Science and Technology Facilities Council

ITRF/LhARA

Conceptual Design Report

UKRI Science and Technology Facilities Council

The LhARA collaboration

H. Ahmed[1], M. Alderton[2], R.A. Amos[3], D.O. Ariyanto[4], C.J. Baker[5], J. Bamber[6], J. Bebbington[7], W. Bertsche[8,9], R. Bingham[2,10], N. Bliss[11], E. Boella[12,9], S. Boogert[8,9], M. Borghesi[13], R. Buckley[7], P.N. Burrows[14,15], G. Casati[16,17], M. Charlton[5], X. Chen[18], J. Clarke[7], B.T. Cox[3], G. Cox[11], T.S. Dascalu[12,9], E. Dolier[2], M. Dosanjh[14,15], N.P. Dover[16,17], C. Dyson[16,17], S. Eriksson[5], A. Fernandez-Rodriguez[19,20], S. Gerlach[21], A. Giaccia[22,23], S. Gibson[24,25], A. Goulden[7], R. Gray[2,9], S. Green[26], T. Greenshaw[27], S. Griffiths[11], D. Gujral[28], H.C. Hall[29], C. Hardiman[30], E.J. Harris[6], C. Hill[11], P.R. Hobson[31], R.P. Hugtenburg[32], A. Isaac[5], M. Johnson[7], W.G. Jones[16,29], P.J. Jurj[16,17], M. King[2], A. Knoll[33], N. Kumar[27,9], T.J. Kuo[16,17,34], A. Kurup[16,17], J.B. Lagrange[34], J. Lascaud[21], A.M. Lombardi[35], K.R. Long[16,17,36], W.G. Luk[37], S. Lyu[18], T.A.M. Masilela[38], P. Matthews[39,40], M. Maxouti[16,17,36], J.M. McGarrigle[16,41], P. McKenna[2,9], R. McLauchlan[30,42], I. McNeish[4], E. Melia[43], K. Middleman[7], Z. Najmudin[16,17], M. Noro[44], S.R. O'Neill[12,9], L. Obst-Huebl[45], U. Oelfke[6], H. Owen[7], C. Palmer[13], F. Parambil[27], K. Parodi[21], J.L. Parsons[43], J. Pasternak[16,17,34], M. Patel[27,9], R. Pattathil[1], M. Pereira[24,25], H. Poptani[27], Y. Prezado[46,20], P. Price[4], T. Price[47], K.M. Prise[48], C. Pugh[7], P. Ratoff[12,9], R. Razak[16,17], F. Romano[49], P. Ruksasakchai[5], M. Sabate-Gilarte[50], Z. Sadur[16], A. Sandhu[51], G. Schettino[52], J. Schreiber[21], W. Shields[24,25], B. Smart[50], R.A. Smith[16], A.M. Snijders[45], D. Spiers[2,9], S. Tantawi[51], J.W.G. Thomason[34], B. Torrance[2], S. Towe[53], T. Underwood[53,3], A. Vick[7], A. Vikhoreva[11], P. Weightman[27], C.P. Welsch[27,9], C. Whyte[2,9], R. Wilson[2], N. Zakhir[16], D.P. van der Werf[5]

UK Research and Innovation

Polaris House

Swindon

SN2 1FL

www.ukri.org

www.lhara.org

1 *Central Laser Facility, STFC Rutherford Appleton Laboratory, Harwell Oxford, Didcot OX11 0QX, UK*
2 *Department of Physics, SUPA, University of Strathclyde, Glasgow G4 0NG, UK*
3 *Dept of Medical Physics and Biomedical Engineering, University College London, WC1E 6BT*
4 *Department of Surgery and Cancer, Imperial College, Hammersmith Hospital London, W12 0NN, UK*
5 *Department of Physics, Faculty of Science and Engineering, Swansea University, Singleton Park, Swansea, SA2 8PP, UK*
6 *Joint Department of Physics, Institute of Cancer Research and Royal Marsden NHS Foundation Trust, Sir Richard Doll Building 28 Oakleaf Avenue, Sutton, London, SM2 5GP*
7 *Accelerator Science and Technology Centre, STFC Daresbury Laboratory, Daresbury, Cheshire, WA4 4AD, UK*
8 *Department of Physics and Astronomy, The University of Manchester, Oxford Rd, Manchester, M13 9PL, UK*
9 *Cockcroft Instituite for Accelerator Science, Keckwick Ln, Daresbury, Warrington WA4 4AD*
10 *Central Laser Facility, STFC Rutherford Appleton Laboratory, Harwell Oxford, Didcot OX11 0QX, UK*
11 *Technology Department, STFC Daresbury Laboratory, Daresbury, Cheshire, WA4 4AD, UK*
12 *Department of Physics, Lancaster University, Bailrigg, Lancaster, LA1 4YW, UK*
13 *School of Mathematics and Physics, Queen's University Belfast, University Road, Belfast, BT7 1NN, Northern Ireland, UK*
14 *Particle Physics, Denys Wilkinson Building, Keble Rd, Oxford, OX1 3RH*
15 *The John Adams Institute for Accelerator Science, University of Oxford, Keble Rd, Oxford, OX1 3RH*
16 *Department of Physics, Imperial College London, Exhibition Road, London, SW7 2AZ, UK*
17 *The John Adams Institute for Accelerator Science, Department of Physics, Imperial College London, Exhibition Road, London SW7 2AZ, UK*
18 *Department of Bioengineering, Imperial College London, Exhibition Road, London, SW7 2AZ, UK*
19 *Institut des Sciences Moléculaires d'Orsay, Rue André Rivière, Bâtiment 520, 91400 Orsay, France*
20 *Institut Curie, Universit PSL, CNRS UMR3347, Inserm U1021, Signalisation Radiobiologie et Cancer, 91400 Orsay, France*
21 *Fakultät für Physik, Lehrstuhl für Medizinische Physik, Ludwig-Maximilians-Universität Münich, Am Coulombwall 1, D-85748 Garching, Germany*
22 *Department of Oncology, University of Oxford, Old Road Campus Research Building, Roosevelt Drive, Oxford, OX3 7DQ, UK*
23 *Department of Radiation Oncology, Stanford University, Stanford, CA 94305, USA*
24 *Department of Physics, Royal Holloway University of London, Egham, Surrey, TW20 0EX, UK*
25 *The John Adams Institute for Accelerator Science, Royal Holloway University of London*
26 *Department of Medical Physics, University Hospital Birmingham Foundation NHS Trust, Edgbaston, Birmingham, B15 2TH, UK*
27 *Department of Physics, University of Liverpool, Liverpool, L69 7ZE, UK*
28 *Imperial College NHS Healthcare Trust, Department of Clinical Oncology, Charing Cross Hospital, London W6 8RF, UK*
29 *CRUK PPI group, Charing Cross Hospital, London, W6 8RF, UK*
30 *Dept. Radiation Physics and Radiobiology, Imperial College Healthcare NHS Trust, London, W2 1NY, UK*
31 *School of Physical and Chemical Sciences, Queen Mary University of London, Mile End Road, London, E1 4NS, UK*
32 *Department of Biomedical Sciences, Faculty of Science and Engineering, Swansea University, Singleton Park, Swansea, SA2 8PP, UK*
33 *Department of Aeronautics, Imperial College London, Exhibition Road, London, SW7 2AZ, UK*
34 *ISIS Neutron and Muon Source, STFC Rutherford Appleton Laboratory, Harwell Oxford, Didcot OX11 0QX, UK*
35 *CERN, CH-1211 Genève 23, Switzerland*
36 *Particle Physics Department, STFC Rutherford Appleton Laboratory, Harwell Oxford, Didcot OX11 0QX, UK*
37 *Department of Computing, Imperial College London, Exhibition Road, London, SW7 2AZ, UK*
38 *Department of Radiation Oncology, University of California San Francisco, San Francisco, CA, 94115, USA*
39 *Rosalind Franklin Institute, Harwell Campus, Didcot, OX11 0QX, UK*
40 *Department of Brain Sciences,Faculty of Medicine, Imperial College London, Exhibition Road, London SW7 2AZ, UK*
41 *Institut Curie, 73 Rue Claude Bernard, 75005, Paris, France*
42 *Department of Physics, Imperial College London, Exhibition Road, London SW7 2AZ, UK*
43 *Department of Cancer and Genomic Sciences, College of Medicine and Health, University of Birmingham, Edgbaston, Birmingham, B15 2TT, UK*
44 *Business Innovation Department, STFC Daresbury Laboratory, Daresbury, Cheshire, WA4 4AD, UK*

45 *Lawrence Berkeley National Laboratory, 1 Cyclotron Road, Berkeley, CA 94720, USA*
46 *University of Santiago de Compostela, Center for Research in Molecular Medicine and Chronic Diseases, 15782, Santiago de Compostela, Spain*
47 *School of Physics and Astronomy, University of Birmingham, Edgbaston, Birmingham, B15 2TT, UK*
48 *Patrick G Johnston Centre for Cancer Research, Queens University Belfast, 97 Lisburn Road, Belfast, BT9 7AE, UK*
49 *INFN Catania, Via Santa Sofia,64 - 95123 Catania - Italy*
50 *Particle Physics Department, STFC Rutherford Appleton Laboratory, Harwell Oxford, Didcot, OX11 0QX, UK*
51 *Arizona State University: Tempe, Arizona, US*
52 *National Physical Laboratory, Hampton Road, Teddington, TW11 0LW, UK*
53 *Leo Cancer Care, Broadview, Windmill Hill, Hailsham, East Sussex, BN27 4RY, UK*

Acknowledgements

The work described here was made possible by a grant from the UK Research and Innovation Infrastructure Fund. Substantial additional support was provided by STFC, CNRS, EPSRC and the institutes that make up the LhARA collaboration. We are grateful for the support of the STFC Project Sponsor, M. Noro, the ITRF Project Board, the ITRF Advisory Committee and its Chair, N. Burnett.

Executive Summary

Motivation

In 2022, the UK Research and Innovation (UKRI) Infrastructure Fund established a two-year Preliminary Activity to develop the conceptual design of the Ion Therapy Research Facility (ITRF) [1]. The ITRF is conceived as a unique, single-site research infrastructure delivering high-dose-rate ions at energies sufficient for the study both *in vitro* and *in vivo* of the fundamental biology that underpins the efficacy of proton and ion beam therapy [2, 3]. The Preliminary Activity was extended for 10 months through a Bridging Award to allow the completion of the approved programme [4].

Cancer is the second most common cause of death globally [5]. Radiation therapy (RT), a cornerstone of cancer treatment, is required in over 50% of cancer patients [6] and is a contributor to ∼40% of cancer cures in England [7], according to England's national cancer registry and oncology treatment datasets [7]. Global utilisation varies due to differences in access [8].

Radiotherapy is most frequently delivered using X-ray photon beams with MeV-scale energies. The energy deposited by X-ray beams rises rapidly as the beam enters the tissue, reaching a maximum at a depth of $\sim 10\,\mathrm{mm}$; it then falls exponentially. The therapeutic dose is proportional to the energy deposited. Modern X-ray-therapy systems maximise the dose delivered to the tumour while minimising dose to healthy tissue by irradiating the patient from a variety of directions with beams of appropriately modulated intensity.

Proton and ion beams offer substantial advantages over X-rays because the dose deposited close to the surface of the tissue is low and remains low until the beam comes to rest when the bulk of the beam energy is deposited in the Bragg peak. Modulating the energy of the proton or ion beam allows the Bragg peak to be localised at the site of the tumour and the therapeutic dose to be conformed to the tumour volume. The dose delivered to healthy tissue in the path of the beam leading up to the Bragg peak is significantly lower than that which an equivalent dose of X-rays would deliver. The sharp fall-off of the energy deposition after the Bragg peak means that almost no damage is done to tissues that lie beyond the Bragg peak.

Proton and ion beam therapy is usually delivered over a period of several weeks in a series of daily sessions. Each session consists of the delivery of a single fraction of $\sim 2\,\mathrm{Gy}$ delivered at a rate of $\leq 5\,\mathrm{Gy/minute}$. The dose in each fraction is usually distributed uniformly over an area of several square centimetres. Exciting evidence of therapeutic benefit has recently been reported when dose is delivered at ultra-high dose-rate, $> 40\,\mathrm{Gy/s}$ ("FLASH" radiotherapy) [9], or provided in multiple mini-beams with diameters of less than 1 mm distributed over a grid with inter-beam spacing of $\sim 3\,\mathrm{mm}$ [10].

To allow systematic and definitive studies to be made of the radiation biology relevant for the development of new treatment regimens and the elucidation of fundamentally new biological mechanisms, the ITRF is required to:

- Be capable of delivering a variety of ion species from proton to carbon, exploiting ultra-high dose rates and novel temporal-, spatial- and spectral-fractionation schemes;

- Have automated, *in-vitro* end stations in which high-resolution, real-time imaging is able to resolve the time-evolution of the biological impact of the beams on the samples; and to

- Have automated *in-vivo* end stations which incorporate real-time imaging of the subject and its tissues, and in which the dose profile is measured shot-by-shot.

ITRF Preliminary Activity

When the ITRF Preliminary Activity was initiated, it was recognised that the laser-hybrid proton/ion source proposed by the international LhARA collaboration could meet the needs of the ITRF [2]. LhARA, the Laser-hybrid Accelerator for Radiobiological Applications [11], exploits a high-power pulsed laser to drive the creation of a large flux of protons or light ions, which are captured and formed into a beam by strong-focusing plasma lenses [12, 13]. The proton/ion beams are then accelerated using a fixed field alternating gradient accelerator (FFA) that preserves the unique flexibility in the time, energy, and spatial structure of the beam afforded by the laser-driven source. The Preliminary Activity was therefore structured to advance the design of LhARA and to tension the laser-hybrid technique with more conventional synchrotron- or linac-based approaches [14].

ITRF/LhARA Conceptual Design Report

This document, the principal deliverable of the Preliminary Activity, presents the conceptual design for LhARA to serve the ITRF. The conceptual design of the accelerator facility is presented in Chapter 2. Comparison of the laser-hybrid solution with the conventional alternatives has allowed the LhARA approach to be confirmed as the baseline design [15]. The conceptual design for the facility is shown in figure 1.

The Preliminary Activity allowed substantial progress to be made on the development of key techniques and prototype systems. In addition to the conceptual design of the accelerator facility, the principal achievements over the Preliminary Activity period are:

- *Implementation of the initial configuration of the PoPLaR, Proof of Principle LhARA Radiobiology, platform on the SCAPA facility at Strathclyde.*
  A permanent-magnet-quadrupole beam line was designed to serve a series of experiments by which to demonstrate capability and establish a track record in the systematic study of radiobiology using laser-driven beams [16]. The delivery of protons with energies in excess of 10 MeV was demonstrated in August 2025 [17]. Bespoke, thin-bottomed, cell dishes were developed and tested at the Birmingham MC40 cyclotron by personnel from the Universities of Birmingham and Oxford [18]. Bespoke diagnostics is also being developed. First biological exposures took place on November 19$^{\text{th}}$ 2025.

- *A detailed specification of the high-power pulsed laser and target system has been developed.*
  Simulation, design and experimental work have been carried out to develop the specification of the laser-driven source for LhARA (see chapter 3). The specification of the LhARA source has been validated through experiments at the University of Strathclyde, Imperial College London, and Queen's University Belfast.

- *The principle of the ion-acoustic dose-profile measurement technique was demonstrated in an exposure on the LION beam line at Ludwig Maximilians Universität, Munich*
  A volume of liquid scintillator was exposed to the laser-driven proton beam on the LION beam line (see chapter 4) [19]. The optical and acoustic signals were detected simultaneously in order to calibrate the acoustic response using the scintillation light. The results are now being prepared for publication, and a follow-up experimental campaign is being discussed.

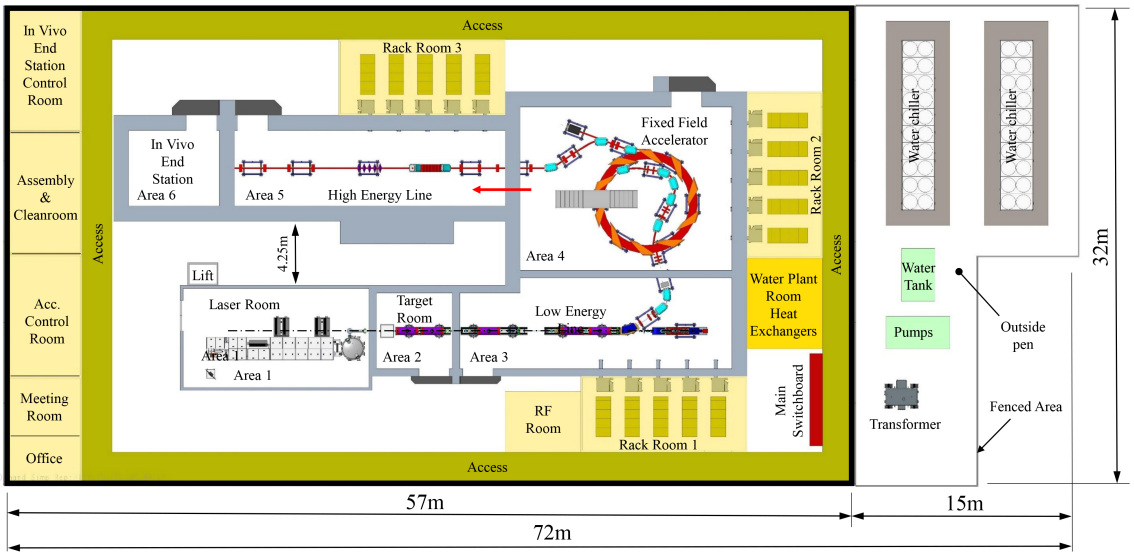

Figure 1: Schematic representation (top view) of the Laser-hybrid Accelerator for Radiobiological Applications (LhARA) integrated within the Ion Therapy Research Facility (ITRF). The figure depicts the accelerator facility, located on the ground floor, which is split into six main areas, each performing distinct functions. In Area 1 (Laser Room), a laser beam is generated and focused onto the proton and ion target located in Area 2 (Target Room). Protons or ions are captured by two electron-plasma lenses before being transported to Area 3 (Low Energy). The beam is then directed to one of two paths: either to the Fixed Field Accelerator (FFA) in Area 4, or to a low-energy *in-vitro* end-station (not shown), situated on the first floor. Beam extracted from the FFA is routed via the High Energy Line (Area 5) to either a high-energy *in-vitro* end-station (not shown, located on the first floor), or to the *in-vivo* End Station (Area 6).

- *The Penning-Malmberg trap on the positron beam line at the University of Swansea has been used to investigate and develop the electron trapping procedure.*
  Trapped-electron densities in excess of $10^{15}\,\mathrm{m}^{-3}$ in small volumes have been obtained and held for periods of 10s of seconds (see chapter 5). The electron density required for the LhARA plasma lenses has therefore been demonstrated. Future experimental and numerical development will focus on extending the volume of the high-density plasma whilst maintaining and extending the excellent plasma stability.

- *An initial specification for the* in-vitro *end stations and the* in-vivo *end station has been drawn up following an international peer-group consultation exercise.*
  The end-station specification is documented in a series of technical notes that define many of the requirements for the end stations and are the basis of future developments (see chapter 6) [15, 20, 21].

The work reported here was carried out by staff at the STFC national laboratories and the collaborating institutes. Much of the simulation and experimental work was carried out by excellent early-career researchers. To date, 4 PhD theses have been defended in the UK on the LhARA programme [19, 22–24] with more in the pipeline. Two theses from Institüt Curie have analysed aspects of the LhARA programme (beam delivery and TOPAS-based evaluation of the beam delivered to the *in-vitro* end station) [25, 26] and a third will be delivered next year. Interest in our programme is growing in France, Spain, the US, and Asia.

The legacy of the UKRI Infrastructure Fund ITRF Preliminary Activity is substantial; not only does this document provide the “blueprint” for the future development of the initiative,

but a new experimental radiobiology programme has been initiated at SCAPA. The technical progress made during the Preliminary Activity has been presented widely at conferences and in seminars at national and international institutes. The collaboration has also been active in making the case for a vibrant programme of R&D aimed at advancing radiotherapy in general and identifying the unique potential of the laser-hybrid approach in this context. Supported enthusiastically by Radiotherapy UK and the Global Coalition for Radiotherapy, the collaboration has engaged with:

- Decision makers, taking part in a number of events organised by Radiotherapy UK in the House of Commons;
- Patient groups, for example presenting the initiative to the Northern Ireland Research Consumer Forum when the collaboration met at Queen's University Belfast [27]; and with the
- Public, presenting LhARA at the 2025 Great Exhibition Road Festival, which was attended by more than 40,000 members of the public, influencers and decision makers. The LhARA presentation at this event was prepared in collaboration with Leo Cancer Care. The collaboration's engagement with the Great Exhibition Road Festival led directly to the opportunity to present the LhARA initiative to President Macron and the French and UK scientific delegations on the occasion of the President's state visit in July 2025.

Over the period of the Preliminary Activity, the collaboration has developed a communication strategy and is now working to communicate its ambitious programme to all its stakeholders.

Taking the LhARA initiative forward

The ITRF Preliminary Activity selected the LhARA technology to serve the facility as it is capable of providing the requisite variety of ion species over the required range of dose rates and temporal-, spatial- and spectral-fractionation schemes [28]. It is proposed that the facility be implemented in two Stages: Stage 1 based on laser-plasma acceleration; and Stage 2 in which the Stage 1 beam line is used as an injector to the FFA. Stage 1 delivers initial capability for *in vitro* research at low energy, followed in Stage 2 by a higher-energy *in vitro* and *in vivo* provision.

The LhARA collaboration now seeks to build on the foundations laid during the ITRF Preliminary Activity to:

- Deliver a systematic and definitive radiation biology programme;
- Prove the feasibility of laser-driven hybrid acceleration; and thereby
- Lay the foundations for the transformation of ion beam therapy.

The efforts of the collaboration will focus on the creation of a self-sustaining, multidisciplinary R&D programme alongside science-delivery and impact-generation programmes that maximise the benefits of the LhARA initiative, with the ultimate goal of building LhARA as an international research facility and developing a clinical particle-beam therapy system with industry.

Contents

List of Figures

List of Tables

CHAPTER 1

Introduction

The LhARA collaboration has been formed to:

Transform proton- and ion-beam cancer therapy by harnessing the unique properties of laser-driven proton and ion beams to deliver a variety of ion species in a single treatment session, exploiting ultra-high dose rates in novel spatial, temporal and spectral fractionation schemes to improve clinical outcomes; and

Make "best in class" treatments available to the many by developing a fully automated system that removes the requirement for a large treatment gantry, thereby reducing footprint and increasing capacity and throughput.

To achieve its goals, the collaboration has defined the LhARA initiative by which to:

- Deliver a systematic and definitive radiation biology programme;
- Prove the feasibility of laser-driven hybrid acceleration; and thereby
- Lay the foundations for the transformation of ion beam therapy.

Central to this initiative is the delivery of the Laser-hybrid Accelerator for Radiobiological Applications (LhARA) to serve the Ion Therapy Research Facility (ITRF). ITRF/LhARA is intended to be a UK-based international facility dedicated to the study of the science of particle beam therapy.

Here we present the Conceptual Design Report for the facility, which will provide:

- *The flexibility to deliver multiple ion species* from proton to carbon over a variety of temporal, spectral, and spatial distributions in a single facility, enabling systematic *in-vitro* and *in-vivo* investigation of the biological response to radiation and allowing direct comparison of different ion species;
- *The advanced automation* required for the study of complex biological endpoints and processes, such as the triggering of the immune system and normal-tissue sparing in FLASH and spatially-fractionated radiation therapy (SFRT);
- *The novel instrumentation* required to study the time evolution of the biochemical processes that determine the therapeutic effect; and
- *The capability to support pre-clinical and biomed-tech R&D*, directly through the experimental programme, and indirectly through the deployment of prototype pre-clinical systems that will enhance the clinical impact of particle beam therapy.

The conceptual design presented here builds on a concept presented in an earlier study [29].

1.1 Background

Cancer affects 1 in 2 people in the developed world, and its prevalence is increasing; CRUK estimates a 30% increase in cases in the UK by 2040. Across the world, cancer is the second most common cause of death, with 17 million new cases diagnosed each year; it is anticipated that this rate will increase to 27.5 million new cases per year by 2040 [30]. RT is used in $\sim$ 50% of all cancer treatments [6] and is instrumental in 40% of cancer cures. The global demand for radiotherapy is projected to rise sharply by 2050, with GLOBOCAN 2022 estimating 33.1 million new cancer cases and 16.5–21.2 million patients needing radiotherapy [31]. Expanding access to radiotherapy by 2050 has the potential to save millions of lives, particularly in low- and middle-income countries. Meeting this projected treatment need requires the development of new radiotherapy modalities that expand efficient and cost-effective treatment options.

Today, radiotherapy is most often provided using X-ray or electron beams. For such beams, the peak dose is deposited close at the surface, after which the dose falls exponentially with depth. This results in a limit on the maximum dose that can be delivered to a deep-seated tumour without delivering an unacceptably large dose to overlying (proximal) healthy tissue. X-rays or electrons that pass through the tumour will also deliver a dose to the tissues that lie behind it. Modern X-ray treatment machines mitigate these effects by delivering the beam from a variety of directions ('fields') to spread the unwanted proximal dose. However, in some cases, this technique still deposits an unwanted dose in sensitive organs close to the tumour. Such unwanted dose can be an issue, for example, in children, where it can produce acute side effects or late effects such as the induction of malignancies later in life [32].

Particle therapy (proton and ion beams) is also used for radiotherapy. Unlike X-rays, which deposit dose continuously as they pass through the body, charged particles gradually lose energy as they travel through tissue. This deceleration produces a pronounced Bragg peak, where the particles release most of their dose at a well-defined depth. That depth (the range of the particle) is determined by the kinetic energy at which the particle enters the patient, allowing for highly targeted dose delivery beyond that which may be achieved with conventional X-rays.

The therapeutic dose can be localised in the tumour by positioning the Bragg peak at the depth of the tumour. Almost no energy is deposited beyond the Bragg peak; therefore, tissues that lie behind the Bragg peak receive almost no dose. This allows a dose to be delivered to the tumour while sparing sensitive organs and substantially reducing the dose to healthy tissue in many treatments [33]. Ions more massive than protons show an enhanced radiobiological effectiveness (RBE) for a given dose [34]. The use of ion beam therapy in combination with emerging immunotherapy techniques has the potential to enhance the effectiveness of radiotherapy [35].

The Particle Therapy Co-Operative Group (PTCOG) lists 146 particle beam therapy facilities worldwide today, of which 17 are capable of delivering carbon ions [36]. Figure 1.1 shows that these facilities are located predominantly in high-income countries; low- and middle-income countries (LMIC) are relatively poorly served. It is estimated that 70% of cancer patients worldwide have limited access to radiotherapy [6] and that 26.9 million life-years could be saved in LMICs if access to RT were improved [37]. This presents both a challenge and an opportunity: developing the necessary techniques and scaling up radiotherapy provision will require significant investment, but experimental platforms such as LhARA can support the investigation of new technologies and approaches that may improve treatment outcomes, enable more effective and potentially more accessible radiotherapy in the future, create new markets, drive economic growth through new skills and technologies, and deliver impact through improvements in health and well-being.

The beams used in particle therapy today provide relatively low dose rates (around 1 Gy/min) with a limited range of temporal and spatial distributions. Recent studies have shown that the efficacy of particle-beam therapy can be substantially improved if the dose is delivered at much higher, ultra-high dose rates ("FLASH" therapy) [38] and/or in multiple spatially distinct beams

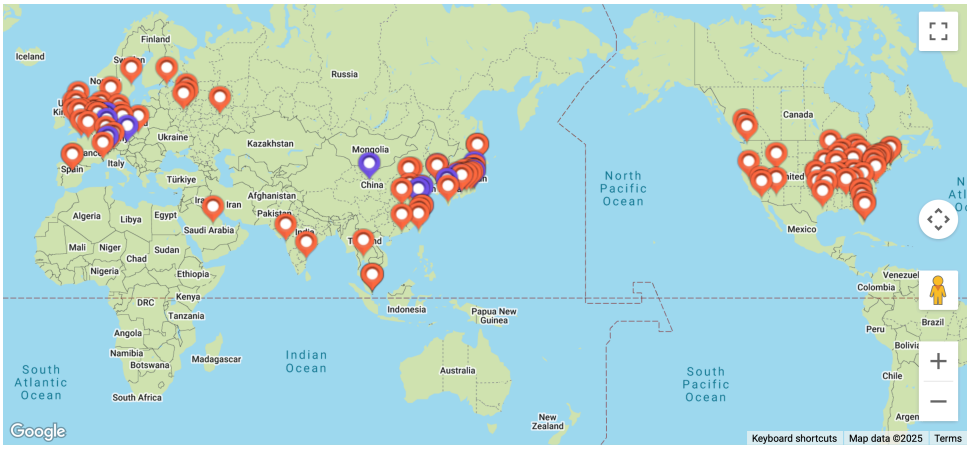

Figure 1.1: Location and number of proton (red) and carbon (blue) ion therapy facilities worldwide. Carbon facilities are available mainly in Germany, Italy and Japan. This figure contains data up to February 2025 and was sourced, with permission, from the PTCOG website [36] in May 2025.

(spatially-fractionated radiotherapy, SFRT) [39]. These results indicate that a new facility incorporating a highly flexible, multiple-ion source is required to enable the fundamental research needed to fully understand the biological effects induced by proton and ion beams and to realise the full potential of particle-beam therapy. This facility will open up key new areas of biological and biomedical research, including the influence of the immune system on the cellular response to radiation, and will allow investigation of the personalisation of particle-beam therapy for the particular patient.

1.2 The case for a systematic study of the radiobiology of proton and ion beams

The nature of the interactions between protons or ions with tissue confers on particle beam therapy (PBT) the advantage that the dose can be precisely controlled and closely conformed to the tumour volume. However, there are significant biological uncertainties in the impact of ionising radiation on living tissue. The flexibility of the LhARA facility allows beams to be delivered in a controlled and varied manner, enabling investigations into these biological effects and supporting the development of new treatment approaches. The efficacy of proton and ion beams is characterised by their relative biological effectiveness (RBE) in comparison to reference photon beams. The treatment-planning software in use today assumes a constant RBE for protons of 1.1 [40]; this means that a somewhat lower proton-delivered dose is needed to produce the same therapeutic effect as would be obtained using X-rays. It is known that RBE depends strongly on many factors, including particle energy, dose, dose rate, the degree of hypoxia, and tissue type [41], but the radiobiology that determines these dependencies is not fully understood. The rapid rise in the rate of energy deposition at the Bragg peak is expected to make the biological effectiveness depend on depth. A number of studies have shown that there can be significant variation in RBE [42–44]. Indeed, RBE values from 1.1 to over 3 have been derived from *in vitro* clonogenic survival assay data following proton irradiation of cultured cell lines derived from different tumours [41, 45, 46]. Some of this variation may be due to the positioning of the cells during irradiation relative to the Bragg peak. RBE values of ~ 3 are accepted for high-LET carbon-ion irradiation, although higher values have been reported [47]; RBE uncertainties for carbon and other ion species are at least as large as they are for protons.

Uncertainties in RBE can lead to incorrect estimation of the dose required to treat a particular tumour. Radiotherapy causes cell death by causing irreparable damage to the cell's DNA. Hence, differences in RBE can also affect the spectrum of DNA damage induced within tumour cells. The larger RBE values, corresponding to higher LET, can cause increases in the frequency and complexity of DNA damage, particularly DNA double-strand breaks (DSB) and complex DNA damage (CDD) where multiple DNA lesions are induced in close proximity [48, 49]. These DNA lesions are a major contributor to radiation-induced cell death as they represent a significant barrier to the cellular DNA repair machinery. Furthermore, the specific nature of the DNA damage induced by ions determines the principal DNA repair pathways employed to effect repair; base excision repair is employed in response to DNA-base damage and single-strand breaks, while non-homologous end-joining and homologous recombination are employed in response to DSBs [48]. Consequently, there is significant uncertainty in the precise radiobiological mechanisms that arise in PBT, and a more detailed and precise understanding is required for optimal patient-treatment strategies to be devised. Detailed systematic studies of the biophysical effects of the interaction of protons and ions, under different physical conditions and with different tissue types, would provide important information on RBE variation and could enable enhanced treatment-planning algorithms to be devised. In addition, studies examining the impact of combination therapies with PBT (e.g. targeting the DNA damage response, but also the tumour microenvironment) are currently sparse, and performing such studies is vital in devising future personalised patient therapy strategies using PBT. Such studies are needed, especially in the case of ion-beam radiotherapy.

1.3 The case for novel beams for radiobiology

In a typical treatment regimen today, the therapeutic dose is provided in a series of daily sessions delivered over a period of several weeks. A session might consist of the delivery of a single fraction of $\sim 2\,\mathrm{Gy}$ delivered at a rate of $\lesssim 5\,\mathrm{Gy/minute}$, the dose in each fraction transversely distributed uniformly over an area conforming to the tumour volume and depth. Passive scattering techniques have given way to active proton scanning, which allows better conformation of the dose to the treatment volume.

Exciting evidence of therapeutic benefit has recently been reported when dose is delivered at high "FLASH" dose rates $\gtrsim 40\,\mathrm{Gy/s}$ [9, 50–52]. Early studies indicated significantly reduced lung fibrosis in mice, reduced skin toxicity in mini-pigs, and reduced side-effects in cats with nasal squamous cell carcinoma. Similarly, therapeutic benefit has been demonstrated in the use of multiple beam segments (with micrometre or submicrometre ($\leq 100\,\mu$m, typically 25-100μm) width beams for MRT or beam widths ranging between 500 and 700μm for MBRT [53]). However, whether the FLASH effect is exhibited above a particular dose-rate threshold and what that threshold might be, if it exists, is still a matter of debate. Further, the radiobiological mechanisms by which therapeutic benefit is generated in FLASH and SFRT are not known and extensive further study both *in vitro* and in appropriate *in vivo* models is required.

LhARA is conceived as a highly flexible facility that is required to elucidate the mechanisms that underlie the biological efficacy of proton and ion beams, and to explore the vast "terra incognita" of the mechanisms by which the biological response to ionising radiation is modulated by the physical characteristics of the beam [54]. Estimates of the doses and dose rates that can be delivered by LhARA were determined using the simulations reported in [29]. These doses and dose rates are presented in table 1.1 and have been adopted as the baseline specification for the LhARA facility presented here.

Table 1.1: Summary of the expected dose per pulse and dose rate that LhARA can deliver, based on Monte Carlo simulations using a bunch length appropriate for the particular energy, particle species and instantaneous dose rate; the average dose rate assumes a 10 Hz repetition rate of the LhARA accelerator source.

	12 MeV Protons	15 MeV Protons	127 MeV Protons	33.4 MeV/u Carbon
Dose per pulse	7.1 Gy	12.2 Gy	9.7 Gy	83.8 Gy
Instantaneous dose rate	0.7×10^9 Gy/s	1.2×10^9 Gy/s	2.3×10^8 Gy/s	1.1×10^9 Gy/s
Average dose rate	71 Gy/s	122 Gy/s	97 Gy/s	838 Gy/s

1.4 Laser-hybrid beams for radiobiology and clinical application

High-power lasers have been proposed as an alternative to conventional proton and carbon-ion facilities for radiotherapy [55–57]. The capability of laser-driven ion beams to generate protons and high-LET carbon ions at FLASH dose rates is a significant step forward for the provision of local tumour control whilst sparing normal tissue. High-power lasers have also been proposed to serve as the basis of electron, proton and ion beams for radiobiology [58–63]. More recent projects (e.g. A-SAIL [64], ELI [65] and SCAPA [66]) also investigated radiobiological effects using laser-driven ion beams and addressed various technological issues [67–71].

The LhARA collaboration's concept is to exploit a laser to drive the creation of a large flux of protons or light ions, which are captured and formed into a beam by strong-focusing plasma lenses. The laser-driven source allows protons and ions to be captured at energies significantly above those that pertain in conventional facilities, thus evading the present space-charge limit on the instantaneous dose rate that can be delivered. Rapid acceleration will be performed using a fixed-field alternating gradient accelerator (FFA), thereby preserving the unique flexibility in the time and spatial structure of the beam afforded by the laser-driven source.

Modern lasers are capable of delivering a joule of energy in pulses that are 10s of femtoseconds in length, at repetition rates of $\gtrsim 10$ Hz. Laser-driven proton and ion sources typically create beams that are highly divergent, have a large energy spread, and an intensity that can vary by up to 40% pulse-to-pulse; the predominant technique is TNSA (target normal sheath acceleration [72]) in which a thin, typically plastic foil is illuminated at a small spot by the incoming laser pulse. Multiple ion species, from proton to carbon, can in principle be produced with a single laser by varying the target foil composition and particle-capture optics.

The LhARA collaboration's vision is that LhARA will prove the principle of the novel technologies required for the development of future therapy facilities. The legacy of the LhARA programme will therefore be: a unique facility dedicated to the development of a deep understanding of the radiobiology of proton and ion beams; and the demonstration in operation of technologies that will allow particle beam therapy to be delivered in completely new regimes.

1.5 LhARA and the Conceptual Design Report

The LhARA facility shown schematically in figure 1.2 has been designed to serve two end stations for *in vitro* radiobiology and one end station for *in vivo* studies. The principal components of Stage 1 of the LhARA accelerator are: the laser-driven proton and ion source; the matching and energy-selection section; beam delivery to the low-energy *in-vitro* end station; and the low-energy abort line, which delivers the beam to a beam dump.

Stage 2 is formed of: the injection line to the fixed-field alternating-gradient accelerator

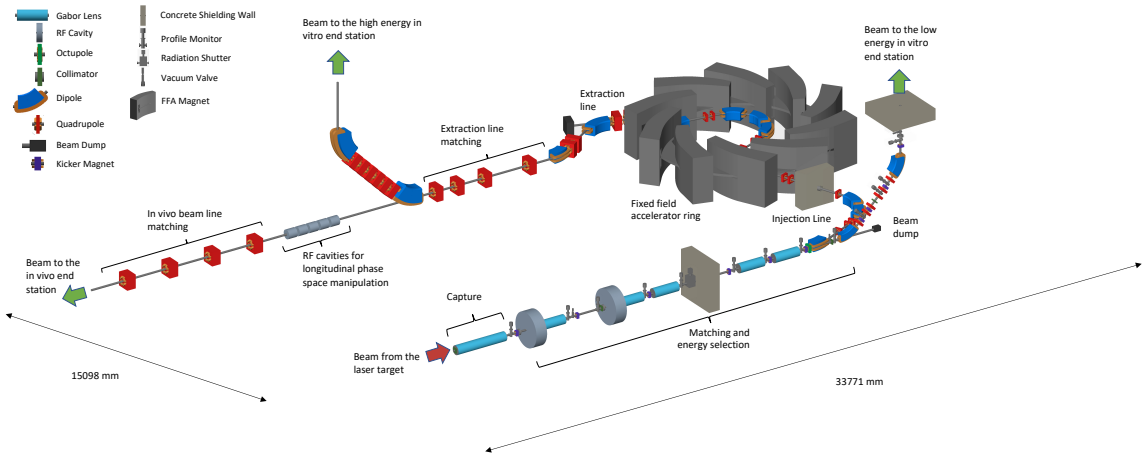

Figure 1.2: A schematic representation of the LhARA accelerator, with all major sections highlighted from the particle source through to LhARA's three radiobiology end stations. All major accelerator components are shown, including the Gabor plasma lenses, FFA magnets, standard dipole and quadrupole magnets, RF cavities, and numerous diagnostic devices.

(FFA); the FFA; the extraction line; the high-energy abort line; beam delivery to the high-energy *in-vitro* end station; and the transfer line to the *in-vivo* end station.

Proton beams with energies of between 10 and 15 MeV will be delivered directly from the Stage 1 laser-driven source to the low-energy *in-vitro* end station via a transfer line. The Stage 2 high-energy *in-vitro* end station and the *in-vivo* end station will be served by proton beams with energy between 15 and 127 MeV and by ion beams, including C^{6+} with energies up to 33.4 MeV/u.

The conceptual design of LhARA and its integration within the ITRF are presented in Chapter 2. The subsequent chapters report on the status of the R&D work at the conclusion of the ITRF Preliminary Activity in June 2025. Chapter 3 focuses on the laser-driven proton and ion source. Chapter 4 describes the programme of measurements of trapped electron plasmas of the type that will form the basis of the Gabor lens. Chapter 5 details the development of the ion-acoustic dose-profile measurement technique. Chapter 6 outlines the considerations relating to the *in-vitro* and *in-vivo* end stations, and provides a summary of the peer-group consultation. The appendices provide additional supporting material: Appendix A summarises the specifications of the alternative synchrotron and linac options, while Appendix B evaluates the facility infrastructure requirements and projected costs.

CHAPTER 2

Facility design

2.1 Overview and key parameters

The LhARA facility, shown schematically in figure 1.2, has been designed to deliver proton beams with energies of between 12 MeV and 15 MeV directly from the laser-driven source to the low-energy *in-vitro* end station via a transfer line. The high-energy *in-vitro* end station and the *in-vivo* end station will be served by proton beams with energy between 15 MeV and 125 MeV and by ion beams (including C^{6+}) with energies up to 33 MeV/u. This configuration makes it natural to propose that LhARA be constructed in two stages: Stage 1 providing a beam to the low-energy *in-vitro* end station; and Stage 2 delivering the full functionality of the facility. The Stage 1 design is mature and includes proposed locations for the plasma (Gabor) lenses, conventional magnets, and auxiliary systems, including RF, diagnostics, and shielding. The concept for Stage 2 is complete and includes the injection line transferring the beam into the fixed-field alternating-gradient accelerator (FFA), the FFA ring, the extraction line, and the transfer lines to the high-energy *in-vitro* and *in-vivo* end stations.‘

The key sections of the LhARA accelerator facility are:

- *Laser-driven proton and ion source*: protons and light ions will be generated using laser-driven acceleration via the target normal sheath acceleration (TNSA) mechanism [73];
- *Proton and ion capture*: Two strong focusing electron-plasma (Gabor) lenses in a single module will capture the divergent flux of particles generated at the target;
- *Matching and energy selection*: Five more Gabor lenses will be used to transport and match the beam into transfer lines that will take it either to the low-energy *in-vitro* end station or to the injection line serving the FFA. Collimators will be used for energy selection;
- *Beam delivery to low energy in-vitro end station*: A 90° vertical bend will transport beam to the low energy *in-vitro* end station;
- *Low-energy abort line*: A transfer line through which the beam may be dumped safely during commissioning, or in fault conditions, leads to a passive beam dump;
- *Injection line for the FFA*: The beam is transported and matched to the injection section of the FFA using a series of dipole and quadrupole magnets;
- *Fixed-field alternating-gradient accelerator*: A 10-cell, single spiral FFA will provide a three-fold increase in beam momentum;
- *Extraction line*: The extraction line from the FFA, composed of dipole and quadrupole magnets, will transport and match the beam into either the high-energy *in-vitro* end station or the *in-vivo* beamline;
- *High-energy abort line*: A transfer line through which the beam may be dumped safely during commissioning, or in fault conditions, leads to a passive beam dump;

- *Beam delivery to high-energy in-vitro end station*: A 90° vertical arc by which beam is delivered to the high-energy *in-vitro* end station; and

- *Transfer line to the in-vivo end station*: The transfer line that delivers beam to the *in-vivo* end station includes a series of quadrupole magnets to match the beam into the end station and RF cavities for longitudinal phase-space manipulation.

The LhARA beam transport systems are required to provide beam to the *in-vitro* and *in-vivo* end stations that are each optimised for radiobiology experiments. This includes beam delivery systems that will provide significant flexibility in the distribution of dose at the end station, including its spatial profile, temporal structure, and energy spectrum. The spot size is defined as the 2σ diameter of the transverse beam profile. A spot size of between 1 and 3 cm is required to achieve uniform irradiation of cell dishes. Magnetically focused minibeams will be provided in both line-focused and spot-focused configurations.

The baseline Stage 1 beamline uses a series of Gabor lenses for beam capture and matching. Gabor lenses offer simultaneous focusing in both transverse planes, much like a solenoid magnet. Whilst Gabor lenses require a solenoid magnet for plasma confinement, the confining field strength is approximately 1/40 of the solenoidal field required to deliver the equivalent focusing strength. Since the strength of the equivalent solenoid often exceeds 1 T, the use of plasma-lens focusing will provide a significant reduction in capital cost and power consumption. The use of conventional (either warm or superconducting) solenoids is retained as an option to mitigate the risk that the Gabor lens development programme later encounters unforeseen complications.

2.2 Accelerator design tools

The accelerator lattices described here were initially designed and optimised in MAD-X [74] and BeamOptics [75]. These codes were used to calculate the nominal beam envelope using conventional transfer-matrix methods to determine the optical functions. Consequently, the results obtained with the two codes agree very well. To assess the detailed beam transport performance, Monte Carlo start-to-end simulations were performed with two particle tracking codes: BDSIM [76] and GPT (General Particle Tracer) [77].

BDSIM is based on the Geant4 [78] toolkit, which makes it possible to track using full electromagnetic field maps and simultaneously to take into account the interaction of particles in material. BDSIM can therefore be used to estimate particle losses and the dose delivered to the end station in a single calculation. For efficiency, conventional BDSIM tracking uses a hybrid scheme in which particles that lie close to a nominal reference trajectory (paraxial particles) are treated using linear transfer matrices. 4^{th} order Runge-Kutta integration using three-dimensional electromagnetic field maps is used to track non-paraxial particles. Field maps were used to track particles through the Gabor lenses using the procedure described in [23]. Field maps were also used in BDSIM for tracking through the octupole magnets that are used to improve the uniformity of the dose delivered to the end stations.

GPT is widely used for the modelling of space-charge forces, which increase the size of the beam, leading to increased beam loss and reduced transmission. Lattices were optimised using `GDFSOLVE`, a GPT utility that uses the multi-dimensional Newton-Raphson method to solve the transport equations when space-charge forces are considered. The space-charge routine used in all GPT simulations here was `spacecharge3Dmesh` using the Poisson solver method `MGCG` with a fixed-sized mesh of $50 \times 50 \times 150$ mesh lines in the orthogonal, x, y, coordinates transverse to the beam and the z coordinate parallel to the beam, respectively. The Gabor lenses were described in GPT using the equivalent solenoid model (see section 2.2.2).

2.2.1 Particle tracking and model differences

Small differences can occasionally be observed when comparing the optical functions obtained from MAD-X, BDSIM, and GPT. MAD-X calculates the evolution of the beam envelope using matrices with no consideration of the actual bunch structure and its matching into the lattice, whereas BDSIM and GPT are Monte Carlo codes that track particles according to a more precise description of the beam line. The calculations of the optical functions in BDSIM and GPT are therefore susceptible to statistical fluctuations that can be caused, for example, by outlier particles either in the spatial or momentum distributions.

The methods used to record particles can also induce artefacts in the optics calculations. MAD-X and BDSIM record the phase space coordinates of particles as they cross planes perpendicular to the beam axis. These planes are often chosen to be at the downstream end of each beamline element. In GPT, however, the phase-space distributions are recorded at points in time. GPT can also record the phase space at a given reference plane; however, this is known occasionally to cause tracking errors that manifest as spurious apparent changes in emittance. Therefore, the spatial recording of phase space was not used in the GPT studies of the LhARA beamline. To make the model comparisons as accurate as possible, the phase space was recorded at the points in time when a nominal 15 MeV proton, travelling along the reference trajectory, would reach the end of each beamline element. This methodology can record the phase space when the end of a bunch (head or tail) is within a magnetic field, whilst the rest of the bunch is in a field-free region; the result is that the phase-space distribution is distorted compared to what would be recorded at a given plane perpendicular to the beam axis.

The distortion of phase space is amplified in GPT when recording the beam at the entrance or exit of a dipole. GPT models require the user to define the coordinate system at the entrance and at the exit of each bending magnet. The beam can be recorded in these coordinate systems, and therefore, no post-simulation transformations of particle coordinates are needed for the calculation of the optical functions. When recording the phase space at these locations, however, only half the bunch (either the head or the tail) is inside the field of the magnet, so the coordinate system in which the head and tail of the bunch are expressed is different. The use of different coordinate systems further distorts the phase-space distributions.

The final major source of difference between the various codes is in the treatment of fringe fields. Both MAD-X and BDSIM calculate the effect of fringe fields in thin elements as an integrated effect applied as a single kick; this is a conventional mathematical technique common to such codes. Fringe fields are only available for dipoles, solenoids, and RF cavities. All electromagnetic elements in MAD-X and BDSIM were therefore considered to have hard-edged fields. GPT constructs the full fringe field that varies with distance from the magnet boundaries.

2.2.2 Simulation of Gabor lenses

A Gabor lens exploits an electron plasma to provide cylindrically-symmetric focusing of a positive ion beam [79]. As the ion beam passes through the electron plasma, it experiences a focusing force directed towards the lens axis that is proportional to the displacement from the centre of the electron plasma at the lens axis. The focusing effect is therefore similar to that provided by a solenoid without introducing the strong coupling of the transverse phase space coordinates that occurs in solenoid focusing.

Detailed theoretical and numerical studies of the focusing effect of the Gabor lens were carried out in earlier work [12, 22, 23]. These studies showed that, for a given focal length, the optical effect of a Gabor lens of uniform electron density, n_e, is well described by a solenoid with field strength given by:

$$B_{\text{sol}} = \sqrt{\frac{2n_e\gamma_0 m_{\text{I}}}{Z\varepsilon_0}}\,; \tag{2.1}$$

where m_I is the ion mass, Z is the ion charge number, ε_0 is the permittivity of free space, and $\gamma_0 = E_{I0}/(m_I c^2)$ where E_{I0} is total energy of the reference particle. This result is important as it allows the initial optimisation of the beamline to be carried out using the solenoid models implemented in MAD-X, BeamOptics, BDSIM and GPT. The first-order transfer matrix for the Gabor lens [23] is used to simulate the Stage 1 beamline both in the LhARAlinearOptics package [80] and in BDSIM, while the full electrostatic field map may also be used in BDSIM.

2.2.3 Coordinate systems

The origin of the LhARA laboratory coordinate system, used to define component positions both for physics calculations and for engineering design, is at the position of the laser focus at the laser-target interaction point [81]. Laboratory coordinates are denoted here using upper-case letters. The Z axis is horizontal and parallel to the nominal capture axis, pointing in the downstream direction from the interaction point. The Y axis points vertically upwards, and the X axis completes a right-handed orthogonal coordinate system. The position of a reference particle originating from the interaction point, as well as its momentum (p_0) and energy (E_0), are described as functions of the distance, s, that the reference particle has travelled from the origin of coordinates.

By convention, particle dynamics in a particle accelerator are described in a local coordinate system defined relative to the position of the reference particle. Local coordinates will be denoted by lower-case letters. The tangent to the reference particle trajectory at s defines the z axis. Therefore, by definition, the reference particle always has $z = 0$. In the laboratory coordinate system, the presence of local electric or magnetic fields may cause the reference particle's trajectory to change. In the neighbourhood of the reference particle, a curved trajectory may be described in terms of an arc of a circle; the local x axis is taken to be in the direction pointing away from the centre of the circle. The third coordinate axis, y, is defined to complete the right-handed orthogonal coordinate system. In local coordinates, the position and direction of a particle in a bunch is expressed in trace space, defined by convention as:

$$\begin{pmatrix} x \\ x' \\ y \\ y' \\ z \\ \delta \end{pmatrix} = \begin{pmatrix} x \\ \frac{\partial x}{\partial s} \\ y \\ \frac{\partial y}{\partial s} \\ \frac{\Delta s}{\beta_0} \\ \frac{\Delta E}{c p_0} \end{pmatrix}; \tag{2.2}$$

where $\beta_0 = p_0 c/E_0$, c is the speed of light, and Δs and ΔE are the difference between the reference-particle and test-particle position and energy, respectively.

In the following, subscripts will be used on the Twiss parameters and other optical quantities to indicate the transverse coordinate x or y to which the parameter applies.

2.3 Stage 1 design and performance

Stage 1 of LhARA will transport the proton and ion beams generated at the laser-driven source to the low-energy *in-vitro* end station. A schematic layout of Stage 1 of LhARA is shown in figure 2.1 and the key parameters of the Stage 1 lattice are presented in table 2.1. The ion flux emerging from the source enters the capture section, which brings the beam from its initial divergent condition to near parallel. The capture section is followed by an energy selection section in which the beam is focused into a collimator. The strength of the cylindrically symmetric, electrostatic focusing provided by the Gabor lens is a function of particle energy. Therefore, by varying the focusing strength, a chosen range of ion energies can be selected.

The matching section brings the beam parallel once more and has the flexibility to produce a range of spot sizes at the end station. The beam shaping section will include an octupole to improve the uniformity of the beam transported to the low-energy *in-vitro* end station, and a switching dipole to send the beam either to the FFA injection line or to the low-energy *in-vitro* end station. If the switching dipole is not powered, the beam is sent to a beam dump. An achromatic vertical arc is used to direct the beam vertically up to the low-energy *in-vitro* end station.

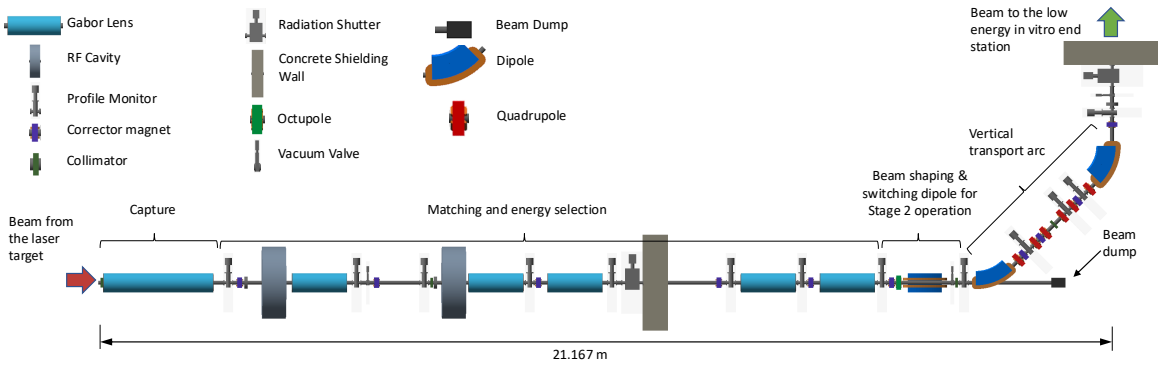

Figure 2.1: Schematic layout of the LhARA Stage 1 beamline. Stage 1 transports the proton and ion beams produced at the laser-driven source to the low-energy *in-vitro* end station. The layout illustrates, in sequence: (1) beam generation at the laser–target interaction point; (2) capture section; (3) matching and energy-selection system; (4) beam-shaping and switching dipole (enabling operation toward Stage 2); (5) vertical transport arc; and (6) delivery of the beam to the low-energy *in-vitro* end station.

2.3.1 Lattice description

The LhARA Stage 1 lattice description starts 100 mm downstream of the target in the direction of the vector normal to the rear surface of the target. The first 50 mm after the target foil is empty. The second 50 mm contains a nozzle with a 2 mm radius opening aperture and an aperture of radius 2.87 mm at its exit. The nozzle is designed to maintain the vacuum gradient between the target chamber and the first Gabor lens, whilst also acting as a collimator for the off-axis ions and other contaminants produced in the laser-target interaction. This allows the first Gabor lens to be positioned to the target, achieving a high capture efficiency.

The capture section immediately follows the vacuum nozzle and consists of two Gabor lenses. Each Gabor lens in LhARA is assumed to contain an 857 mm long electron plasma contained by a cathode voltage of 65 kV. The inner radius of the central electrode is 36.5 mm. The first lens will be operated at the highest possible plasma density to reduce the beam divergence. The second lens will be set to bring the beam parallel with as small a transverse momentum as possible. The physical Gabor lens is assumed to require a space of 150 mm beyond the plasma at each end to accommodate vacuum components and injectors for the electron plasma. The full physical length of a Gabor lens module is therefore considered to be 1157 mm.

The close proximity of the first lens to the target chamber introduces engineering challenges for electron injection, especially if the first and second lenses are constructed as separate components. The first two lenses will therefore be implemented as two separate plasma regions within the same module. The two plasmas will be populated using a single injector, located at the downstream end of the second lens.

A 1645 mm long straight section after the module containing the first two Gabor lenses will contain a profile monitor, a corrector magnet, a wall current monitor, and a 500 mm long

space for an RF cavity that permits control of the bunch length and manipulation of the longitudinal phase space. The parallel beam allows the length of this section to be modified without impacting the machine optics. A third Gabor lens then focuses the beam into an energy-selection collimator at a distance 1771 mm downstream of the lens. Between the lens and the collimator, space is reserved for two profile monitors, a vacuum valve, and a corrector magnet. After the collimator, a second RF cavity will allow further longitudinal phase space manipulation. A pair of Gabor lenses separated by 500 mm then focus the beam once more. The location of the focal plane depends on the optics configuration required to produce the desired spot size at the end station. The space between these two lenses accommodates a further profile monitor and corrector magnet. A 2900 mm long drift section after the fifth Gabor lens allows a 500 mm thick concrete wall to be installed along with a 460 mm long radiation shutter. This arrangement is designed to enable the staged construction of the capture and energy-selection sections whilst the remainder of Stage 1 is being installed. Profile monitors will be positioned on each side of the shielding wall, with a corrector magnet installed downstream of the wall. The remaining space is reserved for the installation of a Wien filter for velocity selection, should the Gabor lenses be replaced by solenoids. A second pair of Gabor lenses, again separated by 500 mm, then brings the beam parallel once more. A profile monitor and corrector magnet will be placed between these lenses. The second parallel beam region allows flexibility in the installation of a shielding wall and other equipment between the final lens and the vertical arc. A profile monitor and corrector magnet will be placed after the final lens.

Radiobiological studies require a variety of dose distributions, ranging from a uniform dose profile across a disc of radius $\sim$ 20 mm to spatially fractionated dose distributions in which the dose is limited to lines or pixels of width $\leq$ 1 mm, the dose falling to zero in the valleys between regions of peak dose. To facilitate the delivery of uniform dose distributions, the beam passes through an octupole magnet before it enters the vertical arc. A magnetic approach to flattening the dose distribution is appropriate for the low-energy beamline at LhARA because the traditional passive scattering technique would be challenging given the low energy of the beam and the potential shot-to-shot variations in flux. In addition, the flexibility to deliver a variety of ion species would require a system capable of switching scattering material depending on the particle species being delivered.

The use of octupole magnets for uniform dose generation exploits third-order focusing to provide a perturbation to the first-order focusing provided by the linear elements upstream. The method has been demonstrated in a number of facilities [82–84]. Non-linear magnets would typically be located where the beam profile is large in one transverse axis and small in the other to reduce aberrations and transverse coupling. The optimal number and location of these magnets, as well as the suitability of using combined function magnets, are still under active investigation.

A space approximately 1 m long is reserved after the octupole for the installation of a switching magnet to direct the beam into the transfer line to the FFA. A vacuum valve is located after the switching dipole drift space. A collimator may be installed after the vacuum valve to remove off-axis particles that received a large kick from the octupole field.

The vertical arc is an achromatic matching section, i.e. it has closed vertical dispersion. Transparent optics are employed, such that the phase advances in both transverse planes are a multiple of π, ensuring that the first-order transfer map through the arc is the identity transformation. The arc consists of two identical, 800 mm-long dipoles and six 100 mm-long quadrupoles. The dipole field required for a 15 MeV proton to bend through $\pi/4$ rad is ≈ 0.55 T. The first of the arc magnets will be a switching dipole which, when powered off, will allow the beam to pass into the Stage 1 abort line. The arc quadrupoles form two identical triplets, with a maximum field gradient of 18 T /m. The field strength at the pole tip for a quadrupole aperture of radius 36.5 mm is ≈ 0.66 T. A momentum-cleaning collimator is located at the centre of the arc, where the vertical Twiss β function is small and vertical dispersion is large. Potential

locations for profile monitors and corrector magnets in the arc have been identified. Further efforts will determine whether additional space for diagnostics is required.

After the arc, a drift space of 2 m is reserved for the installation of elements that will deliver the beam to the *in-vitro* end station at bench height. A corrector magnet, profile monitor, vacuum valve, and wall-current monitor are planned in this space. A 0.5 m-thick concrete wall is included in this space, acting as both shielding and the floor of the end station. A radiation shutter will be installed before the wall. To improve flexibility in the spot sizes that may be delivered to the end station, schemes for producing mini-beams via magnetic focusing are being investigated; this has proven to be challenging given the limited space. Therefore, the possibility of modifying the optics of the arc as part of a mini-beam scheme is being considered. Combined-function magnets incorporating non-linear field components are also being investigated to aid the generation of uniform beams.

2.3.2 Optics and tracking performance

To assess the performance of the design, Stage 1 has been simulated with the codes outlined in section 2.2. The LhARAlinearOptics [80] code was used to generate a beam distribution at the source. Protons with a kinetic energy of 15 ± 0.3 MeV (i.e. a 2% window around 15 MeV) were selected and used for the design and optimisation of the Stage 1 lattice. MAD-X [74] was used to find optical configurations which deliver beams to the end station. GPT [77] was then used to assess the impact of space charge. Finally, BDSIM was used to validate the beam uniformity that can be achieved using the octupole and to estimate the dose delivered to the end station.

2.3.2.1 Particle distributions at the source

The energy and angular distributions of the beam that enters the Stage 1 beamline are considerably different from typical beams in modern particle accelerators, in that the beam originates from a very small spot size at the target, with a significant divergence. The present assumed source distribution, presented in [80], is superior to that used in previous LhARA design iterations in that it does not suffer from unphysical artefacts that were present in previous iterations. Considerable experimental and simulation effort has been expended to model the particle distributions generated via the TNSA mechanism.

Energy spectrum
The typical kinetic energy spectrum produced in target-normal sheath acceleration (TNSA) falls exponentially with kinetic energy before dropping rapidly to zero at a maximum cut-off energy, K_{max}. The kinetic-energy spectrum of the TNSA model presented in [85] is given by:

$$\frac{dN}{dK} = \frac{\mathcal{N}}{\sqrt{2KT_e}} \exp\left(-\sqrt{\frac{2K}{T_e}}\right) ; \tag{2.3}$$

where N is the number of protons or ions produced per unit solid angle, K is the ion kinetic energy, T_e is the hot electron temperature, and $\mathcal{N}$ is a normalisation constant that depends on the laser-pulse duration, t_{laser}.

Equation 2.3 is based on time-limited fluid-dynamical models, which are unable to predict the cut-off kinetic energy accurately. The cut-off energy is taken to be that given by the model described in [86], in which the time over which the laser pulse creates the conditions necessary for acceleration is derived. The kinetic energy cut-off is given by:

$$K_{max} = X^2 K_{i,\infty} ; \tag{2.4}$$

where X is obtained by solving:

$$\frac{t_{\text{laser}}}{t_0} = X\left(1 + \frac{1}{2}\frac{1}{1-X^2}\right) + \frac{1}{4}\ln\left(\frac{1+X}{1-X}\right); \tag{2.5}$$

Here, t_0 is the time over which the ion acceleration may be treated as ballistic and $K_{i,\infty}$ is the maximum possible kinetic energy that could be imparted by the electric field strength of the laser.

Angular distribution
The angular distribution of the flux of protons and ions produced by the TNSA mechanism has been observed to be a cone centred on the normal to the foil surface [87]. This cone has an opening angle 2α which varies as a function of energy, where the envelope angle, α, is defined such that all particles are contained within $\pm\alpha(E)$ of the z axis for a given energy. The opening angle has been observed to decrease as the ion energy increases.

The distribution of the polar angle, θ_S, at which particles are produced at the laser-driven source is generated by defining r' such that:

$$r' = \frac{\partial r}{\partial s}; \tag{2.6}$$

where $r = \sin\theta_S$. x' and y' are sampled independently from the probability density function:

$$g(r') = \frac{3}{4r'^2_m}\left(r'^2_m - r'^2\right); \tag{2.7}$$

where $r'_m = \sin\alpha$. At low kinetic energy ($E \sim E_{min}$), $\alpha(E)$ is taken to be $\sim 20°$. $\alpha(E)$ is assumed to decrease linearly with energy such that:

$$\alpha(E) = 20° - 15°\frac{E}{E_{max}}; \tag{2.8}$$

i.e. $\alpha(E)$ decreases from 20° at $E = 0$ to 5° at E_{max}. Finally, the azimuthal angle, ϕ_S, is chosen from a uniform distribution over the range $0 < \phi_S < 2\pi$.

Transverse spatial distribution
The x and y distributions that are produced are assumed to be independent and to have inverted parabolic distributions with a maximum spread given by the radius of the laser spot that is focused onto the TNSA target.

2.3.2.2 Start-to-end tracking

Nozzle region
The small laser spot size is anticipated to produce a small emitted ion spot size at the exit surface of the target. Such a high density of positively charged ions would usually experience strong space-charge forces. However, it is known that this region also contains large numbers of electrons that are generated by, and are fundamental to, the TNSA mechanism. The electron and ion distributions are expected to co-propagate over an appreciable distance, resulting in overall charge neutralisation and diminished space-charge forces within the beam. The kinetic energy spectrum of the electrons, however, is less well understood than that of the ions, so that the understanding of the dynamics of the beam shortly after the target is limited. It has therefore been assumed that the electrons and ions co-propagate such that the space-charge forces are neutralised over the first 50 mm from the target. At this point, the ions enter the nozzle that separates the target-chamber vacuum from the Gabor-lens vacuum. It is assumed

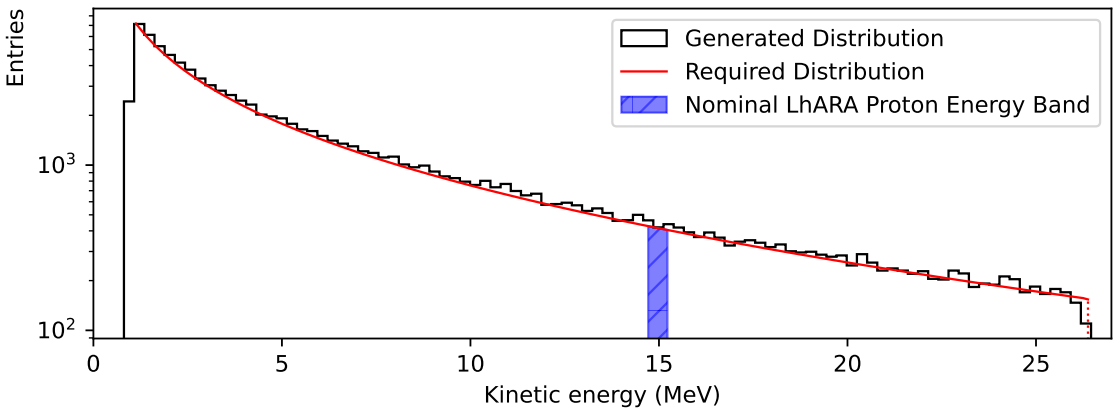

Figure 2.2: Sample generated kinetic energy spectrum of the parameterised beam as a histogram, compared to the required distribution from equation 2.3, shown as a solid red line. LhARA's nominal proton energy band of 15 MeV ±2% is shown in blue.

that the electrons are separated from the ions at the entrance to the nozzle, and space-charge forces must thereafter be considered.

The Stage 1 beamline is required to transport protons with a central energy of 15 MeV. Therefore, particles in a band of 15 ± 0.3 MeV (i.e. 15 MeV ±2%) were selected from the generated TNSA kinetic-energy spectrum. One million simulated protons were generated and tracked using GPT as macroparticles for 50 mm without space-charge forces. A 2 mm radial cut was then applied to represent the aperture of the entrance to the nozzle. Particles passing into the nozzle were tracked for another 50 mm, taking space-charge forces into account; a total bunch charge of 10^9 protons was assumed. A 2.87 mm radial cut was then applied, corresponding to the aperture of the nozzle exit.

The predicted beam distributions and phase space at the exit of the nozzle are shown in figure 2.3. The collimation provided by the nozzle plays a significant role in determining the transverse phase space, since the solid angle subtended by the nozzle is small. The transmitted beam profile exhibits a high degree of uniformity; the flat kinetic energy and temporal distributions are highly correlated as anticipated. The temporal profile of the ion distribution at the target exit is expected to be comparable to the duration of the laser pulse. This is small compared to the time taken for ions to traverse the nozzle; therefore, any temporal structure generated at the target is expected to be lost, given the comparatively broad kinetic energy spread. Similarly, the small transverse spot size, coupled with the broad distribution of transverse momenta, will result in any spatial structure produced at the target being lost.

The final predicted beam dimensions and optical functions are listed in table 2.2. The predicted transmissions at the nozzle entrance and exit are listed in table 2.3. The transmitted beam sample, composed of 41375 protons, is converted to BDSIM and GPT coordinates and used in all subsequent simulations.

Impact of nozzle on beam phase space

The parameterised source simulation described above predicts that the angular divergence of the 2% kinetic energy slice around 15 MeV is approximately a factor of 4 larger than the angular divergence used in earlier simulations [12, 13]. The beam parameters at the exit from the nozzle calculated using the source distributions presented in [12, 13] are summarised in table 2.4. Comparing the values of the beam parameters obtained with the two source simulations, presented in tables 2.2 and 2.4, indicates that the beam parameters entering the Stage 1 beamline are determined by the nozzle, giving confidence in the source term used to optimise the beamlines.

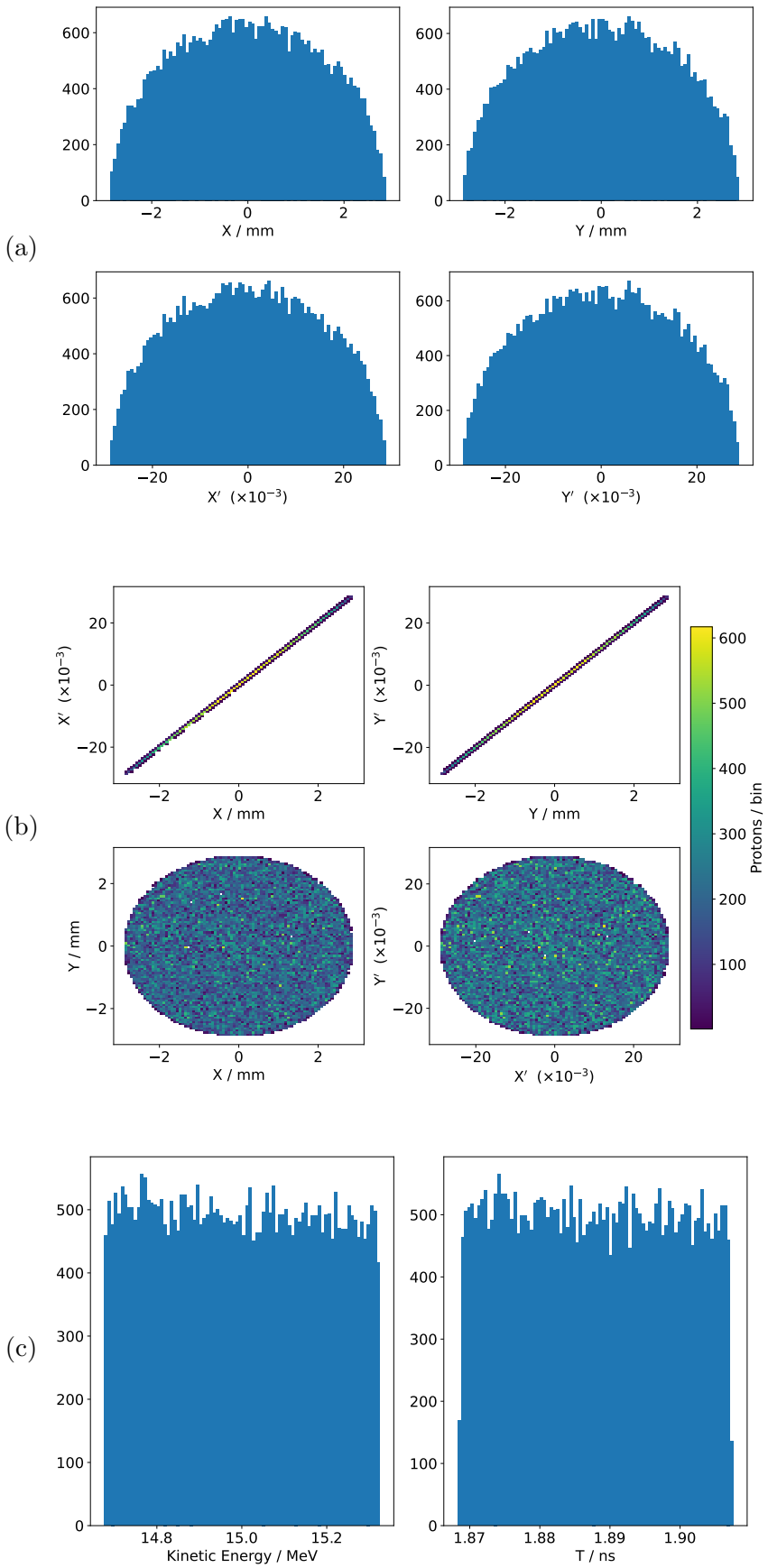

Figure 2.3: Beam phase-space distributions at the nozzle exit, located 100 mm downstream of the laser target. Subfigures (a) and (b) show the transverse phase space; X' and Y' represent the slopes relative to the Z axis. Subfigure (c) shows the longitudinal distribution in kinetic energy and time (T).

At 15 MeV, the RMS angular divergence of the protons emitted from the source is expected to be $\sim 2.75°$. The transmission through the nozzle of protons emitted within the energy range 15 ± 0.3 MeV is presented in table 2.5. The maximum charge collected per pulse is therefore determined by collimation at the nozzle. In order to increase the transmission, and thereby increase the maximum dose per pulse that can be delivered to the end stations, schemes will be explored in which focusing elements are used, such as permanent-magnet quadrupoles placed within the target vacuum space.

Stage 1 nominal design performance

The constraints under which the Stage 1 lattice was derived are:

- Twiss α_x and α_y are zero between the second and third Gabor lenses to give a parallel beam;
- Twiss α_x and α_y are zero at the collimator location after the third Gabor lens to ensure the correct focal length for efficient collimation;
- Twiss α_x and α_y at the end of the seventh lens planes are again zero, and the Twiss β is constrained to yield the $1\,\sigma$ beam radius for the desired spot size, given the emittance values listed in table 2.2; and
- The field strength of the equivalent solenoids for all Gabor lenses was limited to a maximum of 1.4 T.

The last condition was imposed to ensure that the lattice could be implemented using solenoids, should the risk that the Gabor lenses can not be delivered on the required timescale be realised.

Figure 2.4 shows the Twiss β_x and β_y and the dispersion, D_y, for the configuration that delivers a beam with a diameter of 30 mm at the Stage 1 end station. The beam behaves identically in both transverse planes until the start of the vertical arc. The Twiss β_y has a minimum at the location of the arc's momentum-cleaning collimator, whilst the D_y is large. β_x is comparatively large, indicating that a wide aperture in x is required. Collimator settings and cleaning efficiency will be studied in future work.

Solutions for the beam transport optics are shown in figure 2.5. The 1σ beam size in x and y (σ_x and σ_y) along the Stage 1 beam transport line from nozzle exit to Stage 1 end station are shown for five separate spot size configurations ranging from 10 to 30 mm. The beam size is calculated by evaluating:

$$\sigma_{x,y}^2 = \beta_{x,y}\epsilon_{x,y} + D_{x,y}^2\sigma_p^2\,; \tag{2.9}$$

where the β_i are the Twiss beta functions, the ϵ_i are the 2D transverse emittances, the D_i are the dispersions in x and y, and σ_E is the standard deviation of the relative proton-momentum distribution. All subsequent figures that display a MAD-X beam size are calculated using this equation. The beam in figure 2.5 remains symmetric until the vertical arc. The arc transports all spot sizes identically, with a near-identical minimum in σ_y at the location of the momentum cleaning collimator. Solutions for significantly smaller spot sizes could not be found in MAD-X using the current field constraints. Significant modifications to the lattice are likely to be required to achieve this. The use of additional magnets to produce mini-beams after the vertical arc in a "beam-delivery section" is being investigated.

The electron densities that must be confined within each of the first three Gabor lenses, constructed with carbon gas to enable formation of the electron plasma, to produce the desired focusing effect, are listed in table 2.6. The magnetic field strength of the equivalent solenoids is also given. The first three lenses are designed to focus the beam into the energy-selection collimator. Therefore, the strength of these lenses is the same for each of the various configurations described above. The electron densities required in Gabor lenses 4 to 7 to produce beams with

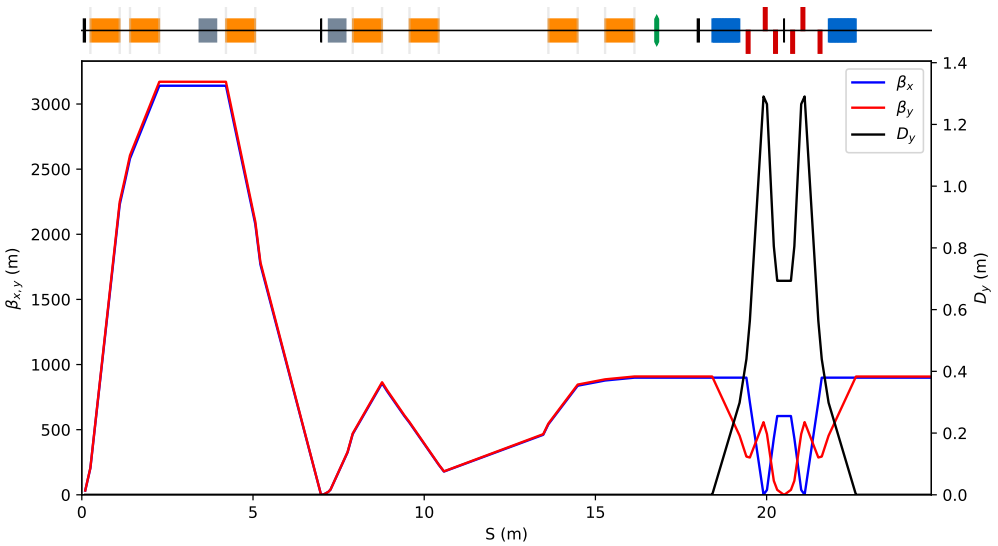

Figure 2.4: Horizontal (β_x, blue) and vertical (β_y, red) Twiss β functions and vertical dispersion (black) along the Stage 1 beam transport line (s) from the nozzle exit to the *in-vitro* end station for the 30 mm spot size configurations. The survey at the top of the plots shows the locations of the Gabor lenses/solenoids (orange), RF cavities (grey), collimators (black), octupole (green), dipoles (blue), and quadrupoles (red).

five different spot sizes at the Stage 1 end station are listed in table 2.7 along with the magnetic field strength of the equivalent solenoids.

In the vertical matching arc, both dipoles have a length of 0.8 m and a deflection angle of 45°. All quadrupoles are 10 cm long, their field gradients are shown in table 2.8.

Model Validation

Figure 2.6 shows the evolution of the beam size in x and y is evaluated using the MAD-X, BDSIM, and GPT models. Space charge was not modelled in the GPT simulation. Differences are observed that originate in small differences in model construction and tracking procedures described in section 2.2.1. The field strengths of the equivalent solenoids used to describe lenses 4–7 in the GPT simulation were adjusted by $< 1\%$ to achieve the agreement shown in the figure. It is likely that differences in the algorithms used to transport particles through the solenoids and their fringe fields is partially responsible for the differences observed. The large jumps in σ_y in the GPT simulation around the arc dipoles are due to the recording of the beam being partially in the dipole field at those locations, meaning that the local coordinate system is not the same as in the other models. The remaining small differences can be attributed to the partial capture of the bunch within the quadrupole magnets. The agreement of the beam dimensions after the arc indicates that, overall, the various models agree well.

The emittance of a particle beam is usually considered to be conserved in accordance with Liouville's theorem. However, emittance is not conserved in the presence of non-linear terms in the equations of motion or when the effect of collisions and dissipative forces, such as space charge, is taken into account. Space-charge effects have not been included; however, when tracking in the equivalent solenoid model, the presence of solenoid fringe fields can introduce a non-linear component to the equations of motion. If the beam entering a solenoid is large and strongly divergent, then its emittance will increase due to the coupling of the phase space coordinates [88]. This condition is met in LhARA in the first solenoid downstream of the source.

To evaluate the impact of emittance growth due to solenoid fringe fields and the coupling of the beam phase space in the two transverse planes, table 2.9 presents the emittance at the

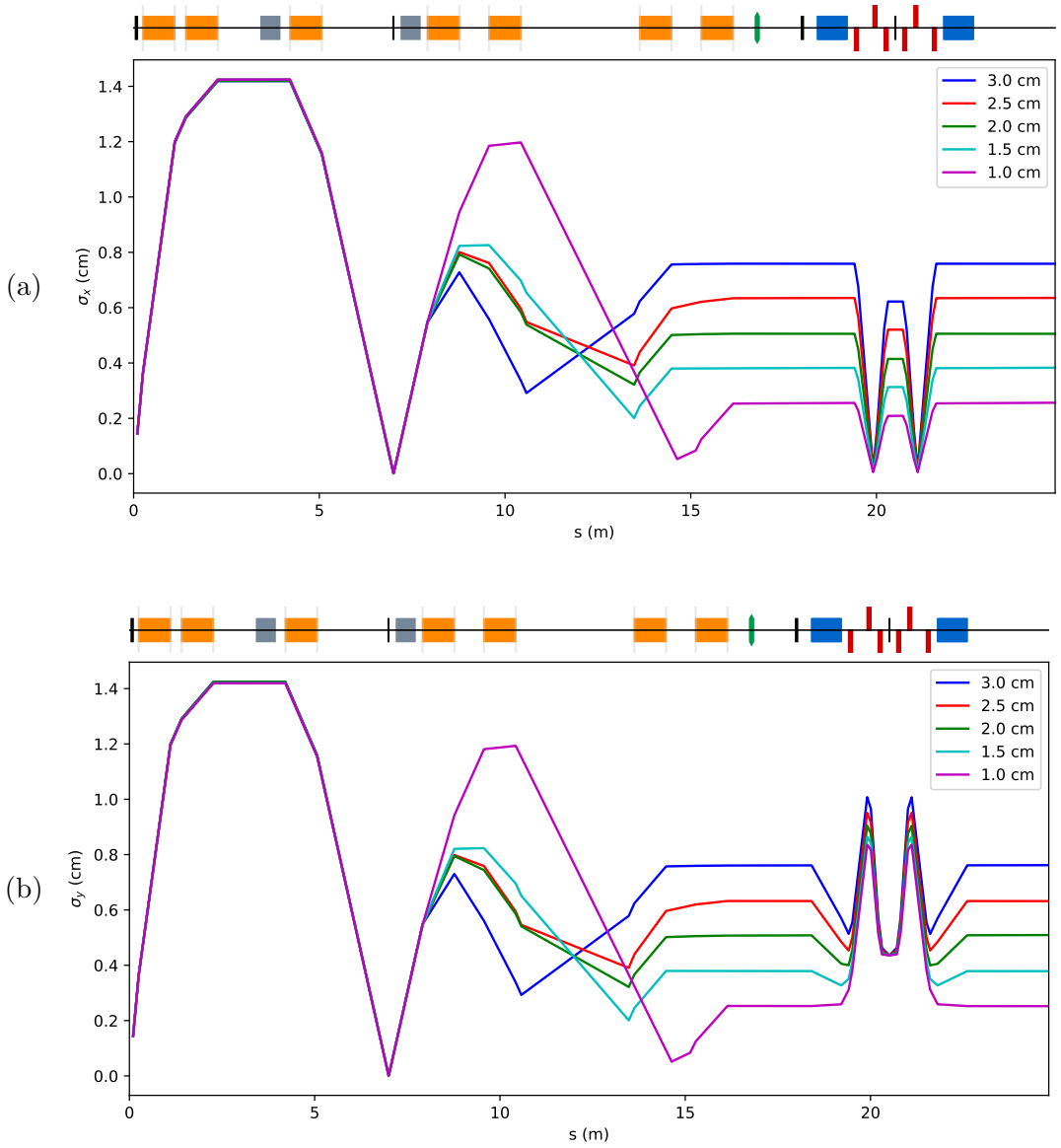

Figure 2.5: Horizontal (σ_x, a) and vertical (σ_y, b) beam size along the Stage 1 beam transport line from the nozzle exit to the *in-vitro* end station. The beam sizes are plotted as a function of beamline length (s) for 5 spot size configurations from 10–30mm. The survey at the top of the plots shows the locations of the Gabor lenses/solenoids (orange), RF cavities (grey), collimators (black), octupole (green), dipoles (blue), and quadrupoles (red).

entrance to the switching dipole evaluated with MAX, BDSIM and GPT. Both BDSIM and GPT integrate the equations of motion using magnetic field maps; the emittance evaluated using these codes is observed to be in close agreement. MAD-X, which propagates the beam using first-order transfer matrices, assumes a constant emittance, and it will therefore remain significantly smaller. The full emittance evolution along the beamline is not shown here as the GPT methodology distorts the optics at the boundaries of elements with external fields. The mean transverse emittance has increased in the BDSIM and GPT simulations by nearly two orders of magnitude compared to that at the nozzle exit (table 2.2).

In the baseline configuration for LhARA, beam transport in the Stage 1 beamline before the vertical arc will exploit the electrostatic focusing provided by the Gabor lenses. The radial

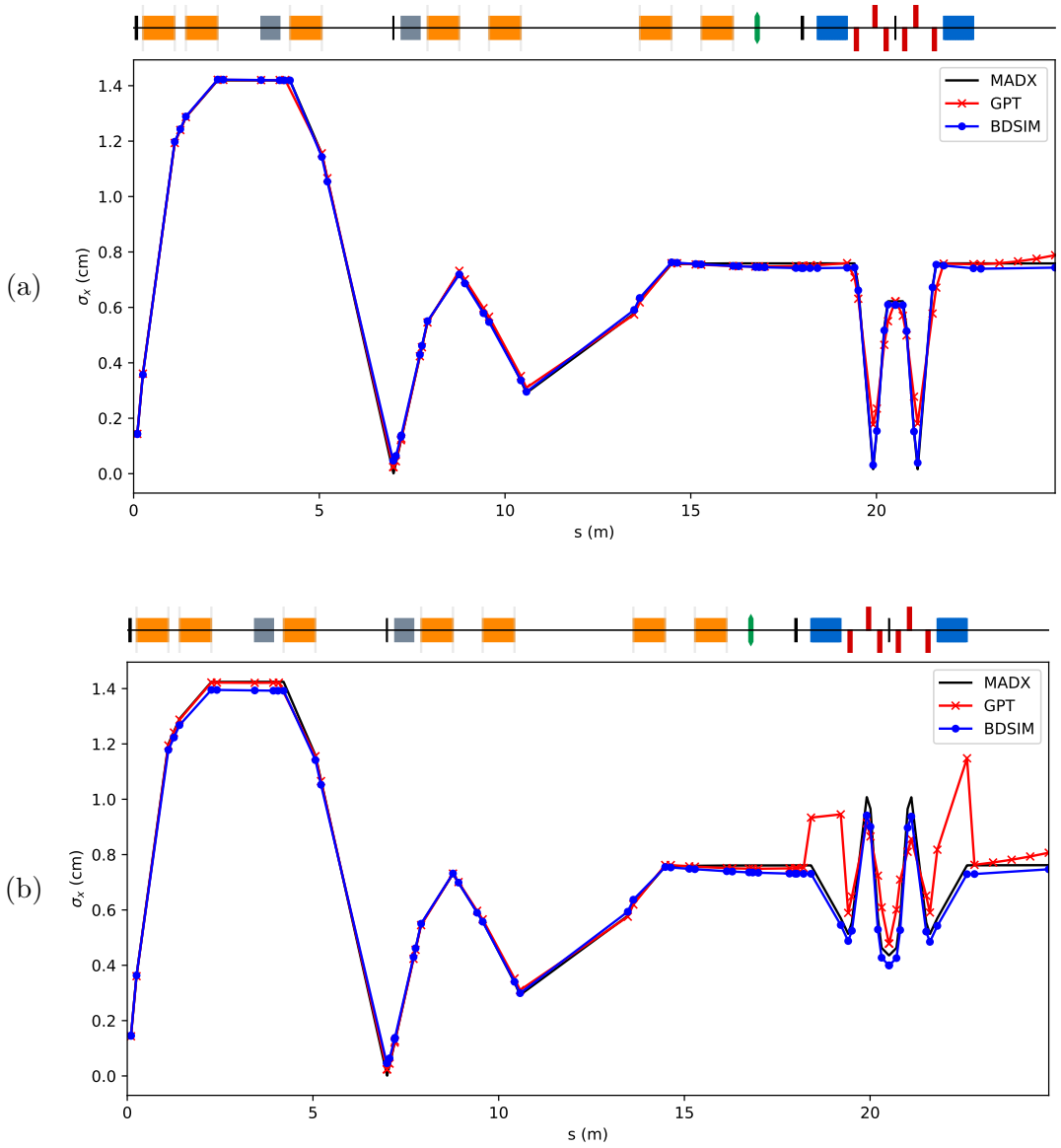

Figure 2.6: Horizontal (σ_x, a) and vertical (σ_y, b) beam size along the Stage 1 beam transport line (s) from the nozzle exit to the *in-vitro* end station. The beam sizes are plotted as a function of beamline length (S) for three simulation models: MAD-X (black), BDSIM (blue), and GPT (red). The survey above the plots show the locations of the model's solenoids (orange), RF cavities (grey), collimators (black), octupole (green), dipoles (blue), and quadrupoles (red).

focusing field produced by the confined electron plasma will be linear, assuming an axially uniform plasma density. The fields in the entrance and exit regions, however, are not yet known as the anode geometry that dictates the confining electric field has not been specified. It is therefore not possible at present to evaluate the degree of emittance growth that will occur in the baseline Stage 1 lattice. Should it be necessary to use the fallback solenoid-focusing lattice, the results presented above indicate that the fringe fields and transverse phase-space coupling will result in significant emittance growth.

The phase space distributions at the Stage 1 end station are shown in figure 2.7 for the nominal optical configuration delivering a 30 mm diameter beam. The spatial distribution is circular and symmetric, with the transverse profiles being approximately parabolic. The sharp

peak in the transverse momentum distribution is characteristic of a parallel beam, with outliers being limited to small angles with respect to the reference axis. The bow-tie-shaped transverse phase-space is believed to be a result of the transverse coupling from the solenoidal field and will be investigated further; however, this distribution is not believed to be detrimental to the exploitation of the beam at the end station. The temporal distribution has naturally broadened due to the energy spread; however, it remains uniform over the pulse duration. The energy spread itself is unchanged.

Impact of space charge

The impact of space charge was evaluated using GPT. Figure 2.8 shows that the evolution of σ_x and σ_y along the Stage 1 lattice is broadly similar when evaluated with and without space-charge forces. The impact of space charge is most noticeable at the nozzle exit as the beam propagates towards the field region of the first Gabor lens. The effect is to increase the emittance such that the beam is divergent as it exits the second Gabor lens. This impacts the downstream optics, with the beam being divergent as it enters the arc, which subsequently does not deliver a parallel beam to the end station. The focus of the third Gabor lens is also no longer at the location of the collimator.

To mitigate the effect of space charge, the GPT model was optimised with `GDFSOLVE`. The strength of the first three solenoids was adjusted to deliver a parallel beam between lenses 2 and 3 and to focus the beam into the collimator. The field strengths were constrained not to exceed 1.4 T. Figure 2.9 shows the evolution of the beam with the re-optimised field strengths. The revised GPT model matches the nominal MAD-X model well. A small discrepancy is observed around the focus after lens 3. This is due to the space-charge forces increasing as the beam is brought to a focus and resulting in a larger focal spot than is possible in the absence of space charge. The close agreement of the re-optimised GPT and nominal MAD-X models after the focus at the collimator shows that the beam can successfully be captured and transported in the presence of space-charge forces. The optimised strengths of the lenses are listed in table 2.10, only small differences from the nominal parameters presented in table 2.6 are observed.

The strengths of the final four equivalent solenoids have also been optimised to mitigate space charge when delivering a variety of spot sizes. The models were configured to deliver the desired spot size in a parallel beam before the start of the vertical arc. The optimised field strengths are then used in the full Stage 1 model with space charge to track from the nozzle to the end station. Figure 2.10 shows the optics for the evolution of the beam size when the lattice is set to deliver spot sizes of 30 mm and 25 mm. While the beam-size requirements are met at the start of the vertical arc, the beam is divergent when it emerges from the vertical arc. This behaviour intensifies with decreasing beam size and is present in the solutions obtained for the 20 mm and 15 mm configurations (not shown here). Solutions could not be found for the 10 mm configuration. The investigation of the origin of this effect and its mitigation continues. It is anticipated that solutions can be found that provide close-to-parallel beams in the final drift.

The phase space distributions at the Stage 1 end station are shown in figure 2.11 for the 30 mm spot-size configuration after optimisation to mitigate space-charge effects. The transverse distributions are in good agreement with those of the nominal design presented in figure 2.7. The energy spread has grown slightly beyond the 2% design target due to space-charge forces. The momentum cleaning collimator, which has not been modelled here, is expected to reduce the kinetic energy spread. Solutions have also been found for the 25, 20, and 15 mm spot size configurations. Optimising the 10 mm beam remains challenging owing to the higher charge density. However, we are confident that solutions will be found and, therefore, that space-charge forces will not significantly impact LhARA's beam-transport performance.

Stage 2 operation

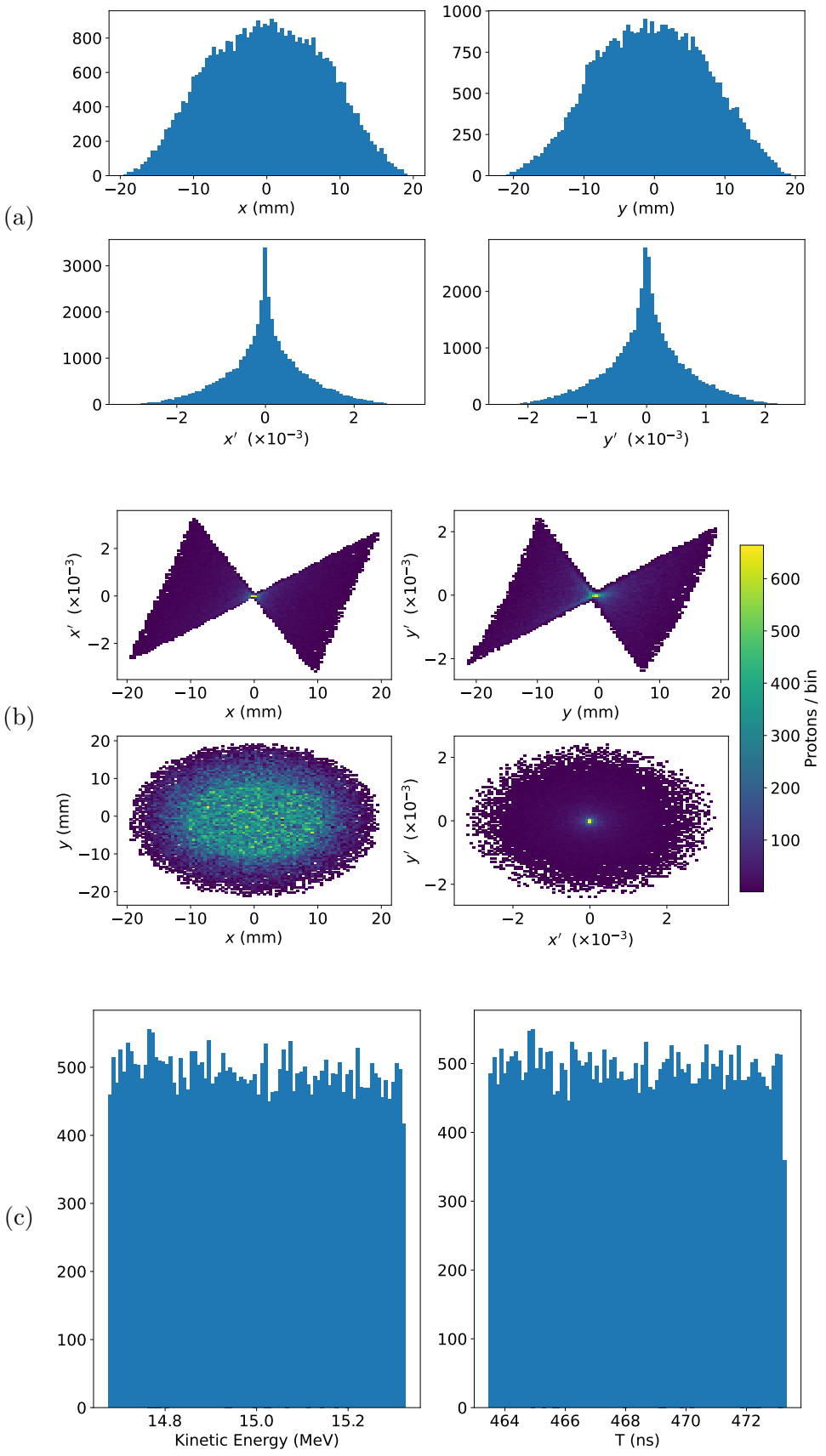

Figure 2.7: Beam phase-space distributions at the Stage 1 end station for the nominal solenoid settings for delivering a 30 mm spot size when not considering space charge effects. Subfigures (a) and (b) show the transverse phase space; X' and Y' represent the slopes relative to the Z axis. Subfigure (c) shows the longitudinal distribution in kinetic energy and time (T).

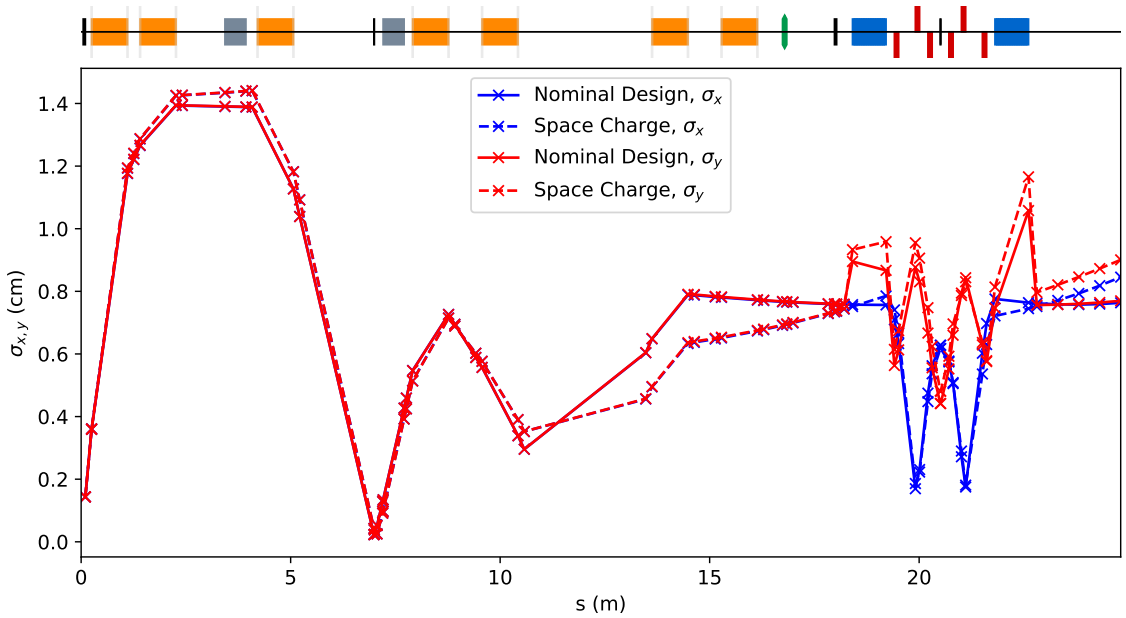

Figure 2.8: Beam size evolution along the Stage 1 beamline, showing horizontal beam size (σ_x, blue) and vertical beam size (σ_y, red) as a function of beamline length (s) before the vertical arc. The solid lines represent the nominal design performance, while the dashed lines account for space charge effects in the model. The survey above the plot indicates the locations of key beamline components: solenoids (orange), RF cavities (grey), collimators (black), octupoles (green), dipoles (blue), and quadrupoles (red).

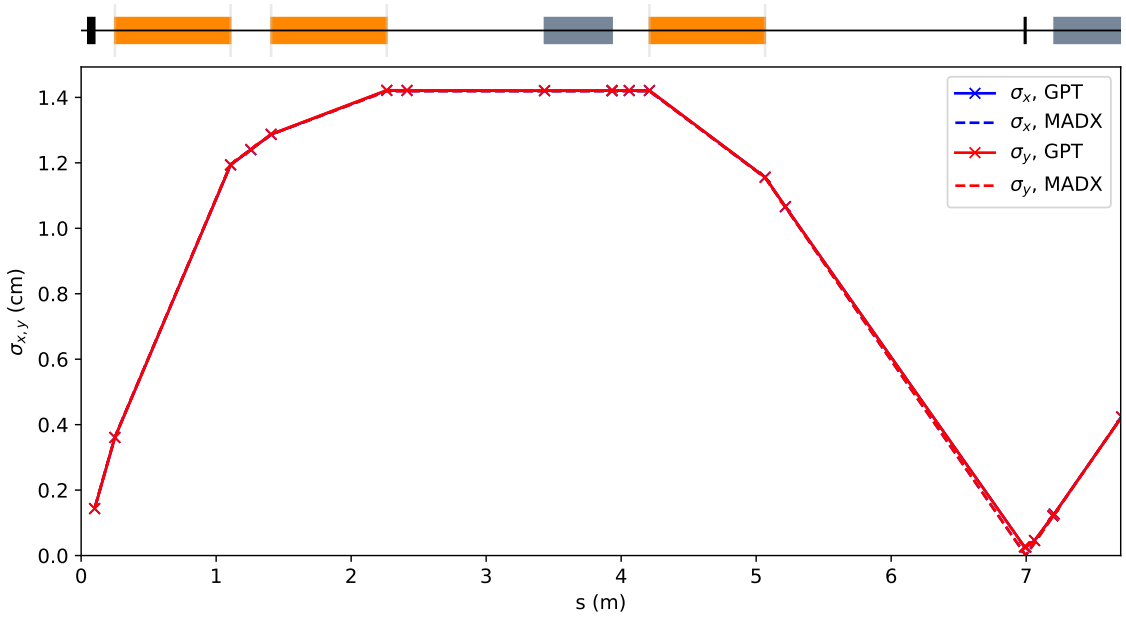

Figure 2.9: Horizontal (σ_x, blue) and vertical (σ_y, red) beam size along the Stage 1 beamline, comparing the nominal MAD-X design (dashed lines) with the GPT model (solid lines). The GPT model includes optimisations in the first three solenoids to mitigate space charge effects between the nozzle exit and the energy selection collimator. The survey above the plot indicates the locations of key beamline components: solenoids (orange) and RF cavities (grey).

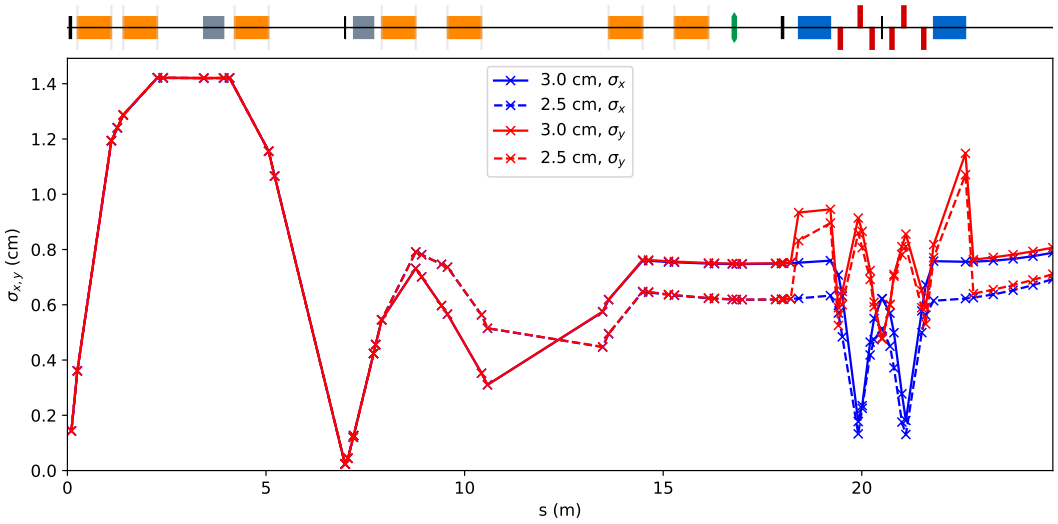

Figure 2.10: Horizontal (σ_x, blue) and vertical (σ_y, red) beam size along the Stage 1 beamline for two spot size configurations: 30 mm (solid lines) and 25 mm (dashed lines), both optimised in GPT for space charge mitigation. The final four lenses are specifically optimised to mitigate space charge effects between the energy selection collimator and the start of the vertical arc. The survey above the plot shows the locations of the model's key beamline components: solenoids (orange), RF cavities (grey), collimators (black), octupole (green), dipoles (blue), and quadrupoles (red).

In Stage 2, the beam will be transported to the FFA via the switching dipole installed before the vertical arc. The initial injection line design described in [12, 13] assumed a Twiss $\beta_{x,y}$ of 50 m and Twiss $\alpha_{x,y}$ of 0 at the start of the switching magnet. The assumed RMS emittance, however, was approximately an order of magnitude larger than that listed in table 2.2. Simulations have shown that the emittance grows as the beam is transported through the equivalent solenoids (see table 2.9). The resulting emittance gives a beam size of 14.2 mm at the switching dipole entrance.

To optimise the model with space charge, only the strengths of the final four equivalent solenoids were varied. The beam is constrained to have Twiss $\alpha_{x,y} = 0$ at the entrance to the switching dipole. The optimisation seeks to deliver Twiss $\beta_{x,y} = 25$ m at the entrance to the switching dipole. This condition is not enforced as strongly as the condition $\alpha_{x,y} = 0$ since the nominal FFA injection-line optics is sufficiently flexible to deliver the values of $\beta_{x,y}$ required at injection to the FFA. Two solutions were found, see figure 2.12, one in which all four lenses are used and a second in which the fifth and sixth lenses are powered off. The required electron plasma densities and the equivalent solenoid field strengths are listed in table 2.11.

2.3.2.3 Generation of a uniform beam profile at the end station

An octupole is used to generate a uniform transverse beam profile at the end station. As GPT does not include a model of an octupole, octupole focusing will be implemented through the importation of a magnetic field map. In the present study, the beam generated using the space-charge optimised GPT model was used in BDSIM for the study of octupole focusing.

A reference plane transverse to the beam axis is placed 150 mm after the end of the final plasma lens (or equivalent solenoid). The particle phase space from the space-charge optimised GPT model recorded at this plane is sampled to restart beam propagation through the arc. The analysis of the impact of space-charge forces presented in section 2.3.2.2 shows that the

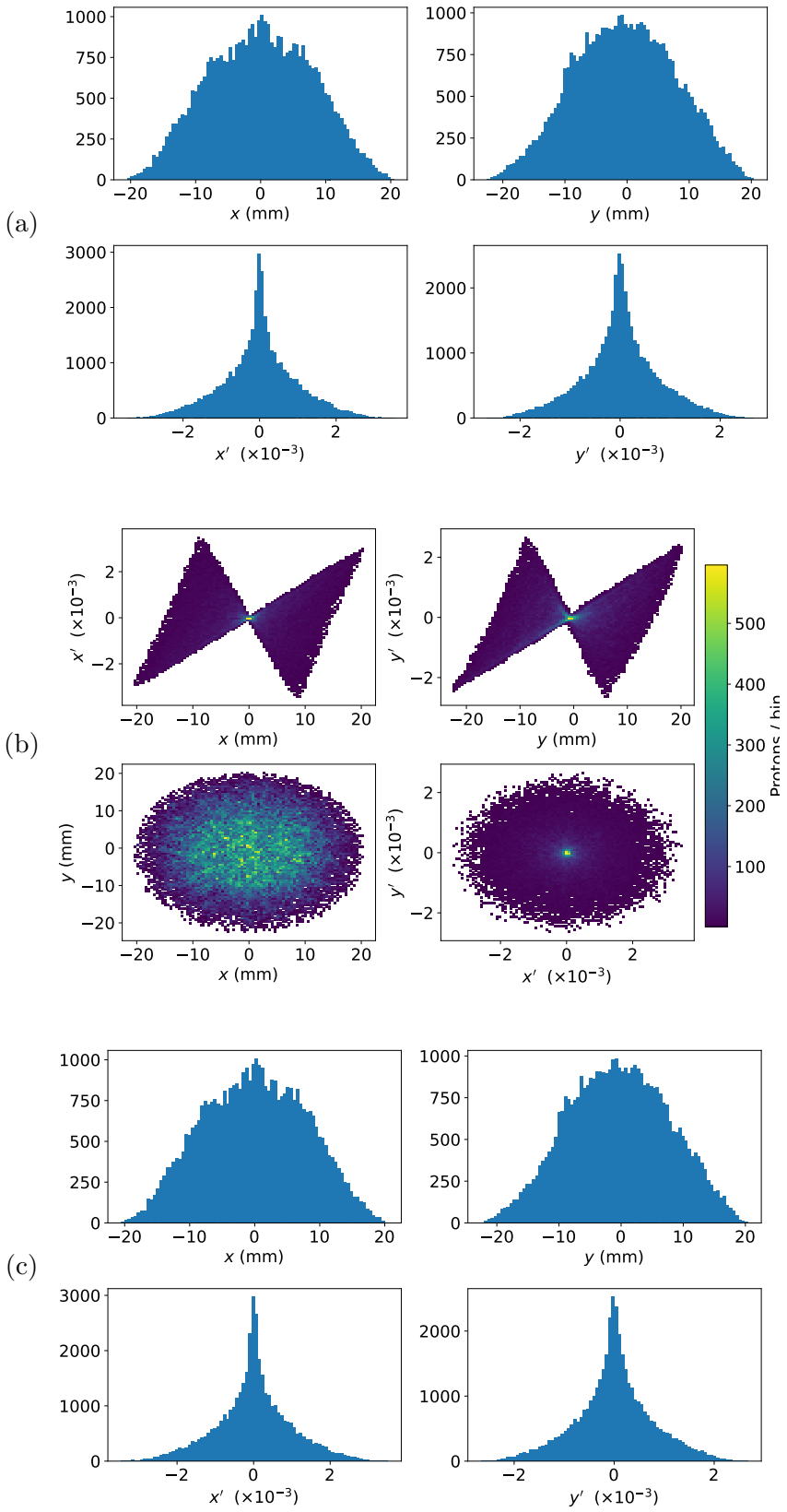

Figure 2.11: Beam phase-space distributions at the Stage 1 end station for the nominal solenoid settings for delivering a 30mm spot size when not considering space charge effects. Subfigures (a) and (b) show the transverse phase space; X' and Y' represent the slopes relative to the Z axis. Subfigure (c) shows the longitudinal distribution in kinetic energy and time (T).

quadrupolar focusing in the arc is unaffected by space charge, making it possible to study the effect of the octupole on the transverse distributions at the end station using BDSIM.

The normalised octupole strength, K_3, is defined in BDSIM as:

$$K_3 = \frac{1}{B_8\rho_0}\frac{d^3B_{8y}}{dx^3}\,; \tag{2.10}$$

where B_8 is the magnetic field strength, B_{8y}, is its component along the y axis, and $B_8\rho_0$ is the nominal magnetic rigidity of the reference particle. Figure 2.13 shows the transverse profiles obtained using $K_3 = 10,000\,\mathrm{m}^{-4}$. The core of the beam is observed to be uniform, but the particle density falls gradually to zero as the radial distance from the centre of the beam increases. Overall, improved transverse uniformity has been demonstrated for a range of octupole strengths. Work continues to obtain a set of parameters for the arc quadrupoles that, together with the octupole, produce a fully uniform profile across the spot at the end station.

2.3.2.4 Modelling the dose delivered to the end station

Depth-dose simulation

To estimate the dose delivered to the end station, a BDSIM model has been developed containing the materials through which the proton beam is expected to propagate, see table 2.12. The air gap is included to provide clearance for the automated positioning of the cell samples. The polystyrene sample container is typical of a cell culture plate. The cell layer is modelled using the physical properties of water. A water layer follows the culture medium.

The dose delivered was evaluated for beams with energies of 10, 12, and 15 MeV. Simulations were performed using a parallel beam with a transverse profile assumed to be Gaussian, with a standard deviation of $\sigma_{x,y} = 2.5\,\mathrm{mm}$, representative of the 10 mm spot size configuration. Where beams for previous end station dose simulations have been mono-energetic, an energy spread of 2% is now defined for all beams to represent the expected beam at the end station and examine the effect on Bragg peak depth, dose, and range straggling. The per-event average dose is recorded, integrated over the $0.1 \times 0.1m$ transverse extent of the model in a $1 \times 1 \times 450$ cell scoring mesh. 10000 protons were simulated, and the scored dose was scaled to the full bunch

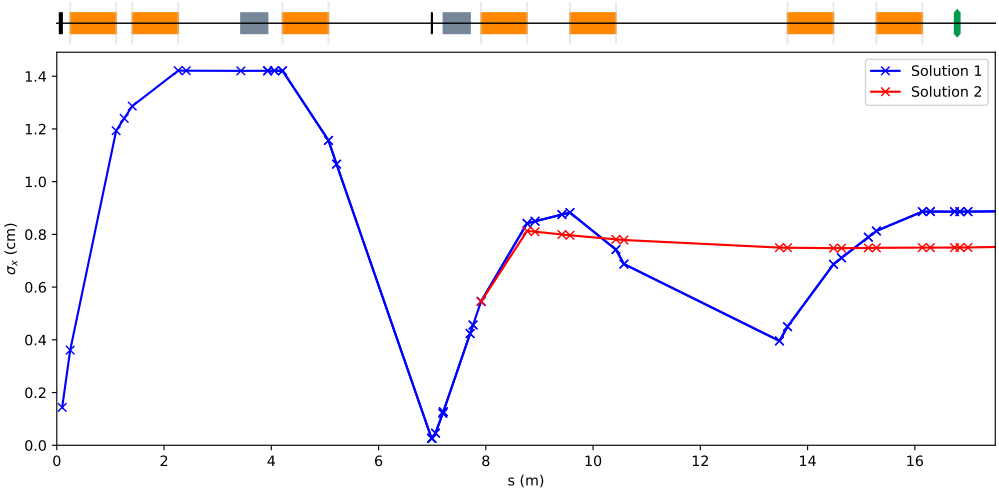

Figure 2.12: Two optics solutions for the Stage 1 beam to meet the conditions at the entrance to the Stage 2 FFA injection line. Solution 1, blue: all four lenses are used. Solution 2, red: the fifth and sixth lenses are powered off. The survey at the top of the plots shows the locations of the model's solenoids (orange) and RF cavities (grey).

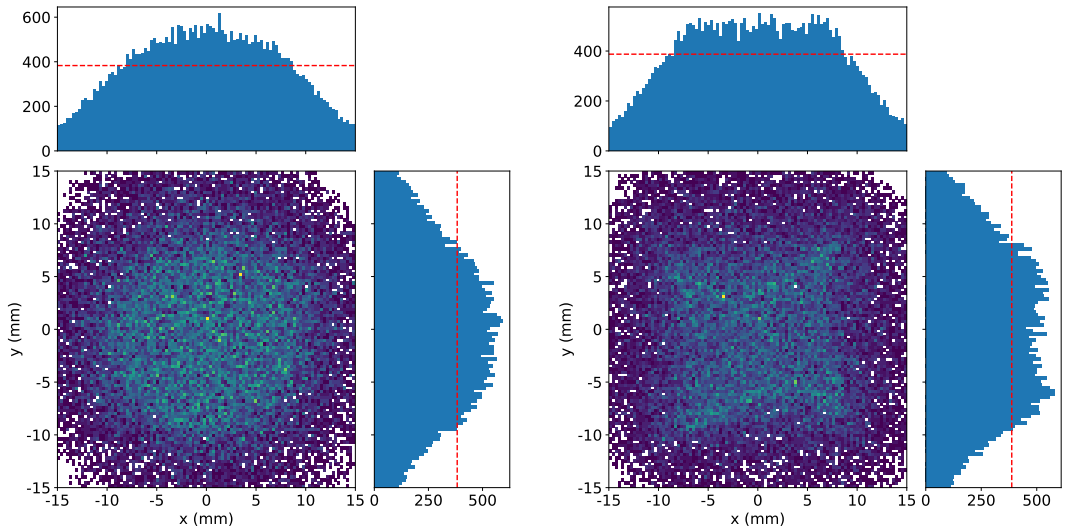

(a) **(b)**

Figure 2.13: Transverse beam profile at the Stage 1 end station for the nominal 30 mm spot size configuration with the octupole field off (a) and on (b) for a normalised $K3$ strength of 10,000 m^{-4}. The red dashed lines indicate the number of particles per bin that would be required for a perfectly uniform profile across the whole transverse distribution.

charge of 10^9 protons. The particle flux at the end of each model component is recorded in BDSIM samplers. Figure 2.14 shows the depth-dose distributions of the three different energy beams. The 10 MeV beam does not reach the cell layer, with the majority of the beams energy lost in the base of the sample container. The 12 MeV beam has the Bragg peak located close to the cell layer. The Bragg peak at this location would result in a significant dose variation across the depth of the cell layer, contributing significant experimental uncertainties. The 15 MeV beam, by comparison, has the cell layer on the proximal slope of the depth dose curve, offering a much shallower dose gradient in the volume. The Bragg peak is contained within the water volume after the cell layer, indicating that a beam stop will not be needed when irradiating cell samples.

The kinetic energy distribution after each model component is shown in figure 2.15 for the 12 MeV and 15 MeV beams. The component causing the largest energy degradation before the cell layer is the sample container, resulting in protons entering the cells at energies of approximately 2.75 MeV and 8.75 MeV for the 12 MeV and 15 MeV beams, respectively. Scattering within the model components results in an increased energy spread that will further contribute to experimental uncertainties.

Dose rate estimations

The dose delivered was estimated by calculating the energy deposited in a single cell scoring-mesh equal in volume to the sensitive volume of a PTW 23343 Markus ion chamber [89]. The cylindrical chamber has a radius of 2.65 mm and a depth of 2 mm, giving a volume of approximately $4.4 \times 10^{-8}\,\mathrm{m}^3$. We remove the cell layer from the end station model and position the scoring mesh such that the flat entrance surface of the volume is co-planar with the boundary of the sample container and water volumes. The dose deposited in water is modelled to avoid the need to consider the response rate of the detector. The dose recorded for a single proton bunch was 12.20 Gy. Using a bunch length of 9.83 ns from figure 2.11 yields an instantaneous

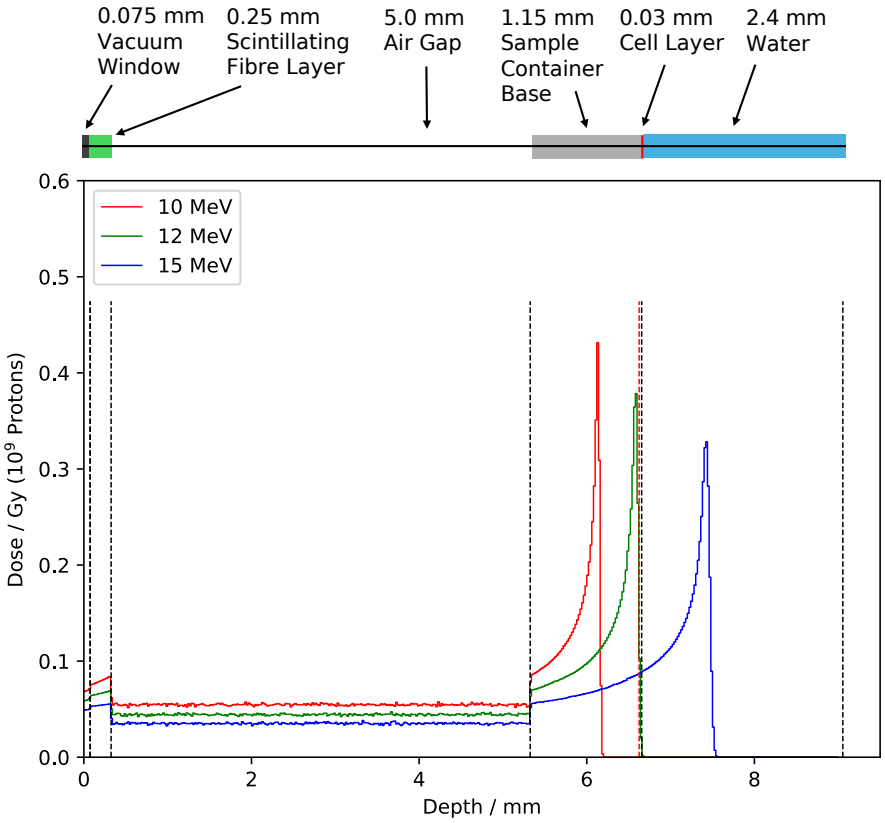

Figure 2.14: Depth dose curves for 10, 12, and 15 MeV proton beams in a BDSIM model of the LhARA Stage 1 *in-vitro* end station. The model includes a vacuum window, scintillation fibres, air gap, sample container, cell layer, and water. 10,000 protons are simulated, and the average dose per proton is scaled to the LhARA total bunch charge of 1×10^9 protons.

dose rate of 1.3×10^9 Gy/s. The average dose rate, assuming a laser repetition rate of 10 Hz, is therefore 124.0 Gy/s. These end-station dose values are summarised in table 1.1.

2.3.2.5 Gabor lens tracking

A confined electron-plasma (Gabor) lens element has been added to BDSIM [90]. The focusing effect of the electron-plasma space charge is simulated without taking into account the small perturbations on the beam produced by the electric and magnetic fields that form the Penning-Malmberg trap. Figure 2.16 shows a comparison of the Twiss β_y and dispersion functions in Stage 1 configuration that delivers a 30 mm beam. The evolution of the beam focused using Gabor lenses is in good agreement with the evolution obtained using the nominal MAD-X model and using solenoid focusing in BDSIM. The figure demonstrates that Gabor lenses are able to deliver a beam that meets the LhARA requirements. Minor alterations ($\leq 1\%$) of the Gabor lens field strengths were required to match the optical performance of the solenoid models. The perturbation to plasma focusing arising from the confining electric and magnetic fields remains to be evaluated.

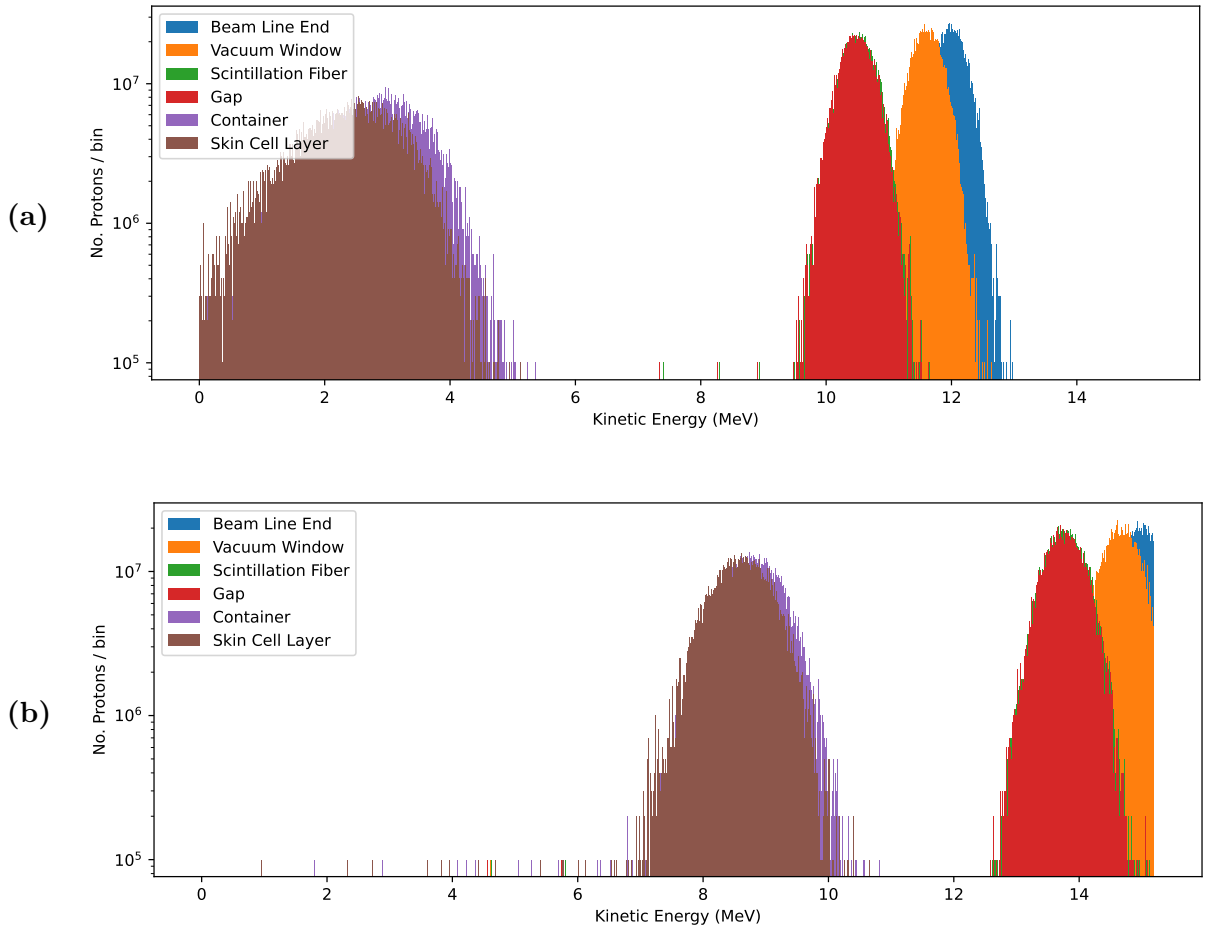

Figure 2.15: Kinetic energy spectrum at the exit of each component in the Stage 1 *in-vitro* end station model for (a) 12 MeV and (b) 15 MeV proton beams.

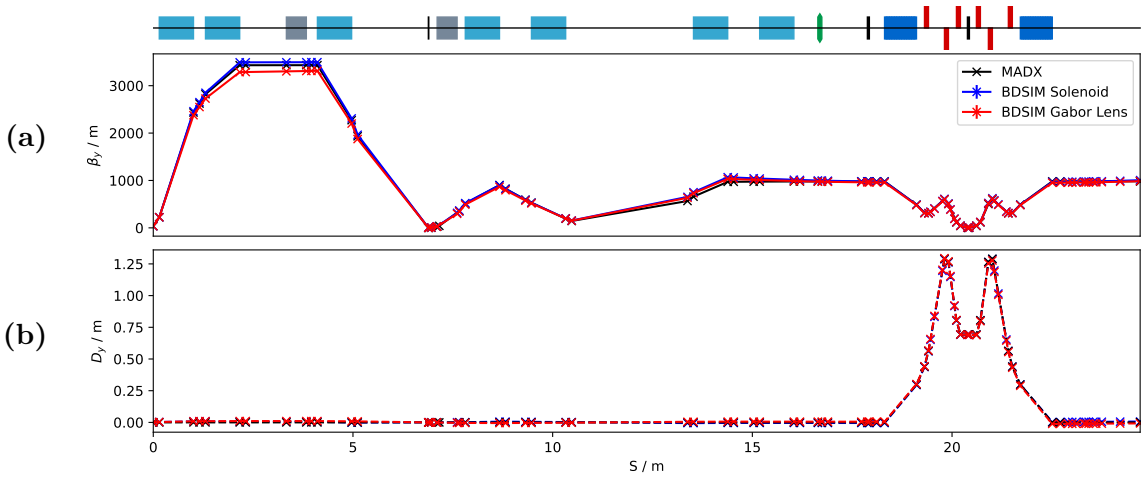

Figure 2.16: The vertical Twiss function (β_y, a) and vertical dispersion (D_y, b) in the nominal MAD-X design (black), in BDSIM with solenoids (blue), and in BDSIM with Gabor lenses (red). The survey above the figure shows the locations of the Gabor lenses (light blue), RF cavities (grey), collimators (black), octupole (green), dipoles (dark blue), and quadrupoles (red).

2.4 Stage 2 design and performance

2.4.1 Post-acceleration and beam delivery to the in-vitro and in-vivo end stations

An FFA based on the spiral scaling principle [91–94] is proposed to boost the ion-beam energy in LhARA in Stage 2. The system is designed to deliver proton beam energies of between 15 MeV and 125 MeV and ion beams, for example C^{6+}, from 4 MeV/u to 33 MeV/u, to the *in-vitro* and *in-vivo* end stations. The FFA is ideal for acceleration in LhARA and for a future clinical system because it has the capability to:

- Operate at arbitrarily large repetition rates; and
- Deliver beams of arbitrary energy between the injection energy and the maximum specified energy.

The first of these capabilities is made possible by the fact that the magnetic field is not ramped during acceleration. The FFA is compact when compared to a synchrotron due to the use of combined function magnets. The large dynamic aperture of an FFA makes the acceleration of multiple ion species straightforward when compared to a cyclotron; the acceleration of a range of ion species from proton to carbon is an essential requirement for LhARA. The structure of the FFA provides the possibility to implement multiple extraction ports.

A typical FFA is able to increase the beam momentum by a factor of three, though a greater factor is achievable. For LhARA, the threefold increase in momentum translates to a maximum proton-beam energy of 127 MeV from an injected 15 MeV beam. For carbon ions (C^{6+}) with the same rigidity, the maximum energy is approximately 33.4 MeV/u. The energy at injection into the FFA determines the beam energy at extraction. The injection energy will be changed by varying the focusing strengths in the Stage 1 beam line from the capture section through to the extraction line and the FFA ring. This will allow the appropriate energy slice from the broad energy spectrum produced at the laser-driven source to be captured and transported to the FFA. The FFA will then accelerate the beam, acting as a three-fold momentum multiplier, which will allow the extraction energy to be varied. This scheme simplifies the injection and extraction systems since their geometry and location can be kept constant.

To provide the capability to perform cell irradiation using protons with a kinetic energy of 15–127 MeV and carbon ions, the extraction line from the FFA leads to a 90° vertical arc that sends the beam to the high energy *in-vitro* end station. If the first dipole of the arc is not energised, beam will be sent to the *in-vivo* end station. The extraction line of the FFA includes a switching dipole that will send the beam to the high-energy beam dump if it is not energised. The key parameters of the Stage 2 lattice are presented in table 2.13. The layout of the FFA, the injection line, and a section of the extraction line are shown in Figure 2.17.

2.4.2 FFA injection line

The FFA injection line begins at a switching dipole after Gabor lens 7. To inject on the inside of the FFA, the injection line crosses the FFA ring between the magnets of two adjacent FFA cells. Modifications to the FFA ring from the design presented in [12] resulted in an increase of the orbit excursions, increasing the required magnet aperture. The engineering design of the beam line as it crosses the FFA is challenging, as it must accommodate not only the injection line itself, but all necessary infrastructure, including shielding, radiation shutters, vacuum pumps, diagnostics, and corrector magnets.

The FFA injection line includes two straight sections. The first, 2.2 m long, accommodates a 0.5 m thick concrete shielding wall, radiation shutter, and all other necessary devices. The

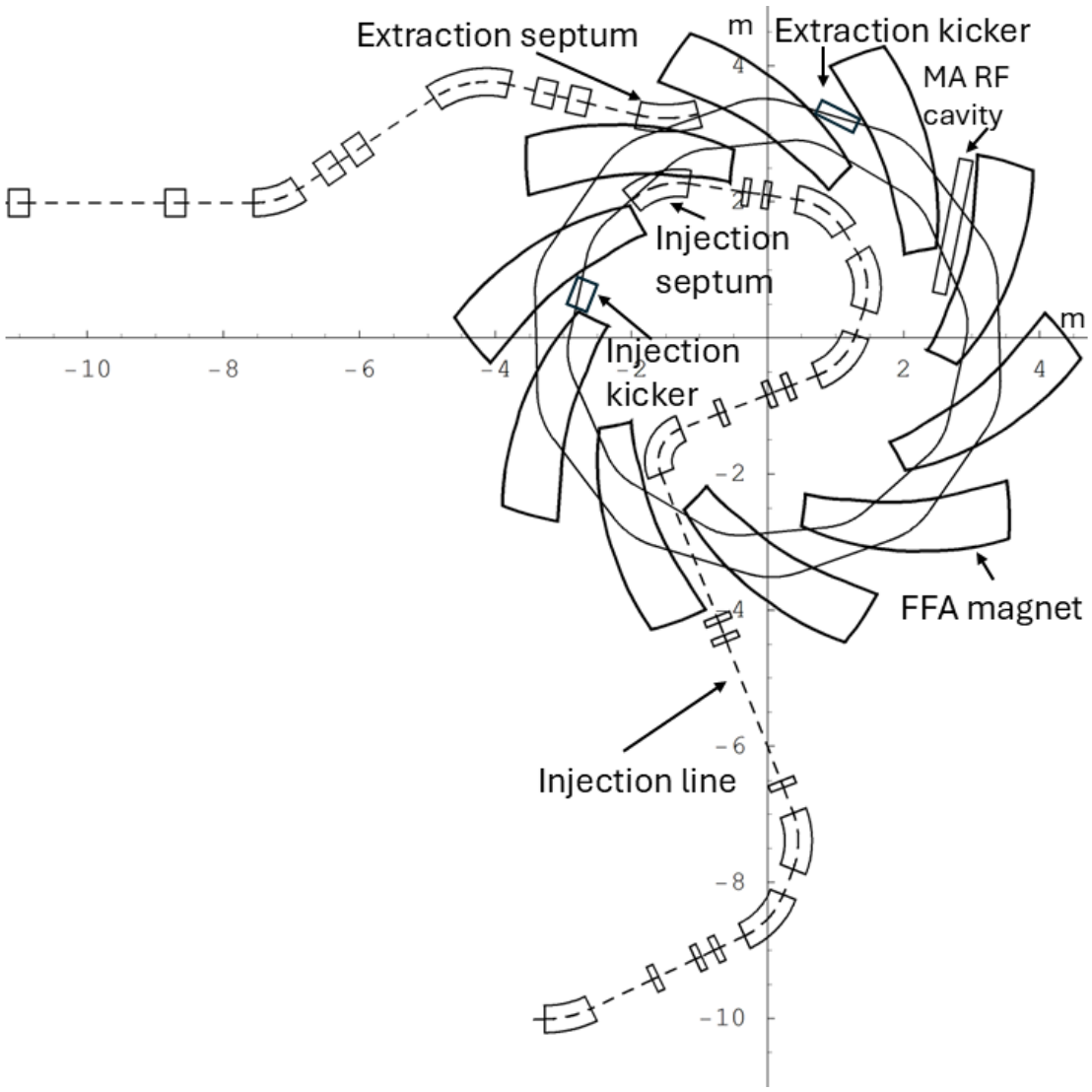

Figure 2.17: Layout of the LhARA FFA ring, including injection and extraction systems, together with the injection line geometry, assuming the FFA magnet shapes corresponding to the design presented here.

second straight section is 1.85 m long to accommodate the FFA crossing. Eleven identical quadrupoles and six dipoles are required. The specifications of the transfer-line magnets are presented in table 2.13 along with the parameters of the switching dipole and injection septum. The total length of the injection line is 17.6 m.

The baseline configuration of the Stage 1 beam line delivers Twiss parameters of $\beta_{x,y} = 50$ m and $\alpha_{x,y} = 0$ downstream at the switching dipole. These values of $\beta_{x,y}$ yield a beam size of $\sigma_{x,y} = 14$ mm due to the emittance growth observed in the evaluation of beam transport through Stage 1. The aperture of the switching dipole would therefore need to be large to avoid unacceptable beam loss.

To address this, the Gabor lenses in Stage 1 were re-optimised using GPT's optimisation utility `GDFSOLVE` to reduce $\beta_{x,y}$ at the switching dipole whilst preserving $\alpha_{x,y} = 0$. The normalised quadrupole strengths were varied with the constraint that the quadrupole strength parameters satisfy $|K_1| \leq 17\,\mathrm{m}^{-2}$. A solution meeting this constraint was found for which $\beta_{x,y} \approx 27$ m at the switching dipole.

The FFA injection line was optimised using a beam with $\alpha_{x,y} = 0$ and $\beta_{x,y} = 27$ m at the

entrance to the switching dipole. The resulting beta functions and dispersion are shown in figure 2.18. The conditions at the end of the injection septum, shown in table 2.14, have been achieved whilst preserving the region of low beta and high dispersion at $s \approx 8\,\mathrm{m}$ for installation of a momentum cleaning collimator.

Engineering designs are being developed for the FFA ring and injection line. Space constraints make the design of the region in which the injection line crosses the FFA challenging. Providing sufficient space for personnel to install and maintain the injection line also remains a concern as the last of the injection-line magnets before the injection septum are close to the FFA magnets. Therefore, the possibility of reducing the severity of these pressures by allowing the transfer line to cross the FFA at an oblique angle was considered. The crossing angle was chosen to be closer to the spiral angle of the FFA magnets, offering greater flexibility for positioning injection-line components. A solution was found that provides the required beam parameters at injection to the FFA whilst also improving access between the line and FFA ring. However, the revised injection-line optics yield large beam sizes at some locations. Work continues to ensure that these excursions do not cause unacceptably large beam loss.

2.4.3 FFA

A spiral FFA scaling ring has been designed for post-acceleration in Stage 2. The spiral scaling principle defines the field profile in the median plane, given as a function of radius measured from the centre of the ring, r, by [91]:

$$B_y = B_0 \left[\frac{r}{r_0}\right]^k F\left(\theta - \ln\left[\frac{R}{r_0}\right]\tan\zeta\right) ; \tag{2.11}$$

where B_0 is the magnetic field at radius r_0, k is the field index, ζ is the spiral angle and F is the flutter function. This field law defines a zero-chromaticity condition, which means the working point of the machine is independent of energy up to field errors and alignment imperfections and avoids the crossing of resonances that would reduce the beam quality and may lead to beam loss. The ring consists of ten symmetric cells, each containing a single combined-function spiral magnet. The choice of the number of cells is a compromise between the size of the orbit excursion, which dictates the radial extent of the magnet, and the length of the straight section, which is required to accommodate injection and extraction. Each of the magnets provides bending, horizontal focusing, and vertical defocusing, while the field at the magnet edges contributes to both horizontal and vertical focusing. These effects allow a stable beam to be obtained in

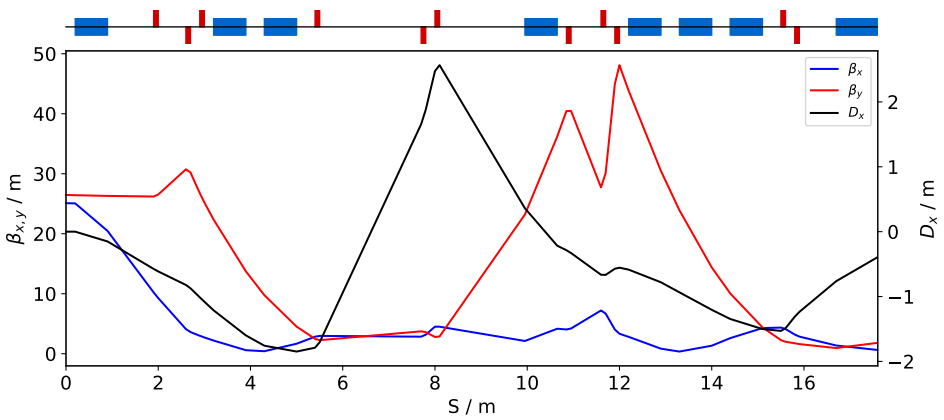

Figure 2.18: Horizontal (β_x, blue) and vertical (β_y, red) Twiss β_x functions, and horizontal dispersion function (D_x, black) along the Stage 2 FFA injection line (s).

both transverse planes using only a single magnet per cell without requiring a negative bend, as is necessary for radial FFA machines, and which significantly reduces the size of the spiral machine. Table 2.13 presents the main design parameters of the FFA ring for LhARA. The betatron functions and dispersion in one lattice cell at injection are shown in figure 2.19.

Normal conducting spiral scaling FFA magnets, similar to the ones needed for LhARA, have been constructed successfully using two different techniques [94, 95]. The first technique used a set of coils distributed along the surface of a flat pole to meet the scaling-field requirement. In the second technique, the scaling-field requirement was achieved by shaping the gap between the poles. The first technique, in which the scaling parameter, k, can be tuned by applying different currents in each coil, was chosen for LhARA as it allows the working point to be kept constant over a variety of modes of operation and allows the extraction energy to be varied. Since the magnetic field of the FFA ring needs to be adjusted to allow the extraction energy to be varied, the use of a laminated magnet design will be considered to allow the time required for the field to be changed to be reduced. The flexibility provided by the distributed coils will also allow k to be changed. Such flexibility will be important if it becomes necessary to move away from a particular resonance or to tune the lattice to a different working point to generate a long pulse using resonant slow extraction [96].

An alternative design based on a double-spiral FFA was proposed in [97]. However, this design would correspond to a larger ring with larger orbit excursion and would require two magnets per cell. Although this design would be very flexible in tuning, it is not considered necessary for LhARA and the single spiral FFA design is retained as the baseline.

2.4.4 Extraction line

Material described in this section corresponds to the design presented in [12].

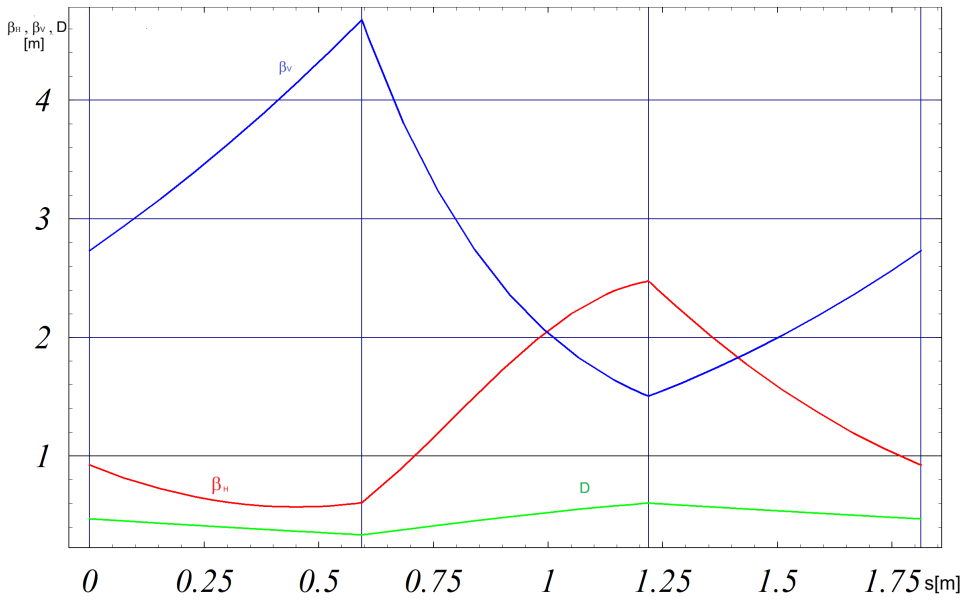

Figure 2.19: Horizontal (red) and vertical (blue) Twiss beta functions (β_x and β_y respectively), and horizontal dispersion (D_x, green) in one FFA cell at injection calculated using hard-edge approximation in [75].

2.4.4.1 Upstream part of the extraction Line

The extraction line design was obtained on the assumption that the emittance of the 127 MeV beam at extraction will be determined by the nominal emittance of the 15 MeV beam at injection, i.e. an initial emittance of $2.8\,\pi$ mm mrad was assumed. However, it may be necessary for the extraction line to accept a higher emittance to accommodate space-charge induced emittance growth, see table 2.9. Acceleration in the FFA ring shrinks the emittance by a factor of three due to adiabatic damping. In this scenario, the normalised emittance is assumed to be conserved from the start of the injection line to the end of the extraction septum. This implies that the physical emittance at extraction from the FFA is $0.93\,\pi$ mm mrad (RMS).

For the extraction of a variety of beam energies, the injection energy will be varied and the ring will always increase the beam momentum by a factor of three. This means the adiabatic damping factor will be the same for each setting and therefore that the emittance at 40 MeV will be the same as at 127 MeV. The assumption that the emittance at extraction is the same for all momenta is valid so long as the optics and apertures that define the beam size are the same for all energies. Space-charge forces will result in an energy-dependent growth of emittance. The size of the space-charge emittance growth in the FFA is yet to be estimated.

The first part of the extraction line collects the beam coming out of the extraction septum of the FFA, which has the optical parameters given in table 2.15. The description of the extraction septum has yet to be updated; therefore, the septum parameters were taken from [12]. The beam then passes through two dipoles of different lengths and four quadrupoles, each of length 0.3 m. The beam propagates antiparallel to the low-energy beam line, which ensures that dispersion is closed. It is important that the dispersion is closed as off-momentum particles will otherwise follow trajectories different to those followed by particles with the design momentum and lead to a significant increase in beam size and beam loss.

The second part of the extraction line consists of four quadrupoles, each of length 0.3 m, which transport the beam to the first dipole of the vertical arc that serves the high-energy *in-vitro* end station. These quadrupoles are used to produce a beam that is close to round and has a size close to that required at the end station. The last four quadrupoles are flexible enough to allow a variety of values of $\beta_{x,y}$ to be accommodated. Figure 2.20 shows the Twiss beta functions for five quadrupole settings that can match beams with $\beta_{x,y} = 410$ m, $\beta_{x,y} = 46$ m, $\beta_{x,y} = 40$ m $\beta_{x,y} = 4.5$ m and $\beta_{x,y} = 0.46$ m.

2.4.4.2 High-energy in-vitro beam line

The high-energy *in-vitro* beam line transports the beam from the exit of the extraction line to the high-energy *in-vitro* end station. The 90° vertical arc is a scaled version of the low-energy arc and consists of two dipoles and six quadrupole magnets. The lengths of the magnets were scaled by a factor of 3 to accommodate the threefold increase in momentum while ensuring that the magnetic fields remain below the saturation limits of normal conducting magnets. The length of the dipoles is therefore 1.2 m and that of the quadrupoles is 0.3 m. The overall length of the arc then becomes 6 m, compared to 4.6 m for the low-energy *in-vitro* arc. This difference in arc length means the high-energy *in-vitro* arc is ~ 0.9 m taller than the low-energy arc.

The arc has been designed to fulfil the following criteria for the beam optics for the Twiss α and β functions, dispersion (D) and dispersion derivative (Dp), and phase advance ($\Delta\mu$):

- $\beta_{x,y,\mathrm{in}} = \beta_{x,y,\mathrm{out}}$;
- $\alpha_{x,y,\mathrm{in}} = \alpha_{x,y,\mathrm{out}} = 0$;
- $D_{x,y,\mathrm{in}} = D_{x,y,\mathrm{out}} = 0$;
- $D'_{x,y,\mathrm{in}} = D'_{x,y,\mathrm{out}} = 0$;

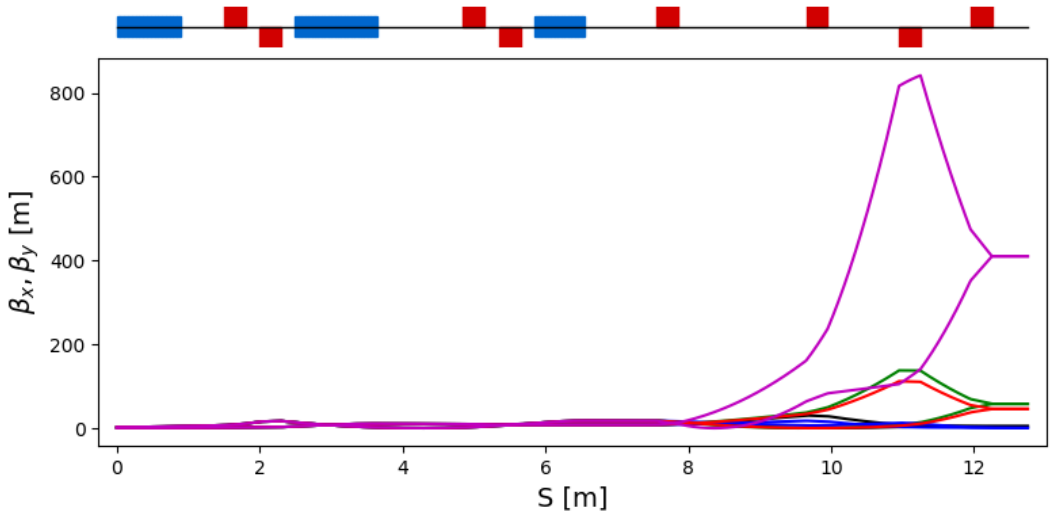

Figure 2.20: β_x and β_y functions for the full range of extraction beam line matching to $\beta_{x,y} = 410\,\text{m}$ (magenta), $\beta_{x,y} = 46\,\text{m}$ (red), $\beta_{x,y} = 40\,\text{m}$ (green), $\beta_{x,y} = 4.5\,\text{m}$ (black) and $\beta_{x,y} = 0.46\,\text{m}$ (blue).

- $\Delta\mu_x = n\pi$, where n is an integer; and
- $\Delta\mu_y = m\pi$, where m is an integer.

The quadrupole strengths that meet these criteria were obtained using MAD-X. The results of the MAD-X optimisation are compared with tracking simulations performed using BDSIM in figure 2.21. The two calculations are in good agreement. The input beam Twiss parameters were taken to be those delivered by the extraction line (see table 2.16), and the phase-space distributions were assumed to be Gaussian. It is expected that the effect of space charge will not be negligible, but that adjustments to quadrupole strengths can be made to compensate for the effect, as was done for the low-energy arc.

2.4.4.3 In-vivo beam line

If the first dipole of the high-energy *in-vitro* arc is not energised, then the beam is sent to the *in-vivo* end station. From the end of the extraction line, a 7.7 m drift is necessary to clear the first bending dipole of the *in-vitro* arc, to provide space for the RF cavities needed for longitudinal phase-space manipulation, and to allow space for diagnostic devices. Following this drift is a further 6.6 m of beam line that includes four quadrupoles, each of length 0.4 m, which are used to perform the final focusing adjustments of the beam delivered to the *in-vivo* end station. A final 1.5 m drift is reserved for scanning magnets to be installed to perform spot scanning and to accommodate the shielding of the *in-vivo* end station.

The optics required to match the input beam parameters are given in table 2.16. The design required a compromise between the competing requirements of: flexibility to match various values of $\beta_{x,y}$; minimisation of the number of magnetic elements in the beam line; and minimisation of the overall length of the beam line. Quadrupole settings were obtained using MAD-X; care was taken to avoid small $\beta_{x,y}$ values throughout the beam line to try to limit both space charge and kinematic effects.

Figure 2.22 shows five sets of quadrupole settings to match $\beta_{x,y}$ values from 410 m to 0.46 m. With the exception of the settings for $\beta_{x,y} = 410\,\text{m}$, for which the minimum $\beta_{x,y}$ is approximately 0.08 m, all settings have a minimum $\beta_{x,y}$ above 0.2 m.

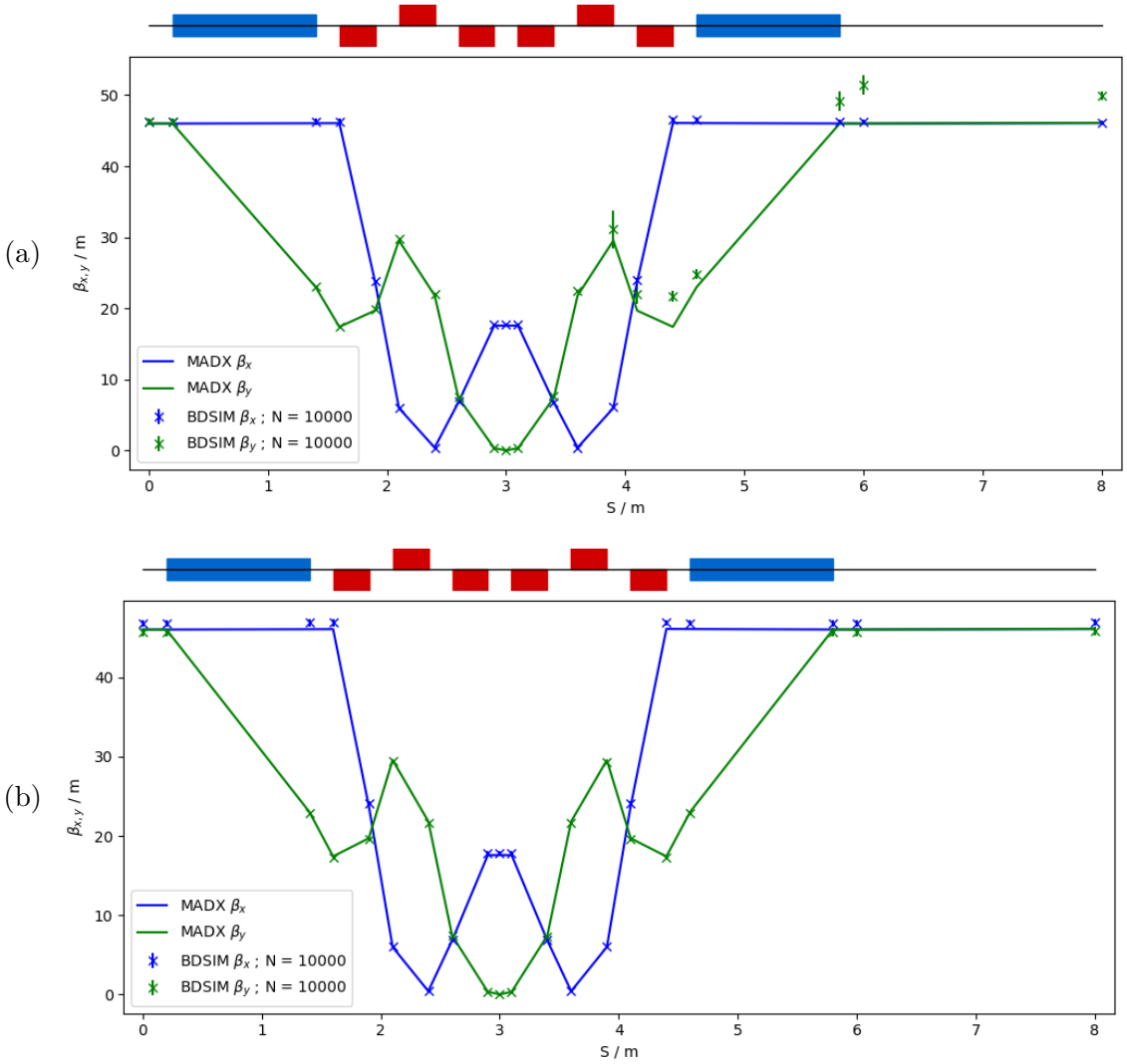

Figure 2.21: Horizontal profile, s, of β_x (blue) and β_y (green) generated by MAD-X compared to BDSIM for a 40 MeV (a) and nominal 127 MeV (b) proton beam passing through the high-energy *in-vitro* arc simulated with 10^4 particles (in BDSIM).

Good agreement between the Twiss beta functions evaluated with BDSIM and MAD-X is presented in figures 2.23 and 2.24. The quadrupoles have been matched to give $\beta_{x,y} = 0.46$ m, $\beta_{x,y} = 46$ m and $\beta_{x,y} = 410$ m. It is expected that the effect of space charge can not be neglected, but that adjustments to the quadrupole strengths can accommodate it. Additional magnets may be required to deliver magnetically-focused minibeams.

2.4.5 Stage 2 dose estimation

To serve the high-energy *in-vitro* end station with proton beams of 127 MeV, we assume a similar design to the low-energy *in-vitro* end station, but with the length of the air gap increased to 50 mm. A water phantom, based upon the PTC T41023 water phantom [98] placed at the end of the air gap, was simulated. The phantom is constructed from PMMA with a wall thickness of 6.95 mm and a beam-entrance window of thickness 3.05 mm. 10^9 protons per bunch and a minimum beam size of 1 mm were assumed. The dose was recorded using a model of the ionisation chamber described in section 2.3.2.4. The volume is positioned such that the pristine

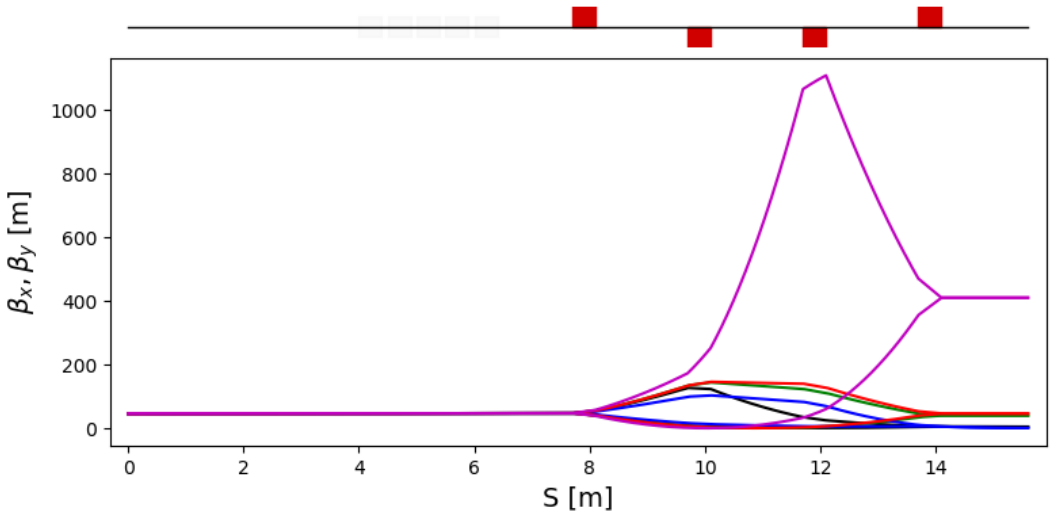

Figure 2.22: β_x and β_y functions for the *in-vivo* beam line matching from initial $\beta_{x,y} = 46\,\text{m}$ to $\beta_{x,y} = 410\,\text{m}$ (magenta), $\beta_{x,y} = 46\,\text{m}$ (red), $\beta_{x,y} = 40\,\text{m}$ (green), $\beta_{x,y} = 4.5\,\text{m}$ (black) and $\beta_{x,y} = 0.46\,\text{m}$ (blue).

Bragg peak was in the centre of the chamber. The estimated dose rates are reported in table 1.1. The energy deposited in the chamber is $4.25 \times 10^{-4}\,\text{J}$ corresponding to a dose of 9.7 Gy. Without phase rotation in the *in-vitro* beam line, the estimated bunch length of a 127 MeV proton beam is 41.5 ns. Therefore, the instantaneous dose rate is 2.33×10^8 Gy/s, and the average dose rate is 96.7 Gy/s when operating at a repetition rate of 10 Hz.

For 33.4 MeV/u carbon ion beams, the Bragg peak range is similar to that of the 15 MeV proton beam in Stage 1. We therefore simulated ion-beam delivery using the Stage 1 end station model. The incoherent space-charge tune shift is proportional to $\frac{q^2}{A}$ and inversely proportional to $\beta^2\gamma^3$, where q is the ion charge, A, its mass number and β, γ are the relativistic parameters. As a result, the intensity of a bunch of carbon ions experiences a space-charge tune shift 12 times as large as that experienced by a proton bunch of the same geometrical size and containing the same number of ions. It is therefore assumed that the maximum flux of carbon ions is a factor of 12 lower than the maximum proton flux. A single pulse of 8.3×10^7 ions deposits $3.69 \times 10^{-3}\,\text{J}$ into the chamber, giving an instantaneous dose rate of 1.1×10^9 Gy/s for a bunch length of 75.2 ns and a corresponding maximum average dose rate of 838 Gy/s.

2.5 Technical Systems

2.5.1 FFA Magnet Design

The FFA ring consists of ten cells, each containing a single combined-function spiral magnet with parameters given in table 2.13. To achieve zero chromaticity during acceleration, the beam has to experience constant focusing independent of radius. To achieve this, the integrated magnetic field in the median plane is constrained to follow the scaling law, equation 2.11, i.e.:

$$(BL) = (BL)_0 \left(\frac{r}{r_0}\right)^{k+1}\,; \tag{2.12}$$

where (BL) is the field integral for an obit of radius r and $(BL)_0$ is the field integral for an orbit with radius r_0. (BL) may then be written in terms of the angle, $\Delta\theta = \theta_{\text{max}} - \theta_{\text{min}}$, subtended

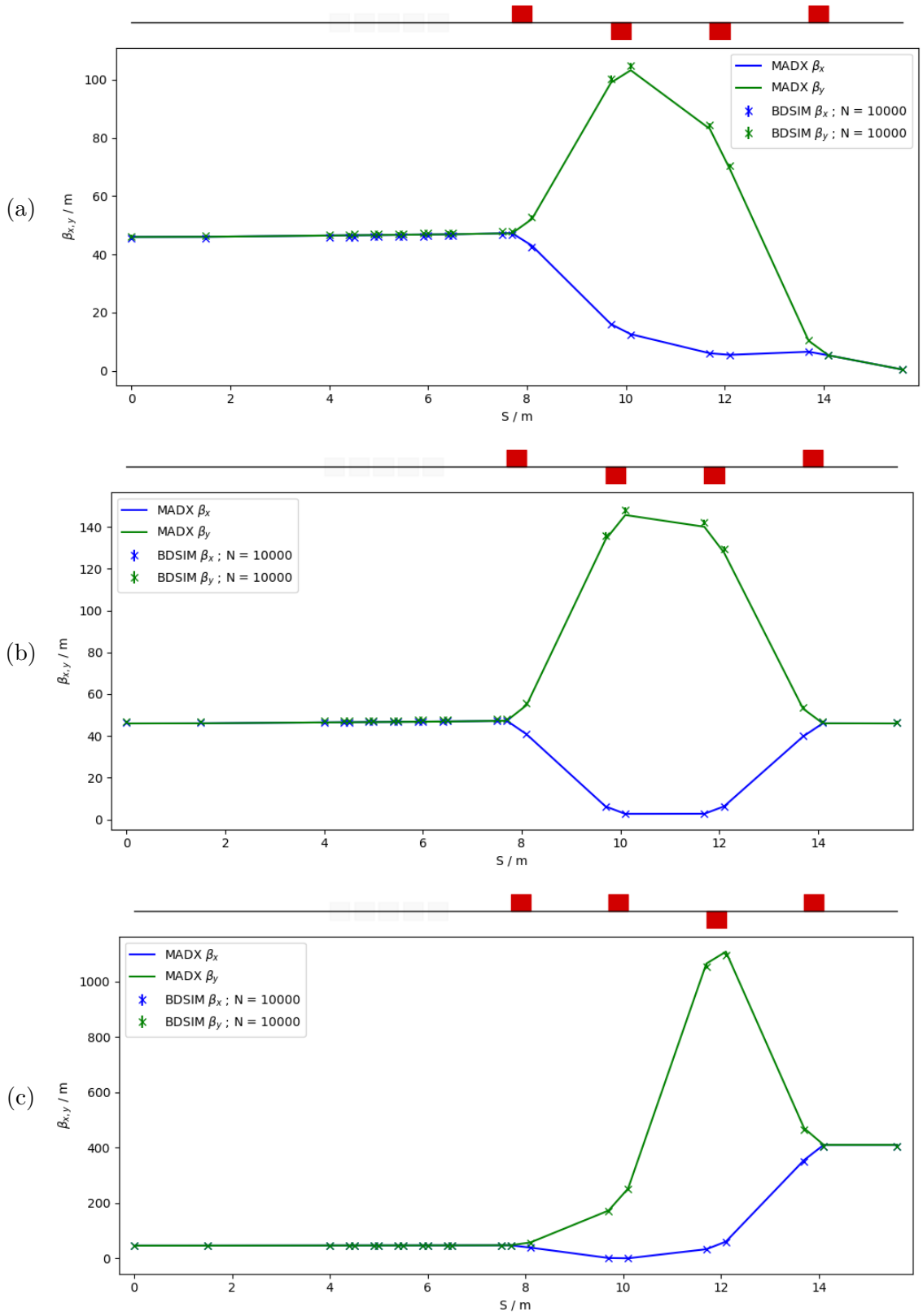

Figure 2.23: Comparison between MAD-X and BDSIM simulations of the Twiss β functions for the *in-vivo* beamline with a 40 MeV proton beam. The quadrupoles are matched to $\beta_{x,y} = 0.46\,\mathrm{m}$ (a), $\beta_{x,y} = 46\,\mathrm{m}$ (b), and $\beta_{x,y} = 410\,\mathrm{m}$ (c), for 10^4 simulated particles.

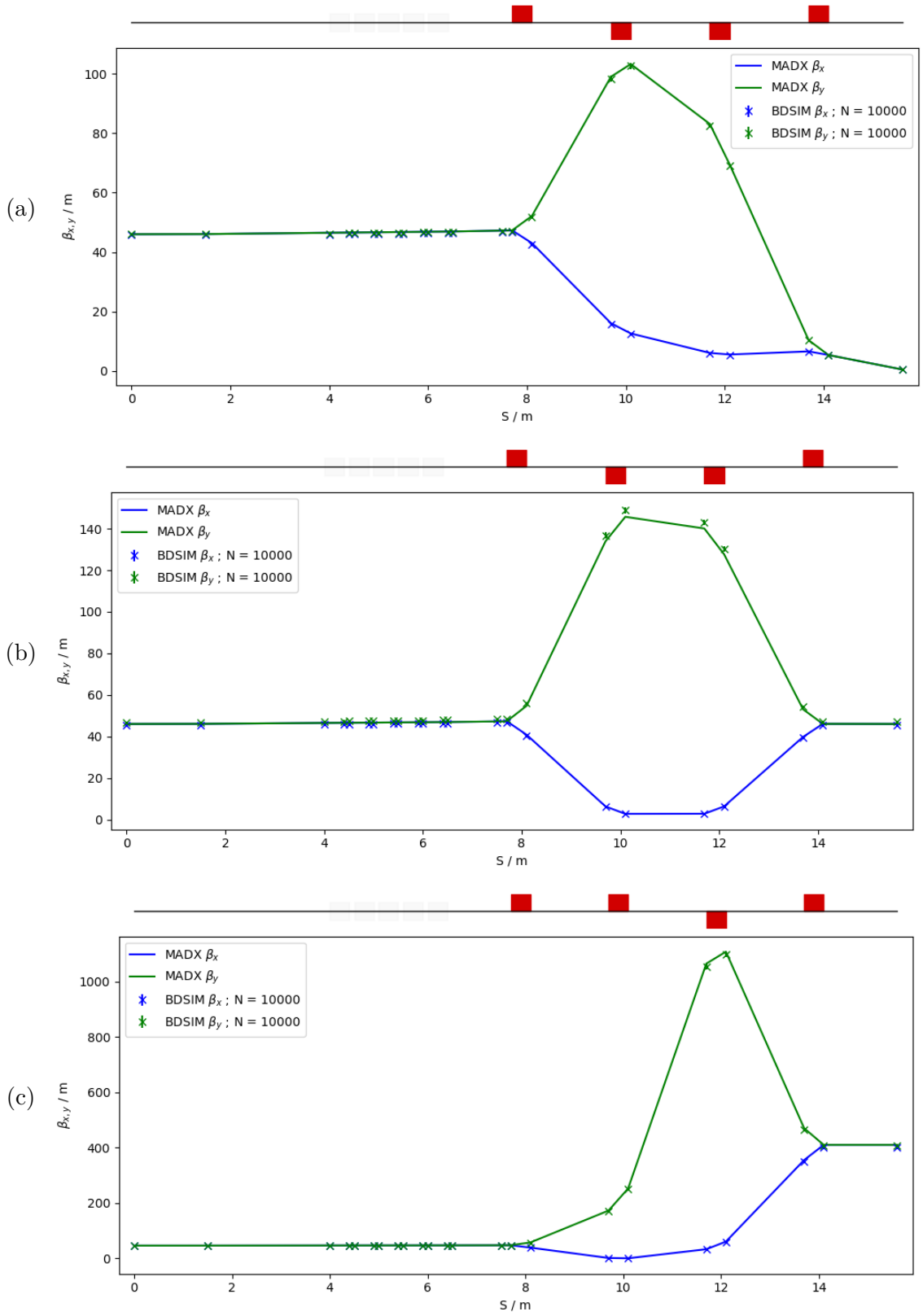

Figure 2.24: Comparison between MAD-X and BDSIM simulations of the Twiss β functions for the *in-vivo* beamline with a 127 MeV proton beam. The quadrupoles are matched to $\beta_{x,y} = 0.46\,\text{m}$ (a), $\beta_{x,y} = 46\,\text{m}$ (b), and $\beta_{x,y} = 410\,\text{m}$ (c), for 10^4 simulated particles.

by the magnet at radius r:

$$(BL) = r \int_{\theta_{\min}}^{\theta_{\max}} B_y d\theta \,; \tag{2.13}$$

where B_y is the vertical magnetic field. Since the field at r is constant, (BL) becomes:

$$(BL) = rB\Delta\theta \,; \tag{2.14}$$

and:

$$(BL)_0 = r_0 B_0 \Delta\theta \,; \tag{2.15}$$

where r_0 is the radius at which $B_y = B_0$, the main dipole field.

The field index, k, may be obtained by evaluating:

$$k = \frac{r}{\int_{\theta_{\min}}^{\theta_{\max}} B_y d\theta} \frac{\partial \int_{\theta_{\min}}^{\theta_{\max}} B_y d\theta}{\partial r} \,; \tag{2.16}$$

The FFA is required to deliver beams over a range of energies; this can be done by adjusting the value of B_0. Power and tune calculations were performed for acceleration of proton beams from 15 MeV to 127 MeV and from 6 MeV to 57 MeV.

The scaling magnetic field is generated using a main coil wrapped around the flat pole and 18 trim coils. A main coil generates the constant dipole field. The trim coils cross the pole face and return towards the outer radius. Powered with different currents, the trim coils generate the required field shape. The trim coil parameters are presented in table 2.17 together with an estimate of the total power required to deliver the various currents.

The configuration of the conductors surrounding the pole can be found in figure 2.25. The trim coils are wrapped in two different vertical layers, with a "0.5-coil" offset between the two layers; this has been shown to improve the field quality in studies conducted for the FFA magnet of the Front End Test Stand (FETS), which has similar properties [99]. The main coil is labelled "0" and has transverse dimensions $75 \times 95\,\mathrm{mm}^2$. The trim coils are labelled 1–18; each coil has transverse dimensions $10 \times 92.5\,\mathrm{mm}^2$.

3D model

A 3D model was created in `OPERA3D` (see figure 2.26) using the specifications given in table 2.13. The magnet is required to create the field profile that delivers a k-index value of 5.23. The `OPERA3D` model was used to optimise the currents in the main and trim coils and to evaluate the field quality. The result is shown in figure 2.27. The deviation of the field on the median

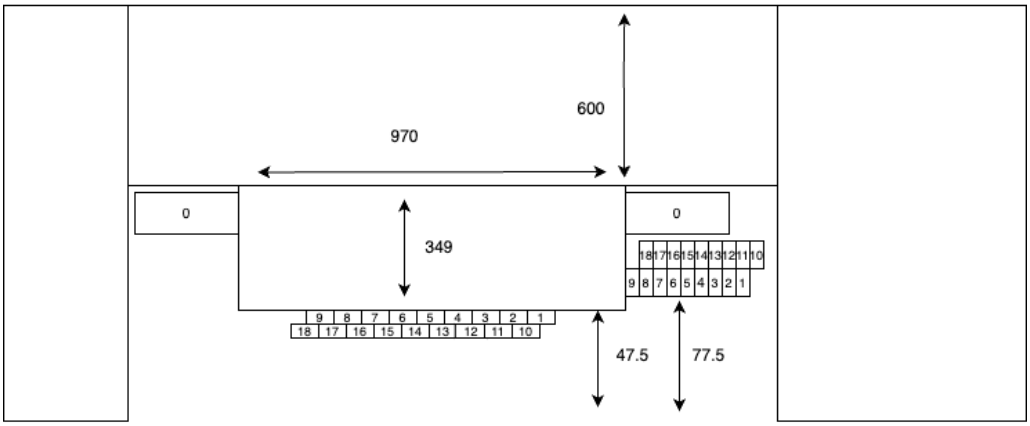

Figure 2.25: Schematic diagram of the cross-section of the FFA magnet. The dimensions of the magnet are labelled in millimetres, and the conductors are labelled from 0–18.

plane computed using OPERA3D from that obtained from the scaling law is within ±0.02% while the difference between the k-index derived from the OPERA3D field map lies within ±1% of the desired value. Field clamps were added to either side of the magnet to ensure that the extent of the fringe field scales with radius and the vertical tune, β_y, is controlled.

The 3D magnetic field map shown in figure 2.28 was used in the tracking code Fixfield [100] to evaluate the horizontal and vertical tunes. The vertical apertures of the clamps were then adjusted to minimise the vertical tune variation; the results are shown in figure 2.29.

The FFA is required to be capable of delivering beams over the energy range specified above. Therefore, the currents have also been optimised for $0.937 \times B_0$ T. This setting allows the acceleration of protons from 6 MeV to 57 MeV. The vertical aperture of the clamps was not changed since the aperture cannot be changed once the clamps have been manufactured. The tune of the beam over this energy range can be found in figure 2.30.

The crossing of low-order resonances during acceleration must be avoided to prevent uncontrolled beam loss. The evolution of the tunes was studied for both ranges of acceleration (15–127 MeV and 6–57 MeV). Figure 2.31 shows the evolution of the tunes in relation to the resonances up to fourth order; the results indicate that the tunes are sufficiently far away from the resonances. Further investigations are underway to decrease the tune spread in case it is necessary to allow a bigger margin of misalignment when manufacturing the magnets.

The dynamic aperture (DA) was determined by tracking through 100 turns at 25 MeV using the 3D field map. A kinetic energy of 25 MeV was chosen as the good field region of the magnets needs to be increased to incorporate the 15 MeV beam. This issue will be addressed. The results presented in figure 2.32 demonstrate that the DA is larger than the physical acceptance of the ring in both the horizontal and vertical plane.

2.5.2 Radio-frequency cavities for FFA

The fixed-field accelerator conceived for Stage 2 is required to deliver a momentum gain of a factor of three. The design parameters of the RF cavities for the acceleration of proton beams are given in table 2.18. The principal parameters are the frequency range of 2.89–6.48 MHz and the voltage-gain per turn of 4 kV. The frequency range will be adjusted for ion beams. Ferrite-loaded and magnetic-alloy-loaded cavities are being considered for the FFA cavity.

The RF cavity for the FETS-FFA [101], which has similar requirements to the LhARA FFA cavity, is being developed by the ISIS synchrotron RF group. Both ferrite cores and magnetic alloy cores are being considered, and measurements of material properties of prototype cores

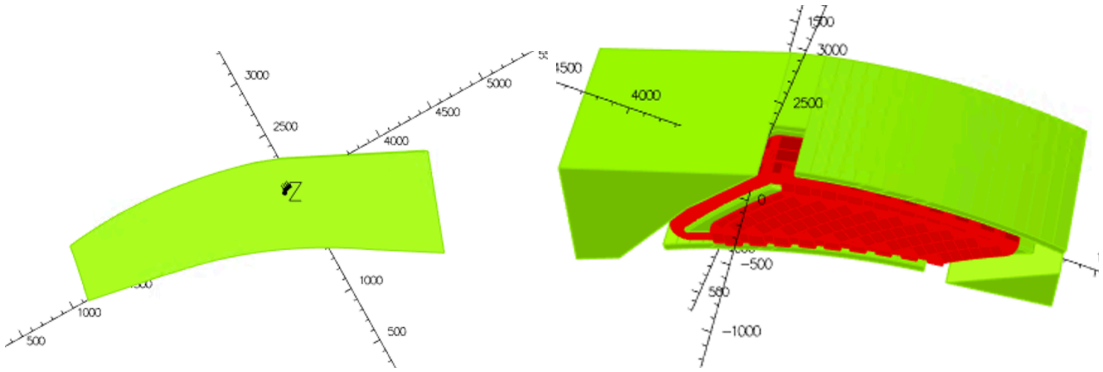

Figure 2.26: A OPERA3D model of the FFA magnet; only the top half of the magnet is shown. The conductors are shown in red with the iron in green. Left: View from above the magnet. Right: View of the magnet from the side. Axis dimensions are in mm.

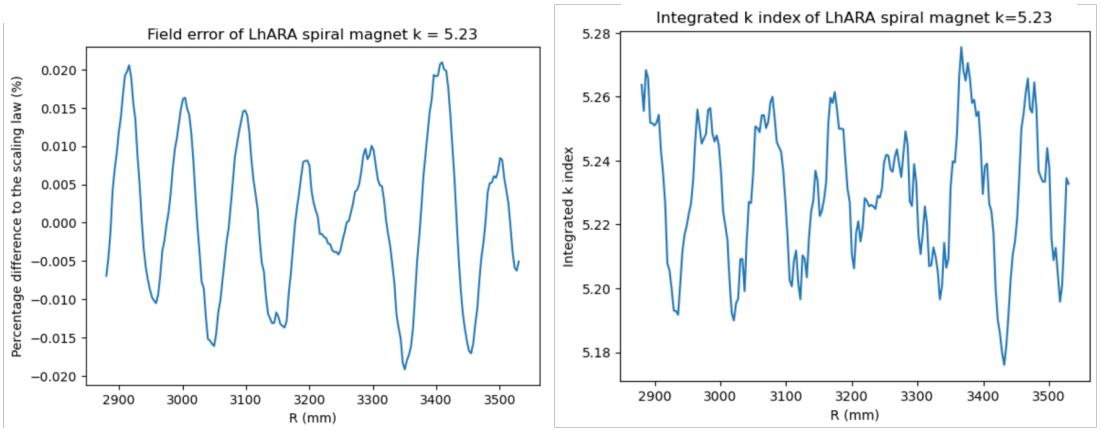

Figure 2.27: Field quality obtained from the OPERA3D model. Left: Difference between the integrated B_y in the model compared to the scaling law. Right: Difference between the k-index, calculated from the integrated B field obtained from the model, compared to the designed value of $k = 5.23$.

are in progress.

Ferrite-loaded cavity

Figure 2.33 shows a schematic diagram of a ferrite-loaded cavity. Details of the analysis of this device can be found in [102]. The bias current, I_{gen}, induces a magnetic field in the ferrite discs and is used to modulate the effective permeability, μ'_p. Variation of I_{gen} allows the resonant frequency to be swept over the required range.

The shunt impedance, R_p, of a ferrite cavity is given by [102]:

$$R_p = N\mu'_p Q f \ln\left(\frac{r_o}{r_i}\right)\mathcal{T}\,; \tag{2.17}$$

where N is the number of core rings, Q is the quality factor of the ring-core material, f is the frequency, $\mathcal{T}$ is the ring-core thickness, and r_i and r_o are the inner and outer radii of the ring cores, respectively. The term $\mu'_p Q f$ is often quoted by manufacturers and is presented for a variety of materials in figure 2.34. The cavity design requires that $\mu'_p Q f$ be measured over the required frequency range and under the anticipated range of operating conditions.

The operation of a ferrite-loaded cavity requires a bias-current power supply, an RF power-amplifier chain, and a low-level RF control system. The bias power supply must be capable of ramping the required current within the period of one acceleration cycle, thereby varying μ'_p.

Magnetic-alloy loaded cavity

Magnetic-alloy (MA) loaded cavities are similar to ferrite-loaded cavities in that they use an inductive core to give a relatively low resonant frequency. In the case of the MA cavity, the permeability and the saturation magnetic field are much higher than for the ferrite cores. This gives the cavity such a large bandwidth that there is no requirement to use a bias current to sweep the resonant frequency. This simplifies the power amplifier and low-level RF systems. However, since the cavity has a low Q value, the power dissipated in the cores will be higher, which will have an impact on the running cost of the cavity.

The metallic ribbon that forms the magnetic-alloy core is wound onto a former that creates the aperture of the cavity. An insulating layer is used to separate adjacent turns. After winding, the core undergoes either an annealing or a nano-crystallisation process. Figure 2.35(a) shows a schematic of the MA-core cavity for the FETS FFA, and figure 2.35(b) shows a photograph of

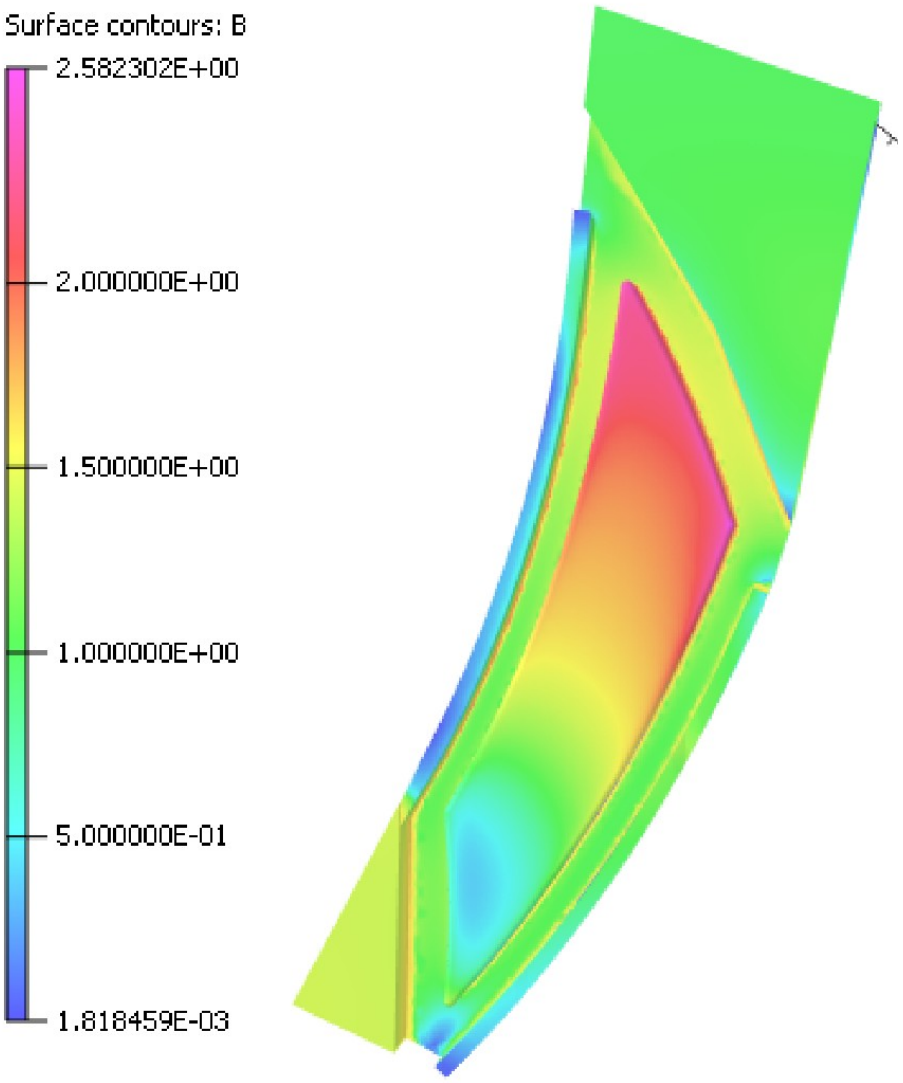

Figure 2.28: Magnetic flux density at the iron surfaces as calculated by `OPERA3D`. Fields can be seen to reach up to 2.66 T at larger radii, which is far into the saturation region. This has an impact on the tune of the beam, which can be corrected by adjusting the vertical apertures of the field clamps. The axis units are mm.

a prototype core purchased by the ISIS synchrotron group to measure the $\mu'_p Qf$ of the material.

Discussion

The ferrite-loaded option requires that the magnetic field in the cores stay below the saturation limit. The addition of more cores will result in a lower magnetic field within each core, but will also increase the length of the cavity. The space between the ring magnets, therefore, imposes a constraint on the number of cores that may be used. The development of a cost model for the cavities will require consideration of the bias power supply, the high-power RF system and the low-level RF system, as well as the estimated running cost.

Magnetic-alloy cores are more complex to manufacture than the ferrite cores and will require a specific QA procedure to ensure that the cores will maintain their performance over the operational period of the facility. Deformation of the MA cores has been observed in cavities operating at high power. This is not expected to be a problem for LhARA owing to the modest cavity gradient required.

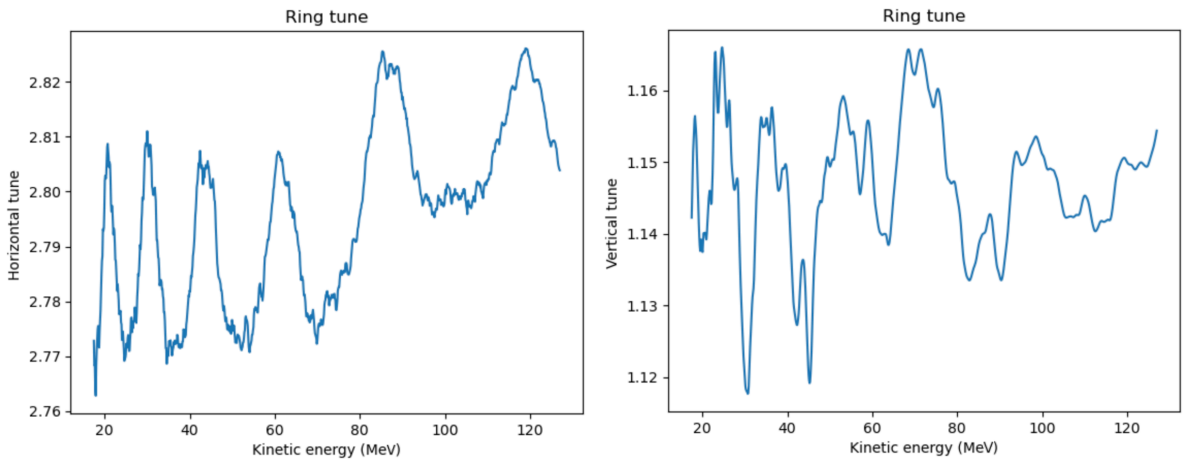

Figure 2.29: Horizontal (left) and vertical (right) tune of the beam (unitless) plotted against the kinetic energy after the currents and the aperture of the clamps have been separately optimised.

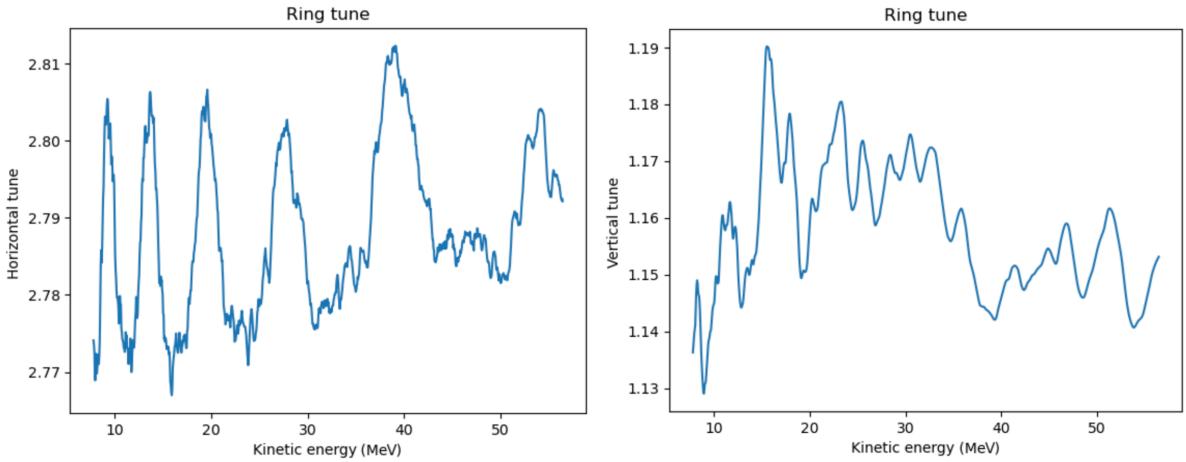

Figure 2.30: Horizontal (left) and vertical (right) tune of the beam (unitless) plotted against the kinetic energy of a range 6-57 MeV. The variation in horizontal tune is smaller compared to the previous case, as the magnet is no longer in the saturation region. However, the variation in vertical tune is larger as the clamp aperture was optimised for the energy range 15-127 MeV.

The limited space between adjacent magnets may require the cavities to be placed parallel to the spiral angle, see figure 2.17. The direction in which the beam crosses the gap between two adjacent magnets in a spiral scaling FFA varies during the acceleration cycle. As a result, it is not possible to arrange the cavity so that the electric field is parallel to the beam trajectory for all energies. This affects the rate of acceleration and induces low-amplitude oscillations in the beam trajectory in the transverse plane. As the rate of acceleration is very low in LhARA, and since the working point is away from low-order resonances, these oscillations are not expected to adversely impact beam quality.

2.5.3 Diagnostic systems

The laser-driven ion source creates a beam with short bunches, each containing a large instantaneous flux. The beam created at the target will have a large peak current, very low emittance,

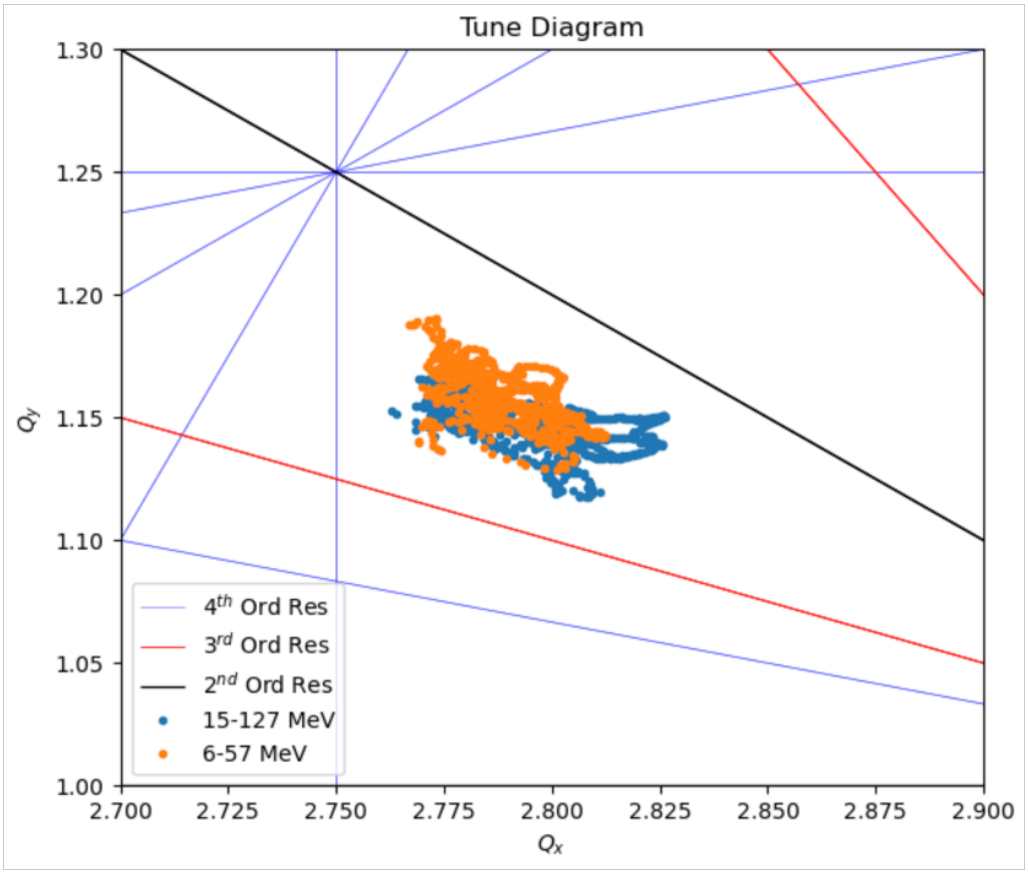

Figure 2.31: It can be seen that the tunes at different energy ranges overlap with one another. The variations in tunes are different, but both are sufficiently far away from any resonance up to the fourth order.

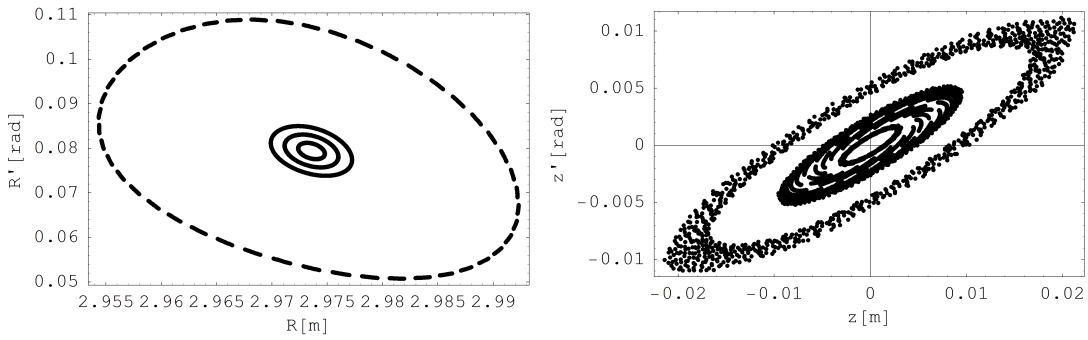

Figure 2.32: Dynamical acceptance study using 3D field map by tracking 100 turns at 25 MeV in [75]. 1σ, 2σ, 3σ, and limits (DA) are shown in both transverse planes, horizontal (left) and vertical (right). Some emittance growth in the vertical plane is visible and may be caused either by inaccurate interpolation or the proximity of a resonance. Note that 1σ emittance corresponds to $2.8\,\pi$ mm mrad.

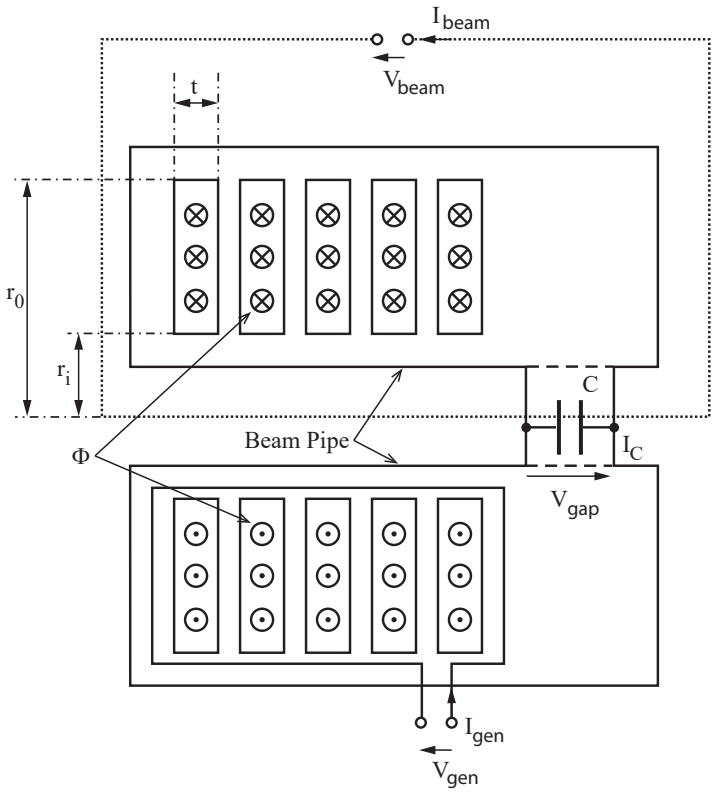

Figure 2.33: Simplified schematic diagram of a ferrite-loaded cavity, adapted from [102]. The current, I_{gen}, is used to excite the ions. The inner radius, r_i, outer radius, r_o, and thickness of the cores, $\mathcal{T}$, are indicated. The magnetic flux, ϕ, runs through the cores as shown. The beam propagates through the cavity from left to right. The capacitance, C, and current, I_C, with the cavity indicated.

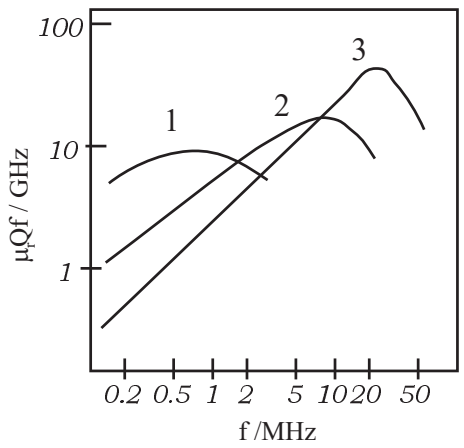

Figure 2.34: $\mu_p' Q f$ plotted as a function of frequency for three different types of ferrite material (1: Ferroxcube 4A, 2: Ferrox-cube 4C, 3: Ferroxcube 4E), adapted from [102].

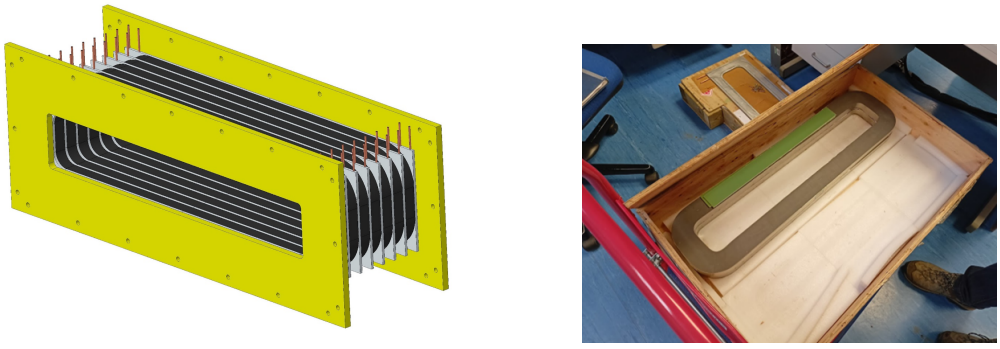

(a) (b)

Figure 2.35: An example magnetic alloy core cavity: (a) is a cavity schematic with cores shown in black and the vacuum flanges plates in yellow, (b) is a prototype core to be tested for the FETS FFA RF cavity.

high brightness, and very short bunch length, but the average current will be low. Emittance growth will occur as the beam propagates through the beamline, and some beam loss is expected. In the absence of phase rotation, the bunch length will also increase, from < 1 ns to the 7–10 ns range in Stage 1, and to tens of ns in Stage 2. The diagnostics required for commissioning and operation of the accelerator facility are discussed below.

Stage 1, FFA injection line to FFA and high-energy-beam transport lines

In Stage 1, the key parameters to be measured are the size of the beam, the beam position, and the beam current. The beam size and beam position can be measured using scintillating screens or secondary electron emission (SEM) grids. In each case, the diagnostic will need to be retracted when not in use. The beam current can be measured non-destructively using wall-current monitors (WCMs). The short bunch makes it likely that passive devices will be required. A similar set of devices will be needed in the FFA injection and extraction lines, and in the transport lines serving the high-energy *in-vitro* and *in-vivo* end stations. Precise measurement of bunch length will be challenging in Stage 1 due to the very short bunch. Bunch shape monitors with sub-ns resolution have been demonstrated [103, 104]. In the extraction line and the high-energy-beam transport lines, the bunch length will be longer, and it may be possible to use WCMs to measure the length of the bunch. Beam loss can be measured using monitors based on plastic scintillators. Such monitors will be placed in the vicinity of the beam pipe in the areas where beam loss is expected.

FFA

An in-depth study is required of the diagnostics necessary to ensure beam parameters can be measured accurately so that magnet, RF or other systems can be optimised and beam losses minimised. The results of a preliminary study of key systems are presented below.

The diagnostic requirements of the FFA are similar to those of a synchrotron of similar size. Synchrotrons are now sufficiently common that a common diagnostics toolkit exists [105]. Both the transverse cross-section of the beam aperture (see table 2.18) and the transverse excursion of the beam within that aperture are much larger in an FFA than in a comparable synchrotron. Some key systems from the synchrotron toolkit that must be adapted for use in an FFA include: beam-loss monitors, beam current monitors, and beam position monitors.

A primary beam particle is said to be lost when it is no longer contained within the acceptance region of either the longitudinal or transverse focusing system. Such a particle will usually collide with the vacuum vessel, generating a secondary shower of particles that can be

detected by a range of possible detectors [106]. Since beam losses in an FFA are not fundamentally different from beam losses in a synchrotron or a linac, detectors from these machines can be used in an FFA without any major modifications. For LhARA, it is necessary to verify that suitable detectors can be found for the low beam energy. Detection of beam losses from a proton beam with an energy between 10 MeV and 20 MeV has been demonstrated at JPARC with plastic scintillator and photomultiplier tubes [107]. This demonstrates that suitable detectors are available and that an appropriate beam-loss monitoring system is feasible. Future studies are needed to optimise the scintillator material and the placement of the monitors and to investigate the signal levels that can be obtained [108].

Beam position can be measured by means of intercepting diagnostics. Such devices are in use at accelerator facilities worldwide. Beam scrapers are fully destructive devices which can provide a measure of a beam's horizontal position when used in combination with a beam-loss monitor or current-sensitive diagnostic [109]. Such scrapers have been demonstrated at the KURRI proton FFA, with an injected beam energy of 11 MeV and an extraction energy of between 100 MeV and 150 MeV. The intensity of the KURRI machine of $\sim 3 \times 10^9$ protons [109] is comparable to that specified for the LhARA FFA. Intercepting wires can also be used to measure a beam's horizontal position and charge distribution. The use of such wires has been demonstrated using a 13.5 MeV proton beam on the KURRI FFA [108]. A peak signal amplitude of ~ 60 mV was obtained. The bunch charge of LhARA is expected to be lower than that of KURRI, making it necessary to consider amplifiers with higher gain. Amplifiers with fifty times the gain and a larger bandwidth than those used at KURRI are available commercially [110]. These observations indicate that intercepting-wire devices are also options for LhARA.

Beam current can be measured using fully destructive Faraday cups. These devices have been demonstrated for bunch charges an order of magnitude below that of LhARA [111], and at energies exceeding that of LhARA [112]. Beam current can also be measured using calibrated non-interceptive, electromagnetic pickups [113]. In principle, these devices are capable of measuring a range of beam parameters, including beam position and betatron tune. Such devices have been demonstrated on accelerators with a wide rectangular aperture [113, 114]. Position-sensitive variants are being investigated for the FETS-FFA [115]. The signal amplitude of a 20 mm long electrostatic beam-position monitor (BPM) for LhARA has been estimated to be ~ 20 mV before amplification. It is therefore reasonable to expect that electromagnetic pickups could be developed for use in the LhARA FFA; position-sensitive variants would need further development. This conclusion is supported by experimental measurements on the KURRI FFA, where post-amplification signal levels on the order of 1 V have been observed on a full-aperture electrostatic pickup. The relatively short bunch length at LhARA would make it vital to assess the impact of resonances on such devices; it is possible that technology such as button BPMs could be adopted.

An RF knock-out method has been developed [116] to measure horizontal tune on any orbit. This technique exploits the horizontal dispersion that causes oscillations to be induced when the beam is accelerated as it passes through the RF cavity. Vertical tune measurements will require a vertical exciter, which may be magnetic or electrostatic. The measurement of betatron tunes may be made using the "Base-Band Q" (BBQ) technique with direct diode detection [117], which allows the measurement of betatron tunes without any external excitation. This method has not yet been demonstrated using an FFA.

2.5.4 Injection and extraction systems for FFA ring

A full aperture, fast injection of the beam will be performed using a magnetic septum, installed on the inner radius of the ring. As shown in figure 2.17, the septum will be followed by a kicker magnet situated in the next lattice cell.

The specification requires that a flux of approximately 10^9 protons be accepted by the ring. The beam at injection (see table 2.19) has a relatively small emittance and short bunch length. Therefore, it is anticipated that space-charge effects will be severe immediately after injection, but will become more relaxed quickly due to debunching during acceleration.

Fast extraction of the beam over the full aperture will be performed using a kicker magnet, followed by a magnetic septum installed in the lattice cell immediately following the cell accommodating the extraction kicker. The extraction kicker will bend the beam outside of the ring as shown in figure 2.17. Table 2.20 summarises the parameters of the injection and extraction elements.

2.5.5 Control and Feedback Systems

The LhARA control system will be a facility-wide monitoring and control system integrating the control of all parts of the facility. The control system will extend from the interface of the equipment being controlled through to the operator, engineering expert, physicist and end-station user. It will include all hardware and software between these bounds, including computer systems, networking, hardware interfaces, programmable logic controllers (PLCs) and field-buses.

The Personnel Safety System (PSS) will be interfaced to, and monitored by, the control system. A separate event-synchronisation system will be implemented as part of the control system to ensure synchronisation of technical sub-systems and critical control operations, and will also provide a common high-resolution time-stamping and/or pulse-numbering capability.

The control system will benefit from existing control-system-equipment standards and knowledge gained from recently implemented ASTeC Radiation Test Facilities, e.g. CLARA. Consideration of technological advancement, e.g. new, more appropriate field-buses or protocols, will continue.

Architecture

The control system will be implemented using the `EPICS` software toolkit. `EPICS` is a proven software toolkit with well-defined interfaces at both the client and server and will enable fast integration and development. The choice of `EPICS` enables the project to take advantage of work done at other laboratories. `EPICS` has been successfully applied on previous projects at STFC, including the ALICE, CLARA, EMMA, ISIS and VELA facilities and on many accelerator projects worldwide. For previous projects, extensive use has been made of `EPICS` Version 3 and more recently `EPICS` Version 7. For LhARA, it will be possible to deploy Version 7 or later and to use the advanced features exposed via the process-variable access (`pvAccess`) protocol, including manipulation and transport of structured data over the network.

The various components of the control system will be connected to a high-speed Ethernet local area network. This will consist of several class C subnets connected to the main site network. Access will be provided to the control system data via `EPICS` gateway systems running access security.

The hardware interface layer of the control system will provide the connection to the underlying subsystems. This will consist of a modular hardware solution of commercial rack-mounted PCs and embedded systems running the Linux operating system, connected to a range of I/O types directly or via selected field buses.

Application software will be installed on central file servers to ensure consistent operation from any console on the control-system network. The control system will be implemented in such a way that it can be expanded and upgraded incrementally as the project proceeds. The control system must be able to be extended to new hardware and software technology. A number of `EPICS` client interfaces will be supported for controls and user application development in high-level languages. This is likely to include both Channel Access and `pvAccess` interfaces

for languages such as `C++/VB` via `.NET`, `Matlab`, `Mathematica` and `Python`.

Controls hardware
The network hardware and commercial PC hardware of the control system will use standards defined by the STFC Digital Infrastructure Department. As far as possible, controls hardware used on recent ASTeC Radiation Test Facilities (RTFs) should be preferred to take advantage of existing expertise and proven hardware standards. This hardware includes:

- *Industrial rack mount PC systems running a Linux operating system, with potential for a real-time kernel, as required*: Existing `EPICS` support is available for interfacing many I/O types, including analogue, digital and serial (RS232/422/485) along with status/interlocking via Ethernet-connected Programmable Logic Controllers;
- *Omron NJ series PLCs*: Status and interlock systems for digital control and machine protection of accelerator hardware and sub-systems. As a replacement for Omron CJ series PLCs deployed on previous ASTeC RTFs, the NJ PLCs will either be integrated directly into the `EPICS` control system using the CIP protocol, or indirectly via a data aggregation tool with EPICS integration via OPC-UA or similar. This will allow PLC data tags to be directly mapped to `EPICS` process variables and/or to `pvAccess` structured data types; and
- *Motion control systems*: Field-bus based systems with remote I/O via EtherCAT. In common with CLARA and building on this experience, these will comprise Beckhoff TwinCAT real-time controllers with EtherCAT-connected motion control and I/O modules. These controllers interface with the `EPICS` control system via Modbus TCP.

Any specialist control requirements will be addressed using dedicated real-time controllers (for example, embedded industrial or FPGA-based hardware). Examples of such systems could include geographically isolated devices or systems that require the computing speed of a dedicated CPU. Any dedicated controllers would be integrated into the `EPICS` environment and software-build processes.

Due to the pulsed nature of the facility, dedicated real-time systems will be required. Likely applications include data acquisition for beam diagnostic measurements or RF system measurements. For previous ASTeC RTF control systems, VMEbus processors and FPGA-based I/O carriers have been used. It is expected that the modular, open standard MicroTCA protocol will be adopted as a replacement for VMEbus. Options for embedded MicroTCA controllers and FPGA carriers will be evaluated further in the Technical Design phase.

Virtualisation
Virtualisation technology will be used both in the server infrastructure layer and, where appropriate, in the EPICS input/output controllers. This will increase flexibility, scalability, reliability and efficiency of the control system by abstracting hardware specifics from the controls software.

Timing and synchronisation system
One of the principal challenges with a network-distributed control system is the synchronisation and accurate time-stamping or pulse numbering of events spread across several physically and logically separated systems. An example of this is the simultaneous measurement of beam diagnostic information along an entire beam transport system. This operation will typically involve collecting beam-synchronous data simultaneously from a number of front-end server systems. Commercially available synchronisation hardware, as used on CLARA, is available for a number of platforms and provides timing outputs for LhARA applications. It will be important to ensure that the master clock used by the timing system is locked to the RF and laser systems. GPS atomic clock synchronisation will be used to distribute an accurate time-stamp via the

timing system, and can also be used to discipline the RF master oscillator.

Interlock systems
The control system will provide a comprehensive interlock and machine protection system ranging from the enforcement of operating limits to the protection of the facility against potentially dangerous operating conditions. The interlock system may be defined using two classes of systems:

High Integrity system: will be used to provide high-speed and fail-safe local protection in situations where serious damage to equipment is likely to occur if fault conditions are allowed to develop. Embedded micro-controllers could be used for this purpose; and

Routine system: is intended to prevent faults causing minor damage to individual machine components or sub-systems. An Omron PLC-based interlock system, based on experience at other facilities, will be used for this purpose.

Both interlock systems will operate independently of `EPICS` with monitoring and control requests marshalled to the interlock systems via `EPICS` for processing via programmed logic. There will also be local systems that supervise individual components, such as RF structures. These systems are not described here.

Personnel Safety System
Personnel safety must be ensured using a *Personnel Safety System* (PSS). This section does not cover details of the protection of personnel from facility hazards. In terms of logic implementation, the PSS would be implemented using Omron safety controllers. The NX controllers make use of Ethernet-based safety protocols and are more suited to a new facility, easing installation and enabling greater scalability and flexibility. Full monitoring of the PSS will be provided through the control system.

Feedback systems
Digital feedback will be required in a number of places. The primary requirements include closed-loop control of amplitude and phase in RF systems as well as water cooling for high-power RF infrastructure and accelerating cavities.

Slow feedback and control, e.g. for water temperature stabilisation, can either be implemented in the commercially-supplied system, or within the control system via PLC or `EPICS` PID control. Ideally, the use of commercial systems should be limited to those that support integration into the control system to allow remote monitoring and control.

For faster, lower-latency feedback and control, direct integration into the control system is required. RF amplitude/phase control will be achieved either by embedding the control directly into the FPGA of the low-level RF (LLRF) controller or using dedicated software directly on the CPU of the LLRF controller. Options for embedded feedback control will be evaluated further in the Technical Design phase.

High-level application software
During operation, high-level applications are required that will communicate via the control system. A mid-level interface is required to abstract the detailed implementation of devices in the control system. This will allow operators and users to interact with sub-systems and devices in a consistent, structured and well-defined way. Options developed and used previously include common C++/Python mid-level interfaces to the control system, CATAP: 'Controls Abstraction To Accelerator Physics'. The `pvAccess` interface using `EPICS` Version 7 or higher will be used to represent sub-systems and devices as consistent, structured data for direct consumption by high-level application software.

2.5.6 Vacuum system

The vacuum system will require several different vacuum regions with a variety of requirements and specifications. The first key area is the target chamber where ions are produced, and there is a significant gas load. This is then directly coupled into the low-energy beamline with Gabor lenses, where performance needs to be optimised to avoid degrading the properties of the plasmas. The high-energy line requires a similar level of vacuum to the low-energy line, whereas the fixed-field accelerator, due to particles recirculating, will require a higher vacuum. The laser system will have a vacuum requirement to maintain beam quality and reduce scattering. The make-up of the end stations is currently unknown, but may require a vacuum. Finally, RF waveguides may be needed where a vacuum system should be used over the more conventional SF_6 gas-filled waveguides because of the negative environmental impact of SF_6.

The currently -assumed vacuum levels are presented in table 2.21 and are based on accelerator-design experience. These values need to be confirmed by simulating the effect of residual gas on beam propagation. Vacuum modelling will then be required to ascertain where vacuum pumps should be placed.

The vacuum system requirements fall comfortably in the ultra-high vacuum region, and therefore, the general design principles for this vacuum regime will be adopted. The Vacuum Quality Assurance Documents developed at Daresbury Laboratory, for modern accelerator applications, provide a good example of design principles that can be adopted.

Vacuum technology

In general, the vacuum system design of LhARA is based on well-tried and well-understood design principles. The machine will be split into vacuum regions separated by gate valves for practical reasons and for machine protection. Dividing the machine into discrete vacuum regions makes it easier to install and commission, whilst at the same time simplifying maintenance and breakdown interventions. In most circumstances, gate valves will be metal. Roughing valves (right-angled valves) will be located in each vacuum region for ease of maintenance.

It is expected that the laser systems and transport lines up to the target chamber, where there could be a gas load from ion production, will be at a lower vacuum specification of 1×10^{-6} mbar. This can use ISO-KF flanges pumped continuously by turbo pumps and dry backing pumps to handle the gas load and achieve the desired working pressures.

It is assumed the beamline requires a higher vacuum specification to maintain beam quality, with the FFA requiring the highest specification due to circulating particles. This area of the accelerator will use ConFlat™ Flange (CF) as the most common type of flange connection for ultra-high vacuum systems and the knife-edge principle to achieve an all-metal vacuum seal. Vacuum will be achieved using pumping carts, a combination of turbo-molecular pumps backed by scroll pumps, to remove gas quickly from the section. Ion pumps with optional NEG (non-evaporable getter) cartridges will then be used for maintaining vacuum during normal operations. Since ion pumps do not have moving parts, they do no introduce vibrations into the system. NEG cartridge pumps, once activated, have the ability to pump without electrical power and may be a useful addition to reduce energy demand.

All vacuum components will undergo a full UHV solvent cleaning procedure to remove contamination before installation. The beamline components will also undergo an ex-situ vacuum bake to 250 C for 24 hours before installation, with a residual gas analysis scan to verify vacuum cleanliness. This will reduce contaminants and surface outgassing and enabling the design pressure of 1×10^{-8} mbar to be reached. To reach the highest vacuum specification envisaged for the FFA and the injection and extraction lines, an *in-situ* bake may be required to reduce the outgassing further.

The low-energy beamline is approximately 26 m of beam pipe with a number of chambers for screen diagnostics and Gabor lenses. Predominantly, this needs to be held at a base pressure of 1×10^{-8} mbar, and will need 19 ion pumps each with 500 l/s pumping speed.

The injection and extraction lines serving the FFA have a total length of 29 m and requiring a further 13 ion pumps. The FFA itself requires a higher specification of vacuum down to around 1×10^{-9} mbar. To achieve such a low pressure with the vessel surface area prepared in the same way as the other beamline sections, 120 ion pumps would be required. Therefore, the FFA vacuum system needs to be baked *in situ*, ideally to over 150 C. This baking would drop the outgassing of the surface considerably, and consequently, the required number of ion pumps would fall to 10.

The high-energy line transfer line provides a further 20 m of beamline, at a similar specification to the low-energy line, and requires 10 ion pumps each of 500 l/s pumping speed.

Vacuum will be achieved using pumping carts, a combination of turbo-molecular pumps backed by scroll pumps, to remove gas quickly from the section. Ion pumps with optional NEG (non-evaporable getter) cartridges will then be used for maintaining vacuum during normal operations. The laser transport lines, target chamber and differential pumping will use turbo-molecular pumps backed by scroll pumps to achieve the desired working pressures.

The vacuum system will be equipped with the relevant diagnostic instrumentation in each section, vacuum gauges (Pirani and Inverted Magnetron) and residual gas analysis. This allows the environment to be monitored, analysed and problem-solving to be carried out when required. The vacuum system will be linked to the controls system for monitoring and to enable machine protection. Interlocks between sections will be used to prevent accidental venting of the machine or catastrophic failure; these will be driven by the diagnostic instrumentation. The control system should have a 'standby' mode, that allows the controlled reduction of the number of running pumps and controllers. In conjunction with the use of NEG pumps, this will allow the electrical power demand to be reduced.

The control system should also be enabled with a 'standby' mode, allowing the controlled reduction of running pumps and controllers. In conjunction with NEG this allows the electrical power demand to be reduced, impacting the CO2 production and running costs.

Initial concept modelling

The mechanical layout and lattice of the accelerator were used to obtain an estimate of the internal surface area of the vacuum vessel. This allows the pumping capacity to achieve the specified vacuum to be calculated. It was assumed that the vessel will predominantly be made of stainless steel and that the vessel will be processed ex-situ. Therefore, the material outgassing figure for stainless steel was used in the vacuum calculations. The beam pipe was assumed to be 100 mm in diameter and to include vessels for installation of diagnostic screens.

The diameter of the Gabor lenses are 250 mm, larger than the assumed beam pipe. The cylindrical surface area of the internal electrodes increases the effective surface area. Each Gabor lens vessel alone requires 1000 l/s of pumping to overcome the outgassing of the surfaces of the lens. This is best achieved by 2 large (500 l/s) ion pumps, one at each end. The first Gabor lens, being twice as long, will require a special case with pumping in the centre to achieve the vacuum specification.

Modelling

A number of iterations of machine layout and calculation of pressure distributions will be required before a satisfactory final scheme of vacuum pumping can be determined. Two areas have been highlighted as challenging from a vacuum perspective and require further investigation to understand whether the design concept will work.

The first is the vacuum connection of the target chamber to the low-energy beam line due to different operating pressures of 10^{-8} and 10^{-6} mbar. The calculation of the conductance of the nozzle between the two will give an understanding of the impact on the vacuum from connecting these two volumes. The nozzle diameter can be optimised between ion beam diameter requirements and vacuum specification. The gas produced from the film target and its trajectory

is unknown and could have an impact on the overall design due to the beaming effect.

The second challenge is the ability to pump the first Gabor lens, as there is a requirement to site it as close to the ion source as possible, leaving little room for a vacuum pump. As the target is a gas source, there will be a higher pressure at one end of the Gabor lens than the other, potentially detrimental to the operation of the lens. Modelling needs to be done to understand the pressure profile in this area. The mechanical design needs to be further understood in this area to enable the inclusion of pumping ports to achieve the Gabor lens operating pressure.

Nozzle conductance

Initial modelling has been carried out on the nozzle between the target chamber and the first Gabor lens. There is a requirement to have a minimum of 2 orders of magnitude pressure difference between the target chamber and the Gabor lens for successful operations. Figure 2.36 shows an engineering image of the Target Chamber and the Gabor Lens, whilst Figure 2.37 provides a closer look at the target and a restrictive nozzle aperture to help minimise the pressure increase between the two chambers during ion beam generation.

Monte-Carlo modelling of target chamber and Gabor lens

The first two vacuum chambers of LhARA were modelled using the computer code Molflow+ [118–120]. which is based on the Monte-Carlo method. Monte-Carlo simulations can be performed only for a closed volume; therefore, the pumping ports are closed by virtual surfaces with the following properties:

1. Gas desorption or gas injection is described by a desorption coefficient; and

2. Pumping is described in terms of the surface area, A, and a sticking probability (or capture factor), a. $a = 0$ corresponds to no pumping speed and $a = 1$ corresponds to an ideal pumping speed (a “black hole”).

Figure 2.38 and 2.39 show the vacuum model of the target chamber and Gabor Lens as set up in the Molflow+ program. It consists of a closed vacuum system starting at the entrance to the target chamber and finishing at the end of the Gabor lens. Figure 2.38 shows a number

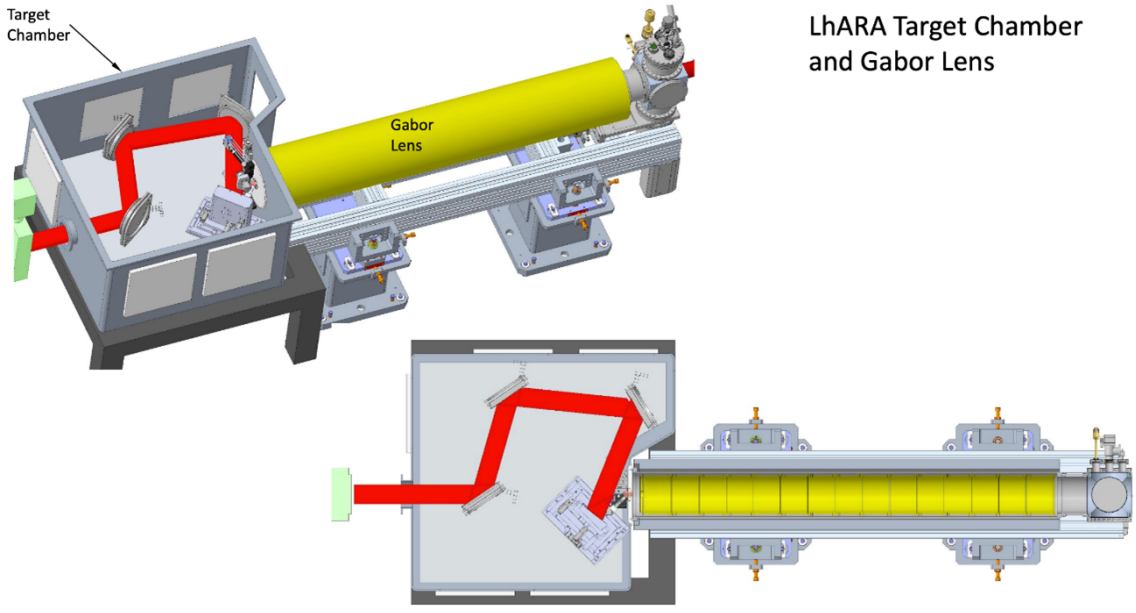

Figure 2.36: Layout of the LhARA target chamber and first Gabor lens.

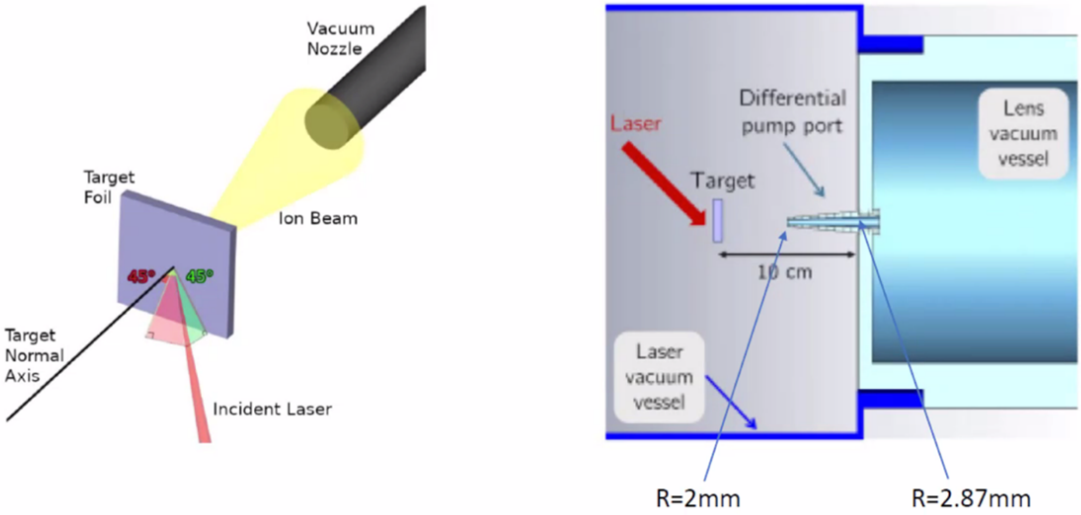

Figure 2.37: Close-up depiction of the target chamber, with restrictive aperture before the Gabor lens.

of different views of the target chamber and Gabor lens in the Molflow+ program. Figure 2.39 shows a close-up image of how the restrictive aperture separates the target chamber from the Gabor lens; it also shows a number of red facets along the structure. These facets were used as a way to calculate the transmission probability of gas molecules along the structure. The transmission probability is the probability of a gas molecule getting from position 'A' to position 'B', 'C' and so on along the structure.

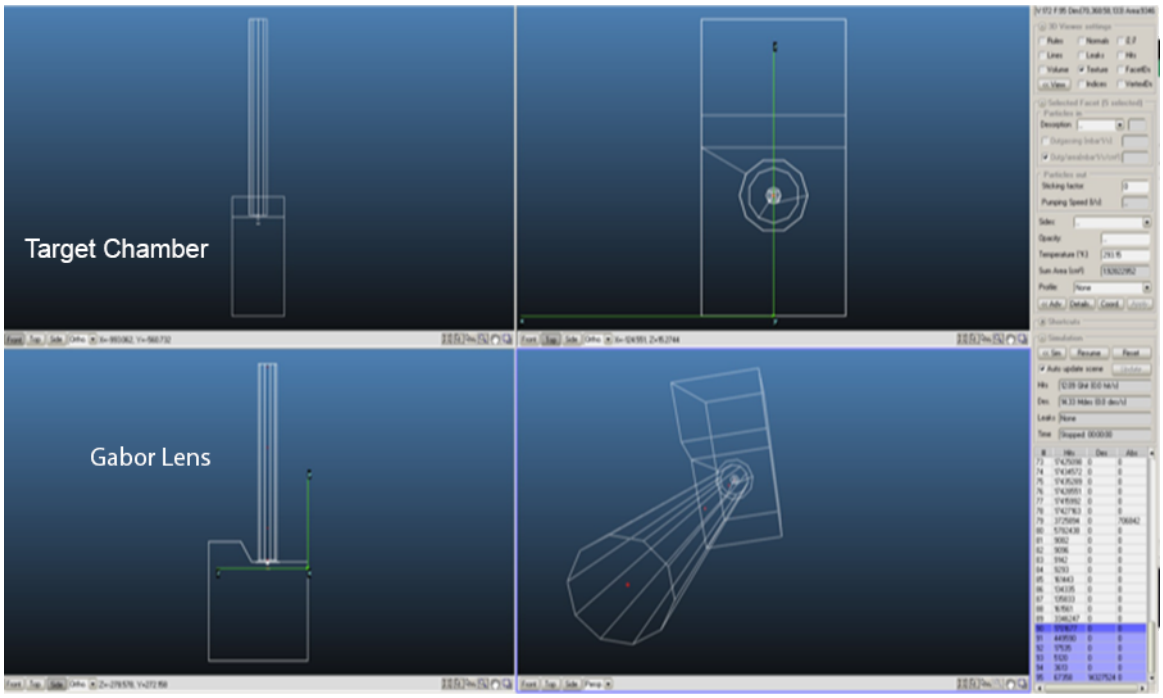

Figure 2.38: Target chamber and Gabor Lens in the Molflow+ program.

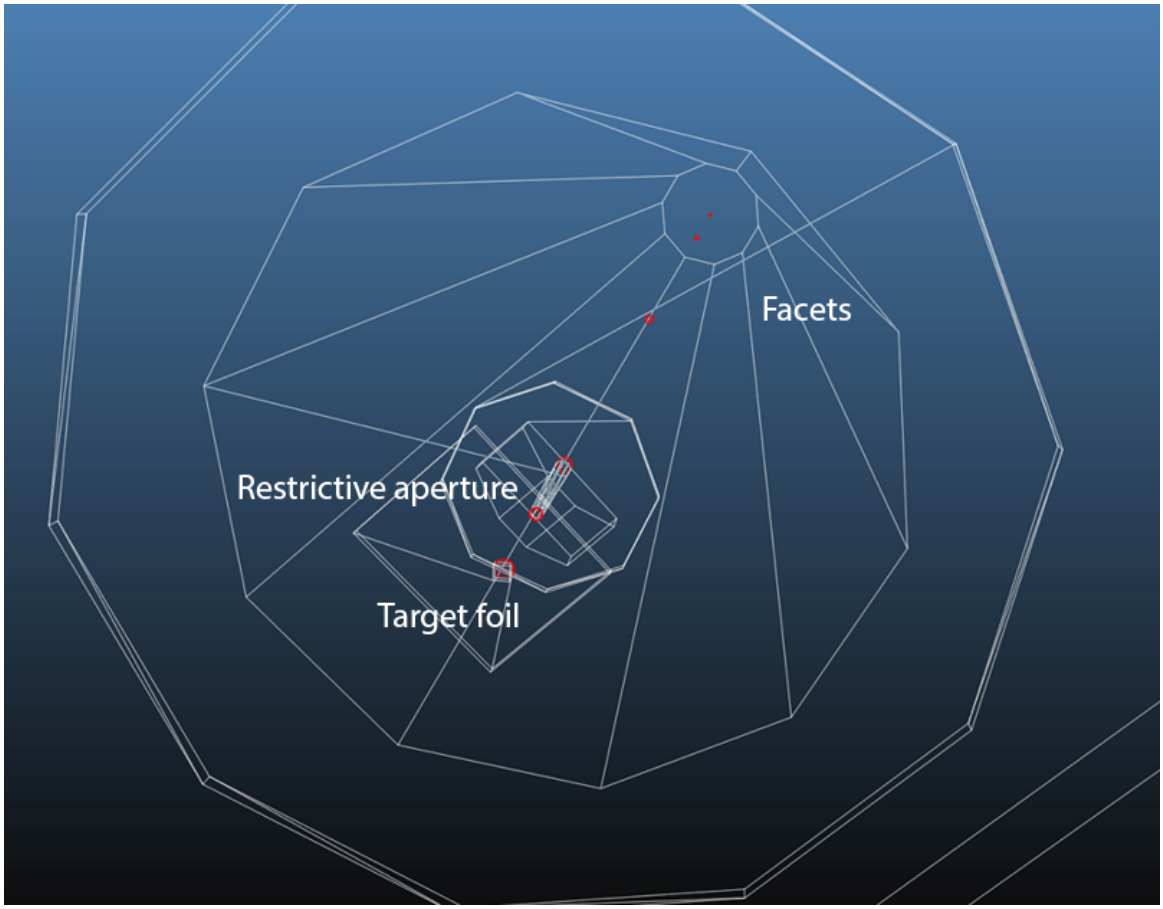

Figure 2.39: Target chamber and Gabor lens in the Molflow+ program.

This study provided a first evalution of the suitability of the vacuum design. The vacuum requirements for first two volumes of the LhARA vacuum system are:

1. Target chamber: 5×10^{-6} mbar; and
2. Gabor lens: 5×10^{-8} mbar.

One of the best ways to consider the effectiveness of a restrictive aperture or differential pumping system is to consider the transmission probability in conjunction with a pressure profile along the structure.

The transmission probability, w, was calculated using the equation:

$$w = \frac{\mathrm{MHit}_j}{N}; \tag{2.18}$$

MHit_j is the number of hits on the j-th facet, and N is the number of generated molecules. Pressure, P, is calculated by evaluating the expression:

$$P = 4\frac{Q\mathrm{MHit}_j}{NA_j v}k_B T; \tag{2.19}$$

where Q is the outgassing rate, A_j is the area of the j-th facet, v is mean molecular velocity, k_B is Boltzman's constant and T is the temperature. Pressure is directly proportional to transmission probability. The results of the simulations for the transmission probability of molecules generated at the target foil and propagated along the beam line and into the Gabor Lens. Table 2.22 below shows the results of the transmission probability.

he requirement of a pressure differential of two orders of magnitude between the target vessel and the Gabor lens implies that the transmission probability must satisfy value of < 0.01 at the exit of the restrictive aperture (the nozzle). There are four result columns in table 2.22. The different columns present the transmission probabilities obtained using different desorption profiles generated at the target foil. In Molflow+, the standard desorption profile from a surface or facet has a cosine profile:

1. Cosine desorption: corresponds to a Lambertian radiator where the probability of the angle of radiation is proportional to the cosine of that angle. This means that particles are more prone to leave a facet perpendicular to the surface.

2. CosineN (CosN) desorption: The same as above, but, the probability is proportional to a chosen power of the cosine of the angle; the higher the exponent is, the greater will be the tendency for the net gas flow to be perpendicular to the surface.

Results are shown for cosine desorption (i.e. CosN=1) and CosN=2, 10, and 100. The transmission probability results meet the requirement $w < 0.01$ in the first three columns (CosN=1, 2 and 10). However, for CosN=100 the transmission probability does not meet the requirement.

The higher the exponent in the CosineN desoption, the greater the 'beaming' effect is in the simulations. For LhARA, it is not anticipated that the 'beaming' effect will be dominant because it is expected that the ion beam generated is likely to have a conventional expansion profile typical of the Cosine desorption profile described above. Therefore, it is reasonable to expect that the current restrictive aperture design that separates the target and Gabor lens will be able to maintain the two orders of magnitude pressure differential the facility specification requires.

To verify the transmission probability results, the Molflow+ program was used to generate a pressure profile from the target to the Gabor lens. A CosN=2 desorption profile was used to generate the pressure profile; the results are therefore expected to match the CosN=2 transmission probability results shown in table 2.22. Figure 2.40 shows the pressure profile facet in the Molflow+ program, and figure 2.41 shows the pressure profile result along the target and Gabor lens chambers. Figure 2.41 shows that the pressure differential between the target chamber and the Gabor lens is more than two orders of magnitude as specified by the facility specification.

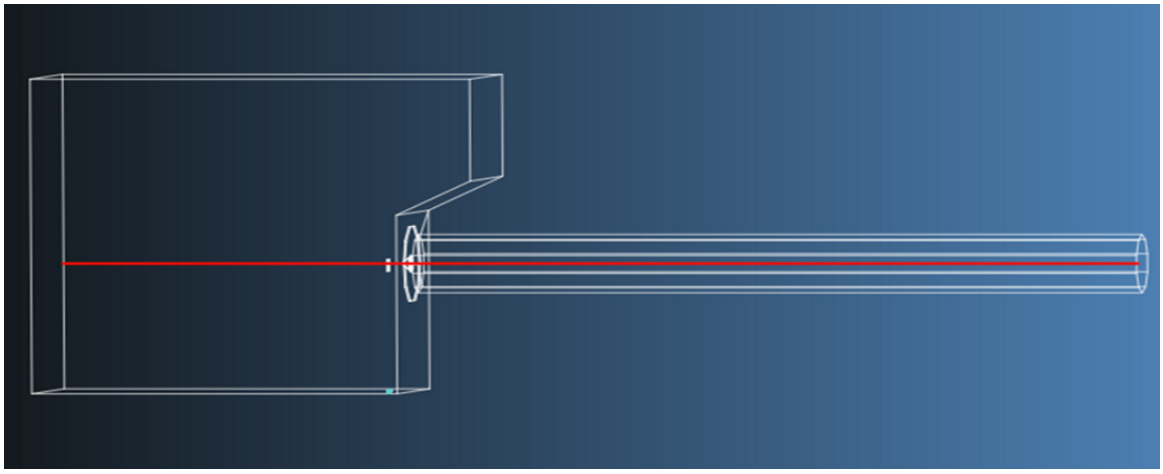

Figure 2.40: Pressure profile facet shown in the Molflow+ program.

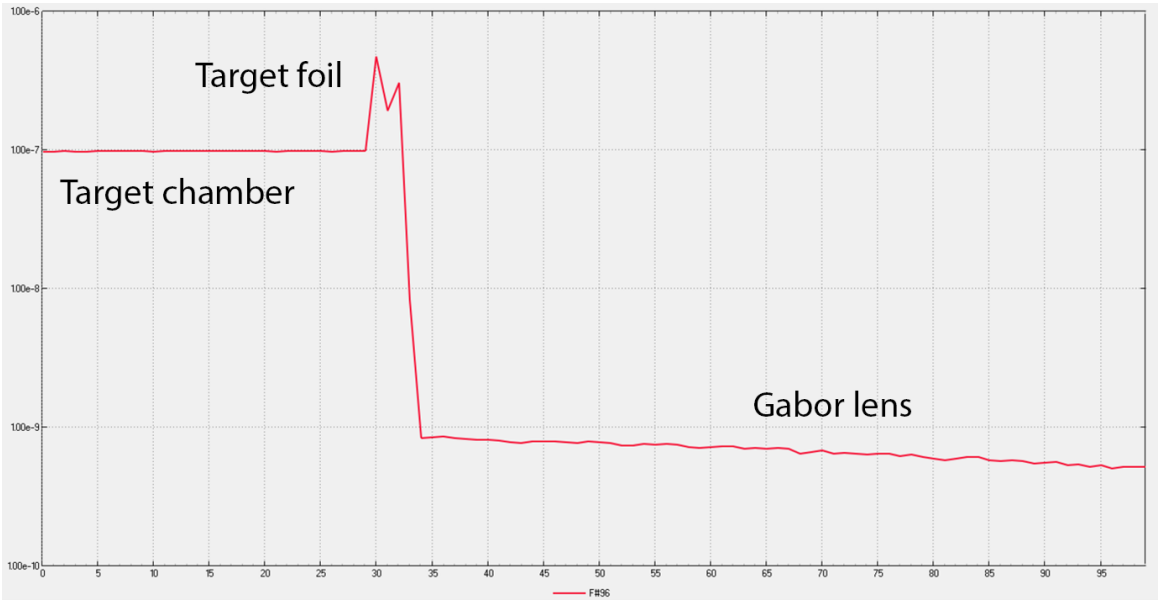

Figure 2.41: Pressure profile result.

Table 2.1: Key parameters of LhARA Stage 1, depicted in figure 2.1. Parameters include the capacities/quantities (with units) of the laser source, the capture section components and the beam transport components.

Parameter	Value / Range	Unit
Laser Parameters		
Central wavelength	800	nm
Energy after amplifier	>18	J
Energy stability (shot to shot)	<2	%
Energy stability (over 12 hours)	<5	%
Pulse length (FWHM)	<50	fs
Pulse length stability	<5	%
Rep. rate	10 (100)	Hz
Contrast at 5 ps	10^{-8}	
Contrast at 10 ps	10^{-9}	
Contrast at 100 ps	10^{-10}	
Laser Delivery Parameters		
Peak power	100	TW
Energy on target	> 10	J
Strehl ratio (measured)	> 0.5	
Angle of incidence	30	degrees
Focal intensity	9×10^{18}	$\mathrm{W/mm^{-2}}$
Proton Energy	15	MeV
Ion Energy	4	MeV/u
Proton and Ion Capture		
Beam divergence at design energy	11	degrees
Gabor lens effective length	857	mm
Gabor lens physical length	1157	mm
Cathode radius	36.5	mm
Maximum voltage	65	kV
Number of Gabor lenses	2	
Alternative technologies: solenoid length	1157	mm
Alternative technologies: solenoid max field	1.4	T
Stage 1 Beam Transport		
Number of Gabor lenses	5	
Number of re-bunching cavities	2	
Number of collimators	2	
Arc total bending angle	90	degrees
Number of bending magnets	2	
Maximum dipole field	0.55	T
Number of quadrupole magnets	6	
Maximum quadrupole field	0.65	T
Number of octupole magnets	1	
Beam pipe aperture radius	36.5	mm

Table 2.2: Beam parameters at the nozzle exit, 100 mm downstream of the target. This parameterised beam was modelled using one million protons with kinetic energies of 15 MeV ±2% and an envelope angular divergence of 11°.

Parameter	Value	Unit
α_x	-355	
α_y	-356	
β_x	35.35	m
β_y	35.51	m
ϵ_x	5.91×10^{-8}	m rad
ϵ_y	5.87×10^{-8}	m rad

Table 2.3: Transmission efficiency of the parameterised beam through the target housing vacuum nozzle. One million protons were simulated with kinetic energies of 15 MeV ±2% and an envelope angular divergence of 11°.

Location	Transmission (%)
Target exit	100
Nozzle entrance	7.9
Nozzle exit	4.1

Table 2.4: Beam parameters at the nozzle exit, 100 mm downstream of the target, with an envelope angular divergence reduced to 2.75°. This parameterised beam was modelled with one million protons with kinetic energies of 15 MeV ±2%.

Parameter	Value	Unit
α_x	-342	
α_y	-342	
β_x	33.89	m
β_y	33.93	m
ϵ_x	5.77×10^{-8}	m rad
ϵ_y	5.75×10^{-8}	m rad

Table 2.5: Transmission efficiency of the parameterised beam through the target housing vacuum nozzle. One million protons were simulated with kinetic energies of 15 MeV ±2%.

Location	Transmission (%)
Target exit	100
Nozzle entrance	87.5
Nozzle exit	55.9

Table 2.6: Estimated electron plasma densities for the first three Gabor lenses for all spot size configurations, and their equivalent solenoid magnetic field strength.

Gabor lens	e^- Density ($\times 10^{15}\ m^{-3}$)	Equivalent solenoid field strength (T)
1	5.188	1.400
2	0.864	0.571
3	1.753	0.814

Table 2.7: Estimated plasma densities for Gabor lenses 4 to 7 for all five spot size configurations, and their equivalent solenoid magnetic field strengths.

Spot size configuration 2σ diameter (cm)		1	1.5	2	2.5	3
Gabor lens	Strength Parameter					
4	e^- plasma density ($\times 10^{15}\, m^{-3}$)	1.524	3.191	3.595	3.509	4.534
	Equiv. solenoid magnetic field (T)	0.759	1.098	1.165	1.151	1.309
5	e^- plasma density ($\times 10^{15}\, m^{-3}$)	1.810	1.484	1.339	1.531	0.758
	Equiv. solenoid magnetic field (T)	0.827	0.749	0.711	0.761	0.535
6	e^- plasma density ($\times 10^{15}\, m^{-3}$)	2.81×10^{-4}	3.437	2.511	2.125	1.632
	Equiv. solenoid magnetic field (T)	1.03×10^{-2}	1.140	0.974	0.896	0.785
7	e^- plasma density ($\times 10^{15}\, m^{-3}$)	5.076	5.63×10^{-4}	0.031	0.183	0.011
	Equiv. solenoid magnetic field (T)	1.385	1.45×10^{-2}	0.107	0.263	0.065

Table 2.8: Field gradients of the quadrupole magnets in the Stage 1 vertical matching arc for a 15 MeV proton beam. Quadrupoles 4, 5, and 6 have the same strengths as quadrupoles 3, 2, and 1, respectively.

Quadrupole	dB_y/dx (Tm^{-1})
1	-12.67
2	17.63
3	-17.71

Table 2.9: Mean RMS transverse emittance at the location of the switching dipole using GPT and BDSIM, which model particle transport in field maps with fringe field modelling.

Tracking Code	Mean RMS Emittance (m rad)
GPT	4.02×10^{-6}
BDSIM	4.06×10^{-6}

Table 2.10: Estimated electron plasma densities for the first three Gabor lenses for all proton spot size configurations, and their equivalent solenoid magnetic field strength when optimised for mitigating space charge effects. The plasma densities will be adjusted accordingly for ion transport.

Gabor lens	e^- Density ($\times 10^{15}\ m^{-3}$)	Equivalent solenoid field strength (T)
1	5.188	1.400
2	0.890	0.580
3	1.765	0.817

Table 2.11: Estimated plasma densities for Gabor lenses 4 to 7 and the equivalent solenoid field strengths for two solutions to meet the proton beam conditions at the entrance of the switching dipole for transport through the Stage 2 FFA injection line. The plasma densities will be adjusted accordingly for ion transport.

Gabor lens	Strength Parameter	Solution 1	Solution 2
4	e^- plasma density ($\times 10^{15}\, m^{-3}$)	3.041	3.341
	Equiv. solenoid magnetic field (T)	1.072	1.123
5	e^- plasma density ($\times 10^{15}\, m^{-3}$)	1.904	0
	Equiv. solenoid magnetic field (T)	0.848	0
6	e^- plasma density ($\times 10^{15}\, m^{-3}$)	1.468	0
	Equiv. solenoid magnetic field (T)	0.745	0
7	e^- plasma density ($\times 10^{15}\, m^{-3}$)	0.661	0.036
	Equiv. solenoid magnetic field (T)	0.500	0.209

Table 2.12: Lengths and materials of components in the BDSIM model of the LhARA Stage 1 end station.

Component	Length (mm)	Material
Vacuum window	0.075	Mylar
Scintillating fibre	0.250	Polystyrene
Air Gap	5.0	Air
Sample Container	1.15	Polystyrene
Cell Layer	0.03	Water
Water	2.4	Water

Table 2.13: Key parameters of LhARA Stage 2.

Parameter	Value / Range	Unit
Injection Line		
Number of bending magnets	7	
Number of quadrupole magnets	11	
FFA		
Machine type	single spiral scaling FFA	
Number of cells	10	
k	5.23	
Spiral angle	53.9	degrees
R_{inj}	2.914	m
R_{ext}	3.477	m
R_{max}	4.61064	m
B_{ext}	1.405	T
Orbit excursion	0.56	m
Magnet packing factor	0.34	
Magnet opening angle	12.24	degrees
Magnet gap - distance between flat poles (full)	95	mm
Max $B\rho_{inj}$	0.562	Tm
Max $B\rho_{ext}$	1.685	Tm
Ring tunes	(2.79, 1.22)	
γ_T	2.516	
RF frequency	1.46-6.51	MHz
h	1, 2 3 or 4	
RF voltage	4	kV/turn
Extraction Line		
Number of bending magnets	2	
Number of quadrupole magnets	6	
Number of vertical arc bending magnets	2	
Number of vertical arc quadrupole magnets	6	
Number of *in vivo* line quadrupole magnets	6	

Table 2.14: Beam parameters at the end of the FFA injection line.

Parameter	Value	Unit
α_x	0.074	
α_y	-0.963	
β_x	0.622	m
β_y	1.819	m
D_x	0.391	m
D'_x	-0.181	m

Table 2.15: Beam parameters at the exit of the extraction septum of the FFA, used as input to the extraction line.

β_x [m]	β_y [m]	α_x	α_y	D_x [m]	D'_x
1.093	2.100	0.692	-0.930	0.551	-0.181

Table 2.16: Beam parameters at the end of the extraction line used to design the high-energy *in-vitro* arc and the *in-vivo* beam line.

β_x [m]	β_y [m]	α_x	α_y	D_x [m]	D'_x
46	46	0	0	0	0

Table 2.17: Coil currents in the FFA preliminary design. The coil number corresponds to the ones labelled in figure 2.25. The power requirement (for this configuration is 21.6 kW per half magnet, or 43.2 kW total per dipole).

Coil Number	Length (m)	Ampere Turn	Power (W)
0	4.81	16545	3600
1	2.37	6908	2930
2	2.61	4795	1560
3	2.85	3883	1120
4	3.09	3184	814
5	3.33	2674	618
6	3.58	2250	470
7	3.82	1921	366
8	4.06	1653	288
9	4.30	1449	234
10	2.77	6908	3430
11	3.02	4795	1800
12	3.26	3883	1270
13	3.50	3184	921
14	3.73	2674	693
15	3.98	2250	523
16	4.22	1921	405
17	4.246	1653	317
18	4.70	1449	256

Table 2.18: Principal parameters for the RF cavities to be used for baseline proton acceleration.

Parameter	Value
Proton RF frequency	2.89–6.51 MHz
Voltage per cavity	4 kV
Bunch intensity	10^9 protons/bunch
Harmonic number	1
Horizontal aperture	650–850 mm
Vertical aperture	$\sim$ 70 mm

Table 2.19: Summary of the main parameters for the proton beam at the injection to the FFA ring. These parameters correspond to the nominal (maximum) kinetic energy mode of operation.

Parameter	Unit	Value
Beam energy	MeV	15
Total relative energy spread		$\pm 2\%$
Nominal physical RMS emittance (both planes)	π m rad	2.8×10^{-6}
Incoherent space charge tune shift		-0.14
Bunching factor		0.023
Total bunch length	ns	8.1
Number of Protons		10^9

Table 2.20: Summary of estimated parameters for the injection/extraction systems of the FFA ring.

Parameter	Unit	Value
Injection septum:		
Nominal magnetic field	T	0.53
Magnetic length	m	0.9
Deflection angle	degrees	48.7
Thickness	mm	10
Full gap	mm	31
Pulsing rate	Hz	10
Extraction septum:		
Nominal magnetic field	T	0.93
Magnetic length	m	0.9
Deflection angle	degrees	28.5
Thickness	mm	10
Full gap	mm	22
Pulsing rate	Hz	10
Injection kicker:		
Magnetic length	m	0.42
Magnetic field at the flat top	T	0.05
Deflection angle	mrad	37.4
Fall time	ns	320
Flat top duration	ns	25
Full gap	mm	31
Extraction kicker:		
Magnetic length	m	0.65
Magnetic field at the flat top	T	0.05
Deflection angle	mrad	19.3
Rise time	ns	110
Flat top duration	ns	40
Full gap	mm	22

Table 2.21: Mean working pressures assumed for each vacuum region.

Subsystem	Mean working pressure (mbar)
Laser systems	TBC
Laser beam conditioning chamber	TBC
Target chamber	1×10^{-6}
Gabor lenses	1×10^{-8}
Low energy line	1×10^{-8}
Low energy *in-vitro* end station	TBC
Fixed Field Accelerator	1×10^{-9}
High energy line	1×10^{-8}
RF Waveguide	1×10^{-8}
High energy *in-vitro* end station	TBC
High energy *in-vivo* end station	TBC

Table 2.22: Transmission probability results. Key: N- Number of hits, P_t- Transmission Probability (w).

	Cosine Desorption		**CosN = 2 Desorption**		**CosN = 10 Desorption**		**CosN = 100 Desorption**	
Position along vessel	N	P_t	N	P_t	N	P_t	N	P_t
Number of gas molecules generated	2,850,083		4,554,821		2,707,689		14,327,524	
Entrance to nozzle (4 mm)	15,761	5.53×10^{-3}	31,061	6.82×10^{-3}	48,074	1.78×10^{-2}	1,701,677	1.19×10^{-1}
Exit of nozzle (5.4 mm)	2,063	7.24×10^{-4}	4,626	1.02×10^{-3}	9,767	3.61×10^{-3}	449,590	3.14×10^{-2}
1/4 way along Gabor Lens	79	2.77×10^{-5}	184	4.04×10^{-5}	383	1.41×10^{-4}	17,535	1.22×10^{-3}
1/2 way along Gabor Lens	28	9.82×10^{-6}	55	1.21×10^{-5}	120	4.43×10^{-5}	5,120	3.57×10^{-4}
End of 1st Gabor Lens	18	6.32×10^{-6}	47	1.03×10^{-5}	79	2.92×10^{-5}	3,613	2.52×10^{-4}

CHAPTER 3

Laser-Driven Ion Source

3.1 Laser-driven ion source

3.1.1 Introduction to laser-driven ion source

The LhARA facility is required to provide an arbitrary bunch structure and variable intensity, including ultra-high instantaneous dose rates for the study of the FLASH effect. It is challenging to deliver such a range of requirements using conventional ion sources, which typically extract ions with energies $E_i \lesssim 100\,\text{keV}$. At such a low energy, the ions move slowly and therefore the mutual repulsion of the ions causes the beam to diverge rapidly. This "space-charge" effect significantly reduces the charge that can be captured in the first focusing element. The maximum dose rate that can be delivered is therefore limited by the space-charge effect at the very start of the accelerator.

This limitation can be overcome by adopting a *laser-driven* ion source [121, 122]. Such a source provides beams at much higher initial energies than a conventional source ($E_i \gg 10\,\text{MeV}$), and with an initially co-moving electron population, which mitigates space-charge forces. Indeed, the proton energy achieved by the source is already sufficient for some *in vitro* applications, without the need for any further acceleration. The initial bunch duration is short, on the same order as the initial laser drive pulse, $\sim 100\,\text{fs}$. This ultrashort bunch duration is maintained only very close to the source and increases with distance.

Ultrashort bunches open up the possibility of delivering ultra-high dose rates on the order of 10^9 Gy per second, a billion times higher than typically used in radiotherapy. Furthermore, the source is fully triggerable, making it 'on-demand'. The source has a low total power consumption, $\lesssim 100\,\text{kW}$. These properties make the laser-driven ion source an ideal technology for LhARA.

This chapter outlines the key system requirements for a laser-driven ion source, including the specification of the laser needed to meet the LhARA requirements. The challenges that remain to be addressed to realise a fully operational laser-driven ion source are discussed, along with a proposed research and development programme by which to address these challenges.

3.1.2 Operation of laser-driven ion sources

The key components of a laser-driven ion source include:

- A high-power laser system and laser pulse characterisation system;
- A laser delivery vacuum chamber and associated laser beamline;
- A target replenishment system and interaction chamber; and
- A source and beam characterisation system.

A high-power laser meeting the LhARA requirements is available commercially. It will be situated in a laser-safety-controlled clean room. The footprint of this room will be determined by the laser specification. The high-power laser for LhARA will rely on the chirped pulse amplification scheme, where the pulse is stretched in time before being amplified and recompressed. The recompression and all subsequent laser transport are done in vacuum to avoid nonlinear

optical effects in air. Therefore, after the output of the final laser amplifier, the laser enters the "compressor" vacuum chamber, which houses the large diffraction gratings used for pulse re-compression. The compressed ultrashort laser pulse is transported into a conditioning chamber, where the pulse undergoes adjustments such as wavefront optimisation using a deformable mirror. Finally, the laser pulse is sent to the interaction chamber, which will be in a different room from the high-power laser. Separating the laser and interaction area brings substantial benefits in safety and the working environment. In the interaction chamber, the laser is reflectively focused onto the target using an off-axis parabolic mirror. The focused laser pulse interacts with the target, generating ions. For the case of relativistically-intense laser pulses, the ions are emitted at high energy ($> 1\,\mathrm{MeV}$), with a relatively high divergence (typically with cone angles $\gtrsim 10°$) and a quasi-thermal energy spectrum. The flux, along with the spatial, spectral and dosimetric properties of the ions, will be measured to evaluate and optimise the performance of the source.

The acceleration process most widely used for laser-driven ion production is Target Normal Sheath Acceleration (TNSA) (figure 3.1). The intense fields of a focused high-power laser overcome atomic potentials and ionise a thin, dense target. Target electrons are accelerated to relativistic energies in micrometre distances [123] and rapidly leave the target at the rear surface to form a strong electrostatic field of order TV/m which accelerates surface ions to energies of tens of MeV or more. The effective accelerating gradients produced are far higher than is possible in conventional accelerating cavities [124–126]. The energy and flux of the accelerated ion beam depend on various laser parameters, such as the laser energy and focal spot size (see section 3.4.3). For example, the ion energy typically increases with increased laser energy and reduced spot size [127].

Development of this mechanism towards applications has made significant progress in recent years [128, 129]. It is now known to be a robust and effective technique. Laser-driven ion beams are fundamentally ultra-short ($< 1\,\mathrm{ps}$) at the source, due to the pulse length of the drive laser. The space-charge limitation of conventional sources is overcome due to the high initial ion energies ($\gg 1\,\mathrm{MeV/u}$) and inherent co-moving electron cloud created in the laser-target interaction. This results in a flexible, on-demand high flux beam with a low transverse normalised emittance [130]. Typically, accelerated ions originate from a thin ($\sim 1\,\mathrm{nm}$) layer of hydrocarbon contaminants on the surface of the target, resulting, predominantly, in the acceleration of protons, carbon and oxygen. Applying established contaminant-removal techniques enables acceleration of the ions in the target bulk material rather than the contaminant layer [131, 132]. This provides a relatively simple way of generating high-energy ions of different

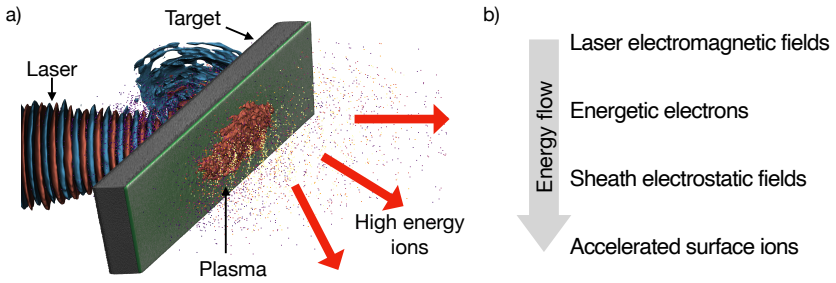

Figure 3.1: a) 3D Particle-In-Cell simulation showing the Target Normal Sheath Acceleration mechanism. A high-power laser is focused from the left onto a thin foil, forming a plasma and heating electrons to relativistic energies. These electrons form a sheath on the surfaces of the foil, rapidly accelerating surface ions. b) Flow diagram showing the transfer of energy from the laser to the ions. Each stage of energy conversion results in energy loss, and maximising the coupling into ions involves minimising this energy loss.

species, increasing the flexibility of the source. It is only recently, however, that high-power laser technology has developed to a stage where challenges related to continuous operation of the source have been addressed [133].

3.1.3 UK expertise in laser-driven ion sources

The UK has an internationally recognised record of leadership in the development of laser-driven ion sources, historically centred around the Central Laser Facility at the Rutherford Appleton Laboratory. Currently, the UK is home to world-class research groups in laser-driven ion sources at Strathclyde, Queen's University Belfast, Imperial College London and the Central Laser Facility. Each of these groups has a track record stretching back decades in performing seminal experimental development in various aspects of the laser-driven ion source. To deliver the laser-driven ion source for LhARA, all four groups are working together to perform critical research and development to de-risk the source, building on a longstanding collaboration in this area. They have previously spearheaded research into the underpinning physics of this technology through research programmes including A-SAIL (EP/K022415/1) and LIBRA (EP/E035728/1), establishing the UK as a world-leader in the field.

Much of this development work requires world-class laser systems for testing purposes. As well as the facilities at the Central Laser Facility, including the Gemini laser and the upcoming Extreme Photon Application Centre (EPAC), recent years have seen the development of significant university-scale laser infrastructure. Strathclyde hosts the Scottish Centre for the Application of Plasma-Based Accelerators (SCAPA) 350 TW laser system, which, in many ways, is a prototype of the laser which will be implemented for LhARA. Smaller facilities at Imperial (Zhi laser) and Queen's (Taranis laser) have lower laser-pulse energy and repetition rate, respectively, but are also able to support critical development work.

Beyond experiments, the ultra-small spatial and temporal scales of the laser-driven ion source necessitate numerical modelling for the behaviour to be understood fully and for the source to be optimised. These plasma simulations require sophisticated codes and large-scale computing resources. The LhARA laser-driven source team has extensive experience in performing state-of-the-art high-fidelity simulations of laser-driven ion sources. These simulations are run on both university-scale high-performance computing clusters and the ARCHER2 UK National Computing Service.

3.1.4 Specification of the laser-driven ion source

The baseline specifications of the laser-driven ion source for LhARA are:

- 10 Hz repetition rate;
- 10^9 protons at 12–15 MeV $\pm 2\%$ at 15 msr divergence;
- 10^8 carbon ions at 4 MeV/u $\pm 2\%$ at 15 msr divergence; and
- Production of other ion species, at energies and fluxes yet to be specified.

These parameters have been demonstrated at multiple laboratories on a single-shot basis and at reduced energies and fluxes at repetition rates up to 1 kHz. The parameters that defined the baseline specification of the LhARA source have never been delivered at 10 Hz. A key challenge is the development of a solution for achieving the required beam parameters at 10 Hz with a scheme compatible with long-term operation without significant downtime or maintenance. There are a number of potential issues that must be addressed to de-risk the facility. These are detailed in the next section.

3.2 Design recommendations

The following section describes the conceptual design of the laser-driven ion source. Further details of how these parameters were chosen are presented in sections 3.4.1 and 3.4.3.

3.2.1 High power laser and laser delivery specification

The high-power laser sets the limit of the ion beam parameters that can be generated. The parameters that specify the laser system and the laser beam delivery are shown in table 3.1. The parameter that has the greatest impact on proton and ion production is the laser energy on target; the number of particles produced will scale linearly (or more quickly) with this parameter.

The conditioning of the laser pulse and the diagnostics required to monitor the beam parameters must also be specified. Firstly, a full-aperture deformable mirror system is required to allow the wavefront to be flattened and to enable the focal spot to reach high Strehl ratios. At the entrance of the interaction chamber, it will be necessary to "pick off" samples of the laser beam. One pick-off will be used as an optical probe, measuring the front surface plasma expansion from the target. A second will be focused down onto the front of the target, arriving before the main pulse to control the plasma-density profile on the front surface. As shown in the modelling presented in section 3.4.3, this scale length is key in extracting the most particles from the source. The specification for this prepulser is still under investigation. The laser also needs to be complemented by a full diagnostic suite, at multiple points in the system. This suite will be used to maintain stable conditions over long time periods, facilitate rapid fault detection and minimise downtime.

Table 3.1: Specifications of the laser system for LhARA.

Parameter	Value	Unit
Laser Parameters:		
Central wavelength	800	nm
Energy before compressor	> 18	J
Energy stability (RMS)	< 2	%
Energy stability (RMS over 12 hours)	< 5	%
Pulse length (FWHM)	< 50	fs
Pulse length stability (RMS)	< 5	%
Rep. rate	10	Hz
Temporal contrast at 5 ps	10^{-8}	
Temporal contrast at 10 ps	10^{-9}	
Temporal contrast at 100 ps	10^{-10}	
Laser delivery parameters:		
Energy on target	> 10	J
Focal spot size (FWHM)	< 3	μm
Strehl ratio (Measured)	> 0.5	
Angle of incidence	30	$^\circ$
Pointing stability	< 5	μrad

3.2.2 Target system requirements

Resources have not yet allowed a full evaluation of all target options. However, a significant period of testing a tape drive target has been possible. Development of other target technologies is taking place at other laboratories. There are still significant unknowns regarding the target selection. It is therefore important to maintain flexibility in both the target-chamber design and the laboratory environment to allow the target system to be updated at a later stage. Moreover, it is likely that a number of different target options will eventually be required depending on the beam delivery requirements. Ideally, the various target options will be arranged on a linear drive to allow switching between targets without the need to open up the interaction vacuum chamber.

Tape targets

As shown in section 3.4.1, tapes are an effective target for proton generation, albeit with outstanding issues in debris production that need to be addressed. Although it is yet to be demonstrated, it is likely that tape-drive targets will be suitable for the generation of oxygen and carbon ions. The production of other ions, for example, aluminium and iron, will require further technical development.

The current specifications of the tape-drive target are shown in table 3.2. A variety of tape materials will allow different ions to be accelerated. Generation of ions other than protons will require an external heating system to remove water or hydrocarbon surface contamination. This may be an external 1 W scale continuous wave laser, a pulsed laser, or some other active heating element. Although these techniques have all been tested at low repetition rate, further research needs to be performed to confirm the viability of these contaminant-removal techniques at 10 Hz.

Liquid jet targets

Liquid jets are currently undergoing rapid development for deployment in laser-driven ion sources. Liquid-jet targets offer numerous advantages over tape targets. These include:

- A thinner target, resulting in a higher flux of high-energy ions;
- The target material is easily replenished; and
- Reduced debris production.

Table 3.2: Envisioned specification for tape target.

Parameter	Value	Unit
Tape drive parameters:		
Tape length	2	km
Shots per tape	200,000	
Continuous operation	5	hours
Tape width	> 1	cm
Tape velocity	0.1	ms^{-1}
Tape stability at focus	< 5	μm
Tape material	varied	%
Tape thickness	< 5	μm

Liquid jets are likely only to provide specific ion species. The generation of protons and deuterium ions has already been demonstrated from water and heavy water jets [134, 135]. It is likely that oxygen could also be accelerated from water targets. It is expected that other organic liquids would result in carbon acceleration. Ion species with the highest charge-to-mass ratio are preferentially accelerated, so to accelerate heavier ions, it is important to minimise the percentage of hydrogen in the liquid. Quantitative predictions or measurements of the ion yield are not yet available.

Other types of target

Other promising target types are being developed, such as:

- Cryogenic targets; and
- Gas targets.

Progress on the development of these techniques and their suitability for LhARA will continuously be monitored.

Cryogenic targets have been shown to deliver performance comparable to that of solid targets [136, 137]. Cryogenic hydrogen can be extruded through shaped apertures to create a flat ribbon suitable for TNSA. The control of the ribbon as it is being extruded is technically challenging, and the extrusion head has to be protected from the laser-plasma interaction. Cryogenic targets would likely be suitable for proton acceleration. It should also be possible to freeze other gases to generate different ion species, although this has not been demonstrated.

None of the targets outlined above can be used to generate helium ions, which are an important ion species for radiobiology. It is possible to use a cryogenic jet to generate helium droplets [138], but these have not yet been tested for use in a laser-driven ion source. It is likely that the beam produced from droplets would be highly divergent and therefore have a low acceptance into the beamline. Due to the difficulties of dealing with liquid helium, gas jets have been considered as a candidate for helium acceleration [139–141]. However, it is hard to generate the high gas densities required to form the critical-density surface that absorbs the laser pulse, and that is needed for TNSA. Furthermore, it is challenging to make thin gas targets. Various groups worldwide, including Imperial College, are investigating schemes to compress gas plumes optically using secondary laser pulses to facilitate the acceleration of ions by laser-plasma mechanisms other than TNSA. The discussion of such schemes, which currently do not meet the LhARA requirements, is beyond the scope of this report.

3.2.3 Source characterisation and monitoring

The laser-driven ion source will require an extensive suite of diagnostics to be used for monitoring and providing data to help stabilise the ion beam.

Laser diagnostics

There will be a suite of laser diagnostics placed just before the interaction chamber. The full aperture laser leakage through a large aperture dielectric mirror will be transported out of the vacuum chamber and onto a diagnostics bench, where the spectrum, energy, the unfocused laser profile (the “near field”), and the focused laser profile (the “far field”) will be measured. A small portion of the laser will also be sampled using a small “pick-off” mirror and sent through a thin vacuum window to monitor the beam’s temporal characteristics (pulse length, spectral phase, temporal-intensity contrast, etc.). It is essential that these diagnostics are used to provide evaluation and feedback in real time.

Target diagnostics

Variation in the laser focus on the target will cause a change in the generated ion beam properties. Therefore, the position of the target with respect to the laser focus needs to be monitored continuously to ensure there is no drift. This will be done by setting up a fixed imaging line perpendicular to the laser axis and imaging the position of plasma emission. Alternatively, monitoring could be performed using retro-reflection techniques.

Plasma diagnostics

Measuring the plasma parameters generated during the laser plasma interaction can give insight into source performance and also help diagnose fault conditions. A laser optical probe will be used to measure the plasma size and density profile just before the interaction point to ensure the source is operating in an optimal regimen. We will also monitor the light emitted at the rear of the target, which is generated by transition radiation from laser-accelerated electrons passing through the rear target surface-vacuum interface. This process is a good proxy for laser absorption.

Destructive ion diagnostics

When commissioning and testing the system, a suite of ion diagnostics will be implemented to generate a spatio-spectral map of the generated ion emission. This will involve both ion-beam profiler devices and high-resolution Thomson parabola energy spectrometers to monitor the different ion species and their spectra. These diagnostics will be removed to enable the injection of the ions into the downstream beamline.

Non destructive ion diagnostics

Due to the large divergence of the laser-generated ion beam, many ions will be emitted at angles too large to be accepted by the Gabor lens. However, the properties of these ions are strongly correlated to those that do go into the beamline. Therefore, measuring the ions on the periphery of the nozzle connecting the source and the Gabor lens should give a strong predictor of the useful source output. The design of this diagnostic will be revised as the source-lens interface develops, but is likely to include measuring the light emission from scintillators placed around the edge of the nozzle, which are differentially filtered.

These non-destructive diagnostics, together with the laser and plasma diagnostics, will be used to provide synthetic profiles of the beam entering the beamline. This approach has already been shown to be highly successful with laser-generated electron beams [142], and can combine with other beam-line and end-station diagnostics to provide further confidence to the user in the parameters of the ion beam.

3.3 Key challenges in source implementation

The main challenges that are still to be addressed to allow the extended operation at high repetition rate of laser-driven ion sources are outlined below. The LhARA laser-driven source R&D programme has been designed to investigate and identify solutions to these issues.

3.3.1 High power drive laser

A commercially developed high-power laser has been specified to drive the ion source. Over the last decade, a number of industrial providers have started to offer lasers capable of driving ion

production. Indeed, the SCAPA laser facility at Strathclyde, where much of the LhARA source development has taken place, uses a commercial laser system. The key challenges affecting both the specification of the laser system and its operation are discussed below.

There are numerous studies of the acceleration of protons from solid targets, which can be used to predict the requirements of the laser system for LhARA. However, there are large differences in performance even for apparently similar laser systems. The differences may have a variety of causes, including diagnostic issues, hidden or undisclosed laser parameters, or limitations in calibration. Furthermore, there are far fewer published studies available on the production of ion species other than protons. Multi-species ion generation is a key requirement for the LhARA source, and currently, there is insufficient data available to make quantitative predictions of how the ion yield will be determined by the laser parameters.

Component failure is relatively common during the operation of high-power laser systems. Failures typically involve damage to optical components or custom electrical devices, which then require replacement. Such issues can prevent laser systems from running at full specification. These risks can partially be mitigated by considering potential operational issues when specifying the laser. For example, if the high-power laser system can provide more laser energy per shot than required for the laser-driven ion source, then the system is robust to a single pump-laser failure and can continue delivering the ion beam while the faulty pump laser is being repaired.

3.3.2 Targetry for ion source

The ion beam properties depend on the target size and density. Typically, sources driven by TNSA have used thin ($\sim \mu$m) solid foils. TNSA can only accelerate the ions on the surface of the target, and therefore, without special treatment, the ions come from hydrocarbon contaminant layers on the target surface. This results in protons dominating the emission, as their charge-to-mass ratio is large compared to carbon and oxygen ions. Other ions from the bulk material of the target can be generated instead by removing the contaminant prior to irradiation, typically with a secondary laser or heating system [132, 143, 144].

LhARA will run for extended periods at 10 Hz. Although high repetition laser-driven ion sources have been demonstrated at relatively low $\sim$ 1 MeV energies [134, 145], the 15 MeV required by LhARA has not been demonstrated in sustained operation. Previous work has relied mainly on the use of individual targets. Tape drives are also being developed that are capable of delivering targets at 10 Hz, to match the increasing repetition rate of high power lasers [127, 146, 147]. However, they have a number of potential difficulties. Firstly, each laser shot will create a damage spot $>$ 1 mm in diameter, and therefore the tape needs to be moved between shots. Assuming a 1 cm space between shots, the laser-driven ion source would use 6 m of tape per minute, or $\sim$ 1 km of tape in a 3-hour session of continuous ion generation. The reel will therefore need to be regularly replaced, and material costs have to be considered. Secondly, laser-driven ion sources typically work most effectively with target thicknesses of the same order as the focal spot size, $\approx 1\,\mu$m. It is unclear whether it is possible to operate a tape drive with such a thin foil that will tear easily when moved after being punctured by the laser interaction. So far, tape drives have only been shown to be usable down to a thickness $\approx 5\,\mu$m [127]. Finally, debris production is a major unsolved problem. It is well known that debris is generated after laser-solid interactions, and this debris coats and damages nearby equipment. Particularly sensitive are the optical components, such as the off-axis parabolic mirror, which focuses the laser. Debris will reduce the reflectivity and degrade the focal spot, resulting in continually worsening performance. Replaceable debris shields can be used, but these have to be very thin in order to minimise nonlinear effects, which would degrade the quality of the focal spot. This means they are relatively fragile. Furthermore, to avoid laser energy loss, they should be treated with an anti-reflection coating, increasing their cost. The optimal design of the debris shield remains to be developed.

There is considerable research effort worldwide on the development of different target-delivery systems beyond foil targets. These include cryogenic ribbons, gas jets, and water-jet sheets, which were discussed in more detail in section 3.2.2. It is hoped that these targets will provide sustainable solutions to the issues with tape targets listed above. However, the target systems are still relatively untested, and it is not yet clear whether they can be used to generate all the different ion species required by LhARA, or whether they are sufficiently stable for routine operation.

3.3.3 Ion beam delivery

LhARA requires high stability of the particle number in the selected energy band in order to deliver a predictable dose to the radiobiological end stations. The stability of laser-driven ion sources has not been greatly explored in the literature. However, long-term studies of laser-driven electron accelerators [148] imply that laser stability is one of the key drivers of instability in the source. Factors that affect stability include focal spot size, transverse jitter, focal spot longitudinal jitter (i.e. defocus), and laser energy. In addition, laser-driven ion sources are also likely to be sensitive to laser contrast and wavefront fluctuation, as well as parameters such as target thickness and position. At the moment, it is challenging to predict the sensitivity of ion source operation to fluctuations in these parameters. This adds uncertainty to the component-stability specifications. As well as shot-to-shot instability, it is typical to see long-term drift during extended operation, which could, for example, be due to long-term alignment drift. Although sources can often be corrected manually, studies have not been carried out on automated ion-source stabilisation to compensate for these effects.

Although the TNSA scheme is known to be a robust mechanism, it is possible there are also inherent plasma or laser-plasma instabilities that may also contribute to output variation. For example, if there is a significant low-density plasma plume on the front side of the target generated by the prepulse, the likelihood of hosing instabilities or laser filamentation instabilities will be increased. It is therefore possible that some working points for the source may have different inherent stability due to plasma processes.

3.3.4 Beamline interface challenges

Laser-driven ion sources produce a variety of different unwanted radiation byproducts (particularly electrons and X-rays from keV up to tens of MeV) and copious electromagnetic noise (i.e. EMP). These unwanted effects are sufficiently different to those that arise in the use of conventional ion sources to cause concern about integration of the laser-driven ion source with the subsequent beamline. The most affected components are likely to be those nearest the ion source, particularly the first Gabor lens. For example, the lens uses electrodes to maintain confinement; these could be affected by the secondary radiation or EMP. The confined single-species electron plasma in the lens will be subject to large fluxes of charged particles, both protons and electrons, that may cause plasma disruption. In recent years, there have been more studies demonstrating laser-driven ion sources combined with various capturing and focusing devices, including quadrupole magnets [149, 150] and pulsed solenoids [128], albeit generally at relatively low repetition rate. Some risk nonetheless remains due to the novelty of the Gabor lens system.

3.4 Current development activities

Work to date has focused on the:

- Demonstration of the LhARA test source at the SCAPA facility;

- Development of source technology towards high repetition rate operation; and
- Prediction of source optimisation through numerical simulation.

These different activities present substantial cross-over and were made possible by a productive collaboration between the University of Strathclyde, Queen's University Belfast, Imperial College London and Lancaster University. Some highlights of the activity are summarised here, and are also covered in greater depth in two detailed milestone reports [151] and [152].

3.4.1 Demonstration of test source at the SCAPA facility

A series of experiments were performed on the SCAPA laser over the period July 2023 to July 2024 to optimise the laser-driven proton source and to develop the methodologies required to characterise the proton source at repetition rates of up to 1 Hz. SCAPA is a 350 TW laser system capable of achieving a maximum of 6.5 J on target in a 25 fs pulse. The beamline serving Bunker B is designed for dense plasma and ion acceleration experiments. The final focus is performed using a short focal length off-axis parabola that enables peak intensities on the order of $5{\times}10^{21}\,\mathrm{W/cm^2}$ to be reached, and is thus ideal to investigate the requirements of the LhARA source. The SCAPA 350 TW laser also has the potential to operate at up to 5 Hz repetition rate. In this section, the performance achieved on the SCAPA system to date is reviewed.

The optimal source performance was found for the highest laser energy ($E = 6.5$ J), shortest pulse ($\tau = 27\,\mathrm{fs}$) and best focus ($\phi = 1.5\,\mu\mathrm{m}$). Variation in the target material between Kapton and steel also proved to be an important factor. Despite similar target thicknesses ($L_{\mathrm{Steel}} = 10\,\mu\mathrm{m}$ and $L_{\mathrm{Kapton}} = 13\,\mu\mathrm{m}$) there is a $\approx 20\%$ increase in the maximum proton energy for the steel relative to the Kapton. A change in target thickness between Kapton of $25\,\mu\mathrm{m}$ and $13\,\mu\mathrm{m}$ did not produce a similar effect, and therefore the performance improvement is unlikely to be due to the difference in target thickness alone. It is likely that the different densities of target material result in a different degree of expansion of the front surface. Hydrodynamic modelling, not shown here, supports this conclusion, indicating that the steel target expands more than the Kapton. This larger expansion can lead to improved coupling of laser energy into fast electrons, which then drives the acceleration of the protons and also indicates the utility of using the preheater beam with the Kapton tape in future experiments.

After these initial data scans to optimise the proton source, a $50 \times 50\,\mathrm{mm^2}$ radiochromic film (RCF) dosimetry stack was placed at a distance $d = 45\,\mathrm{mm}$ from the rear surface of a $L = 10\,\mu\mathrm{m}$ steel tape target. From this measurement, it is possible to produce a calibrated, spatially and spectrally resolved measurement of the proton beam. An example of the proton beam profile measured with this detector is shown in figure 3.2. Here, the proton beam profile for the layer measuring protons with energies of 1.2 MeV and above is shown, as well as the layer measuring protons with energies $\geq 12.6\,\mathrm{MeV}$. These beam profiles are notably different, with the lower energy portion of the beam having a radial, ring-like profile and the higher energy beam having a smooth, flat-top profile. The ring-like structure at low energies has been observed many times in laser-driven proton acceleration and is indicative of electron transport effects within the target, strong magnetic field formation at the rear surface or deformation of the rear surface [153, 154].

For radiobiology experiments relevant for LhARA, protons with energies $E_p \geq 10\,\mathrm{MeV}$ will be selected; therefore, this low-energy structure will not affect the dose deposition profile. Figure 3.2(c) shows a "lineout" through the middle of the beam shown in 3.2(b). The beam profile is close to parabolic with relative symmetry in the x and y dimensions. The extent of the beam as a function of depth within the RCF dosimetry stack is also shown in figure 3.2, allowing the beam divergence to be determined as a function of proton energy. This measurement shows that the divergence decreases monotonically with increasing energy. In the relevant band around

10 ± 1 MeV, a divergence half-angle of $\approx 11°$ is obtained. This relatively low angle of divergence will allow a relatively high capture efficiency in the experiments at SCAPA and at LhARA.

Alongside the beam spatial profile measurement, the proton energy spectrum was also determined using the RCF dosimetry stack. Fig. 3.3 (a) shows the calibrated spectrum and indicates the region of the spectrum to be used in the PoPLaR experiments for radiobiology tests. The measured cutoff for the spectrum on this shot is $E_p = 14 \pm 1$ MeV. This measurement comes from a single laser shot and the spectrum, especially around the cutoff, is subject to shot-to-shot variation. The integrated band around $E_p = 10 \pm 1$ MeV contains 7×10^9 protons.

Given the single-use, film-based nature of the RCF dosimetry stack, it is not possible to build up detailed data scans or a statistical understanding of the performance of the proton source using this approach. Figure 3.3 shows measurements made of the proton beam with a Thomson parabola (TP) spectrometer [155]. The scaling of the proton spectrum accelerated from a steel tape ($L = 10\,\mu$m) over a series of shots (N = 27) in which the laser energy was varied between 0.72 J and 5.75 J is shown in figure 3.3. A maximum proton energy of $E_p = 15.6$ MeV is observed at the highest laser energy on target. Shots where the laser energy measurement was not available are shown as grey lines. The TP spectrometer data is not yet calibrated to yield the number of protons striking the device. The signal is reported instead as counts measured on the CCD camera. The measured maximum proton energy is higher than seen on the RCF dosimetry stack, despite the TP spectrometer being further away from the target (≈ 1 m) than the RCF dosimetry stack and samples a considerably smaller solid angle (0.8 μsr compared to 4 sr). The amplification provided by the micro-channel plate (MCP) detector used gives good sensitivity at the proton cutoff energy, and given the capability to make repeated measurements, a greater chance to observe the highest cutoff energies as the laser energy fluctuates slightly. Figure 3.3 shows a series of direct repeat shots on a Kapton tape (N=23) taken during a scan to measure the stability of the proton spectrum measured with the TP spectrometer. Kapton was used during a series of stability scans since it produced significantly lower EMP, which made it easier to operate at a higher repetition rate. The average maximum proton energy and standard deviation over these repeat shots is found to be $\overline{max(E_p)} = 12.9 \pm 0.5$ MeV. The average flux in the $E_p = 10 \pm 1$ MeV band is found to have a coefficient of variation (CV) of $\frac{\sigma_{10\pm1}}{\overline{N}_{10\pm1}} = 8.4\%$. This value is expressed here as the CV in percentage rather than the standard deviation in absolute terms, given that the TP does not have a proton number calibration at present. The CV of the laser energy during the same data scan was only $\frac{\sigma_{E_L}}{\overline{E_L}} = 0.9\%$ and thus does not explain the variability seen in the integrated proton signal on its own (given our previously observed linear scaling).

In addition to measuring the change in the proton spectrum as the laser energy is varied (and its stability in direct repeat shots) it is important to consider the scaling of the flux within the $E_p = 10 \pm 1$ MeV band as a function of laser energy. Figure 3.3(d) shows the scaling of the number of protons measured on the TP as a function of laser energy. This data indicates that, in order to reach the highest dose possible in this configuration, energy on target is the key parameter. Optimisation of the laser during operation must consider both the laser energy output, the throughput of the compressor, the transmission of the pellicle, and the encircled energy in the focal spot. The results indicate that more than 4 J on target is required to produce protons with energies around 10 MeV. Above this threshold, the flux in the $E_p = 10 \pm 1$ MeV band scales linearly with energy. This insight provides a clear motivation to optimise the energy on target in SCAPA for radiobiology experiments and in the design of the LhARA facility, and the consideration the provision of a significant pulse-energy margin in the laser.

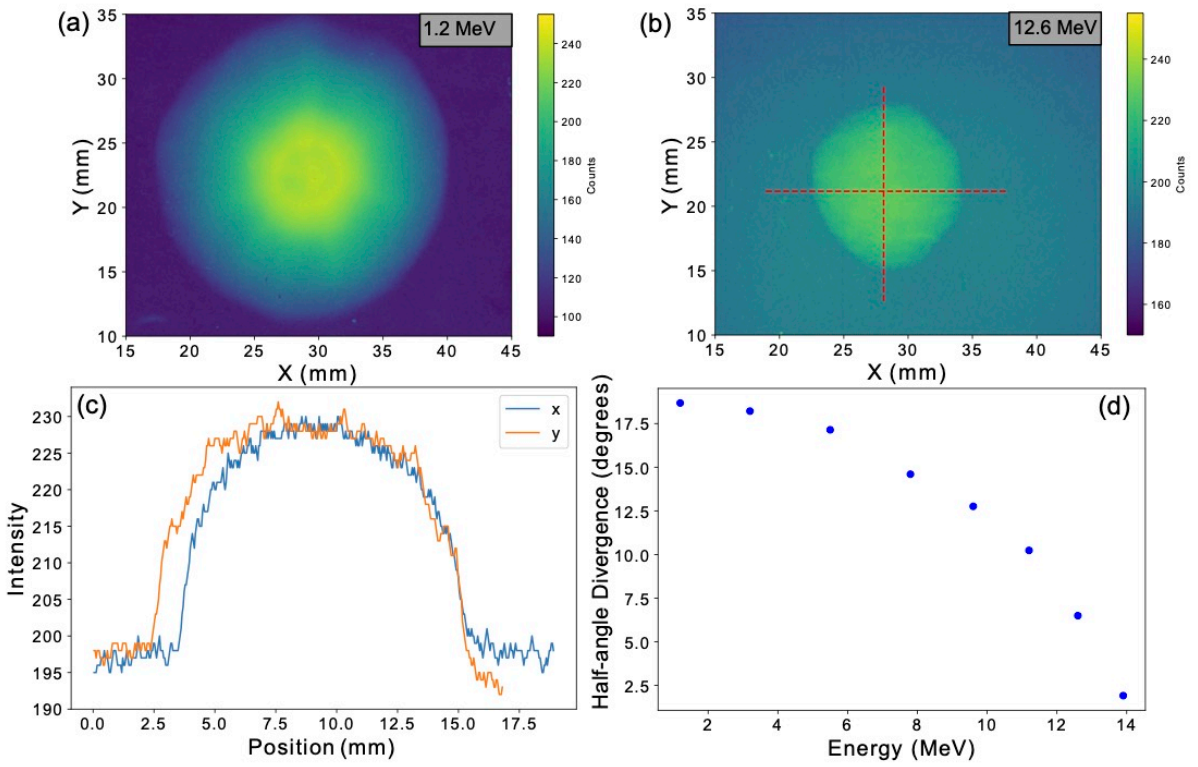

Figure 3.2: Example images of proton beam profile measured using RCF dosimetry stack. (a) Beam profile for 1.2 MeV protons measured on the first layer of RCF dosimetry stack. (b) Beam profile for 12.6 MeV protons measured on the 7$^{\text{th}}$ layer of RCF dosimetry stack, also showing the region of the line out in X- and Y- (c) X- and Y- lineouts of the proton profile measured at 12.6 MeV. (d) Beam divergence as a function of proton energy.

3.4.2 Development of source technology towards high repetition rate operation

The development of instrumentation and diagnostics that are compatible with 10 Hz operation is a key requirement for LhARA. Laser-driven ion sources delivering $\gg 1$ MeV/u ions have, up until the last few years, typically been run in a low repetition rate, single-shot mode (typically $\ll 0.01$ Hz). Over the past two years, significant progress has been made in the move towards high repetition rate, through the experiments at SCAPA and elsewhere. Here, two examples representative of the breadth of work being undertaken are described.

One challenge in developing the source technology is a lack of available beamtime at facilities capable of delivering high-repetition laser-driven ion sources. For example, the SCAPA laser facility is in high demand, and the beamtime available to LhARA is not sufficient for all components to be tested. Therefore, the LhARA collaboration has been developing a new platform for a > 10 Hz laser-driven ion source based at Imperial College London, using the Zhi laser. Zhi is a Ti:Sapphire chirped pulse amplification system capable of delivering 100 mJ pulses with a pulse length of 45 fs at up to 100 Hz. Through the Preliminary Activity, a full laser diagnostic suite has been implemented and tested at 100 Hz. Ion diagnostics include a Thomson parabola, a scintillator-based beam profiler, and a time-of-flight ion spectrometer. The laser reflection is monitored, as well as plasma emission, which is used to study the front surface interaction conditions. The system has been used to irradiate a home-built tape target [147] at a low energy level (3 mJ), and experiments at the full 100 mJ will start within the next few years. Proton energies are expected to be accelerated up to 1 MeV, and the experiment will be used as

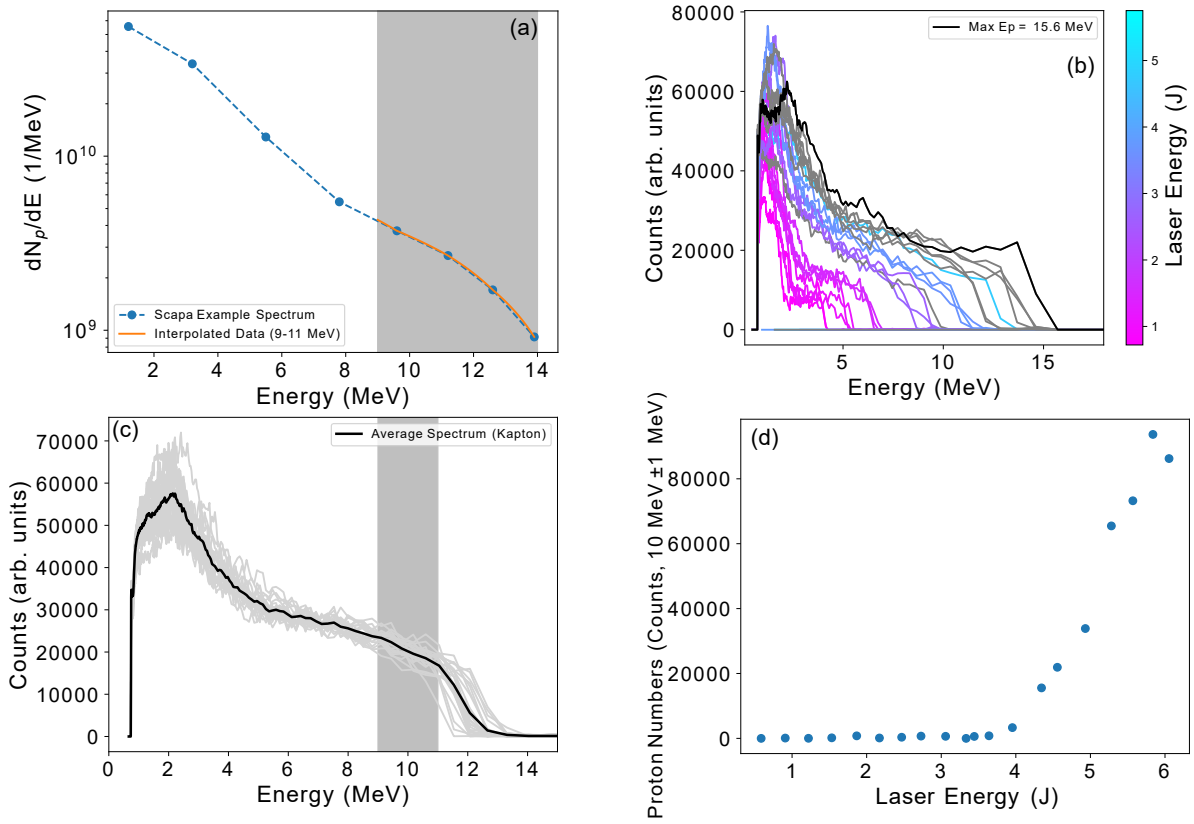

Figure 3.3: (a) Example proton spectrum measured on RCF dosimetry stack with grey box indicating 10 ± 1 MeV region relevant for use in radiobiology experiments. This data was taken with $L = 10\,\mu$m steel tape and laser energy E=6.5 J. (b) Proton spectra measured for N=27 shots over an energy range of $E_L = 0.72 - 5.75$ J on Thomson parabola spectrometer. Energy range is indicated by colour shade from purple to magenta (according to the scale bar), and grey lines represent shots where no laser energy had been recorded. (c) Proton spectra measured over N=23 repeat shots at maximum laser energy. (d) Scaling of the number of protons in an $E_p = 10 \pm 1$ MeV band as a function of laser energy.

a test-bed for targetry, debris mitigation, diagnostics, real-time data analysis and automated beam stabilisation.

In addition to the testing of high repetition-rate lasers, the development of a suite of detectors capable of operating at high repetition rates is essential. Ionising radiation is typically measured at high repetition rate using scintillators. The broadband source energy spectrum and the fluctuating particle flux make it hard to characterise the source. Moreover, at large flux, the effect of quenching of the scintillator response must be taken into account. Measurements must be made in the presence of a large background from electrons and X-rays generated at the target and the surrounding vacuum chamber. A series of studies have been performed at the MC40 cyclotron at the University of Birmingham to inform the scintillator selection for the LhARA diagnostic suite. A variety of different scintillators commonly used in the laser-plasma community were irradiated and their response measured. Example results are shown in figure 3.4. The response of the scintillators to different proton energies was studied, and the high LET quenching was quantified by fitting a standard Birks response curve [156] to the data. Fitting the Birks response facilitates the adaptation of the calibration to the different detector and beam configurations that will be used at LhARA.

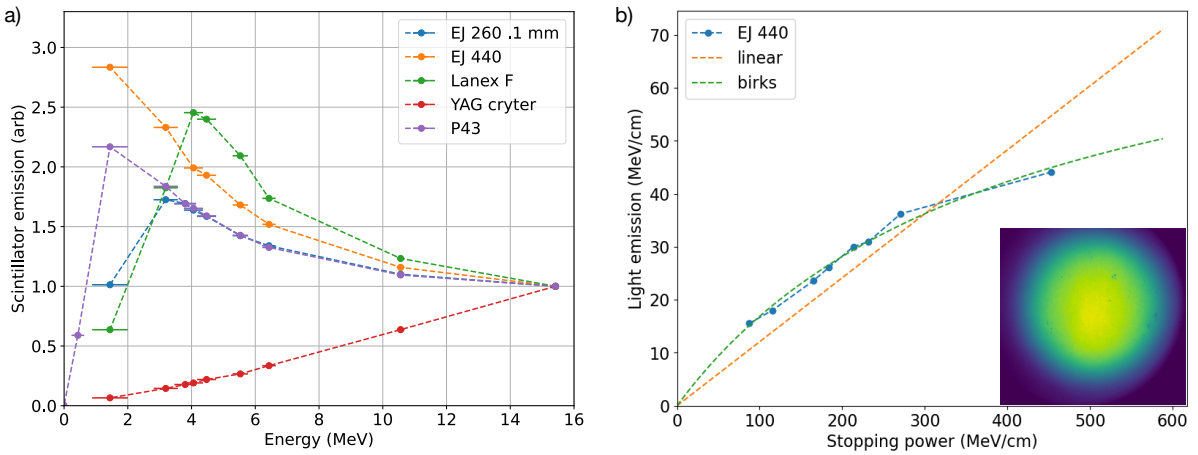

Figure 3.4: (a) Photon emission as a function of energy for a variety of scintillator materials. The photon number is normalised at 15 MeV for ease of comparison. (b) An example extraction of the relationship between light emission and stopping power for one of the scintillators, EJ-440 (Eljen Technology). A Birks relationship is fitted to the curve, with a linear curve also shown as an example of the importance of characterising the nonlinearity properly. Inset is an example of the proton beam profile imaged from the scintillator.

3.4.3 Source optimisation through numerical simulation

To predict a set of optimised proton source parameters for a ≥ 300 TW laser system, a comprehensive series of high-fidelity hydrodynamic and kinetic (particle-in-cell) simulations were carried out. The impact of several laser and target parameters on the acceleration of protons via TNSA from a solid target was investigated. The results predict lower or upper thresholds for the source parameters that will ensure the acceleration of protons with the energy and flux required for LhARA. As in experimental studies, the "cutoff energy" serves as a critical parameter to characterise the effectiveness of ion acceleration using the TNSA mechanism; it is also used here as a principal figure of merit. The cutoff energy refers to the energy at which the broad ion spectrum typical of TNSA begins to exhibit a precipitous decrease in particle number or falls below a certain threshold.

Rationale

The parameters of interest were chosen from those that are known to play a role in the acceleration of protons and ions via TNSA. These are: laser energy [157, 158], focal spot size [157–159], angle of incidence [160], target thickness [161, 162], and pre-expansion of the target before the arrival of the main laser pulse [163–167]. A well-known feature of laser-driven ion sources is the sensitivity to the laser prepulse, which here refers to any laser energy arriving at the target before the high-energy, high-intensity main pulse. Although modern laser systems use numerous techniques to optimise the contrast [168], the wavelength-scale focal spot typically results in significant target ionisation and heating picoseconds to nanoseconds before the main pulse. The pre-pulse results in ablation of the front surface, causing a shock wave to be driven into the target and a plasma plume to be ejected away from the target. When the high-intensity main pulse arrives, it has to travel through the plasma plume up to the dense part of the target. Therefore, the properties of the plasma plume, or "preplasma", can often dominate the laser absorption properties and so determine the characteristics of the ensuing laser-driven ions.

The interaction between the main laser pulse and a plasma is intrinsically non-linear, multi-dimensional, and can be properly simulated only through the kinetic approach. Among the

different possibilities, particle-in-cell (PIC) codes [169] represent the most suitable tool due to the reduced number of physical approximations and the ability to take full advantage of high-performance computing (HPC) resources. The PIC simulations presented here were carried out using the OSIRIS code (version 4.4) [170] on two HPC systems: ARCHER2 (EPCC, UK) [171] and SuperMUC-NG (LRZ, Germany) [172], with most of the simulations using up to 12,288 cores in parallel.

Main predictions

The key results of the campaign of simulations carried out to identify the optimal parameters for the LhARA source are reported in figure 3.5. In summary, in the presence of optimal laser contrast and sharp plasma-to-vacuum transition, very thin targets ($< 2\,\mu$m) and laser intensities $\gg 10^{21}\,\mathrm{Wcm}^{-2}$ are required to extend the proton spectrum beyond 20 MeV and accelerate sufficient protons to energies within the range of interest of (15 ± 0.5) MeV.

General trends and specific conditions which result in optimal acceleration of protons have also been identified. Firstly, while the laser intensity can be increased by varying both the laser energy on target and the focal spot size, the proton energy is observed to scale more rapidly with the laser energy on target (see figure 3.5). Secondly, for fixed laser parameters, a thinner target accompanied by a longer scale-length preplasma on the front surface favours the acceleration of protons to higher energies. The proton cutoff energy is observed to increase approximately linearly with larger preplasma scale length within the range that was tested. Lastly, an incidence angle close to 30° is predicted to enhance the proton cutoff energy by approximately 20% compared to that obtained in the case of normal incidence.

Impact of preplasma

Under all conditions investigated numerically, the presence of a preplasma was observed to yield a harder proton spectrum. The possibility that a pre-pulse would generate the preplasma in front of the target in a more controlled way was also investigated. Simulations of an idealised preplasma (density profile modelled as a hyperbolic tangent function) in front of the target indicate that proton spectra extending beyond 20 MeV can be achieved with targets $> 2\,\mu$m thick and laser intensities $\lesssim 1 \times 10^{21}\,\mathrm{Wcm}^{-2}$. In addition to pushing the energy spectrum to higher values, a long-scale-length preplasma was found to be beneficial to achieve proton beams with a smaller opening angle at the target.

Throughout the campaign of simulations for the LhARA source, the proper modelling of the laser contrast and density profile of the target emerged as important factors which play a significant role in obtaining realistic TNSA proton-energy spectra. Multi-scale simulations which combine outputs from both hydrodynamic and particle-in-cell codes have been developed. This multi-scale approach enables the modelling of the front-surface plasma expansion induced by the laser temporal intensity contrast. Figure 3.5 shows the proton energy spectrum predicted by such a multi-scale simulation, which used a measurement of the laser contrast at SCAPA as an input to the model. These cutoff energies should be regarded as upper bounds, as the 2D geometry used to simulate these results tends to overestimate the cutoff energies.

Given the potential enhancement of the proton energy predicted in the presence of a pre-plasma, a study using 2-D PIC simulations and a differential evolution algorithm was performed to find a preplasma density profile that maximises the proton cutoff energy for a fixed set of laser and target parameters. The results of the study suggest that a foam-like preplasma with a scale-length several micrometres long and with near-critical density can strongly enhance proton acceleration even with the use of not-so-thin tape targets [151]. The formation of a preplasma with an optimal density profile using a laser prepulse represents an alternative to using a laser pulse of higher intensity or a thinner target to extend the proton cutoff energy and particle flux

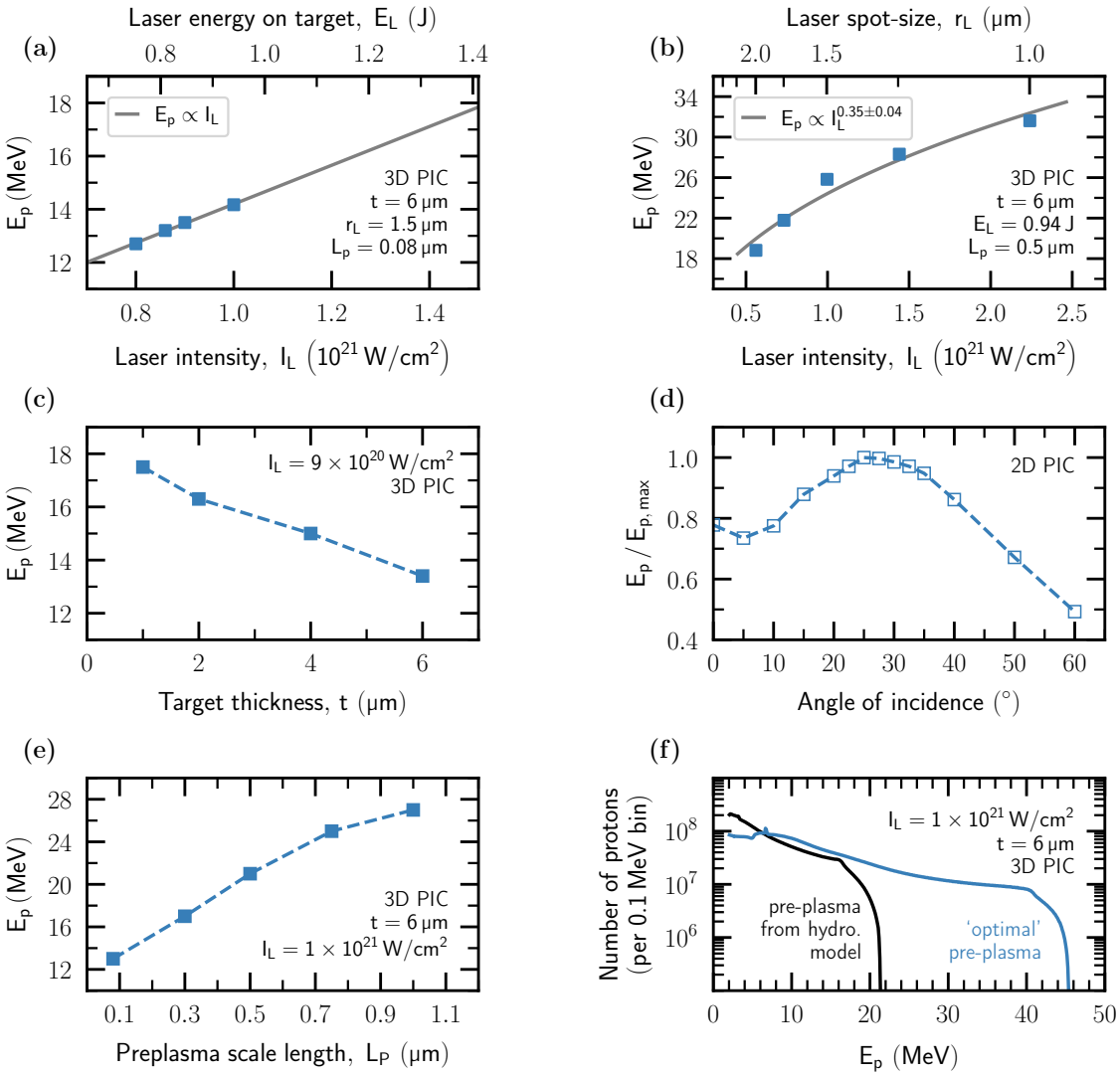

Figure 3.5: Cutoff proton energy, E_p, predicted by particle-in-cell (PIC) simulations modelling a 25 fs laser pulse incident on a tape-like aluminium target when varying: (a) the laser energy on target, (b) the laser spot-size (laser waist, w_0, in the focal plane), (c) the target thickness, (d) the angle of incidence of the laser onto the target, (e) the scale length of the preplasma present in front of the bulk of the target. (f) depicts the proton energy spectra predicted by PIC simulations in the case of using a more realistic preplasma density profile modelled with a separate hydrodynamic simulation versus using a preplasma profile that resulted in an optimisation study aiming to maximise the cutoff proton energy achievable with fixed laser and target parameters. Although Kapton and stainless-steel foils are often used experimentally, aluminium was chosen here as a representative solid-density target with similar interaction characteristics modelled in PIC simulations.

beyond those required for LhARA. Even though a foam-like preplasma is difficult to achieve on a solid target built for high repetition rate, future work will investigate whether similar density profiles can be produced by shaping the laser-contrast curve through the use of controlled pre-pulses or separate laser pulses.

A more elaborate picture of the effect that the preplasma scale length has on the propagation of the laser before it reaches the target is shown in figure 3.6. The two cases highlighted in figure 3.6 correspond to the case of an optimal preplasma density profile and a more realistic one. In each case, the laser-plasma interactions were simulated in three dimensions. The laser considered here has an intensity of $1 \times 10^{21}\,\mathrm{Wcm}^{-2}$, a pulse duration of 25 fs and a 1.5 μm focal spot size. The laser propagation through the preplasma in combination with the kinetic energy density of the electrons originating in the preplasma region indicate part of the mechanism that leads to higher proton cutoff energy in the case of longer scale-length preplasmas (see figure 3.5). When a near-critical low-gradient long plasma is present in front of the target, the laser penetrates through the under-dense plasma, where it undergoes self-focusing and steepening (figure 3.6). When the laser reaches the region where the plasma density is close to the critical density, it expels electrons forming semi-circular cavities (figure 3.6) [123, 164, 173]. The cavities are observed to be less well resolved in the case of the more realistic preplasma with a shorter scale length. In the presence of an extended preplasma, a larger number of electrons reach higher energies (figure 3.6).

Overall, these results indicate that the enhancement of the proton cutoff energy is due to the interplay between the laser pulse self-focusing, pulse steepening, the stochastic heating of fast electrons, and the potential laser filamentation starting at longer preplasma scale lengths [174]. However, further investigations are needed to understand the role of each process in the overall laser-target interaction. Nonetheless, reliable experimental techniques that modify the vacuum-target interface could offer control of these mechanisms and have a strong impact on the effectiveness of accelerating proton beams via TNSA. Thus, one conclusion from the simulations is that it will be important to control and measure the preplasma density profile to create optimal conditions for proton and ion acceleration from solid targets via TNSA. In a scenario in which the highest available laser intensity is used in combination with the thinnest target, controlling the preplasma represents one of the few approaches to increase the maximum achievable proton energy and to increase the accelerated proton flux.

Acceleration of carbon ions

An initial set of high-fidelity 3-D PIC simulations were performed to investigate the acceleration of C^{6+} ions from the back of a tape-like aluminium target. Aluminium is used, comparable to commonly used Kapton or steel foils in PIC simulations. The results show that carbon ions can be accelerated to a maximum energy of approximately half of the maximum energy obtained for protons in units of MeV/u for identical laser and target conditions. This is consistent with the assumption that identical laser and target parameters lead to acceleration fields with equivalent strength, irrespective of the contaminant ion species present on the back surface of the target.

The PIC simulations also indicate that the presence of hydrogen ions in addition to carbon ions on the back surface of the target leads to a lower cutoff energy for the heavier ion species due to screening of the accelerating field. For example, an equal number density of hydrogen and carbon ions on the back of the target was found to lead to a carbon cutoff energy three times lower than that obtained in the case where no other species is present. Thus, a lack of control of the composition of the contaminant layer on a tape target may prove to be a limiting factor in achieving high carbon-ion energies.

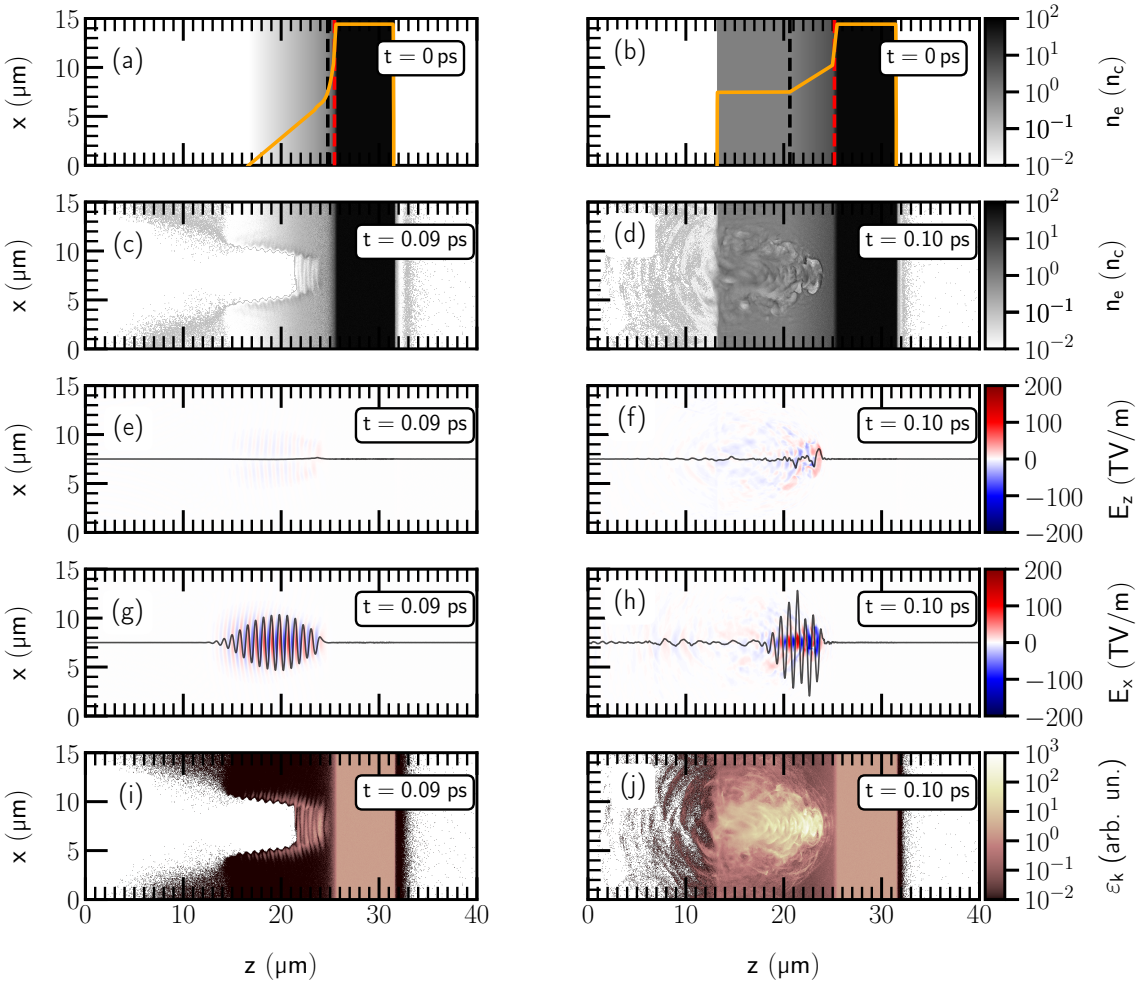

Figure 3.6: 3-D PIC simulations comparing the use of an aluminium target characterised by two distinct preplasma density profiles: a realistic one obtained from a separate hydrodynamic simulation (left column) and an 'optimal' one found as a result of a 2-D scan using a differential evolution scheme (right column)—(a)-(b) electron density at the start of the simulation, (c)-(d) electron density a short time before the laser reaches the bulk of the target, (e)-(f) longitudinal electric field, (g)-(h) transverse electric field, and (i)-(j) electron kinetic energy density. The laser pulse propagates from left to right and hits the bulk of the target at approximately 0.1 ps. The black and red dashed lines in (a),(b) denote the position of the critical density and the relativistic critical density, respectively. The orange lines in (a), (b) show the density lineout along the propagation axis of the laser. The black solid lines in (e)-(h) represent the electric field lineout in the middle of the simulation box.

3.4.4 Near-term plan for laser-driven ion source development

As the previous sections have shown, significant progress has been made towards developing and de-risking the laser-driven ion source for LhARA. The near-term development plan is to continue to address these challenges and to begin to test the source that has been developed at SCAPA to drive scaled-down radiobiology experiments. These are summarised in the following planned milestones.

Demonstration of beam delivery to end station

A series of permanent quadrupole magnets have been installed in the existing target chamber at the SCAPA laser facility downstream of the laser-driven proton source. This setup will be used to demonstrate the transport of the proton beam and to allow measurements of the beam properties at the end station to be performed. These measurements will be interpreted using numerical simulations.

Assessment of beam performance during PoPLaR experiment on SCAPA

The performance of the laser-driven ion source will be diagnosed and monitored while providing the beam for the PoPLaR experiment, and beam stability and integrated system operation will be investigated. These measurements will inform the further development of facility specifications and operational procedures.

Investigation and demonstration of 10 Hz debris and damage challenges at Imperial

The Zhi laser at Imperial College London will be used to demonstrate a laser-driven ion source running at a repetition rate of 10 Hz, matched to the baseline repetition rate of LhARA. Although the source will be generating proton beams with a lower maximum energy than required by LhARA, it will be possible to use the setup to perform studies of debris generation and to evaluate damage to laser-beamline optics and other sensitive components critical to the laser source.

3.5 Recommended future development programme

Section 3.3 summarises the key risks to the successful delivery of the proton and ion source for LhARA. There are further technical challenges which must be addressed when the initial risk-management programme is complete. These have been identified and a programme to solve these challenges has been developed and costed.

3.5.1 Outstanding development requirements

Diagnostic and hardware development

A programme is required to develop instrumentation for the laser-driven ion source. Existing laser, plasma and beam diagnostic techniques will need to be scaled to 10 Hz. This requires implementation of high-throughput data transfer and real-time analysis, which will need to be integrated into an appropriate control system and database. The control system must be able to use the data in an automated feedback system to stabilise the laser-driven ion source. The development of the diagnostic and feedback system for LhARA would be prototyped on the SCAPA laser facility, which can provide laser pulses at 5 Hz, and the Zhi laser, which can operate at 10 Hz.

Novel targetry development

A dedicated target testing platform is required to investigate the stability and long-term operation of novel target types, such as liquid jets. This platform will be developed and operated in collaboration with the Target Fabrication group at the STFC Central Laser Facility who have decades of expertise in targetry for plasma accelerators. The programme will include a test chamber and target diagnostic suite, as well as the construction of the liquid jet target itself. Different designs will be evaluated to determine the best performance and longevity. A portable version of the target will be developed to enable testing at the Zhi and SCAPA laser facilities. The target development will also be supported by state-of-the-art hydrodynamic and kinetic modelling of the target.

Heavy ion source development

A route to generating heavier ions (atomic number $Z \geq 2$) will be developed and tested. This will include a test of contaminant removal from tape drives at high repetition rate to establish whether bulk ion species or oxide layers can efficiently be accelerated at 10 Hz. This will be supported by the development of heavy ion diagnostics, including calibration and construction of a 2D scintillator-based beam profiler. The potential to use liquid or cryogenic targets for heavy ion generation will be evaluated. This will be supported by kinetic particle-in-cell simulations.

High repetition rate operations at full specification

A demonstration experiment at the full LhARA laser will be performed at 5 Hz using the SCAPA facility. This will include initial demonstration of a burst mode operation for up to 1 hour of continuous operation. Feedback from diagnostics will be used to stabilise the source.

Dedicated development beamline at SCAPA

To facilitate this proposed research and development programme, the construction of a new dedicated LhARA ion source development beamline within the Bunker B area of SCAPA is proposed. As shown in figure 3.7, a separate vacuum chamber, diagnostic system and radiobiology end station could be constructed in the existing space. This new beamline would make use of the same laser and many of the same subsystems as the current beamline. The laser beam path can easily be switched between the two beamlines by the introduction of a movable mirror, which would direct the laser in the direction of the new beamline. This new beamline would act as a long-term and modular platform for the development of new targetry, beam capture, ongoing radiobiology work and detector development. In the coming years, there will be increasing pressure on the existing SCAPA beamline for research programmes with different experimental setups. These pressures will make the kind of programmatic access required for LhARA more challenging to sustain. Therefore, a dedicated beamline, enabling integration tests for many of the key components of the LhARA Stage 1 beamline, at relatively low overall cost to the project, would be of significant benefit in demonstrating the feasibility of Stage 1 and would be a substantial aid in addressing the research programme outlined above, which is needed to help de-risk the overall project.

3.5.2 Alternative options

The recommendation for the laser-driven ion source above is configured to meet the baseline demands in terms of particle number and energy. However, one benefit of the laser-driven ion source is its scalability. The source could be reconfigured to provide different beam parameters

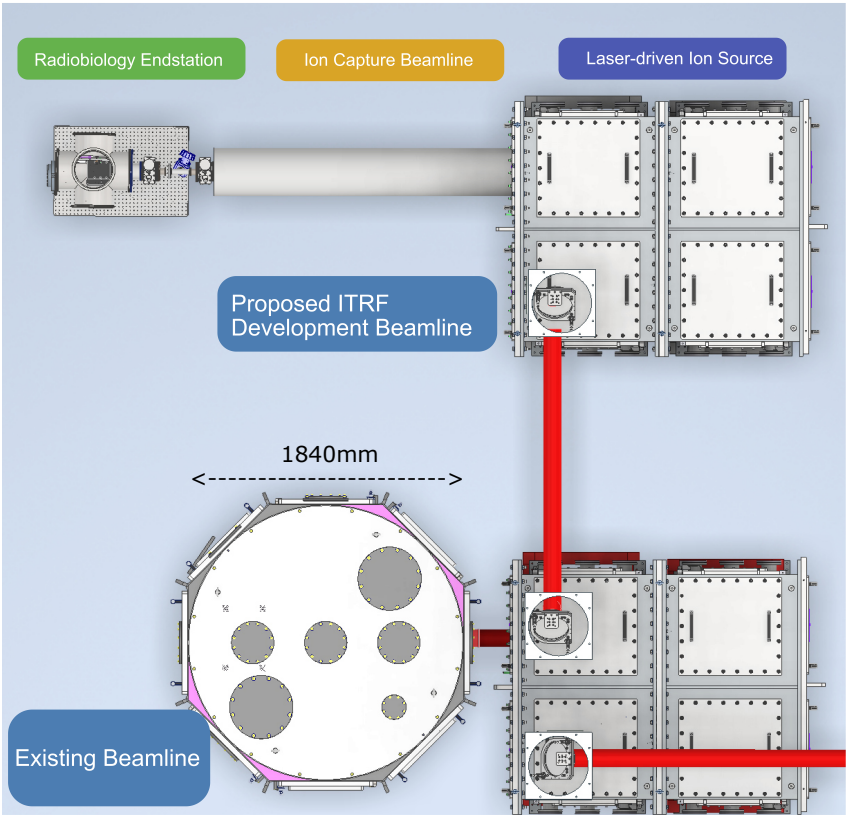

Figure 3.7: Schematic of one possible configuration for a dedicated beamline for ITRF in SCAPA. Shown here is an experimental arrangement in the Bunker B area of SCAPA where the laser is directed to an available space on the other side of the laboratory from the existing beamline. The space enables a modular design which allows independent and long-term development of the laser-driven ion source, capture beamline and the radiobiology end station.

depending on how the beamline demands develop during the project. Here, we give some examples of potential development paths to provide boosted beam parameters from the source.

Higher single-shot yields by increasing laser energy

The baseline energy at which protons are to be captured at LhARA is 15 MeV. This is a useful energy for *in vitro* studies as it is sufficient to allow the protons to penetrate a standard cell dish. Therefore, it could be considered as a minimum value for LhARA Stage 1. The baseline laser-driven ion source for LhARA described above will generate a proton spectrum with a maximum energy significantly larger than 15 MeV, likely to be > 20 MeV. Capturing the beam at an energy higher than 15 MeV would give further flexibility for radiobiology studies. This would include the possibility of controllably varying LET in cell irradiations with protons, or the irradiation of more complex 3D models. The argument against increasing the capture energy is that laser-driven ion sources exhibit a quasi-thermal energy spectrum such that there are fewer particles at higher energy. This then reduces the delivered dose per shot, which both slows data taking and could result in irradiation times exceeding the requirement for a time-averaged dose.

The proton yield of a laser-driven ion source could be increased by using a higher laser energy. The maximum proton energy scales approximately as $\varepsilon_{max} \propto E_L^{0.5}$, where E_L is the laser energy [146, 159]. At the same time, the particle flux also increases, typically near-linearly with the laser energy. Therefore, changing the laser specification (table 3.1) to use a higher laser energy could enable a higher energy Stage 1 design. As an example, the DRACO laser at the

Helmholtz Zentrum Dresden-Rossendorf can reliably generate protons with a maximum energy in excess of 50 MeV using a laser energy of 18 J on target [175]. Fluxes of approximately 10^9 protons have been delivered into a solid angle of 15 msr at 25 MeV with a bandwidth of $\pm 5\,\%$. The high energy of the DRACO laser allows therapeutic doses (≈ 10 Gy) to be delivered in a single shot [176, 177], widening the options for investigating high dose rate and fractionation.

Potential downsides would be a modest increase in the cost of the laser, which would require more amplification, and the laser optical beamline, which would use a larger beam diameter and therefore require larger optics. For a significant increase in laser energy, there may also be issues in designing a laser which can maintain a repetition rate of 10 Hz as thermal management of laser components, such as amplifier crystals and diffraction gratings, becomes increasingly difficult.

Using advanced acceleration mechanisms to boost beam parameters

Although the LhARA baseline design uses the Target Normal Sheath Acceleration method to generate ions, there have been significant advances in recent years in developing new acceleration strategies to improve the performance of the laser-driven ion source. In particular, there is significant interest in targets with a sub-μm thickness, lower than that optimal for TNSA. Instead of accelerating only the surface ions, it has been found that the whole target bulk can be accelerated to higher energies and with higher coupling efficiencies than TNSA. Record maximum proton energies have been measured, first up to around ≈ 100 MeV using a relatively low repetition rate, high energy laser [178], and then up to ≈ 150 MeV using higher repetition rate, medium energy laser systems [179]. Also notable is the significant boost in carbon energies observed in this regimen, up to 30 MeV/nucleon without any special target preparation [180], which is indicative of bulk acceleration.

Challenges remain in harnessing these advanced acceleration mechanisms. Rapid replacement of targets could be an issue, as it is not possible to use tapes with sub-μm thickness. However, this acceleration method is likely to be amenable to liquid jet targets, which can be generated naturally with sub-μm thicknesses. This could be used to generate protons, oxygen, and/or carbon ions, depending on the choice of liquid. Of particular concern is shot-to-shot stability [179], which can cause strong variations in the ion energy and flux. The source of the poor stability is still under investigation, and it is not yet clear whether the interaction can be controlled sufficiently to be usable for flux-sensitive applications, such as LhARA. Although the development of these advanced regimens is beyond the scope of the activities associated with the ITRF, progress in the field should be monitored to see if they should be adopted for LhARA in the future.

CHAPTER 4

Proton and ion capture

4.1 Introduction

The laser-driven proton and ion source produces a flux of particles with a broad energy spectrum and a large angular divergence. Therefore, a large acceptance strong, cylindrically symmetric focusing element is required to capture the beam efficiently. The use of an electron cloud as a focusing element for charged particle beams was first proposed by Gabor in 1947 [79]. Gabor noted that a cloud of electrons uniformly distributed about the axis of a cylindrical vessel would produce an ideal focusing force on a beam of positively charged particles. In the original proposal, an axial magnetic field, produced using a solenoid, was proposed to provide radial confinement while an axial electrostatic field was employed to confine the cloud in the longitudinal direction. The solenoid field causes electrons to spiral around the central axis and confines them in the radial direction. A potential well (trap) was created using a cylindrical anode and grounded electrodes at the ends of the cylindrical volume to confine the electron cloud in the longitudinal direction.

If the motion of electrons captured in the lens under the combined electric and magnetic fields is considered using appropriate boundary conditions, the confinement conditions can be determined [181]. In the radial direction, where there is magnetic confinement and Brillouin flow, the number density of electrons, n_e, is given by:

$$n_e = \frac{\epsilon_0 B_{\mathrm{GPL}}^2}{2m_e} = 5 \times 10^{18}\, B_{\mathrm{GPL}}^2\,;$$

where B_{GPL} is the magnetic field, e the magnitude of the charge on the electron, m_e the mass of the electron, and ϵ_0 the permittivity of free space. In the longitudinal direction, where there is electrostatic confinement, n_e is given by:

$$n_e = \frac{4\epsilon_0 V_A}{eR^2}\,;$$

where R is the radius of the cylindrical anode, which is held at the positive potential V_A. The longitudinal confinement condition imposes a strict limitation on the electron density relative to the anode voltage. In theory, the number density varies with the origin of the electrons; those generated within the trap are better confined than those generated in regions outside the magnetic field. In practice, the number density never reaches the theoretical limit, and an 'efficiency factor' is required to obtain agreement between theory and measurement. Eliminating n_e between the two expressions allows a relationship between the magnetic and electric field strengths to be derived. The theoretical number density of confined electrons in the cloud is then defined by the dimensions of the apparatus and the magnitude of the fields. In the thin lens approximation, the focal length, f, of a Gabor lens can be expressed in terms of the magnetic field and the particle velocity, v_p:

$$\frac{1}{f} = \frac{e^2}{2\epsilon_0}\left[\frac{ZE_0}{P_0^2}\right] B_{\mathrm{GPL}}^2 l\,; \tag{4.1}$$

where Z is the charge state of the ion and E_0 and P_0 are the energy and momentum of the reference particle. The focal length of the Gabor lens is therefore proportional to the kinetic

energy or, equivalently, the square of the momentum, of the incoming beam. By comparison, the focal length for a solenoid is proportional to the square of the momentum, and that of a quadrupole is proportional to the momentum. For a given focal length, the magnetic field required in the Gabor lens is reduced compared to that of a solenoid that would give equivalent focusing:

$$B_{GPL} = B_{sol}\sqrt{Z\frac{m_e}{E_0}}\,; \tag{4.2}$$

where B_{GPL} and B_{sol} are the magnetic fields in the Gabor lens and the equivalent solenoid, respectively. In the case of a proton beam, the reduction factor is 43. So, for example, where a 2 T superconducting solenoid would be required, the magnetic field required for a Gabor lens would only be 47 mT. This means the cost of a Gabor lens can be significantly lower than the cost of a solenoid of equivalent focusing strength. In addition, the electrostatic focusing provided by the Gabor lens, combined with magnetic deflection in the arc, or the FFA injection line, allows particle mass to be selected and makes it possible to deliver a beam containing a single ion species.

The plasma-confinement system described above is commonly known as a 'Penning trap' and has found wide application in many fields [182]. Variations on the Penning trap where axial apertures in the cathodes are introduced, such as the Penning-Malmberg trap [183, 184] are attractive for beam-based applications due to the excellent access provided to the plasma column; see figure 4.1. The properties of these particle traps are well described in the literature, and a wealth of papers are available [185–187]. One feature of these types of Penning trap is the simple harmonic motion of the trapped particles in the combined electric and magnetic fields. This allows detailed investigation of the properties of the trapped particles through their oscillation frequencies. In a lens application, oscillation of the trapped particles is not problematic provided the electron oscillations do not introduce non-uniformity into the plasma cloud, which would degrade the focusing performance. Magnetic confinement fusion provides useful insight; the history of magnetically confined fusion is populated with the discovery and suppression of plasma instabilities and this subject remains the object of much research effort.

As the number density of the trapped particles increases, the growth rate of instabilities increases, and stability becomes more difficult to achieve. It might therefore be expected that a reduction in electron number density would provide a useful means to stabilise the plasma

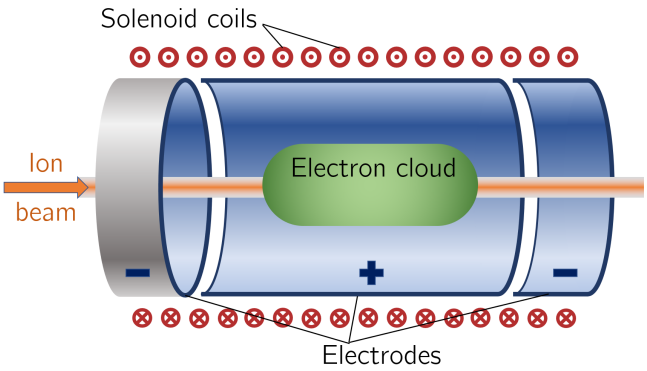

Figure 4.1: Schematic diagram of a Penning-Malmberg trap of the type proposed for use in the Gabor lenses to be used in LhARA, sourced with permission [13]. The solenoid coils and the direction of current flow are indicated by the red circles. The confining electrostatic potential is provided using a central cylindrical anode and two cylindrical negative end electrodes. The ion beam enters on-axis from the left, and the electron cloud is indicated by the green shaded area.

lens. However, the power of the focusing effect is linked to the number density, and so there is a strong driver to maximise the number density. Thus, one design goal for the Gabor lens for LhARA is to maximise the available electron density.

Plasma dynamics causes instabilities in a plasma to grow at characteristic rates. It may therefore be expected that instabilities will appear after an initial stable period. As the beam source proposed for LhARA produces a very short pulse of positively charged particles, it is reasonable to propose a system that uses a transient electron cloud synchronised to the beam source. Gabor lenses can also operate at appreciable vacuum pressures, opening up the possibility of beam space-charge neutralisation, should the application require it.

The Stage 1 beam-transport system requires seven electron-plasma focusing elements, each of length $\sim 1\,\mathrm{m}$. Gabor lenses have many attractive features for the LhARA project, including the possibility of very strong focusing, simple construction, and a low magnetic field. These attractive features come at the cost of vulnerability to electron-plasma instability and operation at relatively high voltage ($> 50\,\mathrm{kV}$).

The status of the research programme carried out using the Penning-Malmberg trap installed in a beam line at Swansea University is described in the section that follows.

4.2 Overview of the Swansea Penning-Malmberg trap beamline

The Swansea positron beamline has been in development since the early 2000s; its current configuration is shown in figure 4.2. It was developed for the study of positron beamline techniques and to facilitate the study of the electron-positron bound state: positronium. Such experiments typically use clouds of positrons with densities orders of magnitude below those required for the electron plasmas of the LhARA Gabor lenses. The most recent major addition to the beamline was made in 2014, during which a Penning trap was added to the positron accumulation system to serve as a third-stage accumulator to enable up to 10^8 positrons to be accumulated; it is this trap which is used to facilitate the studies of electron plasma confinement for LhARA.

The main components of interest for the LhARA studies are shown in figure 4.3. Electrons are confined axially in the central region by nine, cylindrical, gold-plated aluminium electrodes and radially by a water-cooled solenoid that surrounds the vacuum tube and is designed to produce a 400 G (Gauss) field. On either side of the storage trap are stainless steel six-way vacuum crosses, each being evacuated to a base pressure of 10^{-9} mbar by turbo-molecular pumps. Upstream of the solenoid, an electron gun is mounted on a vertical linear manipulator inside the vacuum cross. Downstream, the second cross houses an MCP/phosphor screen installed on an independent linear manipulator. Large-diameter coils are placed on either side of the vacuum

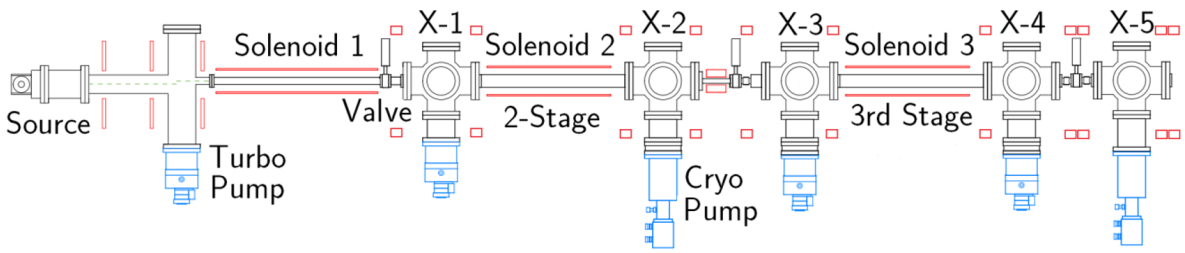

Figure 4.2: Schematic of the full positron beamline with vacuum components in black, pumps in blue and magnetic coils in red. The region between X3 and X4 was used for the LhARA studies and elucidated in figure 4.3.

crosses, roughly in a Helmholtz configuration, to transport the particles. Detailed descriptions of the electron source, storage trap, and detector assembly are provided in the following sections.

4.2.1 Electron source

The electron source is a thermionic electron gun, schematically shown in figure 4.4, mounted on a linear manipulator that controls its vertical position. This allows off-axis electron injection relative to the symmetry axis of the storage trap or injection, precisely aligned with the guiding and trapping magnetic fields. Electrons are emitted from a linear tungsten wire. The emission current can be adjusted by changing the current from the power supply unit (PSU) connected to the filament. To avoid damaging the filament, the current supplied is kept below a maximum value of 3.3 A. The electrons are extracted from the surface of the wire by a fine metallic grid biased to a positive voltage and situated downstream of the filament. The grid bias voltage also determines the 'parallel energy' of the electrons as they exit the source. The energy of the electron beam is dictated by the positive voltage difference between the grid and the filament. A voltage source provides an accelerating voltage of up to 30 V between the hot wire and the grid.

4.2.1.1 Electron beam energy

The energy profile of the electron beam produced by the source is measured to assess the spread of the parallel energy of the electrons that reach the trap. Here, parallel energy denotes the kinetic energy that corresponds only to the axial component of the velocity of a single particle. During a measurement of the beam energy, all but one of the electrodes of the trap are set to ground voltage. The remaining electrode is set to a negative retarding potential that blocks

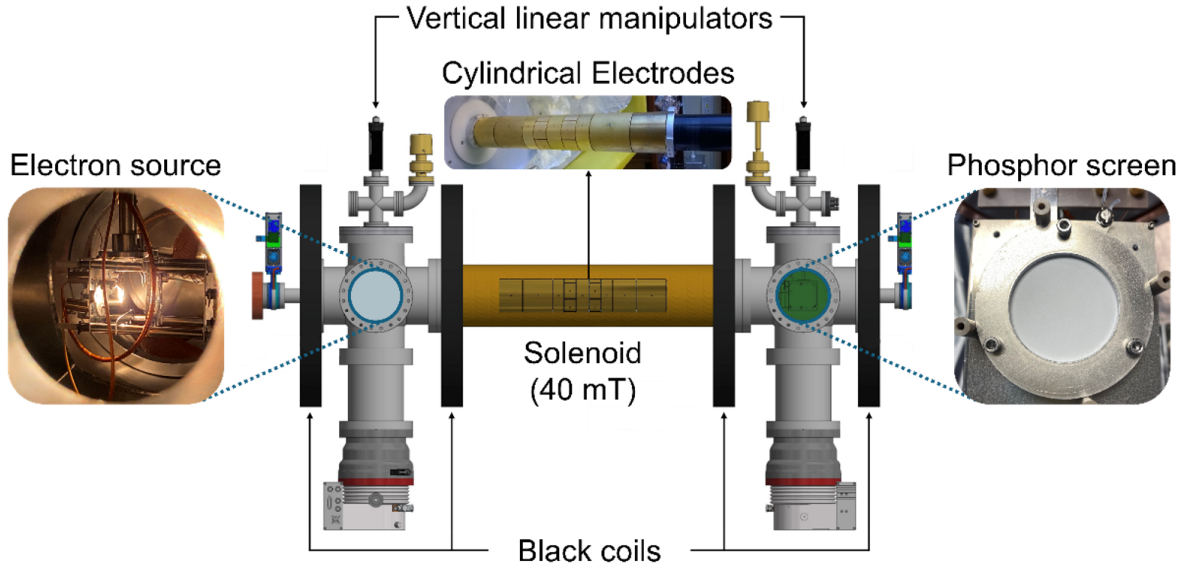

Figure 4.3: The main components of the particle trap of the Swansea positron beamline. The six-way vacuum cross on the left houses an electron source mounted on a vertical linear manipulator. Nine gold-plated aluminium electrodes used for axial trapping of particles are covered by the central solenoid (gold) to confine particles axially. A phosphor screen is mounted on a linear manipulator inside the vacuum cross on the right. Two pairs of Helmholtz coils (labelled Black coils). Each cross is pumped by a turbo-molecular pump.

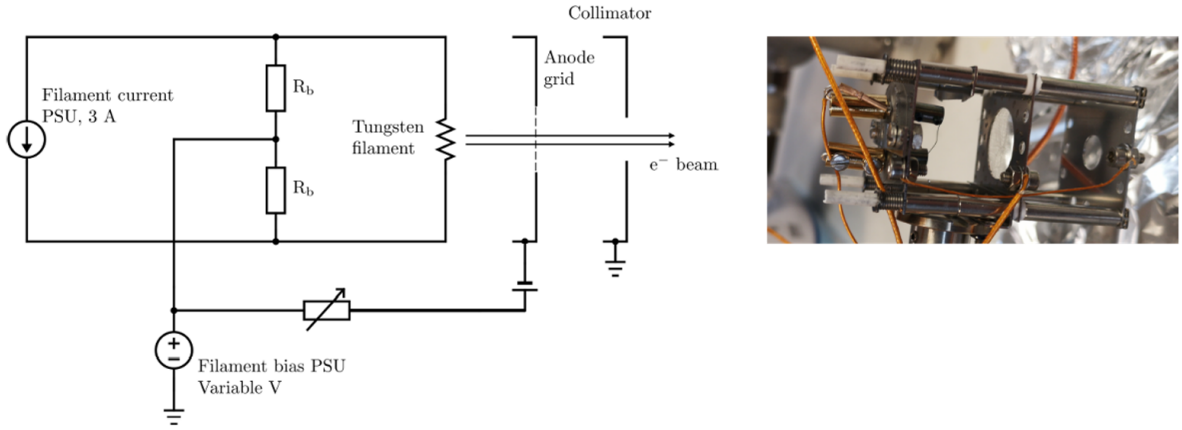

Figure 4.4: Effective circuit diagram of the electron gun used to inject particles into the trap (left). Image of the gun (right) dismounted from the beamline. The tungsten filament is typically heated with 3 A and biased at 30 V. The gun produces an electron beam with an emission current of several tens of μA with an upper limit of about 300 μA.

all the electrons with an energy lower than the equivalent decelerating voltage supplied by the electrode. Measuring the current of the beam that passes the decelerating electrode by scanning the magnitude of the voltage applied to the electrode results in a cumulative distribution of the number of electrons as a function of the blocking voltage, as shown in figure 4.5. The energy profile of the electron beam is then calculated from the cumulative energy distribution. Figure 4.5 shows the energy distribution of the electrons produced by the source for two different extraction voltages. Both measurements show the electron number peaking near the maximum beam energy, which is determined by the acceleration voltage applied to the grid, followed by a sharp drop-off. The electron beam typically has a wide energy spread of about 20 eV with lower particle numbers towards the low-energy tail of the distribution.

4.2.2 Storage trap

The longitudinal and radial confinement of electrons is achieved using the typical Penning-Malmberg trap configuration. The confining fields are generated by cylindrical electrodes surrounded by a solenoid magnet. The gold-plated aluminium electrodes, with an inner diameter of 41 mm, can be biased up to ±140 V and vary in length as shown in figure 4.6. Any two electrodes can be used as end caps of the trap and the distance between the two electrodes determines the length of the resulting electron column. The different lengths of the electrodes allow the longitudinal extent of the volume in which the electrons are confined to be varied by using different combinations of electrodes as the two end caps of the trap. Furthermore, the length of the trapped electron column is influenced by the shape of the axial potential well and, thus, by the voltage applied to the end-cap electrodes. The axial electrostatic potential well is not quadratic, especially for the longer configurations of the trap. Thus, the motion of the electrons is expected to show deviations from that of an ideal Penning trap.

Two of the electrodes have six azimuthal segments for implementing a rotating electric field, known as the 'rotating wall' (RW) technique. This method allows for the radial compression of electron columns by injecting angular momentum into the plasma at a rate that counteracts outward expansion. To ensure electrical isolation, the electrodes are separated by sapphire balls 2 mm in diameter, which are positioned in machined indents at the ends of each electrode, creating a 1 mm gap between adjacent electrodes. Each electrode is connected to a breakout box outside the trap solenoid via a wire, secured by titanium screws to minimise interaction

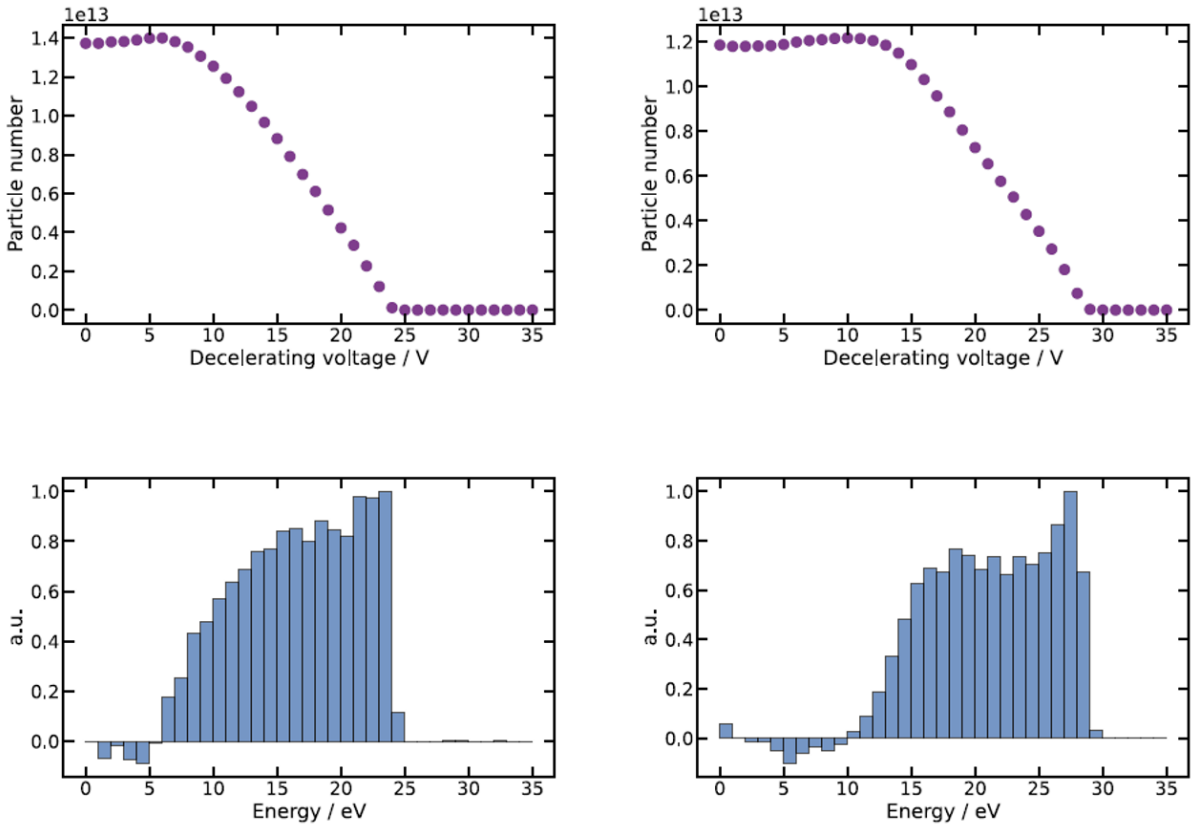

Figure 4.5: Top: The number of electrons measured downstream of the trap as a function of the decelerating voltage applied to one of the cylindrical electrodes of the trap with respect to the potential of the source. Each data point is the average of four separate measurements. The extraction voltage at the source is 25 V and 30 V for the left and right columns, respectively. Bottom: The axial-energy profile of the electrons emitted by the source for the two different extraction voltages.

with the surrounding magnetic field.

4.2.3 Electron imaging assembly

The primary figure of merit for an electron trap is the total number of trapped electrons or the corresponding particle density. In a single experimental sequence, electrons were released by rapidly reducing the bias voltage on the downstream end-cap electrode. The number of electrons ejected was determined by measuring the charge collected on a conductive surface downstream of the trap. Further information on the position of the electrons and their transverse distribution was obtained using a scintillating material coupled with a photo-sensitive detector to pick up the photons produced by the electrons that hit the scintillating material. The principal components of the assembly are the micro-channel plate (MCP) and the phosphor screen (P-screen).

The role of the MCP is to amplify the number of electrons ejected from the storage trap by several orders of magnitude, as the typical number of trapped electrons is insufficient to generate a photon shower large enough for imaging by a camera. The MCP consists of a highly resistive plate, usually made of lead glass, with millions of microscopic channels running from the entry to the exit face. These channels typically have a diameter of 10 μm and are spaced 12 μm apart. An electric field to accelerate the electrons is established within each channel by two conducting layers on the faces of the MCP, which are individually biased to high voltages.

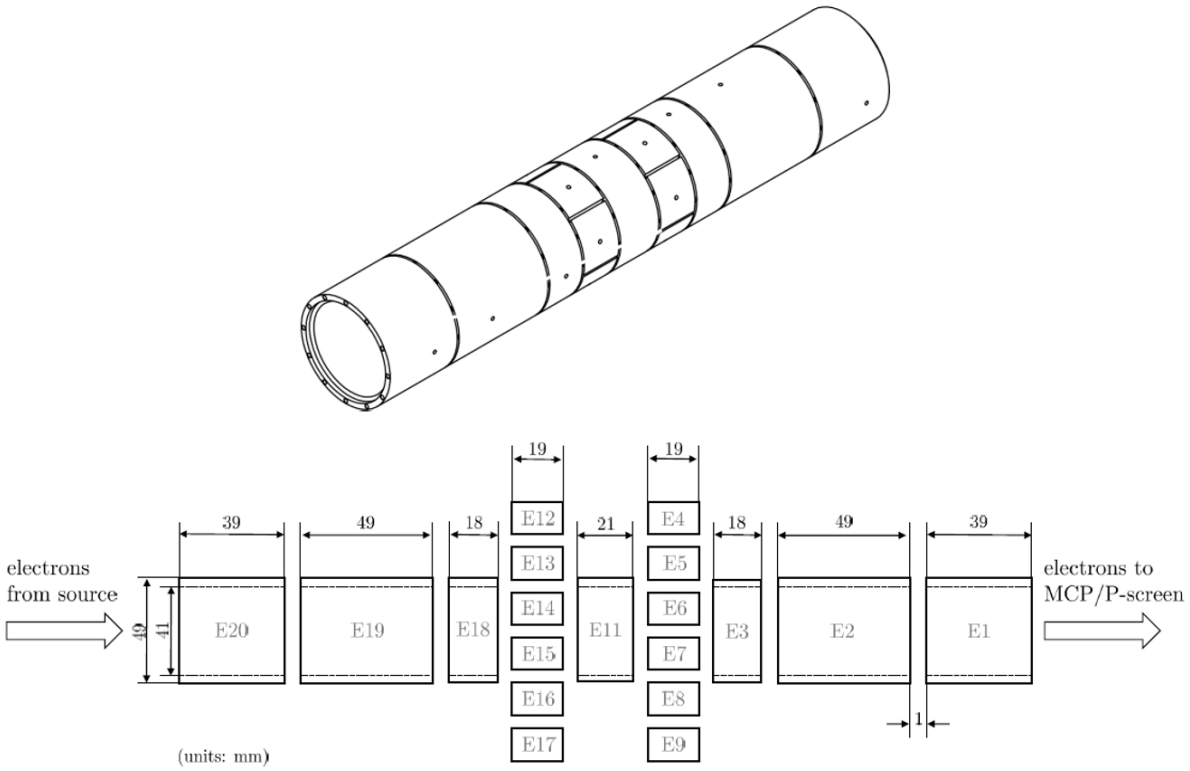

Figure 4.6: Top: Diagram of the electrodes of the electron trap. The electrodes are separated by insulating sapphire spheres, and each has a hole for the electrical connection. Bottom: Schematic of the electrode structure in the storage trap. The electrodes are numbered according to the electrical connections to the external breakout box. Electrodes 4 to 9 and 12 to 17 represent azimuthal segments of two complete ring electrodes designed for the application of rotating electric fields.

The channels are angled relative to the plate's normal axis to maximise the probability of an electron striking the channel walls, releasing secondary electrons in the process. As a result, the MCP functions as millions of parallel continuous dynodes, multiplying the incoming electron signal through successive collisions within each channel, leading to high-gain amplification.

In the LhARA project, the total number of trapped electrons is sufficiently high to be detected by the P-screen alone. Therefore, the MCP and P-screen assembly has been replaced with a P-screen. The holder for the P-screen is designed as illustrated in figure 4.7. The holder is mounted on a vertical linear manipulator inside the vacuum cross downstream of the electron trap (see figure 4.3). The P-screen used in the LhARA project is supplied by Analytical Components and is made of P43 (GdO_2S: Tb). This material emits light in the green part of the visible spectrum when struck by a charged particle, due to the excitation and relaxation of electron-hole pairs. The P-screen is biased with a voltage of 3 kV to allow electrons to pass through the aluminium overlay of the P-screen.

A schematic diagram of the imaging assembly and its functions is shown in figure 4.8. A mirror mounted at a 45° angle behind the screen reflects the scintillation light through a window out of the vacuum system. This light is then captured by a Hamamatsu Orca-R2 CCD camera, processed, and recorded using LabVIEW [188]. The camera is housed in a light-tight box to block ambient light. In front of the P-screen, there is an additional fine mesh grid that helps to create a well-defined electric field in front of the P-screen and can be biased to act as an energy filter. This grid can also be used to protect the P-screen from being damaged by a large number or high density of electrons accidentally striking it (e.g. by allowing the direct transmission of

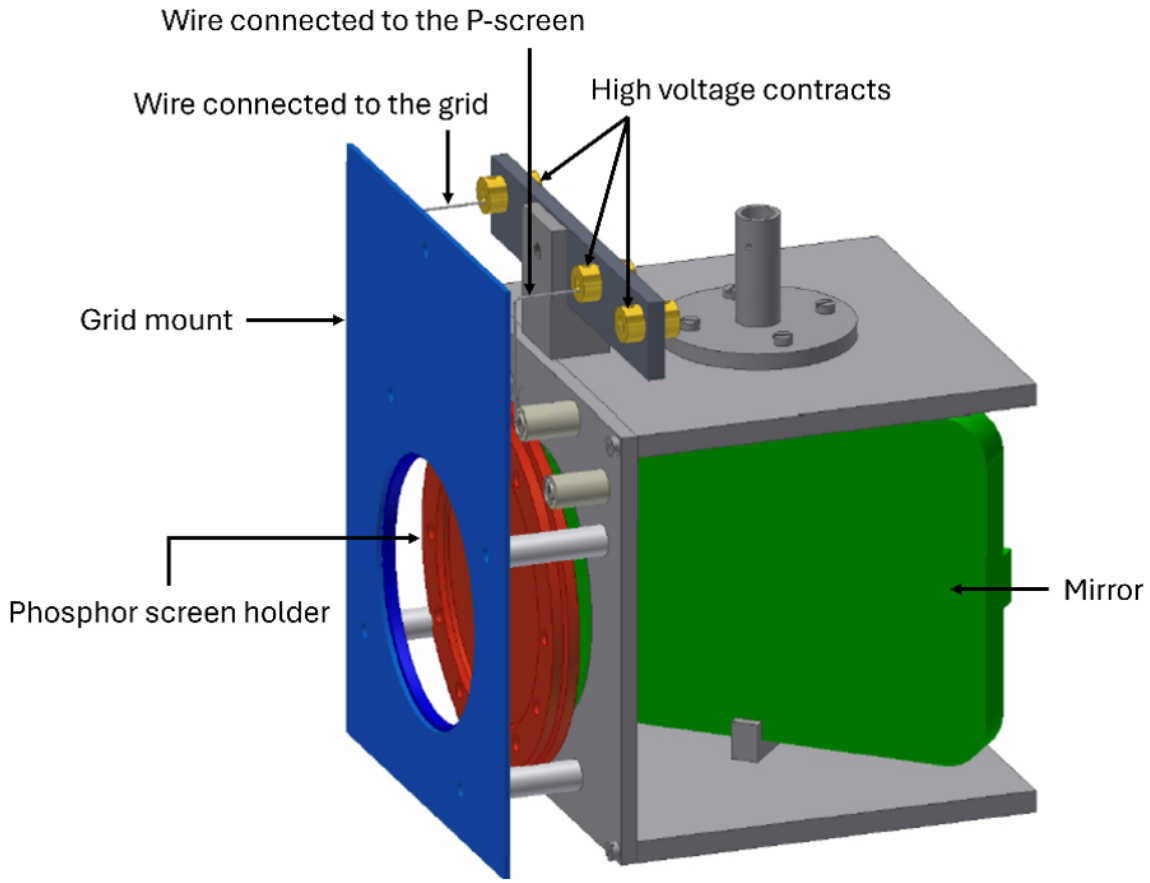

Figure 4.7: The phosphor screen (P-screen) imaging detector: protective grid mount (blue), P-screen holder (red), mirror (green), high voltage contacts (gold) and assembly rig (grey).

electrons from the electron source). Figure 4.9 shows the radial profile of the plasma captured using the new P-screen and the plasma profile obtained with the MCP.

4.3 Modifications to the existing beamline

Upgrades to the existing apparatus to support the LhARA studies are described below. Several components of the positron beamline have been updated, including replacing the MCP with a phosphor screen as described in the previous section, installing a solenoid coil mount, and integrating a high-voltage amplifier to supply the −400 V trap potential.

4.3.1 Installation of solenoid coil mount

A manipulator capable of precisely positioning the solenoid coil used to produce the magnetic field that traps particles radially was designed (see figure 4.10). The manipulator allows the coil position to be adjusted in the transverse and longitudinal directions. The manipulator offers fine-tuning capabilities and reproducible positioning, ensuring precise control over the solenoid coil and will allow study of plasma confinement in precisely-aligned magnetic-field configurations.

With the new manipulator installed, the solenoid coil must be aligned such that its axis coincides with the axis of the trap to ensure that the generated magnetic field is uniform along the length of the trap. Misalignment can introduce radial or transverse magnetic-field components,

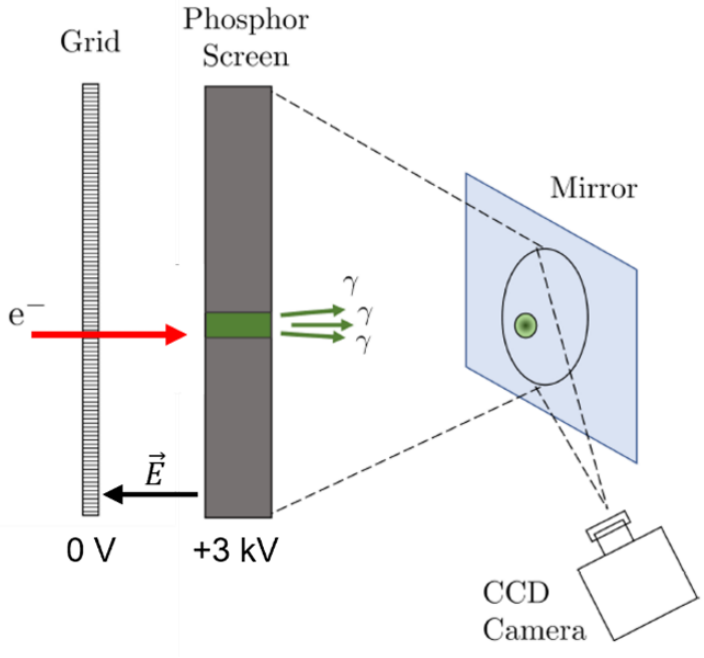

Figure 4.8: Schematic of the detector assembly. An incident electron is converted into a photon signal upon striking the phosphor screen (P-screen). The P-screen typically operates with a bias voltage of 3 kV and has a diameter of 40 mm. A fine mesh grid that helps to create a well-defined electric field in front of the P-screen and can be biased to act as an energy filter. It can also protect the P-screen from damage caused by a large number or high density of electrons accidentally striking the screen.

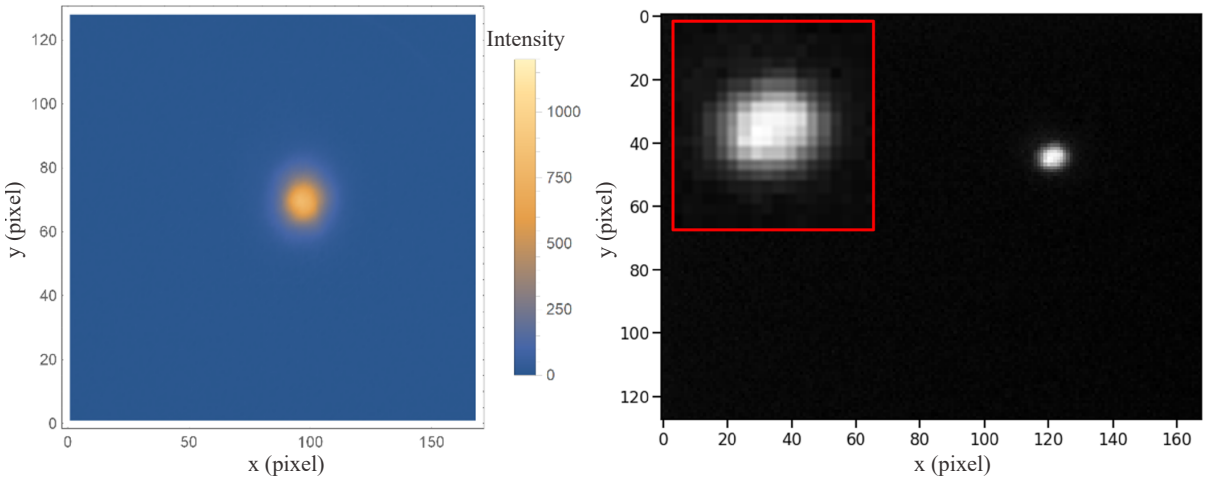

Figure 4.9: Radial profiles of plasma obtained with the new phosphor screen (a) and the high-gain MCP (b).

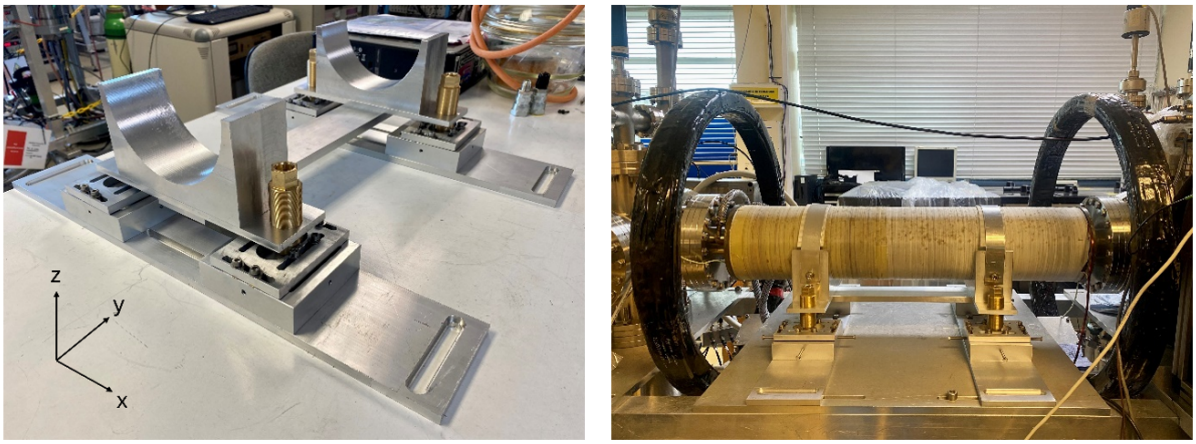

Figure 4.10: The solenoid coil manipulator (left) and the manipulator installed in the Swansea positron beam line (right). The manipulator allows precise adjustments in both the transverse and horizontal directions.

which degrade confinement and lead to electron loss. The solenoid coil is initially positioned roughly to align with the trap axis. The performance was verified by measuring the lifetime of the trapped electron plasma. To optimise the alignment, the solenoid position is adjusted to optimise the electron-cloud lifetime. The optimal coil position results in a plasma lifetime of 2.28 s, as shown in figure 4.11. Details of this measurement are provided in Section 4.5.1.

4.3.2 Integration of high-voltage amplifier for -400 V trap potential

To increase the trapping potential and accommodate a larger electron population, high-voltage amplifiers capable of delivering up to ±400 V were installed. Prior to installation, a thorough calibration of the amplifiers was performed to ensure accurate voltage output and reliable performance. During the calibration process, the input signal to the amplifier was gradually adjusted from -10 V to 10 V, and the corresponding output voltage was measured at each increment.

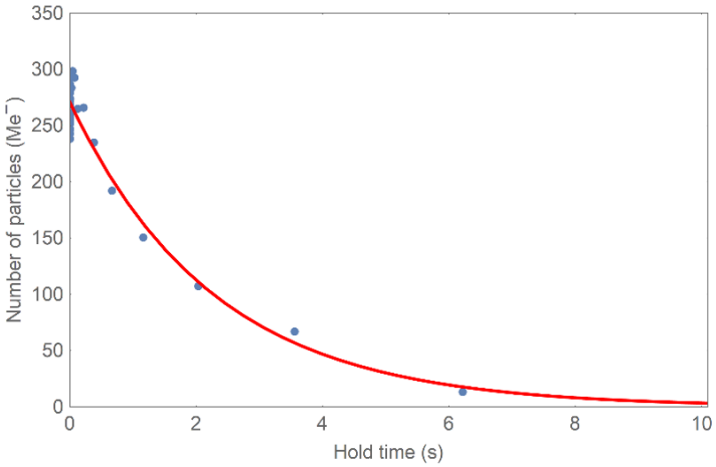

Figure 4.11: A lifetime curve showing the charge within the trap as a function of time. The red line is a fit of the form $ae^{-t/\tau} + b$ with lifetime $\tau = 2.28 \pm 0.35$ s. The cluster of data points at short hold times (near zero) corresponds to independent experimental runs taken on different occasions and does not indicate repeatability or a systematic uncertainty.

The recorded input and output voltages for each step are presented in figure 4.12. The fitted curve indicates that the gain of the amplifiers is 39.64. Following this calibration, the amplifiers were integrated into the experimental setup. The results of trapping electron plasmas under high-voltage conditions are presented in Section 4.5.3.

4.4 Experimental procedure

This section outlines the capture-store-release cycle for measuring the parameters that characterise the electron plasma and summarises the control and data collection systems. Key methods, such as the use of LabVIEW for sequence automation and integration of data acquisition devices, are explained. Finally, the data processing techniques, which are used to analyse the total number of trapped electrons, are described.

4.4.1 Experiment cycle

The capture-store-release sequence consists of three main stages:

- Capture of the electrons from the source into the confinement section;
- Storage and manipulation of the electrons within the trapping electrodes; and the
- Subsequent ejection of the electrons towards the imaging detector.

The experimental sequence is shown schematically in figure 4.13.

Initially, electrons from the source are loaded into the trap by grounding all electrodes except for the electrode at the downstream end, which is raised well above the parallel energy of the incoming electron beam such that the beam is reflected. Typically, the blocking potential is raised to the maximum available voltage of -140 V, which was limited by the voltage amplifier. Subsequently, the upstream end electrode, closer to the electron source, is raised to a potential which is slightly lower than the beam's maximum potential (-28 V), while the downstream end electrode remains at a high potential to fully block the electrons. The most energetic electrons enter the trapping volume and are reflected by the downstream barrier. These electrons lose

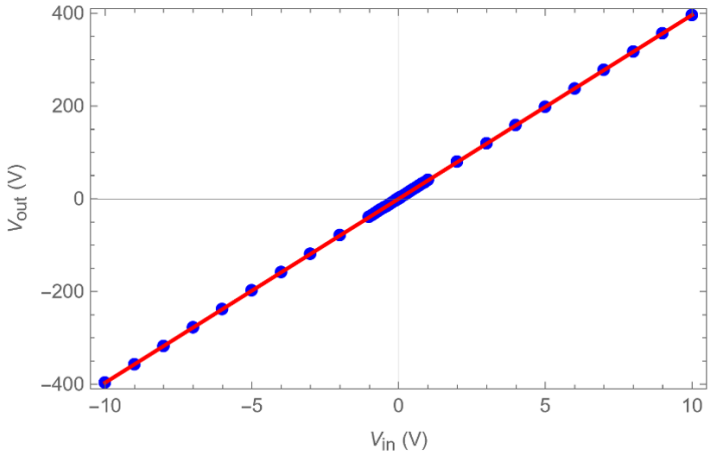

Figure 4.12: A result of high-voltage amplifier calibration demonstrating the relationship between the input signal to the amplifier, ranging from -10 V to 10 V, and the corresponding output voltage. The red line represents a linear fit, indicating that the amplifier gain is 39.64 ± 0.04.

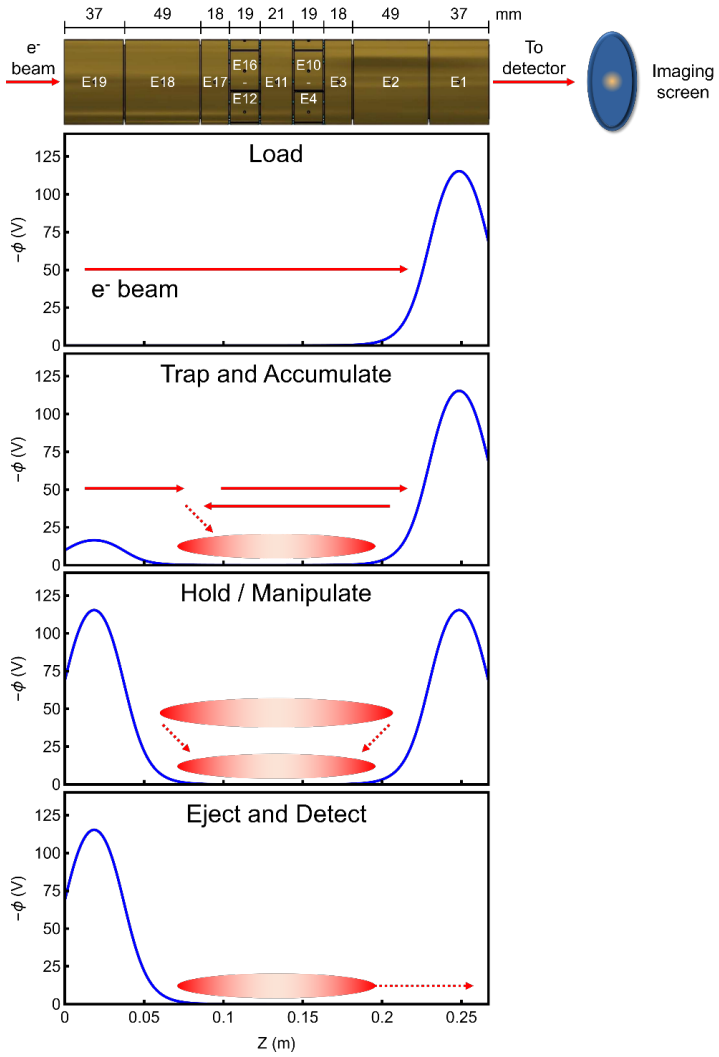

Figure 4.13: A representation of a typical experimental sequence: (A) Reset of the trap potential (B) Electron capture or accumulation by raising the voltage on the upstream end electrodes to a potential slightly lower than the beam's maximum potential, while the downstream end electrode remains at a high potential to block electrons (C) Electron cloud storage, manipulation and study (D) Electron cloud release by lowering the voltage on the end of the trap closer to the phosphor screen. Red arrows indicate electron streams. The blue line shows the on-axis electric potential of the trap, and a drawing of the cylindrical trap electrodes is shown at the top.

energy through collisions with residual gas or via a two-stream instability. If they lose sufficient energy, they cannot pass the entry barrier and become confined.

The axial potential well can be kept open for a long time, up to several seconds, to accumulate electrons. However, as the space-charge density inside the trap increases and electrons that have already been captured spend longer inside the trap, the rate of accumulation will be compensated by the rate of loss of electrons due to radially outward motion. Long accumulation times also lead to significant radial expansion of the trapped electron cloud. At the end of the accumulation interval, the voltage on the upstream end electrode is raised to -140 V to block any further electrons from entering the trap. The space charge is confined in a symmetric potential well for the desired storage time. Lastly, the electron cloud is released by lowering the voltage on the downstream end electrode and travels to the P-screen for detection.

4.4.2 Experiment control and data collection

The study of electron and positron plasmas is carried out using the Swansea positron beamline. Experiments are set up using LabVIEW "virtual instruments", exploiting the graphical user interfaces. The "Sequencer", a key virtual instrument, manages the execution of the sequence (see figure 4.13). The sequencer automates changes in the particle-trap potentials, timing steps, and data acquisition. The Sequencer generates a file that sets variables, produces analogue and digital outputs, and triggers data collection. Running this file operates the experimental setup, allowing for flexible and efficient execution of complex and repetitive experiments.

Several data acquisition devices are integrated with the control system to record data automatically during each experimental sequence as configured by the user. The two primary devices used in this work are:

- **Digitiser**: records the voltage response of the P-screen, which is converted into charge to determine the total number of electrons in the trap. The apparatus can record voltage readings at a maximum sample rate of two giga-samples per second across two separate channels, with 8-bit resolution in a 100 mV to 10 V range. The recording of the data by the digitiser is synchronised with the experimental sequence by a hardware trigger implemented on an FPGA (field-programmable gate array). The digitiser card is configured using LabVIEW, which extracts and saves the data onto disk storage. The resulting files are structured to contain the timestamp of the run, any sequences within the run, and the settings of the digitiser, such as sampling rate and voltage range. The files recorded can subsequently be associated with a specific experimental run by their unique time identifiers. A set of Mathematica scripts is used to extract the raw data from the structured files, display the voltage-time traces, and process parts of the signal. Figure 4.15 shows an example of a digitiser trace from the P-screen detector that resulted from the collection of an electron cloud released from the storage trap.

- **CCD camera**: captures scintillation light from the P-screen. The resulting images are processed to determine the distribution of the electrons. The camera is configured using LabVIEW, which also extracts and saves the image data into a file structure consistent with that produced by the data acquisition from the digitiser. A hardware trigger on an FPGA ensures the synchronisation between the camera acquisition and the sequencer. The stored images can then be paired with the corresponding voltage trace from the digitiser by the unique time and sequence identifiers.

Both the digitiser and the camera can be triggered during a sequence at precise points that are specified in the sequence-control software through individual digital outputs. In most of this work, the camera and the digitiser were triggered when the axial potential barrier of the storage trap was lowered, and the electrons were ejected from the confinement section of the beamline towards the imaging detector.

4.4.3 Data processing

The total number of electrons directly establishes the confinement capabilities of the trap and, in part, determines whether the dynamics of the trapped-electron ensembles correspond to the plasma or the non-interacting, single-particle regime.

To determine the total number of electrons, a digitiser is used to record the voltage-time trace generated by electrons rapidly charging the P-screen. The voltage trace is processed to extract the rapid voltage change when the electrons hit the detector. The change in voltage is then converted into the total charge collected or the corresponding total number of electrons. The total number of electrons is calculated via $N = eV/C$; where e is the electron charge, V is the change in voltage measured by the digitiser when the electrons hit the P-screen, and C is the capacitance of the P-screen and cable, which is calculated from a measurement of the time constant of the resonant circuit. When the P-screen is hit by electrons, it acts as a discharging RC circuit with a known resistance, R=1 MΩ. The exponential decay of the charge in the P-screen circuit is equivalent to the exponential decay of the voltage recorded by the digitiser. An example of the time dependence of the voltage recorded by the digitiser before and after electrons hit the collector is shown in figure 4.14. As the discharge of the resonant circuit corresponds to a voltage decay given by $V = V_0 \exp(-t/\tau_{RC})$, the decaying part of the signal recorded by the digitiser is fitted with the function $a \exp(-(t + t_0)/\tau_{RC}) + b$ to extract the capacitance C. The result shows that $\tau_{RC} = RC = 0.69$ ms, and therefore the capacitance is 0.69 nF.

A typical voltage trace recorded by the digitiser is shown in figure 4.15. Typically, the digitiser is configured to start recording the voltage before the electron signal, with at least 20% of the total acquisition time remaining. The flat trace before the electron signal is used to calculate the average level of electronic noise. When the charged particles hit the P-screen, the voltage drops rapidly. The change in voltage generated by the collected charge is calculated as the difference between the mean value of the recorded signal before the first break point and the mean value of the signal after the second break point.

The P-screen is used to measure the number of electrons that are ejected from the trap and have travelled to the P-screen. For a large radius plasma, charge may not be detected on the P-screen as the plasma radius may exceed the P-screen radius. There can also be losses due to aperture along the beamline and due to magnetic field misalignments. Efficient transport of the electrons is performed using the magnetic coils positioned along the beamline. The generated

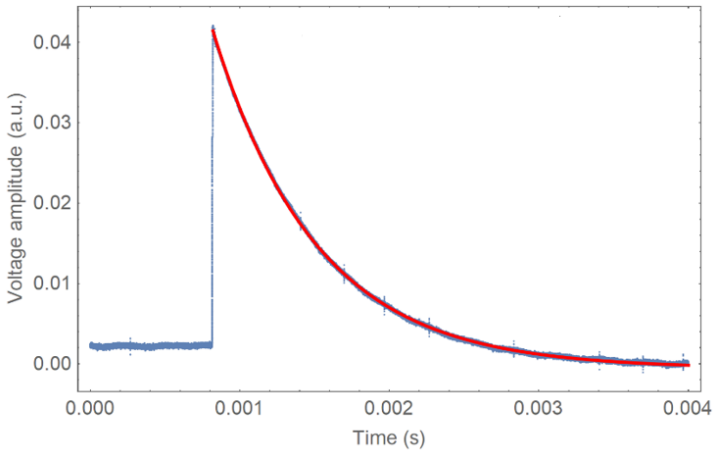

Figure 4.14: The voltage recorded by the digitiser when electrons are collected by the phosphor screen. The electrons hit the screen at around 0.8 ms. The decaying part of the signal is fitted with an exponentially decaying function to extract the time constant of the resonant circuit.

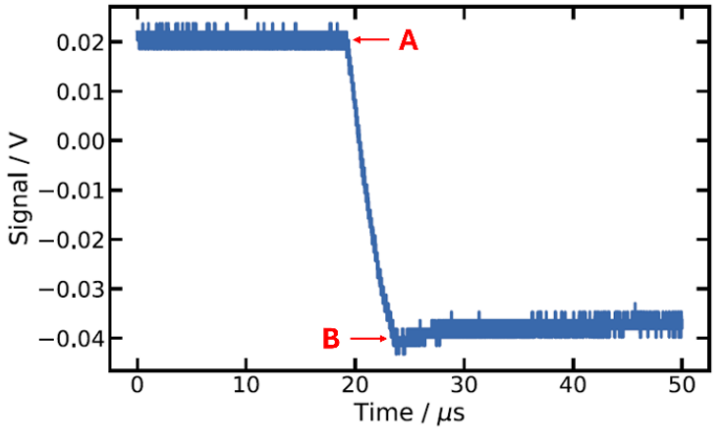

Figure 4.15: An example of a voltage trace recorded by the digitiser when an electron cloud hits the phosphor screen. The signal data recorded starts 20 μs before the charge is collected. The first break point is labelled A and the second B.

magnetic field, in turn, keeps the electrons away from the inner walls of the vacuum chambers.

4.5 Experimental results

This section presents experimental results related to the lifetime and temperature of the electron plasma. The results of investigations into the rotating wall technique are also reported. Rotation frequencies that significantly increase the number of trapped electrons and improve plasma compression are identified.

4.5.1 Electron plasma lifetime

For an electron plasma to work as a focusing lens for ion beams, the lifetime of the electrons must be significantly larger than the transit time of the ions through the plasma. To avoid refilling a plasma lens after the passage of each ion bunch, it is desirable to maintain the plasma at a constant density for time intervals at least on the order of seconds. Here, the lifetime of the electrons was measured for the low-density electron columns.

The lifetime was measured using a large number of electrons trapped using the outermost electrodes (E20 and E1) as end-caps. The electrons were accumulated for 1 s, stored for a certain length of time from microseconds to seconds, and then released towards the P-screen, where the charge was collected and recorded. For each individual storage time, the sequence was repeated five times to obtain the average number of electrons that had been confined. The results, presented in figure 4.11, show that the initial number of electrons is approximately 3×10^8. The plasma profile is illustrated in figure 4.16. The electrons start to be lost gradually, the population being reduced to half the initial number after being confined for $\sim$ 1 s. The plasma undergoes significant expansion (figure 4.16), resulting in a reduced plasma density. The decay of the total number of electrons is well described using an exponential function; a fit to the data yields a lifetime of 2.28 ± 0.35 s. This lifetime was determined using data collected without the use of any active method for reducing the radial loss of electrons, such as the RW technique.

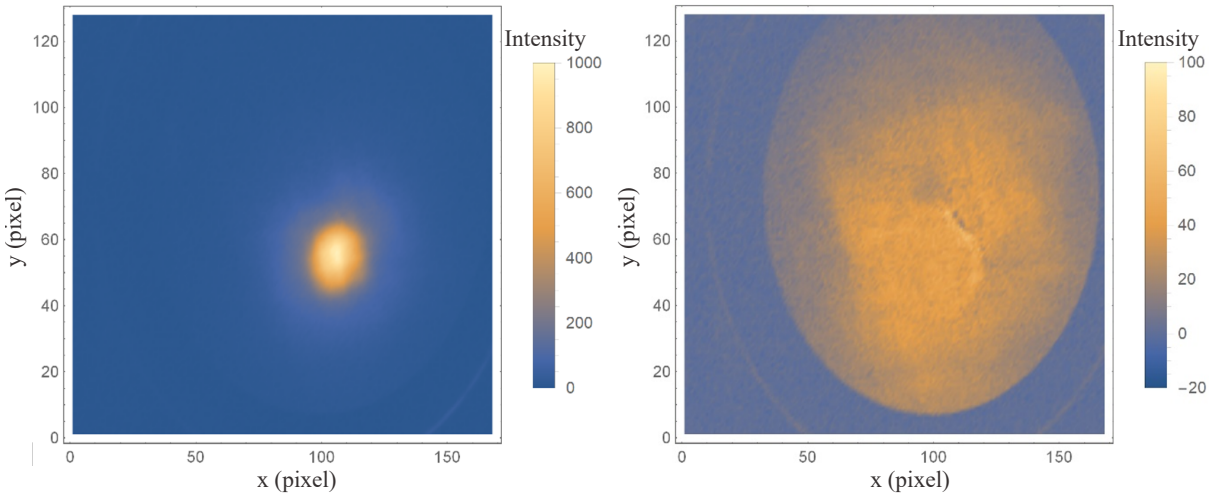

Figure 4.16: Plasma profiles for storage times of 3 μs (left) and 1 s (right), illustrating the evolution of the plasma structure and density.

4.5.2 Application of rotating wall technique

A stable plasma with a long lifetime is crucial for the electron plasma to be used as a focusing element. Techniques such as the RW technique have been developed to enhance the stability and to mitigate the expansion of trapped, non-neutral plasmas.

The RW technique has been instrumental in confining and controlling non-neutral plasma densities since the late 1990s, the first example of which was demonstrated with a magnesium-ion plasma [189]. A cylindrical electrode is subdivided azimuthally into a number of segments, each of which has a sinusoidal voltage applied with matched frequency but different phase. This produces a rotating dipole/quadrupole potential near the centre of the electrode. Two distinct regimes exist depending on the amplitude of the RW and the available cooling mechanisms. The first is the so-called weak drive regime [190] in which the rotating potential is coupled to a plasma-wave (Trivelpiece-Gould mode). The second is the strong-drive regime in which the plasma rotation frequency, which depends on the plasma density, matches the RW frequency, providing control over the plasma density.

RW compression induces heating of the plasma, and the thermal pressure then counteracts compression until equilibrium is reached. Inducing cooling mechanisms or reducing the heating allows greater plasma retention. Cooling can be provided via inelastic collisions with a gas. In general, cooling gases used on the Swansea beamline are CF_4, SF_6, or CO_2. For this work, a supply of CO_2 was connected to the electron-gun vacuum cross so that cooling gas could be admitted into the trapping region. Control of the pressure is achieved using a piezoelectric valve, which may be controlled by a PID controller. A function generator was acquired to drive either of the 6-segmented RW electrodes (shown in figure 4.6 as E4-10 and E12-16).

To compress the electron plasma using the RW technique, the electrons were confined using the outermost electrodes, E20 and E1. A cooling gas pressure of 8×10^{-7} mbar was identified as the optimal condition for the compression experiments. After accumulating electrons for 1 s, a rotating electric field was applied via electrodes E4-10 for 1 s, with frequencies ranging from 1 to 30 MHz and a peak-to-peak amplitude of 2.95 V. Following this, the electron cloud was ejected from the trap for detection.

In the absence of RW application, the electron clouds exhibited a large radius (figure 4.16) with approximately 1.5×10^8 electrons. Figure 4.17 presents the number of electrons as a function of RW frequency, with the optimal frequency, found to be 14 MHz, yielding the highest electron count at 2.4×10^8 electrons and corresponding to a significant plasma compression. The

increase in the number of electrons is attributed to ionisation events between the electrons and the background gas during RW application. The plasma radius was reduced to approximately 1.6 mm, with a peak density of 2.3×10^{14} m^{-3}.

4.5.3 Measurement of electron plasma temperature

The plasma temperature can be used as a tool to quantify the heating and cooling processes involved in manipulating an electron cloud [191–193]. To determine the temperature of an electron cloud, it is first assumed that its parallel velocity distribution at equilibrium follows a Maxwell distribution. By lowering the barrier potential, electrons are allowed to escape from the trap. Consequently, all electrons with a parallel velocity $v_{||}$, such that $mv_{||}^2/2 + e\phi > eV_b$, overcome the potential energy barrier, eV_b, and are collected on the P-screen. The remaining parallel velocity distribution in the trap is:

$$f\left(v_{||}\right) \propto \exp\left(-\frac{mv_{||}^2}{2k_B T_{||}}\right) \text{ if } v_{||} < \sqrt{\frac{2e\left(V_b - \phi\right)}{m}}\,; \tag{4.3}$$

where $T_{||}$ is the temperature of the electrons with a parallel velocity $v_{||}$, V_b is the potential energy barrier, ϕ is the confinement potential, m is the mass of an electron, and e is the charge of an electron.

At the point of escape from the trap, $v_{||} = \sqrt{2e\left(V_b - \phi\right)/m}$ and the number of electrons that escape as a function of barrier potential is:

$$N_E\left(V_b\right) \propto \exp\left(-\frac{e\left(V_b - \phi\right)}{k_B T_{||}}\right)\,; \tag{4.4}$$

We assume that the loss of electrons does not change the trapping potential, meaning $\frac{d\phi}{dV_b} = 0$. Consequently, the gradient obtained from a linear fit to a plot of the natural logarithm of the number of escaped electrons against the barrier potential can be used to extract the temperature. This is given by:

$$\frac{d\ln\left(N_e\right)}{dV_b} = -\frac{e}{k_B T_{||}}\,; \tag{4.5}$$

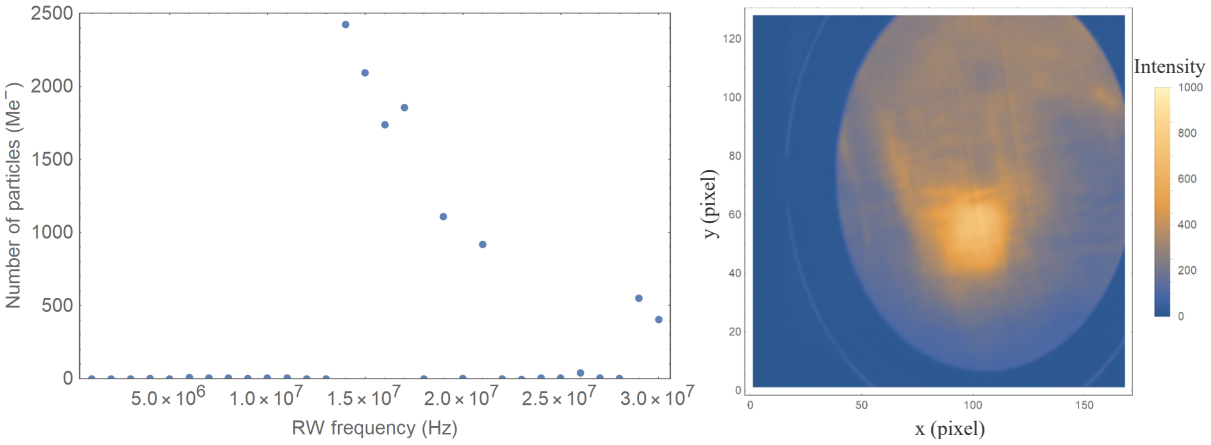

Figure 4.17: (left) Number of trapped electrons as a function of RW frequency with cooling gas. After a 1-second accumulation, the RW is applied for 1 second at 2.95 V peak-to-peak before ejection. (right) Plasma profile at a RW frequency of 14 MHz, showing the high-density region with increased plasma compression.

To measure $T_{||}$, the linear fit is applied to the most energetic tail of the Maxwell-Boltzmann distribution. The uncertainty is estimated to be approximately 5%, which is sufficient to study the cooling performance. For more details, see [192].

To measure the plasma temperature, the plasma was trapped using the experimental sequence described in Section 4.5.2. When the plasma was released by lowering E1, the escaping electrons were detected by the P-screen. During this process, both the detected charge and the voltage applied to E1, which is subsequently used to extract the plasma temperature, were recorded. As the gradient of the detected charge plotted against potential is used to determine the temperature of the plasma, the electrode voltage is not converted to the on-axis potential. This is valid provided the voltage decrease during ejection is linear, as shown in figure 4.18, as the electrode voltage is directly proportional to the potential. In this experiment, the detected charge from the P-screen and the electrode voltage are measured simultaneously. The logarithm of the detected charge is then plotted against the electrode voltage. The resulting data is fitted with the function $a + \log(Q)/T$ to obtain the temperature, as shown in figure 4.19.

4.5.4 Trapping in high-voltage potential wells

From the temperature measurements shown in figures 4.18 and 4.19, it can be observed that electrons begin to escape from the trap when the E1 electrode reaches a bias voltage of approximately -116 V, which closely matches the trap potential depth. This indicates that the trap is fully populated with electrons. To accommodate a larger electron population, the trapping potential was increased using high-voltage amplifiers capable of delivering up to ±400 V.

Electrons were trapped and compressed using the RW technique, following the procedure outlined in Section 4.5.2. Confinement was achieved using the outermost electrodes (E20 and E1), with electrons accumulated for 1 s. A rotating electric field (1–30 MHz, 2.95 V peak-to-peak) was then applied via electrodes E4–10 for 1 s before ejecting the electron cloud for detection. Figure 4.20 shows the number of trapped electrons as a function of RW frequency, with an optimal frequency of 28 MHz yielding an electron number of 1.1×10^9. The corresponding plasma profile is also shown in figure 4.20. The increase in electron number is attributed to enhanced trapping potential and ionisation between electrons and background gas during RW application. The plasma exhibited a radius of 5 mm and a peak density of $1.1 \times 10^{15}\,\mathrm{m}^{-3}$.

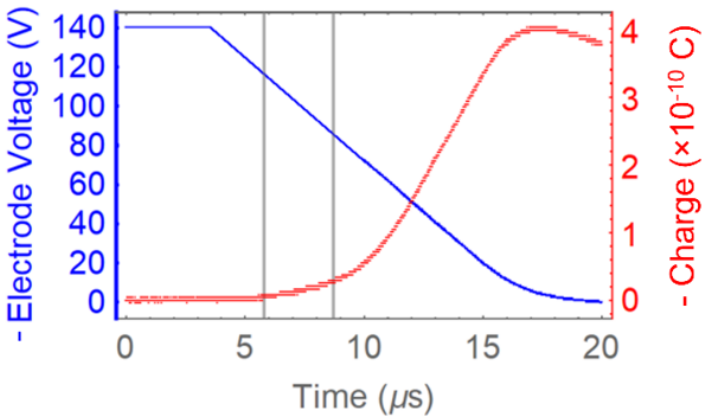

Figure 4.18: An example of the signals from a temperature measurement. The monitored electrode voltage is plotted in blue, and the detected charge from the P-screen as a function of time is plotted in red. As the electrode voltage is decreased, electrons begin to escape, and the detected charge increases until a maximum, at which time all the electrons have been ejected from the trap. The validity of this diagnostic depends on the plasma timescales.

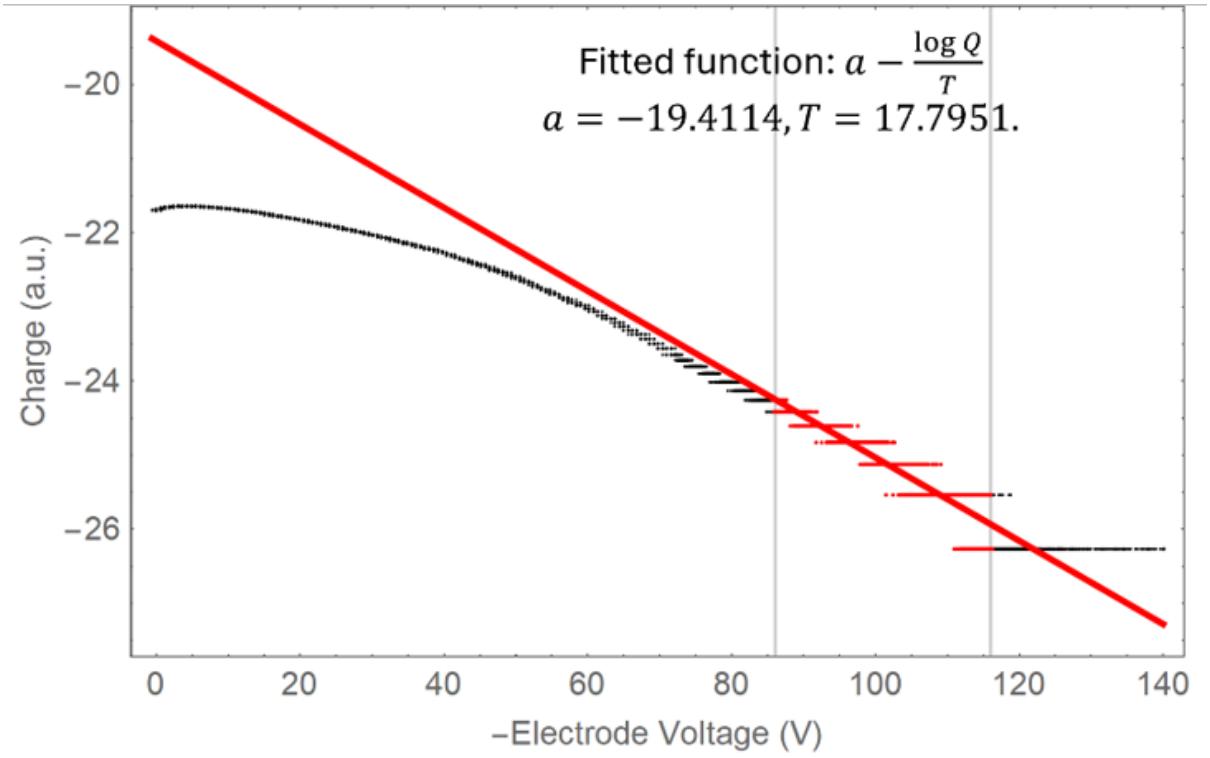

Figure 4.19: An example of the analysed signal from a temperature measurement. The natural logarithm of detected charge from the phosphor screen is plotted as a function of the electrode voltage. From equation 4.5, a linear fit over the region of interest, shown in red, allows the temperature to be obtained.

Notably, a central hole in the plasma was observed, which may result from ions produced during ionisation being trapped within the configuration. Further investigation into the presence of ions in the trap is ongoing.

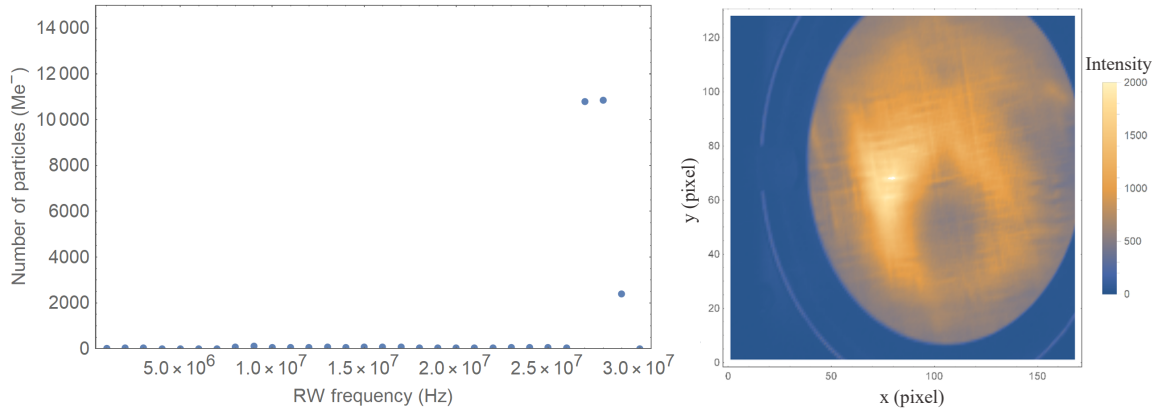

Figure 4.20: (Left) Number of trapped electrons as a function of RW frequency under high-voltage trap potential, with the presence of cooling gas. (Right) Plasma profile at an RW frequency of 28 MHz, giving the high-density region and the central void observed within the plasma.

CHAPTER 5

Ion-acoustic dose-profile measurement

5.1 Introduction

5.1.1 Motivation and concept of the SmartPhantom

The measurement of the dose profile delivered to the *in vitro* and *in vivo* experiments is essential to allow quantitative studies of the biological effects. The dose profile must be measured for each bunch to demonstrate the stability of the beam-delivery systems, to provide feedback to the accelerator, and to allow beam delivery to be terminated when the desired integrated dose has been delivered.

The dose-profile measurement system is therefore required to operate at a repetition rate of at least 10 Hz, i.e. to provide a measurement of the dose profile in less than 100 ms. For LhARA to exploit lasers capable of operating at repetition rates greater than the current baseline of 10 Hz, requires that the dose-profile measurement be completed between laser shots. The ultrasonic, acoustic pressure wave created by the transient pressure increase generated by an ion beam as its energy is transferred to the sample [194] provides a mechanism by which the dose-deposition profile can be measured in real time.

Ultrasound waves are usually detected by transducers that provide a relative, rather than an absolute determination of the delivered dose. Therefore, a novel detector, the SmartPhantom, was designed to measure the three-dimensional dose profile delivered by the passage of nanosecond-scale pulsed ion beams. To calibrate the acoustic response, a liquid scintillator was used as the propagating medium. By detecting the scintillation light and exploiting its known photon yield, an independent measurement of the effective beam range, energy, width and correlation to the particle number was obtained, allowing these optical measurements to be correlated with the acoustic signals and used to determine the absolute three-dimensional deposited dose profile. The detection of the scintillation light emitted during ion beam propagation, combined with the known photon yield, enables the calibration of the acoustic response and the absolute three-dimensional deposited dose profile to be determined.

The performance of the SmartPhantom was evaluated at the Laser-driven Ion (LION) accelerator at the Center for Advanced Laser Applications (CALA) at the Ludwig Maximillian Universität in Munich, Germany [195].

5.1.2 The ion-acoustic effect

As an ion beam traverses a medium, it interacts via Coulomb scattering, transferring its kinetic energy to the atoms in the form of heat. If the duration of the ion pulse is significantly shorter than the stress relaxation time of the medium, the energy remains confined within the system [196]. This condition, commonly known as the stress-confinement criterion, leads to a rapid increase in temperature. Assuming that the temperature rise is short enough to neglect thermal diffusion, the energy is converted into mechanical stress and is released in the form of an acoustic wave. Figure 5.1 illustrates the generation and detection of ion-acoustic waves.

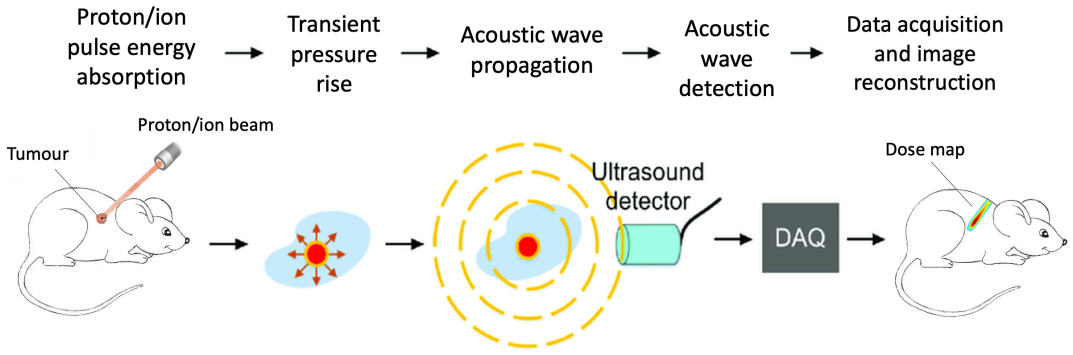

Figure 5.1: Schematic diagram of ion-acoustic-wave generation and detection.

The source pressure distribution at position $\mathbf{r}$ and temperature T, denoted $p_0(\mathbf{r}, T)$, is directly related to the local energy-deposition distribution, $E(\mathbf{r}, T)$, by [197]:

$$p_0(\mathbf{r}, T) = \Gamma(\mathbf{r}, T) E(\mathbf{r}, T)\,; \tag{5.1}$$

where, $\Gamma(\mathbf{r}, T)$ represents the dimensionless Grüneisen parameter, which gives a measure of the efficiency of converting the heat energy into induced pressure. The Grüneisen parameter is given by:

$$\Gamma(\mathbf{r}, T) = \frac{v_s^2 \beta_T}{C_p}\,; \tag{5.2}$$

where v_s is the speed of sound in the medium, β_T is the thermal expansion coefficient, and C_p is the specific heat capacity at constant pressure.

The time evolution of the pressure field is described by the inhomogeneous wave equation:

$$\nabla^2 p(\mathbf{r}, t) - \frac{1}{v_s^2} \frac{\partial^2}{\partial t^2} p(\mathbf{r}, t) = -\frac{\Gamma}{v_s^2} \frac{\partial}{\partial t} \left[E(\mathbf{r}, t) \rho(\mathbf{r}) \right]\,; \tag{5.3}$$

where t denotes time, and $\rho(\mathbf{r}, T)$ is the mass density of the target material at position $\mathbf{r}$ and temperature T [198]. The analytical solution to equation 5.3, which describes the pressure amplitude of the wave at position $\mathbf{r}$ and time t, is given by [198]:

$$p(\mathbf{r}, t) = \frac{1}{4\pi} \frac{\Gamma}{v_s^2} \int_V \frac{dV'}{|\mathbf{r} - \mathbf{r}'|} \frac{\partial^2}{\partial t^2} \left[E(\mathbf{r}', t - \frac{|\mathbf{r} - \mathbf{r}'|}{v_s}) \rho(\mathbf{r}') \right]\,; \tag{5.4}$$

These expressions suggest that the relative dose distribution can be determined by reconstructing the initial pressure distribution $p_0(\mathbf{r}, T)$, provided that the thermophysical properties of the medium are known.

The very short pulses delivered by LhARA (10–40 ns) satisfy the stress-confinement criterion, enabling the generation of ion-acoustic waves. Consequently, the ion-acoustic approach was identified as the most suitable method for real-time monitoring.

5.2 The SmartPhantom

5.2.1 Mechanical design

The computer-aided design (CAD) of the SmartPhantom is illustrated in figure 5.2. The SmartPhantom has a cuboid structure and is made of 5 mm thick aluminium, with the inner volume

measuring 100 mm on each side. The interior is filled with a commercially available liquid scintillator that acts as a beam-energy absorber and is the medium through which the acoustic wave propagates. The beam enters through an air-filled, 15 mm diameter, cylindrical tube sealed with a 50 μm Kapton® (polyimide) foil entrance window. The Kapton foil has a dual role; it acts as both a boundary to avoid spillage of the liquid and removes protons with energies less than 2.1 MeV.

Several acoustic and optical windows are incorporated into the design to allow the detection of various types of signal. The design features four windows: two for mounting optical systems and two for mounting acoustic transducers. Each optical window consists of a 5 mm thick BK7 glass window and a flange to secure the optical components.

The optical windows are positioned perpendicular to one another to image two orthogonal planes; one capturing the scintillation light from the top and the other from the side. The two transducer windows are also positioned orthogonal to one another; one directly opposite to the entrance window, the other opposite to the side optical-glass window. Notably, the transducer windows are significantly larger than those designed for the optical systems. The large size is specified to accommodate matrix transducers not used in the results reported here. In addition, the transducer windows are sealed with black Kapton foils to minimise any internal reflections of scintillation light, and, for the same reason, the entire aluminium detector body was anodised black.

A drip tray was incorporated into the design to collect any liquid scintillator that might leak from the detector, a possible scenario as the transducers would push hard against the Kapton foil. The capacity of the tray was over 1 l to ensure that all the liquid would be collected in the case of a major leak. Lastly, the top lid features two vertical tubes that enable the liquid scintillator to be inserted into the detector and the air to be vented during filling. These tubes enable the entire volume to be completely filled, preventing any air gaps between the liquid scintillator and the glass window, which could introduce reflections or refraction issues.

In addition, custom-designed transducer housings were 3D-printed to hold and secure the transducers perpendicular to the surface of the detector wall on which they were mounted. Two separate housings were made, one for each transducer, their inner surface shaped to match the transducers' contours, which were obtained from 3D scans. The external mounting of the transducers enabled the transducers to be used on either acoustic window as required. Moreover,

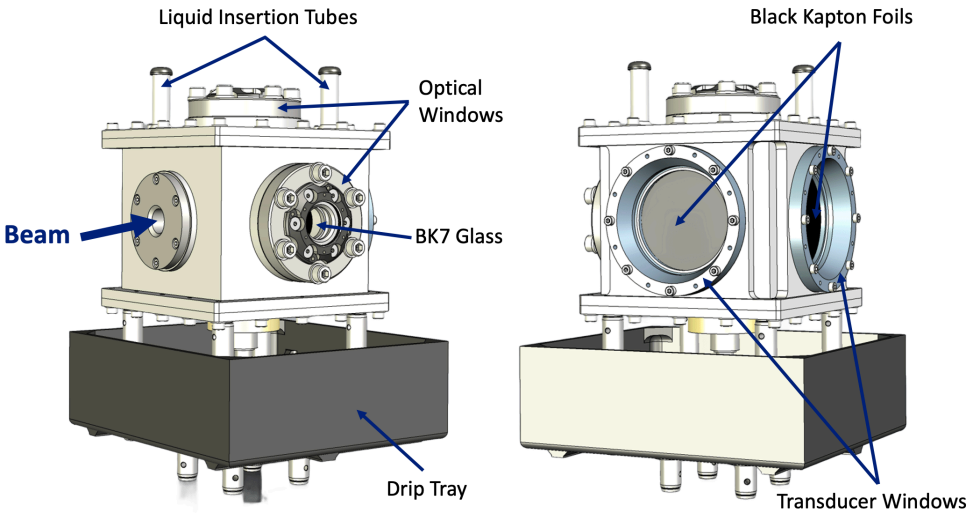

Figure 5.2: Computer-Aided Design rendering of the SmartPhantom, featuring four windows for mounting the optical and acoustic systems. Left: front view. Right: rear view.

the screws within the housings allow the transducers to be fixed firmly in all degrees of freedom, ensuring a precise fit. This arrangement minimised transducer movement, thereby reducing the risk of damage. Lastly, a hole was introduced at the bottom of the SmartPhantom to mount one of the transducers, allowing it to be immersed in the liquid scintillator and used to provide a reference signal. Figure 5.3 shows the CAD model of the SmartPhantom, with the integrated optical systems, transducer housings and immersed transducer.

5.2.2 Ultrasound transducers

Spatial averaging, in addition to temporal averaging, usually improves the signal-to-noise ratio (SNR) in acoustic systems. For this reason, it is proposed that multichannel sensors be employed in the SmartPhantom to record the acoustic signals. The design described below accommodates such sensors. However, the test exposure of the SmartPhantom on the LION beam line employed single-element sensors. A further exposure using the matrix array sensors to allow 3D reconstruction will be carried out in due course.

5.2.2.1 Vantage matrix array ultrasound transducer

To capture signals and reconstruct the pressure distribution in both the axial and radial directions, it is proposed that a Vantage matrix array ultrasound transducer be used. The response of the sensor has a central frequency of 3.5 MHz and a frequency bandwidth of 60% [199]. The array consists of 1024 elements arranged in a 32×32 configuration. For efficient data acquisition, the array is divided into 4 banks, each with 32×8 elements, forming smaller 256-element arrays. The division enables 4:1 multiplexing, allowing the 256 channels of the Vantage system to acquire data from all 1024 elements by switching to different subsets of elements across the banks. Synchronised, real-time, three-dimensional ultrasound data acquisition from all elements can be achieved through this multiplexing scheme in combination with the Vantage system software. Due to the two-dimensional shape of the array, three-dimensional data can be acquired (two spatial and one temporal), and therefore, the transducer is placed on axis with the beam to reconstruct the pressure distribution in all three dimensions.

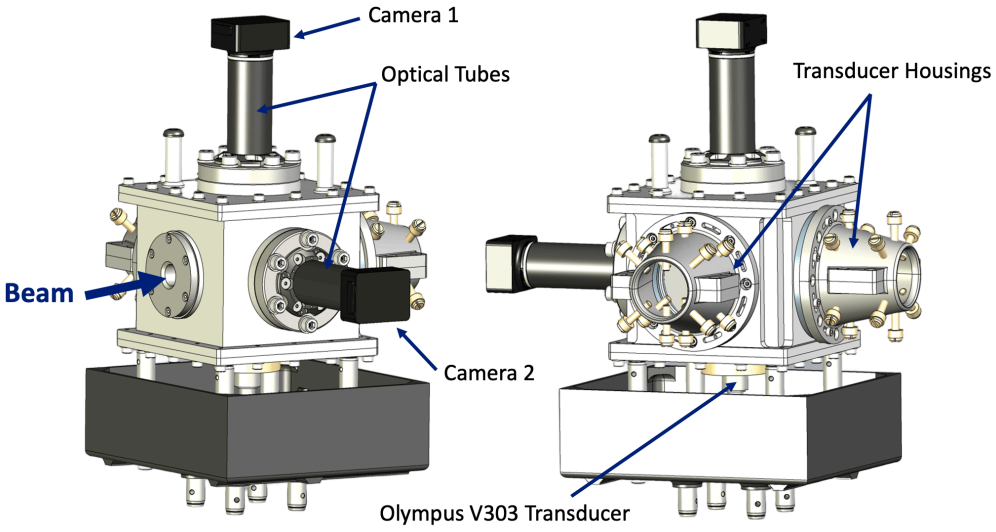

Figure 5.3: Computer-Aided Design rendering of the final version of the SmartPhantom, featuring the optical systems and the transducer housings attached onto the designated windows, along with the Olympus V303 transducer secured at the bottom.

5.2.2.2 GE 9L–D linear array ultrasound transducer

The GE 9L-D linear array transducer is an array of 192 elements, with a centre-to-centre pitch of 0.23 mm [200]. Each element measures 5 mm in length and 0.205 mm in width. The transducer has a field of view of 43.0 mm, making it able to capture ultrasound waves across a wide area. In addition, this transducer has a centre frequency of 5.3 MHz and a frequency bandwidth of 75%. The broadband feature is advantageous as it enables a wide range of frequencies to be recorded. The linear array is placed parallel to the beam axis to reconstruct the plateau region of the energy distribution by capturing the lateral waves. However, the radial dimensions may be more challenging to reconstruct due to the sensor's limited cross-section.

5.2.2.3 Olympus V303 Immersion Transducer

The Olympus V303 immersion transducer is a narrow-band piezoelectric ceramic transducer that can be immersed in water [201]. It consists of a single flat circular element, approximately 13 mm in diameter with an acoustic matching layer for maximum ultrasound transmission. The transducer has a centre frequency of 1 MHz and a frequency bandwidth of 60%, making it suitable for detecting the low-frequency spectrum of the signals. The housing is made of stainless steel, and the transducer's flat surface is placed 24.9 mm from the centre of the SmartPhantom's inner volume, positioned perpendicular to the beam axis. Due to the single-element configuration, this transducer cannot be used to reconstruct an image because it records a single time series.

5.2.2.4 Precision Acoustics ML4X50 piston hydrophone

The Precision Acoustics ML4X50 piston hydrophone is a high-sensitivity, broadband, single-element transducer that has a circular aperture of 23 mm [202]. The hydrophone is a piezoelectric polyvinylidene fluoride (PVDF) foil with gold electrodes, offering a broad and flat frequency response from 300 kHz to 1 MHz, a feature that minimises signal distortion. Due to its ability to detect the low-frequency spectrum of the acoustic signals, this transducer can be used downstream of the Bragg peak, looking up the beam axis, as an alternative to the matrix array but with the expectation of detecting a signal from parts of the plateau region. Furthermore, the ML4X50 piston hydrophone is calibrated, enabling the conversion of voltage to pressure as a function of frequency. This feature makes it ideal for precise dose mapping.

5.2.2.5 Summary

The specifications for the Vantage matrix array, GE 9L-D linear array, Olympus V303 transducer and Precision Acoustics ML4X50 piston hydrophone are tabulated in table 5.1. The specifications include the transducers' centre frequency, bandwidth, number of elements and element-to-element pitch.

5.2.3 Liquid scintillator

Scintillators are materials commonly used in radiation detection and measurement applications due to their ability to emit visible light or other detectable photons when exposed to ionising radiation [203]. When radiation interacts with a scintillator, it transfers energy to the atoms within the material, exciting them to higher energy states. As these excited atoms return to their ground state, they release the excess energy in the form of photons, where the number of photons is proportional to energy deposited. The protons can be detected and counted to quantify the intensity and nature of the incident radiation. Scintillators are available in various forms, including solids and liquids, and come in both organic and inorganic varieties.

Table 5.1: Summary of the key specifications of the ultrasound transducers mentioned in the text. [199–202].

Parameter	Matrix Array	Linear Array	Olympus Transducer	Piston Hydrophone
Image				
Centre Frequency	3.5 MHz	5.3 MHz	1 MHz	0.3–1 MHz
Bandwidth	60%	75%	80%	n/a
Elements	1024 (32x32)	192 (192x1)	1	1
Pitch	0.3 mm	0.23 mm	–	–

Liquid scintillators play an important role in large-scale neutrino experiments due to their efficiency in converting kinetic energy into detectable light with a high yield [204]. These liquids typically consist of three components: a solvent and two fluors. One fluor acts as a light absorber, and the other serves as a wavelength shifter to maximise the fraction of emissions that fall within the detector's sensitivity range. The fluorescent intensity, I, decays exponentially over time, t, as described by:

$$I = I_0 e^{-t/\tau}\,; \tag{5.5}$$

where I_0 is the maximum intensity and τ is the fluorescence decay time constant [205].

The density-normalised scintillation photon yield, L, per unit path length, x, of an ion traversing a scintillating material, is described by:

$$\frac{dL}{dx} = \frac{S\frac{dE}{dx}}{1 + kB\frac{dE}{dx} + C\left(\frac{dE}{dx}\right)^2}\,; \tag{5.6}$$

where S is the scintillation efficiency (i.e., the conversion factor between energy deposition and light production), kB is Birks' constant (a material-dependent quenching parameter), dE/dx is the stopping power, and C is a second-order quenching coefficient [206]. Knowing the stopping power, the total photon yield can be determined through numerical integration.

5.2.3.1 Ultima Gold XR

The liquid scintillator was carefully selected to have a density ($1.005\,\mathrm{g}/cm^3$) close to that of water while exhibiting similar acoustic properties, such as sound speed and signal attenuation. For these reasons, the Ultima Gold XR cocktail was chosen to fill the SmartPhantom volume [207]. The solution has a high flash point ($\sim 150^o$ C) and low toxicity and corrosiveness, making it well-suited for the intended use. Table 5.2 provides the chemical composition of Ultima Gold XR [208], showing that it consists primarily of di-isopropyl naphthalene (DIPN). The scintillator has a refractive index of around 1.54 (15% greater than water), a peak emission wavelength of 427 nm and a light yield of approximately 11200 photons per MeV [209, 210]. The acoustic properties of the scintillator were determined experimentally [211].

Table 5.2: Ultima Gold XR chemical composition [208].

Name	Solvent	Scintillator	Composition [%]
Di-isopropyl naphthalene	✓		40 - 60
Ethoxylated alkylphenol	✓		20 - 40
Bis(2-ethylhexyl) hydrogen phosphate	✓		2.5 - 10
Triethyl phosphate	✓		2.5 - 10
Sodium di-octylsulphosuccinate	✓		2.5 - 10
3,6-dimethyl-4octyne-3,6-diol	✓		1.0 - 2.5
2,5 diphenyloxazole		✓	0 - 1.0
1,4-bis (2-methylstyryl)-benzene		✓	0 - 1.0

5.2.3.2 Imaging Optics

Imaging of scintillation light produced by the proton beam in the liquid scintillator is provided by two identical optical systems which are orthogonal to each other and aligned with the centre of the volume. Each optical system relays the light to the CMOS sensor in a FLIR CM3-U3-31S4M-CS monochrome camera (2048 × 1536 3.45 μm square pixels).

Figure 5.4 shows the system used to capture and image the emitted scintillation light. A 5 mm thick N-BK7 glass flat separates the interior volume of the SmartPhantom from the outside air, as indicated in Figure 5.2. Following this is a lens assembled from two identical achromatic lenses (Edmund Optics #47-638), each with a focal length of 60 mm and an outside diameter of 25 mm. These were inserted as a back-to-back pair to provide an approximate 1:1 conjugate system with symmetry about the central stop of 6 mm diameter. Using a symmetric configuration corrects for coma, distortion and lateral colour. In addition, using achromatic doublets provides correction for axial chromatic and spherical aberrations. To ensure that the images are not saturated, a thin Neutral Density (ND) filter is positioned right after the doublet, before focusing onto the CMOS sensor.

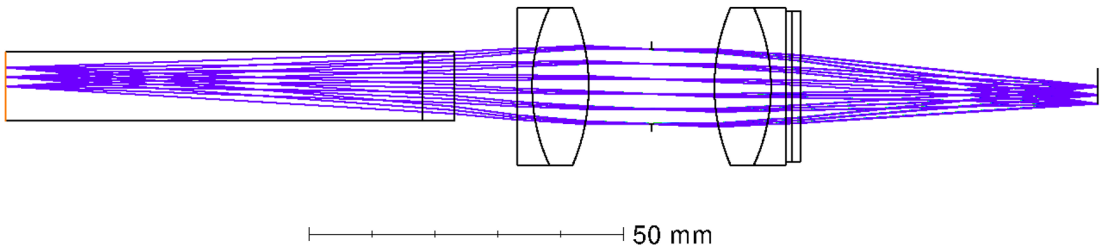

Figure 5.4: The imaging optical system layout. The first volume is the liquid scintillator, then the N-BK7 window. A thin ND filter is shown located just to the right of the second achromatic doublet. The fields shown are at 0°, 1.5° and 3°.

Lastly, the encircled energy for three point sources located at field positions (0°, 1.5° and 3°) is shown in figure 5.5. The system performs best on axis (0.0 mm), with energy tightly concentrated in a small radius, while performance decreases toward the edge of the field, where the image is more spread out due to off-axis aberrations. This indicates increasing image blur

at larger field angles; however, even at 3.0 mm radius, the encircled energy reaches nearly 100% at a radius of around 100 μm and is not a limitation.

5.2.3.3 Optical absorption and acoustic properties

The optical absorption properties of Ultima Gold XR were studied to understand the efficiency at which light is absorbed as it travels through the solution. This property was quantified by measuring the attenuation length, which is the distance over which the intensity of light decreases to approximately $1/e$, i.e. about 36.8%, of its initial value [212].

The optical absorption is typically measured using a spectrophotometer. A light source is used to generate wavelengths within the visible spectrum, which are captured and focused into a prism or grating. These components act as monochromators, dispersing light into different wavelengths. A slit is used to select a specific wavelength, which passes through the sample contained in a cuvette. The transmittance, T, is calculated by dividing the measured intensity of the transmitted light, I_t, by the intensity of the light before it passes through the sample, I_0. The absorbance, A, is then calculated using [213]:

$$A = -log(\frac{I_t}{I_0}) = -log(T)\,; \tag{5.7}$$

Given that absorbance is related to the absorption coefficient, ϵ, the concentration of the sample, $\mathcal{C}$, and the path length, l, using the Beer-Lambert Law:

$$A = \epsilon \mathcal{C} l\,; \tag{5.8}$$

the attenuation length, L_{att}, is calculated using [214]:

$$L_{att} = \frac{1}{\epsilon \mathcal{C}} = \frac{l}{A}\,; \tag{5.9}$$

For the optical absorption measurement, two samples were prepared and evaluated as potential candidates for filling the inner volume of the SmartPhantom: a cuvette containing the Ultima

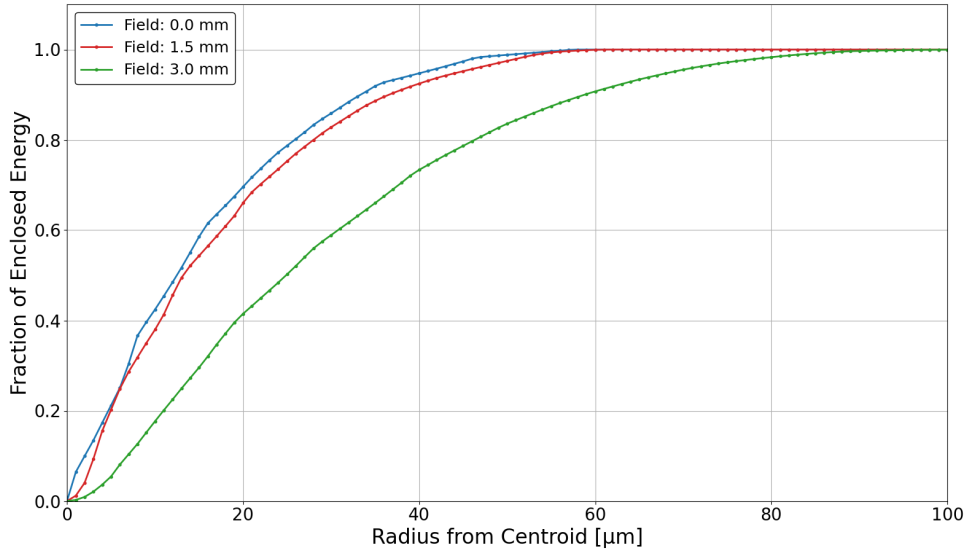

Figure 5.5: Encircled energy for three field positions as a function of radius from the centroid. All wavelengths, with appropriate weighting, are included.

Gold XR cocktail and another containing a 50-50 mixture with distilled water. The optical absorption of these solutions was measured using a spectrophotometer, with an air-filled cuvette serving as a baseline. The cuvettes, each 10 mm wide, were sealed with 3D-printed lids and double-sealed with tape to prevent any spillage. The prepared solutions are shown in figure 5.6.

A 1 nm slit was used and the absorption measurement was performed across the 400 to 550 nm wavelength range at a scanning speed of 0.1 nm/s. Figure 5.7 shows the absorbance as a function of wavelength for the 2 different samples. Both solutions show high absorbance at short wavelengths, towards the UV range, which falls rapidly as the wavelength increases. In addition, the absorbance of the Ultima Gold XR cocktail drops to zero at approximately 430 nm. In contrast, the 50-50 mixture exhibits relatively high absorbance beyond 430 nm, extending in the visible spectrum. This behaviour suggests significant light scattering in the presence of water. Such scattering can interfere with the light emitted due to the energy depositions of the incoming beam and can potentially lead to distorted images. To prevent this, a pure (100%) Ultima Gold XR cocktail was chosen to fill the SmartPhantom. In addition, at 400 nm, the attenuation length is calculated to be 2.96 mm, meaning that the intensity of the light will be reduced by 36.8% after travelling 2.96 mm in the liquid scintillator. In contrast, the attenuation length at wavelengths greater than 430 nm is infinite, suggesting that light emitted at these wavelengths will not be absorbed or scattered.

5.2.3.4 Response and saturation

The linearity of the response and the saturation behaviour of Ultima Gold XR were investigated through a series of experiments conducted at the MC40 cyclotron in Birmingham [215]. Firstly, a small quantity of the Ultima Gold XR cocktail was inserted in a custom-designed 3D-printed cuvette, which was positioned at the cyclotron's exit window. An optical system, comprising an achromatic lens followed by a 1 mm aperture, was used to collimate the scintillation light and focus it onto a PN diode, which generated a photocurrent that was measured using a multimeter. The CAD model of the cuvette and images of the experimental set-up are shown in figure 5.8.

Figure 5.9 shows the measured PN diode current, corrected for dark current, against the current at the Faraday cup for a design proton energy of 26.65 MeV. A straight line fit to the data yielded a Pearson correlation coefficient of 0.991, indicating a strong linear correlation [216].

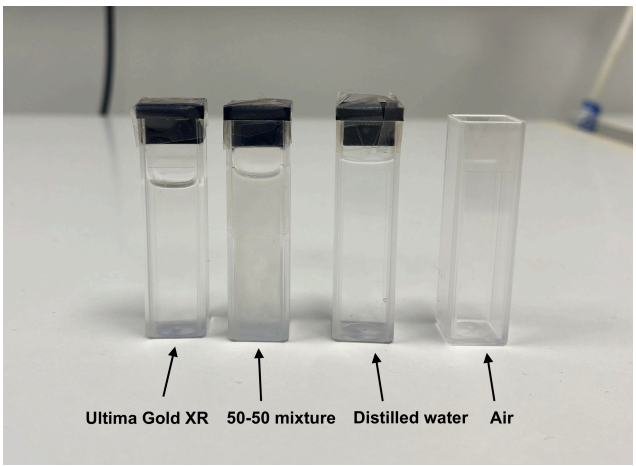

Figure 5.6: Image showing the four cuvettes prepared for measuring the absorbance of Ultima Gold XR and a 50-50 mixture with distilled water using a spectrophotometer. The cuvette containing air was used as a baseline for the measurements.

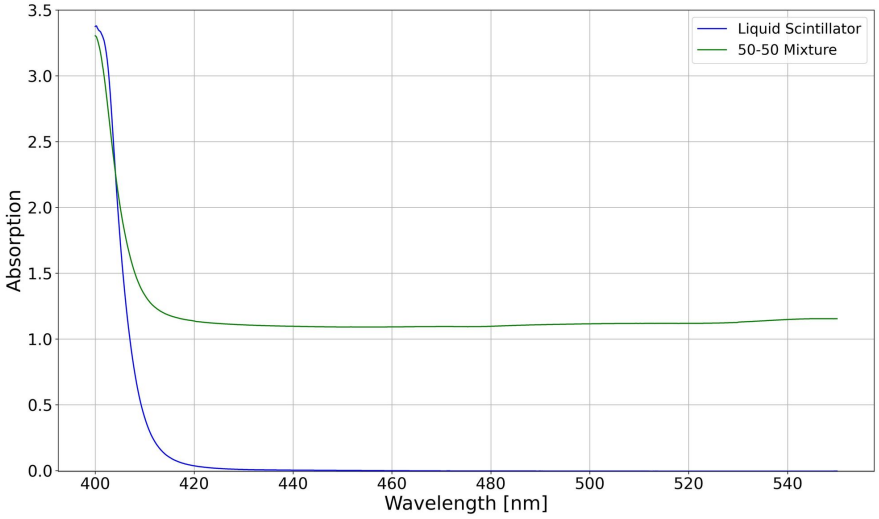

Figure 5.7: Optical absorption spectra of the liquid scintillator (blue) and a 50-50 mixture with distilled water (green), measured using a spectrophotometer. Baseline medium: air.

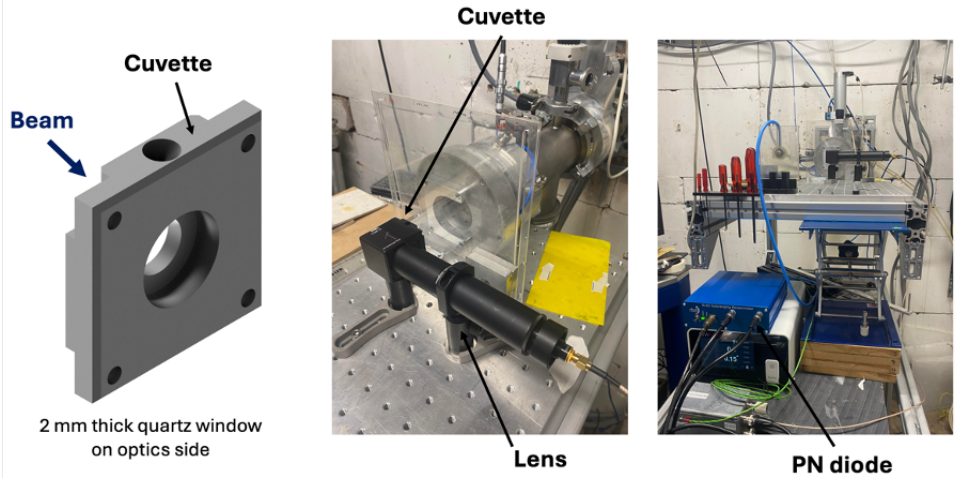

Figure 5.8: Computer-aided design model of the cuvette designed to contain the liquid scintillator (left) and images of the experimental set-up (middle and right) used to study the linearity of the liquid scintillator's response to absorbed dose and saturation behaviour. The experiment was conducted at the MC40 cyclotron in Birmingham [215].

The results demonstrate a linear response up to 1600 nA, suggesting that the liquid scintillator remains unsaturated at this level, with no evidence of quenching.

A second experiment was conducted in which an imaging system, comprising an achromatic lens (25.4 mm diameter, 50.8 mm focal length) and a Chameleon3 CM3-U3-31S4M-CS camera, was mounted on the side of the SmartPhantom through a glass window. To create a narrow beam resembling the one expected at the LION beamline, a 2 mm circular collimator was placed at the entrance window of the SmartPhantom. Moreover, the camera was connected to a laptop operated remotely outside the concrete chamber, enabling real-time light acquisition. An image of the experimental set-up is shown in figure 5.10.

The proton beam current in the cyclotron, and hence the number of particles in the beam, was varied up to 1050 nA. Although the transmission current reached 1050 nA, the combination of the system's transmission ratio and the collimation reduces the delivered beam to an effective flux of 6.6×10^7 protons/s, corresponding to $\sim 9.6 \times 10^7$ protons incident on the sample.

To study different proton energies, the energy of the particles was degraded from an initial energy of 26.65 MeV by placing Perspex sheets of varying thicknesses at the cyclotron's exit window. Specifically, 1, 2 and 3 mm Perspex sheets were used, resulting in proton beam energies of 23.66, 21.25 and 18.59 MeV, respectively.

The camera orientation was adjusted until a clear image of scintillator light induced by the proton beam was obtained. The average pixel intensity of the images was calculated, with the results shown in figure 5.11. The background noise was kept constant by maintaining a consistent camera exposure time of 0.2 s across all runs. Lines of best fit were added to the data to assess the linearity in the liquid scintillator's response. The results confirm that the liquid scintillator exhibits a linear response to the absorbed dose across the energies and particle numbers investigated.

Figure 5.12 shows a colourmap of the pixel intensities of the image obtained with a 26.65 MeV proton beam and 9.6×10^7 protons, corrected for background noise. The beam enters from the left. From the image, it can be seen that the SmartPhantom's entrance window is located at approximately the 850^{th} pixel on the x-axis due to the sudden increase in brightness observed at that point. The pixel brightness appears low and uniform, gradually increasing towards the right, consistent with the energy deposition curve expected for a proton beam. The brightest

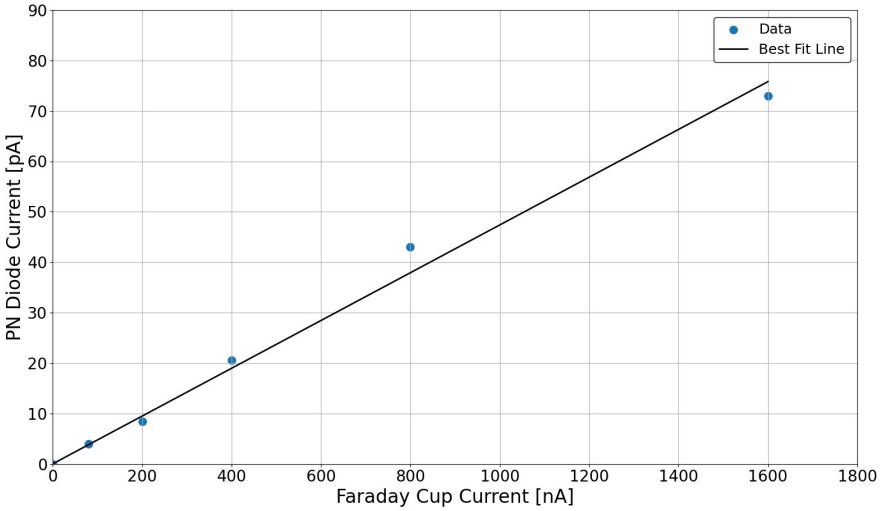

Figure 5.9: Plot of PN diode current against the current measured at the MC40 cyclotron's Faraday cup, using the experimental set-up depicted in figure 5.8 and a 26.65 MeV proton beam. A line of best fit was added to the data and a regression coefficient of 0.991 was calculated, indicating a strong linear correlation with no evidence of quenching in the liquid scintillator.

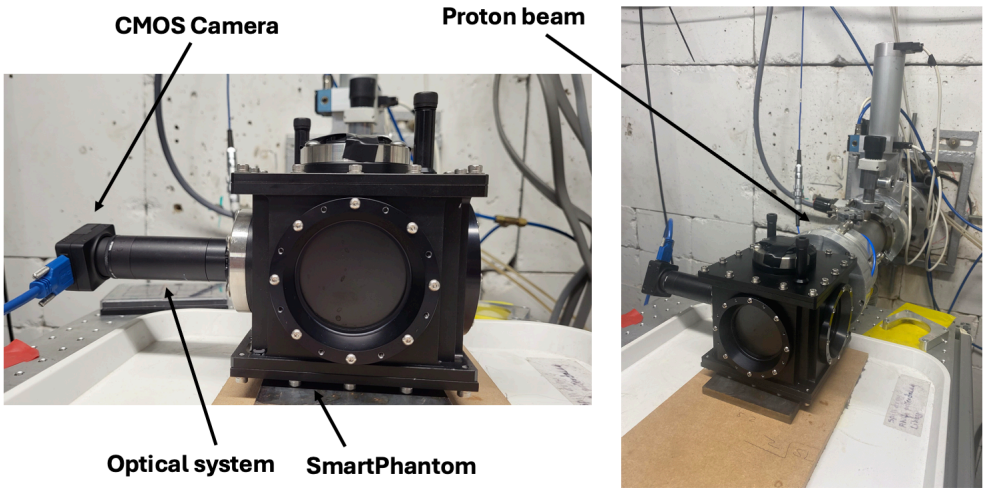

Figure 5.10: Image of the experimental set-up used to capture the scintillation light caused by the passage of the proton beam through the liquid scintillator inside the SmartPhantom at the Birmingham MC40 cyclotron.

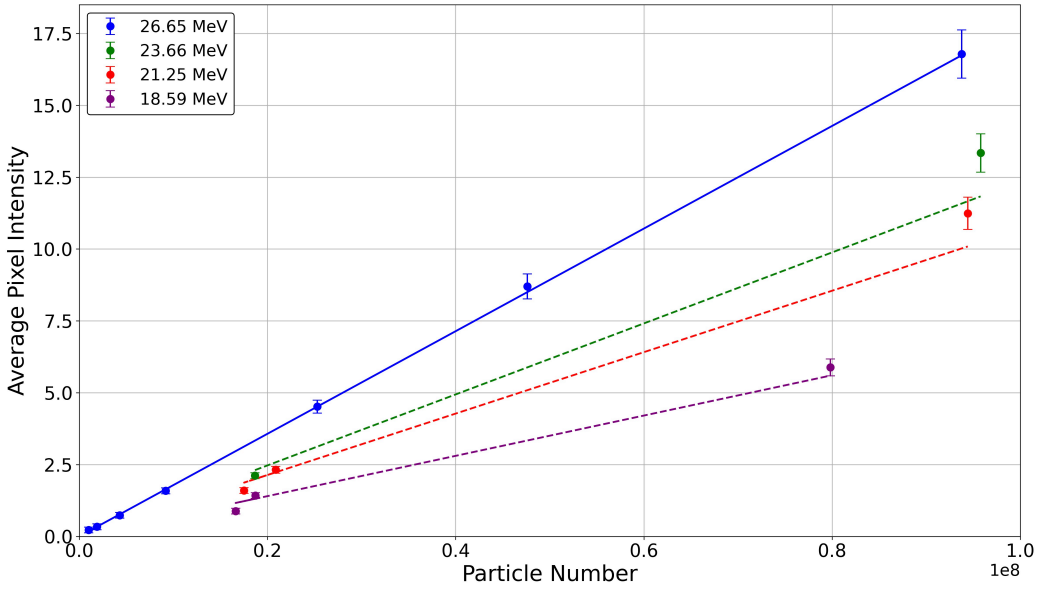

Figure 5.11: Average pixel intensity of the images obtained using the experimental set-up shown in figure 5.10, plotted against particle proton number at various proton energies.

region in the image corresponds to the Bragg peak, beyond which the brightness gradually drops to zero. In addition, the colour scale on the right-hand side of the plot indicates a maximum pixel intensity of approximately 250, suggesting that the image is unsaturated at the given proton beam energy and particle count.

The SmartPhantom coordinate system is defined such that the z direction is parallel to the beam propagation axis, the y direction is vertical and the x-direction completes a right-handed coordinate system. The energy deposition profiles in the z direction and the x-direction were plotted by averaging 60 pixels along the respective black axes. The profiles are shown in figure 5.13, the bin height corresponding to the average pixel intensity. The shape of the projection of the intensity along the z axis resembles the Bragg peak curve, while the transverse

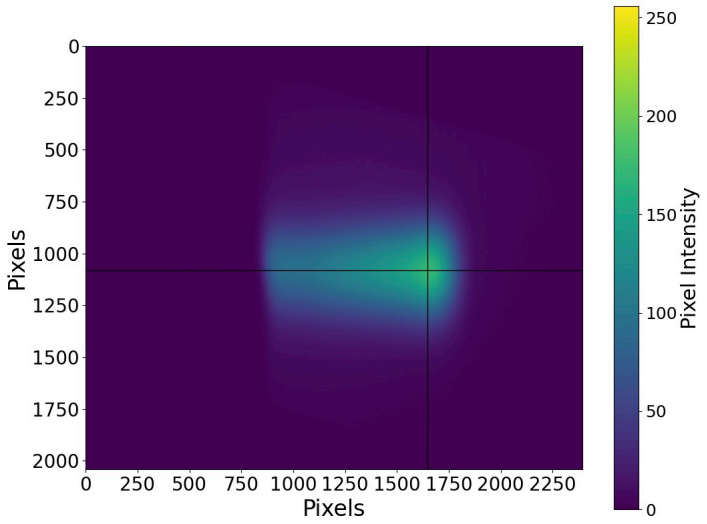

Figure 5.12: Colour map of the image captured with the experimental set-up depicted in figure 5.10 when a 26.65 MeV proton beam of 9.6×10^7 particles propagates through the liquid scintillator. The vertical and horizontal lines indicate the transverse and longitudinal directions, respectively. The teh ADC value recorded by the camera is presented as the Pixel Intensity.

profile indicates that the beam is circular. The ability to extract these profiles from the images obtained suggests that positioning an additional camera orthogonal to the existing setup could provide the y-profile, enabling a three-dimensional reconstruction of the energy deposited by the beam.

5.3 Simulation framework

The SmartPhantom's design was optimised through a simulation pipeline that integrated a parameterised description of the laser-driven source in Python [80] (see section 2.3.2.1), transport through the LION beamline using BDSIM [76], the calculation of energy deposition in the SmartPhantom using Geant4 [78], and acoustic wave generation, propagation, and simulation of the response of the acoustic sensors in k-Wave, a Matlab toolbox [217].

5.3.1 LION beamline

Initially, the LION beamline was simulated using the Beam Delivery Simulation (BDSIM) software [76]. The software tracks particles through the various beamline elements, extracting valuable information about the beam's properties. This information is useful for determining the beam characteristics of particles reaching the detector, understanding the expected energy depositions in the liquid scintillator and characterising the induced acoustic signal. Exploring this information through simulation can help design and optimise the acoustic and optical detection systems.

5.3.1.1 Particle source

A water-leaf target [218] was used to produce the protons for the exposure of the SmartPhantom on the LION beamline at CALA. To simulate the particle production, the parameterisation of the TNSA mechanism described in section 2.3.2.1 [80] was used. The particle source is

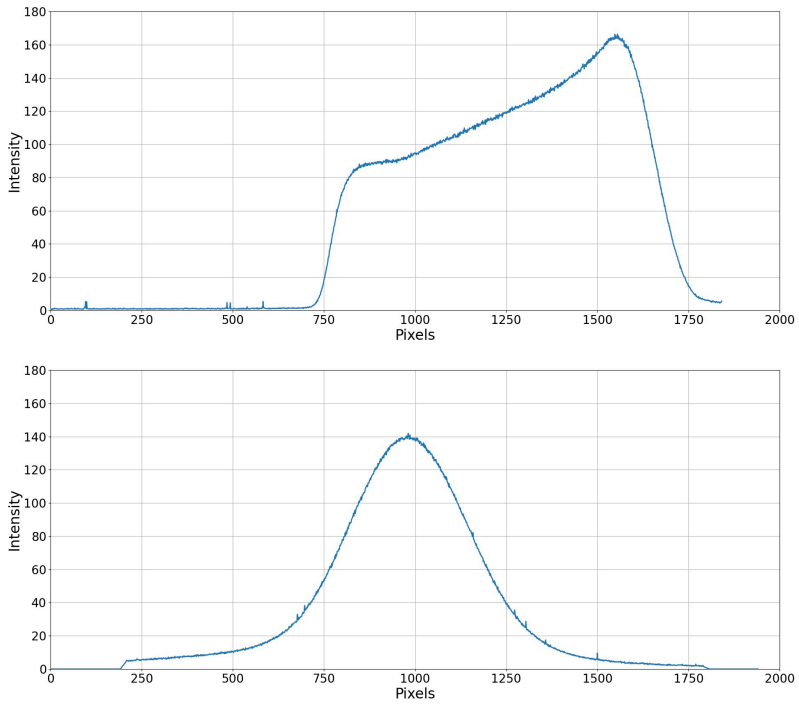

Figure 5.13: Energy deposition profiles of a 26.65 MeV proton beam with 9.5×10^7 protons propagating through the liquid scintillator in the SmartPhantom. Top: longitudinal profile, obtained by averaging 60 pixels along the horizontal black line in figure 5.12. Bottom: transverse profile, obtained from an average of 60 pixels along the vertical line.

driven by a high-intensity 2.5 PW Ti:Sa ATLAS 3000 (Advanced Titanium-Sapphire Laser) laser, operating at a maximum repetition rate of 1 Hz [219]. This laser can deliver pulses up to 28 fs in duration and 70 J of energy. The values of the parameters used in the simulations are given in table 5.3. The generated energy spectrum is shown in figure 5.14 and figure 5.15 shows the generated distributions in spherical polar coordinates. The spatial distributions along the x and y dimensions are assumed to be independent. A FWHM diameter of 10 μm was selected, consistent with values reported in the literature [220].

Table 5.3: Values used in the simulation of the TNSA proton spectra using the algorithm described in section 2.3.2.1.

Parameter	Definition	Value	Unit
E_{laser}	Laser energy	70	J
f	Energy conversion efficiency	$1.2 \times 10^{-15} I^{0.75}$, max=0.5	-
I	Laser intensity	4×10^{20}	W/cm^2
λ	Laser wavelength	0.8	µm
t_{laser}	Laser pulse duration	28×10^{-15}	s
d	Target thickness (plastic foil)	$400 - 600 \times 10^{-9}$	m
θ	Electron half angle divergence	0.436	rad
P_{laser}	Laser power	2.5×10^{15}	W

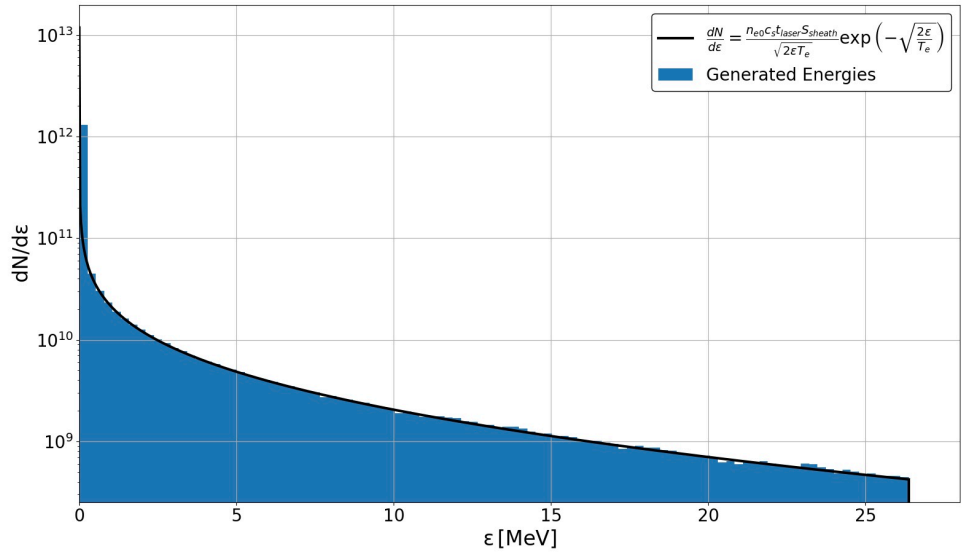

Figure 5.14: Parameterised energy distribution of the laser-driven protons generated at the LION beamline source (blue), based on the specific laser and foil target parameters listed in table 5.3, compared against that obtained using the analytical expression (black).

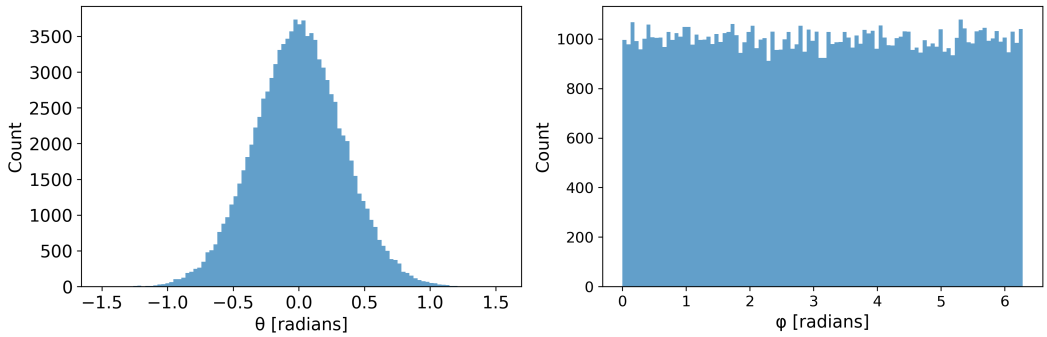

Figure 5.15: Histograms of the divergence angle (left), generated from a Gaussian distribution, and the azimuthal angle (right), uniformly distributed between 0 and 2π, representing the parameterised angular distribution of 100000 particles at the LION beamline source.

5.3.2 Configuration

The LION beamline primarily consists of a quadrupole doublet made up of two permanent magnet quadrupoles (PMQs). To focus a specific beam energy downstream, the quadrupole drifts are adjusted using motorised stages. To achieve a proton beam with a modal energy of 20 MeV, the drift lengths were: 60 mm from the source to the first quadrupole, 56 mm between the two quadrupoles, and 1729 mm from the last quadrupole to the focus. This combination of drift lengths ensures the focal spot occurs inside the SmartPhantom.

Due to the limited aperture of the quadrupoles, not all particles generated at the source are transported along the beamline. Particles that reach the bore of the magnets can cause damage. To prevent this, an elliptical aluminium shielding plate was introduced at the upstream face of the first quadrupole.

The beamline, extending from the source to the exit window, operates in a vacuum. After the exit window, the particles travel through air towards the detector. The LION beamline exit window consists of a 50 μm Kapton foil. Since Kapton is partially transparent, an additional

12 μm aluminium foil is placed behind it to stop electromagnetic radiation. This combination of foils effectively stops protons with an energy below 2.1 MeV.

To decrease the transverse size of the beam and select a range of proton energies, a collimator was placed after the exit window and before the SmartPhantom. An appropriate collimator was selected, based on the modal energy to be focused. For the simulations, an aluminium collimator with a 3 mm circular aperture was chosen that is 5 mm thick. The BDSIM simulation of the LION beamline is shown in figure 5.16. The simulation has been split into two sections: the vacuum section and the air section.

The BDSIM simulation was run multiple times to ensure that around a million protons entered the SmartPhantom. The energy spectrum of the particles at the entrance to the SmartPhantom is shown in figure 5.17. As can be seen from the plot, the beam entering the SmartPhantom has a modal energy of 20.43 MeV and an energy spread of around 1.52 MeV.

Figure 5.18 shows a two-dimensional histogram of the spatial distribution of the particles, with the colour bar indicating the particle count in each bin. There is a higher particle fluence in the central region, which decreases towards the edges, as expected for a quadrupole-doublet-focused beam. In addition, the shape of the beam is elliptical, with a FWHM of 0.77 mm and 0.39 mm along the x and y axes. The total diameter is around 2 mm.

5.3.3 Energy deposition modelling

A detailed simulation of the SmartPhantom was developed in Geant4, see figure 5.19. To examine the impact of the liquid scintillator on the energy depositions, three simulations were run: first with the entire volume filled with water; second with a 50-50 mixture of water and liquid scintillator; and finally using undiluted liquid scintillator. Given the complexity of organic molecules, the physical parameters of the dominant compound, 2,6-Diisopropylnaphthalene (2,6-DIPN, $C_{16}H_{20}$), were used in the simulation.

The Geant4 simulation was split into 0.1 mm cubic voxels and the energy depositions of the particles were written into a three-dimensional matrix. To ensure that the reconstruction of the source from the acoustic signal is sufficiently accurate, the size of the voxels was chosen such that the grid spacing was no more than 25% of the shortest acoustic wavelength generated by the beam. Figure 5.20 shows a comparison of the energy depositions caused by 1 million protons projected along the three orthogonal axes for each liquid. The figure shows that the choice of filling for the SmartPhantom has a minimal impact on the deposited energy distribution, with only around 1.5% variation in the range between water and the liquid scintillator. Figure 5.21

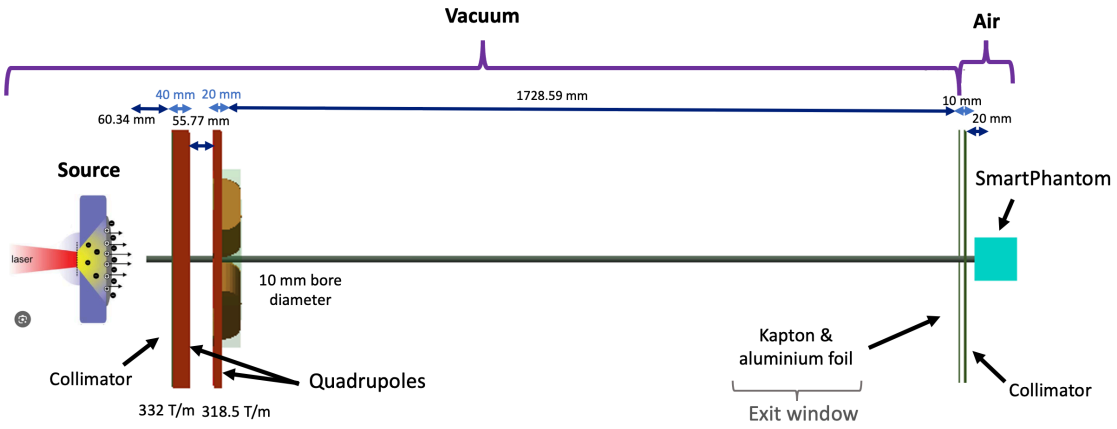

Figure 5.16: Annotated BDSIM diagram of the LION beamline, showing the accelerator elements and drift lengths for focusing a $\sim$ 20 MeV proton beam.

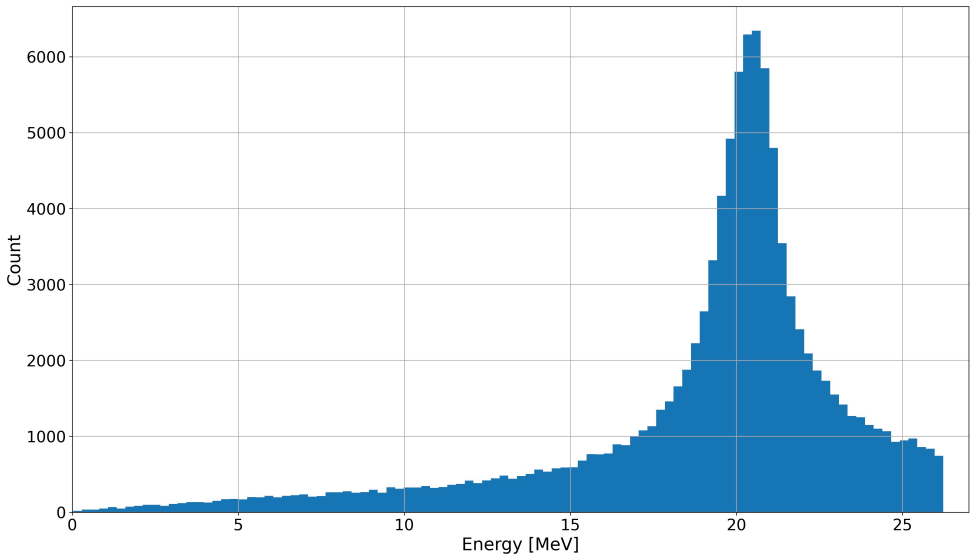

Figure 5.17: Histogram of the simulated energy spectrum of the particles after passing through the LION beamline and focused onto the SmartPhantom.

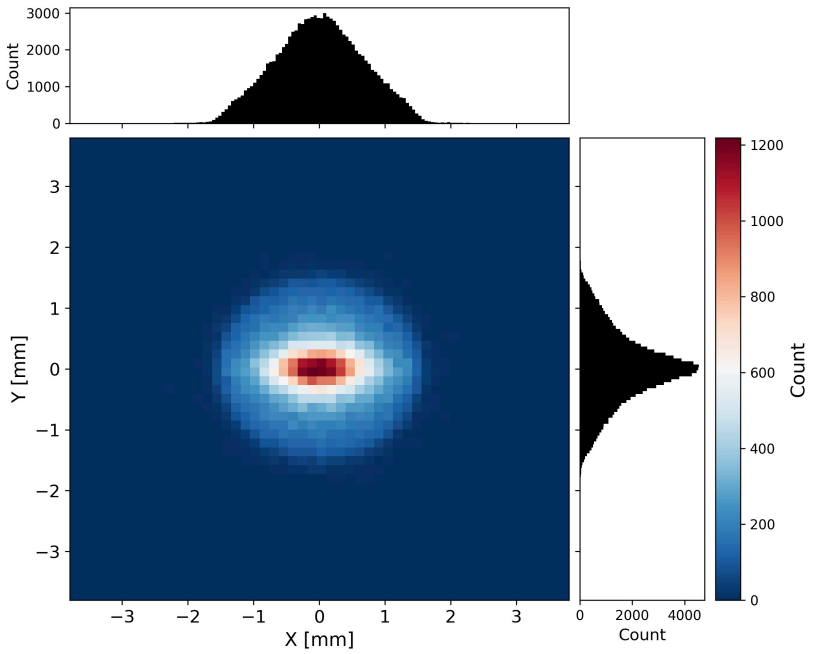

Figure 5.18: The simulated spatial distribution of particles at the LION beamline focus for a nominal beam energy of 20.43 MeV. The focused beam has a FWHM of 0.77 mm and 0.39 mm along the x- and y axes. The total diameter of the beam is approximately 2 mm.

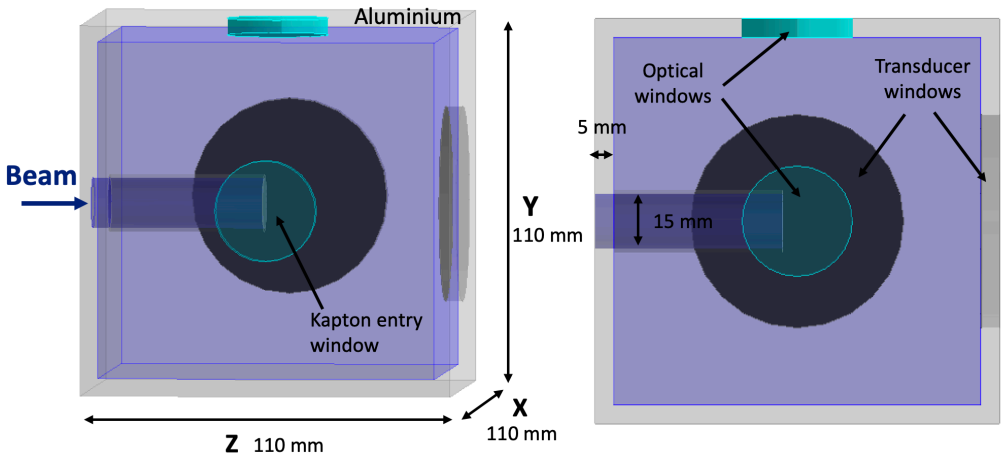

Figure 5.19: Geant4 simulation of the SmartPhantom. Angled view (left), cross-section view (right). The beam, given by the BDSIM simulation, is incident from the left.

shows the deposited energy distribution in the liquid scintillator projected onto each of three orthogonal planes.

5.3.4 Acoustic signal

5.3.4.1 Pressure distribution

The three-dimensional energy depositions from Geant4 were used as the source input for k-Wave [217], which was used to simulate the ion-energy transfer to the medium, the generation of the acoustic waves and their propagation in the three-dimensional space. The pressure value at each voxel was calculated based on the energy deposited in the voxel using equation 5.1. The resulting pressure distribution, in the three orthogonal planes, caused by the passage of the beam in the SmartPhantom is shown in figure 5.22. The pressure distribution determines the characteristics of the induced acoustic signals, which were generated and propagated through space. To ensure that the signals are properly sampled and to prevent artefacts in the reconstructed images, a sampling frequency of 90 MHz was selected as a compromise between accuracy and computational speed.

5.3.4.2 Acoustic wave generation and propagation

Acoustic measurements of the liquid scintillator indicated a speed of sound of approximately 1474 m/s, a 0.5% reduction compared to pure water [211]. Therefore, this value has been used for the simulation. The generation and evolution of the ion-acoustic waves within the SmartPhantom is illustrated in figure 5.23. The figure shows two pressure waves propagating along the z-axis being generated: one arising from the Bragg peak due to the steep pressure gradient and one created at the entrance window, where a boundary between the liquid and air exists, due to the rapid change in the deposited energy density.

Both waves propagate outwards from the heated regions, with a portion of the acoustic wave originating from the Bragg peak travelling towards the Kapton foil. The Kapton-liquid boundary acts as an interface discontinuity due to the difference in acoustic impedance between the two media. Since there is an acoustic mismatch, with the acoustic impedance of air being much lower than that of the liquid, a larger fraction of the wave is reflected. Consequently,

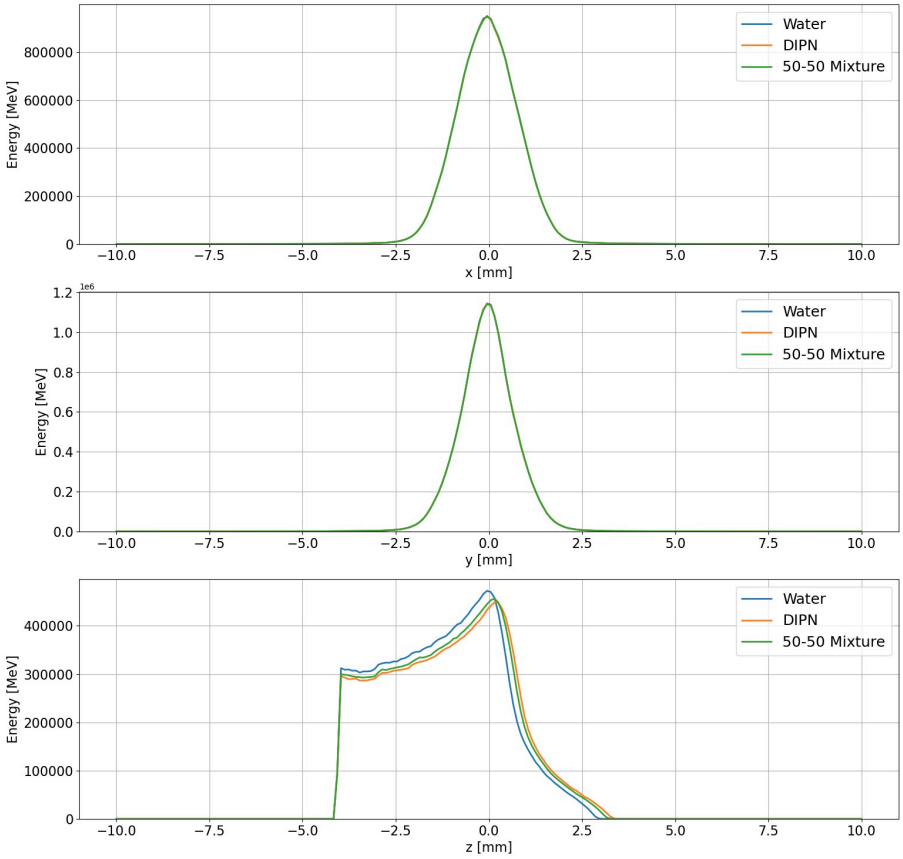

Figure 5.20: Simulated energy depositions, along the three orthogonal axes, caused by particles emerging from the LION beamline and entering the SmartPhantom, for three cases: the entire volume filled with water, a 50-50 mixture of water and liquid scintillator and 100% liquid scintillator.

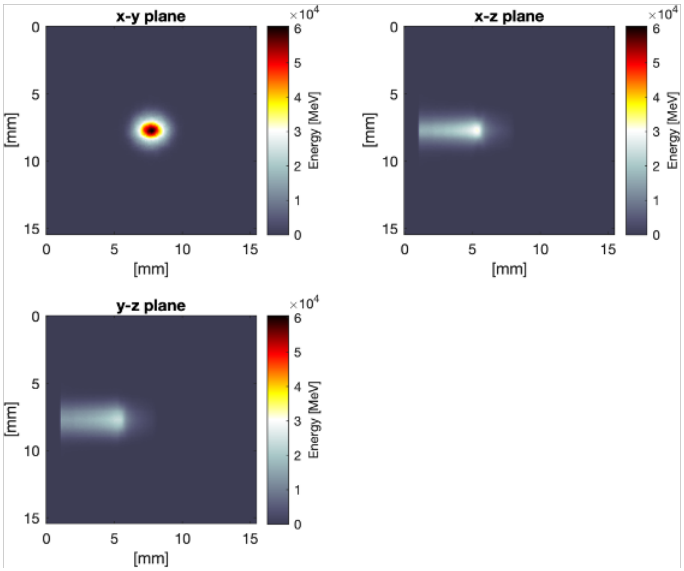

Figure 5.21: Energy depositions in the liquid scintillator inside the SmartPhantom caused by the passage of protons emerging from the LION beamline, as simulated with Geant4. Voxel size: 0.1 mm.

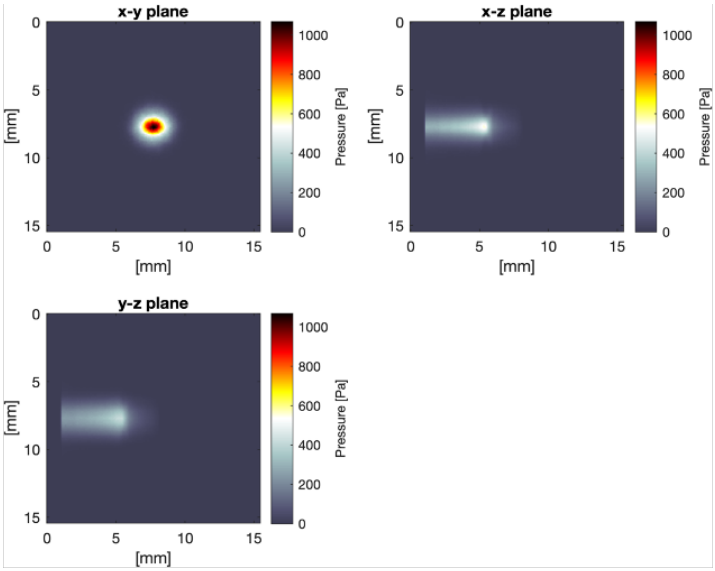

Figure 5.22: Simulated total pressure distribution of particles depositing energy as they propagate through the SmartPhantom, shown in three orthogonal planes. Voxel size: 0.1 mm.

three distinct waves are detected by the transducers, explaining the peaks in the acoustic traces discussed below.

As illustrated in figure 5.23, two different shapes of pressure waves are emitted: the α-wave, a cylindrical wave emitted perpendicular to the beam axis before the Bragg peak, and the γ-wave, a spherical wave emitted from the Bragg peak in all directions. The two waves are highlighted in figure 5.24.

5.3.4.3 Detection and Signal Waveforms

Figure 5.25 illustrates the four transducers and their planned locations relative to the energy depositions of the beam. The Vantage matrix array transducer, shown in the top left, is placed on axis with the beam and the Olympus V303 transducer, shown in the top middle, is aligned axially at the bottom of the SmartPhantom. Similarly, the GE 9L-D linear array transducer, displayed in the top right, is placed axially but oriented parallel to the beam axis and the Precision Acoustics ML4X50 piston hydrophone is used interchangeably with the matrix array, positioned along the beam axis.

All transducers are oriented to face the centre of the SmartPhantom, ensuring that the waves strike their surfaces perpendicularly. In the simulations, the transducers' limited bandwidth has been implemented by applying a Gaussian filter, the centre frequency and bandwidth of which correspond to the transducers' specifications given in Table 5.1.

5.3.5 Signal evaluation

5.3.5.1 Waveforms

The normalised simulated acoustic waveforms that would be recorded by each transducer, according to the k-Wave simulation, are shown in figure 5.26. For the matrix and linear arrays, the average of all the elements is presented. The shape of the traces is influenced by the incoming beam's radius, pulse duration, deposited dose, and the transducer's orientation and depth of detection.

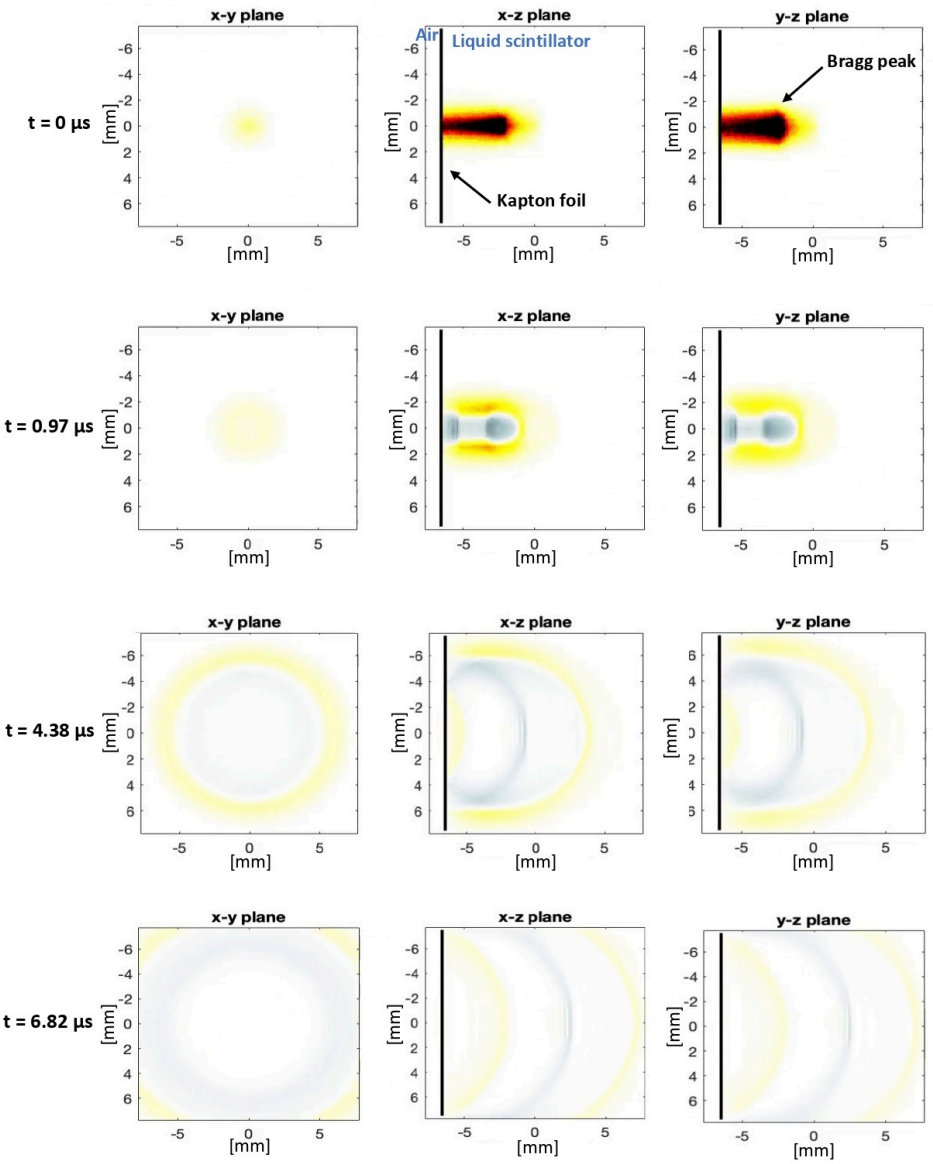

Figure 5.23: Simulated ion-acoustic signal generation and evolution within the SmartPhantom, simulated using k-Wave. Two pressure waves are generated at $t = 0$, originating from the Bragg peak and the entrance window. Both waves propagate outwards, with the second one reflected off the liquid-air interface at the Kapton foil due to acoustic impedance mismatch.

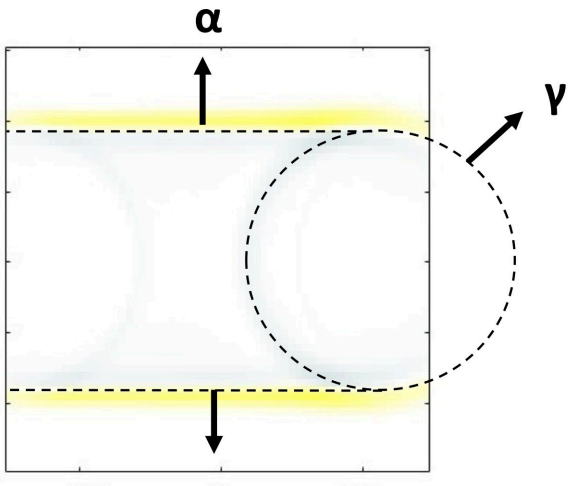

Figure 5.24: An illustration of the two distinct waves emitted as the beam propagates through the SmartPhantom. The α-wave is emitted laterally in the pre-Bragg-peak region, and the γ-wave is emitted at the Bragg peak in all directions. The protons travel from left to right.

Figure 5.26 shows that the Olympus V303 transducer records a signal that starts at approximately 16.6 μs. This delay corresponds to the time required for the ultrasound wave to travel approximately 2.49 cm (the distance between the transducer's surface and the Bragg peak) at a speed of 1474 m/s. The recorded signal shows a high-pressure positive peak, followed by a sudden negative pressure and a plateau. This pattern results from the ion-acoustic effect: the rapid increase in temperature and pressure generates a compression wave, followed by rarefaction as the pressure is released, leading to equilibrium. In addition, the transducer's relatively large cross-sectional area compared to the wavelength of the emitted wave makes it highly directional. This results in a distinct signal originating from the Bragg peak being recorded, with reduced sensitivity to the parts of the signal originating from the off-axis directions. The directional effect and position of the transducer relative to the beam depositions also explain the absence of any oscillations after the dominant peaks.

A similar acoustic time trace is recorded by the linear array, with the signal arriving at approximately 36.7 μs. This corresponds to the time required for the ultrasound wave to travel approximately 5.5 cm at a speed of 1474 m/s. The greater number of elements, compared to the Olympus transducer, enhances the spatial resolution, while the smaller element size eliminates the directionality effect. This improves the detection efficiency of the off-axis signals, resulting in additional compression-rarefaction patterns being observed after the dominant peaks. Furthermore, the improved spatial resolution sharpens the peaks, enabling the array to detect finer variations in the acoustic field. Lastly, unlike the Olympus transducer, the positive signal amplitude is more pronounced than the negative, due to the array's greater sensitivity.

Figure 5.26 also presents the signal recorded by the matrix array, with the waveform displaying more intricate characteristics. Unlike the linear array, the two-dimensional configuration of the matrix array elements enables efficient detection of radially propagating signals. This results in enhanced resolution, evident from the finer peaks observed in the signal trace. In addition, positioning the array on axis relative to the beam enables detection of signals reflected off the entrance window. In the acoustic waveform, this is observed as a spatially inverted signal following the dominant signal from the Bragg peak, attributed to the phase inversion caused by the reflection. Furthermore, the subsequent oscillations arise from waves arriving at various angles and distances, giving rise to intricate patterns in the signal.

Lastly, a similar time trace is recorded by the piston hydrophone, albeit with slightly poorer resolution due to its single-element configuration. This results in the waveform appearing

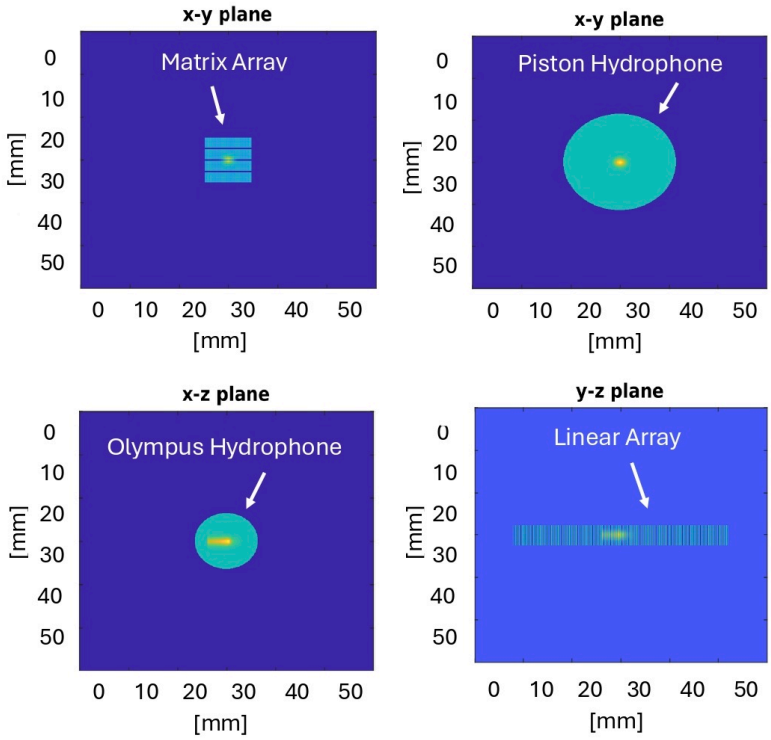

Figure 5.25: k-Wave simulation illustrating the acoustic transducers and their location relative to the beam energy depositions, indicated by the yellow region. The energy depositions depicted are generated by a beam exiting the LION beamline, optimised for a modal energy of 20 MeV, as it passes through the liquid scintillator.

smoother, as the acoustic pressure is averaged across the hydrophone's surface.

5.3.6 Optical Simulation

The interior of the SmartPhantom and the imaging optics were simulated using non-sequential ray-tracing in Ansys Zemax OpticStudio version 2025/R1 (Premium).

Non-sequential ray-tracing was used in a detailed model of the SmartPhantom in order to determine the image of the scintillating volume, including diffuse reflectance from the nominally absorbing surfaces such as the anodised aluminium and the black Kapton. The achromatic doublet lenses had their proprietary anti-reflection coatings included; the BK7 window was uncoated.

Key aspects of the SmartPhantom include the two optical windows, the proton beam entrance tube and the occluding ring that holds the Kapton in place and provides support for the scintillating fibre planes. The imaging optics were discussed in Section 5.2.3.2, and figure 5.27 shows the volumes simulated.

A small sample of both the black Kapton film and the black anodised aluminium were measured for both diffuse and specular reflectance using a PerkinElmer LAMBDA 1050+ spectrophotometer. The average reflectance of the diffuse sphere in the 1050+ spectrophotometer was 98.7% over the range 350 nm to 500 nm. Figure 5.28 shows the diffuse reflectance of our sample of black Kapton. In our optical simulations, we used the value of 8.2% diffuse reflectance (and thus 91.8% absorbance), which is the measured value at 427 nm. The measured specular reflectance at this wavelength was 2.7% and was not included in the simulation. The black anodised aluminium had a maximum diffuse reflectance of 4.7% over the same range.

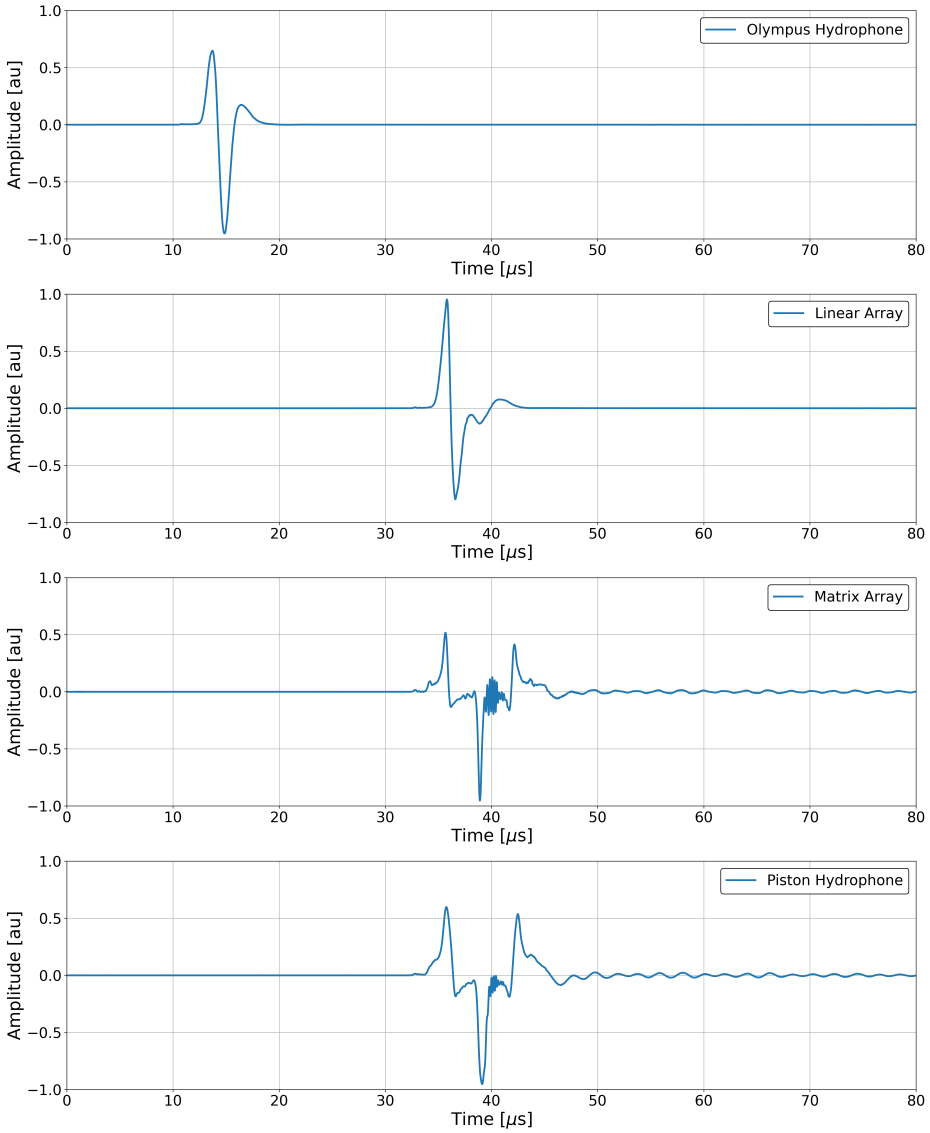

Figure 5.26: Normalised simulated acoustic waveforms recorded by the four transducers: Vantage Matrix Array Ultrasound Transducer, GE 9L-D Linear Array Ultrasound Transducer, Olympus V303 Immersion Transducer and Precision Acoustics ML4X50 Piston Hydrophone, when positioned at the locations displayed in figure 5.25.

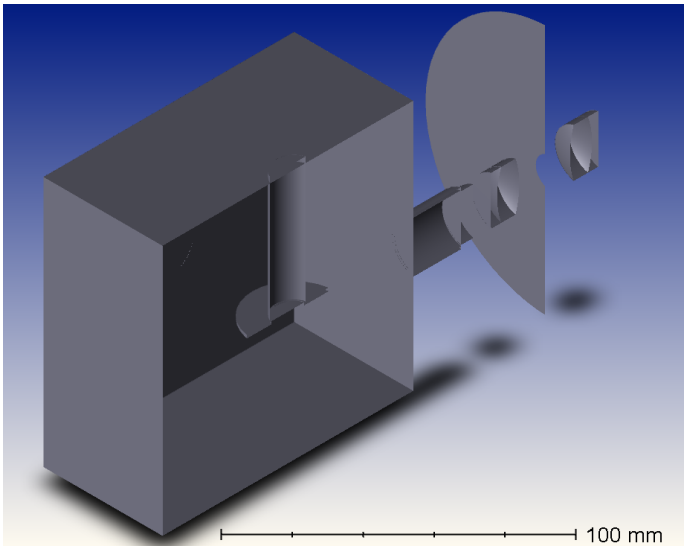

Figure 5.27: Cut-away 3D volume of the SmartPhantom as simulated in Zemax OpticStudio.

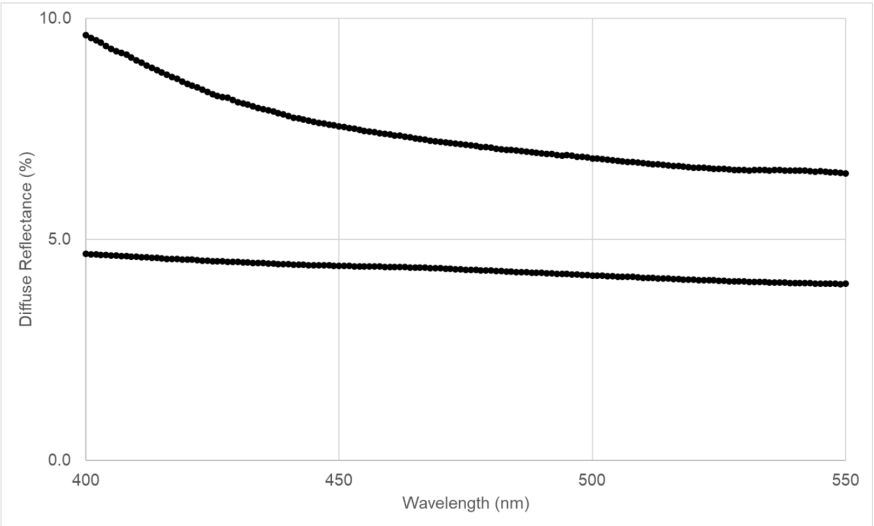

Figure 5.28: Diffuse reflectance of black Kapton (upper curve) and black anodised aluminium (lower curve).

Using non-sequential ray tracing, we simulated the response of a camera imaging an ideal LION beam depositing energy at approximately 20 MeV into the liquid scintillator. All simulations use non-sequential ray tracing with both ray splitting and scattering at every surface. The optical sources represent the Monte Carlo predicted intensity of the light from the liquid scintillator, modelled as fifteen elliptical elements each emitting isotropically with intensities and number of photons weighted by the simulated deposited energy in the volume. Figure 5.29 shows the result of a simulation where each source has equal intensity.

The total number of primary rays traced was 300 million, and a simple Lambertian scattering model was used with three scattered rays produced per scattering event. The minimum relative ray intensity was 0.1%, and polarisation and ray splitting at dielectric boundaries were accounted for.

Figure 5.30 shows the simulated image on the plane of the CMOS camera and a section of the image along the midline. The gradient of the rising edge near the Kapton is clearly smaller than that of the falling edge. This is due to the effect of the support ring, which partially occludes the light collected from the first 1.5 mm of the emitting source.

5.4 Initial detector evaluation

5.4.1 The LION beamline

The SmartPhantom was evaluated at the LION beamline. The liquid scintillator was inserted through the tubes located on the top lid, shown in Figure 5.2. The detector was left undisturbed for a few minutes to allow air bubbles to dissipate, as their presence could affect the acoustic measurements.

Both imaging systems, each composed of two bi-convex lenses, were mounted on each of the optical windows. The piston hydrophone was mounted on the Kapton window opposite the entrance window, and the Olympus V303 transducer was attached inside the SmartPhantom at the bottom. Acoustic matching gel was applied between the piston hydrophone and the black Kapton foil to ensure effective coupling and maximise signal transfer. The SmartPhantom was

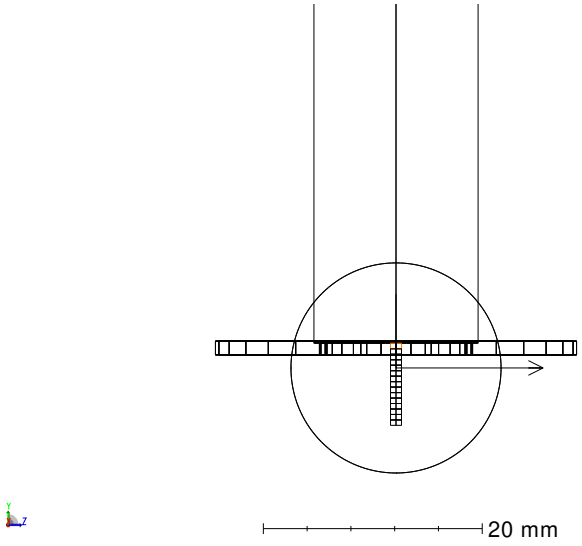

Figure 5.29: View showing the proton beam pipe, the black Kapton film, the support ring and the elliptical sources. The arrow points towards the imaging optics, and the circle represents the second N-BK7 window with an orthogonal view of the sources.

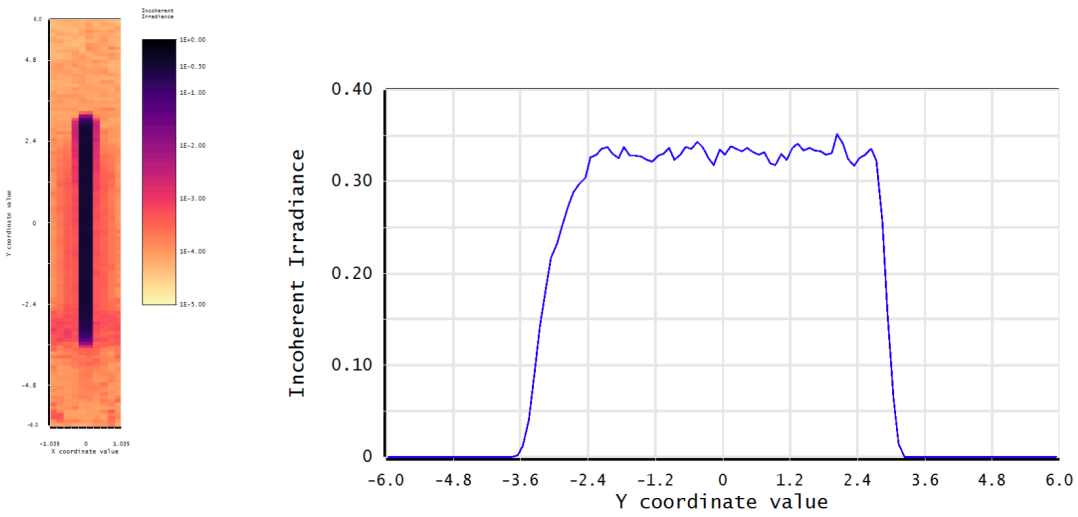

Figure 5.30: The 2D image and a section along the depth axis for a 0.1 mm diameter uniform set of sources. The occluding effect of the ring supporting the black Kapton can be seen in the region between $y = -1.4$ and $y = -1.6$ mm.

then mounted onto a motorised translation stage to enable horizontal and vertical movements to align it with the beam axis. Images of the experimental set-up are shown in figure 5.31.

The transducer signals were recorded using a picoscope [221], while the cameras were read out by the central computer. Three trigger signals were sent through the laser's trigger box: one to each camera via GPIO connectors and one to the picoscope to activate the two transducers simultaneously.

To evaluate the effect of the beam width on the distribution of scintillation light and the shape of the acoustic signals, collimators of various sizes were placed between the beam exit window and the entrance window of the SmartPhantom. The collimators used are shown in figure 5.32 and had circular apertures with diameters of 1, 2, 3 and 4 mm.

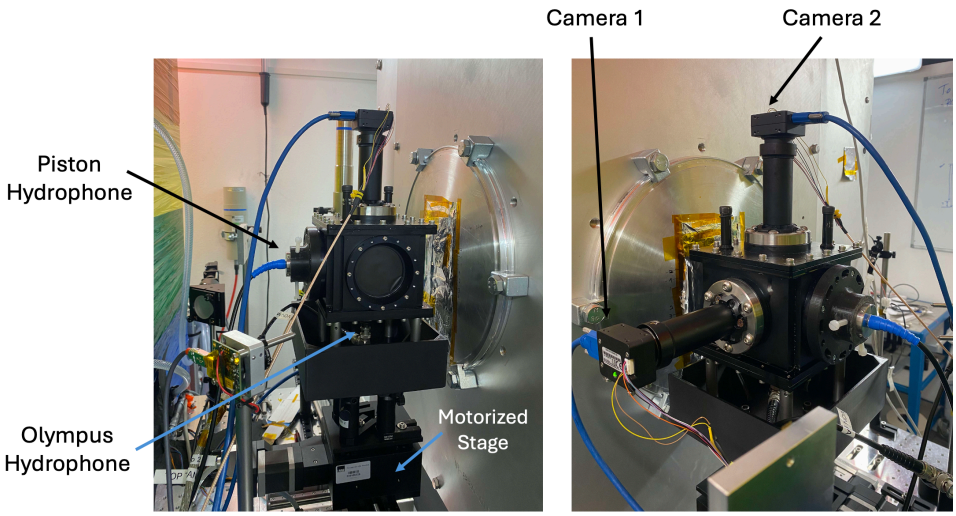

Figure 5.31: Experimental setup showing the SmartPhantom mounted on a motorised translation stage located at the LION beamline's exit window. The piston hydrophone is aligned with the beam axis, and the Olympus V303 transducer is positioned at the bottom.

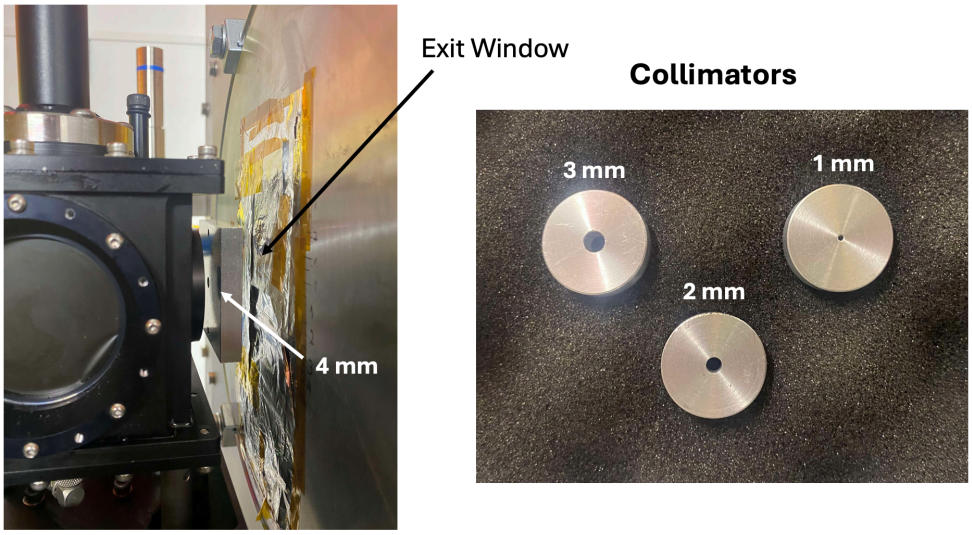

Figure 5.32: Location of the collimators relative to the SmartPhantom and the beam-exit window (left) and image of the collimators showing their respective diameters (right).

5.4.2 Optical and acoustic cross-correlation

Initial experiments were performed without a collimator, relying solely on the 15 mm diameter entrance window of the SmartPhantom for beam collimation. Later tests were conducted using 4 mm and 2 mm collimators mounted in front of the SmartPhantom on a holder fixed to the optical bench. Simultaneous optical and acoustic measurements were acquired using the imaging systems and transducers, while varying the beam energy by adjusting the quadrupole drifts. For conciseness, only the data obtained with the 4 mm collimator will be presented here.

The averaged, background-corrected images obtained using the top and side cameras, for the various beam energies (10 MeV, 12 MeV, 14 MeV, 16 MeV, 18 MeV and 20 MeV) and the 4 mm collimator, are shown in figures 5.33 and 5.34 respectively. The images show that the collimator reduces the cross-sectional area of the beam, as expected. As a result, most of the energy depositions, and hence scintillation light, occur within the camera's field of view. The offset between the energy deposition and the centre of the imaging plane is possibly due to misalignment between the collimator and imaging system. The intensity fluctuations can be attributed to large particle number variation between shots.

Beam profiles were extracted from the images by averaging 60 pixels along the x, y, and z axes as indicated in figure 5.35. The resulting profiles are shown in figures 5.36, 5.37, and 5.38.

The z-profile plots with the 4 mm collimator exhibit sharper peaks compared to the z-profiles without a collimator. This may be because the collimator filters out particles found in the outer radius of the beam that do not have the desired energy; the collimator sharpens the energy spectrum of the focused particles, and hence the Bragg peak appears narrower. Furthermore, as the beam energy increases, a second peak begins to emerge. A possible explanation for this might be the non-optimised drifts between the quadrupole magnets in the beamline.

The x- and y-profiles are narrower when the collimator is placed in front of the detector. Consequently, the camera imaging the y-plane is able to capture a larger fraction of the scintillation light. In addition, the beam is not centred in either plane due to misalignment between the collimator and the detector's centre. Furthermore, camera saturation is observed in the x-plane when the 14 MeV beam propagates through the liquid scintillator, possibly due to a large particle count. The saturation is also evident in the colour map in figure 5.35.

The acoustic signal traces recorded by the Piston hydrophone and Olympus transducer with

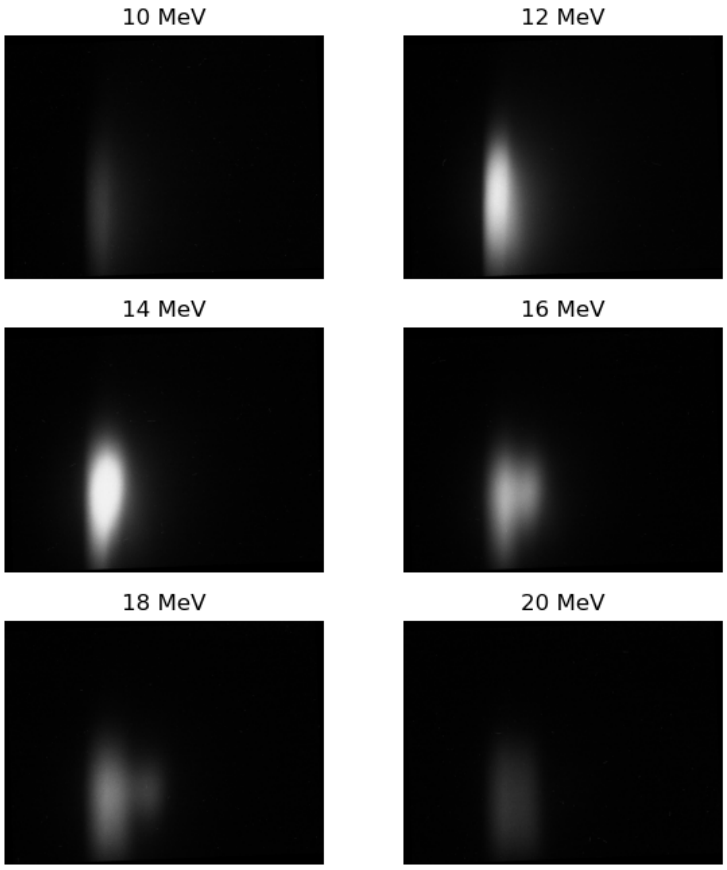

Figure 5.33: Averaged, background-corrected grey-scale images obtained using Camera 2 from the setup shown in figure 5.31. A 4 mm collimator was placed in front of the SmartPhantom.

the 4 mm collimator in front of the SmartPhantom are shown in figures 5.39 and 5.40. The waveform recorded by the piston hydrophone appears noisier compared to the corresponding waveform without a collimator. While the peaks appear at the same time intervals, the amplitudes are significantly smaller due to the lower number of particles entering the SmartPhantom. As a result, the signal features are harder to distinguish, with the 16, 18 and 20 MeV waveforms being dominated by noise.

In contrast, the waveforms recorded by the Olympus transducer are significantly clearer compared to those obtained without a collimator, with two distinct peaks visible in the acoustic traces across all beam energies. This is possibly due to the collimator filtering out particles found at the outer radius of the beam, thereby generating a more compact and well-defined sound wave. In addition, the signals become progressively noisier with increasing beam energy.

The effective range was also estimated using the acoustic traces by calculating the signal envelope. The time difference between the first peak, corresponding to the signal from the Bragg peak, and the third peak, which corresponds to its reflection off the entrance window, was then calculated. This time difference was multiplied by the speed of sound in the liquid scintillator to give twice the range.

The images of the scintillation light do not show distinct peaks and do not allow the effective range to be determined. This is likely to be a consequence of insufficient focusing of the particle beams. Therefore, only the effective ranges determined by the acoustic data were reconstructed, and hence, comparison of the effective range estimated by the two systems was not possible. The acoustic results are presented in figure 5.41. The error on the effective range was calculated using the standard deviation of the fit to the peak.

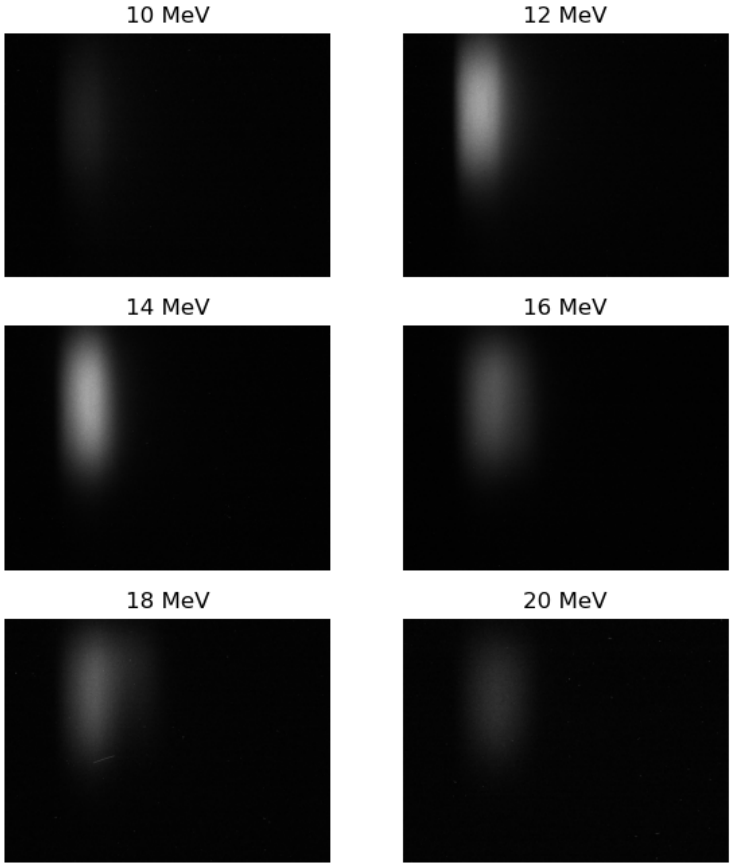

Figure 5.34: Averaged, background-corrected grey-scale images obtained using Camera 1 from the setup shown in figure 5.31, with a trigger window of $\sim 160\mu$s. A 4 mm collimator was placed in front of the SmartPhantom. Each image is the average image from multiple shots at each energy, specifically: 3 shots at 10 MeV, 3 shots at 12 MeV, 3 shots at 14 MeV, 4 shots at 16 MeV, 3 shots at 18 MeV and 3 shots at 20 MeV.

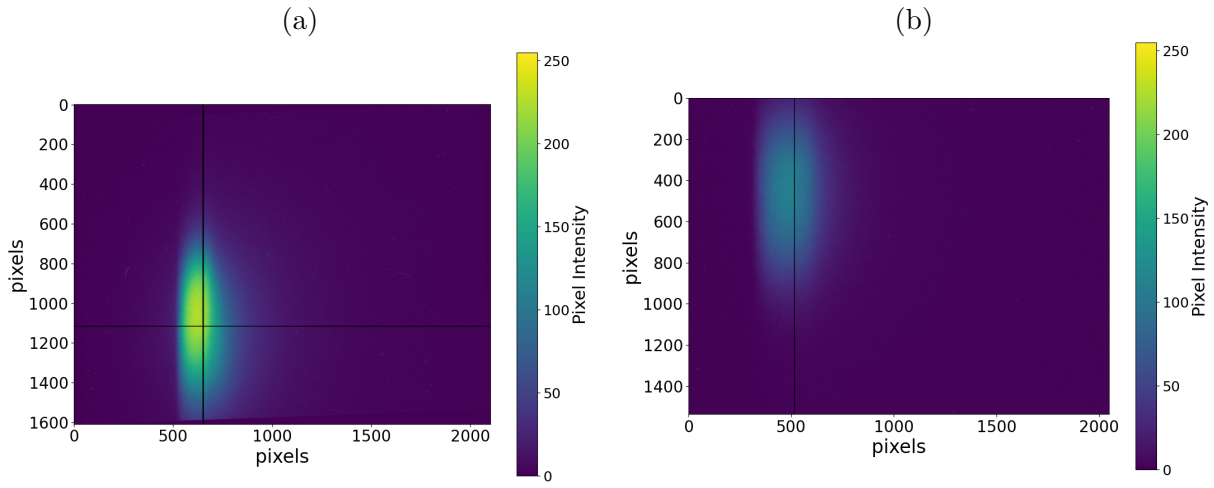

Figure 5.35: Colour maps of pixel intensities from the images obtained using the top camera (a) and side camera (b) when a 12 MeV proton beam passes through the liquid scintillator. The setup included a 4 mm collimator in front of the SmartPhantom.

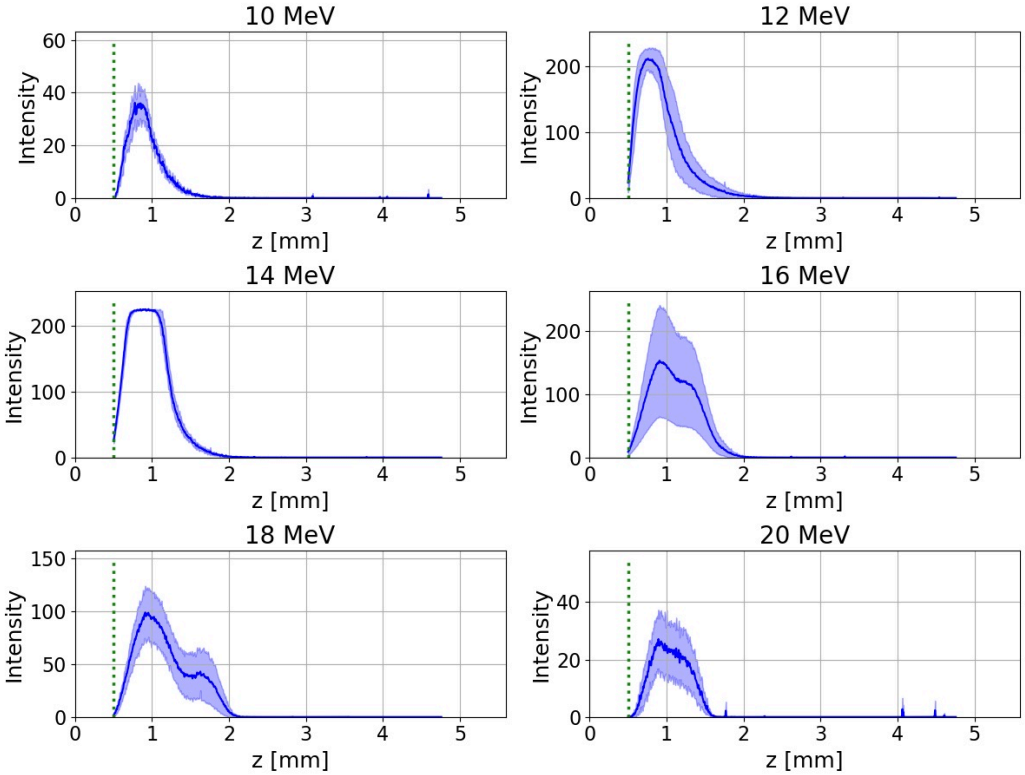

Figure 5.36: Z-profile average of 60 pixels, with a 4 mm collimator, corrected for the 0.5 mm shift observed due to the entrance window flange. The green dotted line marks the estimated position of the entrance window, determined by the peak of the second derivative of the curves.

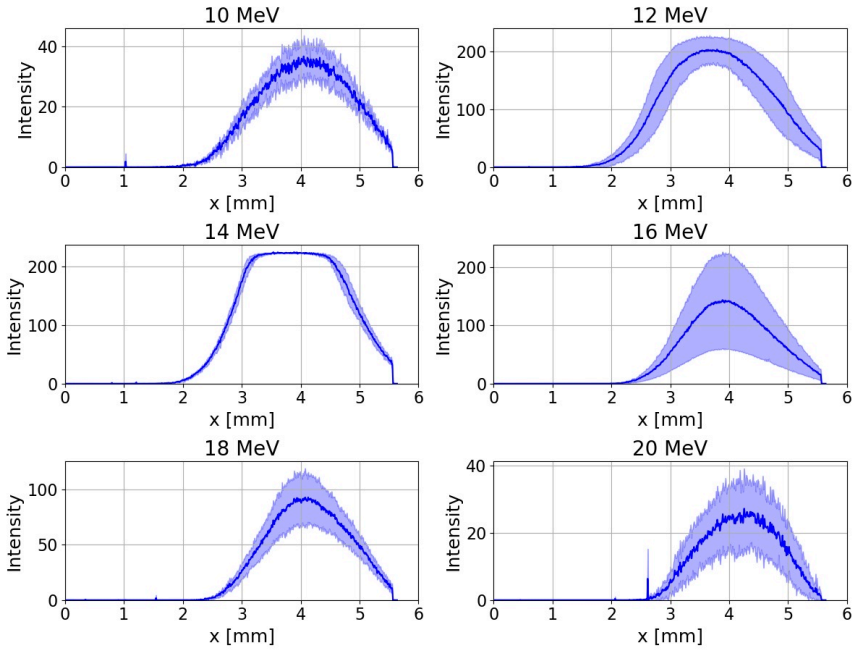

Figure 5.37: X-profile average of 60 pixels from images obtained at various proton energies traversing the liquid scintillator, with 4 mm collimator in front of the SmartPhantom.

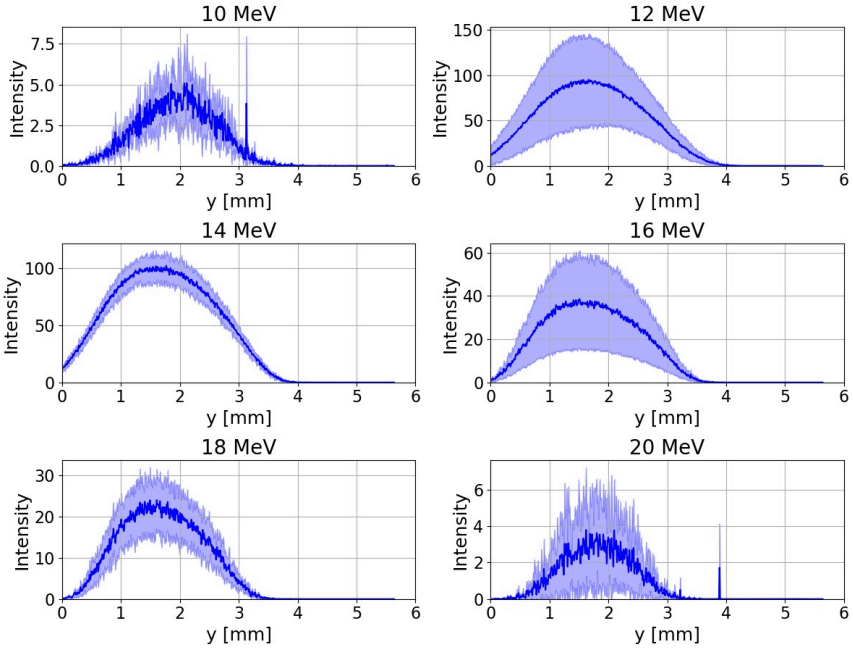

Figure 5.38: Y-profile average of 60 pixels from images obtained at various proton energies traversing the liquid scintillator, with 4 mm collimator in front of the SmartPhantom.

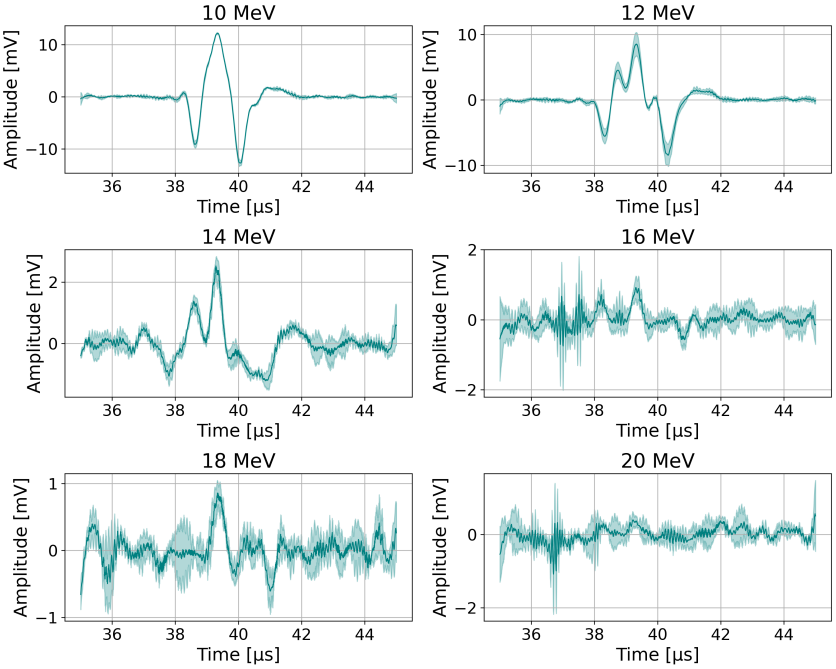

Figure 5.39: Acoustic waveform recorded by the Piston hydrophone, on-axis with the beam, with a 4 mm collimator placed in front of the SmartPhantom. The darker colour waveform shows the average acoustic trace across all shots at each energy. The lighter shade error band demonstrates the standard deviation across the multiple shots, described in the caption of figure 5.34.

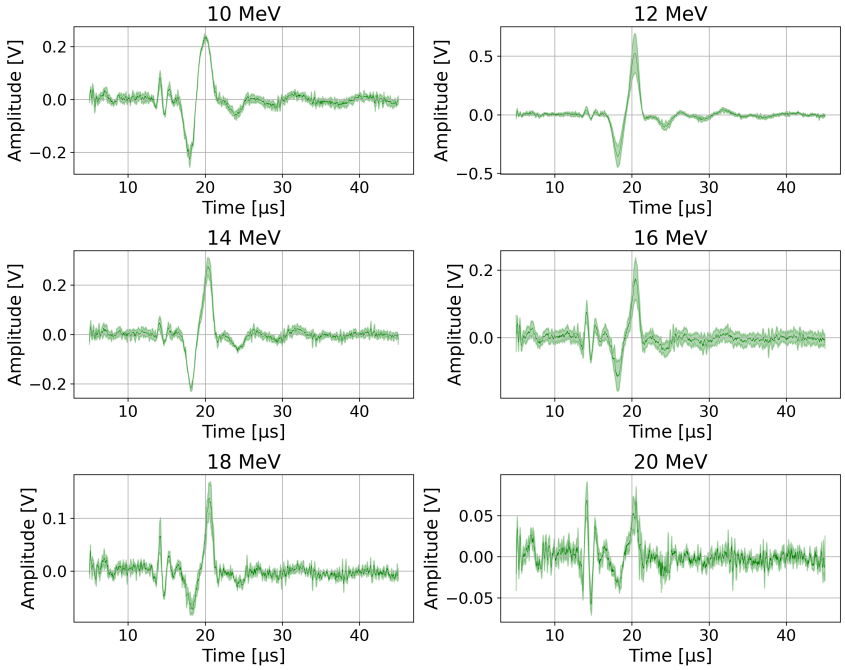

Figure 5.40: Acoustic waveform recorded by the Olympus V303 transducer, immersed from underneath, with a 4 mm collimator placed in front of the SmartPhantom.

The beam width in the x- and y-directions was determined from the x- and y-profiles of the energy depositions along each axis. To calculate the FWHM, polynomial fits were made, and the FWHM and its error were calculated from fitted parameters.

Figure 5.42 shows the calculated FWHM of the beam width along the x-direction based on the optical data for the various collimators used. However, a comparison of the beam width between optical and acoustic data in this direction is not possible as no transducer was positioned facing the defined x-axis. It is evident from the plots that the beam width decreases with the collimator size. In addition, a small decrease in width is also observed as the set energy increases.

The beam width in the y-direction was calculated using the same approach as the width across the x-direction, by applying polynomial fits to the extracted profiles. Unfortunately, the beam width along the y-direction without a collimator could not be determined, as a large fraction of the energy depositions were outside the camera's field of view. The polynomial fits are shown as black dashed lines. The FWHM for each case was calculated from the fits, with the associated errors shown by the lighter blue colour.

For comparison, the beam width in the y-direction was also calculated using the acoustic data. This was done using the acoustic traces obtained from the Olympus V303 transducer, which was positioned facing in the y-direction. The beam width was estimated by calculating the signal envelope and identifying the two dominant peaks, corresponding to the compression and rarefaction waves. Subsequently, the time difference between them was calculated and multiplied by the speed of sound in the liquid scintillator to obtain the beam width in that direction. For the cases where the three signals from the Bragg peak, the entrance window and the Bragg peak reflection off the entrance window overlap, the FWHM of the envelope was used instead. The traces at 10 and 12 MeV without a collimator, as well as at 18 and 20 MeV with a 4 mm collimator, were deemed unusable, as no distinct peaks could be identified. As before, the errors were estimated using the error bands.

Figure 5.43 presents a comparison of the beam width in the y-direction using the various

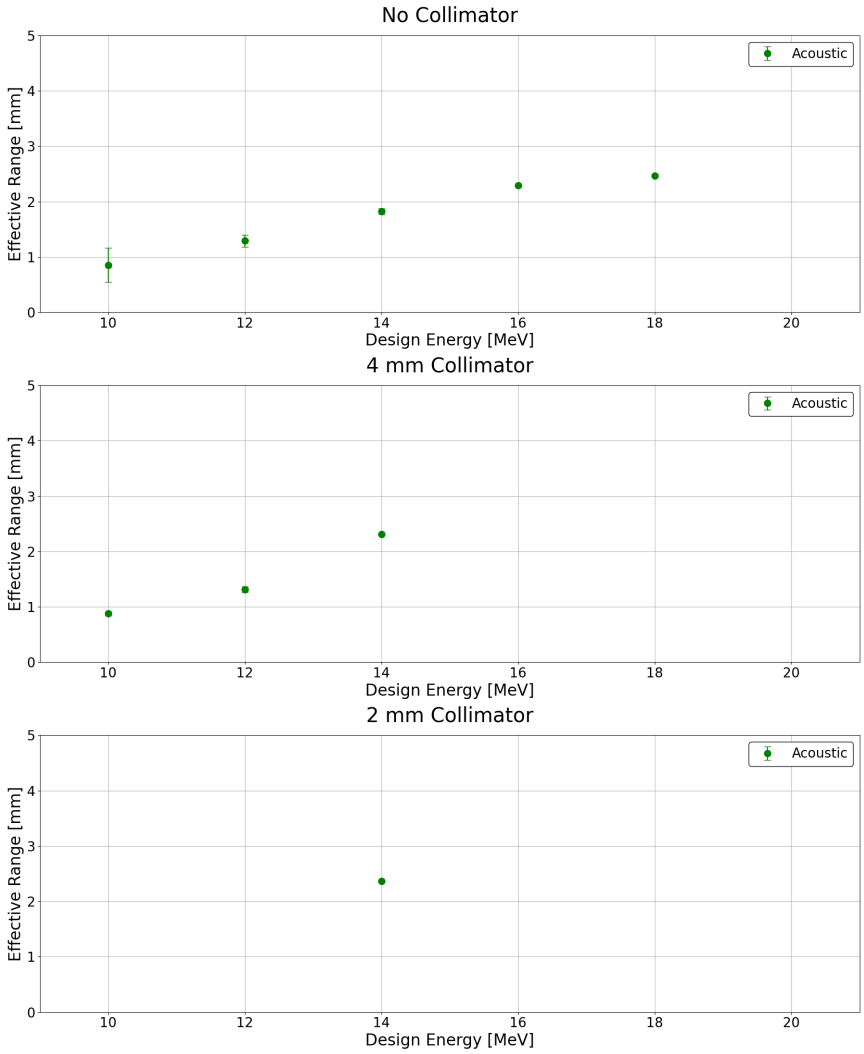

Figure 5.41: Effective range calculated using the peaks observed in the acoustic traces obtained by the piston hydrophone positioned on axis with the beam.

collimator sizes and proton energies investigated, calculated using the optical and acoustic data. The plots reveal that, at all energies, the FWHM of the beam decreases in proportion to the collimator size. In addition, a slight decrease in beam width is observed for a fixed collimator size and increasing modal beam energy, a trend also observed in the data along the x-direction. Furthermore, for the 4 mm and 2 mm collimator data, the calculated optical and acoustic beam widths are in strong agreement, within the associated errors.

Lastly, specific features retrieved from the optical and acoustic data are proportional to the particle number in each bunch, providing additional ways to establish a correlation between the two [222]. In the images obtained, the particle count is directly proportional to the pixel intensity, assuming that no saturation is reached. This is because a higher particle count generates a greater total scintillation-light emission, as there are more particles to deposit energy. The average pixel intensity of each averaged, background-corrected image at each energy and collimator size used was calculated and plotted in figure 5.44.

In the acoustic signals, the number of particles in the bunch is proportional to the signal amplitude. This is because a greater particle count would give a larger beam current and hence larger energy deposition. Specifically, the waveforms recorded by the piston hydrophone, placed on-axis with the beam, were used. However, since the first and third peaks originating from the

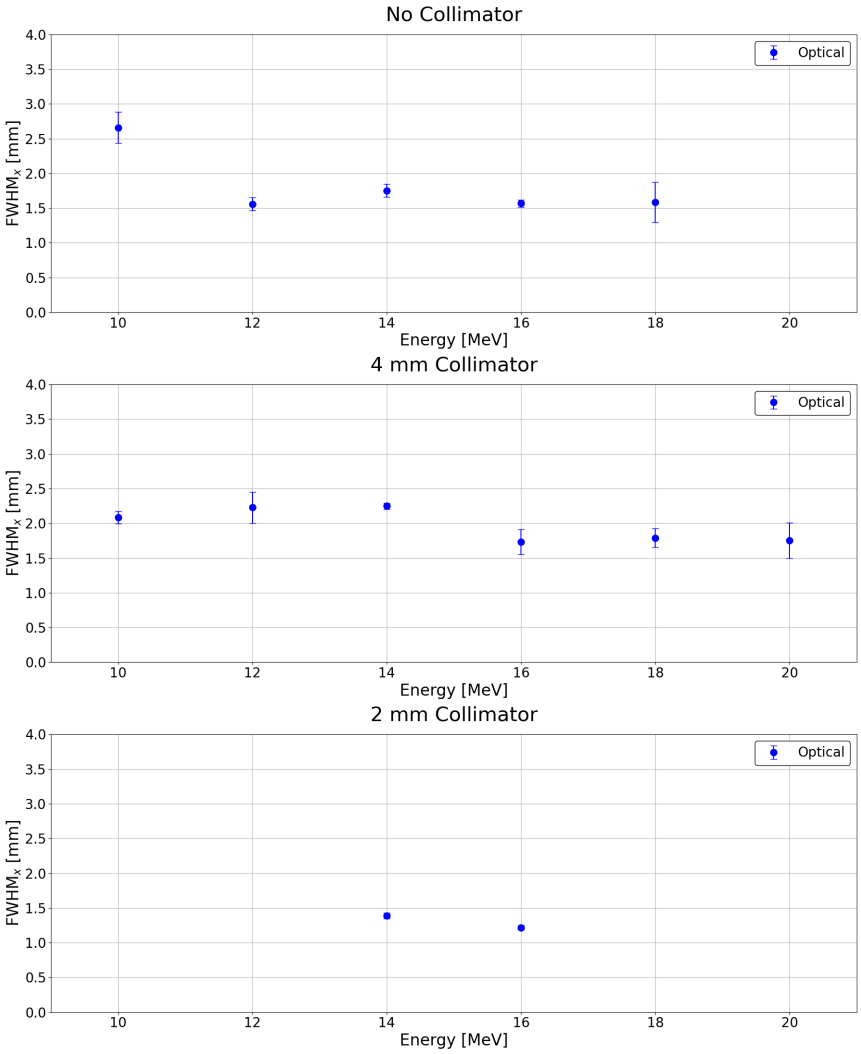

Figure 5.42: Full Width Half Maximum (FWHM) calculation along the x-direction of the beam depositions at the various proton energies and collimator sizes used in the setup.

Bragg peak are influenced by the beam's energy spread, the second peak, originating from the entrance window, was selected for the measurement. The peak was only identified for the data where the peaks were sufficiently distinct.

Figure 5.44 presents a comparison of the amplitude of the entrance window peak from the acoustic waveforms recorded by the piston hydrophone with the average pixel intensity of the images captured during the same shots. Both the average pixel intensity and the amplitude of the acoustic peak decrease as the size of the collimator is reduced. In addition, for a fixed collimator size, both the optical and acoustic data follow a decreasing pattern as the beam set energy increases. This is due to the lower number of particles being focused as a result of the quadrupole doublet focusing mechanism.

However, a significant discrepancy between the values obtained by the two methods is observed for the 10 and 12 MeV set energies. The average pixel intensities at those energies are much lower than expected based on the trend. This can be attributed to the entrance window flange, which occludes the first few millimetres of the energy depositions, resulting in a significant loss of information.

In conclusion, a positive correlation appears to exist between the optical data coming from the scintillation light images and the acoustic data from the recorded acoustic waveforms as the

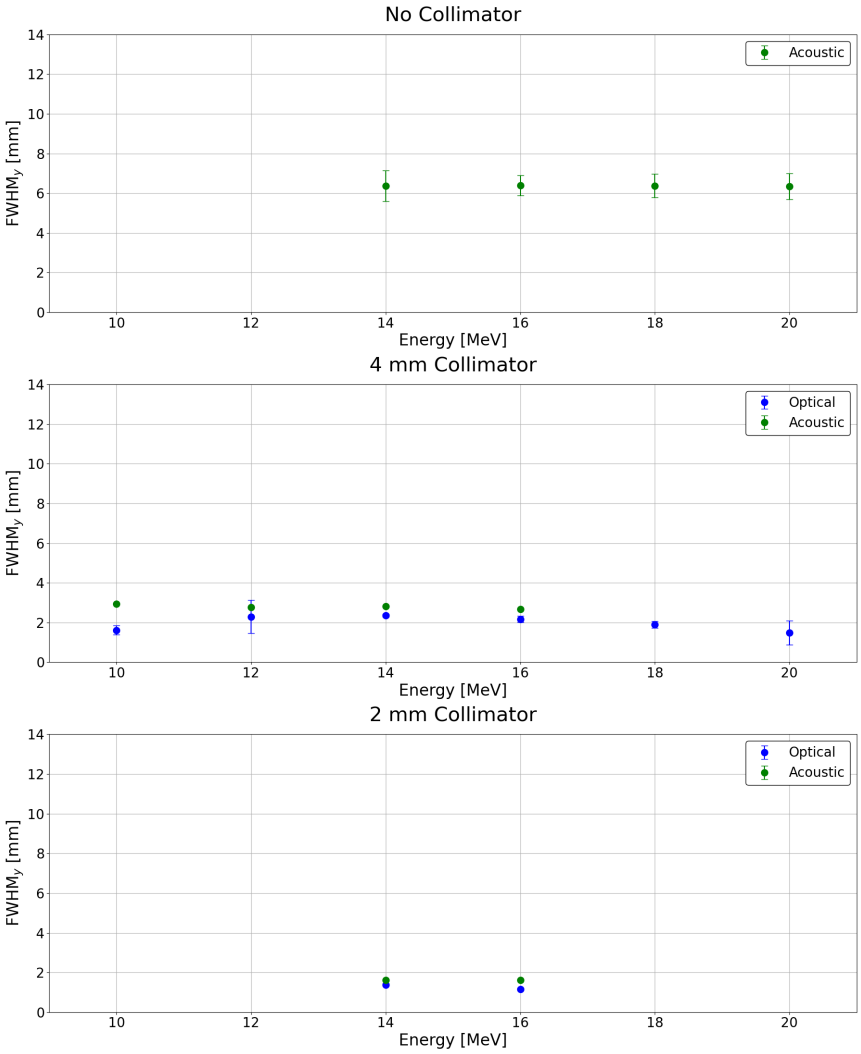

Figure 5.43: Full Width Half Maximum (FWHM) calculation along the y-direction of the beam depositions at the various proton energies and collimator sizes used in the setup.

beam propagates through the SmartPhantom. The shot-by-shot comparisons of the effective range, mean beam energy, beam width and bunch particle number revealed a promising relationship between the two methods. This comparison lays a strong foundation for a calibration mechanism, in which the liquid scintillator will calibrate the acoustic response and yield an absolute determination of the deposited dose.

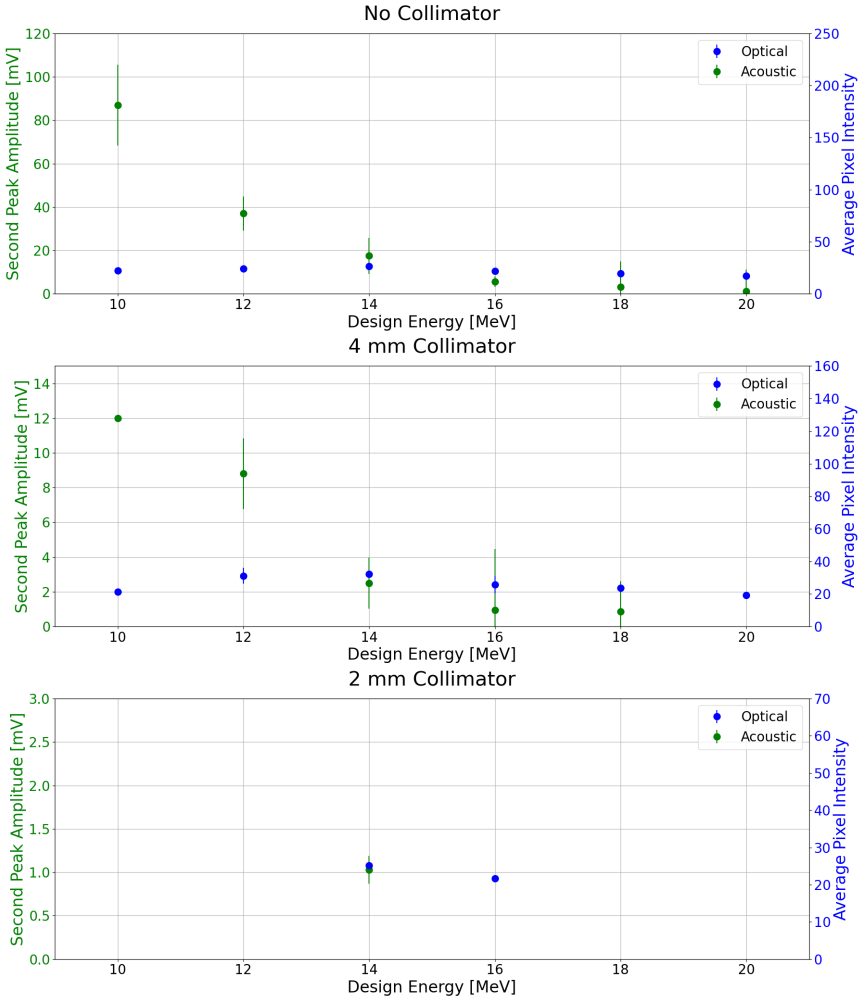

Figure 5.44: Comparison of the entrance window peak amplitude obtained from the Piston hydrophone waveforms (green) and the average pixel intensity from the images obtained during the same shot (blue). Both measurements are related to the particle number in the bunch.

CHAPTER 6

End Stations

6.1 Introduction to the end-stations.

LhARA will support three end-stations: two *in vitro* and one *in vivo*. In Stage 1, a 15 MeV proton beam will serve the low-energy *in-vitro* end-station. In Stage 2, after passing through the FFA, the high-energy 127 MeV proton beam will serve both the high-energy *in-vitro* end station and the *in-vivo* end station. In addition, Stage 2 will provide ion beams up to C^{6+} at energies up to 33.4 MeV/u to both the high energy *in-vitro* and the *in-vivo* end-stations. The expected beam parameters at each end-station are described in Chapter 2, and the specification of the beam energies and dose rates that the facility will deliver are summarised in table 1.1.

The requirements for each end-station are presented in the sections that follow. The end-station design requirements have been derived to address:

- User requirements gathered from consultation meetings;
- A detailed review of existing dosimetry techniques to assess their feasibility for the beams LhARA will deliver; and
- The development of a supersonic-gas-curtain-based ionisation profile monitor for non-destructive beam monitoring in real time.

Each of these aspects is discussed below.

6.2 End-station user requirements

A series of consultation meetings was held to capture the requirements of the radiobiological communities that would be served by the LhARA facility. The first meeting focused on the Stage 1 *in-vitro* end-station, the second on both the Stage 1 and Stage 2 *in-vitro* end-stations, and the third on the Stage 2 *in-vivo* end-stations and associated infrastructure needs. Across the three meetings, 71 unique registrations from across the UK, Europe, North America and Asia were received. Registrations were received from researchers at Universities, national and international laboratories, including CERN, IAEA, PSI, and DKFZ, as well as private companies. The consultation meetings began with short introductions to the LhARA project, with ample time set aside for attendees to discuss their research and requirements. The following list of 10 conclusions (**C1** to **C10**) was drawn from these meetings.

C1: There was strong support for the present baseline vertical beam-delivery concept for the low- and high-energy *in-vitro* end-stations, and therefore the existing baseline of vertical beamlines should be retained.

C2: A specification of 5% for the accuracy and repeatability of the measurement of integrated dose is sufficient for the dose-measurement uncertainty not to dominate the error budget of biological experiments. This should be treated as a hard upper limit with every effort made to minimise the uncertainties.

C3: The end-station designs must be compatible with the dosimetry methods used to achieve C2. Techniques under consideration include ion-acoustic imaging for real-time dose-profile measurement and the gas-curtain profile monitor for beam monitoring. Other techniques will be considered as the R&D programme develops. In addition, the end-stations must be able to incorporate real-time imaging of samples both during and shortly after irradiations in order to exploit the unique timing structures of LhARA.

C4: Any setup and end-station must be simple, robust, reproducible, and cheap for the facility users. With this in mind, the Stage 1 *in-vitro* end-stations are designed to accommodate standard plastic cell dishes with the flexibility to accommodate other cell dishes as required by users.

C5: The cell transportation into the end-stations must be automated in a climate-controlled environment where the temperature and oxygen tension will be set by the user. The end stations must maintain and monitor these parameters to provide users with a history for each irradiation. Two options are under consideration to achieve this. The first is a large environmental chamber which runs from incubator to end-station and back, within which cell dishes are transported. The second would be multiple small environmental chambers in which the cells are loaded, the whole chamber then being transported to the end station.

C6: An X-ray source to be included in the facility to allow control sample and low LET comparisons to be made with cultures in both the Stage 1 and Stage 2 *in-vitro* end-stations.

C7: The experimental complications arising from the use of a low-energy proton beam must be considered carefully, and a validated Monte Carlo simulation will be essential to extract kinetic energy, LET, and beam uniformity profiles.

C8: For the *in vivo* work, an animal house on site is essential as the animals involved in experiments cannot leave the site after irradiation. This prevents contamination of animals.

C9: The development of the specification of the *in-vivo* end-station and its operation should include careful consideration of the range of animals required. Support will be required from external partners, such as the Mary Lyon Centre, regarding the regulations for animal work.

C10: Real-time imaging will be required in the *in-vivo* end-station for animal work to ensure reproducibility and optimal outcomes. The end station must be equipped appropriately.

6.3 Review of dosimetry techniques for ion beams

This section discusses dosimetry techniques suitable for integration into the LhARA end stations. The choice of dosimetry technique typically depends on the type of radiation, dose rates and the level of dose information required. Since the LhARA beam is designed to deliver FLASH doses, the dosimetry must be capable of accurately reporting dose at rates in excess of 40 Gy/s. At such high rates, the large instantaneous current requires the dosimeter response to be independent of rate and for the dose to be reported pulse by pulse.

The work of Romano et. al. [223] provides valuable insights into the dosimetry techniques preferred for ion beams in FLASH-capable accelerators. However, most state-of-the-art ion accelerators achieve only a fraction of the dose rates expected at LhARA, making direct comparison of existing dosimeters challenging due to the lack of relevant literature. In addition, the greater availability of clinical electron beams has resulted in most performance studies focusing on electron beams rather than ion beams. Fortunately, the underlying principles of most of the

dosimeters are the same for electron or proton beams so that the results of electron-beam studies can be used to assess the performance of the technique when applied to proton or ion beams. Therefore, categorising dosimetry techniques by their operating principles offers an overview of their functionality, advantages and limitations for specific beam types.

6.3.1 Charge collection dosimeters

Charge collection dosimeters are the simplest form of detectors and are often considered as most reliable. They operate by exploiting the ion pairs or charges created during irradiation to create a signal. However, these devices have limited sensitivity, suffer from non-linear responses, and saturation effects when dealing with high instantaneous dose rates. Usually, the detector geometry restricts the measurement of dose to a point (1D) or across a plane (2D).

6.3.1.1 Gas-based detectors: ionisation chambers

Ionisation chambers (IC) are considered the gold standard of dosimetry in radiotherapy. The IAEA TRS-398 code [224] serves as a comprehensive guide, offering recommendations for determining absorbed dose in external beam radiotherapy. Ionisation chambers are commonly used in proton therapy facilities for reference dosimetry in water phantoms. However, the measurement is less precise for proton beams than it is for electron beams.

The ion and electron pairs generated in the gas that defines the detection volume of an ionisation chamber are collected by applying an external electric field across a set of electrodes. The applied voltage is usually high enough to ensure that all charges are collected. However, at a higher dose rate, ion pairs can recombine before being swept across the electric field and collected. This can result in a reduction in ion-collection efficiency, resulting in inaccuracies in dose measurement. Boag's model [225] is used to introduce correction factors to account for the efficiency loss due to recombination at moderate dose per pulse. Some commercial ICs, such as the Advanced Markus IC by PTW, can collect ions effectively at dose rates as high as $\sim 300\,\mathrm{Gy/s}$ and a dose per pulse of around 5 mGy. However, in situations with very high instantaneous dose rates and high dose per pulse commonly used in FLASH radiotherapy, Boag's model becomes less accurate. Figure 6.1 shows the response of an IC under FLASH dose rates.

The time resolution of charge-based dosimeters is constrained by the ion-drift velocity (IC), modalities of different charge carriers (solid state detectors), and fundamental parameters such as transit time and minority-carrier lifetime (solid state detectors). ICs usually show a response time ranging from a few ms to hundreds of ms. Silicon diodes can achieve time resolutions on the order of a few milliseconds [229]. Pure diamond detectors, due to their superior electron and hole modalities, offer extremely good resolution on the order of a few ns [230]. Meanwhile, the resolution of most synthetic diamond detectors is determined by the minority carrier lifetime, which is a few microseconds [231]. Hence, real-time dose monitoring is feasible with diodes, diamonds, and ICs.

Petersson et al. [226] investigated ion-recombination effects in the Advanced Markus Ionisation Chamber for FLASH setups. They were able to measure the dose per pulse by accounting for the ion-recombination effects and noted a strong dependence on dose per pulse above 1 Gy. Patriarca et al. [232] used Boag's model to account for recombination effects for their FLASH measurement using cyclotron-based 230 MeV (IBA) proton beam (100 MHz, 2 ns). Their study indicated that the total recombination of ions was around 1% at a maximum mean dose rate of 80 Gy/s. Jorge et al. [233] showed that, at the high dose rate of 1050 Gy/s, despite correcting for ion-recombination effects, ICs can show deviations up to 15%. Beyreuther et al. [234] used a 224 MeV proton beam at a dose rate of 100 Gy/s and concluded that the pulse duration (100ms) was an order of magnitude higher than the ion-collection time for the Advanced Markus cham-

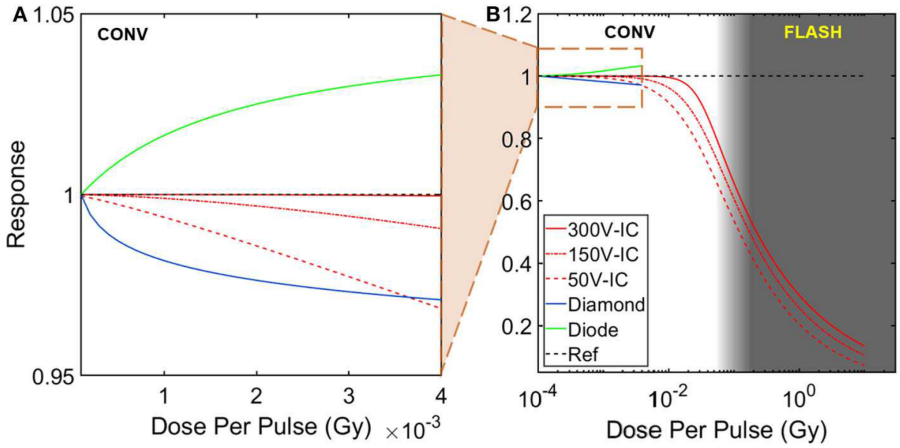

Figure 6.1: Dose per pulse dependency of Advanced Markus Chamber IC, PTW microDiamond, and Isorad Gold diode detectors for conventional (A) and FLASH beams (B). The Advanced Markus Chamber IC is the only charge-based detector tested at FLASH dose rates [226], while the models for the diamond and diode detectors were exclusively tested at conventional dose rates [227, 228].

ber (10 μs). Some studies also attempt to reduce the recombination effects by modifying the IC. For example, the DOSION ionisation chamber [235] has been modified to reduce the recombination below 1% for instantaneous dose rates up to 1 kGy/s. Nonetheless, high pulse repetition frequency in clinical proton beam dosimetry and factors such as volume recombination, along with the limited experimental data in FLASH conditions, particularly for proton beams, pose uncertainties when using ionisation chambers for LhARA-like beams.

6.3.1.2 Solid state detectors

A solid-state detector may be thought of as a solid-state ionisation chamber. This family of detectors consists of semiconductor-based detectors such as silicon diodes, MOSFETs, and diamond detectors. Due to their better sensitivity, solid-state detectors can be made extremely small, offering better spatial resolution compared to gas-filled ionisation chambers. The PTW microDiamond, for instance, achieves a remarkable 1 μm resolution when used in an edge-on configuration. Another high-resolution, charge-based dosimeter is the silicon single-strip detector (SSD), identified as a potential tool for Microbeam Radiation Therapy. The SSD, used at the European Synchrotron Radiation Facility, has very good spatial resolution ($10\mu m$) and a broad dynamic range [236].

The operation principle of an SSD is fundamentally similar to an ionisation chamber, but, instead of forming an ion-electron pair, radiation creates electron-hole pairs. These pairs are caused to drift to the collection electrodes using an electric field. Electron-hole recombination impacts SSD performance: whereas in ICs, direct recombination is the dominant process; recombination in solid state detectors is dominated by indirect recombination due to recombination-generation (RG) centres and impurities that can act as traps [237]. Recombination affects the linearity of the response at high dose rates.

Examples of SSDs include:

Silicon Diodes were first implemented for dosimetry in the 1980s [238] and have since been used routinely for *in vivo* dosimetry. They offer a good spatial resolution due to the high radiation sensitivity relative to the ionisation volume. High spatial resolution with relatively fast response time (microseconds) makes them ideal for *in vivo* dosimetry. Moreover, they can be configured to operate in real-time mode, making them one of the best

candidates for real-time *in vivo* dose measurement for individual pulses such as that of a linear accelerator [239]. Diodes are positioned on the skin of a patient during radiation treatment. They are encapsulated in a material which is usually metallic (e.g. stainless steel).

While ionisation chambers (ICs) experience reduced sensitivity with rising dose per pulse, diodes tend to over-respond at higher dose per pulse [240, 241]. This phenomenon is linked to the process of recombination. RG centres are formed between the valence and conduction bands and are able to capture minority charge carriers, allowing them to recombine with majority charge carriers. At high dose per pulse, the RG centres become saturated with minority charge carriers. Consequently, as shown in figure 6.1, a greater proportion of charges remain unrecaptured, enhancing the overall sensitivity of diodes at elevated dose rates and high dose per pulse. These effects also result in a non-linear dose response.

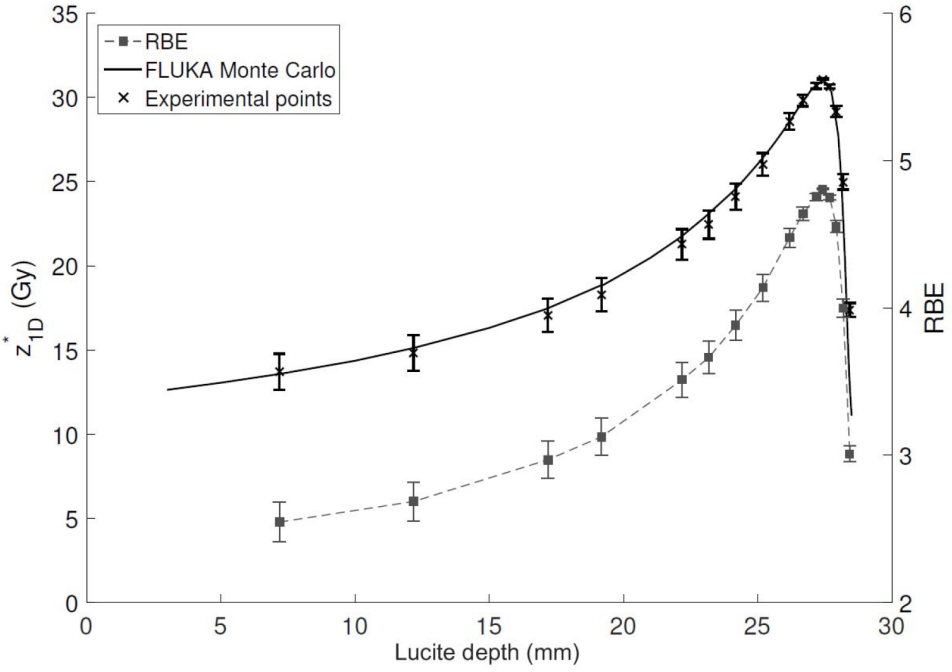

Figure 6.2: Performance of silicon micro-dosimeter near the Bragg Peak region for 115 MeV/u Carbon beam (CNAO Italy) [242]. Relative Biological Effectiveness (RBE) is also shown.

Recently, advanced 3D manufacturing technology, originally created for particle physics experiments at CERN, has allowed silicon micro-dosimeters to be created [243]. These detectors, with micro-machined electrodes, result in faster and more precise silicon micro-dosimeters for ion therapy compared to planar diodes. Prieto-Pena et al. [242] have demonstrated the performance of micro-dosimeters using a 115.23 MeV/u carbon-ion beam (CNAO, Italy) of Gaussian field size 5.1×8.5 mm at a fluence of 5×10^7 $s^{-1}cm^{-2}$, in a water phantom. The authors reported a good agreement of measured dose with Monte Carlo simulations as shown in figure 6.2. Silicon micro-dosimeters promise to improve ultra-high pulse dose rate (UHPDR) dosimetry by reducing recombination effects. Additional factors that must be considered include:

- *Temperature dependence*: A diode will generate dark current even in the absence of radiation due to thermally generated charge carriers. This results in background signals that have to be accounted for. The background signal is strongly temperature-

dependent and increases if the temperature rises during irradiation. Although an offset can be applied before starting a measurement, any changes in the temperature during the measurement will change the diode response.

- *Radiation damage* occurs in the form of displacement of atoms. A displaced atom will act as a recombination centre to capture charge carriers, resulting in a reduction in sensitivity. The rate at which radiation damage occurs depends on the radiation type. For example, damage due to 20 MeV electrons is 20 times faster than damage due to 8 MeV photons [244].
- *Geometrical factor*: the shape and construction of the sensitive surface of the diodes result in the dose becoming a function of the geometry of the system. The dose rate will vary with the angle at which the radiation impinges on the sensitive surface. Certain diode geometries (e.g. dome shaped diodes) reduce the angular dependence, but the dose rate can still vary if the irradiation angle is $> 30°$ from the perpendicular to the diode base plate. The material in which the diode is housed also reduces the sensitivity of the diode for low-energy scattered dose, which forms a substantial part of the dose received in certain radiotherapy treatments like total body irradiation.
- *Calibration* diodes (*in vivo* dosimeters for the most part) are calibrated with the ionisation chamber at the reference depth used for calibration of the beam. A set of correction factors must also to be employed for measurements carried out at different temperatures and beam energy. The correction factors will usually be similar for the same diode type.

The advantages and limitations of diode dosimeters may be summarised as follows:

- *Advantages*: diodes offer a simple and cost-effective way to measure the dose in *in vivo* dosimetry. They offer high sensitivity, real-time readout with relatively simple instrumentation, a degree of robustness and a measurement independent of air pressure.
- *Limitations*: correction factors are required for the dependence of the signal on dose rate, irradiation angle and energy. The varying response with temperature and the spectral range of radiation affects the accuracy of the dose received. Change in sensitivity post-irradiation limits the multi-use applicability of diode dosimeters.

MOSFETs were introduced as dosimeters in radiation therapy in the early 1990s [245]. MOSFETs are very effective in high dose-gradient radiation fields due to their small size and, like diodes, provide good spatial resolution, which is particularly important in IMRT, radiosurgery, and brachytherapy. MOSFETs offer real-time readout with simple instrumentation and ruggedness. Furthermore, dual MOSFET, dual voltage dosimeters are less temperature sensitive, which is advantageous in clinical dosimetry. MOSFETs also enable persistent dose storage due to reduced signal fading over time [246].

A MOSFET has three terminals: the source, the drain and the gate. The source and gate terminals are connected to a p-type substrate built on an n-type base. The gate terminal is connected in-between the source and the drain through a thin SiO_2 layer, which sits on the n-type base. When the gate is biased negatively with respect to the base, the SiO_2 attracts holes, which makes the region near it conductive. A small current, I_{ds}, flows between the source and drain when the bias is increased beyond a threshold voltage, V_{TH}. When the MOSFET is exposed to ionising radiation, the holes are pushed towards the SiO_2 layer and are trapped. Thus, a larger voltage, ΔV_{TH}, is required to generate the same current. The resulting ΔV_{TH} is thus proportional to the absorbed dose as shown in figure 6.3. However, the similarity of the operating principle with that of diodes means that a MOSFET also suffers a non-linearity of response due to recombination effects.

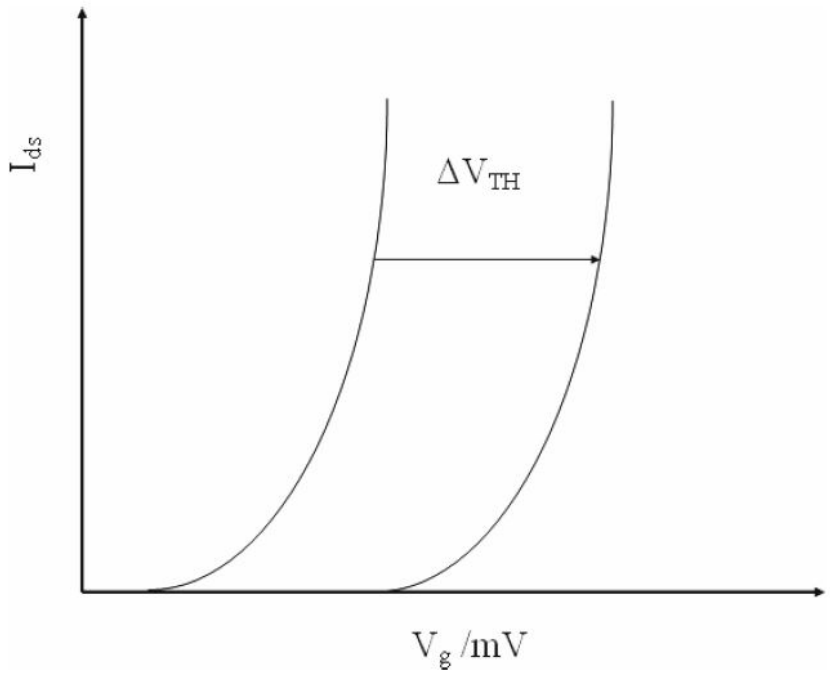

Figure 6.3: Plot of the current-voltage characteristic of a MOSFET. The voltage shift ΔV_{TH} that develops on exposure to radiation is indicated [239].

The relationship between V_{TH} and I_{ds} can be affected by temperature by as much as 4 to 5 mV per °C [247] and great care needs to be taken for MOSFETs to be used *in vivo*. Dual MOSFET, dual voltage dosimeters have been demonstrated to reduce temperature dependencies to about 0.015 mV/°C in the range 0 to 80°C [248].

MOSFETs have a limited lifespan due to an increase in trapped charge in the oxide layer. Depending on the thickness of the oxide layer, the MOSFET saturates after a certain amount of dose. As in the case of a silicon diode, the dose received in MOSFETs is also affected by their orientation with respect to the beamline and also has a response that depends on energy. MOSFETs have been shown to have a linear response with dose rate below 600 MU/min [249].

The advantages and limitations of MOSFET dosimeters may be summarised as follows:

- *Advantages*: Excellent spatial resolution with minimum attenuation due to small size; can be used to monitor the dose rate.
- *Limitations*: Variation of response with energy and incident angle. Response is affected by temperature. Response also changes with accumulated dose, yielding lower accuracy and precision, and a limited lifetime.

Diamond Detectors are gaining popularity for FLASH dose measurement. They are reported to show increased or decreased sensitivity with increasing dose per pulse, depending on their construction, i.e. pure crystals, chemical vapour deposition (CVD), or high-pressure, high-temperature HPHT fabrication [250]. Ade et al. [250] investigated the dose-rate dependence of synthetic diamond detectors in electron beams and evaluated the linearity index for its dependence on electron energy. They found the fitting parameter for some diamond detectors to decrease by as much as 9% when the dose-rate was increased from 2.25 to 3.07 Gy/min. Di Venanzio et al. [251] used a commercial synthetic microDiamond detector type 60019 (PTW Freiburg) in high dose-per-pulse (26–105 mGy per pulse) 6–9 MeV

electron beams produced by an Intra Operative Radiation Therapy (IORT) dedicated accelerator. They observed that the microDiamond response exhibited good linearity in the dose range of 0.2 Gy to 28 Gy with detection sensitivity of 1.29 nC/Gy, showing less than a 1% difference compared to the reference measurement using a Cobalt 60 gamma source. Profile measurements revealed a high spatial resolution, slightly less than that of the silicon diode. Patriarca et al. [232] used the same microDiamond dosimeter for a proof-of-concept study for FLASH irradiation using a proton beam at a dose-per-pulse of a few mGy. The device under responded at higher dose rates.

6.3.1.3 Direct current measurement: Faraday cup

A Faraday cup is a conductive metal cup which accumulates charge when put in the beam's path. It is one of the most common detectors used to measure the beam flux accurately. In pre-clinical FLASH studies, the Faraday cup has been used by multiple authors [252, 253]. The main advantage of Faraday cups is that their response is independent of the effects of saturation, ion collection, and charge-carrier recombination. However, Faraday cups measure the integrated charge instead of the dose and have poor spatial resolution; as a result, they are relatively uncommon in radiotherapy.

6.3.2 Chemical Dosimeters

Chemical dosimeters belong to a group of detectors which have a chemical (sensitive medium) that undergoes structural changes, produces radicals, or changes colour upon irradiation. By layering the sensitive medium in planes, chemical dosimeters can be used to generate 2D or 3D dose distributions. Planar dosimeters also allow for simultaneous measurement of dose profiles, not requiring scanning techniques as in charge-based detectors. Moreover, the structural change during irradiation can also be exploited to provide a permanent record of the dose.

6.3.2.1 Frikie/Alanine dosimeter

The Frikie dosimeter consists of ferrous sulphate as a sensitive medium. Upon irradiation, the ferrous (Fe^{2+}) ions oxidise to ferric ions (Fe^{3+}), which changes the optical density of the active medium. The change in optical density can be read using an external light source. With appropriate calibration, the change in optical density can be used to determine the absolute dose. Studies conducted using these dosimeters have reported instability of radiation-induced species at high dose rate [254, 255], making such detectors less reliable for dose measurement of nanosecond-scale pulses such as those that will be delivered by LhARA.

Alanine dosimeters use alanine, an amino acid, as an active medium. Upon irradiation, alanine forms a stable free radical, the concentration of which is proportional to the dose received. The absorbed dose can be probed using an electron paramagnetic resonance (EPR) spectrometer. Alanine dosimeters exhibit a linear response over a large dynamic range (2 Gy–150 kGy) and are therefore extensively used in pre-clinical FLASH studies [256]. With appropriate setup-dependent corrections, alanine detectors have been shown to produce an accuracy of up to 3% at dose rates of 0.078 Gy/s to 1050 Gy/s [233]. They have excellent dose-rate independence up to 3×10^{10} Gy/s using electron beams [257]. A study conducted at the European Synchrotron Radiation Facility (ESRF) for ultra-high dose rate of (10 kGy/s) using an X-ray source identified alanine as an appropriate dosimeter for X-ray sources [258]. These observations make an alanine dosimeter promising for the high dose rates expected at LhARA.

6.3.2.2 Radiochromic/Radiographic film

Radiochromic films (RCF) are polymeric films that darken during irradiation due to the polymerisation of their active medium. The degree of darkening is quantified by changes in optical density (OD), impacting the transmission of light through the film. The OD change is proportional to the dose received and is measured by analysing the absorption spectrum of transmitted light during readout [259]. Different polymers in the film exhibit varying absorption spectra, leading to colour changes. Stacking multiple films along the depth provides a 3D dose distribution, with each film offering a 2D dose distribution at a particular depth. The response of radiochromic films is independent of energy [260], has high spatial resolution (sub-micron), limited only by the digitising method. The density of the RCF itself is similar to that of tissue. RCF allows for energy-resolved measurements, a technique known as radiochromic film imaging spectroscopy.

Studies by Karsh et al. [261] demonstrated the dose-rate independence of EBT radiochromic film up to 15×10^9 Gy/s using a 20 MeV electron beam with a pulse length of 5 ps. Jaccard et al. [262], in their FLASH dose rate studies using the Oriatron eRT6 electron linear accelerator, concluded that the film remained independent of dose rate up to rates of 8×10^6 Gy/s.

Additional studies focus on quantifying the energy dependence of films for ion beams. Piermattei et al. [263] measured a dose-correction factor for MD-55 for proton beams, accounting for a 5–20% under-response in the Bragg Peak. Daftari et al. [264] conducted further studies on clinical proton beams of 67.3 MeV. Kojima et al. [265] observed significant under-response of MD-1260 for various ion species with increasing linear energy transfer (LET) for 3–45 MeV/u ion beams. Martisikova and Jakel [266] reported a 25–35% under-response for EBT films irradiated by a carbon beam of 100-400 MeV/u, with no under-response for protons down to 50 MeV. Kirby et al. [267] using a cyclotron-produced proton beam demonstrated a consistent flat energy response for EBT and MD-55 films for proton beam energy of 5 MeV and 8-10 MeV respectively, which drops up to 60% for beam energies below that.

Despite the benefits, radiochromic films have major drawbacks, as their measurement is typically offline. While real-time film readout within milliseconds is possible and attempts have been made to read out radiochromic films in real time [268, 269], post-exposure polymerisation complicates real-time dosimetry and is not fully understood.

6.3.2.3 Polymer gels

Polymer gel dosimeters are fabricated from radiation-sensitive chemicals which polymerise as a function of the absorbed radiation dose. Gel dosimeters can be made as a volumetric structure allowing the radiation dose distribution to be recorded in three dimensions with extremely fine resolution [270]. The readout process is similar to that of radiochromic films, but instead of 2D scanning, the readout has to be performed in 3D. As for all chemical dosimeters, diffusion of irradiated species can occur post-irradiation at a high dose gradient, which can affect the measurement. In addition, the complicated readout machinery makes this technique impractical for real-time dose monitoring.

6.3.3 Passive (stimulated) luminescent dosimeters

In general, passive dosimeters enable dose recording for later retrieval during a read-out stage. Passive luminescent dosimeters reveal dose information through the emission of photons during read-out, with the number of photons emitted being proportional to the received dose during irradiation.

Passive luminescent dosimeters work on the principle that introducing impurities into certain crystals creates additional energy levels in the gap between valence and conduction bands, known as meta-stable states. These extra energy levels allow electrons to be trapped during

irradiation. The trapped electrons can be stimulated to escape through the application of sufficient energy, leading to the recombination process and luminescence. Using readout devices such as photomultiplier tubes, the emitted light can be quantified as a measure of the absorbed dose. These dosimeters can be categorised based on the external stimulus applied during readout. Examples include thermoluminescent dosimeters (TLD), optically stimulated luminescent dosimeters (OSLD), or radio-photo luminescence dosimeters. In the absence of the external stimulus, the electrons can remain trapped for long durations. Hence, these dosimeters can only be employed to capture the historical dose delivered during irradiation. Despite this, dosimeters like TLDs and OSLDs have shown excellent dose-rate independence, making them suitable for high dose rate measurements.

6.3.3.1 Thermoluminescent dosimeter

In thermoluminescent dosimeters, the external stimulus is provided by heat. TLDs are widely used and serve as a standard for dose monitoring in any radioactive environment [271]. This is primarily because they are rugged, reusable, offer a linear response to the dose absorbed and offer a record of the dosage received. The reading process partially returns the dosimeter to its previous state, and, with further heating to a high temperature, any remnant metastable electrons can be removed. This heating process, known as annealing, permits the dosimeters to be reused practically indefinitely. Dosimeters are typically bundled together in batches for annealing and calibration. The most commonly used material for TLDs used in radiotherapy is lithium fluoride doped with traces of magnesium and titanium (LiF:Mg,Ti). A new material, lithium fluoride doped with 2% phosphor and traces of magnesium and copper (LiF:Mg,Cu,P)[272], is stated to be more sensitive than LiF:Mg,Ti and has a lower sensitivity and a response that is dependent on energy.

Karzmark [273] tested a LiF TLD over the range 5×10^4 Gy/s to 2×10^{10} Gy/sec and found dose-rate independence up to 2×10^6 Gy/s while Tochilin and Goldstein [274] found the same dosimeter to be dose-rate independent up to 1.7×10^8 Gy/s for X-rays. Karsch et al. [261] studied the response of TLDs and OSLDs using a 20 MeV, pulsed (5 ps), electron beam from a clinical linear electron accelerator, ELBE (the Electron Linac of high Brilliance and low Emittance), at the Helmholtz-Zentrum Dresden-Rossendorf (HZDR). They found both to be dose-rate independent up to 4×10^9 Gy/s within 2%. Jorge et al. [233] compared the LiF-100 TLD (Thermo Fisher, USA) against two dose-rate independent dosimeters, alanine and radiochromic film for FLASH dose using an electron beam from the Oriatron eRT6 linear accelerator (PMB-Alcen, France). The measurement showed that, with setup-dependent corrections, the dose agreement among the three detectors was within 3% for dose rates between 0.078 Gy/s and 1050 Gy/s. In the absence of corrections, dose deviations up to 15% are observed.

The TLD response (also known as the glow curve), measured using a photomultiplier tube, is shown in figure 6.4; the area under the glow curve is proportional to dose. The signal proportionality to dose is maintained up to 1 Gy for LiF:Mg,Ti and 10 Gy for LiF:Mg,Cu,P. TLDs also suffer from a decrease in the thermoluminescence signal between irradiation and readout, known as fading. In the absence of radiation, TLD materials naturally emit a small luminescence background signal, which may be related to chemical reactions on the surface of the dosimeters (called chemiluminescence).

The advantages and limitations of TLDs may be summarised as follows:

- *Advantages*: Multiple use, linear response up to 8 Gy (based on photon and electron beam data [275]).

- *Limitations*: Decrease in the signal due to spontaneous emission of light at room temperature (fading), careful calibration is required, and it can be costly.

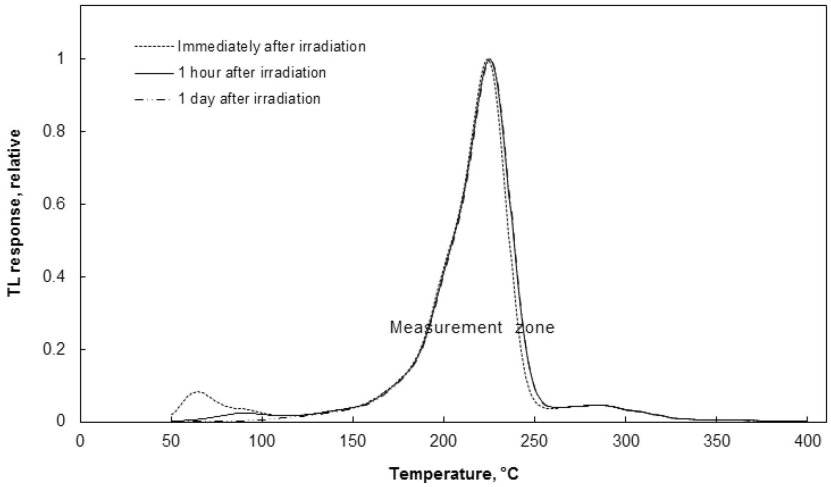

Figure 6.4: TLD 100 glow curve immediately after the irradiation (dots), one hour post-irradiation (solid line) and a day after the irradiation (dash-dot line) [239]. The TL response is presented relative to the peak response as a function of temperature.

6.3.3.2 Optically stimulated luminescence dosimeter

The operation of the optically stimulated luminescence dosimeter (OSLD) is based on two basic processes. Electron-hole pairs created by ionising radiation are trapped in crystal defects. Optical stimulation is used during readout to release the trapped pairs, resulting in electron-hole recombination and luminescence. The luminescence light recorded is proportional to the initial concentration of trapped charges, which, in turn, is proportional to the absorbed dose. OSLDs have been used routinely as passive personal dosimeters for almost a decade, following the successful introduction and development of carbon-doped aluminium oxide (Al_2O_3:C) [276]. Recent articles have started to explore the potential advantages of OSLDs for medical dosimetry [277]. However, best practices are not yet established.

The elements of an OSLD reader are shown schematically in figure 6.5. The reader is composed of a light source for stimulation and a photomultiplier tube (PMT) for light detection. To achieve optimal discrimination between luminescence and stimulation light, the stimulation wavelength must be adjusted in relation to the dosimeter's main luminescence band. Although the simulated light is typically filtered, some photons from the source may still seep into the PMT and impact the dose measurement. A typical Optical Stimulated Light (OSL) response is shown in figure 6.5.

The concept of operation of OSLDs is similar to that of TLDs, except the readout in OSLDs is carried out by simply illuminating the dosimeters. As a result, OSLDs and TLDs share similar characteristics. They are passive dosimeters, require no power or cable, can be made very small for higher spatial resolution, are not affected by electromagnetic interference or air pressure effects, and can be used to measure a wide range of doses. The difference between TLDs and OSLDs is that optical bleaching cannot remove deeper traps in OSLDs, which results in enhanced background signal, thus reducing the sensitivity for doses greater than 10–20 Gy [278].

6.3.3.3 Radio-photo-luminescence glass dosimeters

Radio-photo-luminescence (RPL) glass dosimeters are passive solid-state radiation detectors that were used as personal dosimeters in the 1950s and 1960s and more recently for measurements in beams used for radiation therapy [279, 280]. RPL glass dosimeters are made of silver-activated phosphate glass and generate stable luminescence centres when subjected to ionising radiation. The luminescence centres are read out using a pulsed ultraviolet laser. The

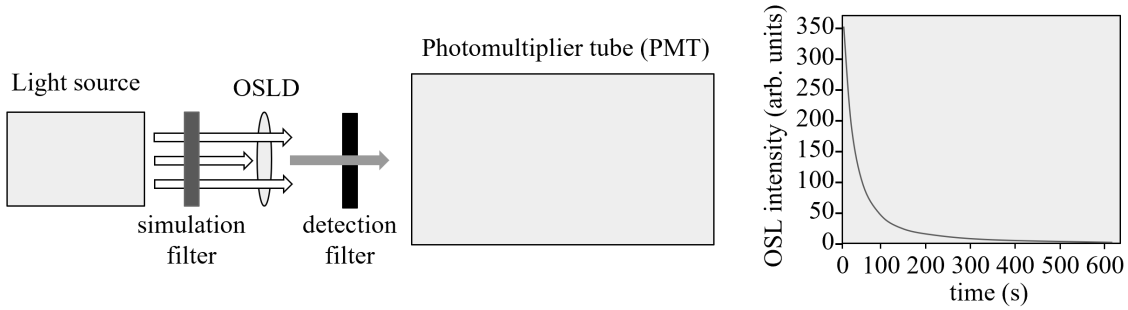

Figure 6.5: Schematic of an OSLD reader (left) and the typical OSLD response (right), adapted from [239].

UV laser stimulates the centres, resulting in orange photoluminescence that may be detected using a photo-detection device. The amount of light emitted is determined by the radiation dose absorbed by the detector.

Stimulation using the UV source does not remove the RPL centres within the detector, allowing for multiple readings. The RPL centres are removed after one hour of annealing at 400°C [281]. RPL dosimeters are millimetre-shaped rods with very low fading properties. The response is independent of temperature and nearly independent of energy for photons with energy greater than 0.2–0.3 MeV.

6.3.4 Active (stimulated) luminescent dosimeters

Active luminescent-based dosimeters belong to the category of detectors that emit photons upon irradiation without external stimulation. The emission of photons occurs almost instantaneously, resulting in the possibility of using the detectors for online monitoring of the dose received. The primary detectors of this type are scintillators and Cherenkov detectors. While the mechanism by which photons are generated is different, both detector types share the property of almost instantaneous photo emission after irradiation.

6.3.4.1 Scintillation detectors

In scintillator detectors, the interaction of certain materials (scintillators) with high-energy photons or charged particles leads to the emission of photons. Scintillating materials can be either organic or inorganic [282, 283], but the scintillation process generally involves three steps: conversion, migration, and luminescence. During scintillation, charged particles excite electrons, causing them to move to a higher energy state within the material. Following this, the electrons migrate to a lower energy state, undergoing radiative de-excitation and returning to their original state. The radiative de-excitation results in luminescence. The mechanism of scintillation is illustrated in figure 6.6 for both organic and inorganic materials.

Organic scintillators are composed of aromatic hydrocarbon compounds. The electrons of the hydrocarbon form energy bands in which the electrons undergo excitations during irradiation. After migration to the appropriate state, radiative de-excitation occurs through electron transitions from the excited singlet state to various vibrational sub-levels of the ground singlet state in a decay timescale of a few nanoseconds. This rapid response enables almost instantaneous emission of photons after irradiation, allowing for real-time dose measurement. Organic scintillators also exhibit excellent tissue equivalence. The simplicity allows for detectors to

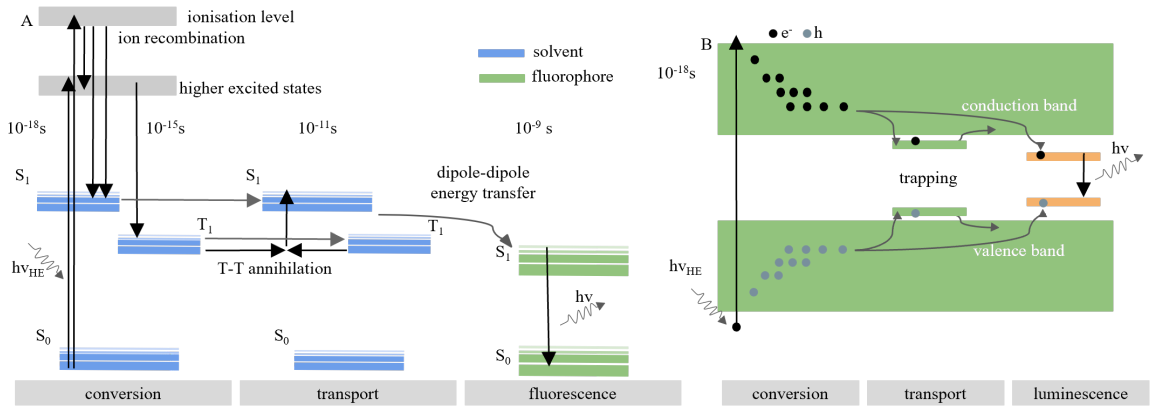

Figure 6.6: Scintillation process in organic (A) and inorganic (B) detectors, adapted from [284].

be miniaturised and the dosimetry of small field beams [285–287]. The commercial detector Exradin W1 (Standard Imaging) serves as a reference for deriving correction factors for other detectors [287].

Plastic scintillation detectors (PSDs) show promise for *in vivo* dosimetry, offering characteristics such as water-equivalent dose detection, energy independence, dose linearity, resistance to radiation damage, and infrequent calibration [288]. Though previously less commercially available, these detectors are now gaining popularity for clinical applications in external beam radiotherapy [281]. A PSD consists of organic scintillating molecules in a polymerised solvent that emits light in proportion to the ionising radiation dose delivered to it. The light is transmitted to a photo-detector using optical fibres. The use of plastic optical fibre as optical guides makes it completely water-equivalent [289].

Inorganic scintillators typically consist of single or poly-crystalline materials doped with impurities acting as luminescent centres. These scintillators, made from high-Z materials, are not tissue-equivalent. However, real-time monitoring and the ability to provide complete 2D dose profiles make scintillators an ideal beam-profile monitoring device. Studies have also demonstrated complete 3D dose distribution measurement using a 3D liquid scintillator detector system for the verification and characterisation of proton beams in real time for intensity and energy-modulated proton therapy [290].

Ashraf et al. [291] employed a time-integrated CMOS camera to measure the spatio-temporal dose distributions in complex stereotactic radiosurgery (SRS) at dose rates up to 200 Gy/s near the Bragg Peak in a radio luminescent phantom. Vigdor et al. [292] used a combination of a xenon gas scintillator and a photomultiplier tube readout to monitor 2D profiles of pulsed and pencil-beam-scanning proton radiotherapy treatments up to a dose rate of 350 Gy/s. In the context of FLASH dose, Favaudon et al. [255] used a 2D scintillating array to monitor beam profiles of electron beams with an overall precision better than $\pm$ 2%, at dose rates from 2×10^2 to 4×10^7 Gy/s with dose per pulse (1 micro second) ranging from 1 mGy to 30 Gy. The detector exhibited excellent dose linearity with increasing dose.

6.3.4.2 Electronic portal imaging device

In *in vivo* dosimetry, an electronic portal imaging device (EPID) is a two-dimensional, image-based instrument [293]. It provides a direct relationship between the measured dose values, the beam profile and the tissue geometry. It is particularly useful for dynamic treatment delivery techniques such as intensity modulated radiation therapy (IMRT). Since this method uses an imaging system, information on the dose distribution relative to the patient's anatomy and the

beam axis is obtained. EPID in *in vivo* dosimetry and patient set-up verification complement each other in the verification of correct treatment execution. The current interest in EPID based on *in vivo* dosimetry is mainly for research. This is due to the fact that developmental work is still ongoing in academic centres [281], and adequate software is not yet commonly available.

6.3.5 Novel approaches

The earlier sections provided insights into various detectors used in dosimetry, highlighting their operational principles, strengths, and limitations in the context of LhARA beam parameters. It becomes evident that most detectors suffer from limitations and so do not qualify as a universal calibration standard for LhARA and motivating the development of the ion-acoustic dose profile measurement technique (see chapter 5). This section summarises novel approaches being developed to address the gap in appropriate dosimetry techniques.

6.3.5.1 Calorimeters

Graphite calorimeters have been established as primary standards for dosimetry in photon [294] and electron [295] beams, with attempts to establish them as reference standards for ion beams as well [296]. The presence of well-established ionisation chambers, serving as gold standards in conventional dosimetry, provided little incentive to explore calorimeters further. With the emergence of high dose rates in the FLASH modality and the recombination limitations associated with ionisation chambers, calorimeters are now considered promising candidates for reference. To conform to the calibration standards based on IAEA TRS-398 [224], the uncertainty in dose measurement in proton beams must be below 2% at 95% confidence level. However, there is limited literature exploring the use of graphite calorimeters for ultra-high dose rate proton beams.

In general, a calorimeter is a device used to measure the energy generated or absorbed during a process. In the context of radiation dosimetry, a graphite calorimeter is used to measure the energy deposited by ionising radiation in a sensitive region (matrix). Graphite is selected as a matrix material because of its low heat capacity and good radiation absorption characteristics. By precise measurement of the temperature increase caused by the energy deposited in the graphite matrix, the radiation dose can be determined.

Palmans et al. [297] conducted a study using a small-body portable graphite calorimeter (SPGC, figure 6.7) developed by the National Physical Laboratory (NPL) on a 62 MeV clinical proton beam at The Clatterbridge Cancer Centre, Wirral, UK. Measurements were carried out for 3747 runs at a dose rate of 15 Gy/min (0.25 Gy/s) with a quasi-continuous beam having a square profile of 3 cm and a uniform dose profile. The dose measured with the SPGC was compared with a cylindrical IC (NE2561) and two plane-parallel ICs (NACP02 SN 6306 and PTW Markus SN 2225) calibrated in terms of absorbed dose to water in a Co-60 beam at NPL.

The study revealed that the relative dose ratio ($D_{W,SPGC}/D_{W,IC}$) varied between 0.983 and 1.019, with standard uncertainties ranging from 1.9% to 2.5%. The authors suggested that the uncertainty in SPGC mainly comes from specific values related to proton stopping power ratios, with a standard uncertainty of 1% (identified from IAEA TRS-398 code), while the ICs have uncertainties of 0.75% for calibrations related to cobalt-60 and electron beams.

Renaud et al. developed a graphite probe calorimeter (GPC) [298], known as the Aerrow detector (see figure 6.8) for clinical application in radiotherapy. The calorimeter demonstrated feasibility for absolute dosimetry in high-energy electron and photon beams. The authors demonstrated [299] the performance of the detector for dose measurements in a water-equivalent solid phantom exposed to high-energy photon (63.5–76.3 MV) and electron (2.3 cm to 8.3 cm) beams. With 72 measurements conducted using the GPC, the standard error on the mean absorbed dose was found to be better than 0.3%, and peak-to-peak variations in the relative response

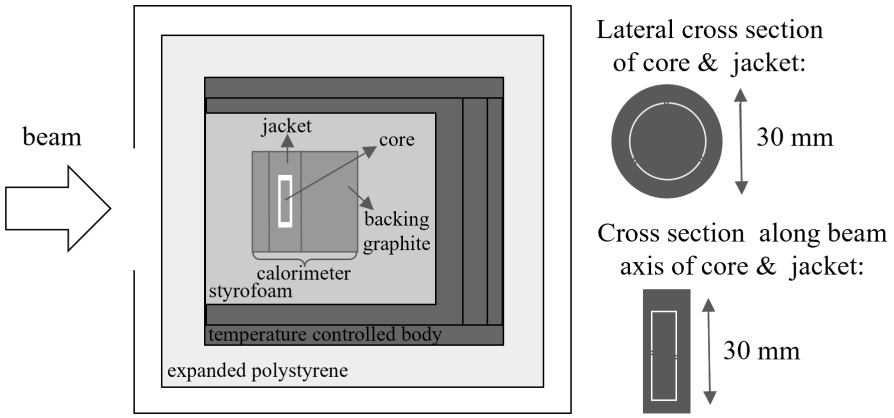

Figure 6.7: Schematics of the small-body portable graphite calorimeter used to measure the dose profile of 62 MeV proton beam at CCO, adapted from [297].

of the GPC were within 1%. The authors concluded that the Aerrow detector, with its energy independence, dose linearity, and dose rate independence, has the potential to serve as an independent absolute dosimeter for both photon and electron beams.

In a subsequent study [300], the authors used the GPC in two distinct modes: quasi-adiabatic and isothermal, and compared dose measurements in a 6 MV photon beam to a calibrated reference ionisation chamber. The average doses measured using the Aerrow were 75.6 ± 0.7 cGy/MU for the quasi-adiabatic mode and 74.7 ± 0.7 cGy/MU for the isothermal mode. In comparison, the dose measured by the ionisation chamber was 76.3 ± 0.7 cGy/MU. The Aerrow detector exhibited dose linearity (characterised by an R^2 value) of 0.9998 in the dose range of 80 cGy to 470 cGy, with dose rate independence observed in the range of 0.5 Gy/min to 5.4 Gy/min. The European Joint Research Project UHDpulse project [301] has recognised Aerrow as a potential redundant dosimeter, offering independent verification of clinical reference doses for nonstandard reference fields.

Recently, Lourenco et al. [302] conducted measurements using the NPL Primary Standard Proton Calorimeter (PSPC) on a pencil proton beam at the CCHMC beamline. This beamline

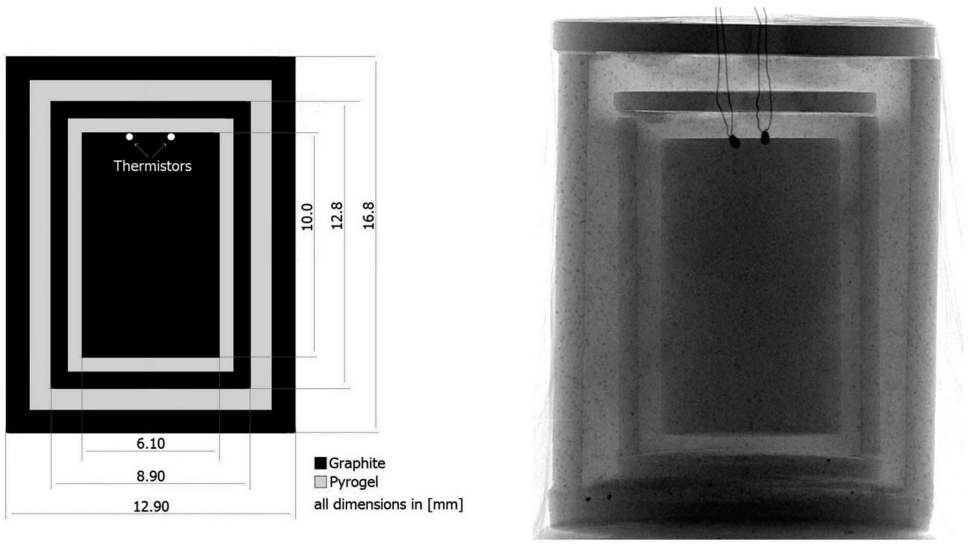

Figure 6.8: Schematic (left) and photograph (right) of the graphite probe calorimeter (also named as Aerrow) for dose measurement at high dose rate [298].

is equipped with a 250 MeV proton cyclotron (ProBeam, USA) upgraded to deliver FLASH [303] irradiation for potential applications in Ultra High Dose Radiotherapy (UHDR). The dose measured by the calorimeter was compared to a set of widely used ionisation chambers (PTW Roos, PTW advance Markus, and IBA PPC05) in terms of absolute measurement accuracy.

The NPL PSPC is a graphite calorimeter with a disk-shaped core with a double layer of graphite jackets and mantle as shown in figure 6.9. Measurements are made in a quasi-adiabatic mode of operation, where the jackets are used to shield the core from ambient temperature effects to deliver temperature measurement accuracy of about 0.1 mK. A set of thermistors are used in the core and the jacket to control the temperature as well as to measure it. The mantle is used to house the printed circuit board (PCB), providing electrical connections and as a support structure. It is expected that the NPL PSPC is dose rate independent.

Measurements were carried out at a water-equivalent depth of 5.2 g/cm^2 by placing graphite build-up plates in front of the measurement equipment. Figure 6.9 shows the accuracy of the calorimeter relative to the ionisation chambers in terms of the ratio of dose measured by the calorimeter to the dose measured by three specific ionisation chambers. Comparisons are reported for six rectangular vertical scanning fields of 5×6, 5×8, 5×10, 5×12, 6×5 and 12×5 cm^2. Monte Carlo simulations using TOPAS [304, 305] and FLUKA [306] codes were used for accurate modelling of beam parameters. Beam parameters in the simulation are benchmarked using a large-area ionisation chamber (IBA StingRay), shown in figure 6.10. The calorimeter was demonstrated to measure the dose rate with overall uncertainty of 0.9% (1σ), in line with the recommendations for reference dosimetry for effective radiotherapy treatments.

6.3.5.2 Cherenkov radiation detectors

Cherenkov radiation is emitted when a charged particle moves faster than light through a material, emitting visible light. Asymmetric polarisation along the particle's path causes relaxation to release energy, creating constructive interference seen as Cherenkov radiation. Its immediate light emission and dose linearity make it excellent for real-time dose monitoring. However, Cherenkov emission has an energy threshold for emission of photons depending on the optical refractive index of the medium [307]. For an electron beam in water (n=1.33), the energy threshold is 264 keV, while in tissue, assuming a refractive index of 1.4, the energy threshold is 219 keV. At energies above the threshold, Cherenkov detectors show an energy dependence as illustrated in the figure 6.11.

Favaudon et al. [255] demonstrated online dose monitoring in FLASH electron beams of pulse width 0.1–2.2 μs at energies of 3.9 and 5.0 MeV. The authors reported a steady increase in the Cherenkov emission with beam energy, pulse duration and dose. Cherenkov radiation has been imaged in real time [308, 309] during multiple clinical radiotherapy treatments.

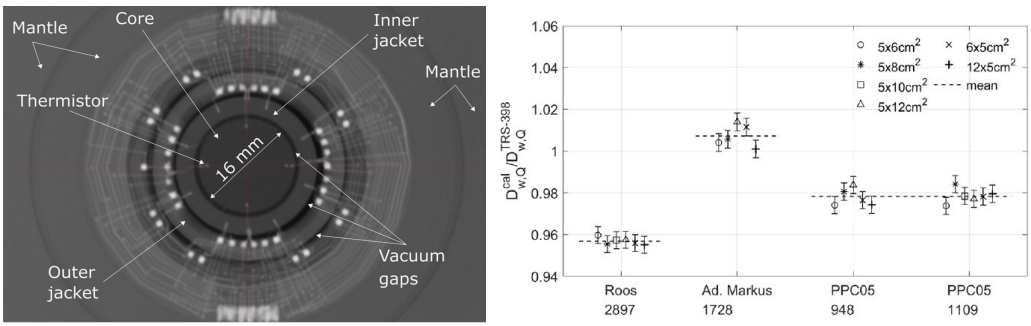

Figure 6.9: On the left panel: NPL PSPC dosimeter. Right panel: Ratio between the dose determined by the NPL PSPC and the dose derived from ionisation chambers for the various fields tested [302].

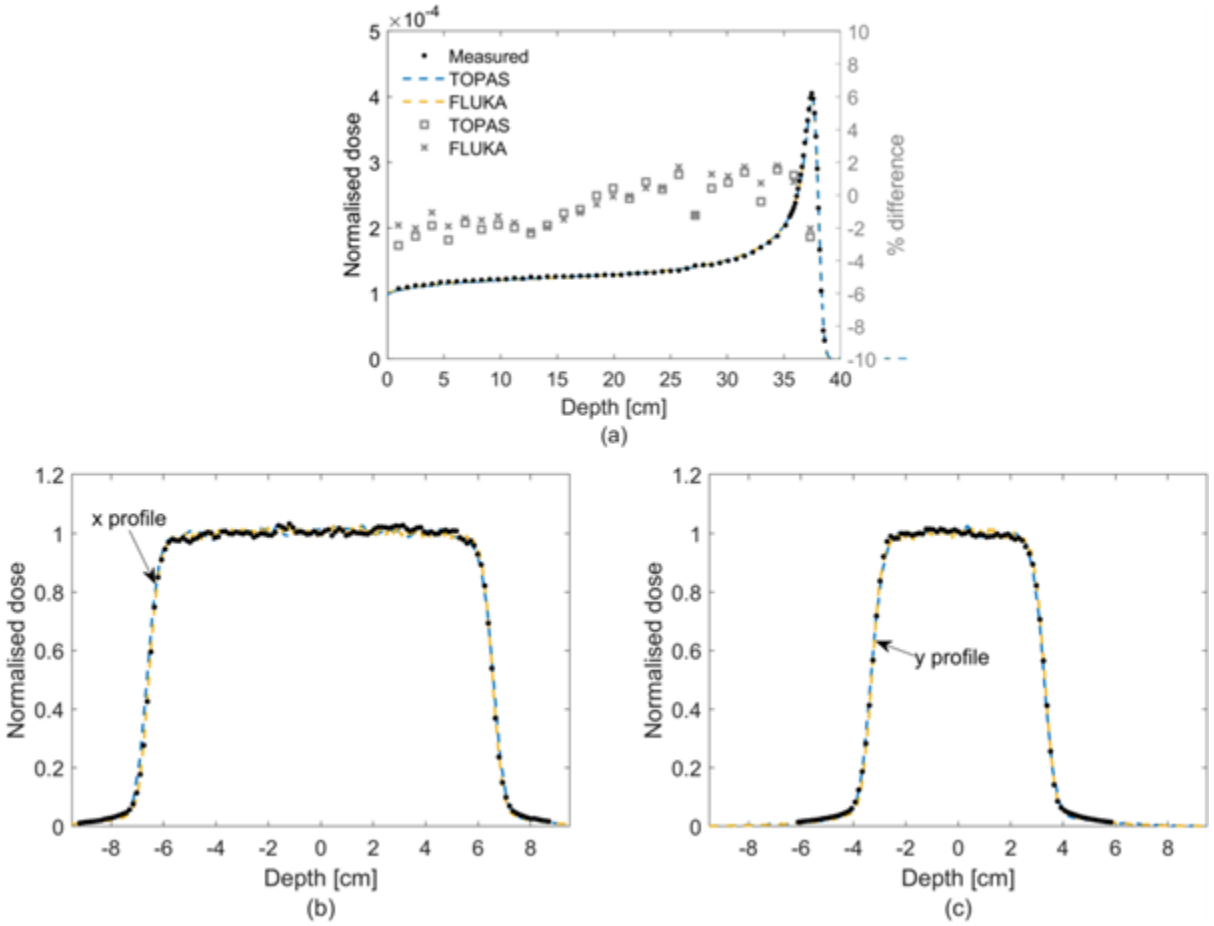

Figure 6.10: Measured and simulated dose distributions for the field $12 \times 5\,\mathrm{cm}^2$. Solid circles represent the measured data, dashed curves represent the simulated data, and open squares and crosses represent the percentage difference between simulated and measured data using TOPAS and FLUKA, respectively [302].

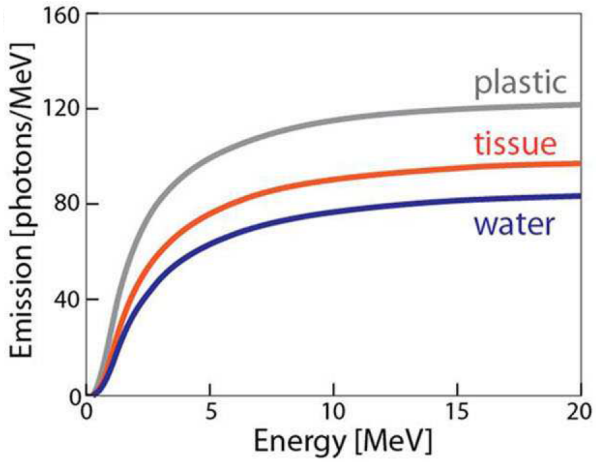

Figure 6.11: Cherenkov emission from electrons generated by incident X-ray photons within a 1 cubic meter volume in different media, with emission per particle normalised to the incident photon energy [308].

Axelsson et al. [310] demonstrated the possibility of monitoring Cherenkov-induced molecular fluorescence to measure the dose profile and dose distribution. They used fluorophore protoporphyrin IX(PpIX), which, when excited by Cherenkov radiation, emits photons. Cherenkov emission was used to measure the dose distribution (see figure 6.12) for electron and photon beams of 6 and 18 MeV. The fluorescence intensity was quantified using the emission spectra of fluorescence for the measurements recorded at different concentrations of PpIX solution in water. Given that the Cherenkov emission is dominated by shorter (blue/UV) wavelengths, which have a short penetration depth in tissue, the fluorophore excitation is also localised to the external beam region.

The method holds promise for *in vivo* dosimetry and real-time monitoring of spatial dose distribution in electron beam therapy. It is particularly applicable to FLASH radiotherapy using clinical electron beams with energies typically exceeding 1 MeV. However, Cherenkov radiation may not be observed from proton beams of equivalent energy due to their lower velocity resulting from their greater mass. The Cherenkov emission threshold for a proton beam is above 500 MeV, exceeding the standard therapeutic proton beam energy range of 70 MeV to 250 MeV. This limits the applicability of Cherenkov detection to electron beams within the energy range of clinical accelerators.

Energy deposition in the Bragg Peak region can result in the emission of secondary electrons with energies greater the threshold for Cherenkov emission. These secondary electrons have the ability to emit Cherenkov radiation, which can be employed in a similar manner.

6.3.6 Summary on dosimetry techniques

A summary of various dosimetry techniques discussed in this section is presented in table 6.1.

6.4 Supersonic gas curtain ionisation profile monitor

Real-time profile and position monitoring of an ion beam enables fast feedback and allows for better control of the beam parameters during beam delivery. In critical situations, such a feedback system can shut off the beam entirely, ensuring safety for the end application. Precise beam control is more crucial for the high instantaneous dose rates anticipated in the LhARA facility. Beam profile monitoring, complemented by other diagnostic tools, can simplify calibration procedures,

Existing online monitoring devices are ideal for calibration and often do not provide real-time information of the important beam parameters, i.e. shape, energy and current distribution. Even those that do offer the possibility of real-time monitoring typically focus on a single parameter. For instance, current transformers can provide instantaneous beam current information, but do not measure the beam's profile or position. Scintillator screens can provide beam position and profile data, but significantly attenuate the beam. Optical transition radiation screens can offer beam profile information, but they require the installation of a metal plate in the beamline, which generates detrimental secondary particles.

As detailed above, existing dosimetry techniques are also inappropriate for use in a real-time feedback system that exploits all beam parameters simultaneously, without disturbing the beam. For example, real-time dosimeters like silicon diodes and MOSFETs, which are attached to the patient's skin, offer limited ability to reconstruct the beam profile. Ionisation chambers installed at the exit of the beamline provide average dose information, but do not capture the beam profile itself and suffer from ion-recombination effects at the high dose rates delivered in FLASH therapy.

As a result, a new approach using a supersonic-gas-curtain-based ionisation profile monitor (SGC-IPM) is being developed to provide all beam parameters in real time. This technique is

Table 6.1: Summary of the characteristics of the dosimetry techniques discussed in the text.

Dosimeter	Absolute Dosimetry	FLASH dosimetry	Dose measurement	Spatial resolution	Response time	Beam perturbation	Dose-rate dependence	Accuracy	Characteristics
Ionisation chamber	Yes	p [232, 234], e [226, 233]	1D, 2D scanning	few mm	10-200μs	Yes	significant $>$ 1 Gy/pulse [226] $>$ 80 Gy/s [232]	1% at 80 Gy/s [232], 15% at 1kGy/s [233], 1% with recombination correction [235]	Ion recombination at high dose rates
Diodes	N	C [242], ph [228, 244]	1D, 2D scanning	sub mm	ms	Mask	Independent at 0.2 Gy/s	2-5%	Radiation damage at high dose rate, over-response at low dose rate
MOSFETs	N	ph [249]	1D, 2D scanning	1mm	ms	Mask	-	-	Temperature dependence [247, 248]
Diamond Detectors	-	p [232], e [250], ph [251]	1D	1 mm	μs	Mask	$>$ 50 mGy/s [250]	1% $<$ 1 mGy/s [232], 9% for $>$ 50 mGy/s	-
Faraday cup	N	-	-	-	-	-	-	up to 1%–2%	Measures total collected charge
Frikie	Y	e [255], ph [254]	1D	2mm	ns	Yes	-	-	High dose rate causes diffusion of radiation-induced species
Alanine	Y	e [257], ph [258]	1D	5mm	Passive	Yes	Independent up to 10^{10} [257, 258]	$>$ 3% up to 1 kGy/s [233]	Decreased accuracy for doses $<$ 10 Gy
Radiochromic films	Potential	p [263, 264, 267] C [265, 266] e [261, 262]	2D	$<$ 1 μm	Passive	Partially transparent	Independent up to 10^{10} [261]	5-20% at Bragg Peak [263], 25-35% for C^{6+} [266, 267]	Under response in high LET field
Polymer gels	-	-	3D	1 μm	Passive	Completely	-	-	Complex measurement and complicated readout machinery
TLD	Y	e [233, 261], ph [274]	1D, 2D array/scan	1 mm	Passive	Mask	Independent up to 10^8 Gy/s [273, 274]	2% for 10^9 Gy/s [261] with corrections, 15% without corrections [233]	Energy dependence, time-consuming, LET dependence
OSLD	Y	ph [274]	1D, 2D array/scan	1 mm	Passive	Mask	Independent up to 10^9 Gy/s [261]	3-5%	Energy dependence, time-consuming, LET dependence
Scintillators	Y	p [291, 292], e [255]	1D, 2D-film	1 mm	ns	Partially transparent	Independent up to 10^7 Gy/s [255]	2% up to 10^7 Gy/s	Real-time readout, water-equivalence, energy independence, dose-linearity, and resistance to radiation damage, no correction factors are required
Cherenkov	e	e [255, 308, 309], Ph [310]	1D, 2D, 3D	1 mm	ps	Partially transparent (affects energy)	-	-	Only applied to electron or photon beams
Calorimeters	Y	p [297, 303], e [299], ph [299, 300]	-	-	-	Completely	Principally independent	$<$ 1% [297, 299, 300]	Bulky, not easy to use, correction factors, time-consuming

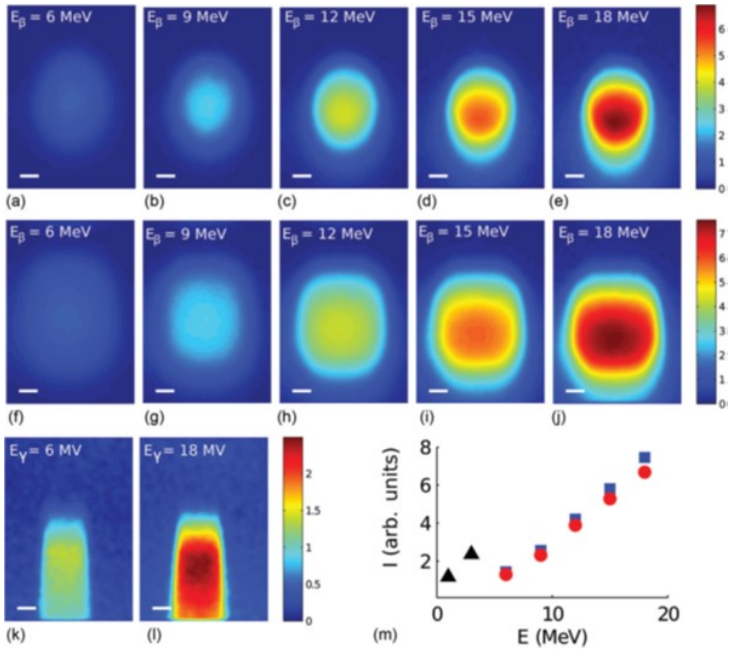

Figure 6.12: Cherenkov emission induced by electrons and photons with varying energies and field sizes. (a-e) show emission from circular electron beams of diameter 3 cm. (f-j) represents the emission from a square beam profile. (k-l) are from gamma rays. (m) shows the intensity averaged over the beam area near the maximum intensity region in the images. The markers 'round' and 'square' represent electron beams with circular and square field sizes, respectively, while the 'triangle' marker denotes photons. For electrons, the energy axis indicates the beam energy, whereas for photons it represents the energy of secondary electrons produced by Compton or photoelectric interaction [310].

derived from an existing instrument installed and operating in the Large Hadron Collider (LHC), which allows the profile of high-energy hadron beams to be measured. The monitor creates a supersonic molecular beam by extracting the core of a free supersonic jet in a vacuum chamber, reshaping it into a gas curtain using a series of masking skimmers. This gas curtain acts as a transparent screen of moving atoms, which is positioned in front of the ion beam. As the ion beam traverses the screen, it interacts with the gas molecules and produces a pattern of ionised atoms in the shape of the beam. The ionised atoms are extracted and sampled to reconstruct the beam profile. The gas curtain's low density, of the order 10^{16} molecules/m^3, and extremely thin structure ensure no measurable detrimental effects on the ion beam, providing a completely non-destructive measurement. Fast ionised-atom collection times, in the microsecond range, combined with a high-gain, fast micro-channel plate detector, enable rapid detection through an extremely low number of ionisation events (~ 1000), facilitating real-time beam monitoring. The number of ionisation events is directly proportional to the beam current, making the system scalable for high-intensity beams, such as those to be delivered by LhARA. In its current stage of development, the device can measure the beam profile, current distribution, and energy fluctuations. The absolute beam energy can theoretically be determined based on the ionisation cross-section for gas-beam interactions, though available data for cross-sections in the energy ranges relevant to LhARA beams remain sparse.

The following sections discuss the progress on the development of the SGC-IPM and ongoing design modifications to suit the end-station requirements of LhARA. The device has been tested to measure the beam profile of proton beams with energies from 4 to 28 MeV and currents from 1 to 30 nA, as well as on carbon beams for various combinations of beam currents (1–100 nA), energies (12–24 MeV), and charge states (C^{2+}–C^{5+}). Low-energy (1–10 MeV) proton

and all carbon beam measurements were conducted at the Pelletron accelerator at the Dalton Cumbria Facility in Whitehaven, UK. Subsequent higher-energy (28 MeV) proton-beam tests, incorporating improvements from earlier trials, were carried out at the MC40 cyclotron facility at the University of Birmingham, UK. The results of these experiments are also discussed in the subsequent subsections.

6.4.1 Beam profile measurement experiments at Dalton Cumbrian Facility

An upgraded gas-jet ionisation profile monitor was integrated into the accelerator beamline at the Dalton Cumbrian Facility (DCF) in Whitehaven. The objective was to conduct proof-of-concept measurements of beam profile and intensity in beams resembling those found in medical-treatment facilities. The measurements encompassed proton and carbon-ion beams of varying sizes, energies, and currents. The results of these experiments highlight the feasibility of such a beam diagnostic and provide valuable insights for its refinement. In this study, the gas-jet monitor is presented as a prospective beam monitor tailored for use in hadron beams.

The integration and testing of the supersonic gas-jet monitor and the measurement of a variety of transverse beam profiles of proton and carbon-ion beams across various beam parameters were successfully conducted. These measurements also point to improvements necessary for the monitor to be able to determine the transverse beam profile in LhARA. The measurement of a nitrogen gas-jet signal using a proton beam obtained after averaging and subtracting the background is given in figure 6.13. The results obtained at DCF have allowed improved estimation of the performance for LhARA to be made.

6.4.2 Beam profile measurement experiments at University of Birmingham

Experiments were carried out at the MC40 cyclotron at Birmingham University in August 2024 to measure the transverse beam profile of low-intensity large beams with energies varying from 10 MeV to 28 MeV.

6.4.3 Design of new ionisation profile monitor

The experiment conducted with proton and carbon beams at DCF highlights the requirement for a dosimeter capable of fast detection that is compact enough to be integrated with medical accelerators. The ion-acoustic approach described in chapter 5 has the potential to be developed into a non-destructive, real-time *in vivo* dose-profile measurement device.

In a complementary approach, an innovative ionisation profile monitor (IPM) system is being developed at the Cockcroft Institute. The realisation of the IPM requires a novel design that is compact and addresses the objectives of field uniformity, background noise reduction, and accounts for recoil and initial velocity effects. The main aim of this development is to reduce acquisition time and thus provide real-time feedback. We designed an IPM and validated it by simulating the electric field distribution and particle trajectories using COMSOL and CST Studio. The 2D distribution of the electric field on the axial plane is given in figure 6.14, and the particle trajectories and beam profile are shown in figure 6.15.

The resulting system successfully achieves reductions in both size and complexity, although it also underscores challenges associated with field distortion. Future efforts will concentrate on overcoming these challenges through manufacturing enhancements and rigorous experimental testing.

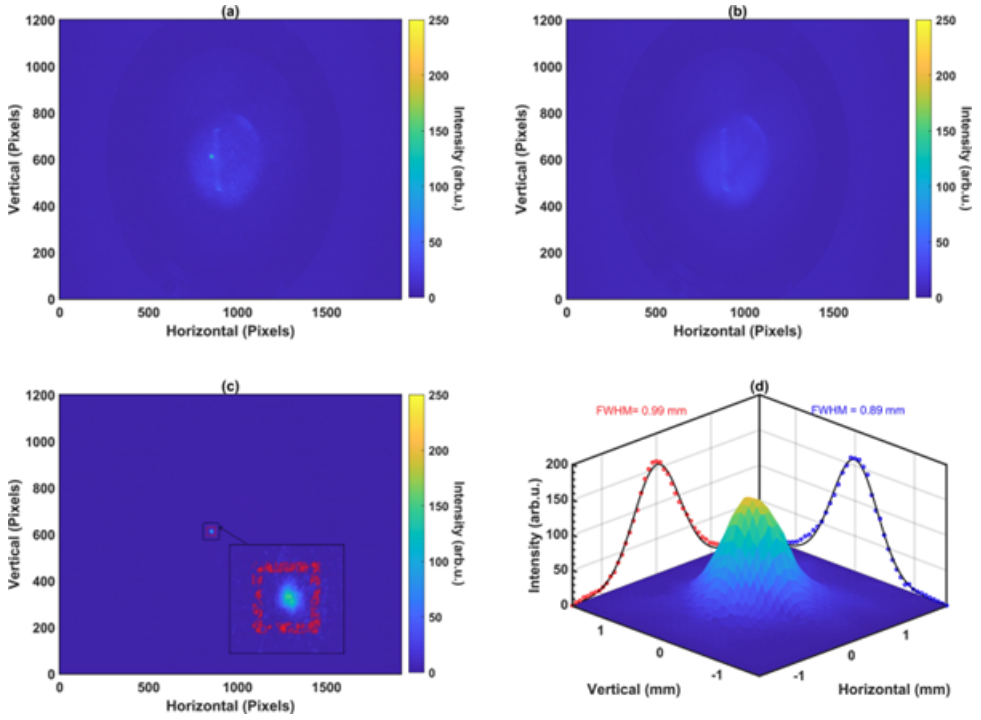

Figure 6.13: Beam Profile measurements for a 6 MeV, 100 NA beam with a 1 s integration time: (a) with the gas curtain on, showing the transverse profile along with beam-induced background ionization, (b) with the gas curtain off, showing only the beam-induced background ionization, (c) after subtracting the images shown in (b) from (a) with ROI marked in red, and (d) beam induced with 2D panels showing the FWHM of Gaussian fits [311].

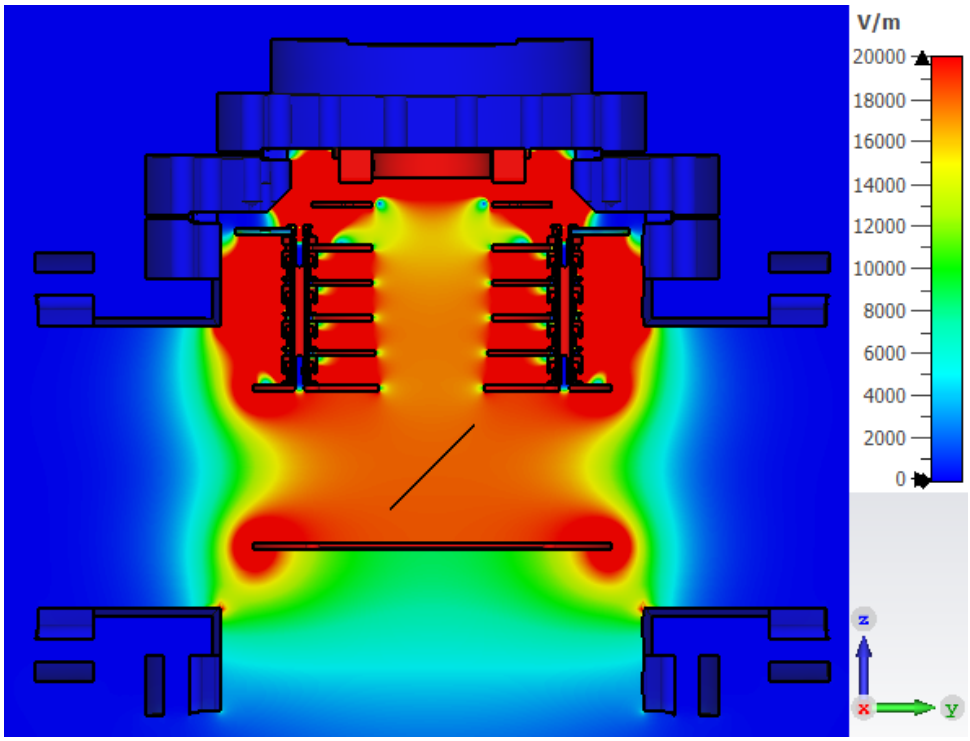

Figure 6.14: 2D distribution of electric field on axial slice plane for IPM with mounting elements.

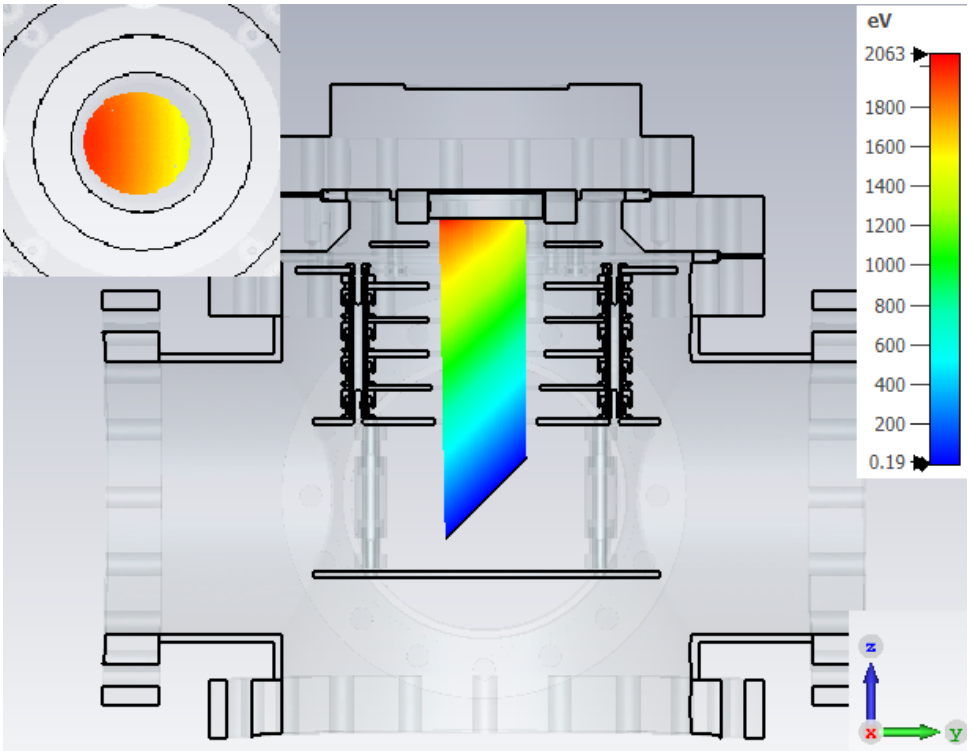

Figure 6.15: 2D distribution of the electric field on the axial slice plane for IPM with mounting elements.

6.4.4 Future work

There are plans to expand experimental studies with the gas-jet system at the Scottish Centre for the Application of Plasma-based Accelerators (SCAPA) in Glasgow.

APPENDIX A

Alternative Technologies

A.1 Introduction

In this appendix, advanced conventional accelerator technologies are compared against the novel laser-hybrid solution, LhARA[13], that has been adopted as the baseline to serve the Ion Therapy Research Facility (ITRF). The scope of this appendix includes the conceptual design of two accelerator schemes to serve a radiobiology research facility. The first alternative is based on a slow cycling synchrotron and the second on a high-frequency linear accelerator. Together, these designs allow quantitative conclusions to be drawn from comparisons between these advanced conventional accelerators and the LhARA baseline. The development of conventional alternatives to serve the ITRF was essential both to establish LhARA as the baseline solution and to provide the basis of the facility-level risk management strategy.

The structure of this appendix is as follows: the requirements that both conventional accelerators should meet are presented in section A.1.1 alongside a review of relevant design studies from the recent literature. Section A.2 describes the design of a facility based on a slow-cycling ($\sim$1 Hz) room-temperature synchrotron, fed from an injector that uses established ion source technologies and acceleration methods. The main parameters for a compact linear accelerator that produces proton bunches at energies relevant to radiobiology experiments, comparable to the LhARA baseline parameters, are summarised in section A.3. Finally, section A.4 details estimates for the dose rates that each system can deliver to its end stations and section A.5 compares the power requirements of each alternative scheme.

A.1.1 Machine requirements

The main requirements for the designs considered in this appendix are:

Choice of Ion Species
Each accelerator should accommodate the ion species that are most likely to be used for radiotherapy. At present, these are expected to be protons (p^+), helium ions ($^4He^{2+}$) and carbon ions ($^{12}C^{6+}$) [312]. Ideally, the design should not exclude the provision of heavier ions that may be of interest to future radiobiology studies, such as oxygen ($^{16}O^{8+}$) or neon ($^{20}Ne^{10+}$) [312, 313].

Machine Parameters
To provide a direct comparison against the baseline LhARA design, each machine should fit within the combined footprint of the LhARA Stage 1 low-energy line and Stage 2 fixed-field accelerator (FFA). Both designs should accommodate beam energies up to the nominal extraction energy of the LhARA FFA: 127 MeV for protons and 33.4 MeV/u for $^{12}C^{6+}$ ions, respectively [13].

Beam Intensity
Both conventional accelerators should achieve beam intensities compatible with the delivery of FLASH dose rates to their end stations. As described in more detail earlier, the FLASH regime is generally defined as a time-averaged dose rate $\gtrsim$ 40 Gy/s. For a

slow-cycling synchrotron, this implies that around $\sim 10^{10}$ ions should be extracted per spill [314].

Choice of Technologies

Consistent with the scope of this appendix, both accelerator designs should be based on accessible, conventional technologies. For instance, the synchrotron dipoles should be normal-conducting, room-temperature magnets rather than high-field superconducting magnets. The machine specifications should not push the limits of conventional technologies beyond what has routinely been achieved in accelerator facilities to date.

A.1.2 Previous Design Studies

In recent years, proposals for advanced radiotherapy machines have primarily focused on compact synchrotrons and high-frequency linear accelerators [314]. Both types of accelerator have an inherent advantage over the more widely used cyclotron since they allow beam extraction over a wide range of energies. This avoids the need for an energy degrader or other energy-modulation system and therefore can allow the delivery of higher beam intensities (and dose rates) to the end stations or treatment rooms [315, 316].

A number of existing radiotherapy facilities, including HIT [317, 318], CNAO [319], and MedAustron [320], have successfully operated synchrotrons based on the PIMMS design [321] for over a decade. More recent proposals have primarily aimed to make synchrotron-based facilities more compact while also providing a significant increase in beam intensity or repetition rate [322]. For example, the Next Ion Medical Machine Study (NIMMS) is an umbrella R&D framework established by CERN to consider designs for next-generation particle radiotherapy machines [323]. The NIMMS project is actively developing several synchrotron designs that are relevant to ITRF, including a superconducting carbon-ion machine [324], and a room-temperature helium-ion synchrotron [325]. Both designs are intended as the basis for a clinical radiotherapy facility, and therefore accommodate beam energies of several hundred MeV/u and intensities up to 10^{10} ions per cycle.

While there are presently no operational proton therapy facilities based on linear accelerators, a number of proposals remain under active development. For example, AVO-ADAM have recently demonstrated a reduced-energy prototype [326] of their LIGHT accelerator design [327]. The LIGHT prototype can deliver proton bunches with a maximum energy of at least 52.9 MeV at repetition rates up to 200 Hz. The full LIGHT accelerator would be capable of 200 Hz operation at energies of at least 200 MeV. The NIMMS project has also proposed a novel 'bent' linac design for both p^+ and $^{12}C^{6+}$ ion beams [323, 328], following earlier designs carried out within the TERA foundation framework.

The following sections provide further details about the NIMMS $^4He^{2+}$ synchrotron (section A.1.2.1) and the AVO-ADAM LIGHT prototype (section A.1.2.2). These designs have been used as the basis for the two conventional accelerators considered later in this appendix.

A.1.2.1 NIMMS Helium-Ion synchrotron

The NIMMS helium synchrotron, shown in figure A.1, has a circumference of ~ 33 m and is designed to deliver $^4He^{2+}$ ions at energies up to 250 MeV/u. The synchrotron lattice is comprised of three identical double-bend achromat (DBA) cells [329], with each cell containing two 60° dipole magnets. Each sector dipole has a bending radius of 2.7 m and a maximum field of 1.65 T, incorporating a small defocusing gradient.

A strong quadrupole at the centre of each bending section is used to cancel the dispersion in the straight sections, which accommodate the injection, extraction and RF hardware in three separate straights. These dispersion-cancelling quadrupoles have additional sextupole windings,

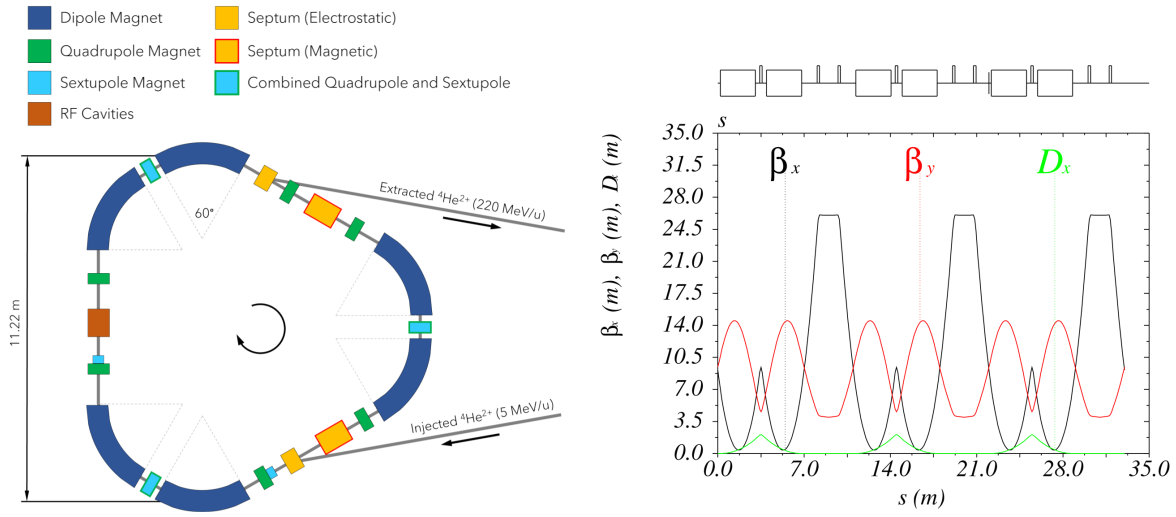

Figure A.1: (a) Schematic layout of the NIMMS $^4He^{2+}$ synchrotron, and (b) preliminary optics for the NIMMS synchrotron, calculated in MAD-X. Both figures adapted from Vretenar *et al.* 2023 [325].

which are used to control the horizontal chromaticity of the lattice. Figure A.1 shows the beam optics functions over the full circumference of the NIMMS $^4He^{2+}$ synchrotron.

The NIMMS designs build on CERN's previous experience with small hadron synchrotrons, which includes the ELENA decelerator [330] at the Antiproton Decelerator (AD) facility. ELENA is a small (30.4 m circumference) synchrotron that decelerates antiprotons ($\bar{p}$) from 5.3 MeV to an extraction energy of only 100 keV. While ELENA operates at far lower beam intensities (typically 10^7 $\bar{p}$ per cycle) and repetition rates (0.01 Hz), it employs many of the technologies that underpin the NIMMS synchrotron designs. For example, the ELENA RF system is based on a wide band (0.14–2 MHz) cavity loaded with magnetic alloy cores, allowing operation over a wide range of energies.

A.1.2.2 AVO–ADAM LIGHT prototype

The AVO-ADAM LIGHT prototype (shown in figure A.2) has a total length of ~ 10 m and was successfully commissioned at CERN between 2015–2019 [326]. Protons are initially extracted from an electron cyclotron resonance (ECR) ion source and guided through a low energy beam transport (LEBT) section at 40 keV. The LEBT section includes a 90° dipole magnet—which is used to disperse unwanted H_2^+ and H_3^+ ions—and a pair of electrostatic plates which are used to chop the beam into $\sim 1\,\mu$s pulses at repetition rates of up to 200 Hz.

The accelerator itself is comprised of a radio frequency quadrupole (RFQ) [331], four side-coupled drift tube linac (SCDTL) modules, and two cell coupled linac (CCL) modules [332]. In this configuration, the linac can deliver p^+ bunches at energies up to 52.9 MeV. However, the LIGHT prototype was intended as a demonstrator for a clinical radiotherapy facility and its maximum beam energy can be increased to 230 MeV by adding additional CCL modules. Such a prototype has been constructed at UKRI-STFC Daresbury Laboratory, and successfully tested to over 230 MeV.

The LIGHT prototype has a number of features that would be beneficial to clinical proton therapy. For example, the energy and intensity of each p^+ pulse can be varied on a shot-to-shot basis at $\gtrsim 100$ Hz [326], the energy being readily varied by adjusting the phase of the CCL modules. As a linear accelerator, the LIGHT prototype also produces proton beams with very small normalised emittances (of order 0.25 mm mrad), which allows the use of smaller magnet

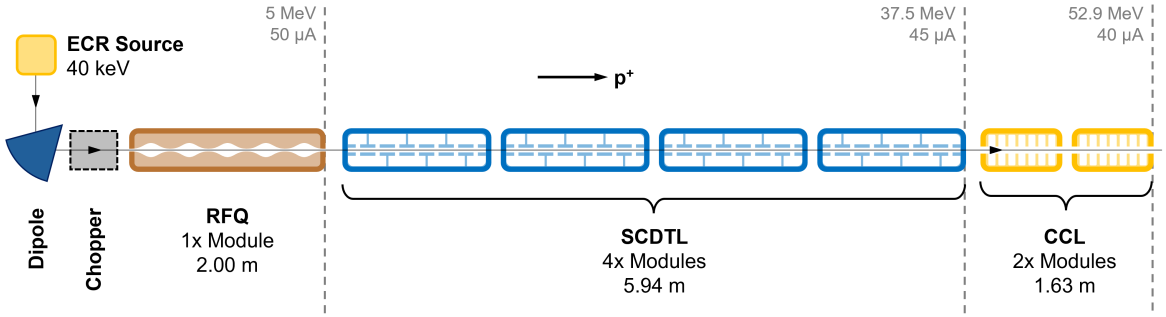

Figure A.2: Schematic showing the layout of the LIGHT prototype machine. Elements are not to scale. The proton beam energy and beam current are annotated at the end of each machine section.

apertures in the beam delivery system and provides for somewhat smaller clinical spot sizes at the patient.

Further details about the AVO-ADAM LIGHT prototype are given in section A.3.

A.2 Synchrotron option

A.2.1 Machine parameters

The NIMMS $^{4}He^{2+}$ synchrotron [325] has been used as the basis for the ITRF synchrotron design, due to its small footprint and large beam intensity. The NIMMS synchrotron is significantly larger than the LhARA FFA and must be scaled down by approximately 30% to fit within a similar footprint. The NIMMS design can readily be scaled to match the size and energy range of the LhARA FFA simply by reducing both the bending radius and the maximum field of its dipole magnets. However, much higher beam energies (up to 84 MeV/u for $^{12}C^{6+}$) can be achieved by increasing the circumference of the synchrotron by around 10% relative to the LhARA FFA size. This would yield a significant advantage, providing greater flexibility in irradiation depth and dose rate at the end stations (see section A.4). The larger, more flexible synchrotron has therefore been chosen here.

Figure A.3 shows a schematic layout of the ITRF synchrotron design, which has a circumference of 23.88 m. Table A.1 lists the specifications for the six sector-dipole magnets. Both the bending radius and maximum field of the dipoles have been reduced compared to the NIMMS design, giving a maximum beam rigidity (at extraction) of 2.70 Tm. This allows the ring to accommodate $^{4}He^{2+}$ and $^{12}C^{6+}$ ions with energies up to 83.5 MeV/u, around 2.5 times higher than the extraction energy of the LhARA FFA. In principle, the dipole magnets can accommodate proton beams with energies up to 300 MeV; however, we anticipate that the maximum proton energy will be limited by the bandwidth of the synchrotron RF system. Assuming an RF bandwidth of 1.0–5.5 MHz, the synchrotron may accelerate proton beams to a maximum energy of 105.5 MeV, comparable to, but a little lower than, the LhARA baseline of 127 MeV.

Tables A.2, A.3 and A.4 outline the preliminary specifications for the dipole, quadrupole and sextupole magnets, respectively, for the main magnet types present in the ITRF synchrotron option design.

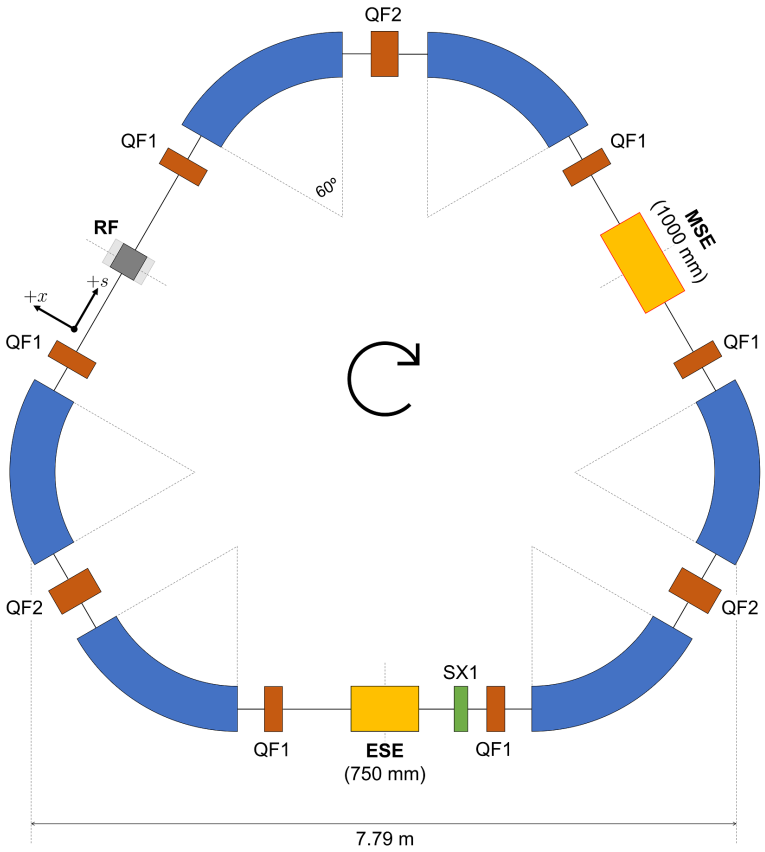

Figure A.3: Schematic showing the preliminary layout of the ITRF synchrotron option. Elements are approximately to scale.

Table A.1: Specifications for the ITRF synchrotron dipole magnets, and the corresponding maximum beam energies for different ion species.

Parameter	**Value**		
Dipole radius [m]	1.80		
Max. dipole field [T]	1.50		
Max. beam rigidity [T m]	2.70		
Ion species	H^{+}	$^{4}He^{2+}$	$^{12}C^{6+}$
Max. beam energy [MeV/u]	105.5	83.5	83.5
Orbital frequency [MHz]	5.50	4.97	4.97

Table A.2: Preliminary parameters for the synchrotron dipole magnets (SB1 in figure A.3). Estimates for the magnet electrical properties and power consumption are based on existing magnet designs [330, 333, 334] and scaling arguments.

Parameter	Value
Bend Angle [°]	60
Bend Radius [m]	1.8
Magnetic Length [m]	1.885
Magnetic Field	
Min. Dipole Field [T]	0.25
Max. Dipole Field [T]	1.50
Quadrupole Coefficient k_1 [m^{-2}]	-0.57
Max. Quadrupole Gradient [T/m]	-1.53
Physical Aperture	
Horizontal [mm]	70
Vertical [mm]	35
Power Requirements	
Windings Resistance [mΩ]	74.8
Max. Current [A]	687
Max. Voltage [V]	51.4
Dissipated Power [kW]	35.4

Table A.3: Preliminary parameters for the synchrotron quadrupole magnets (QF1 and QF2 in figure A.3). Estimates for the magnet electrical properties and power consumption are based on existing magnet designs [334–336] and scaling arguments.

Parameter	Value	
	QF1	**QF2**
Magnetic Length [m]	200.0	300.0
Physical Aperture [mm]	∅80.0	∅80.0
Magnetic Field		
Quadrupole Coefficient k_1 [m^{-2}]	+3.75	+5.35
Max. Quadrupole Gradient [T/m]	+10.1	+14.4
Sextupole Coefficient k_2 [m^{-3}]	-	+5.68
Max. Sextupole Gradient [T/m^2]	-	+15.35
Power Requirements		
Windings Resistance [mΩ]	29.1	87.3
Max. Current [A]	208.9	149.0
Max. Voltage [V]	6.1	13.0
Dissipated Power [kW]	1.27	1.94

A.2.2 Working point

The beam optical functions were calculated primarily using `MAD-X` [74, 338], accessed via the `cpymad` python library [339]. To enable slow extraction using either RF knock-out (RF-KO) or a similar scheme, the synchrotron working point must be established close to a third-order betatron resonance. Figure A.4 shows the preliminary optics at a working point with horizontal tune $Q_x = 2.66$. Figure A.5 shows the location of this working point on a tune diagram, with resonances plotted up to fourth order. By adjusting the strengths of the QF1 quadrupoles (see

Table A.4: Preliminary parameters for the synchrotron resonant sextupole magnet (labelled SXR in figureA.3). Estimates for the magnet electrical properties and power consumption are based on existing magnet designs [334, 337] and scaling arguments.

Parameter	Value
Magnetic Length [m]	150.0
Physical Aperture [mm]	∅80.0
Magnetic Field	
Sextupole Coefficient k_2 [m^{-3}]	20.0
Max. Sextupole Gradient [T/m^2]	54.00
Power Requirements	
Windings Resistance [mΩ]	29.6
Max. Current [A]	51.2
Max. Voltage [V]	1.52
Dissipated Power [kW]	0.08

lattice layout shown in figure A.3), the ring can also be operated at a working point with $Q_x = 2.33$. However, this working point cannot be used in practice, as it provides insufficient phase advance between the electrostatic and magnetic extraction septa (see section A.2.5). Table A.5 summarises the beam optics for our chosen working point with $Q_x = 2.66$.

A.2.3 Injector linac

As in both NIMMS designs, it is proposed that the synchrotron be filled from a conventional injector that resembles CERN Linac 4 [340]. Several ion sources can be connected to the injector

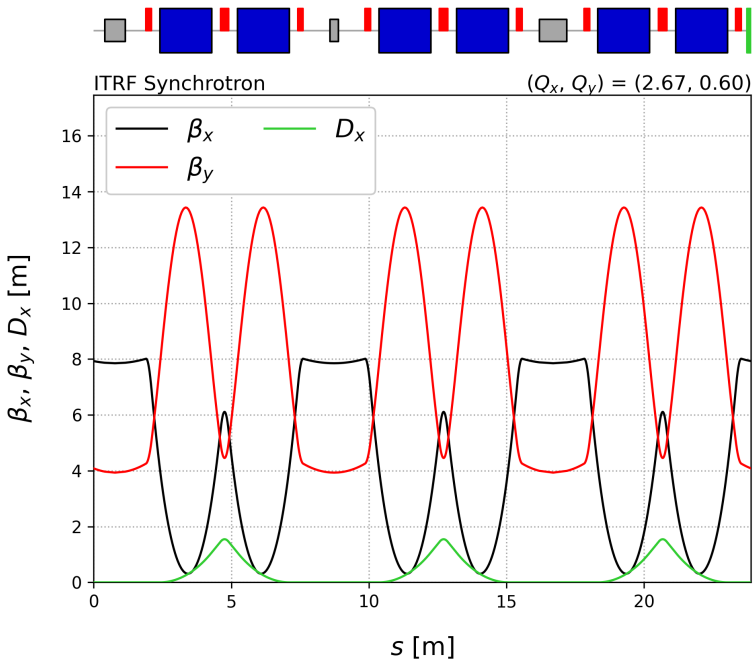

Figure A.4: MAD-X calculation showing the preliminary synchrotron optics, with the machine tuned to a working point close to the third-order resonance $Q_x = 2.66$.

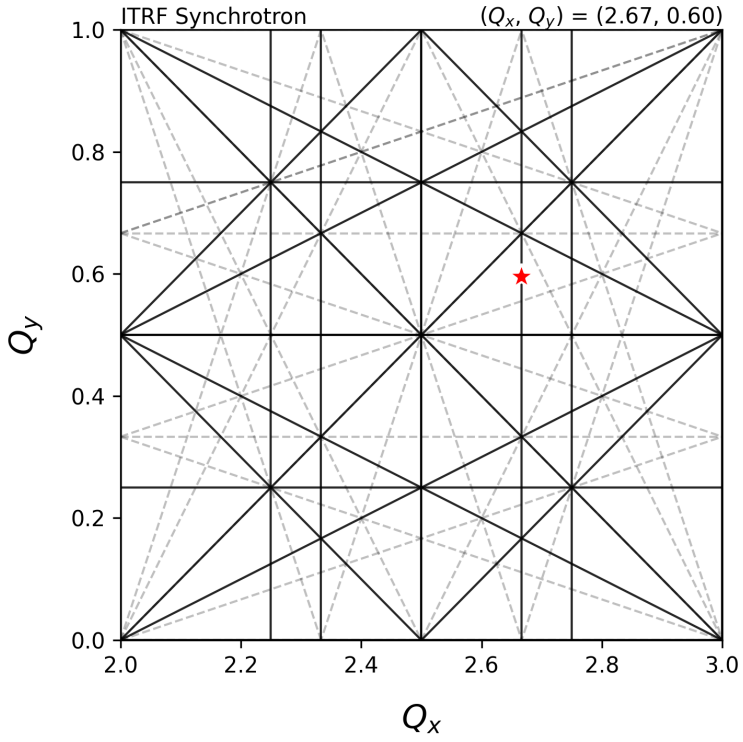

Figure A.5: Tune diagram showing the location of the proposed working point $(Q_x, Q_y) = (2.66, 0.60)$ relative to resonances up to fourth order. The working point is indicated with a red star. Skew resonances are shown as dashed lines.

Table A.5: Summary of beam optics parameters for the synchrotron working point with $Q_x = 2.66$, as shown in figure A.4.

Parameter	**Value**
Focusing Strengths	
QF1 Quadrupoles [m^{-2}]	+3.76
QF2 Quadrupoles [m^{-2}]	+5.35
Sector Dipoles [m^{-2}]	-0.57
Optics functions	
Max. β_x [m]	8.01
Max. β_y [m]	13.4
Max. D_x [m]	1.55
Working Point	
Tune Q_x, Q_y	2.66, 0.60
Natural Chromaticity Q'_x, Q'_y	-3.82, -3.62

via a magnetic switch-yard, allowing a range of ion species to be used interchangeably.

In the NIMMS injector [325], ions are accelerated to a nominal injection energy of 5 MeV/u using a 352 MHz RFQ followed by a single drift tube linac (DTL) tank (of similar design to that of CERN Linac 4). The injection energy of 5 MeV/u was chosen primarily based on the efficiency of typical stripping foils, such as those used to produce $^{12}C^{6+}$ ions from $^{12}C^{4+}$. To mitigate space-charge effects on injection to the synchrotron, protons are accelerated to 10 MeV using a second DTL tank, which can be turned off entirely when working with ions other than protons.

For the purposes of this design, a set of injector parameters based on those of the proposed SEEIST facility [341] is assumed. Table A.6 lists the expected beam current for protons, $^{4}He^{2+}$ and $^{12}C^{6+}$ ions at injection. Commercial ECR ion sources such as the Pantechnik 'Supernanogan' source [342, 343] can provide up to 2 mA of proton current.

A.2.4 Multi-Turn Injection

To accumulate sufficient ions for FLASH extraction during each synchrotron cycle, the beam will be loaded using multi-turn (MT) injection. In this scheme, ions are injected over 15–20 successive turns. Assuming that the injector emittance is much smaller than the synchrotron acceptance, the phase space of the circulating beam is gradually filled with charge, as illustrated in figure A.6. The charge distribution is then smoothed out over subsequent turns via phase-space filamentation.

To estimate the stored intensity for each ion species using the parameters in table A.6, MT injection over 15 turns with an efficiency of 60% [344] is assumed. The maximum number of circulating ions (for both p^+ and $^{4}He^{2+}$) that is predicted to be possible is greater than 10^{10}.

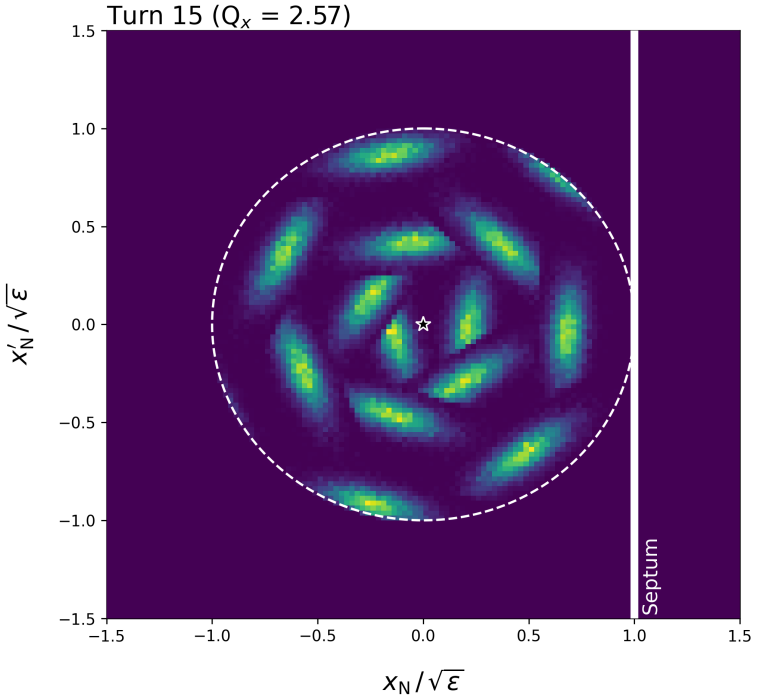

Figure A.6: The distribution of charge density in normalised transverse phase space after MT injection. The distribution was calculated using a toy model, assuming a synchrotron tune of $Q_x = 2.57$ and MT injection over 15 turns. The synchrotron acceptance is shown as a dashed white line, and the septum location is indicated as a solid white line.

The carbon-ion source limits the number of $^{12}C^{6+}$ions that can be accelerated per synchrotron cycle to $\sim 10^9$.

The tune shift due to the transverse defocusing effect of space charge is largest at injection. In general, a space charge tune shift $|\Delta Q| \leq 0.25$ is considered to be acceptable; larger tune shifts may require a resonance compensation scheme. For each ion species, the space charge tune shift in the horizontal plane is [345]:

$$\Delta Q_x = -\frac{Z^2 r_p N_0}{2\pi A \beta^2 \gamma^3 \epsilon_x} \left\langle \frac{2}{1+\sqrt{\epsilon_y \beta_y / \epsilon_x \beta_x}} \right\rangle ; \tag{A.1}$$

where N_0 is the number of circulating ions, r_p is the classical proton radius, ϵ_x is the geometric emittance in the horizontal plane, and A and Z are the atomic mass and charge state of the ion, respectively. The relativistic β and γ functions and beam-optical beta functions $\beta_{x,y}$ are defined as usual. A similar expression can be obtained for the tune shift in the vertical plane.

As shown in table A.6, the space-charge tune shift is within an acceptable bound for each ion species. The number of ions per spill is therefore limited by the injector parameters rather than by space charge considerations, in contrast to the NIMMS designs on which the present lattice was based.

A.2.5 Beam Extraction

A.2.5.1 Resonant Extraction

Slow resonant beam extraction will be achieved using "RF knock-out" (RF-KO). This choice is consistent with the NIMMS $^4He^{2+}$ synchrotron design assumption. In this scheme, the horizontal tune of the synchrotron is set to a third-order resonance (such as $Q_x = 2.66$, as shown in figure A.4), which is excited using one or more resonant sextupole magnets.

Close to a third-order resonance, the ion trajectories in normalised phase space are defined by the Kobayashi Hamiltonian [346, 347]:

$$\mathcal{H} = 3\pi\, \delta Q \left(x_N^2 + {x'}_N^2 \right) + \frac{S}{4} \left(3\, x_N\, {x'}_N^2 - x_N^3 \right) ; \tag{A.2}$$

where $\delta Q = (Q_{\text{ion}} - Q_{\text{res}})$ is the tune distance of the ion from the nearest third-order resonance, and x_N and ${x'}_N$ are the standard particle coordinates in normalised phase space. The parameter S represents the effect of the resonant sextupole, with:

$$S = \frac{1}{2} \beta_x^{3/2}\, l_S\, k_2 ; \tag{A.3}$$

Table A.6: Injector parameters and corresponding stored intensities for different ion species. Injector parameters are based on those of the proposed SEEIST facility [341].

Parameter	**Values**		
	H^+	$^4He^{2+}$	$^{12}C^{6+}$
Linac Current [mA]	2.0	1.0	0.2
Injection Energy [MeV/u]	10.0	5.0	5.0
Orbital Period [MHz]	1.82	1.29	1.29
MT Injection Efficiency [%]		60 %	
Ions After 15 Turns [10^{10}]	6.19	2.18	0.15
Space Charge Tune Shifts			
ΔQ_x	-0.12	-0.01	< 0.01
ΔQ_y	-0.13	-0.02	< 0.01

where l_S and k_2 are respectively the effective length and normalised strength of the resonant sextupole; β_x is the horizontal beta function at the location of that sextupole.

Close to a third-order resonance, the second term of equation A.2 will distort the phase space trajectories of ions into triangular shapes (see figure A.7); ions within a central region of phase space (the 'stable triangle') will follow closed trajectories and remain stable over many turns. However, ions outside of this region are unstable and will eventually follow the separatrices of the Hamiltonian out to large amplitudes.

In the RF-KO extraction scheme, a pair of electrostatic plates are used to kick the beam at frequencies close to the betatron tune [348, 349]. These transverse kicks gradually drive ions out of the stable region of phase space, allowing them to be extracted at the electrostatic extraction septum (labelled ESE in figure A.4). A horizontal kick is imparted to ions that exceed the aperture of the ESE, causing their orbit to deviate from that of the circulating beam. These ions arrive at the magnetic extraction septum (labelled MSE in figure A.3) with a large transverse offset from the main beam, allowing them to be extracted safely from the synchrotron with minimal losses.

Figure A.8 shows the horizontal and vertical phase advance as a function of distance around the synchrotron ring. To maximise the separation between the extracted ions and the circulating beam at the magnetic septum, the septum must be placed at a phase advance of either 90° or 270° from the ESE. As shown in figure A.8, the phase advance between septa is approximately 280° in the proposed synchrotron design.

A.2.5.2 Particle Tracking Simulations

Particle tracking simulations using MAD-X [74, 338] were used to verify that the proposed synchrotron lattice is compatible with slow resonant extraction. In these simulations, a resonant sextupole (labelled SXR in figures A.3 and A.8) was used to excite the third-order resonance at $Q_x = 2.660$. An ion distribution (typically comprising 10^4 macroparticles) was then tracked

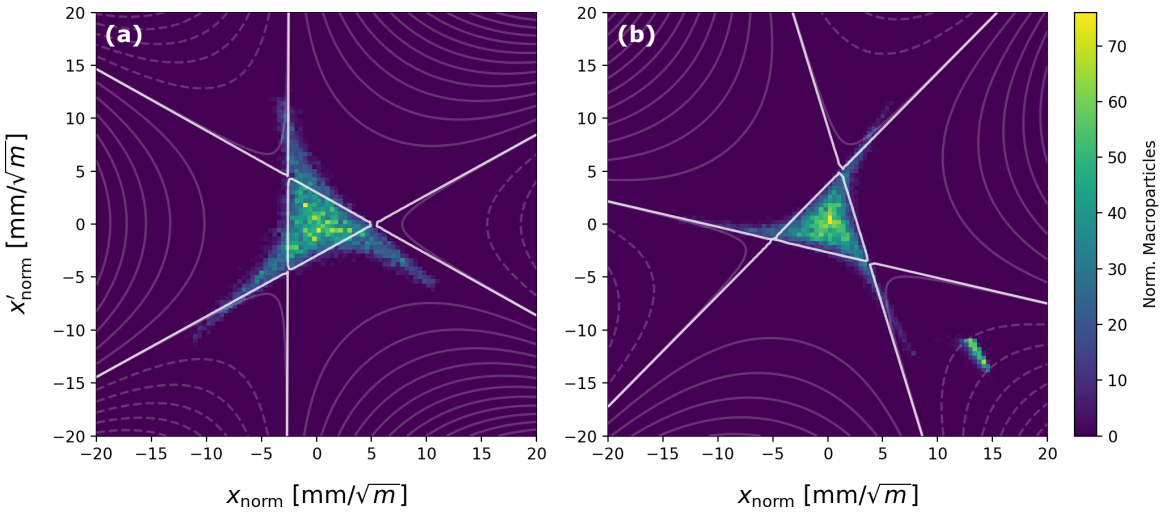

Figure A.7: MAD-X particle tracking simulation showing the (normalised) horizontal phase space of a proton beam during resonant extraction. The phase space is shown (a) immediately after the resonant sextupole and (b) at the magnetic extraction septum (MSE). The smooth lines show the contours of equation A.2. Panel (a) shows only the circulating beam, while (b) also shows ions that have been extracted from the main distribution.

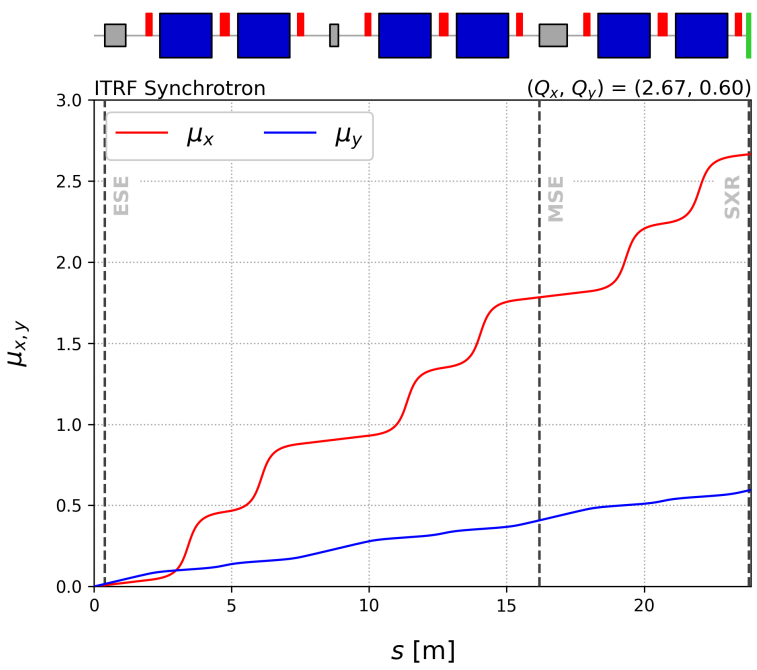

Figure A.8: Horizontal and vertical phase advance (shown in Q units) as a function of longitudinal distance around the synchrotron ring. The locations of the electrostatic (ESE) and magnetic (MSE) extraction septa and resonant sextupole (SXR) are indicated as dashed vertical lines.

around the synchrotron for several hundred turns. If the initial emittance of the simulated beam is chosen to be larger than the stable region of phase space, some ions are initialised on unstable trajectories and quickly exceed the aperture of the electrostatic septum. Figure A.7 shows the phase space of a simulated 100 MeV proton beam during resonant extraction.

We assume an electrostatic septum with an aperture of 25 mm and a deflection angle of 2.5 μrad, similar to the septum currently used in the operating CNAO carbon-ion therapy synchrotron. Ions that exceeded the septum aperture were considered to be extracted and were removed from the simulation, and their coordinates were recorded. These "extracted" ions were then tracked around one full turn of the synchrotron to find their coordinates at the magnetic septum. Figure A.7 also shows the phase space distribution of extracted ions at the MSE. For comparison, the remaining part of the circulating beam is also shown; clearly, the extracted ions have a large transverse separation from the main beam.

These simulations do not include time-dependent elements, such as the kicker used to drive ions out of the stable region of phase space during extraction. Consequently, our simulations were not a full dynamic representation of RF-KO extraction and cannot address the question of how quickly (or slowly) ions were extracted during a typical spill. However, extensive simulations have been carried out for the NIMMS and PIMMS therapy synchrotrons (the latter including those at CNAO and MedAustron) [348, 349]. Previous work has shown that RF-KO schemes can be used to produce a uniform spill over a timescale of 0.1–1.0 s. For the ITRF synchrotron, an extraction timescale of 100 ms corresponds to around 550,000 turns for a proton beam, and around 497,000 turns for either $^{4}\mathrm{He}^{2+}$ or $^{12}\mathrm{C}^{6+}$.

Slow resonant extraction techniques are commonly used in clinical radiotherapy synchrotrons to deliver a steady, well-characterised spill to the patient. However, for radiobiology experiments, single-turn extraction techniques could also be used to deliver the entire spill over a timescale comparable to the revolution period (typically $\lesssim 1\,\mu$s) [322]. In principle, this would allow

the synchrotron to provide much higher instantaneous dose rates. For the ITRF synchrotron, a single orbit takes around 180 ns for 105.5 MeV protons, or 200 ns for 83.5 MeV/u helium or carbon ions.

A.2.6 Operational considerations

The ITRF synchrotron is assumed to be a slow-cycling machine with a repetition rate of around 1 Hz. In any synchrotron, one or more pre-defined cycles are needed to accelerate different ions to a range of extraction energies. The duration of each cycle is primarily determined by inductive effects in the synchrotron dipole magnets, which must ramp up quickly to keep the beam on a closed orbit during acceleration. Typically, the maximum ramp rate for the dipoles in a small, room-temperature synchrotron is of order 2.4 T/s [350].

To estimate the true repetition rate and power requirements of the synchrotron, a number of indicative magnet cycles were considered. The main cycle parameters are listed in table A.7. Each cycle was designed to deliver either p^+, $^4He^{2+}$, or $^{12}C^{6+}$ ions with a mean range of ~ 20 mm in water (see section A.4.1). In each case, the maximum ramp rate of the dipole magnets was limited to 2.4 T/s. We allow at least 100 ms for beam injection and capture, and a further 150 ms for beam extraction at the maximum magnetic field.

Figure A.9 shows the on-axis magnetic field and dissipated power for a single dipole magnet during a typical synchrotron cycle. Calculations are shown for both the p^+ and $^{12}C^{6+}$ cycles described in Table A.7. To estimate the magnet power requirements, it is assumed that the electrical current in the magnet windings is proportional to the on-axis magnetic field. The synchrotron power requirements are discussed further in section A.5.1.

As shown in figure A.9, the 83.5 MeV/u carbon cycle has a duration of 1500 ms, equivalent to a repetition rate of only 0.67 Hz. This is slower than the nominal repetition rate of 1 Hz, meaning that the time-averaged $^{12}C^{6+}$ beam intensity delivered to the end stations will be some-

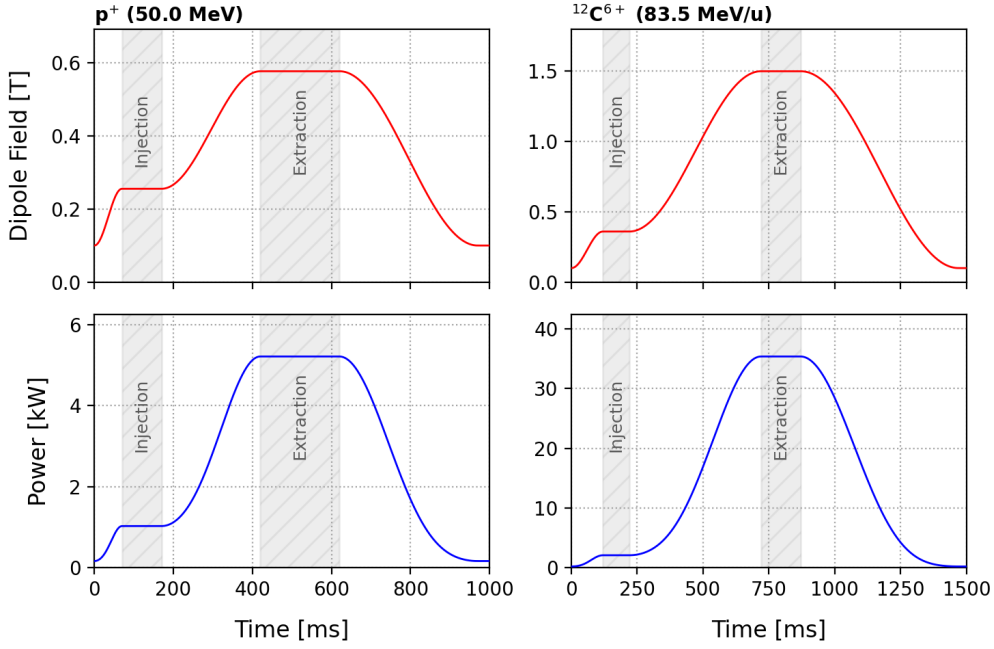

Figure A.9: Indicative synchrotron magnet cycles for 50 MeV protons (left) and 83.5 MeV/u carbon ions (right). Panels (a) and (b) show the main dipole field as a function of time, while (c) and (d) show the power required to generate this field.

Table A.7: Parameters for synchrotron cycles that produce p^+, $^4He^{2+}$, or $^{12}C^{6+}$ bunches, with energies corresponding to a range of ~ 20 mm in water. The cycles for protons and carbon ions are shown in figure A.9

Parameter	**Value**		
Ion Species	p^+	$^4He^{2+}$	$^{12}C^{6+}$
Injection			
Beam Energy [MeV/u]	10.0	5.0	5.0
Dipole Magnetic Field [T]	0.26	0.36	0.36
Extraction			
Ion Range in Water [mm]		20.0	
Beam Energy [MeV/u]	50.0	50.0	83.5
Dipole Magnetic Field [T]	0.58	1.15	1.50
Synchrotron Cycle			
Injection Ramp [ms]	70	120	120
Injection Plateau [ms]	100	100	100
Acceleration Ramp [ms]	250	350	500
Extraction Plateau [ms]	200	150	150
Ramp Down [ms]	350	450	600
Recovery [ms]	30	30	30
Repetition Rate [Hz]	1.00	0.83	0.67

what reduced. The average power dissipated per dipole during the 50 MeV proton (83.5 MeV/u carbon) cycle is approximately 2.6 kW (13.9 kW).

A.3 Linear accelerator option

The AVO-ADAM LIGHT prototype has been used as the basis for understanding the capabilities of a linac option for the ITRF as the LIGHT accelerator is compact and delivers protons and ions over the appropriate energy range. Commissioning data from the original LIGHT prototype can also be used to evaluate the likely performance of a similar machine. While the LIGHT prototype is designed to accelerate proton bunches, several ongoing design studies are examining linacs that can also deliver heavier ions such as $^{12}C^{6+}$ [328]. In principle, these studies could inform the design of a compact linac facility compatible with multiple ion species.

As discussed in section A.1.2.2, the LIGHT prototype (figure A.2) is a ~ 10 m linac that delivers proton bunches at energies up to 52.9 MeV. Protons are initially extracted from an ECR ion source (Pantechnik type Monogan M-1000) [342] and guided through a low-energy beam transport (LEBT) section at an energy of 40 keV. Further acceleration to 5 MeV is achieved within only 2 m by using a compact RFQ (radio-frequency quadrupole) design that was originally developed at CERN [331]. The RFQ operates at the fourth sub-harmonic (750 MHz) of the primary RF frequency (3 GHz), and has a maximum transmission of around 30% [351].

Upon leaving the RFQ, proton bunches are accelerated to their extraction energy using four SCDTL modules, and a pair of CCL modules [332]. Each CCL module has an average accelerating gradient of around 16.5 MV/m. In principle, the maximum beam energy can be increased by simply adding additional CCL modules; the full-scale LIGHT system has 15 CCL modules and a nominal output energy of 230 MeV. AVO-ADAM have publicly reported operation of a second prototype up to a proton energy of around 200 MeV, validating this design. As noted in section A.1.2.2, the extraction energy can be varied on a shot-to-shot basis by varying the RF power distribution between the main accelerating structures; in the LIGHT accelerator this

energy variation can be accomplished at a nominal rate of 200 Hz (the linac pulse repetition rate). When combined with a spot-scanning system, this allows the dose distribution to be tailored in 3D, while avoiding the need for either an energy modulation system [316] or for long energy-switching times (typically $\gtrsim 100$ ms for both synchrotrons and cyclotrons) [352].

Table A.8 lists the main operational parameters for the LIGHT prototype, based on both commissioning data [326, 353–356] and simulation studies [351]. Indicative beam parameters are listed for the end of each machine section. Defining the beam current as the proton current averaged over the duration of a beam pulse and assuming a repetition rate of 200 Hz and a typical pulse duration of 1 μs, the beam has a duty factor of approximately 0.02%. This corresponds to a time-averaged beam current of around 8 nA at the output of the CCL modules.

A.4 Extracted dose rates

A.4.1 Penetration depth

The energy at which the beam enters the biological sample determines the maximum penetration depth. Estimates of the range in water of each ion species (p^+, $^4He^{2+}$ and $^{12}C^{6+}$) at the extraction energies listed in table A.2 are presented below.

The range of an ion beam R_{water} can be estimated using the Bethe-Bloch equation, which describes the mean rate of energy loss for a relativistic ion passing through matter. The equation can be written as [357]:

$$-\left\langle \frac{dE}{dx} \right\rangle = kz^2 \frac{Z}{A} \frac{1}{\beta^2} \left[\frac{1}{2} \ln \frac{2m_e c^2 \beta^2 \gamma^2 T_{\max}}{I^2} - \beta^2 - \frac{\delta(\beta\gamma)}{2} \right] ; \tag{A.4}$$

where Z and A are the atomic number and atomic mass of the absorber, z is the charge of the incident particle, and $I \simeq 11.5Z$ eV is the mean ionisation potential. $T_{max} = 2m_e c^2 \beta^2 \gamma^2 / [1 + 2\gamma m_e / M + (m_e/M)^2]$ is the maximum kinetic energy that can be imparted to an electron in a single collision, $k = 4\pi N_A r_e^2 m_e c^2$, and β and γ are the conventional relativistic factors. $\delta(\beta\gamma)$ is a density correction term. Equation A.4 overestimates the experimentally-achieved range by a few percent [358] but is used to produce the approximate estimates presented below.

In order to use the Bethe-Bloch equation to estimate the range of an ion beam, equation A.4 must be integrated over the path of an ion until it loses most of its initial kinetic energy. A

Table A.8: Specifications for the ITRF linear accelerator option, based on the AVO-ADAM LIGHT prototype commissioned at CERN between 2015 – 2019 [326]. Indicative beam parameters are given for the end of each machine section.

Parameter	**Value**			
Total Length [m]	9.60			
Repetition Rate [Hz]	200			
Min. Pulse Length [μs]	0.50			
Max. Pulse Length [μs]	2.50			
Machine Section	**LEBT**	**RFQ**	**SCDTL**	**CCL**
Number of Modules	1	1	4	2
RF Frequency [GHz]	-	0.75	3.00	3.00
Output Beam Energy [MeV]	0.04	5.00	37.5	52.9
Beam Current [μA]	250	50	45	40
Transmission [%]	-	20	90	90

more straightforward estimate can be obtained using the Amaldi approximation [359]:

$$R_{\text{water}} \simeq 4250\,\text{mm}\,\frac{A}{Z^2}\left(\frac{E_k}{m_p c^2}\right)^{1.82}\;; \tag{A.5}$$

where E_k is the total initial kinetic energy of the ion; this approximation is a refinement of the well-known Bragg-Kleeman relationship [360].

Figure A.10 shows the ranges of $^4He^{2+}$ and $^{12}C^{6+}$ ions with initial energies up to 100 MeV/u. As noted earlier, the extraction energy of the proposed synchrotron has been defined so that carbon ions will penetrate up to 20 mm in water. This provides increased flexibility in user experiments, and may enable *in vivo* experiments with small animal models.

A.4.2 Dose rates for protons

The achievable dose rate depends on the number of ions per spill, repetition rate, beam energy, field size and depth into which the ions are delivered. To illustrate the likely dose rates that may be obtained, two situations were considered:

(a) Target volume with a 3×3 cm field size, extending from a depth of 0–1 cm to enclose a 9 cm^3 volume; and

(b) Target volume with a 1×1 cm field size, extending from a depth of 0–1 cm to enclose a 1 cm^3 volume.

For simplicity, we follow the method outlined in [361]. The basis of this method is to note that the total deposited energy is determined by the number of ions in a spill and by the kinetic

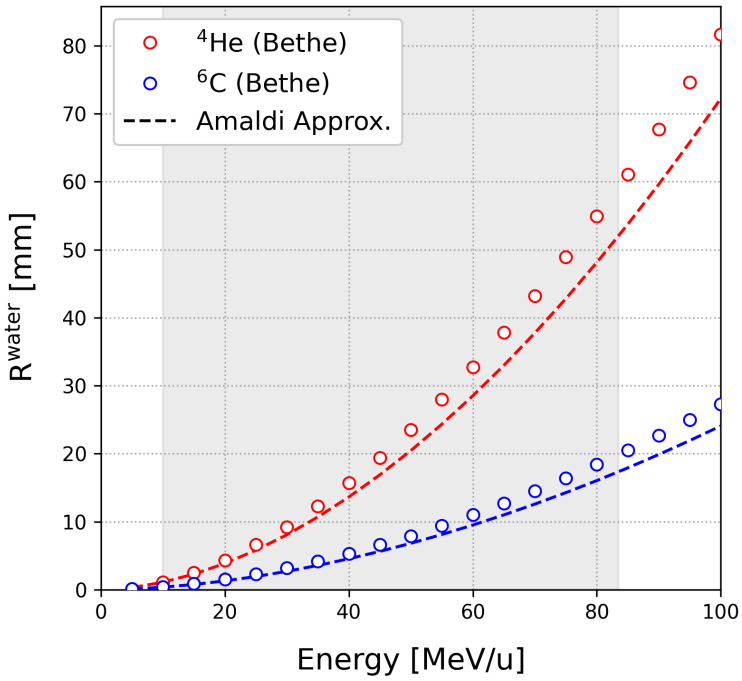

Figure A.10: Penetration depth of $^4He^{2+}$ and $^{12}C^{6+}$ ions in water, as a function of initial beam energy. Penetration depths were calculated analytically using the Bethe-Bloch equation and the Amaldi approximation. The shaded region indicates the energy range of the proposed synchrotron design.

energy of each ion. Assuming that the dose is uniformly deposited over the volume using a spread-out Bragg peak (SOBP) approach, the extraction energy is adjusted for each depth layer to position a Bragg peak at that depth. There will be some additional dose deposited outside the target volume due to multiple Coulomb scattering, but this is a small proportion of the overall energy carried by the incident ions.

Using the Amaldi approximation, equation A.5, for a proton beam to reach a depth of a 10 mm requires a beam energy of 33.7 MeV. The energy required to place a Bragg peak midway through the depth range, i.e. at 5 mm, is approximately 23.1 MeV. Therefore, in this case, 23.1 MeV is used as an estimate of the average energy deposited by a proton within the target volume; 23 MeV is approximately 3.7 pJ per proton.

Table A.9 lists indicative dose rates for the ITRF synchrotron option (section A.2), linear accelerator option (section A.3), and the baseline LhARA design. The leftmost column shows the dose rate estimates that may be obtained from the synchrotron, assuming that protons are extracted using the RF-KO technique (see section A.2.5). With an estimated 5×10^{10} protons per spill, each synchrotron cycle would deposit around 0.184 J. In a 90 mm^3 volume, this corresponds to a dose of 20.5 Gy per spill. Assuming that complete beam extraction is achieved within 100 ms, this corresponds to a dose rate of 205 Gy/s over 100 ms, or a time-averaged dose rate of 20.5 Gy/s over multiple extraction spills at a rate of 1 Hz.

A similar estimate can be made for the smaller target volume (b). The same 0.184 J deposited energy within the smaller volume gives nine times the dose, around 184 Gy per spill. A 100 ms extraction duration would therefore achieve a dose rate of 1840 Gy/s, and a time-averaged dose rate of 184 Gy/s over multiple spills.

The estimated dose rates for protons delivered to the target volume (a) are shown for each accelerator option in figure A.11. The instantaneous dose rate is calculated over the duration of a synchrotron spill or linac pulse, while the time-averaged dose rate is aggregated over many machine cycles. Figure A.11 shows the dose rates that can be achieved with the synchrotron using either resonant extraction (section A.2.5) or single-turn extraction. Similarly, dose rates for the linac option using either the minimum (0.5 μs) or maximum (2.5 μs) pulse length. Changing the extraction mode of the synchrotron only affects the instantaneous dose rate, whereas varying the linac pulse length affects only the time-averaged dose rate.

Operating the synchrotron in a fast (single-turn) extraction mode achieves similar instantaneous dose rates to the baseline LhARA design (of order 10^8 Gy/s). However, while the average dose rate from the synchrotron is limited by its cycling rate (and therefore, the ramp rate of the synchrotron magnets), the LhARA FFA can operate at much higher repetition rates. To illustrate this, figure A.11 includes dose rate calculations for a speculative, future operating mode, in which the LhARA ion source is driven at 1 kHz.

A.4.3 Dose rates for ions

Similar estimates of the achievable dose rates can be made for heavier ions. In the following, estimates are reported for $^4He^{2+}$ and $^{12}C^{6+}$ ions incident upon water volumes (a) and (b) defined above. Helium ions of 23.1 MeV/u kinetic energy have a Bragg peak at 5 mm, while 33.7 MeV/u is needed to reach a depth of 10 mm. Using the same method used for proton beams, but accounting for the lower number of extracted ions, the dose per spill using $^4He^{2+}$ ions is somewhat greater than it is for protons (see table A.9). Carbon-ion dose rates can be calculated the same way; despite the far lower number of ions per spill, the increased kinetic energy carried by each carbon ion means that the dose rate is comparable to that of protons.

Figure A.12 shows the estimated dose rates for each accelerator option, assuming that $^{12}C^{6+}$ ions are delivered to the target volume (a). As in figure A.11, dose-rate estimations are included for both synchrotron extraction modes, and for a speculative 1 kHz LhARA operating mode.

Table A.9: Comparison of dose rates for the synchrotron option (section A.2) using either resonant or single-turn extraction, the linear accelerator option (section A.3, and the baseline LhARA design. Dose rates are estimated for the two indicative volumes (a) and (b) as described in the main text.

Option	**Synchrotron**						**Linac**	**LhARA**	
Extraction Mode	Resonant			Single-turn			-	-	
Particle Species	p^+	$^4He^{2+}$	$^{12}C^{6+}$	p^+	$^4He^{2+}$	$^{12}C^{6+}$	p^+	p^+	$^{12}C^{6+}$
Median Ion Energy [MeV/u]	23.1	23.1	42.2	23.1	23.1	42.2	23.1	23.1	42.2
Ions per Pulse [10^9]	50.0	20.0	1.50	50.0	20.0	1.50	0.25	1.00	0.08
Pulse Duration [μs]		10^5		0.37	0.37	0.28	1.0	0.007	
Repetition Rate [Hz]	1.00	0.83	0.67	1.00	0.83	0.67	200	10	
Target Volume (a)									
Dose per Pulse [Gy]	20.5	32.8	13.5	20.5	32.8	13.5	0.10	0.41	0.75
Dose Rate (Pulse) [Gy/s]	205	328	135	5.6×10^7	9.0×10^7	4.9×10^7	1.0×10^5	5.9×10^7	1.1×10^8
Dose Rate (Average) [Gy/s]	20.5	27.2	9.04	20.5	27.2	9.04	20.5	4.10	7.49
Target Volume (b)									
Dose per Pulse [Gy]	184	295	121	184	295	121	0.92	3.70	6.74
Dose Rate (Pulse) [Gy/s]	1840	2950	1210	5.0×10^8	8.1×10^8	4.4×10^8	9.2×10^5	5.3×10^8	9.6×10^8
Dose Rate (Average) [Gy/s]	184	245	81.3	184	245	81.3	184	36.9	67.4

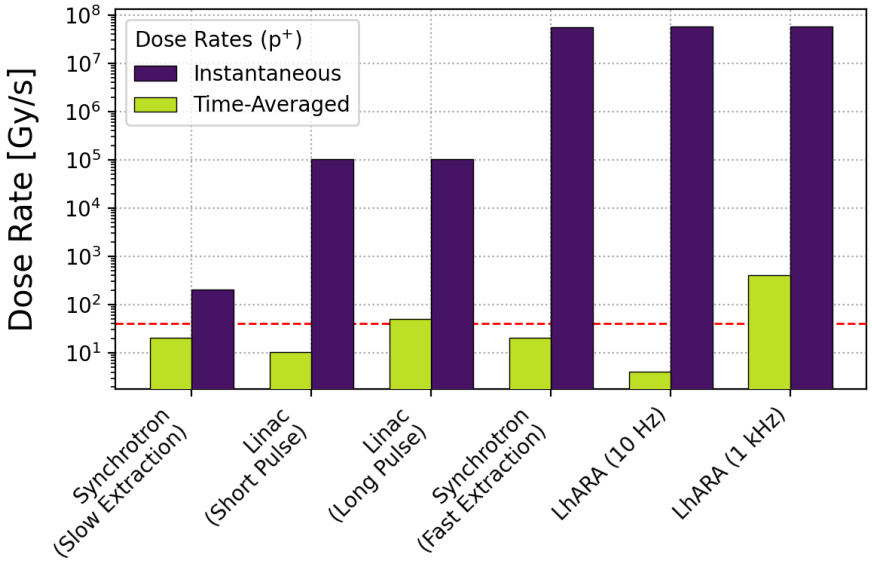

Figure A.11: Indicative dose rates for protons delivered by the synchrotron option (section A.2), the linear accelerator option (section A.3), and the baseline LhARA design. The options are ordered from left to right according to their instantaneous dose rates. The dashed red line indicates the threshold for FLASH dose rates $\gtrsim 40\,\mathrm{Gy/s}$).

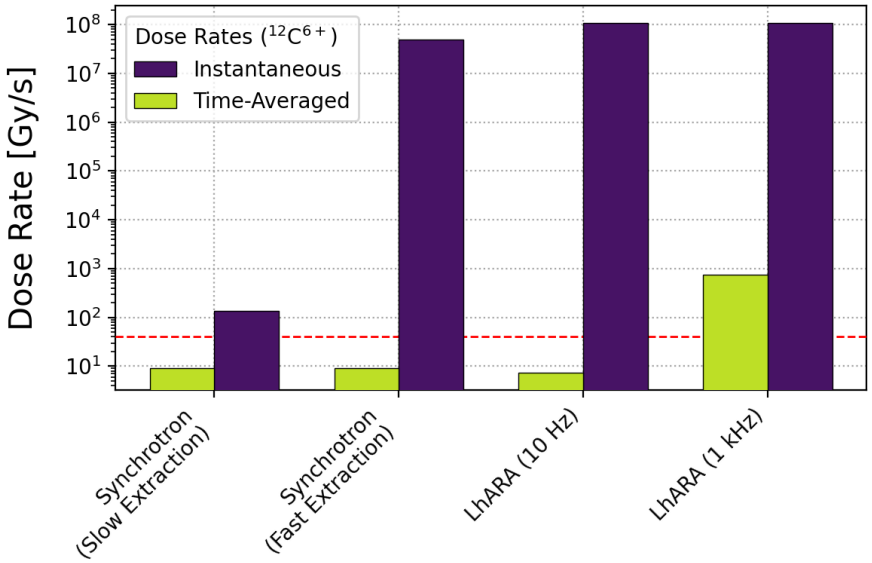

Figure A.12: Estimated dose rates for carbon ions ($^{12}C^{6+}$) delivered by the synchrotron option (section A.2) and the baseline LhARA design. The options are ordered from left to right according to their instantaneous dose rates. The dashed red line indicates the threshold for FLASH dose rates ($\gtrsim 40\,\mathrm{Gy/s}$).

A.4.4 Dose rates discussion

Comparing the estimated dose rates from the different accelerator technology options considered in this study, table A.9, indicates that a conventional accelerator is capable of delivering comparable or greater time-averaged dose rates than the plasma accelerator option exemplified by the LhARA design, with instantaneous dose rates which are nearly as great. However, the key advantage of a plasma option is the ability to achieve a very much shorter pulse duration, here perhaps as much as a hundred times shorter than any conventional technology, in an arbitrary time structure. It is this shorter pulse duration and arbitrary time structure that will enable different experimental regimens applicable to fundamental radiobiology.

A.5 Power requirements

Estimates of the power requirements of the ITRF synchrotron and linear accelerator options (sections A.2 and A.3) are presented below. Since it is beyond the scope of this work to produce a detailed technical design for either option, the estimates are based on simple scaling arguments and reference designs from existing accelerators. In each case, the power requirements of the accelerator in isolation are obtained, i.e., the power requirements of the beamlines serving the end stations and auxiliary services are not considered. As discussed in section A.1.1, the main parameters for each option were chosen to provide a direct comparison against the baseline LhARA design. It is therefore expected that the power requirements of components other than the accelerator itself will remain broadly similar to those outlined in table B.4.

A.5.1 Synchrotron powering

The power requirements of the synchrotron magnets were estimated by scaling a variety of existing, well-documented designs of magnets present in the CNAO [333, 335, 337], SESAME [334] and ELENA [330] synchrotrons, and the European Spallation Source (ESS) [336]. Each reference design was scaled based on its nominal magnetic field, aperture size, and effective magnetic length. Table A.10 lists the estimated power consumption for each family of magnets in the synchrotron lattice (see figure A.3). In general, the power estimates from different reference designs agree to within a few per cent; the values in table A.10 reflect the average for each set of estimates.

As described in section A.2.6, the synchrotron magnets continually cycle between a range of magnetic fields at a rate of around 1 Hz. The average power consumption of the magnets is therefore determined both by their peak power and by the average time spent in each of the synchrotron's main operating modes (see table A.7). To allow a plausible power calculation, we assume that the synchrotron will spend around 12 hours per day delivering 50 MeV proton beams, with the remaining time divided equally between $^{4}He^{2+}$ ions and $^{12}C^{6+}$ ions. The time-averaged values in table A.10 therefore reflect the power dissipated by the magnets over a full day of typical operation.

As described in section A.2.3, the synchrotron is filled from a conventional injector comprised of a 352 MHz radio-frequency quadrupole (RFQ) and two drift tube linac (DTL) tanks. For the purposes of the power calculation, it is assumed that the injector RF stations are equipped with modern solid-state power amplifiers, with an efficiency of around 60%. Consistent with the NIMMS $^{4}He^{2+}$ synchrotron, the total power requirement of the injector is estimated to be around 40 kW. This is a small improvement over the injector linacs of the HIT and CNAO facilities [362], which dissipate around 66 kW of power during normal operation [350].

As discussed in section A.1.2, the synchrotron RF system is based around a single wide-band cavity loaded with magnetic alloy cores. To estimate the average power dissipated by the cavity, we use the simple model described in Shi and Irie (2016) [363]. We assume the cavity geometry

Table A.10: Estimated power requirements of the ITRF synchrotron option (see section A.2). Power estimates for the synchrotron magnets and RF cavity are based on simple scaling arguments as described in the text.

Component	Count	Peak Power [kW]		Average Power [kW]	
		Each	Total	Each	Total
Synchrotron Magnets					
Dipole Magnets	6	35.4	212.2	6.81	40.9
QF1 Quadrupoles	6	1.27	7.62	0.24	1.47
QF2 Quadrupoles	3	1.94	5.82	0.37	1.12
Sextupole	1	0.08	0.08	0.02	0.02
Other Subsystems					
Injector Linac		-	-	-	40.0
Synchrotron RF Cavity		-	-	-	3.42
Vacuum Pumps and Beam Instrumentation		-	-	-	10.0
Cooling (+30%)		-	-	-	29.1
Grand Total					**125.9**

is similar to that of the ELENA synchrotron [330], with two magnetic alloy cores placed on either side of the accelerating gap. The cavity has a frequency range of 1.0–5.5 MHz, with a maximum gap voltage of around 700 V. Based on these parameters, the RF system would dissipate an average power of 3.4 kW; this is broadly consistent with the RF system of the CNAO synchrotron [350].

Following the example of the NIMMS $^4He^{2+}$ synchrotron design [325], we estimate that vacuum pumps and beam instrumentation will dissipate around 10 kW on average. Finally, an additional 30% has been added to the values in table A.10 to account for the power requirements of the cooling system. The total average power over 24 hours required by the synchrotron and its injector is therefore around 74 kW.

Table A.11: Estimated power requirements of the ITRF linear accelerator option (see section A.3).

Parameter	Value		
Machine Section	**RFQ**	**SCDTL**	**CCL**
Number of Modules	1	4	2
Pulsed RF			
Repetition Rate [Hz]	200	200	200
Pulse Length [μs]	5.0	5.0	5.0
Duty Factor	0.1%	0.1%	0.1%
RF Power			
Peak Power [MW]	0.40	2.09	2.21
Average Power [kW]	0.89	2.09	2.21
Other Losses			
Modulator Efficiency		45%	
Total Average Power [kW]	0.89	18.58	9.82
Cooling (+30%) [kW]	0.27	5.57	2.95
Subtotal	**1.16**	**24.2**	**12.8**

A.5.2 Linear accelerator powering

Table A.11 lists the estimated power requirements of the ITRF linear accelerator option. The peak RF power required by each module is based on operational experience with the AVO-ADAM LIGHT prototype, running at its maximum beam energy of 52.9 MeV [326]. For the purposes of the power calculation, we assume that the linac is operated at a fixed repetition rate of 200 Hz, with an RF pulse length of 5 μs. In this operating mode, the total power dissipated by the RF modules is approximately 38.1 kW.

Notably, the average power required by the linear accelerator option is significantly less than the synchrotron option. This reflects a key advantage of high-frequency linear accelerators; since the LIGHT prototype operates at a primary RF frequency of 2.998 GHz (compared to the CNAO injector at 216.8 MHz), the accelerating cavities have much higher shunt impedances [364]. This allows each cavity to generate a stronger accelerating gradient at an equivalent power, leading to reduced power requirements for the facility as a whole.

The maximum proton beam energy of the AVO-ADAM LIGHT prototype is significantly lower than that of the ITRF synchrotron option (105.5 MeV). As discussed in section A.3, the maximum beam energy can be increased by adding additional CCL modules; however, this will also increase the power requirements. Based on the values in table A.11, a linac with 8 CCL modules and a maximum proton energy of ~ 100 MeV would require an average power of approximately 76.4 kW.

APPENDIX B

Infrastructure and costing

B.1 Engineering and infrastructure

B.1.1 Infrastructure

The building and technical infrastructure will require careful planning, design and implementation to ensure the facility delivers on its challenging scientific objectives and provides accommodation that inspires scientific research. Overall, success requires an integrated approach to the high-power laser, target, capture, matching and energy selection of ions, accelerator, end stations, control rooms, building, services, staff and user needs, such as preparation laboratories, offices, meeting rooms and amenities that create a successful research environment.

To develop the requirements, planning and design, the needs of all stakeholders must be included from an early stage of the project to achieve the desired outcome. This section describes the progress and status of the conceptual design of the building and its contents.

Particular attention must be paid at all stages of the design and construction of the building and technical infrastructure to ensure that the challenging performance of the facility can be achieved. The need for equipment stability will be crucial, involving the stringent control of vibration, floor stability and environment control in key areas. The vision is to construct a new purpose-built energy-efficient facility in terms of its design, construction, operation and decommissioning.

The facility concept design floor plan is shown in figure B.1. The design has been driven by the science requirements. Proton and ion beams are generated when a high-power Ti:Sapphire laser impacts a target. Just after the target, Gabor lenses capture and provide matching and energy selection of the proton or ion beams that are then delivered to the Stage 1 experimental areas. Particles are accelerated to the full energy (127 MeV protons or ion beams 34 MeV/u) needed for the Stage 2 experimental areas using a fixed-field alternating-gradient (FFA) accelerator that is injected from the Stage 1 plasma accelerator. Beam transport from the FFA to the *in vivo* experiments is performed by a high-energy beamline.

There are three experimental end stations (see figure B.2), each with a local control room; two end stations will be used for *in vitro* experiments, which are located on the accelerator complex roof at the end of vertical beamlines. The low-energy *in-vitro* end station is served by 15 MeV protons. The second (high-energy) *in-vitro* end station and the *in-vivo* end station use the output of the Stage 2 FFA, which delivers proton beams with energy in the range 15–127 MeV and ions, e.g. carbon, with energies in the range 5–34 MeV/u. The *in-vivo* end station is located on the ground floor in Area 6.

The footprint has been estimated to be 72 m × 32 m of which 57 m × 32 m is the main building footprint next to a 15 m × 32 m fenced outside pen to locate the water cooling chillers, water storage tank, water pumping and transformers (figure B.3). An approximate estimate for these systems has been conducted to inform the cost model; more exact system capacities will be developed as the project develops. The water-cooling plant location has been chosen to be close to the heat exchangers and accelerator equipment with a high cooling load. Similarly, two transformers and the main electrical switchboard are located close to each other to reduce the length and cost of interconnecting cables. A 2.5 m wide access around the circumference of the

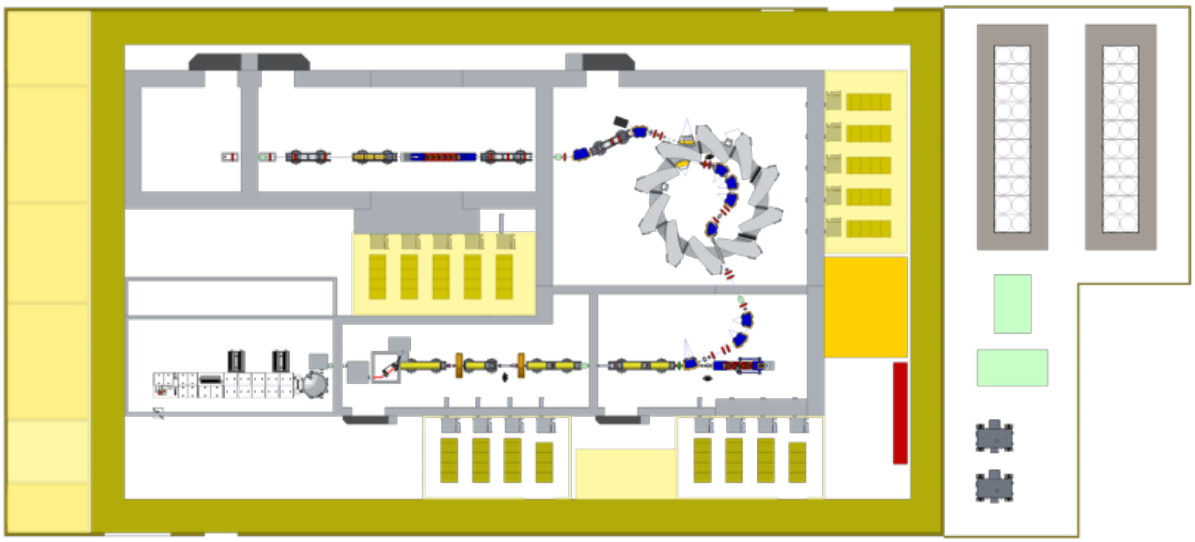

Figure B.1: Facility ground floor plan.

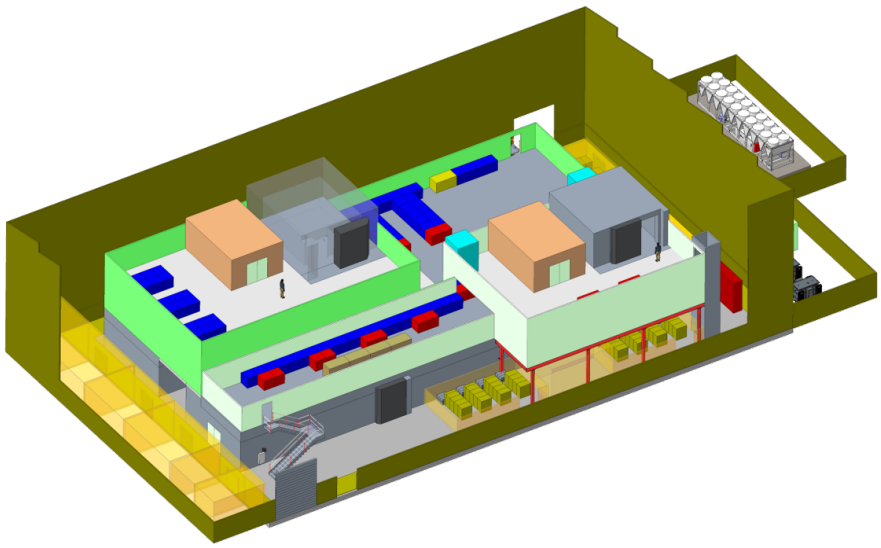

Figure B.2: End stations and research area above the accelerator complex on the 1st floor.

accelerator is proposed to provide equipment access by fork lift.

A cross-section through the building is shown in figure B.5. The overall height is estimated to be 14 m, which allows the installation of an overhead crane to install and decommission the facility. Lifting solutions will also be required inside the radiation enclosures for installation, maintenance and decommissioning. For installation, maintenance and decommissioning of the vertical beamlines, permanently-installed platforms next to the accelerator components are envisaged to provide a safe and efficient working environment. Sliding shield doors are shown in the figures, but labyrinth access will also be considered during the technical design stage.

A saw-tooth roof construction is proposed, comprising a series of ridges with dual pitches on either side. The steeper surfaces at ∼70° are envisaged to have double-glazed windows to admit natural light. The shallower surfaces at ∼35° are proposed for the installation of solar panels facing south, to receive the most direct sunlight.

Two sets of stairs and a lift are proposed for people and light equipment access. Heavy items may be lifted to the accelerator complex roof with the overhead crane.

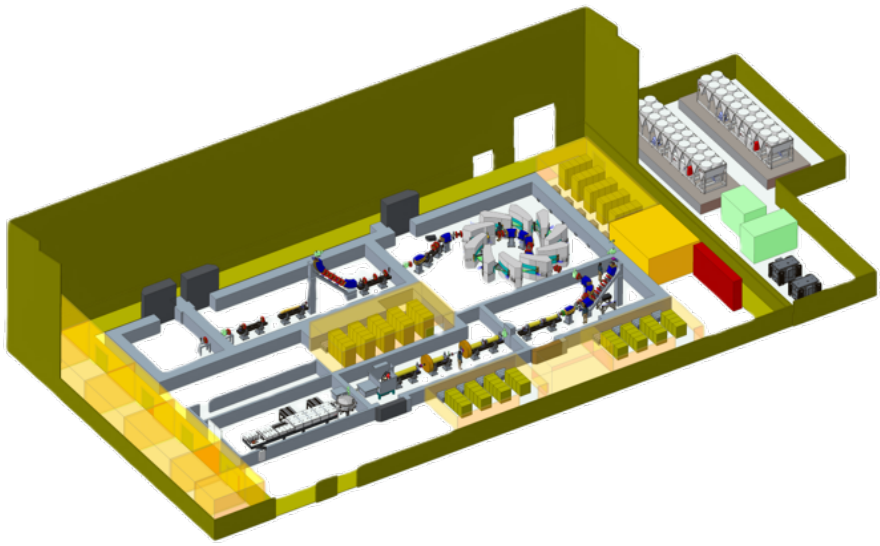

Figure B.3: Accelerator complex with shielding cut away to schematically see equipment.

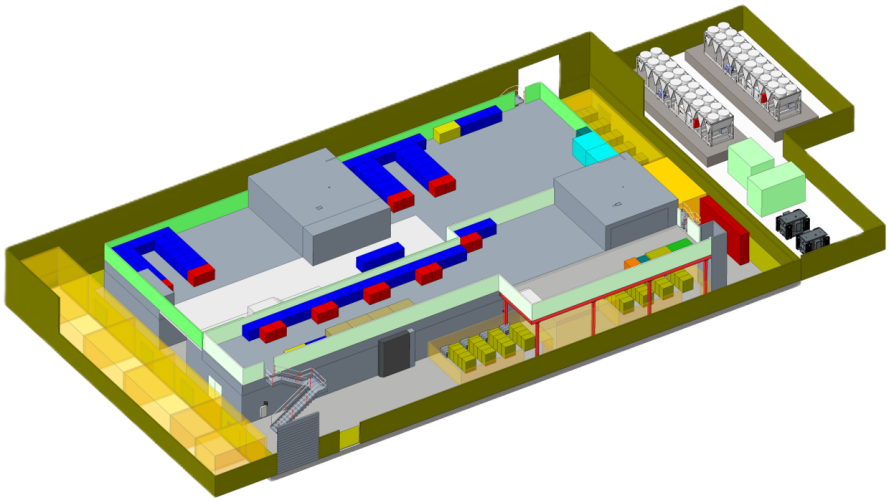

Figure B.4: Water cooling plant and transformer(s) may be seen in outside pen.

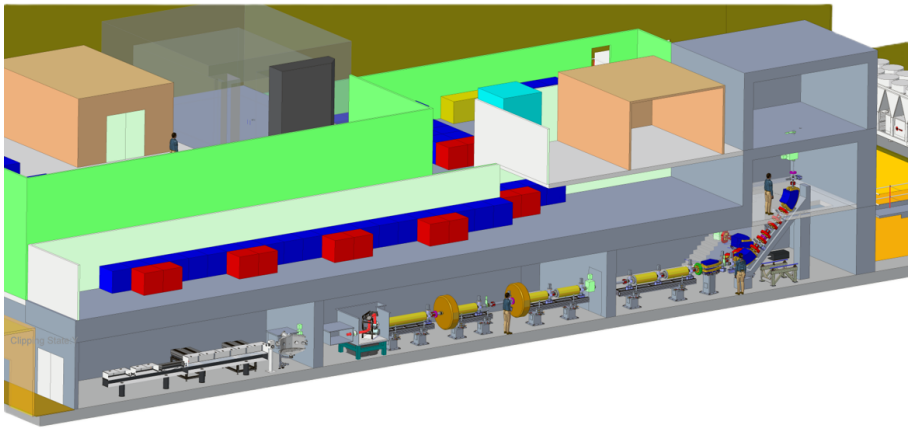

Figure B.5: Cross-section through the facility.

For the accelerator systems shown on the ground floor, 60 power supply, control and instrumentation racks are currently estimated to be needed, as shown in the facility ground floor plan in figure B.1 and table B.1. The estimate will be updated as a more detailed technical specification is generated. The racks will be located in three thermally-insulated air-conditioned rooms to minimise dust and to provide temperature control for the stability of the power supplies.

It is proposed that the laser room will contain an internal technical corridor to house power supplies to reduce the heat dissipation to the room, which has a stringent temperature stability requirement of 20–22°C to better than ±1°C, monitored at less than 2 m from the optical tables. The laser room also requires a humidity of 40–50%, monitored at less than 2 m from the optical tables, and cleanliness to ISO 7 class [365].

B.1.2 Sustainability contributing to Net Zero by 2040

Sustainability aspects of the facility during the planning, design, construction, operation and decommissioning will be crucial to the success of the project and contribute to the green transformation for the UK science estate [366]. The UK Government has committed the nation to achieving net-zero emissions by 2050. This commitment is embodied in international agreements, legislation and policies. The Paris Agreement of COP21 commits the UK to reducing greenhouse-gas emissions by at least 68% by 2030 (compared to 1990 levels). These targets are enshrined in UK Nationally Determined Contributions. The Climate Change Act (2008) sets legally-binding targets overseen by the Climate Change Committee. The UK Net Zero strategy (2021) lays out how emissions reductions will be achieved. These in turn determine policies for UK-funded research and infrastructure development that will, for example, include all future UKRI-funded infrastructures and research. Importantly, STFC aims to reach net-zero carbon emissions by 2040, which is within the timescales of the ITRF facility operation. STFC's goals are laid out in the STFC Environmental Sustainability Action Plan, which includes an energy hierarchy framework to reduce its emissions burden. An accompanying Energy Roadmap and Decarbonisation Plan has been published. STFC is currently developing a suite of guidelines and methods for sustainable design, engineering, procurement and manufacture of its systems.

Technology choices to minimise materials use, power consumption and cooling requirements will be vital. Key examples of technology choices for the accelerator systems that will reduce the carbon footprint of the facility both in construction and in operation, are the plasma lenses in the Stage 1 beamline and the fixed-field accelerator (FFA) that will be used to boost the energy in Stage 2. A geothermal groundwater cooling system is included in the cost model. This will enable efficient heat transfer by recovering heat stored naturally in groundwater or aquifers; the facility's cooling water will pass through heat pumps to yield its low-grade heat

Table B.1: Ground floor power supply, control and instrumentation rack rooms.

Parameter	Equipment	No. of Racks
1	Low Energy Line	20
2	Fixed Field Accelerator	20
3	High Energy Line and *In vivo* end station	20

Table B.2: Laser room size.

Parameter	Description	Size m×m
1	100 TW laser room	13.3×5.5

before being returned to the aquifer at a lower temperature. Solar panels on the saw-tooth building roof design are also proposed (see figure B.5).

Work is in progress to develop UKRI-STFC Sustainability Design Principles [367] that to date encompass:

- Cryogenics;
- Design for manufacture;
- Electrical;
- Sustainable radiation shielding; and
- Vacuum.

The ITRF building design included in the cost model complies with UKRI-STFC Sustainable Building Design Guide V3 [368], which adopts the RIBA Sustainable Outcomes Guide (RIBA, 2019) [369]. The RIBA Guide sets out eight key areas for sustainable performance and a clear process that must be followed for all building projects. By following the RIBA Sustainable Outcomes Guide, the sustainability approach aligns directly to the RIBA Plan of Work (2020) project stages [370]; the RIBA Plan of Work is an industry standard (first set out in 1963 but most recently updated in 2020) and is currently being used with all major new UKRI-STFC building projects. UKRI-STFC has also signed up to targets described in the RIBA 2030 Climate Challenge (RIBA, 2021).

These targets for building sustainability will be altered in future guideline iterations, but are adopted with the aim of achieving Net Zero by 2040. 'Net zero' for building is defined in the UK Government 'Net Zero Estate Playbook' [371] though only for energy in use; embodied carbon and whole-life carbon will be defined later. Due to the uncertainty in this topic, UKRI-STFC currently follows the following hierarchy of design:

- Reducing energy consumption through good design, especially a fabric-first approach and the selection of efficient plant and equipment;
- Installing low-carbon heating and ventilation options;
- Focus on control and benchmarking through a Building Management System to deliver and record continual improvement;
- Installation of renewable generation;
- Where suitable, use of bespoke and innovative technologies (e.g. heat and battery storage, demand-side management and artificial intelligence); and
- Achieving BREEAM [372] 'excellent' or better, as well as the specific targets set out in that standard.

The BREEAM standard is applicable to the building and its operational plant only, and excludes the impact of scientific equipment which will be considered separately. Work is underway within STFC to assess carbon emissions quantitatively during the construction and operation of accelerator facilities, and outcomes from that work will be reflected in future analyses of the emissions associated with the ITRF facility.

B.1.3 Radiation Safety

The Ionising Radiation Regulations 2017 (IRR17 [373]) requires employers to keep exposure to ionising radiation as low as reasonably practicable. Regulation 7 (IRR17) requires that consent is granted by the Health and Safety Executive (HSE) to carry out specified practices, one of which is (IRR17 7.1.d) the consent for the operation of an accelerator. The indicative list of information required to support an application for consent includes:

1. Responsibilities and organisational arrangements for protection and safety;
2. Staff competences, including information and training;
3. Design features of the facility and of radiation sources;
4. Anticipated occupational and public exposures in normal operation;
5. Safety assessment of the activities and the facility in order to:
    a) Identify ways in which potential exposures or accidental and unintended exposures could occur;
    b) Estimate, to the extent practicable, the probabilities and magnitude of potential exposures;
    c) Assess the quality and extent of protection and safety provisions, including engineering features, as well as administrative procedures; and
    d) Define the operational limits and conditions of operation;
6. Emergency procedures;
7. Maintenance, testing, inspection and servicing so as to ensure that the radiation source and the facility continue to meet the design requirements, operational limits and conditions of operation throughout their lifetime;
8. Management of radioactive waste and arrangements for the disposal of such waste, in accordance with applicable regulatory requirements;
9. Management of disused sources; and
10. Quality assurance.

The accelerator complex on the ground floor is proposed to be divided into 6 areas to establish flexibility during the construction, maintenance and operation of the facility. By segregating the controlled areas shown in figure B.1 and figure B.2, access to downstream rooms will be possible when ion beams are present in the upstream controlled areas. This flexibility will allow the project construction duration to be significantly reduced by allowing systems commissioning with beam and installation of downstream areas in parallel. An example is being able to operate the Stage 1 low-energy line while installing the Stage 2 fixed-field accelerator. To achieve that flexibility, radiation shutters will be required to cover each beam pipe aperture in the shielding dividing walls, the shutters interlocked to the access doors controlled within the personnel safety system.

Table B.3 shows the ground floor accelerator complex rooms. The 100 TW laser room is specified to be constructed with thermally insulated panels.

Areas 2 to 8 form the radiation-shielded enclosures. To reduce the volume of concrete, the implementation of composite shielding is being considered. Composite shielding consists of a concrete skin filled with magnetite aggregate. Such a solution has been used in the CALA facility [374], the design was based on previous constructions by Forster [375].

Table B.3: Facility room sizes.

Area	Description	Internal room size (m×m)
2	Target Room	9.4×5
3	Low energy line room	17×6
4	Fixed field accelerator room	14×10.8
5	High energy line room	18×5
6	*in vivo* end station	6×5
7	Low energy *in-vitro* end station	5.5×5.5
8	High energy *in-vitro* end station	5.5×5.5
9	Low energy *in-vitro* end station control station	6.8×3.4
10	High energy *in-vitro* end station control station	6.8×3.4

The construction technique provides significantly improved sustainability due to the reduction in the concrete required. A further development of this technique that is being considered would be to apply the composite approach to shielding blocks rather than *in-situ* casting of the concrete skin. Shielding blocks allow flexibility for cost-effective upgrades and simplification of staged installation and decommissioning. The ability to re-use shielding blocks many times on future facilities further improves sustainability and value for money after the lifetime of the proposed facility.

B.1.3.1 Designation of Areas

IRR17 [373] requires an area to be designated as a Controlled Radiation Area if a person entering that area is likely to receive an annual dose in excess of 6 mSv, or if they are required to follow special procedures intended to restrict their radiation dose or the effects of an accident. The radiation hazard inside the shielded enclosures will generally be negligible when they are not interlocked by the Personnel Safety system (although consideration must be given to components such as collimators and beam dumps, which have the potential for high levels of induced activity after the ion beam has been switched off). Adopting the model used at similar facilities in designating areas, Areas 2 to 8 in table B.3 will be designated as Controlled Radiation Areas on a permanent basis.

IRR17 defines a Supervised Radiation Area as one where it is necessary to keep the conditions of the area under review to determine whether it should be designated as Controlled, or where a person is likely to receive an annual dose in excess of 1 mSv. It is therefore proposed that the surroundings of the accelerator complex are designated as Supervised Radiation Areas, at least for an initial period, whilst environmental dose measurements are made in the surrounding areas within the facility building.

B.1.3.2 Personnel Safety System

The Personnel Safety System will be similar to those in operation at the existing UKRI-STFC facilities in that it will be compliant with IRR17, STFC Safety Code SC40, and is implemented to achieve the required level of risk reduction.

The implementation of interlocks is a complex process that needs to ensure the system achieves adequate levels of risk reduction. Whether this is mechanical or electrical, it is required to follow an interlock lifecycle model to manage the process and ensure consistency in the management of similar safety systems. The implementation of interlocks requires consideration and planning of many aspects, covering a range of areas that are applicable throughout the lifecycle.

There are alternative methods available to comply with the requirements for implementation of interlocks within STFC Safety Code SC40, either:

1. A suitable recognised international standard that covers the lifecycle phases associated with, as a minimum, safety requirements allocation through to decommissioning:

    a) IEC 61508 [376] (or sub-standards, i.e. IEC 62061, IEC 61511, etc.); or

    b) ISO 13849 [377] (With the addition of an IMP, see section 3.5);

2. A process that is equivalent to or better than that detailed within the recognised international standards applicable to interlocks lifecycle implementation.

The application of electrical interlocks is the subject of extensive and detailed guidance and standards, referred to as Functional Safety. The general benchmark of good practice is IEC 61508: Functional safety of electrical/electronic/programmable electronic safety related systems. Functional safety is the accepted term applied to the part of the overall safety of a system that depends on the correct functioning of electrical, electronic and programmable electronic (E/E/PE) safety-related systems and other risk-reduction measures. This would include any mechanical interlocks that contribute to the overall safety of such a system.

IEC 61508 has been used as the basis for industry-specific standards for functional safety, such as:

- IEC 61511: process industry [378]; and
- IEC 62061: machinery [379].

Other standards exist that do not follow this model but are also commonly used and accepted as best practice in industry, such as:

- ISO 138499 [377]: safety of machinery–safety-related parts of control systems.

As an extension to the implementation of functional safety, the use of the lifecycle model for the implementation of mechanical interlocks provides additional controls and consistency across the organisation.

STFC SHE Code 40 requires that a Risk Assessment as per STFC SHE Code 6 (Risk Management) has been carried out for the facility/system under consideration, and that the following inputs are therefore available for that facility/system:

- The Concept;
- The Overall Scope Definition;
- A Hazard and Risk Analysis; and
- Overall Safety Requirements, to reduce risk to a level acceptable to STFC.

Overall Safety Requirements Allocation, in particular, the extent to which the interlock system is required to contribute to the control of risk by reducing the probability of occurrence of the identified hazard(s).

B.1.4 Staged Construction

Site location has not yet been defined for the construction of the proposed facility, but it has been proposed that the facility may benefit from being built at a UKRI-STFC National Laboratory site to take advantage of existing facilities, multidisciplinary technical staff expertise, approved radiation site authorisation, and large electrical power capacity.

It is proposed that the construction of the facility be in 2 stages:

- Stage 1, providing beam to the low-energy *in-vivo* end station, including:
  a) The full building size
  b) The full fenced outer pen to house the water cooling systems and transformer(s)
  c) Laser room
  d) Radiation shielding for areas 1 – 3 and low-energy end station
  e) Laser, accelerator and end station technical systems for:
     - Laser-driven proton and ion source
     - Proton and ion capture section
     - Matching and energy selection section
     - Low energy abort line
     - Beam delivery to low-energy *in-vitro* end station
  f) 1st floor research area for Stage 1
  g) Low energy *in-vitro* end station systems
  h) Low energy *in-vitro* end station control room
  i) Rack room 1
  j) RF room
  k) Main switchboard
  l) Internal water plant room containing heat exchangers and pumping
  m) General technical services for the above-described systems, including electrical distribution, water cooling distribution, HVAC, compressed air and gases
  n) Accelerator control room, meeting room, cleanroom and general office.
  o) EPICs control system for the above systems
  p) Personnel safety system
  q) Two sets of stairs and a light-duty equipment lift to Level 1.

- Stage 2, delivering the full functionality of the facility, including:
  a) Accelerator and end station technical systems for
     - Fixed field accelerator
     - High energy extract line
     - High energy abort line
     - Beam delivery to high-energy *in-vitro* end station
     - Transfer line to the *in-vivo* end station
  b) Radiation shielding for: areas 4 – 6, high-energy *in-vitro* end station and *in-vivo* end station
  c) High energy *in-vitro* end station systems
  d) High energy *in-vitro* end station control room
  e) *in-vivo* end station
  f) *in-vivo* control room

g) *in vivo* experiments preparation room
h) 1st floor research area rearrangement for Stage 2
i) Rack room 2 and 3
j) General technical services for the above-described systems, including electrical distribution, water cooling distribution, HVAC, compressed air and gases
k) EPICs control system for the above systems
l) Upgrade to personnel safety system
m) Upgrade to accelerator control room
n) 3rd set of stairs to Level 1

B.1.5 Key Installation Milestones

The installation and commissioning of the ITRF systems will be coordinated so as to maximise the scientific output of ITRF. Thus, prior to the completion of construction, the goal will be to achieve the following scientific milestones:

Stage 1

- First demonstration of the capture of a laser-driven ion beam using a Gabor lens system;
- Demonstration of the energy selection capabilities of a Gabor lens system;
- Irradiation of cells with a laser-driven ion beam.

Stage 2

- Injection line to the FFA;
- Fixed Field Accelerator (FFA);
- Extraction line from the FFA and the transfer line to the *in-vivo* end station;

Figure B.6: Stage 1 floor plan.

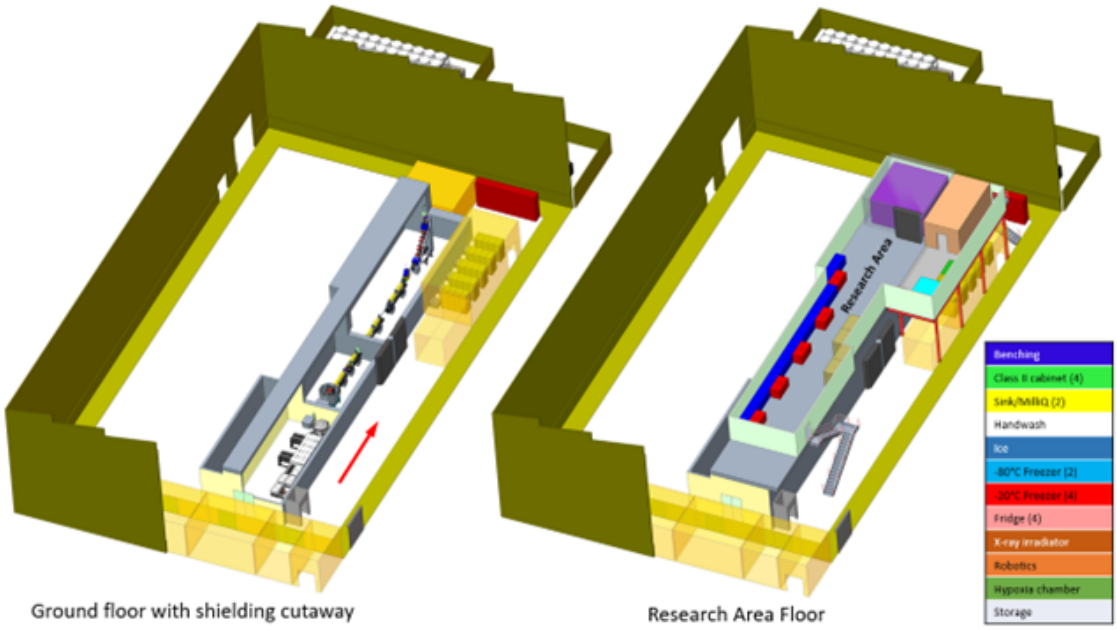

Figure B.7: Stage 1 construction.

- High-energy *in-vitro* arc;
- High-energy *in-vitro* end station; and
- *in-vivo* end station.

B.1.6 Stage 1 Engineering Concept

The engineering CAD model of the laser-driven ion source is in progress, as shown in figure B.8. The CAD model representation of the 100 TW Ti:Sapphire laser and compressor chamber has been provided by Amplitude based on the Pulsar 140 system [12]. However, no decisions have been made on suppliers of equipment at this stage of the project. The laser equipment is shown supported by 2 optical tables (support modules M1 and M2) followed by a compressor chamber (module M3). Figure B.9 shows a provisional representation of the target chamber internal components, which is a conceptual design to be developed over the next 18 months. A motorised vacuum valve has been introduced as an integral part of the nozzle assembly. The valve will allow the low-energy line vacuum region to be isolated from the target chamber vacuum region when the low-energy line is not in use, thereby minimising the risk of contamination of the downstream vacuum regions. Both horizontal and vertical laser-beam configurations have been studied. The vertical configuration, as shown, provides the best access and visibility around the target area. An idea being considered is to mount the 3^{rd} and 4^{th} optic in the chamber on a linear slide to create room between the target and the nozzle when operating at low energy to image the beam from the rear of the tape drive with a camera. The linear slide system would also create additional space for larger target configurations.

Modules labelled M4–M8 are independent support systems, and will be assembled, surveyed and tested prior to installation in the accelerator complex. Power supply, control and instrumentation racks will also be cabled to the modules in the pre-installation assembly area to test the racks and the control system. This proven methodology will solve as many technical issues as possible prior to installation, thus reducing the time taken for installation. Support, alignment and vacuum systems design is based on previous UKRI-STFC facilities. Module M9

is a representation of the 45° girder assembly. Permanently-installed working platforms next to module M9 are envisaged to provide safe and efficient working at height. Internal craneage will also be required in some areas.

B.1.7 Schematic Diagram

A draft schematic diagram of the facility is shown in figure B.10. A large format version with clearer visualisation of the required components is available [380]. A draft device naming convention has been established [381]. The device naming convention has the following benefits:

- Every device in the facility has a unique name;
- Names are used in an appropriate and consistent way;
- Duplicate names can be avoided;
- The function of a device can be derived from its name (and vice versa); and
- Consistency with good practice adopted on previous accelerators constructed and operated successfully.

For these reasons, it is proposed to introduce a formal device naming convention on the ITRF Control System. It is anticipated that the names will be used on the facility schematic, engineering drawings, in technical documents, control system display panels and in informal and formal discussions. The plan is to develop the schematic throughout the Conceptual Design Phase to capture all the equipment required that will inform the CAD model, cost model and schedule development.

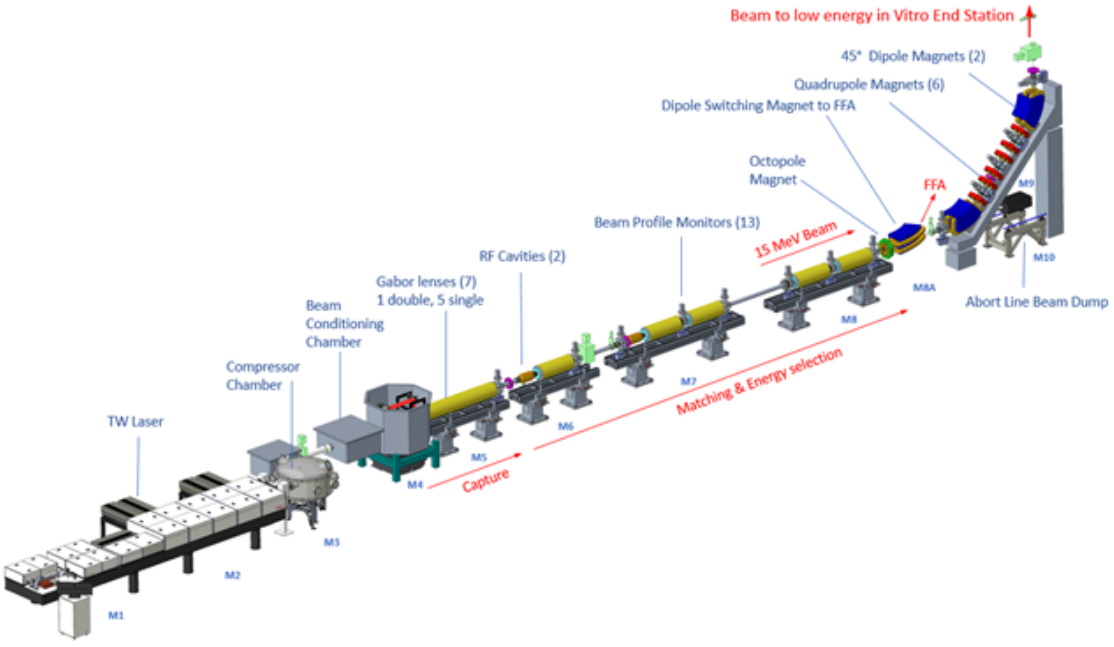

Figure B.8: Stage 1 engineering concept design.

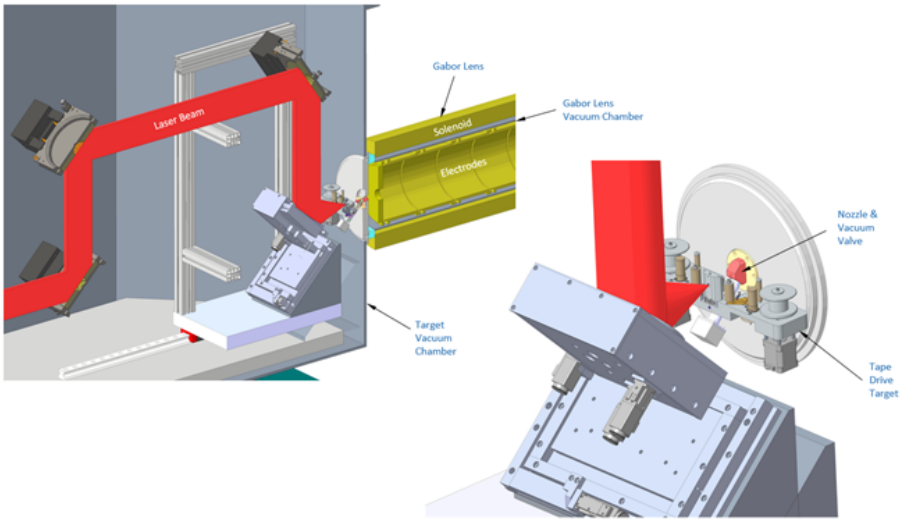

Figure B.9: Concept design of the Target, Conductance Nozzle and 1st Gabor Lens.

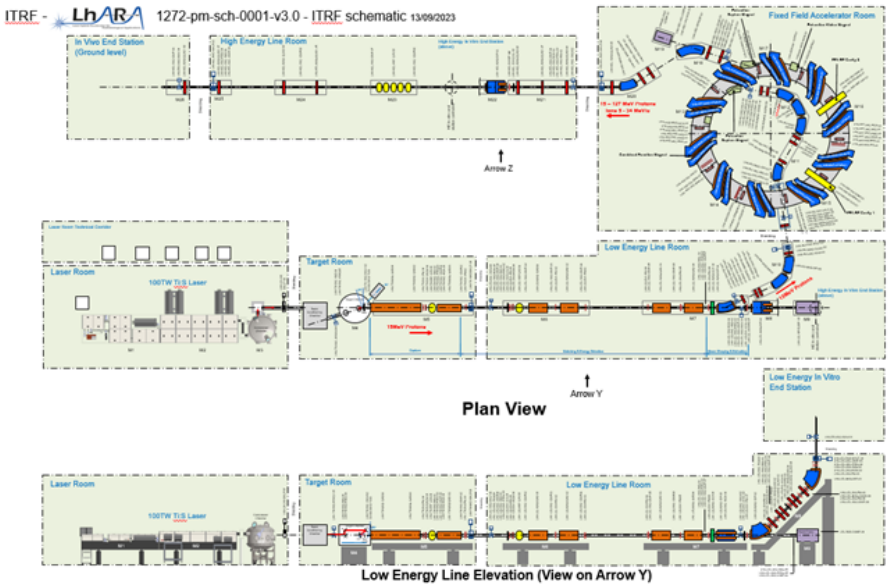

Figure B.10: Schematic diagram of the facility equipment (the representation of the FFA is to scale but does not reflect the design presented in Chapter 2).

B.1.8 Electrical Engineering

B.1.8.1 Electrical Equipment and Services

The number of racks broken down by the equipment served and the estimated power consumption are summarised in table B.4. There are 3 rack rooms proposed to be positioned around the accelerator, each capable of housing 20 standard racks; this even distribution of racks and the numerous local labyrinths minimises the cable lengths, improves energy efficiency and simplifies installation. The location of some equipment is restricted by cable length. The labyrinth design should consider cable routes inside the accelerator and ensure personnel access isn't affected; a possible alternative is to consider high-level cable management.

Although the overall estimated number of racks is 73, the available space in the rack rooms will remain fixed at 60 as it is anticipated that around 20 of the racks will be housed near specialist equipment. These include 4 racks associated with the laser—which needs a dedicated auxiliary room—and the 9 racks for RF systems that will probably be located in an accelerator or RF room. Pulsed power units are expected to be positioned next to the pulsed magnets themselves, to minimise design complexity.

Each rack room will house DC magnet power converter, vacuum, diagnostics, motion control, personnel safety and network equipment. It is envisaged that these rooms will be temperature-controlled at $\pm 1^{\circ}$ C, as this will assist reliable and stable operation. The racks will be mounted on support frames providing a minimum of 300 mm clearance to install cable management. A floating floor will enable easy access to rack equipment and allow the air conditioning to be channelled under the floor and up through the racks, ensuring effective cooling.

Gabor electron-plasma lenses are the baseline for beam transport in Stage 1. This choice is motivated in part by the low power consumption of a Gabor lens when compared to the equivalent solenoid. A conservative approach has been taken when considering the number of racks required for the low-energy line, which will be dominated by the racks' solenoid power converters, should the risk that the Gabor-lens solution can not be developed be realised. An equivalent space of 2 standard racks will be needed to accommodate each of the 90 kW solenoid power converters. The power requirements given below are the installed capacity assuming maximum powering of all systems; this will not occur during operation, and the average power of the accelerator will be significantly lower. The average power consumption of the facility will be determined later and included in the final Conceptual Design Report. The size of the low-energy rack room may need to be increased to house these large solenoid power converters, and rack positions will be dictated by restricted cable length and the substantial size of the magnet cables.

The energy efficiency of the power converters will dictate the rack layout and the heat loading within the rooms. It is highly likely that water cooling will be necessary. The physical size of the FFA and high-energy rack rooms will probably need to increase if the power levels estimated for the magnet power converters are confirmed. The magnet ratings have been scaled from existing magnet designs, with specific reference to similar medical accelerators. The performance of the magnet power converters has not yet been assessed, but it is assumed that the required stability, reproducibility and resolution can be achieved using standard commercially available units. If degaussing or bipolar operation is specified, this will increase the physical size of units and introduce additional cost and technical complexity.

The specification of the pulse power converters of the FFA will be a challenge due to the small circumference (and hence short orbit time) of the accelerator. The low-energy injection septum and kicker power converters should be feasible, although the effects on the circulating particle bunches must be minimised. The fall time of the kicker could be critical to ensure the magnetic field does not affect the circulating bunches, but the low energy will reduce the nominal current required. The rating for the extraction septum and kicker will need to be assessed and optimised, as this could introduce a significant challenge given the extraction

Table B.4: Estimated maximum power consumption and rack quantities; average power loading during operation will be much lower. The figures given here also assume the use of Gabor lenses in the capture line (Line 4 of the table). If an alternative solution based on solenoids were adopted instead, the power requirement would increase by an additional 850 kW.

	Technical Equipment	**No of racks**	**Power/rack kW**	**Total load kW**	**Water cooled kW**	**HVAC kW**
1	Laser	4	12	48	31	17
2	Target	4	2	8	0	8
3	Radio Frequency	5	n/a	186	170	16
4	Gabor Lenses	7	n/a	56	0	56
5	Pulse Power	4	n/a	14	0	14
6	Power Converters (Magnets)	12	n/a	1411	1270	141
	Controls and Instrumentation					
7	Laser	n/a	n/a	0		0
8	Vacuum	6	2	12		12
9	Diagnostics	9	1	9		9
10	Personnel Safety	3	1	3		3
11	Network/Control	3	1	3		3
12	RF Control and Auxiliaries	3	2	6		6
13	Motion Control	6	2	12		12
14	End Stations	n/a	n/a			
	Total Racks and Power (kW)	66		1768		
	Services					
15	Lighting			10		10
16	Climate Control			133		
17	Chiller System			294		
18	Water Pumps			73		
19	Compressed Air			50		
20	Offices/Laboratories			15		15
	Total Ancillary Load (kW)			577		
	Total Power (kW)			2345	1471	332

energy, circumference and the extraction angle. If the kicker needs to be fully energised within the time taken for the beam to complete one orbit, the current in the magnet will need to reach its nominal value within approximately 5 ns. Once the pulse power converter specifications are developed, a review of existing pulse-power technology can be initiated, as this could impact on the final lattice design.

B.1.8.2 Electrical Distribution

The estimated total peak power consumption for the facility is 3.5 MW, which is comparable with other research medical and clinical accelerators of similar energy. The average power consumption will be determined later, and is likely to be significantly smaller; the average powering will also significantly influence the carbon budget of the facility. Given the predicted power consumption, ideally, the chosen location for the facility will need to have an existing high-voltage (HV) sub-station with sufficient spare capacity. However, it is possible to locate the facility on a green field site, but a substantial increase in building cost will be incurred.

The facility will need to be supplied by at least two transformers (for cost purposes), each rated at 2.5 MVA. Although each transformer is not sufficiently rated to provide the total estimated power consumption, there will be enough capacity to operate at the reduced values indicated above. Fault analysis and maintenance is an important consideration when designing the distribution scheme, along with segregation of supplies and conducted harmonics. The electrical infrastructure should mitigate these factors by increasing the number of transformers to offer a minimum of $n + 1$ redundancy; this means potentially installing 3 transformers rated at 2 MVA, with any 2 transformers capable of supporting the entire facility. There must be dual HV incoming supplies connected to local HV ring-main units, with each one feeding a transformer. This philosophy should be cascaded throughout the low-voltage (LV) distribution to ensure that the failure of one circuit does not result in prolonged periods of downtime.

The ITRF will have numerous non-sinusoidal loads such as DC magnet power converters, RF modulators and ion pump power supplies. The harmonic currents generated from such equipment can have an adverse effect on other equipment connected to the distribution system. Ideally, any issues from this should be dealt with at the equipment level. Wherever the facility is built, existing harmonic levels will need to be measured and included in any calculations to ensure compliance with legislation.

Segregation of the mains supply is required to protect sensitive equipment from electrical disturbance caused by, for example, harmonics, sudden changes to load demand, and inrush currents. The point of common coupling between these systems and the sensitive equipment becomes critical and should be considered when designing the electrical infrastructure.

B.1.8.3 Earthing Arrangements

The earthing (or grounding) scheme proposed for ITRF must guarantee the correct operation of power converters, vacuum systems, diagnostic instruments and motion control equipment, and also ensure compliance with safety and EMC requirements from applicable standards.

The primary goal of an earthing system is to ensure personnel safety and protection of installations against damage. Two critical phenomena are lightning and power system faults. These can give rise to the circulation of large currents, which might create hazardous voltages in installation structures. The task of the earthing system in fault conditions is to be a path to the earth for currents, while maintaining minimum voltage differences between any two points of the installation.

The secondary goal of an earthing system is to serve as a common voltage reference and to contribute to the mitigation of electrical disturbances in installations with sensitive and interconnected electronic and electrical systems.

This facility is expected to generate conducted noise at the following frequencies:

- Mains frequency (50 Hz) and multiples of this frequency due to non-linear loads, which make use of uncontrolled rectifiers to convert from AC to DC. There are many examples of sources of noise at these frequencies, which include:
  - All devices that contain a switch-mode power supply;
  - Uninterruptible power supplies; and
  - Inverters for AC motors or pumps.
- High frequency (1kHz to 100 kHz): coming mainly from magnet power converters, and RF system capacitor chargers, due to switching within the converter.

Radiated noise is also expected throughout the RF spectrum emanating from equipment such as:

- Pulsed magnet power supplies for kickers and septum magnets;
- Pulsed power supplies for RF amplifiers such as klystrons; and
- Mobile phones and Wi-Fi signals (common and required across much of the facility), which are a source of radiated noise.

It must also be acknowledged that some specialist equipment may not comply with electromagnetic immunity or susceptibility standards. This may be due to the method of operation or the technology readiness level of the device. Detailed investigation of this equipment and the method of operation must be made to ensure this equipment does not have a detrimental impact on other local systems, and may require incorporating specialist noise reduction techniques.

Best practice for these types of facilities is to install two grounding networks—a safety grounding network and reference grounding network—bonded together. Their design and interconnection will depend on the layout of the accelerator and support areas, such as rack rooms and RF equipment.

B.1.8.4 Cooling System

The cooling system will comprise a primary chilled-water system, secondary de-ionised and general water-cooling circuits, and specific high-stability temperature-control systems for the RF cavities. The proposed use of groundwater to provide up to 2 MW net of primary cooling is being considered as part of the overall cooling solution; if feasible, it will increase the capital cost but would significantly reduce operational costs through energy savings.

The cooling infrastructure would comprise bore holes, water chillers, pumps, heat exchangers, pipework, instrumentation, de-ionisation plant and a SCADA system. The system would have sufficient cooling capacity to satisfy the facility's water cooling and air conditioning requirements.

The total water cooling load is currently estimated to be ∼2.1 MW, which has been included in the cost model.

B.1.8.5 Compressed Air

A compressed air supply and distribution system will be required in ITRF. The anticipated parameters are:

- Pressure: 6 bar; and
- Purity: Compliant with ISO 8573-1:2010 (1:2:1) (Food grade, non-direct contact) [382].

B.1.8.6 Air Conditioning

It is anticipated that a range of air conditioning solutions will be used to match individual room cooling requirements, including DX Comfort cooling systems and water-cooled air-handling units for more sensitive applications. The total air conditioning load is estimated to be ∼0.4 MW.

B.1.9 Bulk Shielding Assessment

Consolidation of source terms
The output of a shielding assessment is entirely dependent on the source terms that are provided to the calculation. A meeting was held at Daresbury Laboratory (1st November 2023) that involved physicists from partner institutions, relevant STFC staff and an external shielding assessor. From this, a set of source terms has been developed for a set of operating modes reflecting the likely operating conditions of ITRF/LhARA (see table B.5).

In addition, the initial plasma source term has been simulated, and all key parameters such as the beam energy distribution, divergence, and initial proton/ion yield have been derived from this. Combining this plasma source with the loss points, each mode of operation has now been described in terms of which source points are engaged and what the particle loss rate is at that point. The source term also contains the operating schedule; the temporal parameters, such as the availability of the machine and the expected duration of "beam on" time and which fraction of this is attributed to each operational mode. The latter are necessary to understand the accumulated exposure and residual activation of components. The bounding source terms for each stage of normal operation are summarised in table B.5.

Shielding assessment
TUV-SUD were engaged to carry out an assessment of the likely shielding requirements for Stage 1 and Stage 2 operation of the ITRF/LhARA facility, based on the source terms identified above. These are documented in TUV-SUD reports NT02602-DAR-LHARA-C01-I1_NPM and NT02602-DAR-LHARA-C02-I1_NPM. Whilst there are a number of limitations in a preliminary assessment of this sort, the required concrete shielding thicknesses, which are < 1 m for Stage 1 and 2–3 m for Stage 2, are determined in part by proton operation at the highest energies. However, the large number of protons and electrons generated at the TNSA source, coupled with the large inherent particle loss at the nozzle, results in a relatively large radiation source term at this location; this materially affects the bulk shielding that is needed to attenuate dose to external personnel.

Some refinement of source terms will be possible, which may allow a reduction in required shielding thicknesses, for example, by improving collimation and beam stop designs, better identification of loss points, and more detailing in the accelerator subsystems, which themselves act in part to attenuate radiation.

Table B.5: Nominal and bounding source terms.

	Stage 1 operation		Stage 2 operation	
	Protons	C^{6+} ions	Protons	C^{6+} ions
Max beam energy (MeV)	15 MeV	48 MeV	127 MeV	400 MeV
Repetition rate (Hz)	100	100	100	100
Particles required at delivery point (#/s)	1×10^{10}	1×10^{9}	1×10^{10}	1×10^{9}

B.1.10 Mechanical Systems Integration Support Concepts

Support systems for accelerator devices are required to be stable, minimise effects due to vibration and include adjustment to facilitate accurate positioning of equipment. The support concepts adopted by ITRF/LhARA have been developed and successfully implemented on other accelerator projects such as CLARA and ESS. The concept adopts a modular system which facilitates assembly and offline testing of accelerator equipment before installation into the accelerator hall, enabling the most efficient use of time, particularly during critical shutdown periods.

Ti:S Laser support system
It is envisaged that the Ti:Sapphire laser system will be procured and supplied by a specialist company; the support for this system will be included during the scope of design and procurement.

Laser target optics support system
For optical support systems, such as the laser target chamber source, it is critical that the optical element supports are isolated from the vacuum chamber, which will deflect during pump down. In figure B.13, optics are shown mounted onto a baseplate, which is isolated from the vacuum chamber with bellows and supported by a synthetic granite block for vibration damping. The vacuum chamber is supported by an independent frame with adjustments available in X, Y and Z.

Accelerator support systems
Each modular support system includes two pedestals and an aluminium extruded beam, as shown in figure B.14. The support pedestals are fabricated in mild steel and consist of a thick-wall support tube with a top and bottom plate. The beam assembly is constructed from rectangular aluminium extrusion, which includes flat surfaces, T-slot features for clamping equipment and ancillary equipment such as electrical and water services. The beam assembly is supported by the pedestals utilising a three-point kinematic system allowing for adjustment in direction Y and also pitch, roll and yaw. Adjustment of the beam in directions X and Z is achieved by translation of a plate using screws.

Accelerator equipment and devices that are assembled to the support beam have independent kinematic support and adjustment, providing translation in X, Y and Z together with pitch, roll and yaw. Figure B.15 shows examples of a quadrupole and corrector magnet assembled

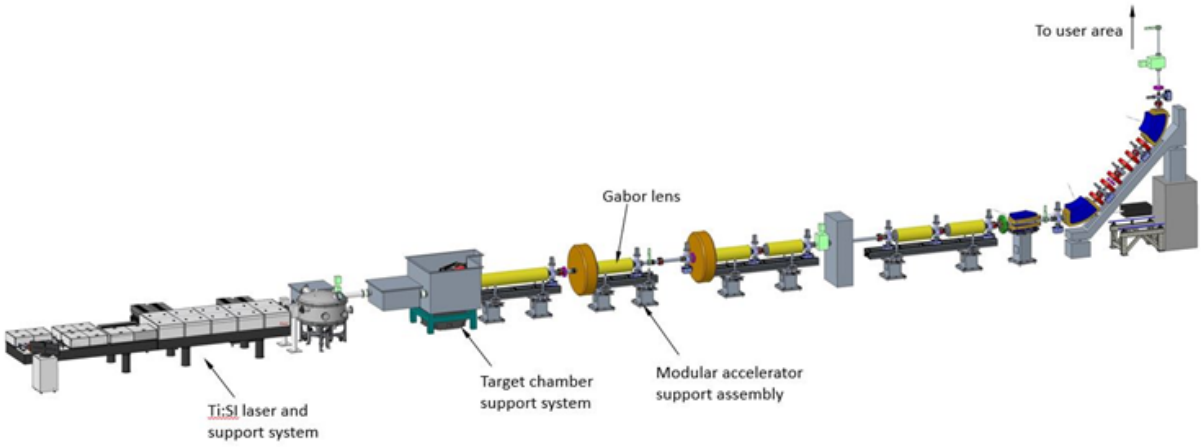

Figure B.11: Stage 1 layout.

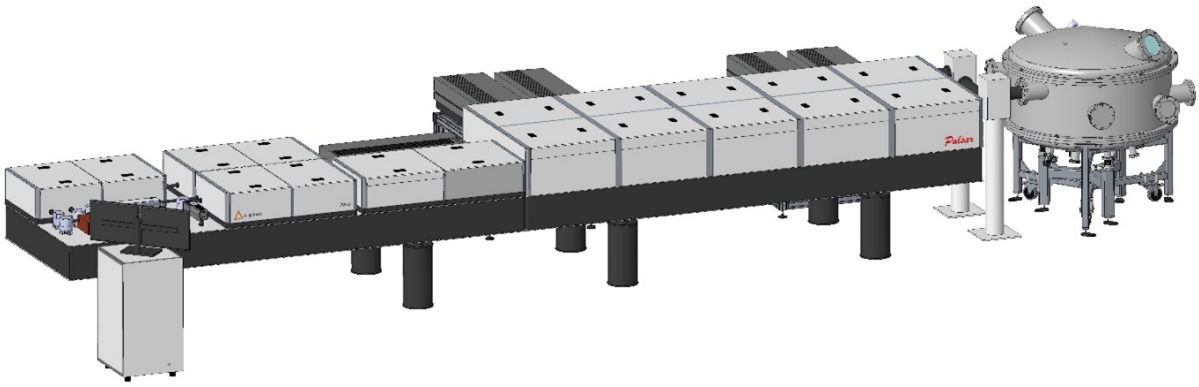

Figure B.12: Laser layout.

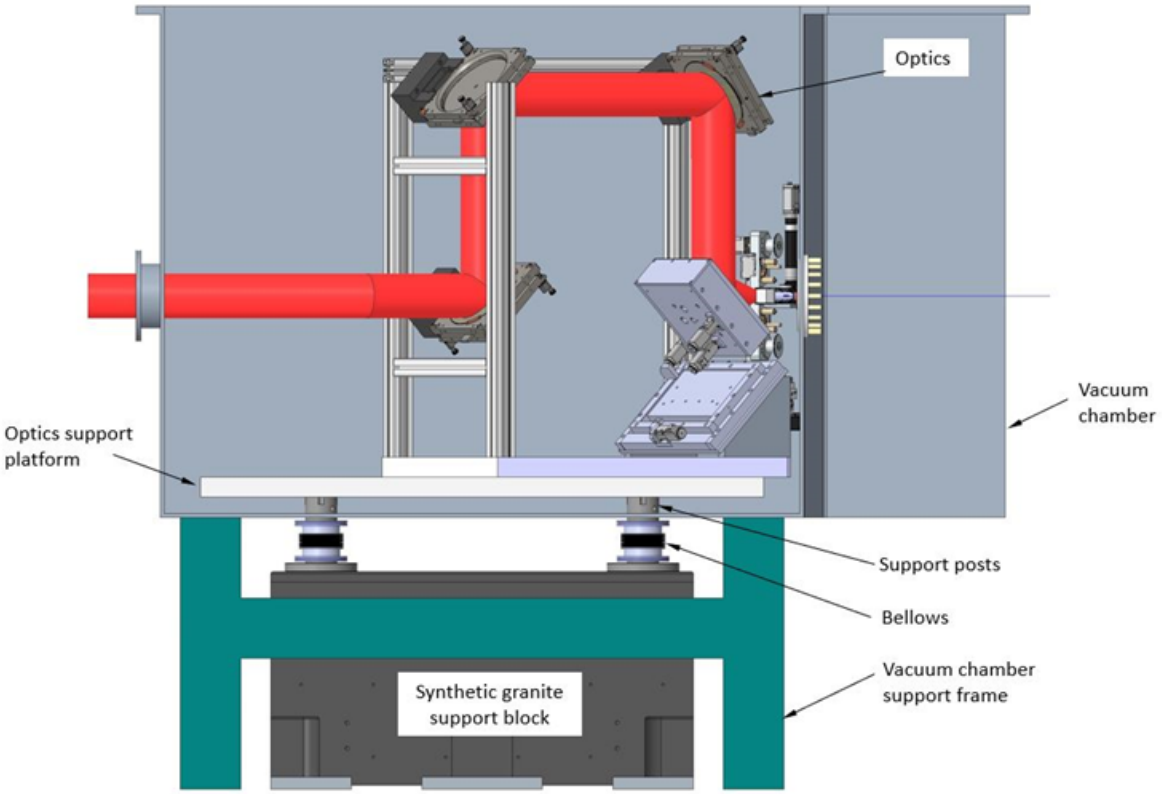

Figure B.13: Source layout.

to a support beam. All accelerator devices will have features for inserting laser-tracker-survey fiducials to enable pre-alignment of each module.

The Gabor lens support features have not been determined at this stage. However, it is envisaged that the proposed modular support beam system would be an appropriate concept, as shown in figure B.16.

Building offline in a modular way also enables the installation of local services, allowing for testing of systems such as vacuum integrity, magnet power and water cooling systems. Following offline testing, the beam assembly module can be transported to the accelerator hall using a lifting beam and attachments. The support pedestals are installed with the bottom plate set 25 mm above the floor, and after levelling, are secured with bolts; a high-strength grout is applied in the gap under the pedestal plate. The pedestals are filled with dry sand to act as a vibration damper. The aluminium beam assembly is located using the three-point kinematic support system and secured with fasteners. Alignment of the beam assembly is achieved using the adjustment features described above and with a laser tracker, which accurately reads back the position of fiducials placed into holes in the corners of the beam assembly. The equipment required to transport the beam vertically to the *in-vitro* end stations will be installed using the same modular system. A concrete block can be used to elevate the support pedestal at one end as shown in figure B.17.

B.2 Cost estimate

The top-level breakdown of the capital costs for the LhARA project is given in table B.6 [383]. The costs are based on those presented in [12] and should be regarded as first estimates that will be challenged and refined as the design-and-development process proceeds. The costs presented in [383] were derived in 2019; therefore, compound inflation (£23M) has been included in the total. Contingency and working margin have been added as indicated in the table. The facility construction cost is taken from the analysis presented in [12]. The cost for the animal house required for the Stage 2 programme was estimated through the peer-group consultation process.

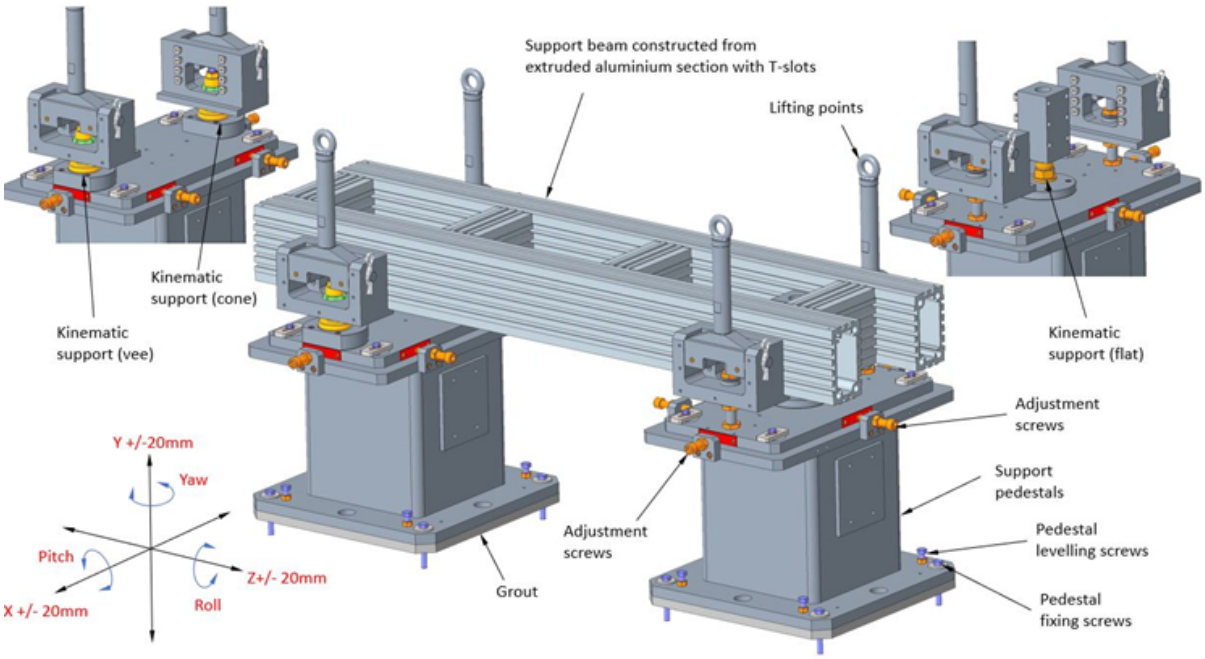

Figure B.14: Support systems.

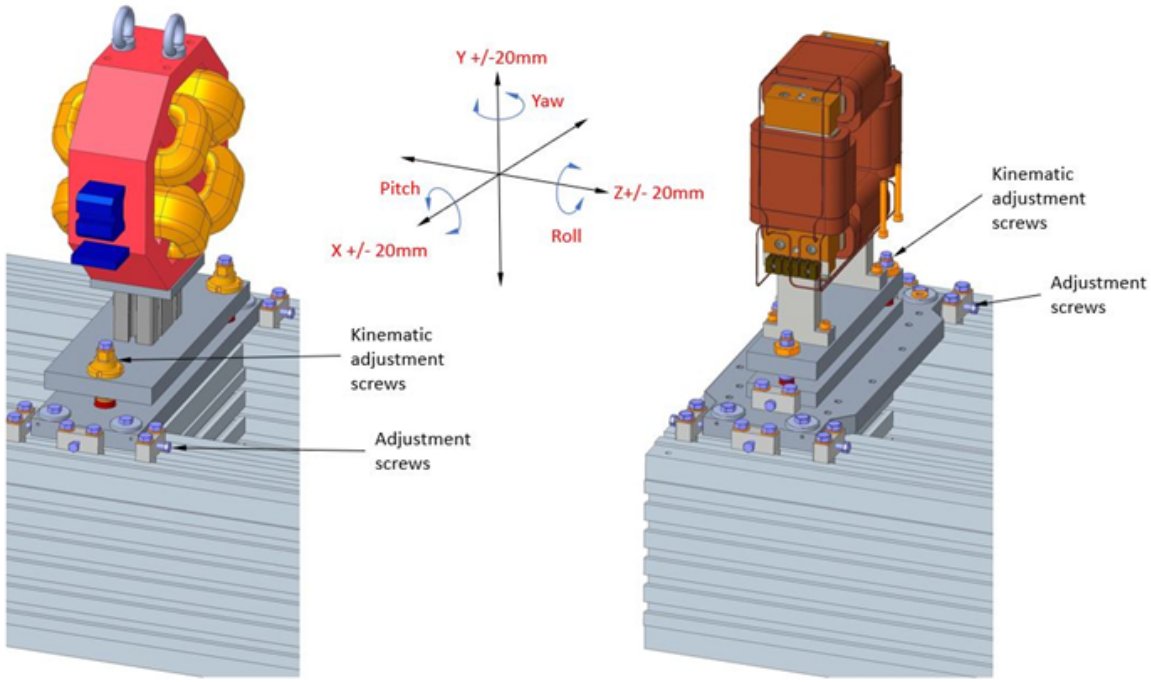

Figure B.15: Kinematic mounts.

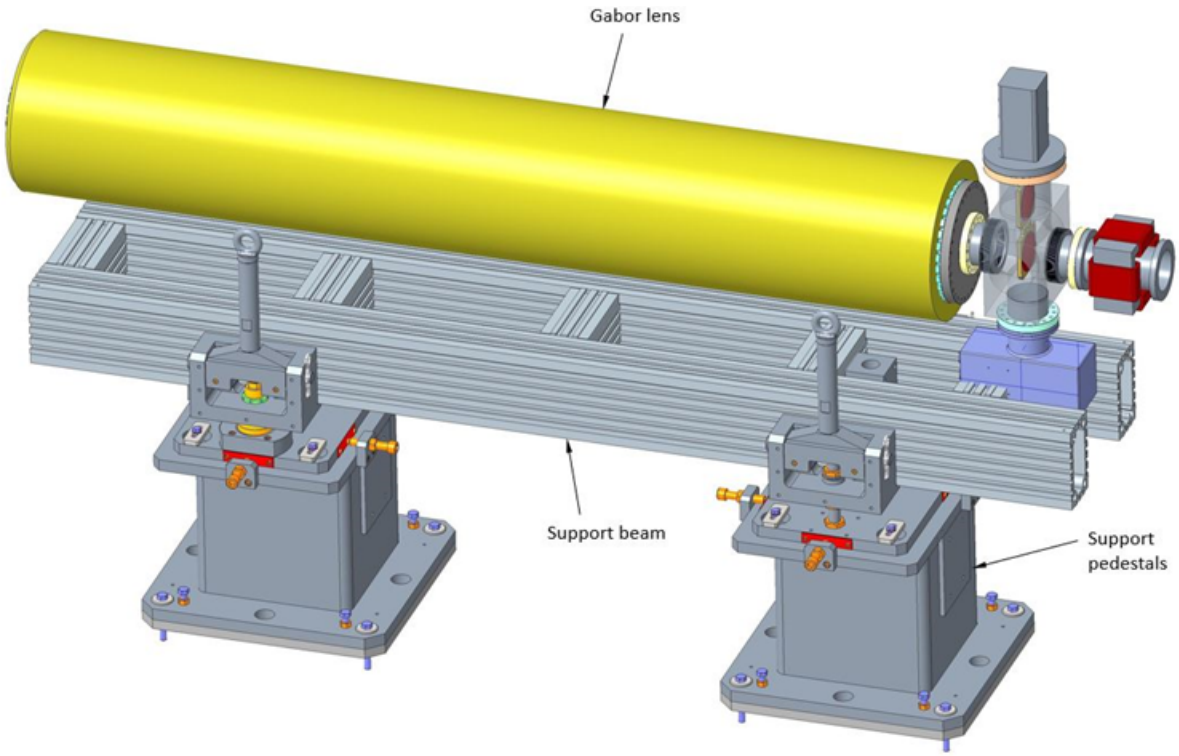

Figure B.16: Gabor lens support system.

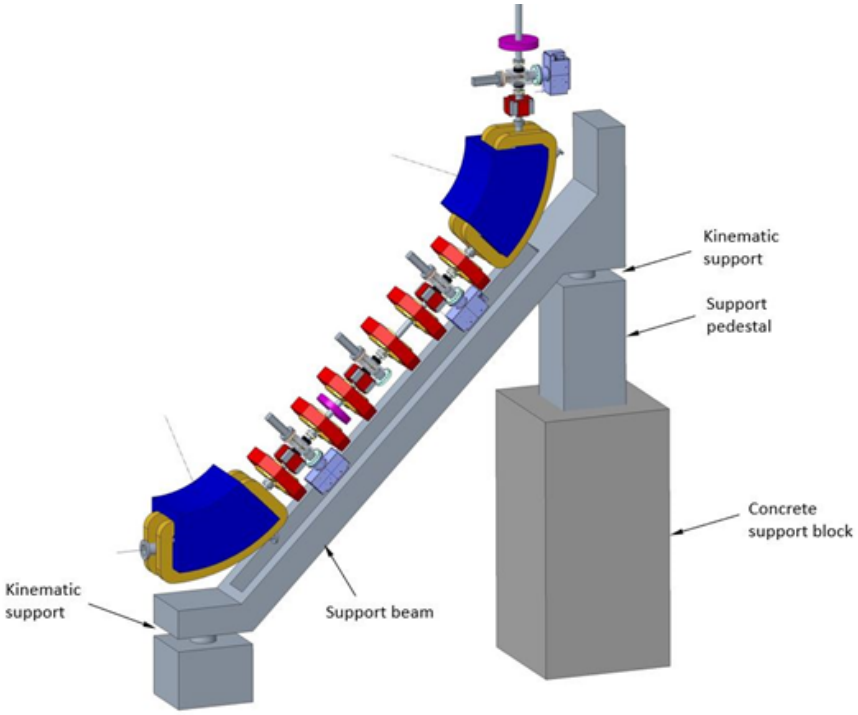

Figure B.17: Stage 1 arc.

The staff cost is based on an updated estimate of the staff effort required to deliver the facility.

Table B.6: Top-level cost breakdown for the ITRF served by LhARA [383].

Item		£M
Facility construction		68
Contingency	20%	14
Working margin	10%	7
Facility construction total		***88***
Animal house		35
Contingency	10%	4
Working margin	5%	2
Animal house total		***40***
Sub-Total - build		**129**
Inflation to 2030	18%	23
Sub-Total - build @2030 costs		**152**
VAT	20%	30
Sub-Total - build @2030 costs inc VAT		182
staff costs @ 2030 rates		***36***
contingency	20%	7
Staff @ 2030 rates inc contingency		**43**
Grand total		**225**

References

[1] UKRI. *Infrastructure Fund projects*. Accessed: 2025-09-21. 2025. URL: https://www.ukri.org/what-we-do/creating-world-class-research-and-innovation-infrastructure/funded-infrastructure-projects.

[2] J Clarke, M Noro, and A Woodcock. *Preliminary details and descriptions; Ion Therapy Research Facility*. Submission to UKRI Infrastructure Fund Advisory Committee. 2021. URL: https://ccap.hep.ph.ic.ac.uk/trac/raw-attachment/wiki/Research/LhARA/Governance/ExecutiveBoard/Meetings/2023/2023-07-05/2021-06-15-ITRF-PrelimAct-Submission-Final.pdf.

[3] ITRF. *LhARA proposals 2021*. Accessed: 2025-09-21. 2021. URL: https://ccap.hep.ph.ic.ac.uk/trac/wiki/Research/DesignStudy/Proposals/2021.

[4] ITR/LhARA. *Ion Therapy Research Facility / LhARA Bridging period 1; project definition5*. https://indico.stfc.ac.uk/event/1060/sessions/869/attachments/2374/4210/LhARA_ITRF_BP1_project_definition.pdf. Accessed: 2025-09-21. 2021.

[5] WHO. *Cancer*. Accessed: 2025-09-21. 2025. URL: https://www.who.int/health-topics/cancer-hash-tab=tab_1.

[6] Niloy R Datta, Susanne Rogers, and Stephan Bodis. "Challenges and Opportunities to Realize "The 2030 Agenda for Sustainable Development" by the United Nations: Implications for Radiation Therapy Infrastructure in Low- and Middle-Income Countries". In: *International Journal of Radiation Oncology*Biology*Physics* 105.5 (2019), pages 918–933. ISSN: 0360-3016. DOI: https://doi.org/10.1016/j.ijrobp.2019.04.033. URL: http://www.sciencedirect.com/science/article/pii/S0360301619306972.

[7] Thomas Mee et al. "The use of radiotherapy, surgery and chemotherapy in the curative treatment of cancer: results from the FORTY (Favourable Outcomes from RadioTherapY) project". In: *The British Journal of Radiology* 96.1152 (October 2023). ISSN: 1748-880X. DOI: 10.1259/bjr.20230334. URL: http://dx.doi.org/10.1259/bjr.20230334.

[8] May Abdel-Wahab et al. "Radiotherapy and theranostics: a Lancet Oncology Commission". In: *The Lancet Oncology* 25.11 (November 2024), e545–e580. ISSN: 1470-2045. DOI: 10.1016/s1470-2045(24)00407-8. URL: http://dx.doi.org/10.1016/S1470-2045(24)00407-8.

[9] Vincent Favaudon et al. "Ultrahigh dose-rate FLASH irradiation increases the differential response between normal and tumor tissue in mice". In: *Science Translational Medicine* 6.245 (July 2014). ISSN: 1946-6242. DOI: 10.1126/scitranslmed.3008973. URL: http://dx.doi.org/10.1126/scitranslmed.3008973.

[10] Stefanie Girst et al. "Proton Minibeam Radiation Therapy Reduces Side Effects in an In Vivo Mouse Ear Model". In: *International Journal of Radiation Oncology*Biology*Physics* 95.1 (May 2016), pages 234–241. ISSN: 0360-3016. DOI: 10.1016/j.ijrobp.2015.10.020. URL: http://dx.doi.org/10.1016/j.ijrobp.2015.10.020.

[11] *LhARA will revolutionise cancer care*. Accessed: 2025-09-22. 2025. URL: https://www.lhara.org.

[12] The LhARA consortium. *The laser-hybrid accelerator for radiobiological applications*. Technical report ech. Rep. CCAP-TN-01. 2020. URL: https://ccap.hep.ph.ic.ac.uk/trac/raw-attachment/wiki/Research/DesignStudy/PreCDR/Review/2020-03-31-LhARA_pre_CDR-d2.0.pdf.

[13] Galen Aymar et al. "LhARA: The Laser-hybrid Accelerator for Radiobiological Applications". In: *Frontiers in Physics* 8 (September 2020). ISSN: 2296424X. DOI: 10.3389/fphy.2020.567738. URL: https://doi.org/10.3389/fphy.2020.567738.

[14] N Bliss, A Goulden, and M Noro. *ASTeC-TD at Daresbury Laboratory Project Management Plan (PMP)*. 1272-pa1-pm-pmp-0001-v13.0-ITRF-2023-09-28. Updated, September 2024. 2022. URL: https://www.ukri.org/wp-content/uploads/2023/05/STFC-310523-DaresburyDevelopment-PlanMarch2023.pdf.

[15] C. Baker et al. *Ion Therapy Research Facility / LhARA: eighteen month progress report*. Technical report LhARA-Gov-PMB-2024-08. 2024. URL: https://ccap.hep.ph.ic.ac.uk/trac/raw-attachment/wiki/Research/LhARA/Documents/LhARA-Gov-PMB-2024-08.pdf.

[16] C Dyson. *Summary of PoPLaR - SCAPA Phase'*. Technical report LhARA-TN-2025-05. 2025. URL: https://ccap.hep.ph.ic.ac.uk/trac/raw-attachment/wiki/Research/LhARA/Documents/LhARA-TN-2025-05.pdf.

[17] B. Torrance. *Developments for the PoPLaR Experiment at SCAPA Bunker B*. Accessed, 22 September 2025. 2025. URL: https://indico.stfc.ac.uk/event/1627/contributions/9480/attachments/3267/5909/LhARA%5C%20Collaboration%5C%20Meeting%5C%2018092025_BT_Development_for_PoPLaR.pptx.

[18] E. Melia. *Radiobiology Preparation and Plans*. Accessed, 22 September 2025. 2025. URL: https://indico.stfc.ac.uk/event/1627/contributions/9474/attachments/3272/5916/180925%5C%20LhARA%5C%20Meeting%5C%20EMelia.pptx.

[19] Maria Macouti. "Development of an Acoustic Dose-Profile Measurement Technique for Short Pulse Proton and Ion Beams". PhD thesis. Imperial College London, July 2025. DOI: https://doi.org/10.25560/121726. URL: https://spiral.imperial.ac.uk/entities/publication/62dd40db-bced-4ecf-ba69-3c593eecd736.

[20] LhARA Project Management Board. *First peer-group consultation meeting*. Technical report LhARA-Gov-PMB-2023-04. 2023. URL: https://ccap.hep.ph.ic.ac.uk/trac/raw-attachment/wiki/Research/LhARA/Documents/LhARA-Gov-PMB-2023-04.pdf.

[21] C. Baker et al. *LhARA/ITRF: twelve month progress report*. Technical report LhARA-Gov-PMB-2023-06. 2023. URL: https://ccap.hep.ph.ic.ac.uk/trac/raw-attachment/wiki/Research/LhARA/Documents/LhARA-Gov-PMB-2023-06-Final.pdf.

[22] Hin Tung Lau. "Medical Applications for Particle Physics". PhD thesis. Imperial College London, February 2022. URL: https://ccap.hep.ph.ic.ac.uk/trac/raw-attachment/wiki/Communication/Theses/2022/2022-02-LAU-HT.pdf.

[23] Titus-Stefan Dascalu. "Study of non-neutral electron plasma lenses for focusing laser-driven ion beams". PhD thesis. Imperial College London, May 2023. URL: https://ccap.hep.ph.ic.ac.uk/trac/attachment/wiki/Communication/Theses/2023/2023-05-DASCALU_TS.pdf.

[24] Josie McGarrigle. "Exploring new approaches in radiotherapy to optimise the design of LhARA". PhD thesis. Imperial College London, January 2026.

[25] Tim Schneider. "Advancing the generation of proton minibeams for radiation therapy". Theses. Université Paris-Saclay, December 2020. URL: https://theses.hal.science/tel-03105944.

[26] Thongchai Masilela. “In silico radiobiological investigations for the advancement of novel RT techniques”. Theses. Université Paris-Saclay, November 2023. URL: https://theses.hal.science/tel-04390290.

[27] *NI Cancer Research Consumer Forum Meet LhARA Researchers*. Accessed, 22 September 2025. 2022. URL: https://cancertrials.hscni.net/ni-cancer-research-consumer-forum-meet-lhara-researchers/.

[28] C Pugh and M Noro. *Close out report*. 1272-pa1-pm-rpt-0001-v0.1-Close Out Report. 2025. URL: https://stfc365.sharepoint.com/sites/itrf/.

[29] G. Aymar et al. “The Laser-hybrid Accelerator for Radiobiological Applications”. In: *arXiv* (May 2020). eprint: 2006.00493 (physics.acc-ph). URL: https://arxiv.org/abs/2006.00493.

[30] Cancer Research UK. *Worldwide cancer incidence statistics*. https://www.cancerresearchuk.org/health-professional/cancer-statistics/worldwide-cancer/incidence. Accessed: 2019-04-13. November 2018.

[31] Hongcheng Zhu et al. “Global radiotherapy demands and corresponding radiotherapy-professional workforce requirements in 2022 and predicted to 2050: a population-based study”. In: *The Lancet Global Health* 12.12 (September 2024), e1945–e1953. ISSN: 2214-109X. DOI: 10.1016/S2214-109X(24)00355-3. URL: https://doi.org/10.1016/S2214-109X(24)00355-3.

[32] Sophia C. Kamran et al. “Therapeutic radiation and the potential risk of second malignancies”. In: *Cancer* 122.12 (March 2016), pages 1809–1821. ISSN: 1097-0142. DOI: 10.1002/cncr.29841. URL: http://dx.doi.org/10.1002/cncr.29841.

[33] Lorenzo Galluzzi et al. “Emerging evidence for adapting radiotherapy to immunotherapy”. In: *Nature Reviews Clinical Oncology* 20.8 (June 2023), pages 543–557. ISSN: 1759-4782. DOI: 10.1038/s41571-023-00782-x. URL: http://dx.doi.org/10.1038/s41571-023-00782-x.

[34] W.T.T. Chu. “Overview of Light-Ion Beam Therapy”. In: *Dose Reporting in Ion Beam Therapy*. Edited by International Atomic Energy Agency and ICRU. Volume 1560. IAEA-TECDOC. Vienna: International Atomic Energy Agency, July 2007. ISBN: 978-92-0-105807-2. URL: https://www-pub.iaea.org/MTCD/Publications/PDF/te_1560_web.pdf.

[35] Jérôme Doyen et al. “Proton beams in cancer treatments: Clinical outcomes and dosimetric comparisons with photon therapy”. In: *Cancer Treatment Reviews* 43 (February 2016), pages 104–112. ISSN: 0305-7372. DOI: 10.1016/j.ctrv.2015.12.007. URL: http://dx.doi.org/10.1016/j.ctrv.2015.12.007.

[36] Particle Therapy Co-Operative Group (PTCOG). *Particle therapy facilities in clinical operation*. October 2025. URL: https://www.ptcog.site/index.php/facilities-in-operation-public.

[37] Rifat Atun et al. “Expanding global access to radiotherapy”. In: *The Lancet Oncology* 16.10 (2015), pages 1153–1186. ISSN: 1470-2045. DOI: https://doi.org/10.1016/S1470-2045(15)00222-3. URL: http://www.sciencedirect.com/science/article/pii/S1470204515002223.

[38] Marco Durante, Elke Brauer-Krisch, and Mark Hill. “Faster and safer? FLASH ultra-high dose rate in radiotherapy”. In: *The British Journal of Radiology* (November 2017), page 20170628. ISSN: 1748-880X. DOI: 10.1259/bjr.20170628. URL: http://dx.doi.org/10.1259/bjr.20170628.

[39] Yolanda Prezado et al. “Spatially fractionated radiation therapy: a critical review on current status of clinical and preclinical studies and knowledge gaps”. In: *Physics in Medicine & Biology* 69.10 (May 2024), 10TR02. ISSN: 1361-6560. DOI: 10.1088/1361-6560/ad4192. URL: http://dx.doi.org/10.1088/1361-6560/ad4192.

[40] Harald Paganetti and Peter van Luijk. “Biological Considerations When Comparing Proton Therapy With Photon The<rapy”. In: *Seminars in Radiation Oncology* 23.2 (2013). Controversies in Proton Therapy, pages 77–87. ISSN: 1053-4296. DOI: https://doi.org/10.1016/j.semradonc.2012.11.002. URL: http://www.sciencedirect.com/science/article/pii/S1053429612001051.

[41] H. Paganetti. “Relative biological effectiveness (RBE) values for proton beam therapy. Variations as a function of biological endpoint, dose, and linear energy transfer”. In: *Phys. Med. Biol.* 59.22 (2014), R419. DOI: 10.1088/0031-9155/59/22/R419. URL: http://stacks.iop.org/0031-9155/59/i=22/a=R419.

[42] B. Jones, S. J. McMahon, and K. M. Prise. “The Radiobiology of Proton Therapy: Challenges and Opportunities Around Relative Biological Effectiveness”. In: *Clinical Oncology* 30.5 (May 2018), pages 285–292. ISSN: 0936-6555. DOI: 10.1016/j.clon.2018.01.010. URL: http://dx.doi.org/10.1016/j.clon.2018.01.010.

[43] Giulia Giovannini et al. “Variable RBE in proton therapy: comparison of different model predictions and their influence on clinical-like scenarios”. In: *Radiation Oncology* 11.1 (May 2016), page 68. ISSN: 1748-717X. DOI: 10.1186/s13014-016-0642-6. URL: https://doi.org/10.1186/s13014-016-0642-6.

[44] Armin Lühr et al. “Relative biological effectiveness in proton beam therapy – Current knowledge and future challenges”. In: *Clinical and Translational Radiation Oncology* 9 (February 2018), pages 35–41. ISSN: 2405-6308. DOI: 10.1016/j.ctro.2018.01.006. URL: http://dx.doi.org/10.1016/j.ctro.2018.01.006.

[45] Pankaj Chaudhary et al. “Relative Biological Effectiveness Variation Along Monoenergetic and Modulated Bragg Peaks of a 62-MeV Therapeutic Proton Beam: A Preclinical Assessment”. In: *International Journal of Radiation Oncology • Biology • Physics* 90.1 (September 2014), pages 27–35. ISSN: 0360-3016. DOI: 10.1016/j.ijrobp.2014.05.010. URL: https://doi.org/10.1016/j.ijrobp.2014.05.010.

[46] J J Wilkens and U Oelfke. “A phenomenological model for the relative biological effectiveness in therapeutic proton beams”. In: *Physics in Medicine and Biology* 49.13 (June 2004), pages 2811–2825. DOI: 10.1088/0031-9155/49/13/004. URL: https://doi.org/10.1088%2F0031-9155%2F49%2F13%2F004.

[47] Christian P Karger and Peter Peschke. “RBE and related modeling in carbon-ion therapy”. In: *Physics in Medicine & Biology* 63.1 (December 2017), 01TR02. DOI: 10.1088/1361-6560/aa9102. URL: https://doi.org/10.1088%2F1361-6560%2Faa9102.

[48] Eirini Terpsi Vitti and Jason L Parsons. “The Radiobiological Effects of Proton Beam Therapy: Impact on DNA Damage and Repair”. In: *Cancers* 11.7 (July 2019), page 946. ISSN: 2072-6694. DOI: 10.3390/cancers11070946. URL: http://dx.doi.org/10.3390/cancers11070946.

[49] Rachel J. Carter et al. “Complex DNA Damage Induced by High Linear Energy Transfer Alpha-Particles and Protons Triggers a Specific Cellular DNA Damage Response”. In: *International Journal of Radiation Oncology*Biology*Physics* 100.3 (2018), pages 776–784. ISSN: 0360-3016. DOI: https://doi.org/10.1016/j.ijrobp.2017.11.012. URL: http://www.sciencedirect.com/science/article/pii/S0360301617341007.

[50] M. C. Vozenin et al. “The Advantage of FLASH Radiotherapy Confirmed in Mini-pig and Cat-cancer Patients”. In: *Clinical Cancer Research* 25.1 (January 2019), pages 35–42. ISSN: 1557-3265. DOI: 10.1158/1078-0432.ccr-17-3375. URL: http://dx.doi.org/10.1158/1078-0432.CCR-17-3375.

[51] M.-C. Vozenin, J. H. Hendry, and C. L. Limoli. “Biological Benefits of Ultra-high Dose Rate FLASH Radiotherapy: Sleeping Beauty Awoken”. In: *Clinical Oncology* 31.7 (July 2019), pages 407–415. ISSN: 0936-6555. DOI: 10.1016/j.clon.2019.04.001. URL: https://doi.org/10.1016/j.clon.2019.04.001.

[52] Varian Medical Systems. “FlashForward Consortium”. In: (2020). URL: https://www.varian.com/about-varian/research/flashforward-consortium.

[53] Weisi Yan et al. “Spatially fractionated radiation therapy: History, present and the future”. In: *Clinical and Translational Radiation Oncology* 20 (January 2020), pages 30–38. ISSN: 2405-6308. DOI: 10.1016/j.ctro.2019.10.004. URL: http://dx.doi.org/10.1016/j.ctro.2019.10.004.

[54] Armin Lühr et al. “ “Radiobiology of Proton Therapy”: Results of an international expert workshop”. In: *Radiotherapy and Oncology* 128.1 (July 2018), pages 56–67. ISSN: 01678140. DOI: 10.1016/j.radonc.2018.05.018. URL: http://www.ncbi.nlm.nih.gov/pubmed/29861141%20https://linkinghub.elsevier.com/retrieve/pii/S0167814018302779.

[55] S.V Bulanov et al. “Oncological hadrontherapy with laser ion accelerators”. In: *Physics Letters A* 299.2 (2002), pages 240–247. ISSN: 0375-9601. DOI: https://doi.org/10.1016/S0375-9601(02)00521-2. URL: http://www.sciencedirect.com/science/article/pii/S0375960102005212.

[56] E. Fourkal et al. “Particle selection for laser-accelerated proton therapy feasibility study”. In: *Medical Physics* 30.7 (2003), pages 1660–1670. DOI: 10.1118/1.1586268. eprint: https://aapm.onlinelibrary.wiley.com/doi/pdf/10.1118/1.1586268. URL: https://aapm.onlinelibrary.wiley.com/doi/abs/10.1118/1.1586268.

[57] Victor Malka et al. “Practicability of proton therapy using compact laser systems”. In: *Medical Physics* 31.6 (2004), pages 1587–1592. DOI: 10.1118/1.1747751. eprint: https://aapm.onlinelibrary.wiley.com/doi/pdf/10.1118/1.1747751. URL: https://aapm.onlinelibrary.wiley.com/doi/abs/10.1118/1.1747751.

[58] S D Kraft et al. “Dose–dependent biological damage of tumour cells by laser–accelerated proton beams”. In: *New Journal of Physics* 12.8 (August 2010), page 085003. DOI: 10.1088/1367-2630/12/8/085003. URL: https://doi.org/10.1088%2F1367-2630%2F12%2F8%2F085003.

[59] F Fiorini et al. “Dosimetry and spectral analysis of a radiobiological experiment using laser-driven proton beams”. In: *Physics in Medicine and Biology* 56.21 (October 2011), pages 6969–6982. ISSN: 1361-6560. DOI: 10.1088/0031-9155/56/21/013. URL: http://dx.doi.org/10.1088/0031-9155/56/21/013.

[60] D. Doria et al. “Biological effectiveness on live cells of laser driven protons at dose rates exceeding 10^9 Gy/s”. In: *AIP Advances* 2.1 (2012), page 011209. DOI: 10.1063/1.3699063. eprint: https://doi.org/10.1063/1.3699063. URL: https://doi.org/10.1063/1.3699063.

[61] K. Zeil et al. “Dose-controlled irradiation of cancer cells with laser-accelerated proton pulses”. In: *Applied Physics B* 110.4 (November 2012), pages 437–444. ISSN: 1432-0649. DOI: 10.1007/s00340-012-5275-3. URL: http://dx.doi.org/10.1007/s00340-012-5275-3.

[62] U. Masood et al. “A compact solution for ion beam therapy with laser accelerated protons”. In: *Applied Physics B* 117.1 (April 2014), pages 41–52. ISSN: 1432-0649. DOI: 10.1007/s00340-014-5796-z. URL: http://dx.doi.org/10.1007/s00340-014-5796-z.

[63] O. Zlobinskaya et al. “The Effects of Ultra–High Dose Rate Proton Irradiation on Growth Delay in the Treatment of Human Tumor Xenografts in Nude Mice”. In: *Radiation Research* 181.2 (2014), pages 177–183. DOI: 10.1667/RR13464.1. URL: https://doi.org/10.1667/RR13464.1.

[64] Queen’s University Belfast. *A-SAIL Project*. URL: https://www.qub.ac.uk/research-centres/A-SAILProject/.

[65] Giuseppe A. P. Cirrone et al. “ELIMED: a new hadron therapy concept based on laser driven ion beams”. In: *Laser Acceleration of Electrons, Protons, and Ions II; and Medical Applications of Laser-Generated Beams of Particles II; and Harnessing Relativistic Plasma Waves III*. Edited by Eric Esarey et al. Volume 8779. International Society for Optics and Photonics. SPIE, 2013, pages 216–225. DOI: 10.1117/12.2026530. URL: https://doi.org/10.1117/12.2026530.

[66] S. M. Wiggins et al. “Application programmes at the Scottish Centre for the Application of Plasma-based Accelerators (SCAPA)”. In: *Relativistic Plasma Waves and Particle Beams as Coherent and Incoherent Radiation Sources III*. Edited by Dino A. Jaroszynski and MinSup Hur. Volume 11036. International Society for Optics and Photonics. SPIE, 2019, pages 93–103. DOI: 10.1117/12.2520717. URL: https://doi.org/10.1117/12.2520717.

[67] L. Manti et al. “The radiobiology of laser-driven particle beams: focus on sub-lethal responses of normal human cells”. In: *Journal of Instrumentation* 12.03 (March 2017), pages C03084–C03084. DOI: 10.1088/1748-0221/12/03/c03084. URL: https://doi.org/10.1088%2F1748-0221%2F12%2F03%2Fc03084.

[68] F. Romano et al. “The ELIMED transport and dosimetry beamline for laser-driven ion beams”. In: *Nuclear Instruments and Methods in Physics Research Section A: Accelerators, Spectrometers, Detectors and Associated Equipment* 829 (2016). 2nd European Advanced Accelerator Concepts Workshop – EAAC 2015, pages 153–158. ISSN: 0168-9002. DOI: https://doi.org/10.1016/j.nima.2016.01.064. URL: http://www.sciencedirect.com/science/article/pii/S0168900216000929.

[69] U Masood et al. “A light-weight compact proton gantry design with a novel dose delivery system for broad-energetic laser-accelerated beams”. In: *Physics in Medicine & Biology* 62.13 (June 2017), pages 5531–5555. DOI: 10.1088/1361-6560/aa7124. URL: https://doi.org/10.1088%2F1361-6560%2Faa7124.

[70] P. Chaudhary et al. “Effectiveness of laser accelerated ultra high dose rate protons in DNA DSB damage induction under hypoxic conditions”. In: *44th EPS Conference on Plasma Physics, EPS 2017*. Volume 44F. European Physical Society (EPS), January 2017, P1.217. URL: https://strathprints.strath.ac.uk/67067/.

[71] Daniele Margarone et al. “ELIMAIA: A Laser–Driven Ion Accelerator for Multidisciplinary Applications”. In: *Quantum Beam Science* 2.2 (2018). ISSN: 2412-382X. DOI: 10.3390/qubs2020008. URL: http://www.mdpi.com/2412-382X/2/2/8.

[72] Matteo Passoni, Luca Bertagna, and Alessandro Zani. “Target normal sheath acceleration: theory, comparison with experiments and future perspectives”. In: *New Journal of Physics* 12.4 (April 2010), page 045012. ISSN: 1367-2630. DOI: 10.1088/1367-2630/12/4/045012. URL: http://dx.doi.org/10.1088/1367-2630/12/4/045012.

[73] M. Roth and M. Schollmeier. "Ion Acceleration—Target Normal Sheath Acceleration". en. In: *CERN Yellow Reports* (2016), Vol 1 (2016): Proceedings of the 2014 CAS–CERN Accelerator School: Plasma Wake Acceleration. DOI: 10.5170/CERN-2016-001.231. URL: https://e-publishing.cern.ch/index.php/CYR/article/view/222.

[74] *MAD- Methodical Accelerator Design*. 2022. URL: http://madx.web.cern.ch/madx.

[75] Y. Chao. "BeamOptics: A symbolic platform for modeling and the solution of beam optics system". In: *tech. rep.* (2000). URL: https://inis.iaea.org/records/ejgw9-wg641.

[76] L.J. Nevay et al. "BDSIM: An accelerator tracking code with particle–matter interactions". In: *Computer Physics Communications* 252 (July 2020), page 107200. ISSN: 0010-4655. DOI: 10.1016/j.cpc.2020.107200. URL: http://dx.doi.org/10.1016/j.cpc.2020.107200.

[77] S Van der Geer and J de Loos. "General Particle Tracer". In: *PulsarPhysics* (). URL: http://www.pulsar.nl/gpt/index.html.

[78] *Geant4*. Accessed: November 2025. URL: https://geant4.web.cern.ch/.

[79] D GABOR. "A Space-Charge Lens for the Focusing of Ion Beams". In: *Nature* 160.4055 (1947), pages 89–90. ISSN: 1476-4687. DOI: 10.1038/160089b0. URL: https://doi.org/10.1038/160089b0.

[80] N. Dover et al. *LhARA linear optics documentation*. Report LhARA-TN-07. Imperial College London, 2025. URL: https://ccap.hep.ph.ic.ac.uk/trac/raw-attachment/wiki/Research/LhARA/Documents/LhARA-TN-2024-07.pdf.

[81] The LhARA collaboration. *Baseline for the LhARA design update*. Technical report CCAP-TN-11. The Centre for the Clinical Application of Particles, Imperial College London, 2022. URL: https://ccap.hep.ph.ic.ac.uk/trac/raw-attachment/wiki/Communication/Notes/CCAP-TN-11-LhARA-Design-Baseline.pdf.

[82] N. Tsoupas et al. "Uniform beam distributions using octupoles". In: *Conference Record of the 1991 IEEE Particle Accelerator Conference*. IEEE, 1991, pages 1695–1697. DOI: 10.1109/pac.1991.164748. URL: http://dx.doi.org/10.1109/PAC.1991.164748.

[83] Eriko Urakabe et al. "Beam-Profile Control Using an Octupole Magnet". In: *Japanese Journal of Applied Physics* 38.10R (October 1999), page 6145. ISSN: 1347-4065. DOI: 10.1143/jjap.38.6145. URL: http://dx.doi.org/10.1143/JJAP.38.6145.

[84] T. Amin et al. "Formation of a uniform ion beam using octupole magnets for BioLEIR facility at CERN". In: *Journal of Instrumentation* 13.04 (April 2018), P04016–P04016. ISSN: 1748-0221. DOI: 10.1088/1748-0221/13/04/p04016. URL: http://dx.doi.org/10.1088/1748-0221/13/04/P04016.

[85] J. Fuchs et al. "Laser-driven proton scaling laws and new paths towards energy increase". In: *Nature Physics* 2.1 (December 2005), pages 48–54. ISSN: 1745-2481. DOI: 10.1038/nphys199. URL: http://dx.doi.org/10.1038/nphys199.

[86] J. Schreiber *et al.* "Analytical Model for Ion Acceleration by High-Intensity Laser Pulses". In: *Physical review letters* 97.045005 (08 2006). DOI: 10.1103/PhysRevLett.97.045005. URL: https://dx.doi.org/10.1103/PhysRevLett.97.045005.

[87] F. Nürnberg et al. "Radiochromic film imaging spectroscopy of laser-accelerated proton beams". In: *Review of Scientific Instruments* 80.3 (March 2009). ISSN: 1089-7623. DOI: 10.1063/1.3086424. URL: http://dx.doi.org/10.1063/1.3086424.

[88] Mohammad Eshraqi, Giuliano Franchetti, and Alessandra M. Lombardi. "Emittance control in rf cavities and solenoids". In: *Phys. Rev. ST Accel. Beams* 12 (2 February 2009), page 024201. DOI: 10.1103/PhysRevSTAB.12.024201. URL: https://link.aps.org/doi/10.1103/PhysRevSTAB.12.024201.

[89] PTW-Freiburg Physikalisch-Technische Werkstatten Dr. Pychlau GmbH. *Ionizing Radiation Detectors*. 2015. Chapter Markus Chamber: Type 23343, page 19. URL: https://www.emf-japan.com/ptw/img/PDF/PTW_all_detectors.pdf.

[90] L. Nevay W. Shields and S. Boogert. "Progress & developments of BDSIM". English. In: *Proc. IPAC'24* (Nashville, TN). IPAC'24 - 15th International Particle Accelerator Conference 15. JACoW Publishing, Geneva, Switzerland, May 2024, pages 2664–2667. ISBN: 978-3-95450-247-9. DOI: 10.18429/JACoW-IPAC2024-WEPR69. URL: https://indico.jacow.org/event/63/contributions/4500.

[91] DW Krest et al. *Fixed field alternating gradient particle accelerators*. Technical report MURA-109, MURA-DWK-KRS-LJL-LWJ-KMT-3. Midwestern Universities Research Association (MURA), 1956. URL: https://lss.fnal.gov/archive/other/mura/MURA-109.pdf.

[92] K. R. Symon et al. "Fixed-Field Alternating-Gradient Particle Accelerators". In: *Phys. Rev.* 103 (6 September 1956), pages 1837–1859. DOI: 10.1103/PhysRev.103.1837. URL: https://link.aps.org/doi/10.1103/PhysRev.103.1837.

[93] J. Fourrier et al. "Spiral FFAG lattice design tools. Application to 6-D tracking in a proton-therapy class lattice". In: *Nuclear Instruments and Methods in Physics Research Section A: Accelerators, Spectrometers, Detectors and Associated Equipment* 589.2 (May 2008), pages 133–142. ISSN: 0168-9002. DOI: 10.1016/j.nima.2008.01.082. URL: http://dx.doi.org/10.1016/j.nima.2008.01.082.

[94] Minoru Tanigaki et al. "Present Status of the FFAG Accelerators in KURRI for ADS Study". In: *EPAC 2006 - Contributions to the Proceedings*. 2006. URL: https://proceedings.jacow.org/a07/PAPERS/THPMA115.pdf.

[95] T. Planche et al. "Design of a prototype gap shaping spiral dipole for a variable energy protontherapy FFAG". In: *Nuclear Instruments and Methods in Physics Research Section A: Accelerators, Spectrometers, Detectors and Associated Equipment* 604.3 (June 2009), pages 435–442. ISSN: 0168-9002. DOI: 10.1016/j.nima.2009.02.026. URL: http://dx.doi.org/10.1016/j.nima.2009.02.026.

[96] R Taylor et al. "Slow Extraction Techniques from Fixed Field Accelerators". In: *Journal of Physics: Conference Series* 2687.2 (January 2024), page 022022. ISSN: 1742-6596. DOI: 10.1088/1742-6596/2687/2/022022. URL: http://dx.doi.org/10.1088/1742-6596/2687/2/022022.

[97] Shinji Machida. "Scaling Fixed-Field Alternating-Gradient accelerators with reverse bend and spiral edge angle". In: *Phys. Rev. Lett.* 119.6 (2017), page 064802. DOI: 10.1103/PhysRevLett.119.064802. arXiv: 1701.06782 [physics.acc-ph].

[98] PTW-Freiburg Physikalisch-Technische Werkstatten Dr. Pychlau GmbH. *User Manual Water Phantom T41023*. 2009. URL: https://ccap.hep.ph.ic.ac.uk/trac/raw-attachment/wiki/Research/Instrumentation/Documentation/Drawings/Water_phantom_T41023_Man_en_73813100_02.pdf.

[99] I. Rodriguez et al. "FFA magnet prototype for high intensity pulsed proton driver". In: *Proc. IPAC'23* (Venice, Italy). International Particle Accelerator Conference 14. JACoW Publishing, Geneva, Switzerland, September 2023, pages 2261–2264. ISBN: 978-3-95-450231-8. DOI: 10.18429/JACOW-IPAC2023-TUPM032. URL: https://jacow.org/ipac2023/doi/jacow-ipac2023-tupm032.

[100] J.-B. Lagrange. "The Particle Tracking Code Fixfield". In: *Proc. IPAC'21* (Campinas, SP, Brazil). International Particle Accelerator Conference 12. https://doi.org/10.18429/JACoW-IPAC2021-TUPAB209. JACoW Publishing, Geneva, Switzerland, August 2021, TUPAB209, pages 1905–1906. ISBN: 978-3-95450-214-1. DOI: 10.18429/JACoW-IPAC2021-TUPAB209. URL: https://jacow.org/ipac2021/papers/tupab209.pdf.

[101] S Machida et al. "Fixed Field Alternating Gradient Accelerator (FFA) Report". In: *STFC-P-2025-001* (July 2025). Preprint. URL: https://epubs.stfc.ac.uk/manifestation/62105503/STFC-P-2025-001.pdf.

[102] Klingbeil H. *Ferrite cavities*. Technical report CERN Yellow Report, CERN-2011-007, 299-317. Darmstadt, GSI, January 2012. URL: https://arxiv.org/pdf/1201.1154.

[103] B. Zwicker et al. "TEST OF A NON-INVASIVE BUNCH SHAPE MONITOR AT GSI HIGH CURRENT LINAC". In: *IBIC'2013*. 2013, MOPC36. URL: https://accelconf.web.cern.ch/ibic2013/papers/mopc36.pdf.

[104] Alexander Feschenko, Viktor Gaidash, and Sergei Gavrilov. "Development and Implementation of Bunch Shape Instrumentation for Ion Linacs". en. In: *27th Russian Particle Accelerator Conference*. JACoW Publishing, Geneva, Switzerland, October 2021. DOI: 10.18429/JACOW-RUPAC2021-MOX02. URL: https://jacow.org/rupac2021/doi/JACoW-RuPAC2021-MOX02.html.

[105] Peter Forck. *Lecture Notes on Beam Instrumentation and Diagnostics*. en. Technical report JUAS. 2011. URL: https://www-bd.gsi.de/conf/juas/juas_script.pdf.

[106] Kay Wittenburg. "Beam Loss Monitors". In: *arXiv* (May 2020). DOI: 10.48550/arXiv.2005.06522. URL: http://arxiv.org/abs/2005.06522.

[107] A Miura et al. "Beam Loss Occurred at DTL Cavity in J-PARC Linac". en. In: *Proceedings of LINAC2012* (2012). URL: https://inspirehep.net/files/a17be9dbd2a01cb12839a1a6b5b23e

[108] "Developments of beam loss monitors for FETS-FFA test ring". English. In: *Proc. 15th International Particle Accelerator Conference* (Nashville, TN). IPAC'24 - 15th International Particle Accelerator Conference 15. JACoW Publishing, Geneva, Switzerland, May 2024, pages 2396–2399. ISBN: 978-3-95450-247-9. DOI: 10.18429/JACoW-IPAC2024-WEPG76. URL: https://indico.jacow.org/event/63/contributions/4345.

[109] S. L. Sheehy et al. "Characterization techniques for fixed-field alternating gradient accelerators and beam studies using the KURRI 150 MeV proton FFAG". In: *Progress of Theoretical and Experimental Physics* 2016.7 (July 2016), 073G01. ISSN: 2050-3911. DOI: 10.1093/ptep/ptw086. URL: http://dx.doi.org/10.1093/ptep/ptw086.

[110] *FEMTO LCA-10K-500M Ultra Low Noise Amplifier*. Technical report. FEMTO Messtechnik GmbH. URL: https://www.femto.de/images/pdf-dokumente/de-lca-10k-500m.pdf.

[111] J. Harasimowicz and C. Welsch. "Faraday cup for low-energy, low-intensity beam measurements at the USR". In: *2010 Beam Instrumentation Workshop, BIW 2010 - Proceedings* (January 2010). URL: https://www.researchgate.net/profile/Carsten_Welsch/publication/44191865_Faraday_cup_for_low-energy_low-intensity_beam_measurements_at_the_USR/links/00b4952a2368c3bbe7000000/Faraday-cup-for-low-energy-low-intensity-beam-measurements-at-the-USR.pdf?_tp=eyJjb250ZXh0Ijp7ImZpcnN0UGFnZSI6InB1YmxpY2F0aW9uIiwicGFnZSI6InB1YmxpY2F0aW9uIn19.

[112] E.M. Donegani et al. "Design and performance of the compact DTL1 Faraday cup for the high-power ESS NCL". In: *Nuclear Instruments and Methods in Physics Research Section A: Accelerators, Spectrometers, Detectors and Associated Equipment* 1047 (February 2023), page 167827. ISSN: 0168-9002. DOI: 10.1016/j.nima.2022.167827. URL: http://dx.doi.org/10.1016/j.nima.2022.167827.

[113] Tomonori Uesugi et al. “Study of Beam Injection Efficiency in the Fixed Field Alternating Gradient Synchrotron at KURNS”. In: *Proceedings of the 10th Int. Particle Accelerator Conf.* IPAC2019 (2019). DOI: 10.18429/JACOW-IPAC2019-WEPGW040. URL: http://jacow.org/ipac2019/doi/JACoW-IPAC2019-WEPGW040.html.

[114] B. G. Loach and B. Southworth. *A 7 GeV Proton Synchrotron*. Technical report NIRL/R/44. 1965. URL: https://epubs.stfc.ac.uk/manifestation/39567584/NIRL-R-44.pdf.

[115] D. W. Posthuma De Boer. *Optimisation of a Beam Position Monitor for the FETS-FFA*. en. September 2024. URL: https://indico.rcnp.osaka-u.ac.jp/event/2375/contributions/13797/.

[116] Y. Takahoko and M. Takashima. *Measurement of betatron tunes in KURRI FFAG Main ring*. 2009. URL: https://ffag.pp.rl.ac.uk/FFAG/FFAG09J_HP/slides/Takahoko-FFAG09j.pdf.

[117] M. Gasior. *Base-Band Q (BBQ) Measurement with Direct Diode Detection (3D)*. URL: https://mgasior.web.cern.ch/pro/bbq/index.html.

[118] CERN. *MolFlow / SynRad documentation — molflow.docs.cern.ch*. [Accessed 07-01-2026]. URL: https://molflow.docs.cern.ch/about/.

[119] CERN. *MolFlow / SynRad documentation — molflow.docs.cern.ch*. [Accessed 07-01-2026]. URL: https://molflow.docs.cern.ch/.

[120] R. Kersevan and J.-L. Pons. “Introduction to MOLFLOW+: New graphical processing unit-based Monte Carlo code for simulating molecular flows and for calculating angular coefficients in the compute unified device architecture environment”. In: *Journal of Vacuum Science &; Technology A: Vacuum, Surfaces, and Films* 27.4 (June 2009), pages 1017–1023. ISSN: 1520-8559. DOI: 10.1116/1.3153280. URL: http://dx.doi.org/10.1116/1.3153280.

[121] Hiroyuki Daido, Mamiko Nishiuchi, and Alexander S Pirozhkov. “Review of laser-driven ion sources and their applications”. In: *Reports on Progress in Physics* 75.5 (April 2012), page 056401. ISSN: 1361-6633. DOI: 10.1088/0034-4885/75/5/056401. URL: http://dx.doi.org/10.1088/0034-4885/75/5/056401.

[122] Andrea Macchi, Marco Borghesi, and Matteo Passoni. “Ion acceleration by superintense laser-plasma interaction”. In: *Reviews of Modern Physics* 85.2 (May 2013), pages 751–793. ISSN: 1539-0756. DOI: 10.1103/revmodphys.85.751. URL: http://dx.doi.org/10.1103/RevModPhys.85.751.

[123] S. C. Wilks et al. “Absorption of ultra-intense laser pulses”. In: *Physical Review Letters* 69.9 (August 1992), pages 1383–1386. ISSN: 0031-9007. DOI: 10.1103/physrevlett.69.1383. URL: http://dx.doi.org/10.1103/PhysRevLett.69.1383.

[124] E. L. Clark et al. “Energetic Heavy-Ion and Proton Generation from Ultraintense Laser-Plasma Interactions with Solids”. In: *Physical Review Letters* 85.8 (August 2000), pages 1654–1657. ISSN: 1079-7114. DOI: 10.1103/physrevlett.85.1654. URL: http://dx.doi.org/10.1103/PhysRevLett.85.1654.

[125] R. A. Snavely et al. “Intense High-Energy Proton Beams from Petawatt-Laser Irradiation of Solids”. In: *Physical Review Letters* 85.14 (October 2000), pages 2945–2948. ISSN: 1079-7114. DOI: 10.1103/physrevlett.85.2945. URL: http://dx.doi.org/10.1103/PhysRevLett.85.2945.

[126] S. C. Wilks et al. “Energetic proton generation in ultra-intense laser–solid interactions”. In: *Physics of Plasmas* 8.2 (February 2001), pages 542–549. ISSN: 1089-7674. DOI: 10.1063/1.1333697. URL: http://dx.doi.org/10.1063/1.1333697.

[127] N.P. Dover et al. "Demonstration of repetitive energetic proton generation by ultra-intense laser interaction with a tape target". In: *High Energy Density Physics* 37 (November 2020), page 100847. ISSN: 1574-1818. DOI: 10.1016/j.hedp.2020.100847. URL: http://dx.doi.org/10.1016/j.hedp.2020.100847.

[128] Florian-Emanuel Brack et al. "Spectral and spatial shaping of laser-driven proton beams using a pulsed high-field magnet beamline". In: *Scientific Reports* 10.1 (June 2020). ISSN: 2045-2322. DOI: 10.1038/s41598-020-65775-7. URL: http://dx.doi.org/10.1038/s41598-020-65775-7.

[129] Jianhui Bin et al. "A new platform for ultra-high dose rate radiobiological research using the BELLA PW laser proton beamline". In: *Scientific Reports* 12.1 (January 2022). ISSN: 2045-2322. DOI: 10.1038/s41598-022-05181-3. URL: http://dx.doi.org/10.1038/s41598-022-05181-3.

[130] M. Borghesi et al. "Multi-MeV Proton Source Investigations in Ultraintense Laser-Foil Interactions". In: *Physical Review Letters* 92.5 (February 2004). ISSN: 1079-7114. DOI: 10.1103/physrevlett.92.055003. URL: http://dx.doi.org/10.1103/PhysRevLett.92.055003.

[131] M. Hegelich et al. "MeV Ion Jets from Short-Pulse-Laser Interaction with Thin Foils". In: *Physical Review Letters* 89.8 (August 2002). ISSN: 1079-7114. DOI: 10.1103/physrevlett.89.085002. URL: http://dx.doi.org/10.1103/PhysRevLett.89.085002.

[132] P Sommer et al. "Laser-ablation-based ion source characterization and manipulation for laser-driven ion acceleration". In: *Plasma Physics and Controlled Fusion* 60.5 (March 2018), page 054002. ISSN: 1361-6587. DOI: 10.1088/1361-6587/aab21e. URL: http://dx.doi.org/10.1088/1361-6587/aab21e.

[133] Colin N. Danson et al. "Petawatt and exawatt class lasers worldwide". In: *High Power Laser Science and Engineering* 7 (2019). ISSN: 2052-3289. DOI: 10.1017/hpl.2019.36. URL: http://dx.doi.org/10.1017/hpl.2019.36.

[134] John T Morrison et al. "Corrigendum: MeV proton acceleration at kHz repetition rate from ultra-intense laser liquid interaction (2018 New J. Phys. 20 022001)". In: *New Journal of Physics* 20.6 (June 2018), page 069501. ISSN: 1367-2630. DOI: 10.1088/1367-2630/aac5d1. URL: http://dx.doi.org/10.1088/1367-2630/aac5d1.

[135] F. Treffert et al. "High-repetition-rate, multi-MeV deuteron acceleration from converging heavy water microjets at laser intensities of 1021 W/cm2". In: *Applied Physics Letters* 121.7 (August 2022). ISSN: 1077-3118. DOI: 10.1063/5.0098973. URL: http://dx.doi.org/10.1063/5.0098973.

[136] Lieselotte Obst et al. "Efficient laser-driven proton acceleration from cylindrical and planar cryogenic hydrogen jets". In: *Scientific Reports* 7.1 (August 2017). ISSN: 2045-2322. DOI: 10.1038/s41598-017-10589-3. URL: http://dx.doi.org/10.1038/s41598-017-10589-3.

[137] Martin Rehwald et al. "Ultra-short pulse laser acceleration of protons to 80 MeV from cryogenic hydrogen jets tailored to near-critical density". In: *Nature Communications* 14.1 (July 2023). ISSN: 2041-1723. DOI: 10.1038/s41467-023-39739-0. URL: http://dx.doi.org/10.1038/s41467-023-39739-0.

[138] Rico Mayro P. Tanyag et al. "Disintegration of diminutive liquid helium jets in vacuum". In: *The Journal of Chemical Physics* 152.23 (June 2020). ISSN: 1089-7690. DOI: 10.1063/5.0004503. URL: http://dx.doi.org/10.1063/5.0004503.

[139] L. Willingale et al. “Collimated Multi-MeV Ion Beams from High-Intensity Laser Interactions with Underdense Plasma”. In: *Physical Review Letters* 96.24 (June 2006). ISSN: 1079-7114. DOI: 10.1103/physrevlett.96.245002. URL: http://dx.doi.org/10.1103/PhysRevLett.96.245002.

[140] O. Tresca et al. “Spectral Modification of Shock Accelerated Ions Using a Hydrodynamically Shaped Gas Target”. In: *Physical Review Letters* 115.9 (August 2015). ISSN: 1079-7114. DOI: 10.1103/physrevlett.115.094802. URL: http://dx.doi.org/10.1103/PhysRevLett.115.094802.

[141] V. Ospina-Bohórquez et al. “Laser-driven ion and electron acceleration from near-critical density gas targets: Towards high-repetition rate operation in the 1 PW, sub-100 fs laser interaction regime”. In: *Physical Review Research* 6.2 (June 2024). ISSN: 2643-1564. DOI: 10.1103/physrevresearch.6.023268. URL: http://dx.doi.org/10.1103/PhysRevResearch.6.023268.

[142] M.J.V. Streeter et al. “Laser Wakefield Accelerator modelling with Variational Neural Networks”. In: *High Power Laser Science and Engineering* (January 2023), pages 1–9. ISSN: 2052-3289. DOI: 10.1017/hpl.2022.47. URL: http://dx.doi.org/10.1017/hpl.2022.47.

[143] B. M. Hegelich et al. “Spectral properties of laser-accelerated mid-Z MeV/u ion beams”. In: *Physics of Plasmas* 12.5 (May 2005). ISSN: 1089-7674. DOI: 10.1063/1.1915350. URL: http://dx.doi.org/10.1063/1.1915350.

[144] D. Jung et al. “Laser-driven 1 GeV carbon ions from preheated diamond targets in the break-out afterburner regime”. In: *Physics of Plasmas* 20.8 (August 2013). ISSN: 1089-7674. DOI: 10.1063/1.4817287. URL: http://dx.doi.org/10.1063/1.4817287.

[145] Bixue Hou et al. “MeV proton beams generated by 3 mJ ultrafast laser pulses at 0.5 kHz”. In: *Applied Physics Letters* 95.10 (September 2009). ISSN: 1077-3118. DOI: 10.1063/1.3224180. URL: http://dx.doi.org/10.1063/1.3224180.

[146] Muhammad Noaman-ul-Haq et al. “Statistical analysis of laser driven protons using a high-repetition-rate tape drive target system”. In: *Physical Review Accelerators and Beams* 20.4 (April 2017). ISSN: 2469-9888. DOI: 10.1103/physrevaccelbeams.20.041301. URL: http://dx.doi.org/10.1103/PhysRevAccelBeams.20.041301.

[147] N. Xu et al. “Versatile tape-drive target for high-repetition-rate laser-driven proton acceleration”. In: *High Power Laser Science and Engineering* 11 (2023). ISSN: 2052-3289. DOI: 10.1017/hpl.2023.27. URL: http://dx.doi.org/10.1017/hpl.2023.27.

[148] A.R. Maier et al. “Decoding Sources of Energy Variability in a Laser-Plasma Accelerator”. In: *Physical Review X* 10 (2020), page 31039. DOI: 10.1103/PhysRevX.10.031039.

[149] M. Nishiuchi et al. “Focusing and spectral enhancement of a repetition-rated, laser-driven, divergent multi-MeV proton beam using permanent quadrupole magnets”. In: *Applied Physics Letters* 94.6 (February 2009), page 061107. ISSN: 1077-3118. DOI: 10.1063/1.3078291. URL: http://dx.doi.org/10.1063/1.3078291.

[150] Minjian Wu et al. “Collection and focusing of laser accelerated proton beam by an electromagnetic quadrupole triplet lens”. In: *Nuclear Instruments and Methods in Physics Research Section A: Accelerators, Spectrometers, Detectors and Associated Equipment* 955 (March 2020), page 163249. ISSN: 0168-9002. DOI: 10.1016/j.nima.2019.163249. URL: http://dx.doi.org/10.1016/j.nima.2019.163249.

[151] T.S. Dascalu et al. *ITRF/LhARA milestone M2.1 report: Baseline simulations of the future LhARA proton and ion source*. Technical report LhARA-TN-2024-08. 2024. URL: https://ccap.hep.ph.ic.ac.uk/trac/raw-attachment/wiki/Research/LhARA/Documents/LhARA-TN-2024-08.pdf.

[152] R.J. Gray et al. *ITRF/LhARA milestone M2.2 report: First SCAPA Ion Source Simulations and Experiments*. Technical report LhARA-TN-2024-09. 2024. URL: https://ccap.hep.ph.ic.ac.uk/trac/raw-attachment/wiki/Research/LhARA/Documents/LhARA-TN-2024-09.pdf.

[153] E. L. Clark et al. "Energetic Heavy-Ion and Proton Generation from Ultraintense Laser-Plasma Interactions with Solids". In: *Physical Review Letters* 85.8 (August 2000), pages 1654–1657. ISSN: 1079-7114. DOI: 10.1103/physrevlett.85.1654. URL: http://dx.doi.org/10.1103/PhysRevLett.85.1654.

[154] F. Nürnberg et al. "Radiochromic film imaging spectroscopy of laser-accelerated proton beams". In: *Review of Scientific Instruments* 80.3 (March 2009). ISSN: 1089-7623. DOI: 10.1063/1.3086424. URL: http://dx.doi.org/10.1063/1.3086424.

[155] D.C. Carroll et al. "A modified Thomson parabola spectrometer for high resolution multi-MeV ion measurements—Application to laser-driven ion acceleration". In: *Nuclear Instruments and Methods in Physics Research Section A: Accelerators, Spectrometers, Detectors and Associated Equipment* 620.1 (August 2010), pages 23–27. ISSN: 0168-9002. DOI: 10.1016/j.nima.2010.01.054. URL: http://dx.doi.org/10.1016/j.nima.2010.01.054.

[156] J B Birks. "Scintillations from Organic Crystals: Specific Fluorescence and Relative Response to Different Radiations". In: *Proceedings of the Physical Society. Section A* 64.10 (October 1951), pages 874–877. ISSN: 0370-1298. DOI: 10.1088/0370-1298/64/10/303. URL: http://dx.doi.org/10.1088/0370-1298/64/10/303.

[157] Muhammad Noaman-ul-Haq et al. "Parametric scalings of laser driven protons using a high repetition rate tape drive target system". In: *Nuclear Instruments and Methods in Physics Research Section A: Accelerators, Spectrometers, Detectors and Associated Equipment* 909 (2018). 3rd European Advanced Accelerator Concepts workshop (EAAC2017), pages 164–167. ISSN: 0168-9002. DOI: https://doi.org/10.1016/j.nima.2018.02.108. URL: https://www.sciencedirect.com/science/article/pii/S0168900218302961.

[158] J. Fuchs et al. "Laser-driven proton scaling laws and new paths towards energy increase". In: *Nature Physics* 2.1 (December 2005), pages 48–54. ISSN: 1745-2481. DOI: 10.1038/nphys199. URL: http://dx.doi.org/10.1038/nphys199.

[159] N. P. Dover et al. "Effect of Small Focus on Electron Heating and Proton Acceleration in Ultrarelativistic Laser-Solid Interactions". In: *Physical Review Letters* 124.8 (February 2020). ISSN: 1079-7114. DOI: 10.1103/physrevlett.124.084802. URL: http://dx.doi.org/10.1103/PhysRevLett.124.084802.

[160] D C Carroll et al. "Carbon ion acceleration from thin foil targets irradiated by ultrahigh-contrast, ultraintense laser pulses". In: *New Journal of Physics* 12.4 (April 2010), page 045020. DOI: 10.1088/1367-2630/12/4/045020. URL: https://dx.doi.org/10.1088/1367-2630/12/4/045020.

[161] A. J. Mackinnon et al. "Enhancement of Proton Acceleration by Hot-Electron Recirculation in Thin Foils Irradiated by Ultraintense Laser Pulses". In: *Phys. Rev. Lett.* 88 (21 May 2002), page 215006. DOI: 10.1103/PhysRevLett.88.215006. URL: https://link.aps.org/doi/10.1103/PhysRevLett.88.215006.

[162] T. Ceccotti et al. "Proton Acceleration with High-Intensity Ultrahigh-Contrast Laser Pulses". In: *Phys. Rev. Lett.* 99 (18 November 2007), page 185002. DOI: 10.1103/PhysRevLett.99.185002. URL: https://link.aps.org/doi/10.1103/PhysRevLett.99.185002.

[163] Y. Sentoku et al. “High-energy ion generation in interaction. of short laser pulse with high-density plasma”. In: *Applied Physics B 2002 74:3* 74 (3 February 2014), pages 207–215. ISSN: 1432-0649. DOI: 10.1007/S003400200796. URL: https://link.springer.com/article/10.1007/s003400200796.

[164] Leonida A. Gizzi et al. “Enhanced laser-driven proton acceleration via improved fast electron heating in a controlled pre-plasma”. In: *Scientific Reports* 11.1 (July 2021). ISSN: 2045-2322. DOI: 10.1038/s41598-021-93011-3. URL: http://dx.doi.org/10.1038/s41598-021-93011-3.

[165] L. Chopineau et al. “Identification of Coupling Mechanisms between Ultraintense Laser Light and Dense Plasmas”. In: *Phys. Rev. X* 9 (1 March 2019), page 011050. DOI: 10.1103/PhysRevX.9.011050. URL: https://link.aps.org/doi/10.1103/PhysRevX.9.011050.

[166] P. McKenna et al. “Effects of front surface plasma expansion on proton acceleration in ultraintense laser irradiation of foil targets”. In: *Laser and Particle Beams* 26.4 (November 2008), pages 591–596. ISSN: 1469-803X. DOI: 10.1017/s0263034608000657. URL: http://dx.doi.org/10.1017/S0263034608000657.

[167] S. Keppler et al. “Intensity scaling limitations of laser-driven proton acceleration in the TNSA-regime”. In: *Phys. Rev. Res.* 4 (1 January 2022), page 013065. DOI: 10.1103/PhysRevResearch.4.013065. URL: https://link.aps.org/doi/10.1103/PhysRevResearch.4.013065.

[168] Hiromitsu Kiriyama et al. “Enhancement of pre-pulse and picosecond pedestal contrast of the petawatt J-KAREN-P laser”. In: *High Power Laser Science and Engineering* 9 (2021). ISSN: 2052-3289. DOI: 10.1017/hpl.2021.51. URL: http://dx.doi.org/10.1017/hpl.2021.51.

[169] John M. Dawson. “Particle simulation of plasmas”. In: *Rev. Mod. Phys.* 55 (2 April 1983), pages 403–447. DOI: 10.1103/RevModPhys.55.403. URL: https://link.aps.org/doi/10.1103/RevModPhys.55.403.

[170] R. A. Fonseca et al. “OSIRIS: A Three-Dimensional, Fully Relativistic Particle in Cell Code for Modeling Plasma Based Accelerators”. In: *Computational Science — ICCS 2002*. Springer Berlin Heidelberg, 2002, pages 342–351. ISBN: 9783540477891. DOI: 10.1007/3-540-47789-6_36. URL: http://dx.doi.org/10.1007/3-540-47789-6_36.

[171] ARCHER2. *ARCHER2–UK National Supercomputing Service*. Accessed: May 2024. 2024. URL: https://www.archer2.ac.uk/.

[172] LRZ. *SuperMUC-NG*. Accessed: May 2024. 2024. URL: https://doku.lrz.de/supermuc-ng-10745965.html.

[173] F. TSUNG et al. “CO2 Laser acceleration of forward directed MeV proton beams in a gas target at critical plasma density”. In: *Journal of Plasma Physics* 78.4 (February 2012), pages 373–382. ISSN: 1469-7807. DOI: 10.1017/s0022377812000189. URL: http://dx.doi.org/10.1017/S0022377812000189.

[174] R J Gray et al. “Laser pulse propagation and enhanced energy coupling to fast electrons in dense plasma gradients”. In: *New Journal of Physics* 16.11 (November 2014), page 113075. DOI: 10.1088/1367-2630/16/11/113075. URL: https://dx.doi.org/10.1088/1367-2630/16/11/113075.

[175] T. Ziegler et al. “Proton beam quality enhancement by spectral phase control of a PW-class laser system”. In: *Scientific Reports* 11.1 (April 2021). ISSN: 2045-2322. DOI: 10.1038/s41598-021-86547-x. URL: http://dx.doi.org/10.1038/s41598-021-86547-x.

[176] Marvin Reimold et al. “Time-of-flight spectroscopy for laser-driven proton beam monitoring”. In: *Scientific Reports* 12.1 (December 2022). ISSN: 2045-2322. DOI: 10.1038/s41598-022-25120-6. URL: http://dx.doi.org/10.1038/s41598-022-25120-6.

[177] Josefine Metzkes-Ng et al. “The dresden platform is a research hub for ultra-high dose rate radiobiology”. In: *Scientific Reports* 13.1 (November 2023). ISSN: 2045-2322. DOI: 10.1038/s41598-023-46873-8. URL: http://dx.doi.org/10.1038/s41598-023-46873-8.

[178] A. Higginson et al. “Near-100 MeV protons via a laser-driven transparency-enhanced hybrid acceleration scheme”. In: *Nature Communications* 9.1 (February 2018). ISSN: 2041-1723. DOI: 10.1038/s41467-018-03063-9. URL: http://dx.doi.org/10.1038/s41467-018-03063-9.

[179] Tim Ziegler et al. “Laser-driven high-energy proton beams from cascaded acceleration regimes”. In: *Nature Physics* 20.7 (May 2024), pages 1211–1216. ISSN: 1745-2481. DOI: 10.1038/s41567-024-02505-0. URL: http://dx.doi.org/10.1038/s41567-024-02505-0.

[180] Nicholas P. Dover et al. “Enhanced ion acceleration from transparency-driven foils demonstrated at two ultraintense laser facilities”. In: *Light: Science &; Applications* 12.1 (March 2023). ISSN: 2047-7538. DOI: 10.1038/s41377-023-01083-9. URL: http://dx.doi.org/10.1038/s41377-023-01083-9.

[181] J. Pozimski and M. Aslaninejad. “Gabor lenses for capture and energy selection of laser driven ion beams in cancer treatment”. In: *Laser and Particle Beams* 31.4 (October 2013), pages 723–733. ISSN: 1469-803X. DOI: 10.1017/s0263034613000761. URL: http://dx.doi.org/10.1017/S0263034613000761.

[182] Richard C Thompson. “PENNING TRAPS”. In: *Trapped Charged Particles*. Advanced Textbooks in Physics. WORLD SCIENTIFIC (EUROPE), September 2015, pages 1–33. ISBN: 978-1-78634-011-5. DOI: doi:10.1142/9781786340139_0001. URL: https://doi.org/10.1142/9781786340139%7B%5C_%7D0001.

[183] J. S. deGrassie and J. H. Malmberg. “Waves and transport in the pure electron plasma”. In: *The Physics of Fluids* 23.1 (1980), pages 63–81. DOI: 10.1063/1.862864. URL: https://aip.scitation.org/doi/abs/10.1063/1.862864.

[184] J. H. Malmberg et al. “Experiments with pure electron plasmas”. In: *AIP Conference Proceedings* 175.1 (1988), pages 28–74. DOI: 10.1063/1.37613. URL: https://aip.scitation.org/doi/abs/10.1063/1.37613.

[185] D. L. Eggleston. “Confinement of test particles in a Malmberg–Penning trap with a biased axial wire”. In: *Physics of Plasmas* 4.5 (1997), pages 1196–1200. DOI: 10.1063/1.872299. URL: https://doi.org/10.1063/1.872299.

[186] M. Amoretti et al. “Cylindrical Penning trap for the study of electron plasmas”. In: *Review of Scientific Instruments* 74.9 (2003), pages 3991–3997. DOI: 10.1063/1.1602931. URL: https://doi.org/10.1063/1.1602931.

[187] J Fajans and A Schmidt. “Malmberg–Penning and Minimum-B trap compatibility: the advantages of higher-order multipole traps”. In: *Nuclear Instruments and Methods in Physics Research Section A: Accelerators, Spectrometers, Detectors and Associated Equipment* 521.2 (2004), pages 318–325. ISSN: 0168-9002. DOI: https://doi.org/10.1016/j.nima.2003.11.194. URL: http://www.sciencedirect.com/science/article/pii/S0168900203031127.

[188] ni. *Test and Measurement Systems, a part of Emerson — ni.com*. [Accessed 31-10-2025]. URL: https://www.ni.com/en.html.

[189] X.-P. Huang et al. “Steady-State Confinement of Non-neutral Plasmas by Rotating Electric Fields”. en. In: *Physical Review Letters* 78.5 (February 1997), pages 875–878. DOI: 10.1103/physrevlett.78.875. URL: http://dx.doi.org/10.1103/PhysRevLett.78.875.

[190] A. W. Trivelpiece and R. W. Gould. “Space Charge Waves in Cylindrical Plasma Columns”. In: *J. Appl. Phys.* 30 (11 November 1959), pages 1784–1793. DOI: 10.1063/1.1735056. URL: https://pubs.aip.org/aip/jap/article-abstract/30/11/1784/162595/Space-Charge-Waves-in-Cylindrical-Plasma-Columns?redirectedFrom=fulltext.

[191] Bret Robert Beck. “Measurement of the Magnetic and Temperature Dependence of the Electron-Electron Anisotropic Temperature Relaxation Rate”. PhD thesis. University of California, San Diego, January 1990. URL: https://ui.adsabs.harvard.edu/abs/1990PhDT.......143B.

[192] D. L. Eggleston et al. “Parallel energy analyzer for pure electron plasma devices”. en. In: *Physics of Fluids B: Plasma Physics* 4.10 (October 1992), pages 3432–3439. DOI: 10.1063/1.860399. URL: http://dx.doi.org/10.1063/1.860399.

[193] B. R. Beck, J. Fajans, and J. H. Malmberg. “Temperature and anisotropic-temperature relaxation measurements in cold, pure-electron plasmas”. en. In: *Physics of Plasmas* 3.4 (April 1996), pages 1250–1258. DOI: 10.1063/1.871749. URL: http://dx.doi.org/10.1063/1.871749.

[194] WFSA Resource Library. *The Physics Of Ultrasound – Part 1*. Accessed: 2024-05-19. URL: https://resources.wfsahq.org/atotw/the-physics-of-ultrasound-part-1/.

[195] T. F. Rösch et al. “Laser-driven ION (LION) acceleration at the centre for advanced laser applications (CALA)”. In: *2017 Conference on Lasers and Electro-Optics Europe & European Quantum Electronics Conference (CLEO/Europe-EQEC)*. Munich, Germany, 2017, pages 1–1. DOI: 10.1109/CLEOE-EQEC.2017.8087795. URL: https://doi.org/10.1109/CLEOE-EQEC.2017.8087795.

[196] A. A. Richards. “Acoustic imaging: Seeing with sound”. In: *Alien vision: Exploring the electromagnetic spectrum with imaging technology*. 2nd. SPIE Press, 2011. Chapter 5, pages 115–125. ISBN: 9780819485359. DOI: 10.1117/3.883085.ch5. URL: https://doi.org/10.1117/3.883085.ch5.

[197] K. C. Jones, W. Nie, J. C. H. Chu, et al. “Acoustic-based proton range verification in heterogeneous tissue: simulation studies”. In: *Physics in Medicine and Biology* 63.2 (January 2018). Published 2018 Jan 11, page 025018. DOI: 10.1088/1361-6560/aa9d16. URL: https://doi.org/10.1088/1361-6560/aa9d16.

[198] J. Lascaud et al. “Investigating the accuracy of co-registered ionoacoustic and ultrasound images in pulsed proton beams”. In: *Physics in Medicine and Biology* 66.18 (September 2021). PMID: 34438378, page 185003. DOI: 10.1088/1361-6560/ac215e. URL: https://doi.org/10.1088/1361-6560/ac215e.

[199] pmgroup. *Vantage Systems*. Accessed 22 June 2025. 2015. URL: https://verasonics.com/vantage-systems/.

[200] GE Healthcare. *9L-D, Ultrasound | GE HealthCare Service Shop USA*. https://services.gehealthcare.com/gehcstorefront/p/5499510. Online; accessed 22 July 2024.

[201] Olympus. *Immersion Transducers*. https://www.olympus-ims.com/en/ultrasonic-transducers/immersion/. Online; accessed 22 June 2025.

[202] Precision Acoustics Ltd. *ML4X50 Piston Hydrophone*. https://www.acoustics.co.uk/product/piston-hydrophone/. Online; accessed 2 June 2025.

[203] Daniel Robertson et al. “Optical artefact characterization and correction in volumetric scintillation dosimetry”. In: *Physics in Medicine and Biology* 59.1 (December 2013), pages 23–42. ISSN: 1361-6560. DOI: 10.1088/0031-9155/59/1/23. URL: http://dx.doi.org/10.1088/0031-9155/59/1/23.

[204] C Athanassopoulos et al. “The liquid scintillator neutrino detector and LAMPF neutrino source”. In: *Nuclear Instruments and Methods in Physics Research Section A: Accelerators, Spectrometers, Detectors and Associated Equipment* 388.1–2 (March 1997), pages 149–172. ISSN: 0168-9002. DOI: 10.1016/s0168-9002(96)01155-2. URL: http://dx.doi.org/10.1016/s0168-9002(96)01155-2.

[205] G. F. Knoll. *Radiation Detection and Measurement*. 4th edition. Hoboken, N.J.: John Wiley & Sons, 2010. URL: https://indico-tdli.sjtu.edu.cn/event/171/contributions/2123/attachments/982/1592/Knoll4thEdition.pdf.

[206] XueGang Chu et al. “Development of novel water equivalent liquid scintillator”. In: *Radiation Measurements* 136 (August 2020), page 106391. ISSN: 1350-4487. DOI: 10.1016/j.radmeas.2020.106391. URL: http://dx.doi.org/10.1016/j.radmeas.2020.106391.

[207] PerkinElmer, Inc. *Safety data sheet: Ultima Gold XR (Catalog No. 6013119)*. Revvity. [PDF]. 2020. URL: https://www.revvity.com/product/ultima-gold-xr-2x5-l-6013119.

[208] Magdalena Dianu and Corneliu Podina. “The safety of environment in final disposal of Ultima Gold scintillation liquid cocktail used for determination of radioactive content in various samples at Cernavoda Nuclear Power Plant”. In: *Revue Roumaine de Chimie* 52 (2007), pages 509–519. URL: https://revroum.lew.ro/wp-content/uploads/2007/RRC_5_2007/Art%2008.pdf.

[209] Karsten Kossert. “Measurement of wavelength-dependent refractive indices of liquid scintillation cocktails”. In: *Applied Radiation and Isotopes* 82 (December 2013), pages 382–388. ISSN: 0969-8043. DOI: 10.1016/j.apradiso.2013.10.005. URL: http://dx.doi.org/10.1016/j.apradiso.2013.10.005.

[210] Paul G. Hoertz et al. “Response of organic liquid scintillators to fast neutrons and gamma radiation”. In: *Radiation Physics and Chemistry* 84 (March 2013), pages 59–65. ISSN: 0969-806X. DOI: 10.1016/j.radphyschem.2012.06.044. URL: http://dx.doi.org/10.1016/j.radphyschem.2012.06.044.

[211] Maria Maxouti et al. “Preliminary evaluation of the correspondence between ion-acoustic signals and luminescence from the absorption of pulsed proton beams in a liquid scintillator”. In: *2025 IEEE International Ultrasonics Symposium (IUS)*. IEEE, September 2025, pages 1–4. DOI: 10.1109/ius62464.2025.11201445. URL: http://dx.doi.org/10.1109/IUS62464.2025.11201445.

[212] Hellenica World. *Attenuation length*. Accessed: 17-11-2025. URL: https://www.hellenicaworld.com/Science/Physics/en/Attenuationlength.html.

[213] K. Vo. *Spectrophotometry*. https://www.avantes.com/support/theoretical-background/introduction-to-spectrometers/?gad_source=1&gbraid=0AAAAAD-Bb4L_L9nIs3dC_9IXgbqFxWP3X&gclid=CjwKCAiAjp-7BhBZEiwAmh9rBZC5zY8C1KfO2JeRBt_TzsQ2ZG_rpIg-9Gqqq8AAIy8ANSOmJAHz-BoCDPwQAvD_BwE. Accessed: 23 Jun. 2025. 2022.

[214] Edinburgh Instruments. *Beer Lambert Law | Transmittance & Absorbance*. 2023. URL: https://www.edinst.com/blog/the-beer-lambert-law/.

[215] University of Birmingham. *MC40 Cyclotron Facility - The Birmingham Centre for Nuclear Education and Research*. [online] Available at: https://www.birmingham.ac.uk/research/activity/nuclear/about-us/facilities/mc40-cyclotron-facility [Accessed 30 Jul. 2024].

[216] D. Nettleton. *Pearson Correlation - an overview*. 2014. URL: https://www.sciencedirect.com/topics/computer-science/pearson-correlation.

[217] k-Wave Project. *k-Wave: A MATLAB toolbox for the time domain simulation of acoustic wave fields*. Accessed: 2022-03-19. URL: http://www.k-wave.org.

[218] L. R. He et al. "Stable high-energy proton acceleration with water-leaf targets driven by intense laser pulses". In: *Phys. Rev. Res.* 7 (2 May 2025), page 023190. DOI: 10.1103/PhysRevResearch.7.023190. URL: https://link.aps.org/doi/10.1103/PhysRevResearch.7.023190.

[219] LMU Munich. *ATLAS - Pulse. Petawatt Users, Lasers, Sources and Experiments - LMU Munich*. Accessed: 2023-03-13. URL: https://www.pulse.physik.uni-muenchen.de/research/high-power/atlas/index.html.

[220] F. Nürnberg et al. "Radiochromic film imaging spectroscopy of laser-accelerated proton beams". In: *Review of Scientific Instruments* 80.3 (2009), page 033301. DOI: 10.1063/1.3086424. URL: https://doi.org/10.1063/1.3086424.

[221] Tequipment.net. *PicoScope 6404D PC-Based Oscilloscope*. https://www.tequipment.net/Pico/6404D/PC-Based-Oscilloscopes/. Accessed: 2025-02-16. 2025.

[222] Sonja Gerlach. "Ionoacoustics for Three-Dimensional Particle Bunch Monitoring". en. Dissertation. LMU München, Faculty of Physics, 2023. DOI: 10.5282/EDOC.32840. URL: https://edoc.ub.uni-muenchen.de/id/eprint/32840.

[223] Francesco Romano et al. "Ultra-high dose rate dosimetry: Challenges and opportunities for FLASH radiation therapy". In: *Medical Physics* 49.7 (2022), pages 4912–4932. DOI: https://doi.org/10.1002/mp.15649. eprint: https://aapm.onlinelibrary.wiley.com/doi/pdf/10.1002/mp.15649. URL: https://aapm.onlinelibrary.wiley.com/doi/abs/10.1002/mp.15649.

[224] IAEA. *Absorbed Dose Determination in External Beam Radiotherapy*. Technical Reports Series 398. Vienna: International Atomic Energy Agency, 2006. ISBN: 92-0-102200-X. URL: https://www.iaea.org/publications/5954/absorbed-dose-determination-in-external-beam-radiotherapy.

[225] Fabio Di Martino et al. "FLASH Radiotherapy With Electrons: Issues Related to the Production, Monitoring, and Dosimetric Characterization of the Beam". In: *Frontiers in Physics* 8 (November 2020). ISSN: 2296-424X. DOI: 10.3389/fphy.2020.570697. URL: http://dx.doi.org/10.3389/fphy.2020.570697.

[226] Kristoffer Petersson et al. "High dose-per-pulse electron beam dosimetry — A model to correct for the ion recombination in the Advanced Markus ionization chamber". In: *Medical Physics* 44.3 (2017), pages 1157–1167. DOI: https://doi.org/10.1002/mp.12111. URL: https://aapm.onlinelibrary.wiley.com/doi/abs/10.1002/mp.12111.

[227] Luis Brualla-González et al. "Dose rate dependence of the PTW 60019 microDiamond detector in high dose-per-pulse pulsed beams". In: *Physics in Medicine and Biology* 61.1 (December 2015), N11. DOI: 10.1088/0031-9155/61/1/N11. URL: https://dx.doi.org/10.1088/0031-9155/61/1/N11.

[228] Amarjit S. Saini and Timothy C. Zhu. "Dose rate and SDD dependence of commercially available diode detectors". In: *Medical Physics* 31.4 (2004), pages 914–924. DOI: https://doi.org/10.1118/1.1650563. eprint: https://aapm.onlinelibrary.wiley.com/doi/pdf/10.1118/1.1650563. URL: https://aapm.onlinelibrary.wiley.com/doi/abs/10.1118/1.1650563.

[229] D.K. Schroder. "Carrier lifetimes in silicon". In: *IEEE Transactions on Electron Devices* 44.1 (1997), pages 160–170. ISSN: 0018-9383. DOI: 10.1109/16.554806. URL: http://dx.doi.org/10.1109/16.554806.

[230] S. F. Kozlov et al. “Preparation and Characteristics of Natural Diamond Nuclear Radiation Detectors”. In: *IEEE Transactions on Nuclear Science* 22.1 (1975), pages 160–170. ISSN: 0018-9499. DOI: 10.1109/tns.1975.4327634. URL: http://dx.doi.org/10.1109/TNS.1975.4327634.

[231] Jan Isberg et al. “High Carrier Mobility in Single-Crystal Plasma-Deposited Diamond”. In: *Science* 297.5587 (2002), pages 1670–1672. DOI: 10.1126/science.1074374. URL: https://www.science.org/doi/abs/10.1126/science.1074374.

[232] Annalisa Patriarca et al. “Experimental Set-up for FLASH Proton Irradiation of Small Animals Using a Clinical System”. In: *International Journal of Radiation Oncology*Biology*Physics* 102.3 (2018), pages 619–626. ISSN: 0360-3016. DOI: https://doi.org/10.1016/j.ijrobp.2018.06.403. URL: https://www.sciencedirect.com/science/article/pii/S0360301618314044.

[233] Patrik Gonçalves Jorge et al. “Dosimetric and preparation procedures for irradiating biological models with pulsed electron beam at ultra-high dose-rate”. In: *Radiotherapy and Oncology* 139 (2019). FLASH radiotherapy International Workshop, pages 34–39. ISSN: 0167-8140. DOI: https://doi.org/10.1016/j.radonc.2019.05.004. URL: https://www.sciencedirect.com/science/article/pii/S0167814019304037.

[234] Elke Beyreuther et al. “Feasibility of proton FLASH effect tested by zebrafish embryo irradiation”. In: *Radiotherapy and Oncology* 139 (2019). FLASH radiotherapy International Workshop, pages 46–50. ISSN: 0167-8140. DOI: https://doi.org/10.1016/j.radonc.2019.06.024. URL: https://www.sciencedirect.com/science/article/pii/S0167814019329640.

[235] Guillaume Boissonnat et al. “Characterization and performances of DOSION, a dosimetry equipment dedicated to radiobiology experiments taking place at GANIL”. In: *Nuclear Instruments and Methods in Physics Research Section A: Accelerators, Spectrometers, Detectors and Associated Equipment* 856 (2017), pages 1–6. ISSN: 0168-9002. DOI: https://doi.org/10.1016/j.nima.2016.12.040. URL: https://www.sciencedirect.com/science/article/pii/S0168900216313079.

[236] M.L.F. Lerch et al. “Dosimetry of intensive synchrotron microbeams”. In: *Radiation Measurements* 46.12 (2011). Proceedings of the 16th Solid State Dosimetry Conference , September 19-24 , Sydney , Australia, pages 1560–1565. ISSN: 1350-4487. DOI: https://doi.org/10.1016/j.radmeas.2011.08.009. URL: https://www.sciencedirect.com/science/article/pii/S1350448711004215.

[237] Muhammad Ramish Ashraf et al. “Dosimetry for FLASH Radiotherapy: A Review of Tools and the Role of Radioluminescence and Cherenkov Emission”. In: *Frontiers in Physics* 8 (August 2020). ISSN: 2296-424X. DOI: 10.3389/fphy.2020.00328. URL: http://dx.doi.org/10.3389/fphy.2020.00328.

[238] Ben Mijnheer et al. “DIODE IN VIVO DOSIMETRY FOR PATIENTS RECEIVING EXTERNAL BEAM RADIATION THERAPY”. In: *AAPM REPORT* 87 (February 2005), pages 1–84. URL: https://www.aapm.org/pubs/reports/RPT_87.pdf.

[239] *Development of Procedures for In Vivo Dosimetry in Radiotherapy*. Human Health Reports 8. Vienna: INTERNATIONAL ATOMIC ENERGY AGENCY, 2013. ISBN: 978-92-0-141610-0. URL: https://www.iaea.org/publications/8962/development-of-procedures-for-in-vivo-dosimetry-in-radiotherapy.

[240] Sara Neira et al. “A kinetic model of diode detector response to pulsed radiation beams”. In: *Physics in Medicine and Biology* 64.20 (October 2019), page 205007. DOI: 10.1088/1361-6560/ab4460. URL: https://dx.doi.org/10.1088/1361-6560/ab4460.

[241] Paul A. Jursinic. "Dependence of diode sensitivity on the pulse rate of delivered radiation". In: *Medical Physics* 40.2 (2013), page 021720. DOI: https://doi.org/10.1118/1.4788763. eprint: https://aapm.onlinelibrary.wiley.com/doi/pdf/10.1118/1.4788763. URL: https://aapm.onlinelibrary.wiley.com/doi/abs/10.1118/1.4788763.

[242] Juan Prieto-Pena et al. "Microdosimetric Spectra Measurements on a Clinical Carbon Beam at Nominal Therapeutic Fluence Rate With Silicon Cylindrical Microdosimeters". In: *IEEE Transactions on Nuclear Science* 66.7 (July 2019), pages 1840–1847. ISSN: 1558-1578. DOI: 10.1109/tns.2019.2921453. URL: http://dx.doi.org/10.1109/TNS.2019.2921453.

[243] C. Fleta et al. "3D cylindrical silicon microdosimeters: fabrication, simulation and charge collection study". In: *Journal of Instrumentation* 10.10 (October 2015), P10001. DOI: 10.1088/1748-0221/10/10/P10001. URL: https://dx.doi.org/10.1088/1748-0221/10/10/P10001.

[244] G Rikner and E Grusell. "General specifications for silicon semiconductors for use in radiation dosimetry". In: *Physics in Medicine and Biology* 32.9 (September 1987), pages 1109–1117. ISSN: 1361-6560. DOI: 10.1088/0031-9155/32/9/004. URL: http://dx.doi.org/10.1088/0031-9155/32/9/004.

[245] Martin J. Butson et al. "A new radiotherapy surface dose detector: The MOSFET". In: *Medical Physics* 23.5 (May 1996), pages 655–658. ISSN: 2473-4209. DOI: 10.1118/1.597702. URL: http://dx.doi.org/10.1118/1.597702.

[246] Paolo Scalchi, Paolo Francescon, and Priyadarshini Rajaguru. "Characterization of a new MOSFET detector configuration for in vivo skin dosimetry". In: *Medical Physics* 32.6Part1 (2005), pages 1571–1578. DOI: https://doi.org/10.1118/1.1924328. eprint: https://aapm.onlinelibrary.wiley.com/doi/pdf/10.1118/1.1924328. URL: https://aapm.onlinelibrary.wiley.com/doi/abs/10.1118/1.1924328.

[247] Tsang Cheung, Martin J Butson, and Peter K N Yu. "Effects of temperature variation on MOSFET dosimetry". In: *Physics in Medicine and Biology* 49.13 (June 2004), N191–N196. ISSN: 1361-6560. DOI: 10.1088/0031-9155/49/13/n02. URL: http://dx.doi.org/10.1088/0031-9155/49/13/N02.

[248] M. Soubra, J. Cygler, and G. Mackay. "Evaluation of a dual bias dual metal oxide-silicon semiconductor field effect transistor detector as radiation dosimeter". In: *Medical Physics* 21.4 (April 1994), pages 567–572. ISSN: 2473-4209. DOI: 10.1118/1.597314. URL: http://dx.doi.org/10.1118/1.597314.

[249] BPaul Ravindran, ASathish Kumar, and SD Sharma. "Characteristics of mobile MOSFET dosimetry system for megavoltage photon beams". In: *Journal of Medical Physics* 39.3 (2014), page 142. ISSN: 0971-6203. DOI: 10.4103/0971-6203.139002. URL: http://dx.doi.org/10.4103/0971-6203.139002.

[250] N. Ade et al. "The dose rate dependence of synthetic diamond detectors in the relative dosimetry of high-energy electron therapy beams". In: *Radiation Physics and Chemistry* 98 (2014), pages 155–162. ISSN: 0969-806X. DOI: https://doi.org/10.1016/j.radphyschem.2014.02.003. URL: https://www.sciencedirect.com/science/article/pii/S0969806X14000413.

[251] C. Di Venanzio et al. "Characterization of a microDiamond detector in high-dose-per-pulse electron beams for intra operative radiation therapy". In: *Physica Medica* 31.8 (2015), pages 897–902. ISSN: 1120-1797. DOI: https://doi.org/10.1016/j.ejmp.2015.06.008. URL: https://www.sciencedirect.com/science/article/pii/S1120179715001489.

[252] Eric S. Diffenderfer et al. “Design, Implementation, and in Vivo Validation of a Novel Proton FLASH Radiation Therapy System”. In: *International Journal of Radiation Oncology*Biology*Physics* 106.2 (2020), pages 440–448. ISSN: 0360-3016. DOI: https://doi.org/10.1016/j.ijrobp.2019.10.049. URL: https://www.sciencedirect.com/science/article/pii/S0360301619340556.

[253] Jing Hu and Joshua L. Rovey. “Faraday cup with nanosecond response and adjustable impedance for fast electron beam characterization”. In: *Review of Scientific Instruments* 82.7 (July 2011), page 073504. ISSN: 0034-6748. DOI: 10.1063/1.3610649. eprint: https://pubs.aip.org/aip/rsi/article-pdf/doi/10.1063/1.3610649/16007678/073504_1_online.pdf. URL: https://doi.org/10.1063/1.3610649.

[254] Mel O’Leary et al. “Observation of dose-rate dependence in a Fricke dosimeter irradiated at low dose rates with monoenergetic X-rays”. In: *Scientific Reports* 8.1 (March 2018), page 4735. ISSN: 2045-2322. DOI: 10.1038/s41598-018-21813-z. URL: https://doi.org/10.1038/s41598-018-21813-z.

[255] Vincent Favaudon et al. “Time-resolved dosimetry of pulsed electron beams in very high dose-rate, FLASH irradiation for radiotherapy preclinical studies”. In: *Nuclear Instruments and Methods in Physics Research Section A: Accelerators, Spectrometers, Detectors and Associated Equipment* 944 (2019), page 162537. ISSN: 0168-9002. DOI: https://doi.org/10.1016/j.nima.2019.162537. URL: https://www.sciencedirect.com/science/article/pii/S0168900219310666.

[256] Marie-Catherine Vozenin et al. “The Advantage of FLASH Radiotherapy Confirmed in Mini-pig and Cat-cancer Patients”. In: *Clinical Cancer Research* 25.1 (January 2019), pages 35–42. ISSN: 1078-0432. DOI: 10.1158/1078-0432.CCR-17-3375. eprint: https://aacrjournals.org/clincancerres/article-pdf/25/1/35/2049875/35.pdf. URL: https://doi.org/10.1158/1078-0432.CCR-17-3375.

[257] H. Kudoh et al. “Response of alanine dosimeters at very high dose rate”. In: *Applied Radiation and Isotopes* 48.4 (1997), pages 497–499. ISSN: 0969-8043. DOI: https://doi.org/10.1016/S0969-8043(96)00281-3. URL: https://www.sciencedirect.com/science/article/pii/S0969804396002813.

[258] Yasser S. Soliman et al. “A comparative dosimetry study of an alanine dosimeter with a PTW PinPoint chamber at ultra-high dose rates of synchrotron radiation”. In: *Physica Medica* 71 (2020), pages 161–167. ISSN: 1120-1797. DOI: https://doi.org/10.1016/j.ejmp.2020.03.007. URL: https://www.sciencedirect.com/science/article/pii/S1120179720300600.

[259] Azam Niroomand-Rad et al. “Radiochromic film dosimetry: Recommendations of AAPM Radiation Therapy Committee Task Group 55”. In: *Medical Physics* 25.11 (1998), pages 2093–2115. DOI: https://doi.org/10.1118/1.598407. eprint: https://aapm.onlinelibrary.wiley.com/doi/pdf/10.1118/1.598407. URL: https://aapm.onlinelibrary.wiley.com/doi/abs/10.1118/1.598407.

[260] Sujatha Pai et al. “TG-69: Radiographic film for megavoltage beam dosimetry”. In: *Medical Physics* 34.6Part1 (2007), pages 2228–2258. DOI: https://doi.org/10.1118/1.2736779. eprint: https://aapm.onlinelibrary.wiley.com/doi/pdf/10.1118/1.2736779. URL: https://aapm.onlinelibrary.wiley.com/doi/abs/10.1118/1.2736779.

[261] L. Karsch et al. “Dose rate dependence for different dosimeters and detectors: TLD, OSL, EBT films, and diamond detectors”. In: *Medical Physics* 39.5 (April 2012), pages 2447–2455. ISSN: 2473-4209. DOI: 10.1118/1.3700400. URL: http://dx.doi.org/10.1118/1.3700400.

[262] Maud Jaccard et al. “High dose-per-pulse electron beam dosimetry: Usability and dose-rate independence of EBT3 Gafchromic films”. In: *Medical Physics* 44.2 (2017), pages 725–735. DOI: https://doi.org/10.1002/mp.12066. eprint: https://aapm.onlinelibrary.wiley.com/doi/pdf/10.1002/mp.12066. URL: https://aapm.onlinelibrary.wiley.com/doi/abs/10.1002/mp.12066.

[263] A. Piermattei et al. “Radiochromic film dosimetry of a low energy proton beam”. In: *Medical Physics* 27.7 (2000), pages 1655–1660. DOI: https://doi.org/10.1118/1.599032. eprint: https://aapm.onlinelibrary.wiley.com/doi/pdf/10.1118/1.599032. URL: https://aapm.onlinelibrary.wiley.com/doi/abs/10.1118/1.599032.

[264] Inder Daftari et al. “An application of GafChromic MD-55 film for 67.5 MeV clinical proton beam dosimetry”. In: *Physics in Medicine and Biology* 44.11 (October 1999), pages 2735–2745. ISSN: 1361-6560. DOI: 10.1088/0031-9155/44/11/304. URL: http://dx.doi.org/10.1088/0031-9155/44/11/304.

[265] T. Kojima et al. “3–45MeV/u ion beam dosimetry using thin film dosimeters”. In: *Radiation Physics and Chemistry* 68.6 (2003). 75th Birthday dedication to Bill L. McLaughlin, pages 975–980. ISSN: 0969-806X. DOI: https://doi.org/10.1016/j.radphyschem.2003.02.001. URL: https://www.sciencedirect.com/science/article/pii/S0969806X03005140.

[266] Maria Martisikova and Oliver Jakel. “Dosimetric properties of Gafchromic® EBT films in monoenergetic medical ion beams”. In: *Physics in Medicine & Biology* 55.13 (June 2010), page 3741. DOI: 10.1088/0031-9155/55/13/011. URL: https://dx.doi.org/10.1088/0031-9155/55/13/011.

[267] Daniel Kirby et al. “LET dependence of GafChromic films and an ion chamber in low-energy proton dosimetry”. In: *Physics in Medicine & Biology* 55.2 (December 2009), page 417. DOI: 10.1088/0031-9155/55/2/006. URL: https://dx.doi.org/10.1088/0031-9155/55/2/006.

[268] Alexandra Rink, I. Alex Vitkin, and David A. Jaffray. “Suitability of radiochromic medium for real-time optical measurements of ionizing radiation dose”. In: *Medical Physics* 32.4 (2005), pages 1140–1155. DOI: https://doi.org/10.1118/1.1877832. eprint: https://aapm.onlinelibrary.wiley.com/doi/pdf/10.1118/1.1877832. URL: https://aapm.onlinelibrary.wiley.com/doi/abs/10.1118/1.1877832.

[269] Pierluigi Casolaro et al. “Real-time dosimetry with radiochromic films”. In: *Scientific Reports* 9.1 (March 2019). Accessed January 12, 2024, page 5307. DOI: 10.1038/s41598-019-41705-0. URL: https://doi.org/10.1038/s41598-019-41705-0.

[270] C Baldock et al. “Polymer gel dosimetry”. In: *Physics in Medicine & Biology* 55.5 (February 2010), R1. DOI: 10.1088/0031-9155/55/5/R01. URL: https://dx.doi.org/10.1088/0031-9155/55/5/R01.

[271] P Andreo J Izewska. “The IAEA/WHO TLD postal programme for radiotherapy hospitals”. In: *Radiother Oncol.* 54(1) (January 2000), page 65. DOI: 10.1016/s0167-8140(99)00164-4. eprint: https://pubmed.ncbi.nlm.nih.gov/10719701/. URL: https://doi.org/10.1016/s0167-8140(99)00164-4.

[272] Y.S. Horowitz (INVITED). “LiF:Mg,Ti Versus LiF:Mg,Cu,P: The Competition Heats Up”. In: *Radiation Protection Dosimetry* 47.1-4 (May 1993), pages 135–141. ISSN: 0144-8420. DOI: 10.1093/oxfordjournals.rpd.a081718. eprint: https://academic.oup.com/rpd/article-pdf/47/1-4/135/50979462/rpd_47_1-4_135.pdf. URL: https://doi.org/10.1093/oxfordjournals.rpd.a081718.

[273] C J Karzmark, John White, and J F Fowler. "Lithium Fluoride Thermoluminescence Dosimetry". In: *Physics in Medicine & Biology* 9.3 (July 1964), page 273. DOI: 10.1088/0031-9155/9/3/302. URL: https://dx.doi.org/10.1088/0031-9155/9/3/302.

[274] E. Tochilin and N. Goldstein. "Dose Rate and Spectral Measurements from Pulsed X-ray Generators". In: *Health Physics* 12.12 (December 1966), pages 1705–1714. ISSN: 0017-9078. DOI: 10.1097/00004032-196612000-00007. URL: http://dx.doi.org/10.1097/00004032-196612000-00007.

[275] Raffaele Liuzzi et al. "Dose-Response of TLD-100 in the Dose Range Useful for Hypofractionated Radiotherapy". In: *Dose-Response* 18.1 (February 2020). ISSN: 1559-3258. DOI: 10.1177/1559325819894081. URL: http://dx.doi.org/10.1177/1559325819894081.

[276] M.S. Akselrod et al. "Highly Sensitive Thermoluminescent Anion-Defect Alpha-Al2O3:C Single Crystal Detectors". In: *Radiation Protection Dosimetry* 33.1-4 (October 1990), pages 119–122. ISSN: 0144-8420. DOI: 10.1093/oxfordjournals.rpd.a080771. eprint: https://academic.oup.com/rpd/article-pdf/33/1-4/119/47982211/rpd_33_1-4_119.pdf. URL: https://doi.org/10.1093/oxfordjournals.rpd.a080771.

[277] V Schembri and B J M Heijmen. "Optically stimulated luminescence (OSL) of carbon-doped aluminum oxide for film dosimetry in radiotherapy". In: *Med. Phys.* 34.6Part1 (June 2007), pages 2113–2118. ISSN: 2473-4209. DOI: 10.1118/1.2737160. URL: http://dx.doi.org/10.1118/1.2737160.

[278] Paul A. Jursinic. "Changes in optically stimulated luminescent dosimeter (OSLD) dosimetric characteristics with accumulated dose". In: *Medical Physics* 37.1 (2010), pages 132–140. DOI: https://doi.org/10.1118/1.3267489. eprint: https://aapm.onlinelibrary.wiley.com/doi/pdf/10.1118/1.3267489. URL: https://aapm.onlinelibrary.wiley.com/doi/abs/10.1118/1.3267489.

[279] Fujio Araki et al. "Measurements of Gamma-Knife helmet output factors using a radiophotoluminescent glass rod dosimeter and a diode detector". In: *Medical Physics* 30.8 (2003), pages 1976–1981. DOI: https://doi.org/10.1118/1.1587451. eprint: https://aapm.onlinelibrary.wiley.com/doi/pdf/10.1118/1.1587451. URL: https://aapm.onlinelibrary.wiley.com/doi/abs/10.1118/1.1587451.

[280] Hideyuki Mizuno et al. "Feasibility study of glass dosimeter postal dosimetry audit of high-energy radiotherapy photon beams". In: *Radiotherapy and Oncology* 86.2 (2008), pages 258–263. ISSN: 0167-8140. DOI: https://doi.org/10.1016/j.radonc.2007.10.024. URL: https://www.sciencedirect.com/science/article/pii/S0167814007005312.

[281] Ben Mijnheer et al. "In vivo dosimetry in external beam radiotherapy". In: *Med Phys.* 40(7) (July 2013), page 070903. DOI: 10.1118/1.4811216. eprint: https://pubmed.ncbi.nlm.nih.gov/23822404/. URL: https://doi.org/10.1118/1.4811216.

[282] Sam Beddar and Luc Beaulieu, editors. *Scintillation Dosimetry*. 1st. CRC Press, 2016. ISBN: 9781315362632. DOI: 10.1201/9781315372655. URL: http://dx.doi.org/10.1201/9781315372655.

[283] J. B. Birks. *The Theory and Practice of Scintillation Counting*. Oxford: Pergamon Press, 1964, page 671. ISBN: 9780080104720. DOI: 10.1016/c2013-0-01791-4. URL: http://dx.doi.org/10.1016/C2013-0-01791-4.

[284] Martin Nikl. "Scintillation detectors for x-rays". In: *Measurement Science and Technology* 17.4 (February 2006), R37. DOI: 10.1088/0957-0233/17/4/R01. URL: https://dx.doi.org/10.1088/0957-0233/17/4/R01.

[285] Hamza Benmakhlouf and Pedro Andreo. “Spectral distribution of particle fluence in small field detectors and its implication on small field dosimetry”. In: *Medical Physics* 44.2 (January 2017), pages 713–724. ISSN: 2473-4209. DOI: 10.1002/mp.12042. URL: http://dx.doi.org/10.1002/mp.12042.

[286] Bagher Farhood et al. “Different dosimeters/detectors used in small-field dosimetry: Pros and cons”. In: *Journal of Medical Signals & Sensors* 8.3 (2018), page 195. ISSN: 2228-7477. DOI: 10.4103/jmss.jmss_3_18. URL: http://dx.doi.org/10.4103/jmss.JMSS_3_18.

[287] Božidar Casar et al. “A novel method for the determination of field output factors and output correction factors for small static fields for six diodes and a microdiamond detector in megavoltage photon beams”. In: *Medical Physics* 46.2 (December 2018), pages 944–963. ISSN: 2473-4209. DOI: 10.1002/mp.13318. URL: http://dx.doi.org/10.1002/mp.13318.

[288] Louis Archambault et al. “Toward a Real-Time In Vivo Dosimetry System Using Plastic Scintillation Detectors”. In: *International Journal of Radiation Oncology*Biology*Physics* 78.1 (), pages 280–287. ISSN: 0360-3016. DOI: 10.1016/j.ijrobp.2009.11.025. URL: https://www.sciencedirect.com/science/article/pii/S0360301609035664.

[289] A S Beddar, T R Mackie, and F H Attix. “Water-equivalent plastic scintillation detectors for high-energy beam dosimetry: II. Properties and measurements”. In: *Physics in Medicine and Biology* 37.10 (October 1992), page 1901. DOI: 10.1088/0031-9155/37/10/007. URL: https://dx.doi.org/10.1088/0031-9155/37/10/007.

[290] Sam Beddar et al. “Exploration of the potential of liquid scintillators for real-time 3D dosimetry of intensity modulated proton beams”. In: *Medical Physics* 36.5 (2009), pages 1736–1743. DOI: https://doi.org/10.1118/1.3117583. eprint: https://aapm.onlinelibrary.wiley.com/doi/pdf/10.1118/1.3117583. URL: https://aapm.onlinelibrary.wiley.com/doi/abs/10.1118/1.3117583.

[291] Muhammad Ramish Ashraf et al. “Optical imaging provides rapid verification of static small beams, radiosurgery, and VMAT plans with millimeter resolution”. In: *Medical Physics* 46.11 (2019), pages 5227–5237. DOI: https://doi.org/10.1002/mp.13797. eprint: https://aapm.onlinelibrary.wiley.com/doi/pdf/10.1002/mp.13797. URL: https://aapm.onlinelibrary.wiley.com/doi/abs/10.1002/mp.13797.

[292] S E Vigdor et al. “A gas scintillator detector for 2D dose profile monitoring in pencil beam scanning and pulsed beam proton radiotherapy treatments”. In: *Physics in Medicine & Biology* 62.12 (May 2017), page 4946. DOI: 10.1088/1361-6560/aa6ce2. URL: https://dx.doi.org/10.1088/1361-6560/aa6ce2.

[293] Wouter van Elmpt et al. “A literature review of electronic portal imaging for radiotherapy dosimetry”. In: *Radiotherapy and Oncology* 88.3 (September 2008), pages 289–309. ISSN: 0167-8140. DOI: 10.1016/j.radonc.2008.07.008. URL: http://dx.doi.org/10.1016/j.radonc.2008.07.008.

[294] Jan Seuntjens and Simon Duane. “Photon absorbed dose standards”. In: *Metrologia* 46.2 (March 2009), S39. DOI: 10.1088/0026-1394/46/2/S04. URL: https://dx.doi.org/10.1088/0026-1394/46/2/S04.

[295] M R McEwen and A R DuSautoy. “Primary standards of absorbed dose for electron beams”. In: *Metrologia* 46.2 (March 2009), S59. DOI: 10.1088/0026-1394/46/2/S05. URL: https://dx.doi.org/10.1088/0026-1394/46/2/S05.

[296] S. Rossomme et al. “Reference dosimetry for light-ion beams based on graphite calorimetry”. In: *Radiation Protection Dosimetry* 161.1-4 (December 2013), pages 92–95. ISSN: 0144-8420. DOI: 10.1093/rpd/nct299. eprint: https://academic.oup.com/rpd/article-pdf/161/1-4/92/9582976/nct299.pdf. URL: https://doi.org/10.1093/rpd/nct299.

[297] Hugo Palmans et al. “A small-body portable graphite calorimeter for dosimetry in low-energy clinical proton beams”. In: *Physics in Medicine & Biology* 49.16 (August 2004), page 3737. DOI: 10.1088/0031-9155/49/16/019. URL: https://dx.doi.org/10.1088/0031-9155/49/16/019.

[298] James Renaud et al. “Development of a graphite probe calorimeter for absolute clinical dosimetry”. In: *Medical Physics* 40.2 (2013), page 020701. DOI: 10.1118/1.4773870. eprint: https://aapm.onlinelibrary.wiley.com/doi/pdf/10.1118/1.4773870. URL: https://aapm.onlinelibrary.wiley.com/doi/abs/10.1118/1.4773870.

[299] James Renaud, Jan Seuntjens, and Arman Sarfehnia. “Sci-Sat AM: Radiation Dosimetry and Practical Therapy Solutions - 03: Energy dependence of a clinical probe-format calorimeter and its pertinence to absolute photon and electron beam dosimetry”. In: *Medical Physics* 43.8Part3 (2016), pages 4959–4959. DOI: 10.1118/1.4961857. eprint: https://aapm.onlinelibrary.wiley.com/doi/pdf/10.1118/1.4961857. URL: https://aapm.onlinelibrary.wiley.com/doi/abs/10.1118/1.4961857.

[300] James Renaud et al. “Aerrow: A probe-format graphite calorimeter for absolute dosimetry of high-energy photon beams in the clinical environment”. In: *Medical Physics* 45.1 (2018), pages 414–428. DOI: 10.1002/mp.12669. eprint: https://aapm.onlinelibrary.wiley.com/doi/pdf/10.1002/mp.12669. URL: https://aapm.onlinelibrary.wiley.com/doi/abs/10.1002/mp.12669.

[301] Andreas Schüller et al. “The European Joint Research Project UHDpulse – Metrology for advanced radiotherapy using particle beams with ultra-high pulse dose rates”. In: *Physica Medica* 80 (2020), pages 134–150. ISSN: 1120-1797. DOI: 10.1016/j.ejmp.2020.09.020. URL: https://www.sciencedirect.com/science/article/pii/S1120179720302362.

[302] Ana Lourenco et al. “Absolute dosimetry for FLASH proton pencil beam scanning radiotherapy”. In: *Scientific Reports* 13.2054 (April 2023), pages 1–11. ISSN: 0003-6951. DOI: 10.1038/s41598-023-28192-0. eprint: https://www.nature.com/articles/s41598-023-28192-0. URL: https://doi.org/10.1038/s41598-023-28192-0.

[303] Jean Bourhis et al. “Treatment of a first patient with FLASH-radiotherapy”. In: *Radiotherapy and Oncology* 139 (October 2019), page 18. DOI: 10.1016/j.radonc.2019.06.019. URL: https://doi.org/10.1016/j.radonc.2019.06.019.

[304] J Perl et al. “TOPAS: An innovative proton Monte Carlo platform for researchand clinical applications”. In: *Med. Phys.* 39 (November 2012), page 6818. DOI: 10.1118/1.4758060. eprint: https://aapm.onlinelibrary.wiley.com/doi/10.1118/1.4758060. URL: https://doi.org/10.1118/1.4758060.

[305] Bruce Faddegon et al. “The TOPAS tool for particle simulation, a Monte Carlo simulation tool for physics, biology and clinical research”. In: *Physica Medica* 72 (April 2020), pages 114–121. ISSN: 1120-1797. DOI: 10.1016/j.ejmp.2020.03.019. URL: http://dx.doi.org/10.1016/j.ejmp.2020.03.019.

[306] T.T. Bohlen et al. “The FLUKA Code: Developments and Challenges for High Energy and Medical Applications”. In: *Nuclear Data Sheets* 120 (June 2014), page 211. DOI: 10.1016/j.nds.2014.07.049. eprint: https://www.sciencedirect.com/science/article/abs/pii/S0090375214005018. URL: https://doi.org/10.1016/j.nds.2014.07.049.

[307] Harley Harris. Ross. “Measurement of .beta.-emitting nuclides using Cerenkov radiation”. In: *Analytical Chemistry* 41.10 (August 1969), pages 1260–1265. ISSN: 0003-2700. DOI: 10.1021/ac60279a011. URL: https://doi.org/10.1021/ac60279a011.

[308] Adam K Glaser et al. “Optical dosimetry of radiotherapy beams using Cherenkov radiation: the relationship between light emission and dose”. In: *Physics in Medicine & Biology* 59.14 (June 2014), page 3789. DOI: 10.1088/0031-9155/59/14/3789. URL: https://doi.org/10.1088/0031-9155/59/14/3789.

[309] Gabriel Adrian et al. “The FLASH effect depends on oxygen concentration”. In: *The British Journal of Radiology* 93.1106 (December 2019). ISSN: 1748-880X. DOI: 10.1259/bjr.20190702. URL: http://dx.doi.org/10.1259/bjr.20190702.

[310] Johan Axelsson et al. “Cerenkov emission induced by external beam radiation stimulates molecular fluorescence”. In: *Medical Physics* 38.7 (June 2011), pages 4127–4132. ISSN: 2473-4209. DOI: 10.1118/1.3592646. URL: http://dx.doi.org/10.1118/1.3592646.

[311] Milaan Patel et al. “Supersonic gas curtain based ionization beam profile monitor for FLASH proton beam therapy”. In: *Frontiers in Oncology* Volume 15 - 2025 (2025). ISSN: 2234-943X. DOI: 10.3389/fonc.2025.1694310. URL: https://www.frontiersin.org/journals/oncology/articles/10.3389/fonc.2025.1694310.

[312] Karen Joy Kirkby et al. “Heavy charged particle beam therapy and related new radiotherapy technologies: The clinical potential, physics and technical developments required to deliver benefit for patients with cancer”. In: *The British Journal of Radiology* 93.1116 (December 2020), page 20200247. ISSN: 1748-880X. DOI: 10.1259/bjr.20200247. URL: http://dx.doi.org/10.1259/bjr.20200247.

[313] Yolanda Prezado et al. “A Potential Renewed Use of Very Heavy Ions for Therapy: Neon Minibeam Radiation Therapy”. In: *Cancers* 13.6 (March 2021), page 1356. ISSN: 2072-6694. DOI: 10.3390/cancers13061356. URL: http://dx.doi.org/10.3390/cancers13061356.

[314] H. X. Q. Norman et al. “Review of Technologies for Ion Therapy Accelerators”. In: (May 2021). DOI: 10.48550/ARXIV.2105.08103. URL: https://arxiv.org/abs/2105.08103.

[315] Alexander Gerbershagen et al. “The advantages and challenges of superconducting magnets in particle therapy”. In: *Superconductor Science and Technology* 29.8 (June 2016), page 083001. ISSN: 1361-6668. DOI: 10.1088/0953-2048/29/8/083001. URL: http://dx.doi.org/10.1088/0953-2048/29/8/083001.

[316] Hywel Owen, Antony Lomax, and Simon Jolly. “Current and future accelerator technologies for charged particle therapy”. In: *Nuclear Instruments and Methods in Physics Research Section A: Accelerators, Spectrometers, Detectors and Associated Equipment* 809 (February 2016), pages 96–104. ISSN: 0168-9002. DOI: 10.1016/j.nima.2015.08.038. URL: http://dx.doi.org/10.1016/j.nima.2015.08.038.

[317] A Dolinskii. “The Synchrotron of the Dedicated Ion Beam Facility for Cancer Therapy, Proposed for the Clinic in Heidelberg”. In: *Proc. EPAC’08*. JACoW Publishing, June 2000, pages 2509–2511. URL: https://api.semanticscholar.org/CorpusID:16742893.

[318] C. Kleffner et al. “The Heidelberg Ion Therapy (HIT) Accelerator Coming Into Operation”. In: *Proc. EPAC’08*. JACoW Publishing, June 2009, pages 426–428. DOI: 10.1063/1.3120065. URL: http://dx.doi.org/10.1063/1.3120065.

[319] S. Rossi. “The status of CNAO”. In: *The European Physical Journal Plus* 126.8 (August 2011). ISSN: 2190-5444. DOI: 10.1140/epjp/i2011-11078-8. URL: http://dx.doi.org/10.1140/epjp/i2011-11078-8.

[320] M. Benedikt and A. Wrulich. "MedAustron—Project overview and status". In: *The European Physical Journal Plus* 126.7 (July 2011). ISSN: 2190-5444. DOI: 10.1140/epjp/i2011-11069-9. URL: http://dx.doi.org/10.1140/epjp/i2011-11069-9.

[321] *Proton-Ion Medical Machine Study (PIMMS) Part II*. May 2000. URL: https://cds.cern.ch/record/449577/.

[322] Ying Shi et al. "Design of a rapid-cycling synchrotron for flash proton therapy". In: *Nuclear Science and Techniques* 34.10 (October 2023). ISSN: 2210-3147. DOI: 10.1007/s41365-023-01283-3. URL: http://dx.doi.org/10.1007/s41365-023-01283-3.

[323] Maurizio Vretenar and Elena Benedetto. "New accelerator designs: NIMMS". In: *Health and Technology* 14.5 (May 2024), pages 945–955. ISSN: 2190-7196. DOI: 10.1007/s12553-024-00882-3. URL: http://dx.doi.org/10.1007/s12553-024-00882-3.

[324] H X Q Norman et al. "Performance Study of the NIMMS Superconducting Compact Synchrotron for Ion Therapy with Strongly Curved Magnets". In: *Proc. IPAC'22*. JACoW Publishing, June 2022, pages 3014–3017. ISBN: 9783954502271. DOI: 10.18429/JACoW-IPAC2022-THPOMS028. URL: https://jacow.org/ipac2022/doi/JACoW-IPAC2022-THPOMS028.html.

[325] M Vretenar et al. "A compact synchrotron for advanced cancer therapy with helium and proton beams". In: volume 2420. 1. IOP Publishing, January 2023, page 012103. DOI: 10.1088/1742-6596/2420/1/012103. URL: http://dx.doi.org/10.1088/1742-6596/2420/1/012103.

[326] Alberto Degiovanni et al. "Design, integration, and commissioning of the first linac for image guided hadron therapy prototype". In: *Physical Review Accelerators and Beams* 27.5 (May 2024). ISSN: 2469-9888. DOI: 10.1103/physrevaccelbeams.27.054701. URL: http://dx.doi.org/10.1103/PhysRevAccelBeams.27.054701.

[327] A Degiovanni, P Stabile, and D Ungaro. "LIGHT: A Linear Accelerator for Proton Therapy". In: *Proc. NAPAC'16*. JACoW Publishing, October 2016, pages 1282–1286. ISBN: 9783954501809. URL: https://cds.cern.ch/record/2314160/files/frb1io02.pdf.

[328] Vittorio Bencini, Luigi Palumbo, and Alessandra Lombardi. "Design of a Novel Linear Accelerator for Carbon Ion Therapy". In: (June 2019). URL: https://indico.cern.ch/event/820103/contributions/3466526/attachments/1866208/3068883/Seminar_20190620_vb.pdf.

[329] Xuanhao Zhang. "Lattice Design of a Carbon-Ion Synchrotron based on Double-Bend Achromat Lens". In: (July 2020). DOI: 10.48550/ARXIV.2007.11787. URL: https://arxiv.org/abs/2007.11787.

[330] Chohan V. *Extra Low ENergy Antiproton (ELENA) Ring and its Transfer Lines Design Report*. April 2014. DOI: 10.5170/CERN-2014-002. URL: https://cds.cern.ch/.

[331] M Vretenar et al. "A Compact High-Frequency RFQ for Medical Applications". In: *Proc. LINAC'14*. JACoW Publishing, August 2014, pages 935–938. ISBN: 9783954501427. DOI: 10.13140/2.1.1217.4084. URL: https://www.researchgate.net/doi/10.13140/2.1.1217.4084.

[332] V Khan et al. "Simulations and Measurements of the CCL Modules of the LIGHT Accelerator". In: *Proc. IPAC'18*. JACoW Publishing, April 2018, pages 429–431. ISBN: 9783954501847. DOI: 10.18429/JACoW-IPAC2018-MOPML015. URL: http://jacow.org/ipac2018/doi/JACoW-IPAC2018-MOPML015.html.

[333] G Brianti, M Giesch, and S Rossi. *Dipole of the CNAO Synchrotron*. 1998. URL: https://cds.cern.ch/record/450834/files/open-2000-160.pdf.

[334] A Milanese, E Huttel, and M Shehab. "Design of the Main Magnets of the SESAME Storage Ring". In: *Proc. IPAC'14*. JACoW Publishing, June 2014, pages 1292–1294. ISBN: 9783954501328. DOI: 10.18429/JACoW-IPAC2014-TUPRO105. URL: http://JACoW.org.

[335] G Borri. *Main Quadrupole of the CNAO Synchrotron*. 1999. URL: https://cds.cern.ch/record/450836/files/open-2000-162.pdf.

[336] Roland Garoby et al. "Corrigendum: The European Spallation Source Design". In: *Physica Scripta* 93 (12 December 2018), page 129501. ISSN: 0031-8949. DOI: 10.1088/1402-4896/aaecea. URL: https://iopscience.iop.org/article/10.1088/1402-4896/aaecea.

[337] S Rossi. *The Sextupole of the CNAO Synchrotron*. 1999. URL: https://cds.cern.ch/record/450837/files/open-2000-163.pdf?version=1.

[338] H. Grote and F. Schmidt. "Mad-X - an upgrade from mad8". In: *Proceedings of the 2003 Particle Accelerator Conference*. IEEE, 2003, pages 3497–3499. DOI: 10.1109/pac.2003.1289960. URL: http://dx.doi.org/10.1109/PAC.2003.1289960.

[339] T. Gläßle, K. Levinsen, and K. Fuchsberger. *The cpymad Python Library (1.14)*. 2024. URL: https://hibtc.github.io/cpymad/.

[340] J. Vollaire et al. *Linac4 design report*. Edited by Maurizio Vretenar. Volume 6/2020. CERN Yellow Reports: Monographs. Geneva: CERN, September 2020. DOI: 10.23731/CYRM-2020-006. URL: https://e-publishing.cern.ch/index.php/CYRM/issue/download/121/96.

[341] U Amaldi et al. *A Facility for Tumour Therapy and Biomedical Research in South-Eastern Europe*. September 2019. DOI: 10.23731/CYRM-2019-002. URL: https://doi.org/10.23731/CYRM-2019-002.

[342] *Pantechnik ECR Ion Sources*. 2024. URL: https://www.pantechnik.com/ecr-ion-sources/.

[343] M. Muramatsu and A. Kitagawa. "A review of ion sources for medical accelerators (invited)". In: *Review of Scientific Instruments* 83.2 (February 2012). ISSN: 1089-7623. DOI: 10.1063/1.3671744. URL: http://dx.doi.org/10.1063/1.3671744.

[344] E Benedetto. *Carbon Ion Compact Medical Synchrotron: Key Parameters*. May 2022. URL: https://cds.cern.ch/record/2812328/.

[345] D. Carey et al. "Chapter 4 . Space Charge and Beam Stability". In: 2001. URL: https://api.semanticscholar.org/CorpusID:198904491.

[346] L. Badano et al. "Synchrotrons for Hadron Therapy: Part I". In: *Nuclear Instruments and Methods in Physics Research Section A: Accelerators, Spectrometers, Detectors and Associated Equipment* 430 (2-3 July 1999), pages 512–522. ISSN: 01689002. DOI: 10.1016/S0168-9002(99)00206-5. URL: https://linkinghub.elsevier.com/retrieve/pii/S0168900299002065.

[347] P. J. Bryant. "Resonant Extraction". In: *CERN Yellow Reports: School Proceedings*. Volume 5. CERN, 2018, pages 315–344. ISBN: 9789290834762. DOI: 10.23730/CYRSP-2018-005.315. URL: https://inspirehep.net/literature/1723478.

[348] R Taylor et al. "Slow Extraction Modelling for NIMMS Hadron Therapy Synchrotrons". In: *Journal of Physics: Conference Series*. Volume 2420. 1. IOP Publishing, January 2023, page 012101. DOI: 10.1088/1742-6596/2420/1/012101. URL: http://dx.doi.org/10.1088/1742-6596/2420/1/012101.

[349] Florian Kühteubl. “Design Study of Radio Frequency Knockout Slow Extraction for the MedAustron Synchrotron”. In: (2020). URL: https://repositum.tuwien.at/bitstream/20.500.12708/1297/2/Kuehteubl%20Florian%20-%202020%20-%20Design%20study%20of%20radio%20frequency%20knockout%20slow...pdf.

[350] G Bisoffi et al. “Energy Comparison of Room Temperature and Superconducting Synchrotrons for Hadron Therapy”. In: *Proceedings of IPAC2022* (2022), pages 3080–3083. DOI: 10.18429/JACoW-IPAC2022-THPOMS049. URL: https://jacow.org/ipac2022/doi/JACoW-IPAC2022-THPOMS049.html.

[351] A M Lombardi et al. “Beam Dynamics in a High Frequency RFQ”. In: *Proc. IPAC’15*. JACoW Publishing, May 2015, pages 2408–2412. ISBN: 9783954501687. DOI: 10.18429/JACoW-IPAC2015-WEYB2. URL: http://jacow.org/ipac2015/doi/JACoW-IPAC2015-WEYB2.html.

[352] Jacobus M. Schippers and Antony J. Lomax. “Emerging Technologies in Proton Therapy”. In: *Acta Oncologica* 50 (6 August 2011), pages 838–850. ISSN: 0284-186X. DOI: 10.3109/0284186X.2011.582513. URL: http://dx.doi.org/10.3109/0284186X.2011.582513.

[353] A Degiovanni et al. “Status of the Commissioning of the LIGHT Prototype”. In: *Proc. IPAC’18*. JACoW Publishing, April 2018, pages 425–428. ISBN: 9783954501847. DOI: 10.18429/JACoW-IPAC2018-MOPML014. URL: http://www.ptcog.ch/index.php/patient-.

[354] G. de Michele et al. “Commissioning Status of the LIGHT Development Machine”. In: *Proc. LINAC’18*. JACoW Publishing, September 2020, pages 352–354. ISBN: 9783954501946. DOI: 10.18429/JACoW-LINAC2018-TUPO013. URL: http://jacow.org/linac2018/doi/JACoW-LINAC2018-TUPO013.html.

[355] V Dimov et al. “Beam Commissioning of the 750 MHz Proton RFQ for the LIGHT Prototype”. In: *Proc. IPAC’18*. JACoW Publishing, April 2018, pages 658–660. ISBN: 9783954501847. DOI: 10.18429/JACoW-IPAC2018-TUPAF002. URL: http://jacow.org/ipac2018/doi/JACoW-IPAC2018-TUPAF002.html.

[356] A Jeff et al. “A Diagnostic Test Bench for the LIGHT Accelerator”. In: *Proc. IPAC’18*. JACoW Publishing, April 2018, pages 1808–1811. ISBN: 9783954501847. DOI: 10.18429/JACoW-IPAC2018-WEPAF001. URL: http://jacow.org/ipac2018/doi/JACoW-IPAC2018-WEPAF001.html.

[357] R L Workman et al. “Review of Particle Physics”. In: *Progress of Theoretical and Experimental Physics* 2022 (8 August 2022). ISSN: 2050-3911. DOI: 10.1093/ptep/ptac097. URL: https://academic.oup.com/ptep/article/doi/10.1093/ptep/ptac097/6651666.

[358] Morad Kh Hamad. “Bragg-curve Simulation of Carbon-Ion Beams for Particle-Therapy Applications: A Study with the GEANT4 Toolkit”. In: *Nuclear Engineering and Technology* 53 (8 August 2021), pages 2767–2773. ISSN: 2234358X. DOI: 10.1016/j.net.2021.02.011. URL: http://dx.doi.org/10.1016/j.net.2021.02.011.

[359] E Benedetto et al. *Comparison of Accelerator Designs for an Ion Therapy and Research Facility*. December 2020. URL: https://sapinski.web.cern.ch/physics/pub/SEEIIST/NIMMS_Note_1_final.pdf.

[360] W. H. Bragg and R. Kleeman. “On the Particles of Radium, and Their Loss of Range in Passing Through Various Atoms and Molecules”. In: *The London, Edinburgh, and Dublin Philosophical Magazine and Journal of Science* 10 (57 September 1905), pages 318–340. ISSN: 1941-5982. DOI: 10.1080/14786440509463378. URL: http://dx.doi.org/10.1080/14786440509463378.

[361] Hywel Owen et al. “Hadron Accelerators for Radiotherapy”. In: *Contemporary Physics* 55 (2 April 2014), pages 55–74. ISSN: 00107514. DOI: 10.1080/00107514.2014.891313. URL: http://dx.doi.org/10.1080/00107514.2014.891313.

[362] B Schlitt. "Commissioning and Operation of the Injector Linacs for HIT and CNAO". In: *Proc. LINAC'08*. JACoW Publishing, September 2008, pages 720–724. URL: https://jacow.org/LINAC08/papers/WE205.pdf.

[363] Hua Shi and Yoshiro Irie. "Study of a Magnetic Alloy-Loaded Cavity for Compact Synchrotrons". In: *Chinese Physics C* 40 (2 February 2016). ISSN: 16741137. DOI: 10.1088/1674-1137/40/2/027002. URL: http://dx.doi.org/10.1088/1674-1137/40/2/027002.

[364] Ugo Amaldi, Saverio Braccini, and Paolo Puggioni. "High Frequency Linacs for Hadrontherapy". In: *Reviews of Accelerator Science and Technology* 02 (01 January 2009), pages 111–131. ISSN: 1793-6268. DOI: 10.1142/s179362680900020x. URL: http://dx.doi.org/10.1142/s179362680900020x.

[365] International Organization for Standardization. *ISO 14644-1:2015; Cleanrooms and associated controlled environments — Part 1: Classification of air cleanliness by particle concentration*. 2015. URL: https://www.iso.org/standard/53394.html.

[366] UKRI. *Green transformation for UK science estate*. 2023. URL: https://www.ukri.org/news/green-transformation-for-uk-science-estate/.

[367] STFC. *STFC Sustainability Design Principles*. 2023. URL: https://stfc365.sharepoint.com/sites/SPADE/SitePages/Sustainable-Design-Principles.aspx.

[368] STFC. *STFC Sustainable Building Design Guide V3*. 2023. URL: https://www.stfc.ac.uk.

[369] RIBA. *RIBA Sustainable Outcomes Guide (RIBA, 2019)*. 2019. URL: https://www.engc.org.uk/engcdocuments/internet/website/RIBA%20Sustainable%20Outcomes%20Guide%202019.pdf.

[370] RIBA. *RIBA 2030 Climate Challenge (RIBA, 2021)*. 2021. URL: https://www.architecture.com/about/policy/climate-action/2030-climate-challenge.

[371] UK Government. *Net Zero Estate Playbook*. November 2021. URL: https://www.gov.uk/government/publications/net-zero-estate-playbook.

[372] bregroup. *BREEAM*. 2023. URL: https://bregroup.com/products/breeam/.

[373] UK Government. *The Ionising Radiations Regulations 2017 (UK Statutory Instruments No. 1075)*. 2017. URL: https://www.legislation.gov.uk/uksi/2017/1075/contents/made.

[374] Franz S Englbrecht et al. "Radiation protection modelling for 2.5 Petawatt-laser production of ultrashort x-ray, proton and ion bunches: Monte Carlo model of the Munich CALA facility". In: *Journal of Radiological Protection* 40.4 (September 2020), page 1048. DOI: 10.1088/1361-6498/aba8e4. URL: https://dx.doi.org/10.1088/1361-6498/aba8e4.

[375] Forster Ingenieurgesellschaft. *Sandwich Construction; Forster Bau Ingolstadt — forster-bau.de*. [Accessed 04-12-2025]. URL: https://forster-bau.de/leistungen/.

[376] International Electrotechnical Commission. *Functional safety of electrical/electronic/programmable electronic safety-related systems*. International Electrotechnical Commission, 2010. DOI: 10.3403/BSEN61508. URL: https://doi.org/10.3403/BSEN61508.

[377] International Standards Organisation. *ISO 13849-1:2015; Safety of machinery — Safety-related parts of control systems — Part 1: General principles for design*. 2015. URL: https://www.iso.org/standard/69883.html.

[378] International Electrotechnical Commission. *IEC 61511-1:2016+AMD1:2017 CSV Consolidated version; Functional safety - Safety instrumented systems for the process industry sector - Part 1: Framework, definitions, system, hardware and application programming requirements*. 2017. URL: https://webstore.iec.ch/publication/61289.

[379] International Electrotechnical Commission. *IEC 62061:2021; Safety of machinery - Functional safety of safety-related control systems*. 2021. URL: https://webstore.iec.ch/publication/59927.

[380] ITRF. *ITRF draft schematic diagram. 1272-pa1-pm-sch-0001-v3.0-ITRF schematic*. 2023. URL: https://stfc365.sharepoint.com/sites/ITRF/.

[381] LhARA. *LhARA draft device naming convention proposal. Document: 1272-pa1-ctrl-rpt-0001-v0.5-LhARA-device-naming*. 2023. URL: https://stfc365.sharepoint.com/sites/ITRF/.

[382] International Organization for Standardization. *ISO 8573-1:2010; Compressed air*. 2010. URL: https://www.iso.org/standard/46418.html.

[383] *ITRF facility cost v1.0*. ITRF Facility cost_v1.0 from LhARA.xksx. 2023. URL: https://stfc365.sharepoint.com/sites/itrf/.